Transactions of the ASME

Journal of Applied Mechanics

Published Quarterly by The American Society of Mechanical Engineers

VOLUME 48 • NUMBER 1 • MARCH 1981

EDITORIAL STAFF
Editor, **J. J. JAKLITSCH, JR.**
Production Editor, **RONNIE HEANEY**
Prod. Asst., **BETH DARCHI**

APPLIED MECHANICS DIVISION
Chairman, **R. M. CHRISTENSEN**
Secretary, **R. C. DiPRIMA**
Technical Editor, **C. S. HSU**
Associate Editors, **S. T. ARIARATNAM**
T. BELYTSCHKO
S. C. COWIN
L. B. FREUND
W. G. GOTTENBERG
M. HOLT
T. R. KANE
A. S. KOBAYASHI
S. LEIBOVICH
P. A. LIBBY
U. S. LINDHOLM
L. E. MALVERN
J. J. McCOY
R. T. SHIELD
T. C. T. TING
G. A. WEMPNER

POLICY BOARD, COMMUNICATIONS
Chairman and Vice-President
I. BERMAN

Members-at-Large
M. J. RABINS
J. E. ORTLOFF
J. W. LOCKE
W. J. WARREN

Policy Board Representatives
Basic Engineering, **F. LANDIS**
General Engineering, **CAROLYN F. PHILLIPS**
Industry, **J. E. ORTLOFF**
Power, **R. E. REDER**
Research, **G. P. COOPER**
Codes and Stds., **L. L. ELDER**
Nom. Com. Rep., **J. W. LOCKE**

Business Staff
345 E. 47th St.
New York, N. Y. 10017
(212)644-7789

Mng. Dir., Pub., **J. J. FREY**

OFFICERS OF THE ASME
President, **CHARLES E. JONES**
Deputy Executive Director
and Assistant Secretary, **PETER CHIARULLI**
Secretary & Treasurer, **ROBERT A. BENNETT**

Journal of Applied Mechanics (ISSN 0021-8936) is edited and published quarterly at the offices of The American Society of Mechanical Engineers, United Engineering Center, 345 E. 47th St., New York, N. Y. 10017. ASME-TWX No. 710-581-5267, New York. Second Class postage paid at New York, N. Y., and at additional mailing offices.

CHANGES OF ADDRESS must be received at Society headquarters seven weeks before they are to be effective. Please send old label and new address.

PRICES: To members, $30.00, annually; to nonmembers, $60.00. Single copies $20.00 each., Add $5.00 for postage to countries outside the United States and Canada.

STATEMENT from By-Laws. The Society shall not be responsible for statements or opinions advanced in papers or . . . printed in its publications (B7.1, Par. 3).

COPYRIGHT © 1981 by the American Society of Mechanical Engineers. Reprints from this publication may be made on condition that full credit be given the TRANSACTIONS OF THE ASME, JOURNAL OF APPLIED MECHANICS, and the author, and date of publication be stated.

INDEXED by the Engineering Index, Inc.

TECHNICAL PAPERS

(Contents continued on Page 216)

Downloaded 04 May 2010 to 171.66.16.34. Redistribution subject to ASME license or copyright; see http://www.asme.org/terms/Terms_Use.cfm

CONTENTS (CONTINUED)

BRIEF NOTES

DISCUSSIONS

BOOK REVIEWS

ERRATUM

(Contents continued on Inside Back Cover)

CONTENTS (CONTINUED)

X. de Saint Victor
Doctor in Mechanics.

D. P. Ly
Doctor of Sciences.

D. Bellet
Professor.

Groupe de Rhéologie,
Institut de Mecanique des Fluides,
Laboratoire Associé au CNRS,
2, rue Charles Camichel,
31071 Toulouse Cedex, France

Numerical and Experimental Simulations of Pseudoplastic Transient Pipe Flows

The purpose of this work is to develop and to compare different methods for the determination of startup flows of a pseudoplastic fluid in pipes under a varying pressure gradient. Three methods are proposed:

1. *A method involving a finite-difference calculation.*
2. *A method using an approximation of the acceleration term in the equation governing the phenomenon.*
3. *An experimental method based on measurements of local velocities by means of Laser-Doppler anemometry.*

The most interesting point of this work is the good agreement observed between the three methods in the non-Newtonian case.

Introduction

In case of startup flow of an incompressible fluid of Newtonian behavior in a rigid cylindrical tube, the solution of the momentum equation can be obtained analytically. The first research worker who studied this phenomenon seems to be Gromecka who solved the problem when the fluid is suddenly exposed to a constant pressure gradient [1]. Later, Szymanski extended the solution to a varying pressure gradient [2]. Other workers tried to obtain this solution by use of Laplace transform technique [3, 4]. Let us notice that only one publication points out an experimental determination of local velocities [4]. These works can be found in Fig. 1.

As it can be seen in Fig. 1, the Newtonian case is the most studied one because the linearity of governing equations allows obtaining an analytical solution.

When one considers non-Newtonian fluids, one can see that there are very few publications including only two in the pseudoplastic case. Edwards, Nellist, and Wilkinson study pulsed flows and startup flows under a constant pressure gradient [5] as did also Sestak and Charles [6] who study the same problem of startup flow using a technique developed by Targ and Slyoskin [7] to solve some problems of Newtonian transport phenomena.

Moreover, it is interesting to note that the pressure gradient is generally taken constant by most authors except by Atabek who studied the startup of a Bingham plastic [8] and by Etter who considered an Oldroyd's fluid [9] (Fig. 2) for nonconstant pressure gradients.

We propose to study by three different methods the startup flow in pipes of an Ostwaldian fluid submitted to a varying pressure gradient.

Equations Governing the Phenomenon

In case the rheological behavior of the fluid is described by the power law of Ostwald-de Waele we have

$$\tau_{rz} = K\frac{\partial u}{\partial r}\left|\frac{\partial u}{\partial r}\right|^{n-1} \tag{1}$$

where

τ_{rz} = shear stress
K = consistency
u = longitudinal velocity
r = radial position
n = behavior index

and the Navier-Stokes equation reduces to

$$\rho\frac{\partial u}{\partial t} = -\frac{\partial p}{\partial z} + \frac{1}{r}\frac{\partial}{\partial r}(r\tau_{rz}) \tag{2}$$

where ρ is the density and t is the time with the initial condition

$$u(r, 0) = 0, \quad \forall r \tag{3}$$

Contributed by the Applied Mechanics Division for publication in the JOURNAL OF APPLIED MECHANICS.

Discussion on this paper should be addressed to the Editorial Department, ASME, United Engineering Center, 345 East 47th Street, New York, N. Y. 10017, and will be accepted until June 1, 1981. Readers who need more time to prepare a Discussion should request an extension from the Editorial Department. Manuscript received by ASME Applied Mechanics Division, February, 1980; final revision, April, 1980.

FLUID / AUTHOR	NEWTONIAN	NON NEWTONIAN INELASTIC	VISCO-ELASTIC
GROMEKHA (1882)	★		
SZYMANSKI (1932)	★		
ATABEK (1962)	★		
ATABEK (1964)		★	
ETTER (1965)			★ ✱
SESTAK (1968)		★ ✱	
AVULA (1969)	★ ○		
DOWNING (1971)	★		
WATERS (1971)			★
AVULA (1971)	✱ ○		
DUGGINS (1972)		✱	
EDWARDS (1972)		★ ✱	
DUGGINS (1972)		✱	
KATAOKA (1975)	○ ●		
MASLIYAH (1975)	★ ○		
I.M.F.T. (1976)	★ ○ ●		
de SAINT VICTOR	★ ✱ ○ ●	★ ✱ ○ ●	

★ analytic method

○ experimental determination of pressure gradient

✱ numerical method

● experimental determination of velocities

Fig. 1 Main literature references and different methods used

	$\frac{\partial p}{\partial z}$ = cste	$\frac{\partial p}{\partial z}$ = f(t)
GROMEKHA	□	
SZYMANSKI	□	□
ATABEK		□
ATABEK		⊡
ETTER		▥
SESTAK	⊠	
AVULA		□
DOWNING		□
WATERS	▥	
AVULA	□	
DUGGINS	⊡	
EDWARDS	⊠	
DUGGINS	⊡	
KATAOKA	□	
MASLIYAH	□	
I.M.F.T.		□
de S^t VICTOR	□ ⊠	□ ⊠

□ newtonian fluid

⊠ pseudoplastic fluid

⊡ Bingham plastic

▥ viscoelastic fluid

Fig. 2 Functional forms of the longitudinal pressure gradient used in different works on startup flows in pipes

and the boundary conditions

$$u(R, t) = 0, \quad \forall t \quad \text{(no-slip condition at the wall)} \tag{4}$$

R is the tube radius

$$\frac{\partial u}{\partial r}\Big/_{r=0} = 0, \quad \forall t \quad \text{(symmetry of the flow about the center line)} \tag{5}$$

In addition, the pressure gradient must be prescribed as a function of time, i.e.,

$$\frac{\partial p}{\partial z} = -\rho A f(t) \tag{6}$$

where ρA is the amplitude of the pressure gradient.

Substituting for τ_{rz} into equation (2) from equation (1) and introducting the dimensionless variables

$$\xi = \frac{r}{R}; \quad t^* = \frac{\omega t}{2\pi}; \quad u^* = \frac{u}{\bar{u}}$$

where ω is the pulsation and

$$\bar{u} = \frac{n}{1+3n}\frac{R^{1/n+1}}{(2K)^{1/n}}(\rho A)^{1/n}$$

leads to the following system of equations:

$$\beta^2 \frac{\partial u^*}{\partial t^*} = Nf(t^*) + \frac{1}{\xi}\frac{\partial}{\partial \xi}\left[\xi \frac{\partial u^*}{\partial \xi}\left|\frac{\partial u^*}{\partial \xi}\right|^{n-1}\right] \tag{7a}$$

$$u^*(\xi, 0) = 0, \quad \forall \xi \tag{7b}$$

$$u^*(1, t^*) = 0, \quad \forall t^* \tag{7c}$$

$$\frac{\partial u^*}{\partial \xi}\Big/_{\xi=0} = 0, \quad \forall t^* \tag{7d}$$

We notice that there are two new dimensionless parameters

$$N = 2\left(\frac{1+3n}{n}\right)^n \tag{8}$$

$$\beta^2 = \frac{\rho\omega\bar{u}^{1-n}R^{n+1}}{2\pi K} \tag{9}$$

The momentum equation (7a) is nonlinear and an analytical solution is impossible, hence we propose the first method of solution.

First Method of Solution

This method involves a finite-difference calculation. The grid used in the solution is shown diagrammatically in Fig. 3.

The radius of the tube is varied from the value $\xi = 0$ at the tube axis to the value $\xi = 1$, at the wall of the tube. It is divided into intervals $\Delta\xi = 0.05$.

The second variable t^* is varied from the initial value $J = 1$ to $J = L$ corresponding to steady-state conditions. The step Δt^* equals 10^{-3}.

Let us write down the partial derivatives of velocity in finite-difference form. We have

$$\frac{\partial u^*}{\partial t^*} = \frac{1}{\Delta t^*}(u^*_{I,J} - u^*_{I,J-1}) + o(\Delta t^*) \tag{10}$$

$$\frac{\partial u^*}{\partial \xi} = \frac{1}{\Delta \xi}(u^*_{I,J} - u^*_{I-1,J}) + o(\Delta \xi) \tag{11}$$

Thus we can write equation (7a) in finite-difference form

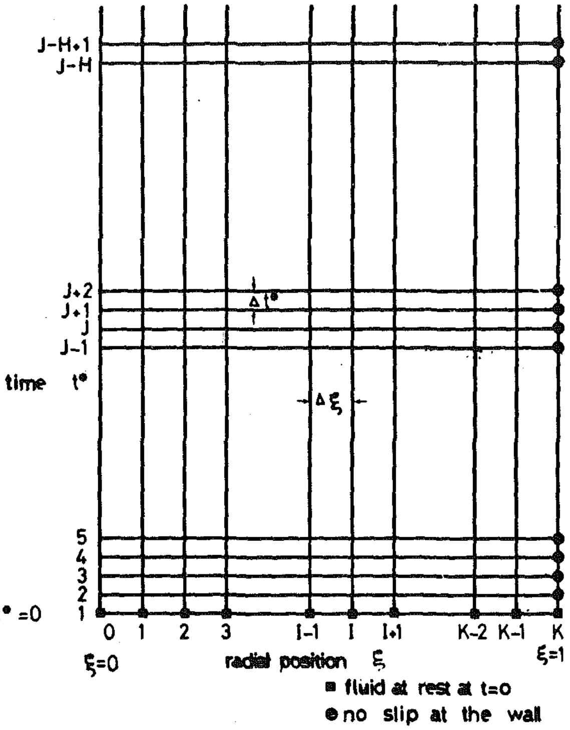

Fig. 3 Grid used in the finite-difference method

$$u^*_{I,J} = u^*_{I,J-1} + \frac{\Delta t^*}{\beta^2}\left\{Nf(t^*) + \frac{1}{\xi\Delta\xi^{n+1}}\right.$$
$$\times\left[\left(\xi + \frac{\Delta\xi}{2}\right)(u^*_{I+1,J} - u^*_{I,J})|u^*_{I+1,J} - u^*_{I,J}|^{n-1}\right.$$
$$\left.\left. - \left(\xi - \frac{\Delta\xi}{2}\right)(u^*_{I,J} - u^*_{I-1,J})|u^*_{I,J} - u^*_{I-1,J}|^{n-1}\right]\right\} \quad (12)$$

To equation (12), we must add

$$u^*_{I,1} = 0, \quad \forall I \quad \text{(initial condition)} \quad (13)$$

$$u^*_{K,J} = 0, \quad \forall J \quad \text{(no-slip at the wall)} \quad (14)$$

However, it is noted that the viscous term in equation (7*a*) includes the fraction $1/\xi$ and hence it will be undefined when $\xi = 0$, i.e., on the tube axis, so it is necessary to establish another expression for this value.

From l'Hopital's rule, we have

$$\lim_{\xi\to 0}\frac{1}{\xi}\frac{\partial}{\partial\xi}\left[\xi\frac{\partial u^*}{\partial\xi}\left|\frac{\partial u^*}{\partial\xi}\right|^{n-1}\right] = 2\frac{\partial}{\partial\xi}\left[\frac{\partial u^*}{\partial\xi}\left|\frac{\partial u^*}{\partial\xi}\right|^{n-1}\right] \quad (15)$$

Proceeding as previously, one obtains

$$2\frac{\partial}{\partial\xi}\left[\frac{\partial u^*}{\partial\xi}\left|\frac{\partial u^*}{\partial\xi}\right|^{n-1}\right]$$
$$= \frac{2}{\Delta\xi^{n+1}}\{(u^*_{I+1,J} - u^*_{I,J})|u^*_{I+1,J} - u^*_{I,J}|^{n-1}$$
$$- (u^*_{I,J} - u^*_{I-1,J})|u^*_{I,J} - u^*_{I-1,J}|^{n-1}\} \quad (16)$$

However, it is advisable to use there as boundary condition the symmetry of flow, i.e.,

$$u^*_{I-1,J} = u^*_{I+1,J} \quad (17)$$

Thus we obtain the simplified equation at the tube axis

$$u^*_{I,J} = u^*_{I,J-1} + \frac{\Delta t^*}{\beta^2}\left\{Nf(t^*)\right.$$
$$\left. + \frac{1}{\Delta\xi^{n+1}}(u^*_{I+1,J} - u^*_{I,J})|u^*_{I+1,J} - u^*_{I,J}|^{n-1}\right\} \quad (18)$$

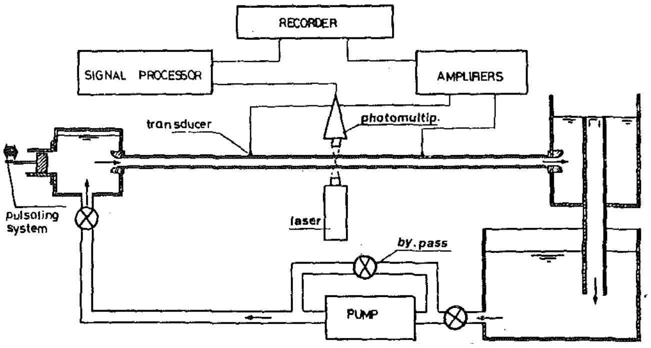

Fig. 4 Diagram of the experimental setup for the study of startup flows; transparent pipe with upstream and downstream tanks; Laser-Doppler anemometer and the electronic devices used

The calculation is started at $J = 2$ choosing a distribution of near zero velocities calculated using the expression of velocity for a steady non-Newtonian flow, i.e.,

$$u = \frac{n}{n+1}\left(\frac{N}{2}\right)^{1/n}(1 - \xi^{1/n+1})(10^{-6}) \quad (19)$$

Second Method of Solution

According to this method, the acceleration term in equation (2) is replaced by its mean value taken along the tube radius; see [7].

$$\frac{\partial u}{\partial t} \simeq \frac{1}{R}\int_0^R \frac{\partial u}{\partial t}\,dr = \varphi(t) \quad (20)$$

Substituting equation (20) into the momentum equation and assuming that $\partial\rho/\partial z = -\rho Af(t)$, we have

$$\frac{d}{d\xi}\left[\xi\frac{dv}{d\xi}\left|\frac{dv}{d\xi}\right|^{n-1}\right] = \frac{\rho R^{n+1}}{K\bar{u}^n}[\varphi(t) - Af(t)] \quad (21)$$

where $v = u/\bar{u}$ and $\xi = r/R$.

Solving this equation with boundary conditions (4) and (5) gives

$$v(\xi, t) = \frac{n}{n+1}\left(\frac{N}{2A}\right)^{1/n}(\xi^{1+1/n} - 1)\chi(t) \quad (22)$$

where

$$\chi(t) = [\varphi(t) - Af(t)]|\varphi(t) - Af(t)|^{1/n-1} \quad (23)$$

Now, it is necessary to determine the unknown function $\chi(t)$. To do this, it is enough to differentiate $v(\xi, t)$ with respect to time and to integrate the obtained result with respect to ξ, i.e.,

$$\frac{\partial v}{\partial t} = \frac{n}{n+1}\left(\frac{N}{2A}\right)^{1/n}(\xi^{1+1/n} - 1)\frac{d\chi(t)}{dt} \quad (24)$$

But, from equation (20), we have

$$\int_0^1 \frac{\partial v}{\partial t}\,d\xi = \frac{1}{\bar{u}}\varphi(t)$$

$$\frac{1}{\bar{u}}\varphi(t) = \frac{n}{n+1}\left(\frac{N}{2A}\right)^{1/n}\frac{d\chi(t)}{dt}\int_0^1(\xi^{1+1/n} - 1)d\xi \quad (25)$$

Finally, we obtain

$$\frac{d\chi(t)}{dt} = -\frac{2n+1}{n}\left(\frac{2A}{N}\right)^{1/n}\frac{1}{\bar{u}}[Af(t) + \chi(t)|\chi(t)|^{n-1}] \quad (26)$$

The solutions of the system formed by this equation and equation (22) are found numerically using the Runge-Kutta method.

Third Method of Solution

The third used method is an experimental one.

Experimental Model. The main aim of the experimental model is to apply either a steady, or sinusoidal, or pulsed pressure gradient at the choosen instant to the fluid at rest (Fig. 4).

This installation is composed of four parts: a rigid tube, a steady

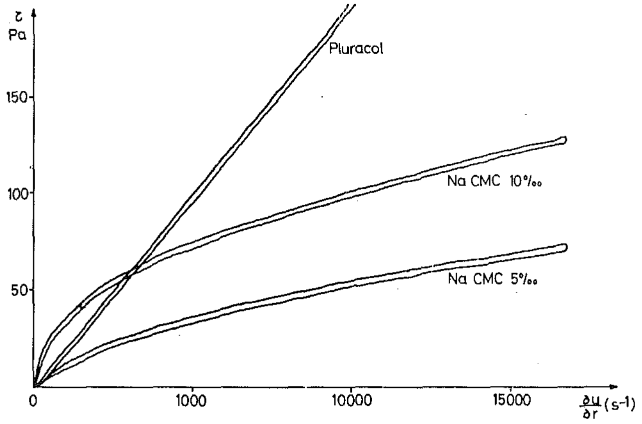

Fig. 5 Examples of rheograms for pseudoplastic behavior obtained with solutions of Na CMC in water; effect of the concentration; comparison with a Newtonian solution of Pluracol

t (s) \ ξ	0		0,3		0,6		0,9	
	FD	A	FD	A	FD	A	FD	A
1	0,75529	0,75643	0,72563	0,72674	0,59078	0,59163	0,21325	0,21348
2	1,28556	1,28699	1,19522	1,19647	0,89113	0,89188	0,28670	0,28688
3	1,59352	1,59500	1,46469	1,46599	1,05907	1,05987	0,32705	0,32722
4	1,76868	1,77014	1,61779	1,61909	1,15426	1,15508	0,34987	0,35005
5	1,86810	1,86955	1,70469	1,70598	1,20829	1,20911	0,36282	0,36300
6	1,92454	1,92597	1,75403	1,75529	1,23897	1,23977	0,37018	0,37035
7	1,95660	1,95799	1,78204	1,78328	1,25637	1,25717	0,37435	0,37453

relative error $< 10^{-3}$

Fig. 6 Comparison between velocities obtained in transient newtonian flows by a finite-difference method (FD) on one hand and an analytical Method 1, on the other

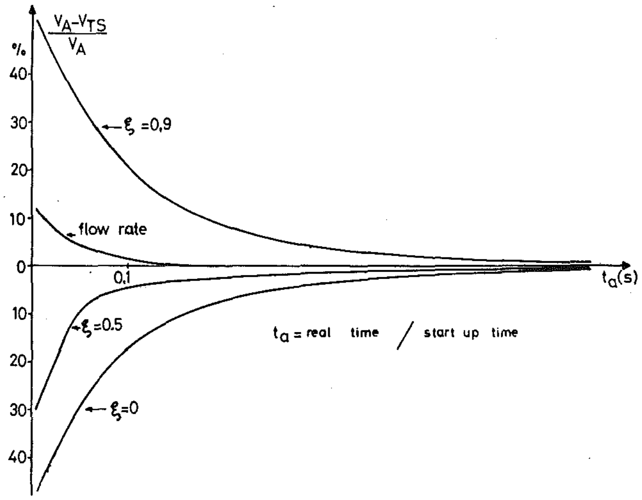

Fig. 7 Comparison of relative error of the determination of velocity in the case of the analytical method (V_A) and the method based on an approximation of the acceleration term (V_{TS}) for different radial position ξ in the pipe; variation of the relative error with flow rate

flow system, a pulsed flow generator, and a starting device which allows accurate timing of the pressure gradient in periods of successive phases.

The rigid tube is made of plexiglas, it is 3 m long, internal diameter is 35 mm, and thickness 2.5 mm. It is set horizontally and due to its transparency it allows visualization of the flow and measure the local velocities with a Laser-Doppler anemometer. (L.D.A.)

Constant flow rates are obtained by a variable speed pump placed in the return circuit.

The pulsed flow generator transforms the rotational movement of a variable speed motor into a sinusoidal translational movement which is transmitted to a piston moving in a cylinder.

The starting device allows the pump and the pulsed flow generator to start simultaneously. The L.D.A. allows the velocity measurement at a single point of a section of the duct. So, it was necessary to start the flow always at the same value of the pressure gradient in order to be able to investigate the whole cross section of the tube. The problem has been solved using a movable switch allowing the piston to be stopped always in the same position.

The fluids studied are of two types

1 Aqueous solutions of Pluracol V 10 giving Newtonian flows.
2 Aqueous solutions of high organic polymers, sodium carboxymethyl-cellulose (Na CMC) the behavior of which is non-Newtonian. Different values of the behavior index n and fluid consistency K can be easily obtained by varying the concentration of water. The rheograms (shear stress/shear rate curves) have been obtained using a Shirley-Ferranti cone-plate rheometer (Fig. 5).

The velocity profiles have been determined by a frequency tracker type Laser-Doppler anemometer Mark 1. For oscillatory or pulsed flows, the use of a Doppler frequency shift system consisting of a BRAGG's acustic-optic modulator allowed accurate measurements of the phase angle and the direction of the velocity.

The experimental pressure gradient is obtained from the output of two pressure transducers. The analytical form of the observed pressure gradient is determined by a graphical method and is used in the momentum equation (Fig. 8).

Results

First of all, we compare the results obtained by each method with the analytical one obtained in the Newtonian case corresponding to a behavior index $n = 1$ (see the Appendix).

The use of the finite-difference method shows that a relative error of about 0.1 percent has been committed (Fig. 6). So it seems that this method is the best one but it is also the most difficult one to use and the time of calculation is long.

The second method, using the approximation of the acceleration term in the momentum equation, does not give such good results in the Newtonian case as the first one (Fig. 7). One can observe that the relative error committed in the value of the local velocities is great at the beginning, but it becomes less than 10 percent shortly after this beginning. It is interesting to note that the relative error of mean velocities, therefore of the flow rates is small.

The agreement between analytical and experimental methods is good. Fig. 8 shows a comparison of results obtained at pulsed pressure gradient. The continuous lines represent the results obtained by the analytical method and the points the experimental ones.

Non-Newtonian Case

We have compared the various, methods proposed for the non-Newtonian case by utilizing Newtonian flow. We present in Fig. 9 the curves of relative errors between the first and the second method for different values of pseudoplasticity.

For, when K is a constant, one can see that the error decreases with the behavior index n. That is to say that the approximation used in the acceleration term in the momentum equation is increasingly accurate as the pseudoplastic character becomes more pronounced.

This is because the velocity profiles become flatter when the behavior index n decreases. So, at every radial position ξ the true value of the acceleration term $\partial u/\partial t$ is nearer to its mean value.

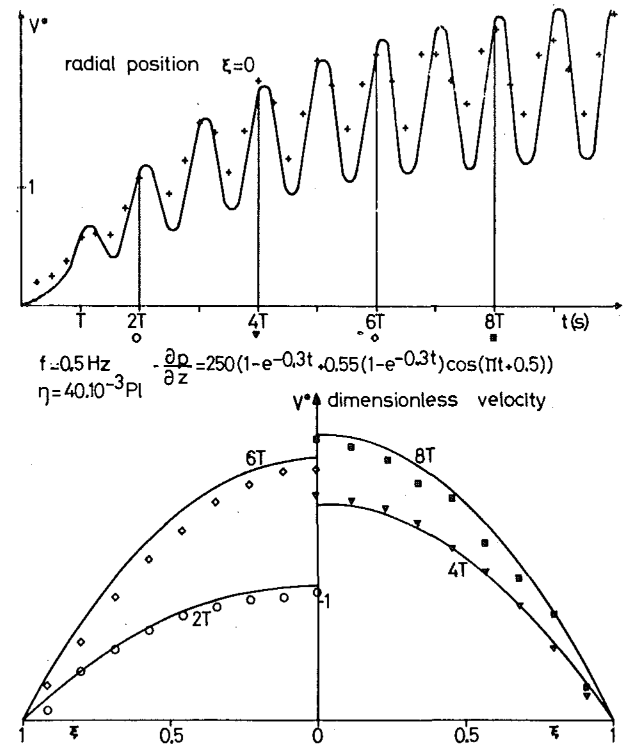

Fig. 8 Evaluation of flow velocities experimentally and numerically obtained in case of startup of Newtonian pulsed flows

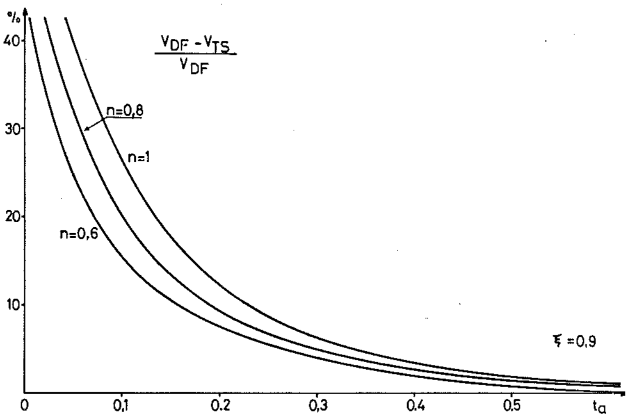

Fig. 9 Effect of behavior index upon relative errors

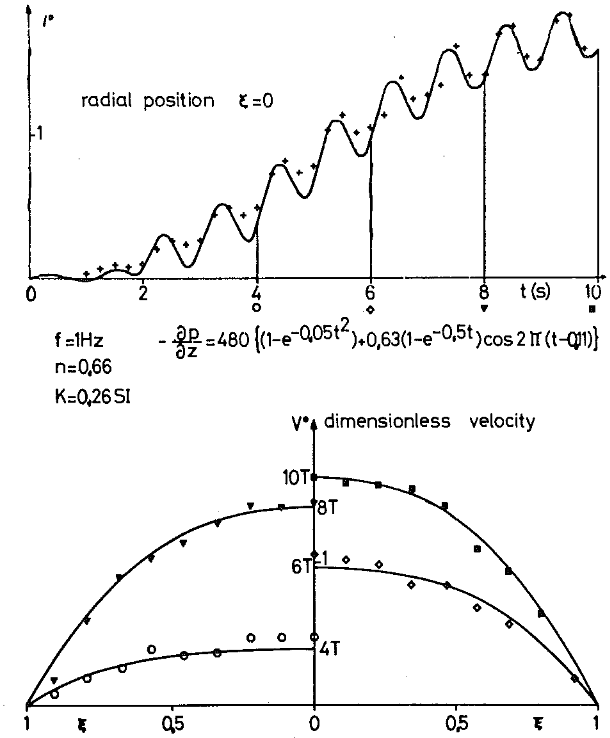

Fig. 10 Evaluation of flow velocities experimentally and numerically obtained in case of a startup of pseudoplastic pulsed flows

The next figure shows the evolution for a pulsed pressure gradient during the startup flow (Fig. 10). The continuous lines represent the results obtained by the finite-difference method and the points correspond to the experimental results.

Conclusion

A literature survey allowed us to notice the special character of this problem. There were not many works available in the Newtonian case and very few in non-Newtonian inelastic case. We tried to solve the problem by several methods

1 An analytical method in the case of Newtonian flows (see the Appendix).

2 A finite-difference method solve directly the equations governing the phenomenon.

3 A method using an approximated acceleration term which allows an analytical solution to be used before the numerical calculation.

4 An experimental method using Laser-Doppler anemometry.

A comparison of the different methods allows us to notice the very good precision of the finite-difference method. The method using an approximated acceleration term, although it is less accurate, also gives satisfying results. On the other hand, this second method is very interesting because it requires much less calculation time than the finite-difference method. Moreover, this method gives very good results when one is only interested in flow rates.

Let us point out at last the good agreement between the results obtained by the four different methods of calculation.

References

1 Gromecka, I. S., *A Contribution to the Theory of Viscous Flow in Narrow Cylindrical Tubes,* (in Russian), Kazanyi University Press, 1882.

2 Szymanski, P., "L'hydrodynamique du fluide visqueux," *Journal de Math. Pures Appliquées,* Vol. 11, série 9, 1932, pp. 67–107.

3 Avula, X. J. R., "A Combined Method for Determining Velocity of Starting Flow in a Long Circular Tube," *Journal of the Physical Society of Japan,* Vol. 27, 1969, pp. 497–502.

4 Ly, D. P., Bellet, D., and Bousquet, A., *Transient Regimes of Unsteady State Flow of Viscous Fluids,* Euromech 73, Aix-enProvence, France, 1976.

5 Edwards, M. F., Nellist, D. A., and Wilkinson, W. R., "Unsteady Laminar Flows of Non-Newtonian Fluids in Pipes," *Chemical Engineering Science,* Vol. 27, 1972, pp. 295–306.

6 Sestak, J., and Charles, M. E., "An Approximate Solution for the Startup Flow of a Power Law Fluid in a Tube," *Chemical Engineering Science,* Vol. 23, 1968, pp. 1127–1137.

7 Slyoskin, N. A., and Targ, S. M., *Dynamics of Viscous Incompressible Fluids,* ed., Moscou, 1955.

8 Atabek, H. B., "Startup Flow of a Bingham Plastic," *Zeistschrift für angewandte Mathematik und Mechanik,* Vol. 11, 1964, pp. 332–333.

9 Etter, I. and Schowalter, W. R., "Unsteady Flow of an Oldroyd Fluid in a Circular Tube," *Transactions of the Society of Rheology,* Vol. 9:2, 1965, pp. 351–369.

10 Atabek, H. B., "Development of Flow in the Inlet Region of a Circular Tube Starting From Rest," *Zeitschrift für angewandte Mathematik und Physik,* Vol. 13, 1962, pp. 417–430.

11 Downing, C. G., "Transient Flow in the Hydrodynamic Entrance Regions of Long Closed Ducts," *AIChE Journal,* Vol. 17, 1971, pp. 322–325.

12 Waters, N. D., and King, M. J., "The Unsteady Flow of an Elastico-

Viscous Liquid in a Straight Pipe of Circular Cross Section," *Journal of Phys. D Applied Physic,* Vol. 4, 1971, pp. 204–211.

13 Avula, X. J. R., "Startup Flow in the Entrance Region of a Circular Tube," *Zeistschrift für angewandte Mathematik und Mechanik,* Vol. 51, 1971, pp. 517–526.

14 Duggins, R. K., "The Commencement of Flow of a Bingham Plastic Fluid," *Chemical Engineering Science,* Vol. 27, 1972, pp. 1991–1996.

15 Duggins, R. K., "The Buildup From Rest of Some Non-Newtonian Flows," *BHRA Fluid Engineering,* International Conference on Pressure Surges, September 6–8, 1972, B3-21, B3-28.

16 Kataoka, K., Kawabato, T., and Miki, K., "The Startup Response of Pipe Flow to a Step Change in Flow Rate," *Chemical Engineering Science,* Vol. 8, 1975, pp. 266–271.

17 Masliyah, J. H., and Schook, C. A., "Laminar Transient Flow in Pipes," *The Canadian Journal of Chemical Engineering,* Vol. 53, 1975, pp. 469–475.

18 de Saint Victor, X., "Régimes transitoiresd'écoulements Non-Newtoniens," *Thèse de Spécialité,* Toulouse, France, 1979.

APPENDIX

Newtonian Case—Analytical Solution (4)

$n = 1$ for Newtonian fluids and the consistency K converges to the dynamic viscosity η. The momentum equation (7a) becomes linear and can be written

$$\frac{\partial^2 u^*}{\partial \xi^2} + \frac{1}{\xi}\frac{\partial u^*}{\partial \xi} - \mathrm{Re}^* \frac{\partial u^*}{\partial t)} = -8f(t^*) \tag{27}$$

where $u^* = u/\bar{u}$, $\bar{u} = Ar^2/8\nu$ where ν is the kinematic viscosity

$$\mathrm{Re}^* = \frac{\omega R^2}{2\pi\nu}$$

with the same initial and boundary conditions as in the non-Newtonian case.

Solving equation (1) by means of the Laplace's transform leads us to the equation

$$U(\xi, s) = \frac{8}{\mathrm{Re}^*}\frac{1}{s}\left[1 - \frac{J_0(i\sqrt{\mathrm{Re}^* s}\,\xi)}{J_0(i\sqrt{\mathrm{Re}^* s})}\right]F(s) \tag{28}$$

where

$$U(\xi, s) = \int_0^\infty e^{-st^*}u^*(\xi, t^*)dt^* \tag{29}$$

$$F(s) = \int_0^\infty e^{-st^*}f(t^*)dt^* \tag{30}$$

s = the symbolic parameter.

Applying successively both theorems of convolution and residues to expression (28), we can find the transform inverse of $U(\xi, s)$

$$u^*(\xi, t^*) = \frac{16}{\mathrm{Re}^*}\sum_{n=1}^{\infty}\frac{J_0(a_n\xi)}{a_n J_1(a_n)} \times \int_0^{t^*} f(t^* - t')e^{-1/Re^* a_n{}^2 t'}dt' \tag{31}$$

where a_n are the positive zeros of the function J_0, such as $J_0(a_n) = 0$, J_0, J_1 = Bessel's functions of first kind of 0 and 1 order.

K. M. Kalumuck
P. W. Huber
Assoc. Mem. ASME

Department of Mechanical Engineering,
Massachusetts Institute of Technology,
Cambridge, Mass. 02139

A Perturbation Analysis of Fluid-Structure Interactions in a Model Test System[1]

A perturbation analysis of fluid-structure interactions in a model test system of controlled flexibility excited by a complex hydrodynamic transient is presented. The analysis demonstrates the important features of the perturbation method and its implementation. Comparison of predictions with experiment provides a test of the analytical procedure and its underlying assumptions. The results illustrate the important effect of transient liquid mass redistribution on the flexible system response.

Introduction

Reference [1] outlines a perturbation method for analyzing the response of fluid-filled flexible structures undergoing complex hydrodynamic transients and develops the criteria for the applicability of this method. In this paper we compare predictions based on perturbation method calculations with experimental results obtained in a simple test system. This paper has three purposes: to demonstrate the implementation of a perturbation method fluid-structure interaction (FSI) calculation in a simple system, to explore the basic physics of FSI in a system undergoing a complex hydrodynamic transient, and to provide one set of tests for verifying the numerous underlying assumptions of the perturbation method. The development of a general algorithm for modeling FSI phenomena was not one of our goals.

Summary of Experiments

Fig. 1 shows a schematic of the cylindrical single downcomer test system partially filled with water in which our FSI experiments were conducted. Detailed descriptions of the test system, experimental procedure, and results have been documented elsewhere [2]. Only those experiments and results analyzed in this paper are summarized here. The test system's sidewalls and top are made of thick steel and are effectively rigid. The base consists of an interchangeable aluminum plate clamped at its periphery. Changing the base plate thickness introduces different degrees of structural flexibility into the system. The rigid structure system characteristics are obtained by use of a 1.9-cm-thick base plate. Sidewall taps enable pressure measurements to be taken at several stations in the liquid pool.

A hydrodynamic transient initiated by the opening of a fast acting valve is generated by injection of air from a large constant pressure reservoir or "drywell." The pressure beneath the plate is maintained constant at the initial pool surface pressure throughout the transient. The air injection forces the water out of the downcomer and forms a bubble that rapidly grows and redistributes the water in the pool causing the pool to "swell." Fig. 2 shows the pool swell history traced from high-speed film records in a geometrically similar rigid plexiglass system subject to a properly scaled but otherwise identical hydrodynamic transient initiated at $t = 0$. A dimensionless time $t^* = t\sqrt{g/2a}$, where a is the pool radius, has been defined in accordance with the hydrodynamic scaling laws for this system [3].

Typical pressure histories measured along the sidwall 5 cm above the base plate are presented in Fig. 3 where the measured pressures have been nondimensionalized by the constant reservoir (drywell) pressure, P_D. The top oscillogram shows the rigid system pressure history containing a very rapid rise in pressure at the time the downcomer is cleared of water followed by a much more gradual change. The other three oscillograms show the measured pressure histories for plate thicknesses of 0.2, 0.16, and 0.1 cm [2].

Perturbation Method Analysis

Governing Equations. Fig. 4 shows schematically the governing equations and boundary conditions used in implementing a perturbation method analysis for our test system. These follow directly from those outlined in [1]. The shaded liquid region, in which we ignore the presence of the downcomer, is bounded by four surfaces $S_1, \ldots, S_4$. The governing liquid region equations are

$$P \equiv P_R + P_p \qquad (1)$$

$$\nabla^2 P_p = 0$$

where P is the pressure in the flexible system, P_R is the pressure in an identical rigid system undergoing an identical hydrodynamic

---

[1] Work sponsored by the U. S. Nuclear Regulatory Commission, Office of Nuclear Regulatory Research under Contract No. 04-77-011.

Contributed by the Applied Mechanics Division for publication in the JOURNAL OF APPLIED MECHANICS.

Discussion on this paper should be addressed to the Editorial Department, ASME, United Engineering Center, 345 East 47th Street, New York, N. Y. 10017, and will be accepted until June 1, 1981. Readers who need more time to prepare a Discussion should request an extension from the Editorial Department. Manuscript received by ASME Applied Mechanics Division, January, 1980; final revision, June, 1980.

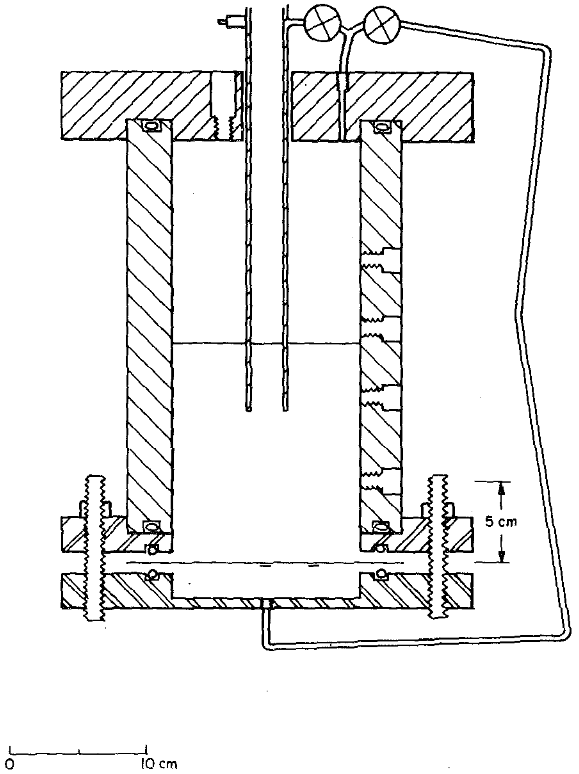

Fig. 1 Schematic of test system

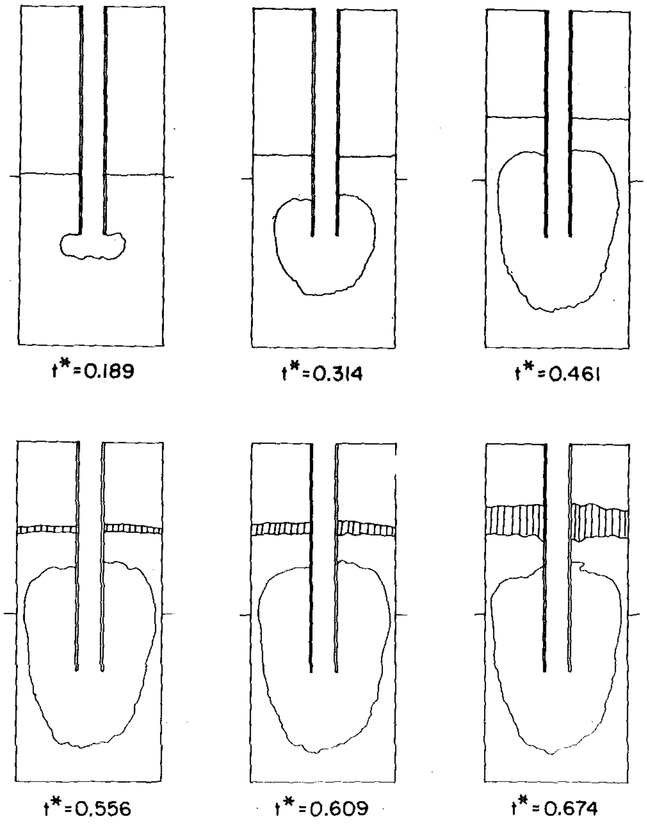

Fig. 2 Pool swell history traced from high speed films; hatch marks indicate growth of interface instability

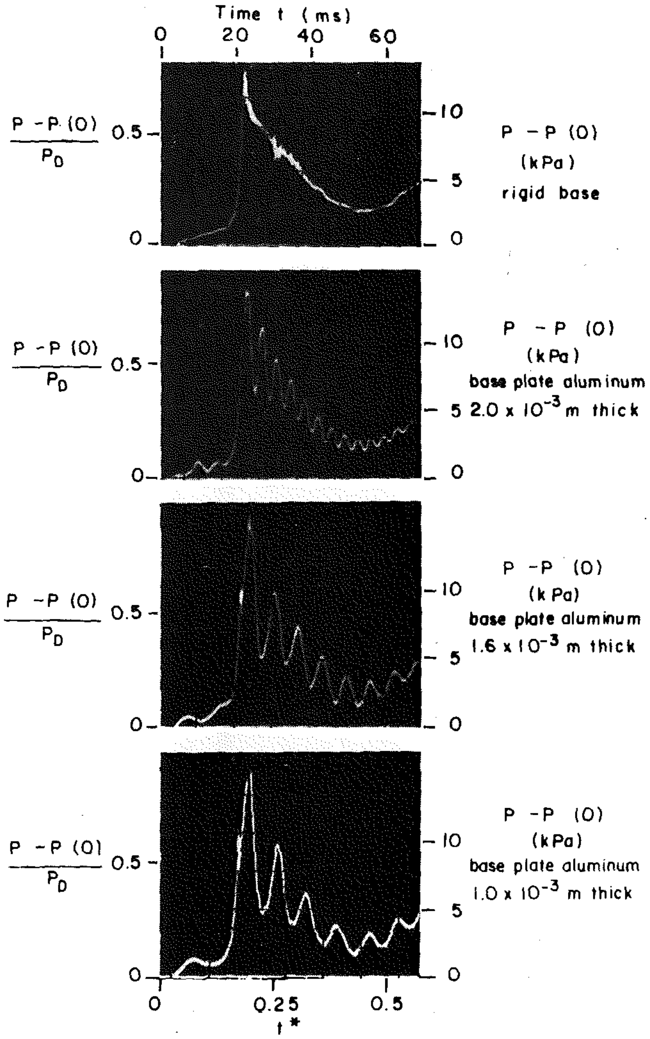

Fig. 3 Experimental pressure histories on pool sidewall 5 cm above the base plate ($z/a = 0.7$)

transient and P_p is the perturbation pressure. The free-surface boundary condition is

$$P_p = 0 \quad \text{on} \quad S_1, S_2 \tag{2}$$

where S_1 is the pool surface (approximated as horizontal throughout the transient) and S_2 is the bubble surface. The solid wall boundary conditions are

$$\frac{\partial P_p}{\partial r} = 0 \quad \text{on} \quad S_3 \tag{3}$$

$$\frac{\partial P_p}{\partial z} = \rho \frac{\partial^2 w}{\partial t^2} \quad \text{on} \quad S_4, \tag{4}$$

where S_3 is the rigid sidewall, S_4 is the initial plate-fluid interface, z is measured vertically upward from S_4, r is measured radially outward from the center of S_4, w is the downward plate displacement from S_4, and ρ is the liquid density. A further approximation is made here in neglecting the small plate deformation due to the initial hydrostatic loading. Hence, S_4 is taken as being perfectly flat. The displacement w shown in Fig. 4 is exaggerated for clarity.

The governing equation and boundary conditions for the clamped circular base plate are

$$D\nabla^4 w = P_R + P_p \quad \text{on} \quad S_4 \tag{5}$$

$$w = 0 \quad \text{and} \quad \partial w/\partial r = 0 \quad \text{at} \quad r = a \tag{6}$$

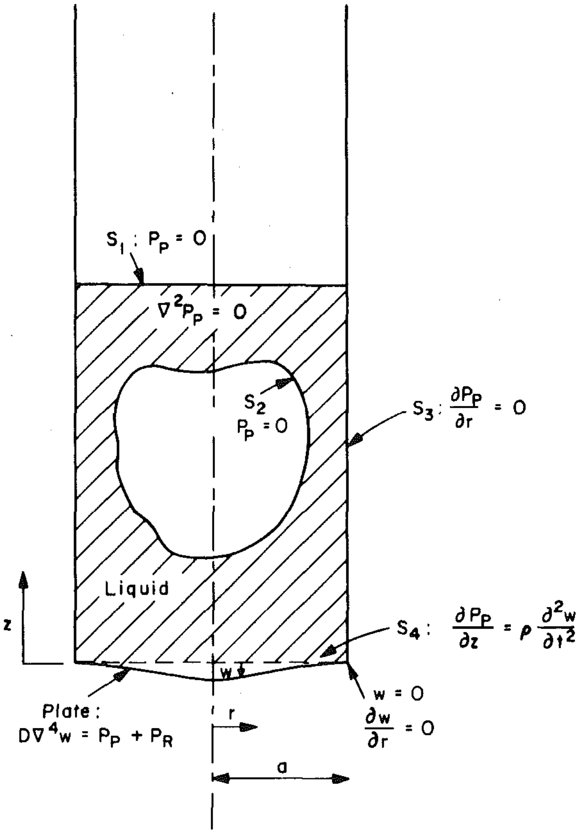

Fig. 4 Equations and boundary conditions for perturbation calculation

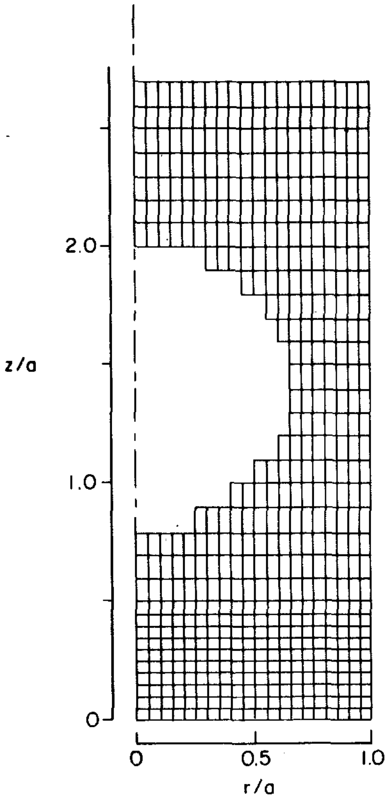

Fig. 5 Typical fluid domain computation mesh (here for $t^* = 0.314$)

$$\partial w/\partial r = 0 \quad \text{and} \quad D \frac{\partial}{\partial r} \nabla^2 w = 0 \quad \text{at} \quad r = 0. \tag{7}$$

Here D is the plate flexural rigidity and P_R is the hydrodynamically induced pressure in the rigid system. Experiments have shown P_R to be uniform over the base plate [4]—varying only with time. In equation (5), the plate inertia has been neglected—an assumption easily justified for our system by the much larger water inertia felt by the plate through P_p. The test system and imposed hydrodynamic transient are axisymmetric. This leads to boundary condition (7). Equation (5) enables the plate to be viewed as moving through a series of quasi-static states.

For solution of (5)–(7), a Green's function approach is adopted. The Green's function for this problem is found to be [5]

For $b \leq r$:

$$\hat{w}(r, b) = \frac{1}{8\pi D} \left[\frac{(a^2 - r^2)(a^2 + b^2)}{2a^2} + (b^2 + r^2) \ln \frac{r}{a} \right]; \tag{8a}$$

For $b \geq r$:

$$\hat{w}(r, b) = \frac{1}{8\pi D} \left[\frac{(a^2 - b^2)(a^2 + r^2)}{2a^2} + (b^2 + r^2) \ln \frac{b}{a} \right]. \tag{8b}$$

Here b is the radial position of an arbitrary annular load. The plate displacement is then given by

$$w(r, t) = \int_0^a 2\pi b [P_R(t) + P_p(r = b, z = 0, t)] \hat{w}(r, b) db. \tag{9}$$

The plate displacement is also related to the plate acceleration

$$w(r, t) \equiv \int_0^t \int_0^t \frac{\partial^2}{\partial t^2} w(r, t) dt\, dt. \tag{10}$$

The complete set of equations to be solved then consists of the liquid (1) and structure (9) equations, boundary conditions (2)–(4), and identity (10). Coupling between the fluid and structure equations occurs through both boundary condition (4) and the loading in equation (9).

Computational Model. The technique adopted to solve the set of governing equations and their boundary conditions is a numerical time stepping one. A fully implicit second-order accurate five-point finite-difference scheme utilizing central differencing in an axisymmetric geometry as presented in [6] is used in the fluid domain. The radial derivatives are expanded prior to discretization. Appropriate forms of second-order accurate boundary conditions are used. A detailed description of the scheme employed can be found in [7]. The finite-difference equations are solved in a two-dimensional time varying mesh. A typical mesh employed is shown in Fig. 5. Two different axial mesh spacings are used such that the mesh point density is greater in the lower region of the pool than in the upper region. This provides a sufficient number of points between the bubble and the base plate to resolve the pressure gradient at the plate with reasonable accuracy. The number of mesh points varied with time from about 500 to 600. The location of each mesh point is fixed in time, but points are removed as the bubble grows and added as the pool rises. Mesh points are denoted by a pair of indices (i, j), $i = 1, \ldots, I$; $j = 1, \ldots, J$. The radial (r) and axial (z) mesh spacings are denoted by δr and δz such that $r = (i - 1)\cdot\delta r$ and $z = (j - 1)\cdot\delta z$. The derivative boundary conditions (3) and (4) are approximated by the introduction of a fictitious set of mesh points. The perturbation pressure $P_{i,j}^k$ at the point (i, j) and time step k (the subscript "p" being dropped for brevity) is set to zero for points that are along the pool or bubble surface or within the bubble. The equations corresponding to these points are removed prior to solution. The remaining set of fluid domain simultaneous equations can be expressed as

$$\mathbf{A}^k \mathbf{P}_p^k = \mathbf{F}^k. \tag{11}$$

Here, $\mathbf{A}^k$ is a square, nonsymmetric matrix containing the coefficients of the unknown $P_{i,j}^k$ arranged along five diagonals and is of order $(I)\cdot(J - 1) - N_B$ where N_B is the number of mesh points lying on the surface of or within the bubble. $\mathbf{P}_p^k$ is a column vector whose elements are the unknown $P^k_{i,j}$. $\mathbf{F}^k$ is a column vector which contains the inhomogenous terms of the mesh point equations. The equations comprising (11) are arranged in the order $(1, 1), \ldots, (I, 1), \ldots, (1, j), \ldots, (i, j), \ldots, (I, j), \ldots, (1, J-1), \ldots, (I, J-1)$.

The Green's function solution (9) to the plate equation is numerically integrated. In general, by selecting the radial locations of the plate nodes to correspond to those of the fluid mesh, one can express the downard displacement w^k_i at node i and time step k as

$$w^k_i = \sum_{l=1}^{I} C_{i,l}(P^k_{l,1} + P^k_R), \quad i = 1, \ldots, I \tag{12}$$

where P^k_R is the value of P_R along the base plate at time step k. The expressions for $C_{i,l}$ depend upon the Green's function expression $\hat{w}$ (8) and the integration scheme. Investigation of the behavior of the product $b\hat{w}$ shows that it varies more rapidly with radius than does the load, $P^k_{l,1} + P^k_R$. Thus a Simpson's rule integration is performed over a much smaller interval than the mesh spacing (typically $\delta r/8$). Values of the perturbation pressure between mesh points are obtained by interpolation using a piecewise quadratic curve fit to the values of $P^k_{l,1}$. The interpolation weights are also accounted for in the values of $C_{i,l}$.

The displacement at node i is obtained from the acceleration history at that node from (10) using a double trapezoidal integration. For zero initial displacement, velocity, and acceleration, this can be expressed at time $t = k\delta t$ (where δt is the time step size) as

$$w^k_i = \tilde{w}^{k-1}_i + \frac{1}{4}\delta t^2 \left(\frac{\partial^2 w}{\partial t^2}\right)^k_i, \quad i = 1, \ldots, I, \tag{13a}$$

where

$$\tilde{w}^{k-1}_i = \delta t^2 \sum_{l=1}^{k-1} (k-l) \left(\frac{\partial^2 w}{\partial t^2}\right)^l_i. \tag{13b}$$

Calculation of the flexible system response involves the simultaneous solution of four sets of linear algebraic equations: the fluid finite-difference equations (11), the plate displacement equations (12), relation (13), and a discretized form of equation (4) which can be expressed as

$$\left(\frac{\partial P_p}{\partial z}\right)^k_{i,1} = \rho \left(\frac{\partial^2 w}{\partial t^2}\right)^k_i. \tag{14}$$

These equations are reduced to a single system of equations by combining (12) and (13) and substituting the result by use of (14) into $\mathbf{F}^k$ of (11). The resulting expression for $\mathbf{F}^k$ is a function of $\mathbf{P}^k_p$. Rearrangement of this set of equations leads to a new set of equations to be solved for the unknown perturbation pressures

$$\mathbf{A}^{*k}\mathbf{P}^k_p = \mathbf{F}^{*k}. \tag{15}$$

The elements of $\mathbf{F}^{*k}$ are given as

$$F^{*k}_m = 8\rho \frac{\delta z}{\delta t^2}\left(P^k_R \cdot \sum_{l=1}^{I} C_{m,l} - \tilde{w}^{k-1}_m\right), \qquad m = 1, \ldots, I$$

$$F^{*k}_m = 0, \quad m > I. \tag{16}$$

The elements of $\mathbf{A}^{*k}$ are given by $A^{*k}_{m,n} = A^k_{m,n} + C_{m,n}$ when both $m \le I$ and $n \le I$ and by $A^{*k}_{m,n} = A^k_{m,n}$ whenever $m \ge I$ or $n \ge I$.

The matrix $\mathbf{A}^{*k}$ is banded with a bandwidth of $2I + 1$. The presence of nonzero elements arising from the $C_{m,l}$ expressions precludes a solution by a block tridiagonal algorithm. A standard banded matrix solution routine was used to solve equation (15) for $\mathbf{P}^k_p$ at each time step.[2] We did not attempt to develop a more efficient solution algorithm that would take advantage of the many zero elements within the band of $\mathbf{A}^{*k}$. After $\mathbf{P}^k_p$ is found from (15), w^k_i and $(\partial^2 w/\partial t^2)^k_i$ are found from equations (12)–(14).

It is interesting to note a possible interpretation of the effect of equations (12)–(14) on the fluid equations (11). Using these equations, the pressure gradient normal to the plate can be expressed as

$$\left(\frac{\partial P_p}{\partial z}\right)^k_{i,1} = \rho \frac{4}{\delta t^2}\left(\sum_{l=1}^{I} C_{i,l}P^k_{l,1} + P^k_R \cdot \sum_{l=1}^{I} C_{i,l} - \tilde{w}^{k-1}_i\right). \tag{17}$$

The term $\tilde{w}^{k-1}_i$ is known from the history of the plate motion and does not depend on any quantities at time step k. At any time step, then, all unknown quantities are expressed in terms of the perturbation pressure field. The structure can be viewed as imposing a special type of boundary condition or constraint on the fluid: the normal perturbation pressure gradient at any point of the plate-fluid interface is a function of the pressure at every point of the interface (17). This is simply the result of the boundary integral nature of the problem.

Due to the fully implicit nature of the solution algorithm, the time step size is not limited by a stability criterion. It is limited, however, by a resolution requirement. That is, δt must be small enough to adequately resolve the expected frequencies of oscillation. With this in mind, δt was selected such that a minimum of about eight time steps occurred within the experimentally observed oscillation period.

The liquid configuration as a function of time is an input to the model. The bubble is approximated as an ellipsoid with three parameters fit by trending from the observed bubble history (Fig. 2). The boundary is further approximated by taking it to lie along the mesh lines which are closest to the computed boundary. The change in the location of the pool surface is computed from continuity once the change in bubble volume is known and is also approximated to lie along a mesh line. A comparison of approximated bubble shapes and pool heights with those observed is shown in Fig. 6 for three selected times.

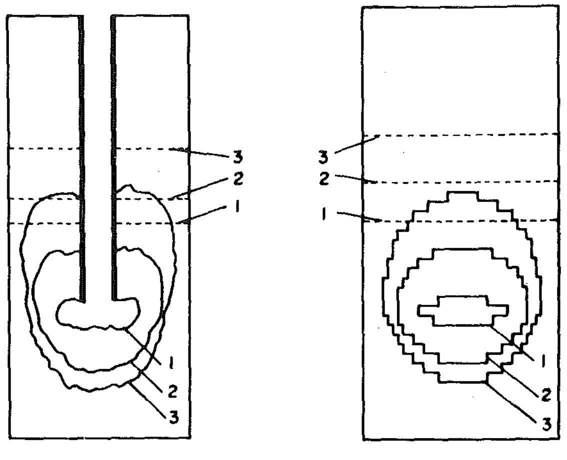

Experimentally observed **Model input**

configuration	time (t^*)
1	0.189
2	0.314
3	0.461

Fig. 6 Experimentally observed liquid configurations and corresponding model inputs at three sample times

Also input to the model is the experimentally determined rigid system base plate pressure history ($P_R(t)$ in equation (9)) and the rigid system pressure history at all other locations at which the flexible system response is desired. With this information, the complete perturbation pressure field is calculated at each time step. The predicted flexible system pressure is then the sum of the computed perturbation pressure and the rigid system pressure at the location of interest.

Perturbation Method Predictions and Comparison With Experiment

The predicted flexible system perturbation pressure amplitudes vary significantly throughout the pool. Fig. 7 shows the predicted 0.2 cm flexible base plate system pressure history nondimensionalized by P_D at two sidewall locations and two base plate locations. The 0.1

---

[2] LEQT1B from the International Mathematical and Statistical Libraries, Inc.—"IMSL."

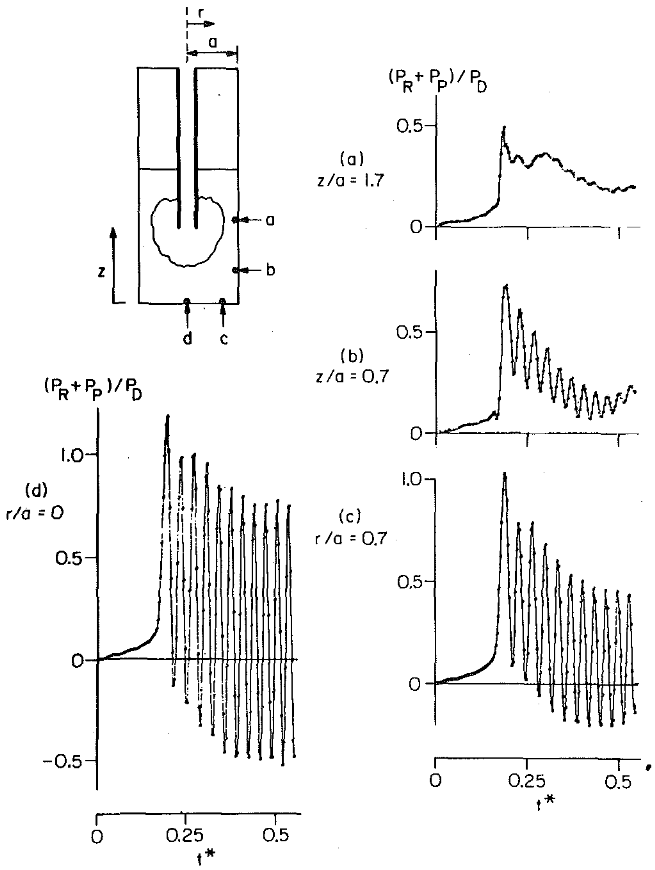

Fig. 7 Model pressure history predictions for the 0.2 cm base plate; calculated values are shown connected by straight lines

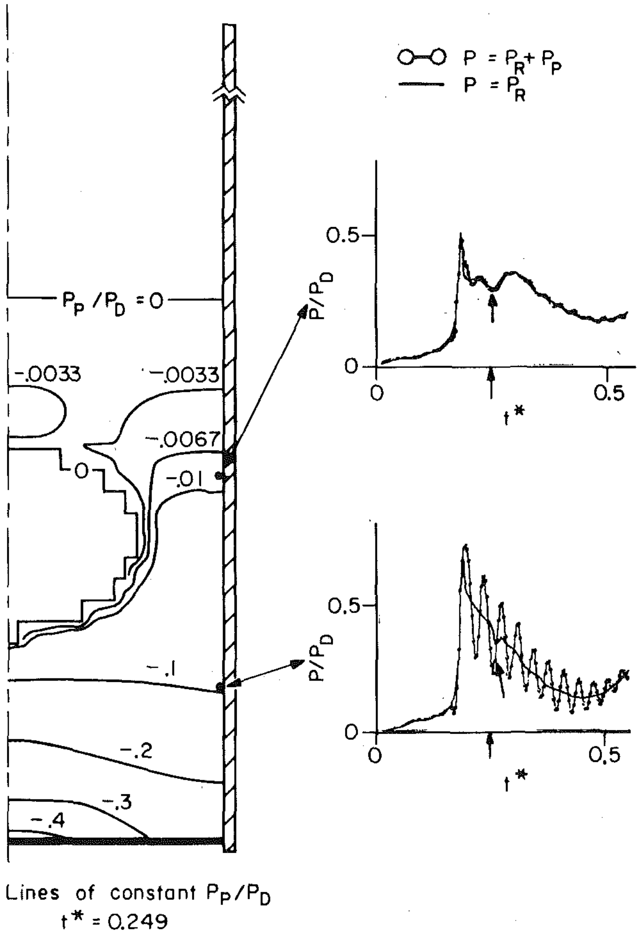

Fig. 8 Predicted perturbation pressure field at $t^* = 0.249$

cm base plate case exhibits similar behavior. The peak value of the flexible system pressure varies by about a factor of 2.5 between stations (a) and (d) of Fig. 7. The perturbation pressures are largest at the base plate and decrease to zero at all liquid-gas interfaces. In Fig. 7(d) the line or zero absolute system pressure is at $(P_p + P_R)/P_D = -0.33$. The predicted flexible system pressures dip below this value several times in the central region of the plate. This suggests the possibility of some cavitation occurring in the experimental tests which has not been investigated experimentally nor accounted for in our model. The maximum predicted flexible system pressure at the plate center represents an overshoot of about 50 percent when compared to the rigid system plate pressure.

Fig. 7 also shows that the predicted perturbation pressure amplitudes decay after their first peak at rates which vary throughout the pool. That a decay should be predicted at all is at first surprising since the model does not account for structural damping or fluid viscosity. The decay is, in fact, the result of the liquid redistribution driven by the bubble growth. Otherwise identical calculations conducted without a growing bubble exhibited no perturbation decay.

Figs. 8 and 9 show the predicted perturbation pressure distributions at two selected times. They illustrate the change with time of this distribution and thus the relative importance of the perturbations in various regions of the pool. The figures also include the predicted flexible system response and measured rigid system pressures along the sidewall at $z/a = 0.7$ and $z/a = 1.7$. The predicted flexible system pressures at the instants of time at which the P_p isobars are calculated are indicated by arrows on the pressure histories. In the region of the pool at elevations less than that of the bubble, the perturbation pressures are large (of the same order as the rigid system pressures) and decrease with elevation roughly linearly. At elevations at or above that of the bottom of the bubble they are much smaller. Thus it appears that there are two regions of influence within the pool: one beneath the bubble and relatively near the plate in which FSI effects are important and a second near and above the bubble in which the influence of the plate oscillation is much less. As the bubble grows, its region of influence grows and the large amplitude perturbation isobars ($|P_p/P_D| \gtrsim 0.1$, say) move closer to the plate. Such behavior leads to the predicted decay in perturbation amplitudes. (In comparing the magnitudes of P_p/P_D in Figs. 8 and 9, it must be remembered that these figures represent different times in the oscillation cycle.)

Model pressure history predictions on the pool sidewall at $z/a = 0.7$ are compared with experiment for the cases of a 0.1 cm and a 0.2 cm thick base plate in Figs. 10 and 11. A brief comparison of the predicted frequency content, peak pressures, and decay rates with those experimentally observed is presented in Table 1. Values of the per cycle decay rates, d, are calculated from the formula

$$P_{p,n} \equiv P_{p,0}(1 - d)^n \tag{18}$$

where n is the number of cycles considered, $P_{p,0}$ is the amplitude of the perturbation pressure at the beginning of the first cycle considered, and $P_{p,n}$ is the amplitude n cycles later. The agreement is generally good. The initiation of a large amplitude decaying oscillation at the "spike" in the rigid system pressure history is clear in both calculations and experiment. For both plate thicknesses, an increase in perturbation frequency with time is predicted and observed experimentally. For both plates, the predicted frequencies are somewhat lower than observed experimentally (25–30 percent low for the 0.1 cm plate and 15–20 percent low for the 0.2 cm plate). For the 0.1 cm plate the model predicts a slight (2 percent) undershoot in comparing the peak value of the flexible system pressure history to that of the rigid system while an overshoot of about 21 percent is observed experimentally. The model predicts an overshoot of about 6 percent for the

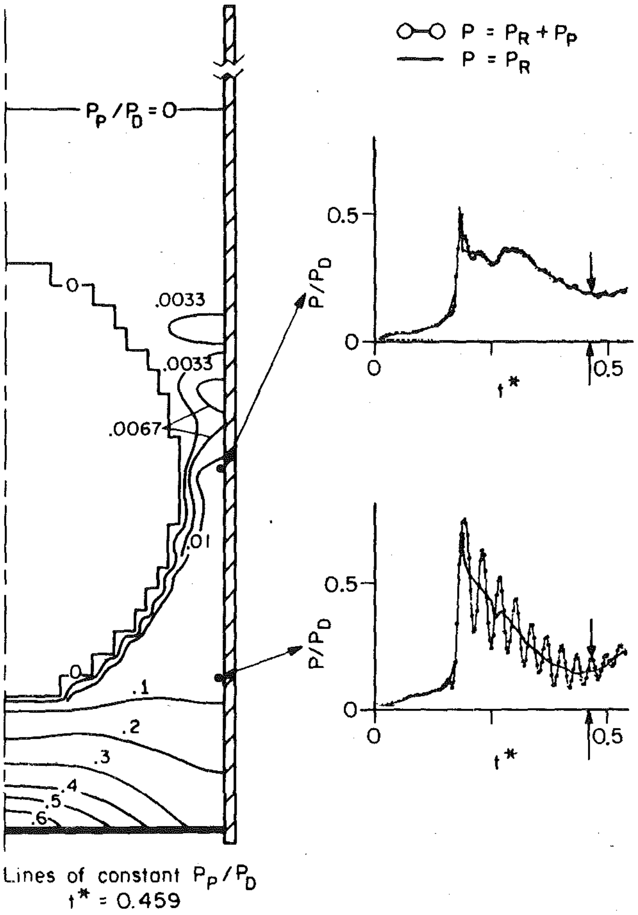

Fig. 9 Predicted perturbation pressure field at $t^* = 0.459$

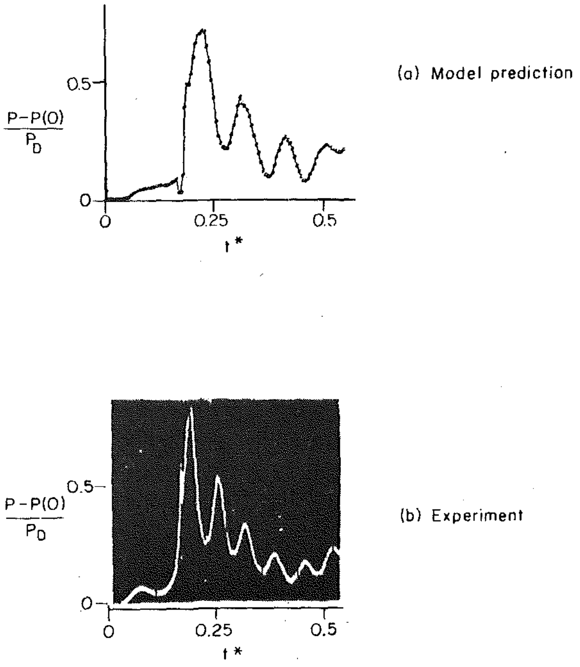

(a) Model prediction

(b) Experiment

Fig. 10 Comparison of sidewall perturbation calculation with experiment: 0.1 cm base plate, $z/a = 0.7$

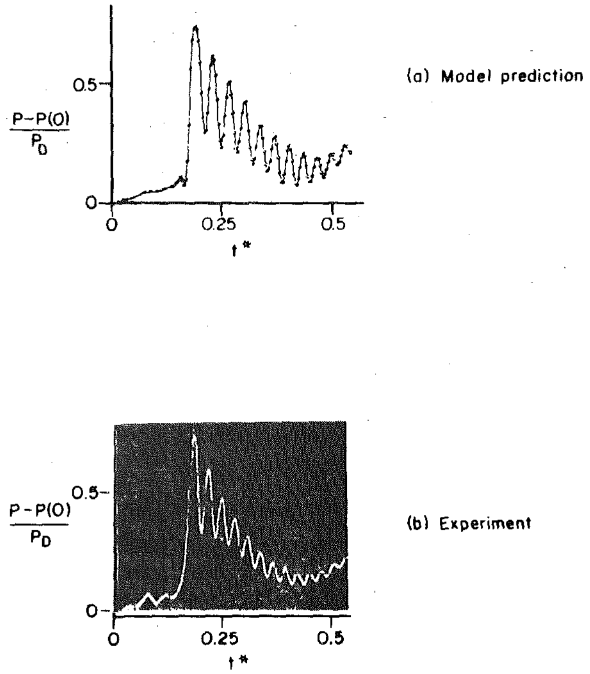

(a) Model prediction

(b) Experiment

Fig. 11 Comparison of sidewall perturbation calculation with experiment: 0.2 cm base plate, $z/a = 0.7$

Table 1 Comparison of predicted flexible system sidewall pressure histories with experiment at $z/a = 0.7$

	0.1 cm base plate		0.2 cm base plate	
	Prediction	Experiment	Prediction	Experiment
$\frac{(P_P + P_R)_{\max}}{(P_R)_{\max}}$	0.98	1.21	1.06	1.06
Frequency (Hz) Average	95[1]	135[1]	250[2]	295[2]
Low (single cycle)	90	125	220	275
High (single cycle)	110	145	265	320
Decay rate[3] Peak to peak	0.35	0.37	0.18	0.23
Trough to trough	0.15	0.39	0.18	0.23

[1] Averaged over the first 7 cycles (beginning with the first peak in flexible system pressure occurring after $(P_R)_{\max}$).

[2] Averaged over the first 12 cycles.

[3] Computed from equation (18). The first 4 cycles are used for $h = 0.1$ cm; the first 10 cycles are used for $h = 0.2$ cm.

0.2 cm plate which agrees well with experiment. The predicted model decay rates are somewhat low but comparable to those observed.

Model predictions at $z/a = 1.7$ are compared with experiment for the 0.2 cm plate case in Fig. 12. Both the measured and predicted flexible system pressure histories differ little from the rigid system history. They exhibit minor perturbations shortly after the rigid system history peak and essentially no perturbations at later times.

Discussion

Our calculations and comparisons with experiment illustrate the essential features of a perturbation method FSI analysis and demonstrate both the simplicity and promise of this method. Relatively few refinements have been implemented in our calculations primarily

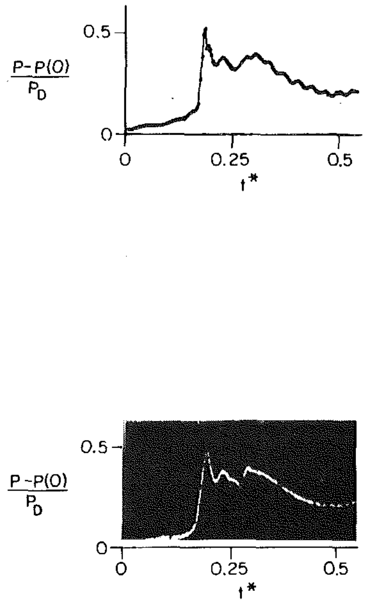

(a) Model prediction

(b) Experiment

Fig. 12 Comparison of sidewall perturbation calculation with experiment: 0.2 cm base plate, z/a = 1.7

Table 2 Evaluation of perturbation method criteria for our test system

Characteristic and physical quantities:

L_w 0.08 cm(1)	L_g 14 cm	ρ_l 1000 kg/m^3
0.01 cm(2)	τ_R 0.04 s	ρ_g 0.08 kg/m^3 (3)
L_R 14 cm	τ_e 0.007 s	μ 0.001 kg/ms
L_λ 14 cm	τ_w 0.01 s(1)	c_l 1500 m/s
L_0 14 cm	0.0035 s(2)	c_g 330 m/s

Criterion(4)	Value for test system 0.1 cm plate	 0.2 cm plate
(1) $\tau_w/\tau_R \ll 1$	0.25	0.09
(2) $\frac{\tau_w}{\tau_R}\frac{L_R}{L_\lambda} \ll 1$	0.25	0.09
(3) $\tau_e/\tau_w \lesssim 1$	0.7	2
(4) $L_w/L_\lambda \ll 1$	0.006	0.0007
(5) $L_w/L_0 \ll 1$	0.006	0.0007
(6) $L_w/L_g \ll 1$	0.006	0.0007
(7) $(L_0/c_l\tau_w)^2 \ll 1$	0.00009	0.0007
(8) $(L_\lambda/c_l\tau_w)^2 \ll 1$	0.00009	0.0007
(9) $(L_g/c_g\tau_w)^2 \ll 1$	0.002	0.015
(10) $\rho_l L_\lambda^2/\mu\tau_w \gg 1$	2,000,000	5,600,000
(11) $\rho_g L_g/\rho_l L_0 \ll 1$	0.00008	0.00008

(1) For a 0.1 cm base plate.
(2) For a 0.2 cm base plate.
(3) Based on an initial gas (air) pressure of approximately 6 kPa.
(4) Taken from [1].

because the agreement between prediction and experiment is near the level of experimental repeatability [2, 4]. The comparisons presented here are not intended to be an exhaustive verification of the perturbation method, but rather to provide one systematic test of the procedure and its underlying assumptions. Our predictions illustrate the important effect that liquid mass redistribution has on both the frequency content and the amplitude of the flexible system's pressure fluctuations. The analysis and results can be contrasted to those of a lumped parameter model [2] which requires prior specification an "effective" pool depth (or "added liquid mass") and is unable to predict any detailed FSI response features.

The criteria for the applicability of the perturbation method are evaluated for our test system in Table 2 where ρ_l and ρ_g are the liquid and gas densities, and c_l and c_g are the speeds of sound in the liquid and gas, and μ is the liquid viscosity. Characteristic length and time scales used are defined as [1]:

L_R = hydrodynamic length over which velocity gradients occur
L_λ = smallest wall oscillation wavelength
L_g = gas region dimension
L_0 = pool (fluid domain) dimension
L_w = wall displacement during oscillation (estimated from the rigid system pressures)
τ_R = hydrodynamic time (estimated from the rigid system bulk fluid motion)
τ_w = longest period for wall oscillation
τ_e = minimum excitation time constant

The length scales L_R, L_λ, L_0, and L_g are all taken to be the plate diameter. Both τ_R and τ_e are estimated from the rigid base plate pressure history. Table 2 shows that all criteria are easily satisfied except for (1) and (2) for the 0.1 cm base plate system. Thus the perturbation method assumptions should introduce negligible error with the possible exception of some nonlinear coupling effects [1] between the perturbed and unperturbed motions not being accounted for in the analysis of the 0.1 cm plate system.

In developing a model for our test system we have made several additional assumptions not central to the perturbation method. Omission of the downcomer should introduce negligible error. It is partly enclosed by the air bubble and is in a region of very small $|P_p|$. The approximation of the pool surface as flat and horizontal (neglecting the growth of irregular pool surface instabilities; see Fig. 2) should be of minor importance for similar reasons. The initial static plate deflection due to the weight of the water is an order of magnitude less than those during pool swell and is easily neglected.

The better agreement between prediction and experiment for the 0.2 cm plate than for the 0.1 cm plate may be largely due to plate tension effects which have been neglected in the model plate equation. Neglecting tension relative to bending stress for a circular clamped plate of thickness h deforming under a uniform load q will introduce an error that can be estimated from [8]:

$$\frac{qa^4}{64\,Dh} = \frac{w_{\max}}{h} + \frac{1+\nu}{2}\left(\frac{w_{\max}}{h}\right)^3 \tag{19}$$

where $w_{\max}$ is the maximum plate displacement and ν is Poisson's ratio. The first term on the right-hand side of (19) is due to bending and the second is due to tension. If we take q to be the maximum value of P_R on the plate, the estimated errors in $w_{\max}$ are 21 percent and 0.2 percent for plate thickness of 0.1 cm and 0.2 cm, respectively. Since tension stiffens the plate, its inclusion in the model would increase the predicted frequencies—enhancing agreement with experiment for the thinner plate. Modification of the predicted peak pressure overshoot should also occur.

The input data—bubble shape and size, P_R on the plate, and P_R at various sidewall locations—were obtained from several different experimental runs, and model predictions are compared to data from yet other runs. To compensate for experimental variability, the time coordinates of the data were shifted a small amount so that they would be equivalent in each set of data. Typically this shift was less than 2 percent of the total time period under consideration ($t^* < 0.01$)—well within the bounds of experimental variability [4].

To save computation time, the liquid configuration was changed at each time step only during the initial period of bubble growth. At later times ($t^* \gtrsim 0.25$), the liquid configuration was modified every fifth time step for the 0.2 cm plate system. Thus the input bubble growth lags the experimental records. This results in a maximum error of about 6 percent in bubble "radius." Such an underapproximation of bubble size will lower the predicted perturbation frequencies and decay rates.

The run-to-run experimental initial liquid depth variation was about 2 percent [2]. The initial liquid depth used in the calculations is about 6 percent higher than the nominal experimental value. This should result in a prediction of frequencies that are about 3 percent low.

Based on simple tests of our algorithm we believe the errors introduced by the numerical schemes to be at most of the same order as the other uncertainties previously discussed. As described earlier, provisions for increased accuracy were made in situations where it was believed useful such as an increased number of mesh points between the bubble and the plate and integration of the plate equation over an interval smaller than the fluid mesh spacing. Due to the finite time step size, the peak in the rigid system pressure history will be missed unless it occurs at a time step. For the 0.2 cm plate system model, this leads to an underestimation of the input rigid base plate pressure peak by about 2½ percent.

Conclusions

The perturbation method is a promising practical tool for modeling FSI problems involving complex hydrodynamic transients. It allows the use of both experimental and analytical data from rigid systems subjected to identical hydrodynamic transients. The implementation of the perturbation method is much easier than alternate approaches which involve the simultaneous solution of the nonlinear hydrodynamic equations and the structural equations.

Our analytical and experimental investigation of FSI phenomena in a simple test system of controlled flexibility has demonstrated the important effects that liquid mass redistribution has on both the frequency content and the spatial and temporal amplitude distributions of the perturbation pressures.

Acknowledgment

The authors wish to acknowledge many helpful discussions with Prof. Ain Sonin during the course of this work.

References

1 Huber, P. W., Kalumuck, K. M., and Sonin, A. A., "Rationale for a Perturbation Method for Analyzing Fluid-Structure Interactions in BWR Pressure-Suppression Containment Systems," U.S. Nuclear Regulatory Commission NUREG/CR-1313, February 1980. See also, Sonin, A. A., "Rationale for a Linear Perturbation Method for the Flow Field Induced by Fluid-Structure Interactions," to appear in ASME JOURNAL OF APPLIED MECHANICS.

2 Huber, P. W., and Javadi, Y. B., "Fluid-Structure Interactions in Pressure-Suppression Pools: Small-Scale Experiments and Analysis," ASME *Journal of Pressure Vessel Technology,* Vol. 102, 1980, pp. 194–201.

3 Sonin, A. A., and Huber, P. W., "On the Scaling Laws for Air Clearing in Water-Type Pressure Suppression Systems," ASME *Journal of Heat Transfer*, Vol. 100, No. 4, 1978, pp. 601–604.

4 Anderson, W. G., Huber, P. W., and Sonin, A. A., "Experimental Tests of the Scaling Laws for Air Clearing in Water-Type Pressure Suppression Systems," ASME *Journal of Heat Transfer,* Vol. 100, No. 4, 1978, pp. 605–612.

5 Timoshenko, S., and Woinowsky-Krieger, S., *Theory of Plates and Shells,* McGraw-Hill, New York, 1959, pp. 63–67.

6 Weber, C., "Calculation of Potential Fields and Electron Trajectories Using an Electronic Computer," *Philips Technical Review,* Vol. 24, No. 4/5, 1962/63, pp. 130–143.

7 Kalumuck, K. M., Engineer's Degree Thesis, M.I.T. Department of Mechanical Engineering, Sept. 1979.

8 Den Hartog, J. P., *Advanced Strength of Materials,* McGraw-Hill, New York, 1952, Chapter 4.

T. L. Geers
Senior Staff Scientist.
Mem. ASME

C. -L. Yen
Research Scientist.

Lockheed Palo Alto Research Lab,
Applied Mechanics Laboratory,
3251 Hanover Street,
Palo Alto, Calif. 94304

Nonlinear Response of an Elastic Cylindrical Shell to a Transient Acoustic Wave

Governing equations are developed for the nonlinear response of an infinite, elastic, circular cylindrical shell submerged in an infinite fluid medium and excited by a transverse, transient acoustic wave. These equations derive from circumferential Fourier-series decomposition of the field quantities appearing in appropriate energy functionals, and from application of the "residual potential formulation" for rigorous treatment of the fluid-structure interaction. Extensive numerical results are presented that provide understanding of the phenomenology involved.

1 Introduction

Although the literature is replete with analytical studies of the linear dynamic response of submerged structures, the dynamic instability of such structures has received relatively little attention [1]. In 1965, Di Maggio [2] studied the unstable dynamic response of an infinite flat plate with a sinusoidal imperfection in one direction subjected to an in-plane static loading in that same direction; the plate was suddenly released so as to interact with an acoustic medium on one side of the plate. He found that, in the vast majority of cases, the acoustic medium may be treated in the incompressible approximation. In 1972, Deng and Popelar [3] studied the parametric instability of a submerged cylindrical shell initially undergoing sinusoidal breathing motions. They also found that the acoustic medium could be accurately treated as imcompressible. References [4–6] report analyses of dynamically excited, submerged shells that exhibit instability characteristics. In all of these, however, approximate treatments of the fluid-structure interaction are used, which raises questions regarding the accuracy of the results.

This paper presents a rigorous treatment of the nonlinear response of an infinite, elastic, circular cylindrical shell excited by a transverse, transient acoustic wave. The field quantities appearing in appropriate kinetic-energy, potential-energy, and work-potential functionals are expanded in circumferential Fourier series, and high-order terms are eliminated in a consistent manner. The residual potential formulation [7–9], which constitutes an exact formulation, is used to treat the fluid-structure interaction. The resulting modal response equations provide a complete and rigorous description of the dynamic processes.

The modal response equations are integrated numerically in time for excitation by plane waves of rectangular pressure-profile. Transient response histories are provided that display:

1 Modal response as a function of incident-wave magnitude.
2 The effects of ambient hydrostatic pressure and "live-load" forcing terms (i.e., terms that account for finite translations and rotations of the shell).
3 Shell response at various locations.
4 The impact of flexural stiffness on mode participation.

2 Governing Equations

Consider the two-dimensional, plane-strain motions of the submerged, infinite, circular cylindrical shell shown in Fig. 1. The shell is excited by a transient acoustic wave that first contacts the shell at $\theta = \pi$. The shell is thin and remains elastic at all times; geometric nonlinearity is considered, however, which introduces the possibility of dynamic instability.

2.1 Energy Expressions. Kinetic and strain-energy expressions for the cylindrical shell of Fig. 1 are:

$$T = \tfrac{1}{2}\rho_0 h \int_0^{2\pi} (\dot{v}^2 + \dot{w}^2) a\, d\theta$$

$$U = \tfrac{1}{2} \int_0^{2\pi} \int_{-h/2}^{h/2} \sigma_\theta \epsilon_\theta \, dz\, a\, d\theta \tag{1}$$

where $\dot{v} = \partial v/\partial t$, etc., σ_θ is the circumferential stress, ϵ_θ is the circumferential strain, and z is the thickness coordinate. Stress-strain and strain-displacement relations for the shell are [10]

$$\sigma_\theta = \frac{E}{1-\nu^2}\epsilon_\theta$$

$$\epsilon_\theta = \frac{1}{a}\left(\frac{\partial v}{\partial \theta} + w\right) + \frac{1}{2a^2}\left(\frac{\partial w}{\partial \theta} - v\right)^2 - \frac{z}{a^2}\left(\frac{\partial^2 w}{\partial \theta^2} - \frac{\partial v}{\partial \theta}\right) \tag{2}$$

Contributed by the Applied Mechanics Division of THE AMERICAN SOCIETY OF MECHANICAL ENGINEERS, for presentation at the 1981 Joint ASME/ASCE Applied Mechanics, Fluids Engineering, and Bioengineering Conference, University of Colorado, Boulder, Colo., June 22–27, 1981.

Discussion on this paper should be addressed to the Editorial Department, ASME, United Engineering Center, 345 East 47th Street, New York, N.Y. 10017, *and will be accepted until June 1, 1981. Readers who need more time to* prepare a Discussion should request an extension from the Editorial Department. Manuscript received by ASME Applied Mechanics Division, May, 1980; final revision, July, 1980. Paper No. 81-APM-10.

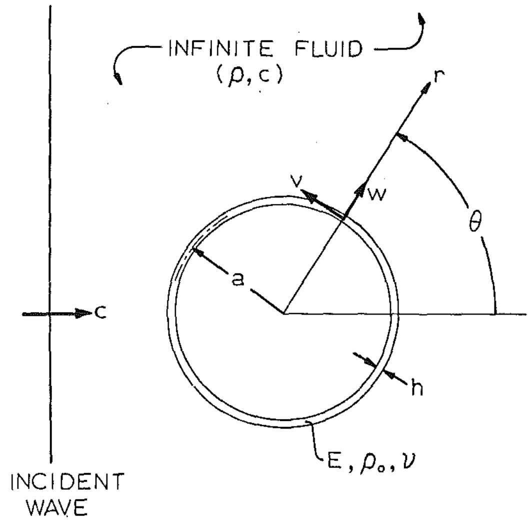

Fig. 1 Infinite, elastic, circular, cylindrical shell submerged in an infinite acoustic medium

where only first-order geometric nonlinearities are considered. The introduction of (2) into (1) then yields

$$U = \frac{1}{2}\frac{Eh}{(1-\nu^2)_a}\int_0^{2\pi}\left\{\left[\frac{\partial v}{\partial\theta} + w + \frac{1}{2a}\left(\frac{\partial w}{\partial\theta} - v\right)^2\right]^2 + \frac{h^2}{12a^2}\left(\frac{\partial^2 w}{\partial\theta^2} - \frac{\partial v}{\partial\theta}\right)^2\right\}d\theta \quad (3)$$

An expression for the work potential appropriate to a pressure field acting on the surface of a smooth shell has been provided by Cohen [11]. For the present problem, that expression reduces to

$$\Pi = \int_0^{2\pi}\left[p\left(a + \frac{\partial v}{\partial\theta} + w\right)w + \frac{1}{2}\left(a\frac{\partial p}{\partial r} - p\right)w^2 + \frac{1}{2}pv^2 + vw\frac{\partial p}{\partial\theta}\right]_{r=a} d\theta \quad (4)$$

where $p = p(r, \theta, t)$ denotes the total pressure field. Although Cohen lists continuity of the pressure field as a requirement for the existence of the work potential, it is easily shown that a more lenient requirement is satisfactory, viz., that the pressure field contain a finite number of integrable discontinuities.

Now the displacement and pressure fields may be expanded in Fourier series as follows:

$$v(\theta,t) = \sum_{n=1}^{\infty} v_n(t)\sin n\theta$$

$$w(\theta,t) = \sum_{n=0}^{\infty} w_n(t)\cos n\theta$$

$$p(r,\theta,t) = \sum_{n=0}^{\infty} p_n(r,t)\cos n\theta \quad (5)$$

Also, the $n \neq 0$ Fourier coefficents for v and w may be transformed into extensional and flexural coefficients as follows [9]:

$$v_n = n\,e_n - \frac{1}{n}f_n$$

$$w_n = e_n + f_n \quad (6)$$

The incorporation of (5) and (6) into (1), (3), and (4) then yields

$$\frac{T}{\pi\rho_0 ah} = \dot{w}_0^2 + \frac{1}{2}\sum_{n=1}^{\infty}\left[(n^2+1)\,\dot{e}_n^2 + \left(\frac{n^2+1}{n^2}\right)\dot{f}_n^2\right]$$

$$\frac{U}{\pi Eh/(1-\nu^2)a} = \underline{w_0}^2 + \frac{1}{2}\sum_{n=1}^{\infty}\left[\underline{\underline{\underline{(n^2+1)^2 e_n^2}}} + \underline{\underline{\frac{h^2}{12a^2}}}\,n^2\left(2n\,e_n + \underline{\underline{\frac{n^2-1}{n}}}f_n\right)^2\right]$$

$$+ \frac{1}{2}\frac{w_0}{a}\sum_{n=1}^{\infty} g_n^2 + \frac{1}{4a}\sum_{l=1}^{\infty}\sum_{m=1}^{\infty}\sum_{n=1}^{\infty}(l^2+1)\,e_l g_m g_n\left[\delta_{(m+l)n} + \delta_{(m-l)n}\right]$$

$$+ \frac{1}{32a^2}\sum_{k=1}^{\infty}\sum_{l=1}^{\infty}\sum_{m=1}^{\infty}\sum_{n=1}^{\infty} g_k g_l g_m g_n\left[\delta_{(k-l)0}\,\delta_{(m-n)0} + \delta_{(k-l)(m+n)}\right.$$

$$\left. - \delta_{(k+l)(m-n)} - \delta_{(k-l)(m+n)} + \delta_{(k+l)(m+n)}\right]$$

$$\frac{\Pi}{\pi a} = \underline{2p_0{}^a\,w_0} + \sum_{n=1}^{\infty}\underline{\underline{\underline{p_n{}^a}}}\,(\underline{\underline{e_n}} + \underline{\underline{f_n}}) + \frac{1}{2}\frac{\partial p_0{}^a}{\partial r}\sum_{n=1}^{\infty}(e_n + f_n)^2$$

$$+ \frac{p_0{}^a}{2a}\sum_{n=1}^{\infty}\left[(3n^2+1)\,e_n^2 + 2(n^2-1)e_n f_n - \left(\frac{n^2-1}{n^2}\right)f_n^2\right]$$

$$+ \left(\frac{p_0{}^a}{a} + \frac{\partial p_0{}^a}{\partial r}\right)w_0^2 + \frac{w_0}{a}\sum_{n=1}^{\infty}\left(p_n{}^a + a\frac{\partial p_n{}^a}{\partial r}\right)(e_n + f_n)$$

$$+ \frac{1}{2a}\sum_{n=1}^{\infty}\sum_{m=1}^{\infty}\left\{(p_{m-n}{}^a + p_{m+n}{}^a)\left[\left(m + \frac{1}{2}\right)e_m - \frac{1}{2}f_m\right]\right.$$

$$\left. + \left(\frac{a}{2}\right)\left(\frac{\partial}{\partial r}p_{m-n}{}^a + \frac{\partial}{\partial r}p_{m+n}{}^a\right)(e_m + f_m)\right\}(e_n + f_n)$$

$$+ \frac{1}{2a}\sum_{n=1}^{\infty}\sum_{m=1}^{\infty}\left\{\frac{1}{2}(p_{m-n}{}^a - p_{m+n}{}^a)\left(me_m - \frac{1}{m}f_m\right)\left(ne_n - \frac{1}{n}f_n\right)\right.$$

$$\left. - \left[(m-n)\,p_{m-n}{}^a + (m+n)\,p_{m+n}{}^a\right]\left(me_m - \frac{1}{m}f_m\right)(e_n + f_n)\right\} \quad (7)$$

(*Cont.*)

where $p_n{}^a = p_n(a,t)$, $\partial p_n{}^a/\partial r = [\partial p_n(r,t)/\partial r]_{r=a}$, $g_n = 2ne_n + [(n^2 - 1)/n]\,f_n$, $e_{m-n} = p_{m-n} = 0$ for $m \lesseqgtr n$, and the δ_{ij} are Kronecker deltas. Equations (7) constitute the basic energy expressions required for the present study.

2.2 Elimination of High-Order Terms. It is now appropriate to eliminate from (7) those terms of order higher than that necessary for a consistent formulation. For this purpose, the $n = 0$ pressure harmonic is taken to be of the order of the critical buckling pressure for the shell, which is [12]

$$P_C = \frac{Eh^3}{4(1-\nu^2)a^3} \quad (8)$$

Hence $p_0{}^a \sim E(h/a)^3$, so that the two singly underlined terms in (7), which govern linear, static, axisymmetric response, yield $w_0/a \sim (h/a)^2$. Next, flexural displacements are taken as $f_n/a \sim h/a$, so that the doubly underlined terms, which govern linear, static, flexural response, yield $p_n{}^a \sim E(h/a)^4$. Finally, the triply underlined terms, which govern linear, static, nonaxisymmetric-extensional response, yield $e_n/a \sim (h/a)^3$. The use of these order-or-magnitude relations in (7), followed by the elimination of terms of order $(h/a)^6$ and higher, yields the simplified energy expressions

$$\frac{T}{\pi\rho_0 ah} = \dot{w}_0^2 + \frac{1}{2}\sum_{n=1}^{\infty}\left(1 + \frac{1}{n^2}\right)\dot{f}_n^2$$

$$\frac{U}{\pi Eh/(1-\nu^2)a} = w_0^2 + \frac{1}{2}\sum_{n=1}^{\infty}\left[\frac{(\gamma h)^2}{12a^2}n^2 + \frac{w_0}{a}\right]\alpha_n^2 f_n^2 + \frac{1}{32a^2}\sum_{k=1}^{\infty}\sum_{l=1}^{\infty}\sum_{m=1}^{\infty}\sum_{n=1}^{\infty}\Delta_{klmn} f_k f_l f_m f_n$$

$$\frac{\Pi}{\pi a} = 2p_0{}^a w_0 + \sum_{n=1}^{\infty} p_n{}^a f_n - \frac{p_0{}^a}{2a}\sum_{n=1}^{\infty}\frac{\alpha_n}{n}f_n^2 + \frac{1}{2}\frac{\partial p_0{}^a}{\partial r}\sum_{n=1}^{\infty} f_n^2 \quad (9)$$

where $\alpha_n = (n^2 - 1)/n$ and $\Delta_{klmn} = \alpha_k\alpha_l\alpha_m\alpha_n\,[\delta_{(k-l)0}\,\delta_{(m-n)0} + \delta_{(k-l)(m-n)} - \delta_{(k+l)(m-n)} - \delta_{(k-l)(m+n)} + \delta_{(k+l)(m+n)}]$. Note that, because $\alpha_1 = 0$, the lower limits of six of the summations in (9) may be changed from 1 to 2.

A few remarks about (9) are in order. First, nonaxisymmetric-extensional response fails to appear as a significant energy contributor. Second, in the reduction of (7) to (9), it has been assumed that $a|\partial p_n{}^a/\partial r| \sim |p_n{}^a|$ for all n. Third, the last of (9) contains no nonlinear terms involving p_n; this implies that the last term in the integrand of (4) is unimportant. Fourth, a nondimensional parameter γ has been introduced into the flexural strain-energy term to permit consideration of a sandwich shell consisting of two concentric shells of thickness $h/2$ separated by a uniform core of negligible mass and in-plane stiffness. Such a shell serves as a convenient plane-strain model for a stiffened shell [7, 13]. With D as the sandwich shell's flexural stiffness, $\gamma^2 = 12(1 - \nu^2)D/Eh^3$. Finally, the simplified expression for the shell's strain energy is positive-definite; this is readily seen by observing that, with $w(\theta,t) = w_0(t) + f(\theta,t)$, it constitutes a Fourier-series decomposition of the expression [cf. (3)]

$$U = \frac{1}{2}\frac{Eh}{(1-\nu^2)a}\int_0^{2\pi}\left\{\left[w_0 + \frac{1}{2a}(f' + f^*)^2\right]^2 + \frac{(\gamma h)^2}{12a^2}(f'' + f)^2\right\}d\theta \quad (10)$$

where a prime denotes a θ-derivative and the asterisk a θ-integral. This corresponds to the use of Rayleigh's inextensibility assumption, i.e., $w = -\partial v/\partial\theta$ for nonaxisymmetric shell response [14].

It is interesting to examine results produced by (9) in certain special circumstances. First, consider the nonaxisymmetric, linear, free vibrations of a hydrostatically pressurized shell. In this case, $p_0(r,t) = P_H$, $p_n(r,t) = 0$ for $n \neq 0$, and the flexural displacements are infinitesimal. The application of Lagrange's equation [15]

$$\frac{d}{dt}\left(\frac{\partial L}{\partial \dot{q}}\right) - \frac{\partial L}{\partial q} = 0 \quad (11)$$

where $L = T - U - \Pi$, then yields, for $q = w_0$,

$$w_0 = -\frac{(1-\nu^2)a^2}{Eh}P_H \quad (12)$$

For $q = f_n$, the application of Lagrange's equation yields

$$\rho_0\left(1 + \frac{1}{n^2}\right)\ddot{f}_n + \frac{E}{(1-\nu^2)a^2}\left\{\left[\frac{(\gamma h)^2}{12a^2}n^2 + \frac{w_0}{a}\right]\alpha_n{}^2 - (1-\nu^2)\frac{P_H a}{Eh}\left(\frac{\alpha_n}{n}\right)\right\}f_n = 0 \quad (13)$$

The introduction of (12) into (13), followed by the assumption of sinusoidal free vibration, yields the modal natural frequency equation

$$\omega_{fn}{}^2 = \left(\frac{c_0}{a}\right)^2\frac{(\gamma h)^2}{12a^2}\left(\frac{n^2}{n^2+1}\right)(n^2-1)^2(1 - P_H/P_{Cn}) \quad (14)$$

where $c_0{}^2 = E/\rho_0(1-\nu^2)$ is the plate velocity for the shell material and $P_{Cn} = \rho_0 c_0{}^2 (h/a)(n^2 - 1)(\gamma h)^2/12a^2$ is the critical pressure for the nth flexural mode; note that $P_{C2} = P_C$ [cf. (8)]. Equation (14) clearly corresponds to the flexural frequency equation for a pressurized ring [16].

Next, consider the response of an unpressurized shell to nearly uniform radial impulse-excitation. The application of Lagrange's equation, (11), to the simplified energy expressions, (9), yields for axisymmetric extensional and nonaxisymmetric flexural response

$$(a/c_0)^2\ddot{w}_0 + w_0 + \frac{1}{4a}\sum_{n=2}^{\infty}\alpha_n{}^2 f_n{}^2 = 0$$

$$(a/c_0)^2\frac{n^2+1}{n^2}\ddot{f}_n + \left[\frac{(\gamma h)^2}{12a^2}n^2 + \frac{w_0}{a}\right]\alpha_n{}^2 f_n + \frac{1}{32a^2}\sum_{k=2}^{\infty}\sum_{l=2}^{\infty}\sum_{m=2}^{\infty}\Delta_{klm}{}^{(n)}f_k f_l f_m = 0 \quad (15)$$

where $\Delta_{klm}{}^{(n)} = \Delta_{klmn} + \Delta_{klnm} + \Delta_{knlm} + \Delta_{nklm}$ and the discussion following (9) has been utilized.

These equations are similar to equations presented in [17–19] which treat this particular problem in considerable detail. Equations (15) are superior, in fact, to the corresponding equations in those references because only (15) exhibit *all* of the following characteristics:

1 $n = 1$ rigid-body motion is decoupled from $n = 0$ breathing motion.

2 Linear-vibration frequencies for the flexural modes are given by the first of (14) with $P_H = 0$.

3 The associated strain-energy expression is positive-definite.

From this brief examination of two special cases, it is concluded that (9) are suitable for the present analysis. This suitability derives from the consistent elimination of high-order terms from appropriate energy expressions.

2.3 Fluid-Structure Interaction. A rigorous formulation of the fluid-structure interaction, which must be considered in conjunction with (9), may be constructed as follows [7–9]. First, fluid pressure and radial fluid-particle velocity are expressed as derivatives of a fluid velocity potential as

$$p = -\rho\dot{\varphi}$$
$$u = \partial\varphi/\partial r \quad (16)$$

Second, the total acoustic field is treated as the superposition of an acoustic field for the (known) *incident wave* and an acoustic field for the (unknown) *scattered wave,* i.e.,

$$\varphi(r,\theta,t) = \varphi_I(r,\theta,t) + \varphi_S(r,\theta,t) \quad (17)$$

Third, compatibility of radial fluid-particle velocity and radial shell velocity is enforced at the wet surface of the shell as

$$u(a,\theta,t) = \dot{w}(\theta,t) \quad (18)$$

Finally, the wave equation and radiation condition for each circumferential harmonic of the scattered wave [see (7)] are replaced by the equivalent residual-potential relation

$$\frac{\partial\varphi_{Sn}}{\partial r} + \frac{1}{c}\dot{\varphi}_{Sn} + \frac{1}{2r}\varphi_{Sn} = \frac{1}{r}\varphi_{Rn} \quad (19)$$

in which the residual potential φ_{Rn} is given by the convolution relation

$$\varphi_{Rn}(r,t) = -\int_0^t r_n(r,t')\,\varphi_{Sn}(r,t-t')\,dt \quad (20)$$

where the r_n are characterisitic functions that resemble step-exponential functions [7].

Equations (16)–(19) may now be utilized to produce, for each circumferential harmonic, the fluid-structure interaction relations

$$p_n{}^a = -\rho\,(\dot{\varphi}_{In}{}^a + \dot{\varphi}_{Sn}{}^a)$$
$$\frac{\partial p_n{}^a}{\partial r} = -\rho\ddot{w}_n$$
$$\dot{w}_n + \frac{1}{c}\dot{\varphi}_{Sn}{}^a + \frac{1}{2a}\varphi_{Sn}{}^a = u_{In}{}^a + \frac{1}{a}\varphi_{Rn}{}^a \quad (21)$$

where $\varphi_{Rn}{}^a = \varphi_{Rn}(a,t)$ is obtained from (20). These equations constitute the optimum form of the information required for a rigorous treatment of the fluid-structure interaction.

2.4 Modal Response Equations. Convenient nondimensional equations may be obtained through introduction of the following convention:

$$\hat{p} = p^a/\rho c^2, \quad \hat{w} = w/a, \quad \hat{t} = ct/a \quad (22)$$

Application of this convention to (9) yields

$$\frac{T}{\pi\rho a^2c^2} = \left(\frac{\rho_0 h}{\rho a}\right)\left\{\dot{\hat{w}}_0{}^2 + \frac{1}{2}\sum_{n=1}^{\infty}\left(1 + \frac{1}{n^2}\right)\dot{\hat{f}}_n{}^2\right\}$$

$$\frac{U}{\pi\rho a^2c^2} = \left(\frac{\rho_0 h}{\rho a}\right)\left(\frac{c_0}{c}\right)^2\left\{\hat{w}_0{}^2 + \frac{1}{2}\sum_{n=2}^{\infty}\left[\frac{(\gamma h)^2}{12a^2}n^2 + \hat{w}_0\right]\alpha_n{}^2\hat{f}_n{}^2 + \frac{1}{32}\sum_{k=2}^{\infty}\sum_{l=2}^{\infty}\sum_{m=2}^{\infty}\sum_{n=2}^{\infty}\Delta_{klmn}\hat{f}_k\hat{f}_l\hat{f}_m\hat{f}_n\right\}$$

$$\frac{\Pi}{\pi\rho a^2c^2} = 2\hat{p}_0\hat{w}_0 + \sum_{n=1}^{\infty}\hat{p}_n\hat{f}_n - \frac{1}{2}\hat{p}_0\sum_{n=2}^{\infty}\frac{\alpha_n}{n}\hat{f}_n{}^2 + \frac{1}{2}\hat{p}_0'\sum_{n=1}^{\infty}\hat{f}_n{}^2 \quad (23)$$

where $\dot{\hat{w}}_0 = d\hat{w}_0/d\hat{t}$, $\dot{\hat{f}}_n = d\hat{f}_n/d\hat{t}$, $\hat{p}_0' = [\partial\hat{p}_0/\partial\hat{r}]_{\hat{r}=1}$, and the discussion following (9) has been utilized. In like fashion, nondimensionalization of (21) and (20) yields

$$\hat{p}_n = -(\mathring{\varphi}_{In} + \mathring{\varphi}_{Sn})$$

$$\hat{p}_n' = -\overset{\circ\circ}{w}_n$$

$$\overset{\circ\circ}{w}_n + \mathring{\varphi}_{Sn} + \frac{1}{2}\hat{\varphi}_{Sn} = \hat{u}_{In} + \hat{\varphi}_{Rn}$$

$$\hat{\varphi}_{Rn} = -\hat{r}_n * \hat{\varphi}_{Sn} \tag{24}$$

where the asterisk denotes temporal convolution. Note that all nondimensional acoustic-field quantities in (23) and (24) pertain to the wet surface of the shell.

The application of Lagrange's equation, (11)–(23), followed by the appropriate utilization of (24) and the second of (6) with e_n neglected, yields the nondimensional modal response equations for the submerged shell

$$\mu\overset{\circ\circ}{w}_0 + \mu\beta w_0 + \frac{1}{4}\mu\beta\sum_{n=2}^{\infty}\left(\frac{n^2-1}{n}\right)^2 f_n{}^2 - \mathring{\varphi}_{S0} = \mathring{\varphi}_{I0}$$

$$\mu\frac{n^2+1}{n^2}\overset{\circ\circ}{f}_n + \left\{\mu\beta\left[\xi(n^2-1)^2 + \left(\frac{n^2-1}{n}\right)^2 w_0\right] + \frac{n^2-1}{n^2}\right.$$

$$\left.\times(\mathring{\varphi}_{I0} + \mathring{\varphi}_{S0}) - \overset{\circ\circ}{w}_0\right\}f_n + \frac{\mu\beta}{32}\sum_{k=2}^{\infty}\sum_{l=2}^{\infty}\sum_{m=2}^{\infty}\Delta_{klm}{}^{(n)}f_k f_l f_m - \mathring{\varphi}_{Sn} = \mathring{\varphi}_{In}$$

$$\mathring{w}_0 + \mathring{\varphi}_{S0} + \frac{1}{2}\varphi_{S0} = u_{I0} + \varphi_{Ro}$$

$$\mathring{f}_n + \mathring{\varphi}_{Sn} + \frac{1}{2}\varphi_{Sn} = u_{In} + \varphi_{Rn}$$

$$\varphi_{Rn} = -r_n * \varphi_{Sn} \tag{25}$$

where all circumflexes have been dropped, and where $\mu = \rho_0 h/\rho a$, $\beta = (c_0/c)^2$ and $\xi = (\gamma h)^2/12a^2$. The nondimensional critical buckling pressure for the shell is, from (8), $P_C = 3\,\mu\,\beta\,\xi$.

Equations (25) constitute the modal response equations neeeded for a rigorous analysis of the nonlinear dynamic response of a submerged, infinite, elastic, circular, cylindrical sandwich shell excited by a transverse, transient acoustic wave. They lend themselves to step-by-step numerical integration in time, producing modal response histories that, through (6) with e_n neglected and through (5), yield corresponding shell response histories. From (2), (5), and (6) with e_n neglected, extensional and flexural strain response histories may be obtained as

$$\epsilon_\theta{}^e = w_0 + \frac{1}{2}\left(\sum_{n=1}^{\infty}\frac{n^2-1}{n}f_n \sin n\theta\right)^2$$

$$\epsilon_\theta{}^f = z\sum_{n=1}^{\infty}(n^2-1)\,f_n\cos n\theta \tag{26}$$

where z is nondimensional [see (22)]. For the sandwich shell described after (9), the distance from the neutral axis to the outer shell fiber is given by

$$|z|_{\max} = \frac{h}{4}\left[1 + \sqrt{1 + \frac{4}{3}(\gamma^2-1)}\right] \tag{27}$$

3 Numerical Results

The numerical results presented in this section have been generated by the application of fourth-order Runge-Kutta numerical integration to the first four of (25) and the use of trapezoidal integration for the last of (25). A variable incrementing procedure with $0.002 \lessdot \Delta t \lessdot 0.2$, has been used. Results have been obtained for two steel shells submerged in sea water, all characterized by $\rho_0/\rho = 7.72$, $c_0/c = 3.53$, and $a/h = 100$. The two shells differ in terms of their γ-values, which are 5 and 10; these values correspond to moderate and heavy stiffening of a uniform homogeneous shell. The shells are excited by plane acoustic waves of rectangular pressure profile that make initial contact at time $t = 0$ along the line $\theta = \pi$. The generalized excitation functions for these waves are given by

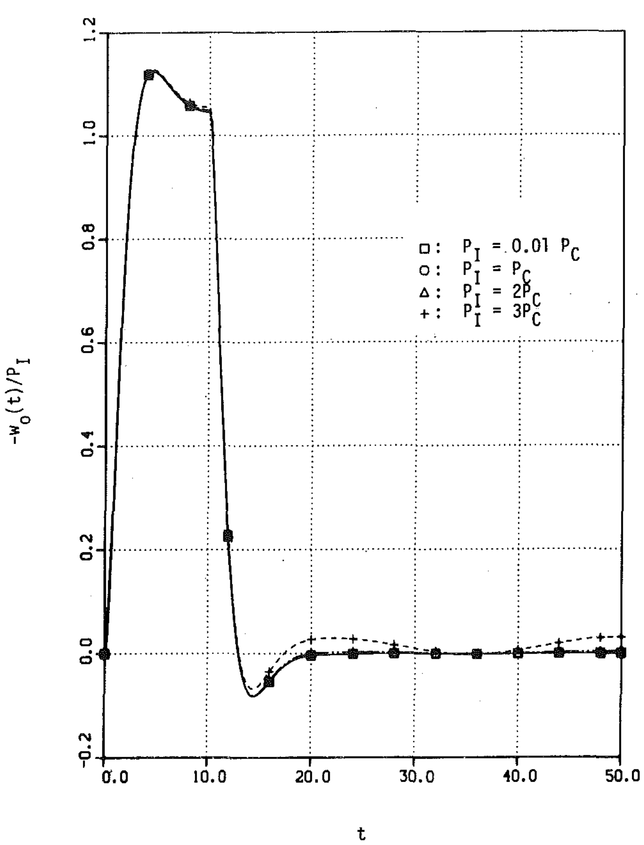

Fig. 2 $n = 0$ displacement of the $\gamma = 10$ shell to rectangular incident waves with $T = 10$

$$\mathring{\varphi}_{In}(t) = (-1)^{n+1}\frac{\epsilon_n}{\pi}P_I\int_0^{\pi} g(t - 1 + \cos\zeta)\cos n\zeta\, d\zeta$$

$$u_{In}(t) = (-1)^{n+1}\frac{\epsilon_n}{\pi}P_I\int_0^{\pi} g(t - 1 + \cos\zeta)\cos\zeta\cos n\zeta\, d\zeta \tag{28}$$

where $\epsilon_n = 1$ for $n = 0$ and $\epsilon_n = 2$ for $n \geqq 1$, P_I is the maximum value of the incident-wave pressure profile, and $g(t) = \mathrm{H}(t) - \mathrm{H}(t - T)$, where $\mathrm{H}(t)$ is the Heaviside step-function and T is the pulse duration. Note that all of the preceding quantities are nondimensional, having been normalized in accordance with (22).

3.1 Modal Response. Fig. 2 shows displacement response histories for the ($n = 0$) breathing mode of the $\gamma = 10$ sandwich shell when excited by broad, rectangular, incident waves of duration $T = 10$. The pressure magnitudes of these waves vary from 1–300 percent of the critical buckling pressure for the shell [see (8), or the discussion following (25)]. Note that all responses are normalized to the magnitude of the incident wave, so that coalescence of response histories implies linearity of response. In this connection, it is seen that the response for $P_I = P_C$ and $P_I = 2P_C$ are virtually coincident with the (linear) response for $P_0 = 0.01\ P_C$; nonlinear effects are discernible for $P_I = 3P_C$, but they are relatively unimportant.

Velocity response histories for the ($n = 1$) translational mode are shown in Fig. 3. Nonlinear effects are barely discernible. This implies that the last term in the last of (23) is of negligible importance because, without it, the $n = 1$ mode is totally uncoupled from the other modes and is governed by purely linear equations [see (25) and the second of (24)].

The $n = 2$ lobar mode is the one that exhibits significant nonlinear behavior, as shown by the displacement response histories of Fig. 4. The response may be conveniently described as occuring in four phases: an "envelopment phase," which extends from $t = 0$ to $t = 2$, a "pressurization phase," which extends from $t = 2$ to $t = T$, a "development phase," which extends from $t = T$ to $t = T + 2$, and a "free vibration phase," which extends onward from $t = T + 2$. During the

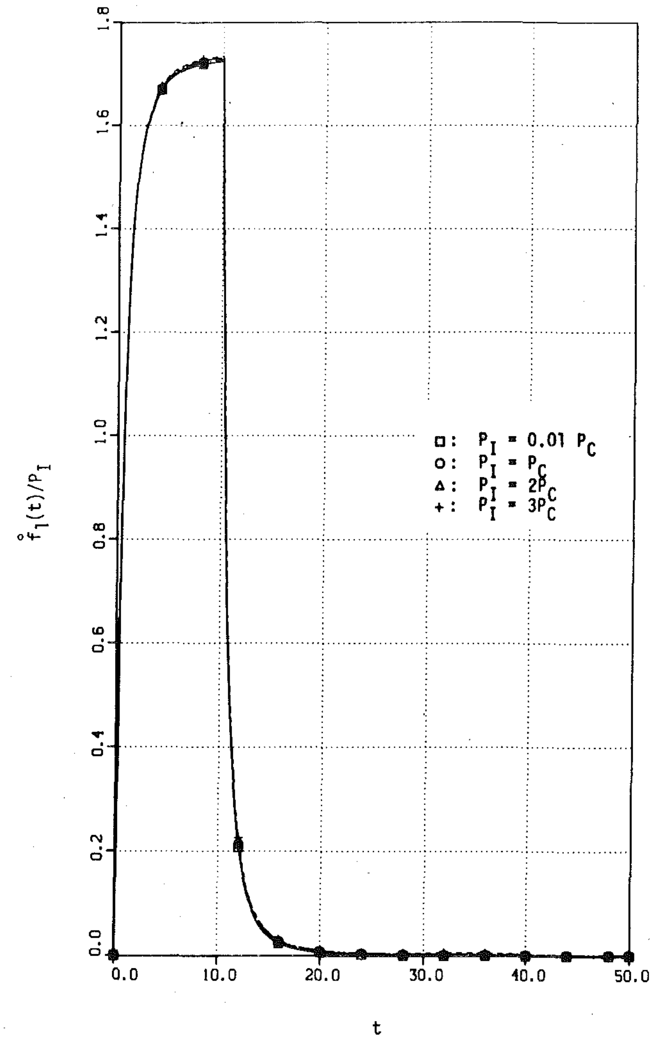

Fig. 3 $n = 1$ velocity response of the $\gamma = 10$ shell to rectangular incident waves with $T = 10$

envelopment phase, in which the incident wave front is passing over the shell, the response is essentially linear. The pressurization phase, in which the shell is essentially hydrostatically pressurized by the incident wave, is characterized by either oscillatory or exponential response, depending upon the magnitude of P_I. During the development phase, in which the back of the rectangular incident wave is passing over the shell, the response exhibits sudden, but modest reversal. Finally, the free-vibration phase is characterized by low-frequency sinusoidal motion. Clearly, the appearance of response overshoot during the free vibration phase depends upon exponential growth experienced during the pressurization phase, which, in turn, depends upon the magnitude of P_I.

Displacement response histories for the $n = 3$ lobar mode are shown in Fig. 5. The preceding description of $n = 2$ response is applicable here also. Especially visible in the $n = 3$ response histories is the virtually undamped nature of the sinusoidal motions during the free-vibration phase. This indicates that the surrounding fluid provides very small acoustic-radiation damping for these motions, which is to be expected when the characteristic structural wavelength $2\pi a/n$ is much smaller than the acoustic wavelength c/f, where f is the frequency of oscillation [1]. The $n = 4$ and $n = 5$ lobar modes have been included in these $\gamma = 10$ shell calculations, but exhibit peak displacements substantially smaller than that of the $n = 3$ mode. Hence response histories are not shown for these modes.

It is instructive to examine dynamic instability of the flexual modes

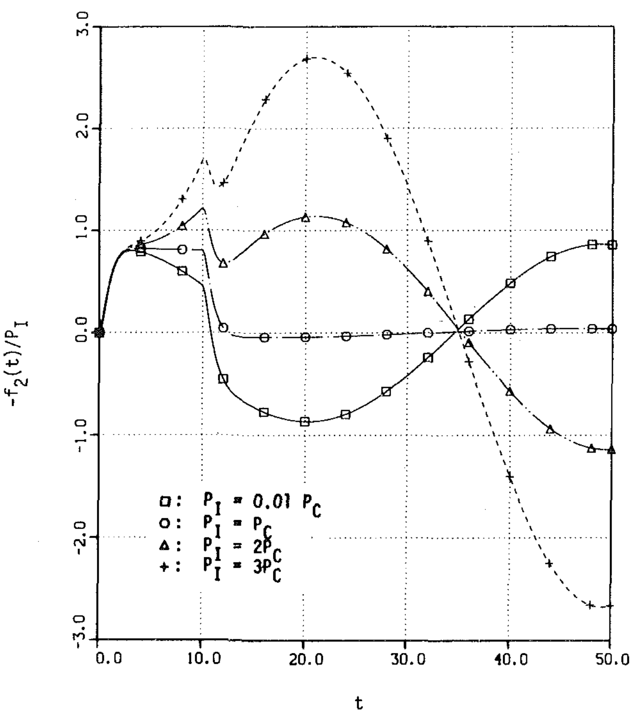

Fig. 4 $n = 2$ displacement response of the $\gamma = 10$ shell to rectangular incident waves with $T = 10$

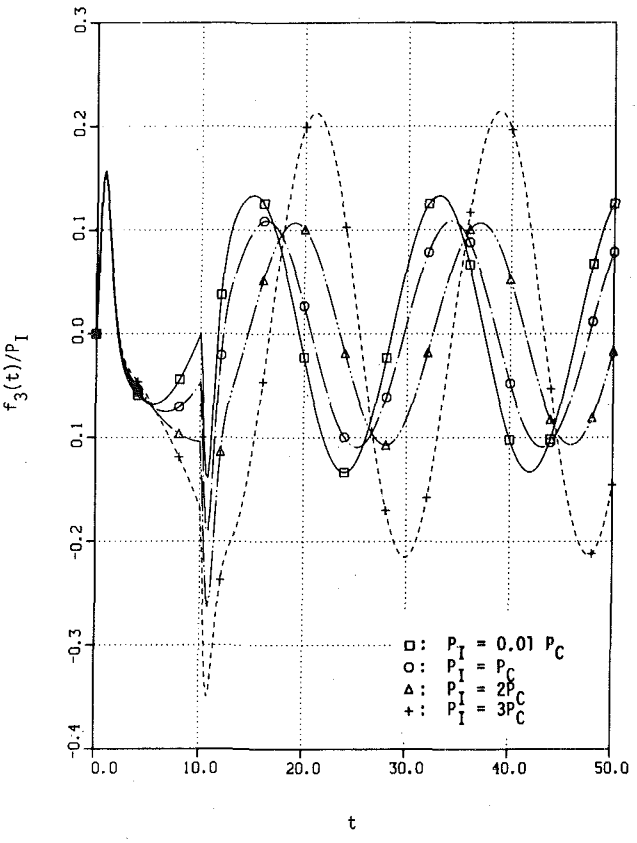

Fig. 5 $n = 3$ displacement response of the $\gamma = 10$ shell to rectangular incident waves with $T = 10$

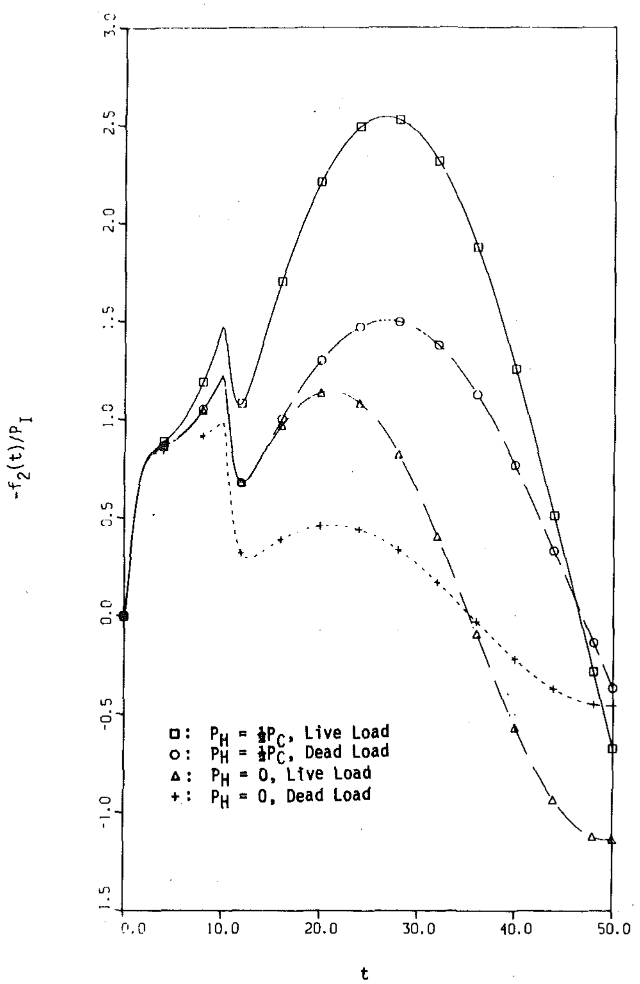

Fig. 6 $n = 2$ **displacement response of the** $\gamma = 10$ **shell to a rectangular incident wave with** $T = 10$, $P_I = 2P_c$

during the pressurization phase. During this phase, $n = 0$ displacement is approximately equal to the hydrostatic value

$$w_0(t) \approx -\frac{P_I}{\mu\beta} \tag{29}$$

Also, flexural response is relatively slow, so that $\dot{\varphi}_{Sn} \ll \varphi_{Sn}$ and, from the last of (25) and [7],

$$\varphi_{Rn} \approx -\varphi_{Sn}\int_0^\infty r_n(t')dt' = -\left(n - \frac{1}{2}\right)\varphi_{Sn} \tag{30}$$

Hence the fourth of (25) yields, with $u_{In} = 0$ for $n \gtrsim 2$, $2 \lesssim t \lesssim T$ [9],

$$\varphi_{Sn} \approx -\frac{1}{n}\dot{f}_n \tag{31}$$

Equations (29) and (31), along with the approximations $\dot{\varphi}_{S0} \approx 0$, $\ddot{w}_0 \approx 0$ and neglect of the triple summation in the second of (25), yield for flexural response during the pressurization phase

$$\left(\mu\frac{n^2+1}{n^2} + \frac{1}{n}\right)\ddot{f}_n + (n^2 - 1)\,(P_{Cn} - P_I)\,f_n = 0 \tag{32}$$

where $P_{Cn} = (n^2 - 1)\mu\beta\zeta$. This equation exhibits the effect of added fluid mass associated with low-frequency shell response; it also indicates that shell response is oscillatory for $P_I < P_{Cn}$ and exponential for $P_I > P_{Cn}$, as seen in Figs. 4 and 5. It is worth noting that, with the removal of P_I, (32) also governs flexural mode response during the free-vibration phase.

Modal response histories for excitation by incident step-exponential waves with decay constant $\lambda = 1$ are provided in [20]. These exhibit behavior similar to that observed in Figs. 2–5, with significant nonlinear effects appearing only in the $n \gtrsim 2$ harmonics.

3.2 Ambient Hydrostatic Pressure and Live Load. It is interesting to examine the effects of ambient hydrostatic pressure on the shock response of the $\gamma = 10$ shell. The modifications in (25) required for such an examination merely involve the replacement of w_0 by $w_0 - P_H/\mu\beta$ and of $\dot{\varphi}_{I0}$ by $\dot{\varphi}_{I0} - P_H$ where P_H is the magnitude of the hydrostatic pressure. With these replacements, the first of (25) remains the same, except that it now pertains to breathing motions about a static equilibrium radius of $1 - P_H/\mu\beta$. The second of (25) changes only to the extent that the term $\xi(n^2 - 1)^2$ is now multiplied by $(1 - P_H/P_{Cn})$, where P_{Cn} is given after (32).

For static stability, P_H must be less than the smallest of the P_{Cn}, which is $P_{C2} = P_C = 3\mu\beta\xi$. Hence the reduction in static equilibrium radius cannot exceed 3ξ, which is very small. Thus the principal effect of ambient hydrostatic pressure is the reduction of flexural stiffness, *which is a destabilizing influence.*

It is also interesting to examine inaccuracies introduced into transient response computations by the neglect of the "live-load" terms in (4). These terms account for the effects of finite translations and rotations of the shell on the work done by the normal pressure loading as referenced to the undeformed shell surface. All the terms in (4) except $p \cdot a \cdot w$ are live-load terms; when processed through the Fourier-decomposition and term-elimination operations of Subsections 2.1 and 2.2, they appear in nondimensional form as the last two summation terms in the last of (23). Following the application of Lagrange's equation (11) and the introduction of the fluid-structure interaction equations (24), live-load effects manifest themselves as the terms $[(n^2 - 1)/n^2]\,(\dot{\varphi}_{I0} + \dot{\varphi}_{S0})$ and $\ddot{w}_0$ in the second of (25).

Response computations designed to demonstrate the effects of ambient hydrostatic pressure and live load have been performed for the $\gamma = 10$ sandwich shell excited by both $T = 10$, $P_I = 2P_C$ rectangular and (in [20]) $\lambda = 1$, $P_I = 5P_C$ exponential incident waves. As would be expected, $n = 0$ and $n = 1$ response is unaffected by the introduction of ambient hydrostatic pressure or the omission of live-load terms in (25). In contrast, the response behavior of the $n = 2$ flexural mode is substantially affected, as indicated in Fig. 6. It is clear from this figure that ambient hydrostatic pressure and live load are both significant destabilizing influences for this mode.[1] The higher modes are much less influenced, however, as indicated by the $n = 3$ response histories of Fig. 7.

3.3 Shell Response. Modal response histories for $0 \le n \le 5$ have been superposed in accordance with (5) and (26) to construct the shell response histories of Fig. 8–10, which pertain to excitation by a $T = 10$, $P_I = 2P_C$ recntangular incident wave. Shown in Fig. 8 are deformational displacement histories, which constitute displacement histories with rigid-body motion removed, i.e., $w_D(\theta,t) = w(\theta,t) - f_1(t)\cos\theta$. It is seen that the effects of ambient hydrostatic pressure and live load are significant for excitation by the rather broad rectangular pulse; they are less significant, however, for narrower pulses.

Fig. 9 shows radial velocity histories at two points on the shell. The effects of the ambient hydrostatic pressure and live load are clearly negligible. Strain response histories are shown in Fig. 10 at locations selected to emphasize flexural and nonlinear-extensional contributions to total strain. The coincidence of the w_0 and $\epsilon_\theta{}^e$-histories in the figure demonstrates that the nonlinear-extensional term in the first of (26) is minuscule. This, along with the smallness of the flexural strain history, demonstrates that the strain response of the shell is dominated by the $n = 0$ breathing mode. Hence, peak strain in the shell is accurately estimated as

$$|\epsilon|_{\max} \approx (P_I{}^{-1}|w_0|_{\max}) \cdot NP_C \tag{33}$$

where $N = P_I/P_C$. For the shell of Fig. 2, for example, $P_I{}^{-1}|w_0|_{\max}$

---

[1] A development like that which produced (32), but which includes ambient hydrostatic pressure and excludes live-load terms, leads to a prediction of the coalescence, for $0 \le t \lesssim 10$, of the response histories of Fig. 10 with the circle and triangle designators.

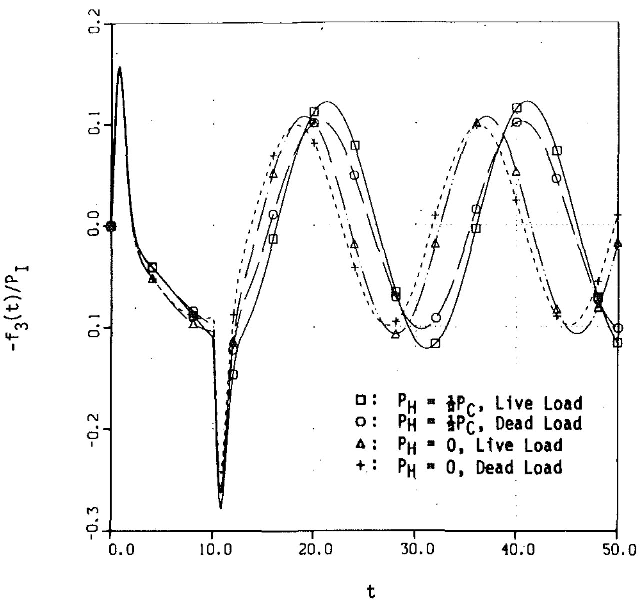

Fig. 7 $n = 3$ displacement response of the $\gamma = 10$ shell to a rectangular incident wave with $T = 10$, $P_I = 2P_C$

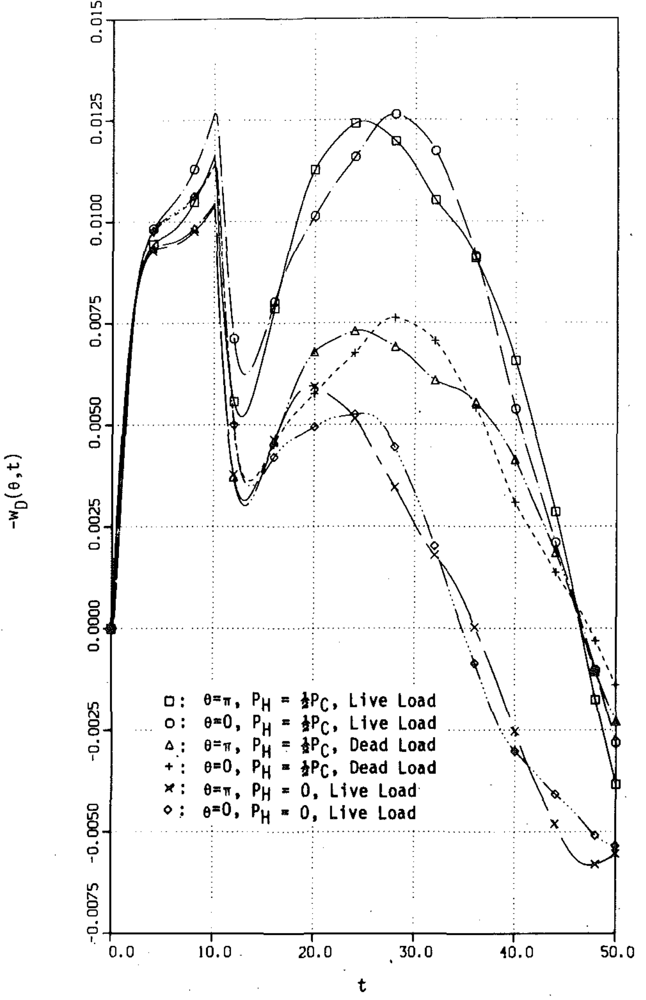

Fig. 8 Deformational displacement response of the $\gamma = 10$ shell to a rectangular incident wave with $T = 10$, $P_I = 2P_C$

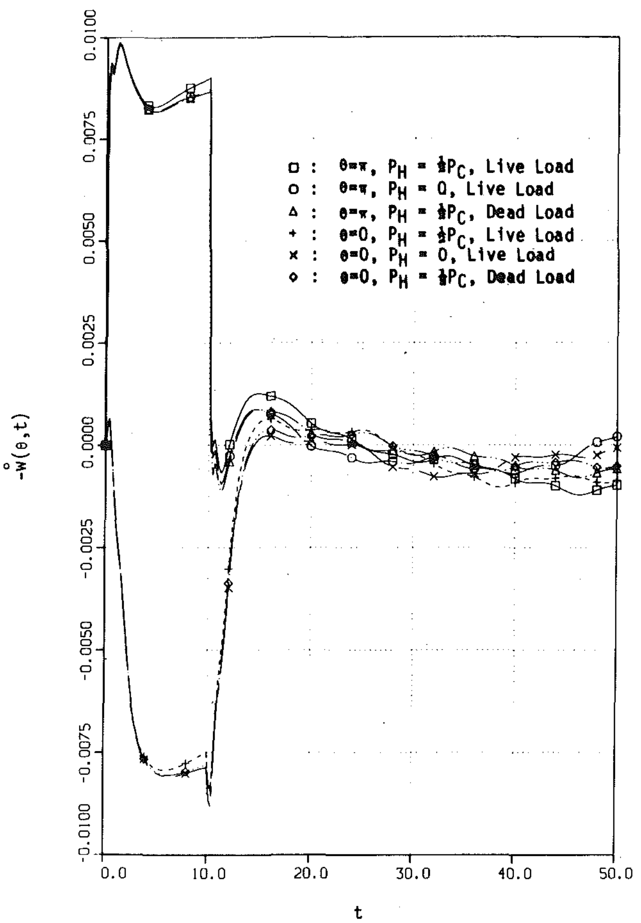

Fig. 9 Radial velocity response of the $\gamma = 10$ shell to a rectangular incident wave with $T = 10$, $P_I = 2P_C$

$= 1.125$ and $P_C = 3\mu\beta\xi_r = 2.405 \times 10^{-3}$; hence $|\epsilon|_{\max} \approx 0.27N$ percent, as suggested by Fig. 10.

3.4 Flexural Stiffness Effects. It is informative to compare the response behavior of a moderately stiffened ($\gamma = 5$) shell with that of the heavily stiffened ($\gamma = 10$) shell of Fig. 2–10. As the flexural stiffness of a sandwich shell is proportional to γ^2 [see the discussion preceding (10)], the P_C-value for the moderately stiffened shell is only one-quarter of that for the heavily stiffened shell. Hence, in order to maintain proper calibration between the excitation levels for the two shells, P_I-values of 0.04 P_C, 4 P_C, 8 P_C, and 12 P_C are used for the moderately stiffened shell.

Figs. 11–14 show modal response histories for the $\gamma = 5$ shell. A comparison of the first of these with Fig. 2 indicates that nonlinear effects in $n = 0$ response are more pronounced for the $\gamma = 5$ shell than they are for the $\gamma = 10$ shell; even so, they remain relatively unimportant. Rigid-body $n = 1$ response of the $\gamma = 5$ shell is virtually a duplicate of Fig. 3 in which nonlinear effects are barely discernible.

Fig. 12, which pertains to $n = 2$ response, displays significant nonlinear behavior, as does Fig. 4 for the $\gamma = 10$ shell. For the same value of $P_I \gtrsim P_C$, an $n = 2$ response peak during the free-vibration phase for the $\gamma = 5$ *shell considerably exceeds its counterpart for the* $\gamma = 10$ shell. This is suggested by (32), which predicts exponential response growth for $P_I > P_{C2} = P_C$ during the pressurization phase. For example, for the $\gamma = 5$ shell with $P_I = 12\,P_C$, the stiffness coefficient multiplying f_2 is $-3 \cdot 11 \cdot P_C = -99 \cdot \mu\beta \cdot 25\,h^2/12a^2$, which exceeds in magnitude its counterpart for the $\gamma = 10$ shell with $P_I = 3$ P_C, which is $-3 \cdot 2 \cdot P_C = -18 \cdot \mu\beta \cdot 100h^2/12a^2$.

It is clear that the nonlinear response of a flexural mode to rectangular-wave excitation depends critically upon the "initial conditions" for the pressurization and free-vibration phases and the value

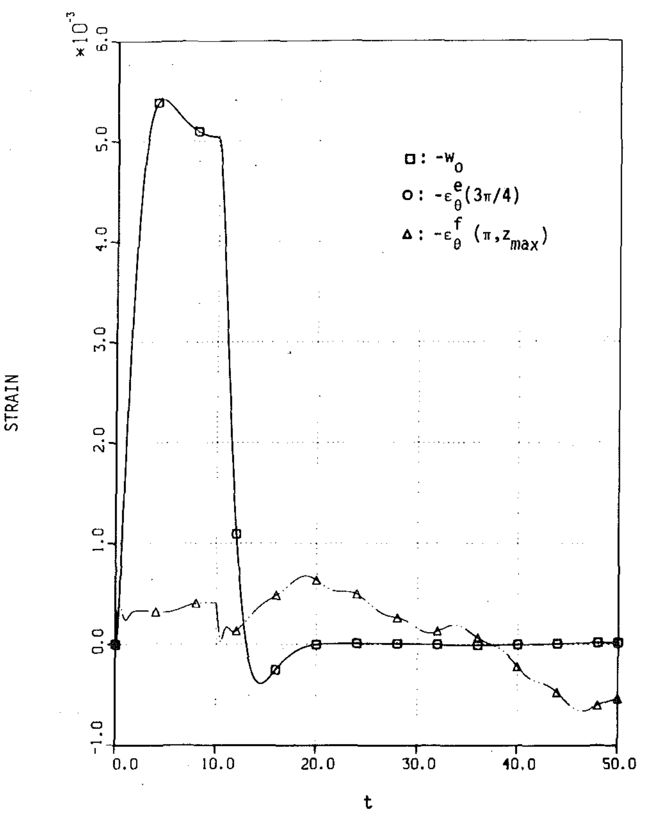

Fig. 10 Strain response of the $\gamma = 10$ shell to a rectangular incident wave with $T = 10$, $P_I = 2P_C$

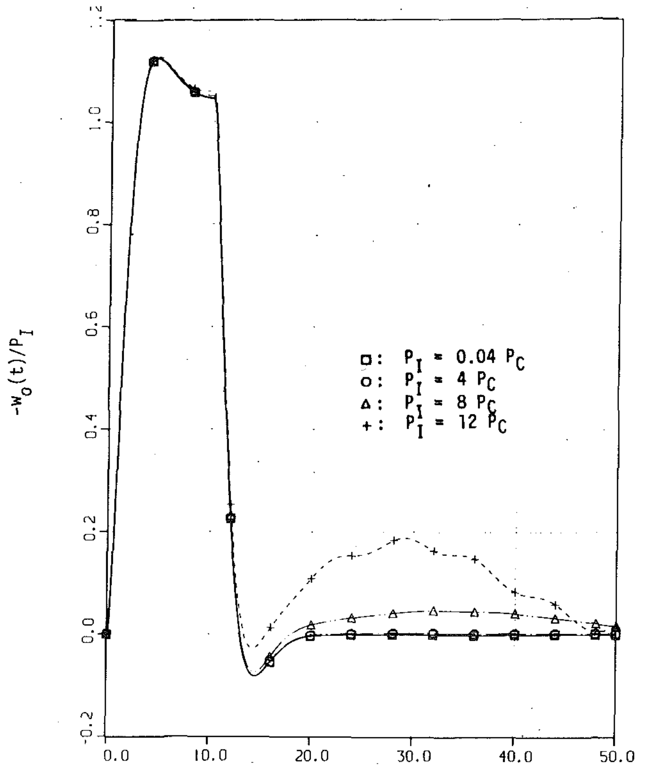

Fig. 11 $n = 0$ displacement response of the $\gamma = 5$ shell to rectangular incident waves with $T = 10$

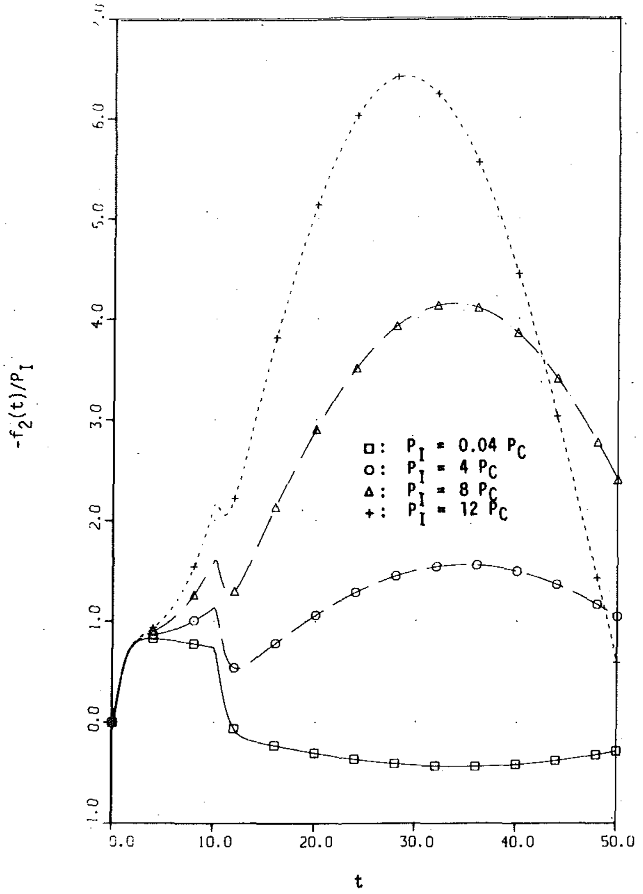

Fig. 12 $n = 2$ displacement response of the $\gamma = 5$ shell to rectangular incident waves with $T = 10$

of the pressurization-phase "stiffness" parameter in (32). With $P_I = NP_C$, (32) predicts exponential growth during the pressurization phase for those modes whose modal index satisfies the inequality $n < (3N + 1)^{1/2}$. Hence a large value of N implies that many flexural modes may contribute significantly to shell response, while a small value of N implies that only the lowest flexural modes need be considered. This is illustrated in Fig. 13, which shows that the $n = 4$ mode of the $\gamma = 5$ shell responds strongly, especially for $P_I = 12\ P_C$. This is in contrast to $n = 4$ response for the $\gamma = 10$ shell, which is so small that it is not even included in the discussion of Subsection 3.1.

The increased participation of the higher flexural modes in the response of the $\gamma = 5$ shell suggests that flexural strain might now play a much more important role than that portrayed in Fig. 10 for the $\gamma = 10$ shell. This is not the case, however, as shown in Fig 14, because the increase in flexural mode response is essentially negated by the decrease in the distance between the outer fibers of the shell. There is a discernible nonlinear-extensional contribution to total strain, but it is hardly significant.

The preceding comparison of $\gamma = 5$ and $\gamma = 10$ shell response illustrates the dissimilarities between the response behavior of moderately stiffened and heavily stiffened shells to a given incident wave. The contrast between an unstiffened shell and a moderately stiffened shell is even greater. For example, $P_I = 8\ P_C$ for $\gamma = 5$ corresponds to $P_I = 200\ P_C$ for $\gamma = 1$. Thus, for this incident-wave magnitude, (32) predicts exponential growth during the pressurization phase for the $n < 25$ flexural modes of the $\gamma = 1$ shell, while it predicts such growth for only the $n < 5$ flexural modes of the $\gamma = 5$ shell. Experimental observations of short-structural-wavelength instability are reported in [21, 22].

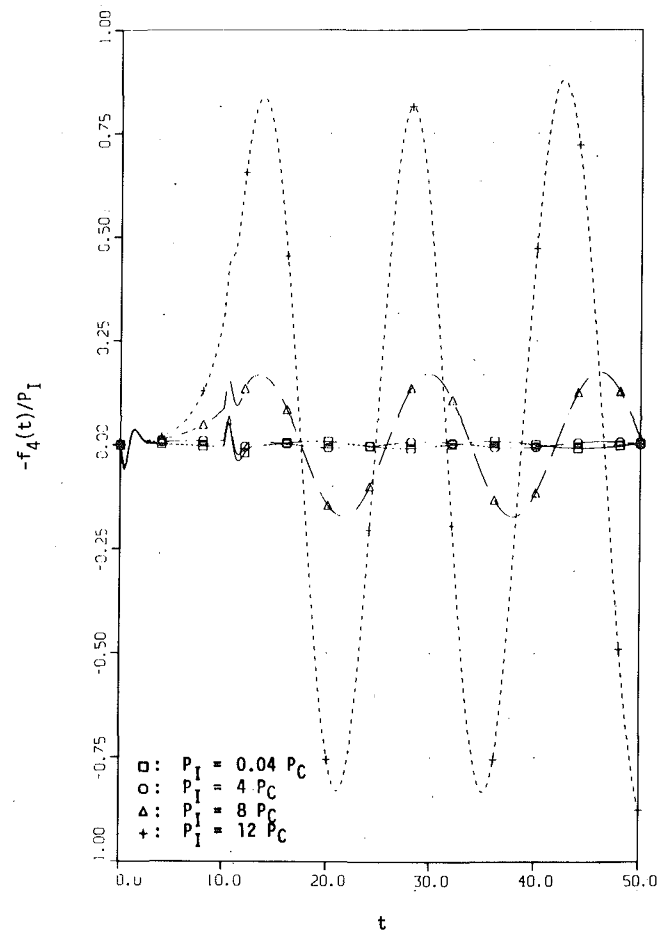

Fig. 13 $n = 4$ **displacement response of the** $\gamma = 5$ **shell to rectangular incident waves with** $T = 10$

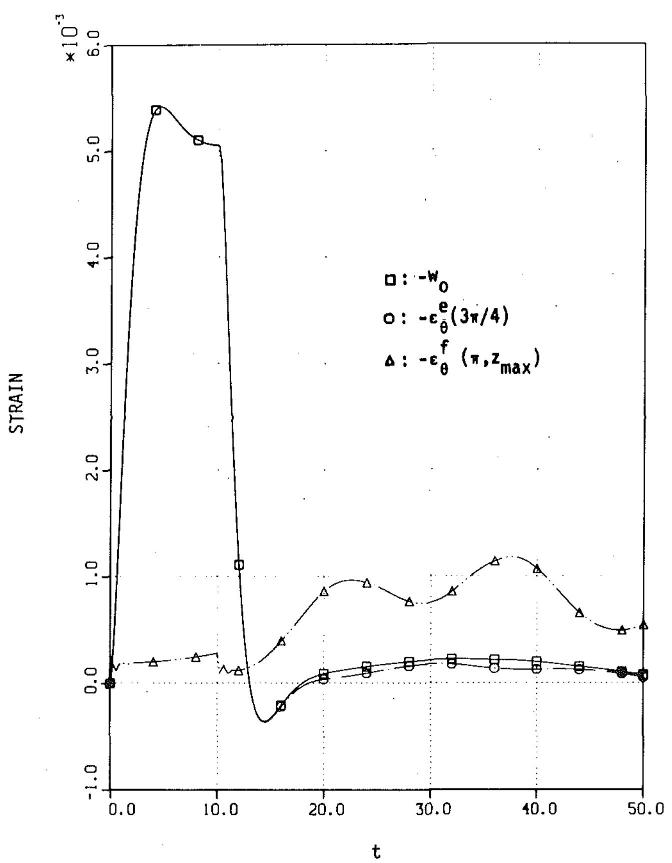

Fig. 14 Strain response of the $\gamma = 5$ **shell to a rectangular incident wave with** $T = 10$, $P_I = 8P_C$

Conclusions

This study has dealt with the dynamic instability of an infinite, elastic, submerged, circular cylindrical shell excited by a transverse, transient acoustic wave. Circumferential Fourier decomposition of the field quantities appearing in appropriate energy functionals, followed by consistent elimination of high-order terms, has led to rather simple shell response equations with satisfactory attributes. The fluid-structure interaction has been treated rigorously in accordance with the residual potential formulation, which has been used successfully in a number of previous studies.

Numerical results have been presented in the form of transient response histories pertaining to excitation by plane waves of rectangular pressure-profile. Examination of these results has led to the following conclusions:

1 Dynamic instability effects are significant only with respect to flexural shell response.

2 The dynamically unstable flexural response that occurs while the incident-wave profile passes over the shell profoundly affects subsequent free-vibration flexural response.

3 For peak total strains smaller than 1 percent, only the lowest flexural modes of a heavily stiffened shell experience dynamic instability; if the degree of stiffening is reduced, however, higher flexural modes exhibit such instability until, in the limit of an unstiffened shell, numerous flexural modes are involved. Hence, the response of an unstiffened shell to a given incident wave is significantly different than that of an appreciably stiffened shell to the same wave.

4 $n = 0$ breathing motion dominates strain response, and quasi-linear (especially $n = 1$ translational) motions dominate velocity response; nonlinear flexural motions are important only with regard to deformational displacement response, i.e., displacement response exclusive of rigid-body translation.

5 As a consequence of the preceding conclusions, live-load forcing terms and ambient hydrostatic pressure substantially affect deformational displacement response, but have minor impact on velocity and strain response.

6 The live-load terms in the surface-pressure work potential that involve pressure gradients may be neglected [see (4)].

Acknowledgments

The authors express their appreciation to their colleagues B. O. Almroth, F. A. Brogan, and P. G. Underwood for their valuable suggestions regarding both theoretical and computational aspects of this study. Additional thanks are due Dr. Nicholas Basdekas of the Office of Naval Research for sharing his knowledge of the literature. This study was sponsored by the Defense Nuclear Agency under Contract No. DNA0001-78-C-0029.

References

1 Geers, T. L., "Transient Response Analysis of Submerged Structures," *Finite Element Analysis of Transient Nonlinear Structural Behavior*, Belytschko, T., Osias, J. R., and Marcal, P. V., eds., AMD, Vol. 14, ASME, New York, 1975, pp 59–84.

2 DiMaggio, F. L., "Effect of an Acoustic Medium on the Dynamic Bucklin of Plates," ASME JOURNAL OF APPLIED MECHANICS, Vol. 23, June 1959, pp. 201–206.

3 Deng, Z.-F., and Popelar, C. H., "Dynamic Stability of a Cylindrical Shell in an Acoustic Medium," *Journal of the Acoustical Society of America*, Vol. 52, No. 5, Nov. 1972, pp. 1430–1436.

4 Mnev, Y. N., and Pertsev, A. K., *Hydroelasticity of Shells*, FTD-MT-24-119-71, Foreign Technology Division, Wright-Patterson Air Force Base, Ohio, Aug. 1971.

5 Grigoliuk, E. I., and Gorshkov, A. G., *Nonstationary Hydroelasticity of Shells*, Sudostroenie, Leningrad, 1974, translated by M. D. Friedman, LMSC-D567983, Lockheed Missiles and Space Company, Sunnyvale, Calif., Nov. 1977.

6 Longhitano, R., and Klosner, J. M., "Nonlinear Dynamics of Submerged Hemispherical Shells," AE/AM Rpt. No. 74-4, Polytechnic Institute of New York, New York, Feb. 1974.

7 Geers, T. L., "Excitation of an Elastic Cylindrical Shell by Transient Acoustic Wave," ASME JOURNAL OF APPLIED MECHANICS, Vol. 36, Sept. 1969, pp. 459–469.

8 Geers, T. L., "Residual Potential and Approximate Methods for Three-Dimensional Fluid-Structure Interaction Problems," *Journal of the Acoustical Society of America*, Vol. 49, No. 5, May 1971, pp. 1505–1510.

9 Geers, T. L., "Scattering of a Transient Acoustic Wave by an Elastic Cylindrical Shells," *Journal of the Acoustical Society of America*, Vol. 51, No. 5, May 1972, pp. 1640–1651.

10 Sanders, J. L., "Nonlinear Therories for Thin Shells," *Quarterly of Applied Mathematics*, Vol. 21, No. 1, Apr. 1963, pp. 21–26.

11 Cohen, G. A., "Conservativeness of a Normal Pressure Field Acting on a Shell," *AIAA Journal*, Vol. 4, No. 10, Oct. 1966, p. 1886.

12 Brush, D. O., and Almroth, B. O., *Buckling of Bars, Plates, and Shells*, McGraw-Hill, New York, 1975.

13 Forrestal, M. J., "Response of an Elastic Cylindrical Shell to a Transverse Acoustic Pulse," ASME JOURNAL OF APPLIED MECHANICS, Vol. 35, Sept. 1968, pp. 614–616.

14 Lord Rayleigh, *Theory of Sound*, 2nd ed., Vol. 2, Dover Press, New York, 1975.

15 Slater, J. C., and Frank, N. H., *Mechanics*, McGraw-Hill, New York, 1947.

16 Liessa, "Vibration of Shells," NASA SP-288, National Aeronautics and Space Administration, Washington, D.C., 1973.

17 Goodier, J. N., and McIvor, I. K., "The Elastic Cylindrical Shell Under Nearly Uniform Radial Impulse," ASME JOURNAL OF APPLIED MECHANICS, Vol. 31, June 1964, pp. 259–266.

18 Lindberg, H. E., "Stress Amplification in a Ring Caused by Dynamic Instability," ASME JOURNAL OF APPLIED MECHANICS, Vol. 41, June 1974, pp. 392–400.

19 Hubka, W. F., "Dynamic Buckling of the Elastic Cylindrical Shell Subjected to Impulsive Loading," ASME JOURNAL OF APPLIED MECHANICS, Vol. 41, June 1974, pp. 401–411.

20 Geers, T. L., and Yen, C.-L., "Dynamic Instability of an Elastic Cylindrical Shell Excited by a Transient Acoustic Wave," DNA 5026Z, Defense Nuclear Agency, Washington, D.C., July 1979.

21 Anik'ev, I. I., Vorotnikova, M. I., and Kononenko, V. O., "Some Experimental Results on the Effect of a Lateral Shock Wave in Water on Cylindrical Shells," *Prikladnaia Mekhanika*, Vol. 7, No. 9, 1971, pp. 106–109.

22 Anik'ev, I. E., and Vorotnikova, M. I., "An Experimental Method for Investigating Nonsteady-State Deformation of Shells Acted on by a Shock Wave," *Izv. ANSS R, Mekhanika Tverdogo Tela*, Vol. 10, No. 6, 1975, pp. 141–145.

M. J. Forrestal
D. B. Longcope
F. R. Norwood

Sandia National Laboratories
Albuquerque, New Mex. 87185
Mems. ASME

A Model to Estimate Forces on Conical Penetrators Into Dry Porous Rock[1]

A model to predict the forces on conical-nosed penetrators for normal impact into dry rock targets is developed. The target medium is described by a linear hydrostat, a linear shear failure-pressure relation, and the material density. A cylindrical cavity expansion approximation to the target response permits one-dimensional wave propagation calculations in the radial coordinate. The equations of motion are reduced, via a similarity transformation, to a nonlinear ordinary differential equation. This equation is solved numerically by a shooting technique which employs an asymptotic expansion to the solution near the wave front. Results include stress wave profiles in the target and curves for the stress on the penetrator nose as a function of its velocity for a wide range of realistic target parameters. Finally, results from the theory are compared with the deceleration history of a penetrator in a field test and reasonable correlation is observed.

Introduction

The penetration of projectiles into targets has been studied for a wide range of applications, many of which are discussed in [1–3]. For geological targets interest is usually focused on the prediction of penetration depth, penetrator deceleration history or stresses on the nose. For the calculation of these quantities, recent solution techniques may be grouped into three main categories:

1 Empirical equations for final depth of penetration based on full scale test data [4–6].

2 Models which use a cylindrical [7, 8] or spherical [9, 10] expansion approximation to the target response and allow for one-dimensional wave propgation.

3 Detailed numerical solutions which employ two-dimensional wave codes [2, 11].

All of these approaches have advantages and limitations which must be considered for a given application.

The present investigation falls into category (2) and is concerned with the prediction of forces on conical-nosed penetrators during normal impact into dry rock targets. The cylindrical cavity expansion approximation considers the target as thin independent layers normal to the penetration direction and allows only radial target motion, which is reasonable for sharply pointed penetrators. The constitutive description of the target contains minimum detail; a linear hydrostat and a linear shear failure-pressure relation. This material description matches closely triaxial test data of cored field samples [12, 13] from the Sandia Tonopah Test Range, Nevada. The present material description is different from that used in the other cavity expansion solutions which model the targets with locked hydrostats.

Results of this study include stress wave profiles in the target and families of curves for the stress on the penetrator nose as a function of its velocity for a wide range of realistic target parameters. Target wave profiles indicate that the stress diminishes rapidly with distance from the penetrator nose when shear strength is significant. Finally, results from the theory are used to calculate the rigid-body deceleration history of a full-scale penetrator which entered a layer of Mt. Helen welded tuff. This prediction is compared with measurements from two on-board accelerometers [14] and reasonable agreement is found.

Formulation of the Problem

A rigid projectile with a conical nose penetrates a uniform target medium with normal incidence. The problem is axisymmetric and is further simplified by applying the cylindrical cavity expansion approximation. As shown in Fig. 1, this approximation considers the target as thin layers normal to the direction of penetration and simplifies the analysis to one-dimensional wave propagation in the radial coordinate. This model assumes that all motion in individual target layers is one-dimensional, radial, and independent of any other layer.

---

[1] This work was supported by the U. S. Department of Energy.

Contributed by the Applied Mechanics Division of THE AMERICAN SOCIETY OF MECHANICAL ENGINEERS, for presentation at the 1981 Joint ASME/ASCE Applied Mechanics, Fluids Engineering, and Bioengineering Conference, University of Colorado, Boulder, Colo., June 22–27, 1981.

Discussion on this paper should be addressed to the Editorial Department, ASME, United Engineering Center, 345 East 47th Street, New York, N. Y. 10017, and will be accepted until June 1, 1981. Readers who need more time to prepare a Discussion should request an extension from the Editorial Department. Manuscript received by ASME Applied Mechanics Division, April, 1980; final revision, September, 1980. Paper No. 81-APM-15.

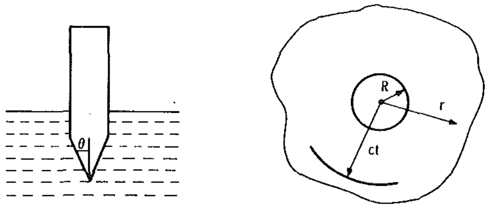

Fig. 1 Geometry of the problem

The target medium is described by a linear hydrostat, a linear shear failure-pressure relation [15], and density. Many rock materials with low water content can be modeled with these idealizations; e.g., see the data for Mount Helen welded tuff shown in Figs. 2 and 3. These hydrostat and shear failure data were obtained from static triaxial tests of cored field samples from the Sandia Tonopah Test Range, Nevada. Additional data at high strain rates with gas gun experiments [16] have shown rate effects to be negligible.

An idealized layer of target material is expanded by a conical nose with half cone angle θ as shown in Fig. 1. The equations of momentum and mass conservation in cylindrical, Lagrangian coordinates are

$$\rho_0 r \frac{\partial^2 u}{\partial t^2} = -(r+u)\frac{\partial \sigma_r}{\partial r} - (\sigma_r - \sigma_c)\frac{\partial}{\partial r}(r+u) \tag{1a}$$

$$\rho_0 r = \rho(r+u)\left(1 + \frac{\partial u}{\partial r}\right) \tag{1b}$$

where ρ_0, ρ are the initial and current densities, u is the radial displacement, and σ_r, σ_c are the radial and circumferential components of Cauchy stress, taken positive in compression. Elastic strains are neglected and the material is described by the hydrostat

$$p = K(1 - \rho_0/\rho) = K\eta \tag{2a}$$

and the shear failure-pressure relation

$$\tau = \sigma_r - \sigma_c = \mu p \tag{2b}$$

where p is the hydrostatic pressure

$$p = \tfrac{1}{3}(\sigma_r + 2\sigma_c) \tag{2c}$$

In equation (2c) it is assumed that $\sigma_z = \sigma_c$ during a penetration event, which matches the physical situation for triaxial tests [12]. Equations (2b,c) are combined to give

$$\sigma_r = (1 + 2\mu/3)p. \tag{2d}$$

Equations (2a, b, d) are used to eliminate the stress components from equations (1a, b) which become

$$\rho_0 r \frac{\partial^2 u}{\partial t^2} + (1 + 2\mu/3)K(r+u)\frac{\partial \eta}{\partial r} + \mu K \eta \left(1 + \frac{\partial u}{\partial r}\right) = 0 \tag{3a}$$

$$\eta + \frac{\partial u}{\partial r} + \frac{u}{r}\left(1 + \frac{\partial u}{\partial r}\right) = 0 \tag{3b}$$

The conical penetrator traveling at constant velocity V_z begins to open a circular cavity in a given layer at time $t = 0$. This displacement at the cavity wall, Lagrangian coordinate $r = 0$, is given by

$$u(0, t) = Vt, \qquad V = V_z \tan\theta. \tag{4}$$

The other boundary condition requires that the radial displacement at the wave front is zero and the formulation of the cavity expansion problem is complete.

Analyses

Similarity Solution. In this section equations (3a, b) are solved by the similarity method which reduces the partial differential equations to nonlinear ordinary differential equations. As discussed in [17], similarity transformations have been previously applied to problems in gas dynamics with the Eulerian spatial description.

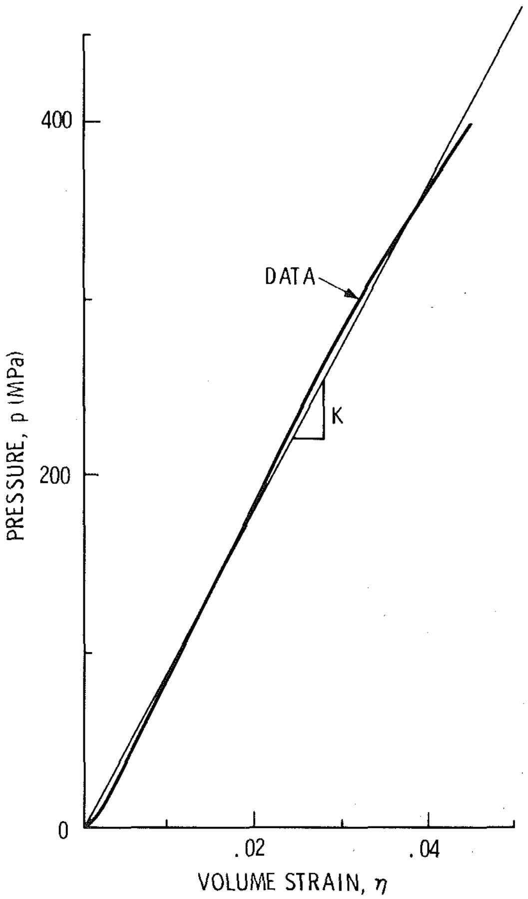

Fig. 2 Idealized linear hydrostat and data from [12]

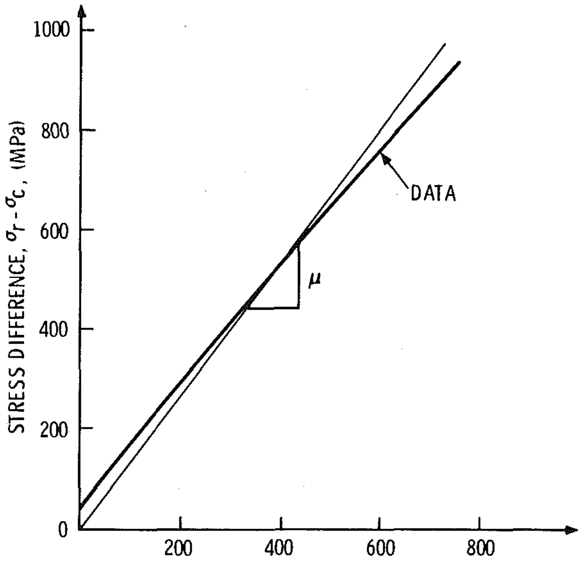

Fig. 3 Idealized linear shear failure relation and data from [12]

Following the procedures outlined in [17], the dimensionless variables $\bar{u}$, ξ are introduced

$$u(r, t) = ct\bar{u}(\xi) \tag{5a}$$

$$\xi = r/ct, \qquad c^2 = (1 + 2\mu/3)K/\rho_0 \tag{5b}$$

The wave-front velocity c for the medium described by equations (2a, b, c) is obtained from the momentum and mass conservation equations across the wave front [15]. The dimensionless radial coordinate ξ ranges from $\xi = 0$ corresponding to the position of the expanding cavity to $\xi = 1$ which is the location of the wave front. Equation (2*a*) indicates that η is dimensionless and no transformation is required for this variable. With these transformations the equations of motion and mass conservation become

$$\xi^3 \frac{d^2\bar{u}}{d\xi^2} + (\xi + \bar{u})\frac{d\eta}{d\xi} + \left(\frac{3\mu}{3 + 2\mu}\right)\eta\left(1 + \frac{d\bar{u}}{d\xi}\right) = 0 \qquad (6a)$$

$$\eta + \frac{d\bar{u}}{d\xi} + \frac{\bar{u}}{\xi}\left(1 + \frac{d\bar{u}}{d\xi}\right) = 0 \qquad (6b)$$

The boundary conditions at the cavity wall and wave front are

$$\bar{u}(0) = V/c, \qquad \bar{u}(1) = 0. \qquad (6c)$$

During the analysis phase of this study it was found that the additional transformation

$$\bar{u}(\xi) = \bar{U}(\xi) - \xi \qquad (7)$$

could condense the length of equations and a single equation in $\bar{U}$ is given by

$$\left(\frac{\xi^4 - \bar{U}^2}{\bar{U}}\right)\frac{d^2\bar{U}}{d\xi^2} + \left[\frac{\bar{U}}{\xi} + \frac{\bar{\mu}\xi}{\bar{U}}\right]\frac{d\bar{U}}{d\xi} - (1 + \bar{\mu})\left(\frac{d\bar{U}}{d\xi}\right)^2 = 0 \qquad (8a)$$

in which

$$\bar{\mu} = 3\mu/(3 + 2\mu) \qquad (8b)$$

The boundary conditions are

$$\bar{U}(0) = V/c, \qquad \bar{U}(1) = 1 \qquad (8c)$$

and the radial stress in the medium is given by

$$\sigma_r = (1 + 2\mu/3)K\eta, \qquad \eta = 1 - \frac{\bar{U}}{\xi}\frac{d\bar{U}}{d\xi} \qquad (9)$$

Numerical Procedure and Results. Equation (8*a*) is a nonlinear, ordinary differential equation and its solution is obtained numerically by a Runge-Kutta integrating subroutine [18]. For this numerical procedure the equivalent system

$$\frac{d\bar{U}}{d\xi} = \xi N \qquad (10a)$$

$$\frac{dN}{d\xi} = \frac{(1 + \bar{\mu})\xi\bar{U}N^2 - \xi(\bar{\mu} + \xi^2)N}{\xi^4 - \bar{U}^2} \qquad (10b)$$

is introduced. The integrating routine requires initial values of $\bar{U}$ and N specified at an end point, but for this application boundary conditions are specified at $\xi = 0$ and $\xi = 1$. Consequently, an iterative shooting method is used. The usual procedure is to guess a value of N at the starting point, perform the integration, and compare the computed value of $\bar{U}$ at the other end of the interval with the specified value. If necessary, the process is repeated with a new value of N until agreement is reached in the computed and specified values of $\bar{U}$. This process is modified in the solution of equations (10*a*, *b*) because of the singularity at $\xi = 1$ in equation (10*b*).

Special treatment is given to the end points, $\xi = 0$ and $\xi = 1$. Equation (8*a*) has an apparent singularity at $\xi = 0$ which is removed by the choice of equations (10*a*, *b*). An actual singularity exists at the wave front $\xi = 1$ and numerical values from asymptotic expansions are used to start the integration at a point near the wave front. Expansions for $0 < 1 - \xi \ll 1$ which satisfy the condition $\bar{U}(1) = 1$ are

$$\bar{U} = \xi + A(1 - \xi)^\beta + \ldots, \qquad \xi \to 1 \qquad (11a)$$

$$N = 1/\xi[1 - \beta A(1 - \xi)^{\beta-1} + \ldots], \qquad \xi \to 1 \qquad (11b)$$

$$\beta = (3 + \bar{\mu})/2 \qquad (11c)$$

where A is an undetermined constant and . . . indicates higher-order terms. Equation (11*a*) indicates a singularity in the second derivative of $\bar{U}$ for $\bar{\mu} < 1$ ($\mu < 3$) which is a practical range for this study. These expansions are determined in the usual way by assuming $\bar{u} = \bar{U} - \xi$ has the form $(1 - \xi)^\beta$ and substituting into equation (8*a*) to determine β.

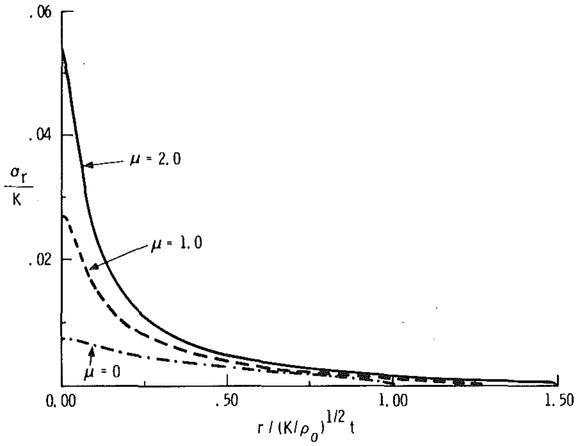

Fig. 4 Radial stress profiles for $V/(K/\rho_0)^{1/2} = 0.047$

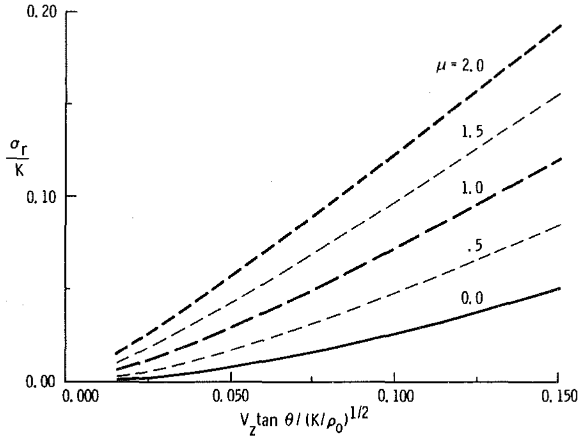

Fig. 5 Radial stress component on the conical nose

An expression is derived which gives a crude, but adequate initial estimate of A to start the numerical procedure. A three term Taylor series for $\bar{U}$ about $\xi = 0$ which satisfies condition (8*c*) is developed.

$$\bar{U} = V/c + B\xi^2 + \ldots, \qquad \xi \to 0 \qquad (12)$$

where B is an unknown constant. Then $\bar{U}$ and its derivative from equations (11*a* and 12) are matched at an appropriate point, $\xi = V/c$, to determine A and B. The resulting expression for A is

$$A = \frac{V/c}{2(1 - V/c)^{\beta-1}[1 - (1 - \beta/2)V/c]} \qquad (13)$$

The strategy for the numerical solution is to use the asymptotic expansions to start the solution at a point slightly less than $\xi = 1$ and integrate toward $\xi = 0$ where the numerical integration is well behaved. Using equation (12) an initial value of A is estimated, and $\bar{U}$ and N are evaluated at $\xi = 1 - 10^{-6}$ from equations (11*a*, *b*). Next, the numerical integration of equations (10*a*, *b*) is performed up to the point $\xi = 10^{-6}$, although it can be performed arbitrarily close to $\xi = 0$. Depending on the difference $\bar{U} - V/c$ at $\xi = 10^{-6}$, a new estimate for A is made and the process repeated until the difference in $\bar{U} - V/c$ is less than 10^{-6}.

Computed values of $\bar{U}$, $d\bar{U}/d\xi$ and equations (9) are used to produce the results of Figs. 4–6. The stress profiles in Fig. 4 are for a single cavity expansion velocity and three values of the shear strength pa-

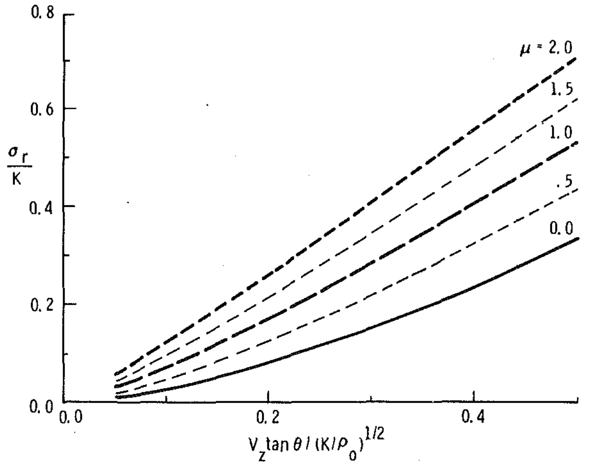

Fig. 6 Radial stress component on the conical nose

rameter. These profiles show the wave-front stresses are zero, as indicated by equations (9, 11a), and that the radial stress increases monotonically from the wave front to the cavity boundary. Fig. 4 also shows the effect of shear strength and that radial stress diminishes rapidly with distance from the penetrator nose when shear strength is important. Figs. 5 and 6 give generalized curves for the radial component of stress at the cavity surface as a function of the cavity expansion velocity for a realistic range of values of the target shear strength parameter for dry rock targets. As discussed in the next section, the curves in Figs. 5 and 6 may be easily used to predict stress on a penetrator nose.

Force on the Penetrator and Deceleration. The similarity solution for this problem indicates that the radial stress component at the cavity wall or the surface of the conical penetrator is constant for a given velocity V. Thus the stress distribution on the conical nose is spatially constant. The incremental radial ring force on the conical nose for a thin target layer with thickness dz is

$$dF_r = 2\pi\sigma_r(0)R(z)dz \tag{14a}$$

and the incremental axial force is

$$dF_z = dF_r \tan\theta \tag{14b}$$

thus

$$F_z = 2\pi\sigma_r(0)\int_0^l z\tan^2\theta\, dz = \pi\bar{r}^2\sigma_r(0) \tag{15}$$

where $\bar{r}$ is the radius of the penetrator aft body, l is the nose length, and $\sigma_r(0)$ can be obtained from Figs. 5 and 6.

As will be discussed later, acceleration-time is measured in field tests. Convenient formulas for acceleration as a function of time or penetration distance can be obtained by linearizing the data in Figs. 5 and 6. These data have only slight curvature and can be linearized without substantial loss of accuracy. For linear curves which pass through the origin, the radial stress and axial resisting force can be written as

$$\sigma_r = \alpha V_z \tan\theta(K\rho_0)^{1/2} \tag{16a}$$

$$F_z = \alpha\pi\bar{r}^2 V_z \tan\theta(K\rho_0)^{1/2} \tag{16b}$$

where α is the slope of the linear fit to the curves in Figs. 5 and 6.

The axial velocity V_z is now permitted to vary with time. From equation (16b) the equation for rigid-body motion of the penetrator with mass m is

$$m\frac{dv}{dt} = -bv, \quad b = \alpha\pi\bar{r}^2\tan\theta(K\rho_0)^{1/2} \tag{17}$$

Equation (17) with the initial condition $v(t = 0) = V_0$ has solutions

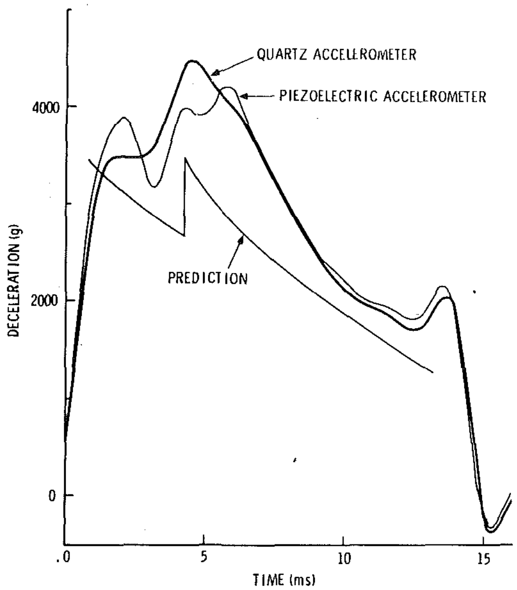

Fig. 7 Deceleration-time measurements and prediction for a field test

$$s = mV_0/b[1 - \exp(-bt/m)] \tag{18a}$$

$$v = V_0\exp(-bt/m) \tag{18b}$$

$$a = -bV_0/m\exp(-bt/m) \tag{18c}$$

for distance, velocity, and acceleration. From equations (18a, b, c)

$$v = V_0[1 - sb/mV_0] \tag{18d}$$

$$a = -bV_0/m[1 - sb/mV_0] \tag{18e}$$

which describe velocity and deceleration as a function of penetration depth.

Comparison With a Field Test

There is currently only one penetrator test into a natural, undisturbed rock layer for which acceleration-time data have been successfully retrieved [14] and the appropriate material data are available. The target was a layer of welded tuff located at the Sandia, Tonopah Test Range, Nevada. Details of the site characterization and the material properties required to apply the predictions derived in this study are presented in [12]. For this test, the penetrator had total length 1.52 m (60.0 in.), outer diameter 0.165 m (6.50 in.), an ogive nose profile with 9.25 CRH (caliber radius head), nose length 0.495 m (19.5 *in.), and mass 182 kg (400 lb). The penetrator was accelerated to a* vertical velocity of 411 m/s (1350 ft/s) with a Davis Gun [19]. A 53.2 kg (117 lb) pusher plate which fits the internal diameter of the gun barrel is attached to the end of the penetrator and follows the penetrator until the pusher plate impacts the rock surface. Two accelerometers (Endevco 225-MZ piezoelectric and Kistler 805 A quartz) were packaged within the penetrator and these acceleration-time data, filtered to 500 Hz, are shown in Fig. 7. The data were filtered in order to estimate the rigid-body motion of the penetrator and eliminate the vibrations associated with mounting the instrumentation package.

The theory derived in this study is for a penetrator with a conical nose; whereas, the penetrator used in the field test had an ogival nose shape. Based on several hundred full-scale soil penetration tests, Young [4, 5] presents nose performance coefficents for several ogival and conical nose shapes. These deceleration and final depth of penetration data indicate that a 9.25 CRH (caliber radius head) nose and a conical nose with half-conical angle $\theta = \tan^{-1}(1/4)$ are nearly identical. The analysis used for comparison with this rock penetration test assumes that the ogival nose is equivalent to a conical nose with $\theta = \tan^{-1}(1/4)$. Material data required for application of the theory are

$$\rho_0 = 1.97 \times 10^3\ \mathrm{kg/m^3}, \qquad K = 9.52 \times 10^3\ \mathrm{MPa}, \qquad \mu = 4/3;$$

as deduced from Figs. 2 and 3.

With the foregoing data the resisting stress on the penetrator nose can be obtained from Fig. 5; $V_z \tan\theta/(K/\rho_0)^{1/2} = 0.047$, $\sigma_r/K = 0.037$. From equation (18c) with $\alpha = 0.80$ the deceleration-time profile can be calculated and this prediction is compared with the field measurements in Fig. 7. For this calculation, it is assumed that no deceleration takes place until 0.329 m (1.08 ft) which corresponds to the distance of full nose penetration of the assumed conical nose shape. After nose penetration, equation (18c) predicts an exponential decay. At 1.52 m (5.0 ft) the pusher plate impacts the target surface, and is removed from the penetrator; this sudden mass change causes a deceleration jump. At this position $s = 1.52$ m (5.0 ft), a new initial value problem is begun without the pusher plate mass. As indicated by the data in Fig. 7, the penetrator comes to rest suddenly at $s = 2.6$ m (8.6 ft). At this distance the penetrator does not have enough kinetic energy to open a cavity as large as the penetrator aft body. The analytical model presented herein does not predict this phenomena.

Summary and Discussion

A model to estimate forces on penetrators for normal impact into hard geological targets is presented. The target medium is described by a linear hydrostat, a linear shear failure-pressure relation and the material density. These simple constitutive laws represent triaxial test data [12, 13] on two different dry rock layers at the Sandia, Tonopah Test Range, Nevada. The mathematical solution for the model is obtained by similarity methods and generalized solution curves for a wide range of practical parameters are presented. Finally, a comparison of this theory with a field test into a natural, undisturbed rock layer is presented and reasonable correlation is observed.

The model provides a quantitative estimate of force on the penetrator nose with minimum detail about the constitutive description of the material. Along with the previously stated approximations to the problem, the Coulomb frictional stresses tangent to the penetrator nose are neglected. Measurements of dynamic friction between rock and steel were performed with a rotating steel wheel arrangement [20] and data obtained for velocities up to 30 m/s which is an order-of-magnitude lower than the velocity range required for this application. No attempt was made to quantify Coulomb frictional effects in this study, but the inclusion of this effect would produce larger predicted accelerations than those shown in Fig. 7.

Acknowledgment

The authors thank D. L. Hicks for suggesting similarity methods, and L. F. Shampine and D. E. Amos for helpful suggestions related to the numerical evaluation.

References

1 Backman, M. E., and Goldsmith, W., "The Mechanics of Penetration of Projectiles Into Targets," *International Journal of Engineering Science*, Vol. 16, 1978, pp. 1–99.

2 Byers, R. K., Yarrington, P., and Chabai, A. J., "Dynamic Penetration of Soil Media by Slender Projectiles," *International Journal of Engineering Science*, Vol. 16, 1978, pp. 835–844.

3 Longcope, D. B., and Grady, D. E., "Initial Response of a Rock Penetrator," ASME JOURNAL OF APPLIED MECHANICS, Vol. 45, No. 3, Sept. 1978, pp. 559–564.

4 Young, C. W., "Depth Prediction for Earth Penetrating Projectiles," *Journal of Soil Mechanics and Foundation*, Division of ASCE, May 1969, pp. 803–817.

5 Young, C. W., "Empirical Equations for Predicting Penetration Performance in Layered Earth Materials for Complex Penetrator Configurations," SC-DR-0523, Sandia Laboratories, Albuquerque, New Mex., Dec. 1972.

6 Bernard, R. S., "Depth and Motion Prediction for Earth Penetrators," Technical Report S-78-4, U.S. Army Engineer Waterways Experiment Station, Vicksburg, Miss., June 1978.

7 Norwood, F. R., "Cylindrical Cavity Expansion in a Locking Soil," SLA-74-0201, Sandia Laboratories, Albuquerque, New Mex., July 1974.

8 Yarrington, P., "A One-Dimensional Approximate Technique for Earth Penetration Calculations," SAND 77-1126, Sandia Laboratories, Albuquerque, New Mex., Sept 1977.

9 Yew, C. H., and Stirbis, P. P., "Penetration of Projectile Into Terrestrial Target," *Journal of the Engineering Mechanics Division*, ASCE, EM2, Apr. 1978, pp. 273–286.

10 Davie, N. T., "A Method for Describing Nearly Normal Penetration of an Ogive Nosed Penetrator Into Terrestrial Targets," SAND 79-0721, Sandia Laboratories, Albuquerque, New Mex., June 1979.

11 Wagner, M. H., Fulton, C. C., and Kreyenhagen, K. N., "Finite-Difference Code Analyses of Earth Penetrator Dynamics in Rock Media," DNA 4069T, California Research and Technology, Inc., Woodland Hills, Calif. 91367, Nov. 1976.

12 Butters, S. W., Swolfs, H. S., and Johnson, J. N., "Field Laboratory and Modeling Studies on Mount Helen Welded Tuff for Earth Penetrator Test Evaluation," DNA 4085F, Terra Tek, Salt Lake City, Utah, Aug. 1976.

13 Cooley, C. H., "Laboratory Tests on Antelope Tuff for Rock Penetration Studies," Terra Tek, Salt Lake City, Utah, to be published.

14 Patterson, W. J., Sandia Laboratories, Albuquerque, Letter to P. Hadala, Waterways Experimental Station, Vicksburg, Miss., June 1976.

15 Christescu, N., *Dynamic Plasticity*, Chapter IX, North-Holland Publishing Company, Amsterdam, 1967.

16 Grady, D. E., and Hollenbach, R. E., "Impact Studies on a Tonopah Test Range Welded Tuff," SAND 76-0104, Sandia Laboratories, Albuquerque, New Mex., June 1976.

17 Zeldovich, Y. B., and Raizer, Y. P., *Physics of Shock Waves and High-Temperature Hydrodynamic Phenomena*, Vol. II, Chapter XII, Academic Press, 1967.

18 Shampine, L. F., and Watts, H. A., "Practical Solution of Ordinary Differential Equations by Runge-Kutta Methods," SAND 76-0585, Sandia Laboratories, Albuquerque, New Mex., Dec. 1976.

19 Young, C. W., "Status Report on High Velocity Soil Penetration Program," SAND 76-0291, Sandia Laboratories, Albuquerque, New Mex., Sept. 1976.

20 Gaffney, E. S., "Measurements of Dynamic Friction Between Rock and Steel," DNA 4161F, Systems, Science and Software, La Jolla, Calif. 92038, Oct. 1976.

G. R. Johnson

Engineering Fellow,
Defense Systems Division,
Honeywell, Inc.,
Hopkins, Minn. 55343

Dynamic Analysis of Explosive-Metal Interaction in Three Dimensions

This paper demonstrates the capability to perform three-dimensional computations for explosive-metal interaction problems with complex sliding surfaces. An analysis is performed for an explosive device which accelerates a metal liner known as a self-forging fragment. Results are presented to show the effects of off-center detonation, asymmetric liner thickness, and asymmetric explosive density for an otherwise axisymmetric device. These three-dimensional conditions have little effect on the linear velocities, but they do introduce significant angular velocities to the self-forging fragment. Unlike projectile-target impact computations, which require only a single sliding surface between the projectile and the target, the explosive devices have multiple, intersecting, three-dimensional sliding surfaces between the expanding explosive gases and the various metal portions of the devices. Included are descriptions of the specialized "search routines" and the "double-pass" approach used for the explosive-metal interfaces.

Introduction

Recently there has been much interest in explosive devices which accelerate a metal liner known as a self-forging fragment [1–4]. Unlike a conical-shaped charge, which forms a high velocity jet consisting of multiple particles [5], a self-forging fragment remains essentially intact and eventually forms a relatively rigid body as it travels at a constant velocity after being accelerated by the explosive. The primary uses for such devices involve military and mining applications where it is desirable to deliver a large amount of kinetic energy to a distant location. Many of these devices are axisymmetric, such as that shown in the upper portion of Fig. 1. Although the dynamic formation of such devices has been accurately simulated in two dimensions [1–4], little is known about the effect of three-dimensional, asymmetric, variations from a baseline axisymmetric configuration.

This paper contains two related items of interest; a numerical technique for explosive-metal interaction problems with complex sliding interfaces, and an analysis of three-dimensional asymmetric variations for an explosive device. Although the EPIC-3 computer code has been used to simulate high velocity impact problems involving projectile-target interaction [6], for the explosive-metal devices in Fig. 1, the sliding surface computations are significantly more complicated. The analysis examines the three-dimensional effects of off-center detonation, tapered liners, and variable density explosive, as shown in the lower portion of Fig. 1. These variations are ±10 percent of the nominal conditions and are generally greater than would be experienced in the fabrication of actual devices.

Computational Approach

A description of the basic EPIC-3 code is given in reference [6]. It is based on an explicit, finite-element, Lagrangian formulation which uses constant strain tetrahedral elements. The additional features for explosive-metal interaction are described herein.

Explosive Formulation. For explosive detonation, the hydrostatic pressure is obtained by a procedure similar to that used in the two-dimensional HEMP code [7]. The pressure, determined by the Gamma law, is given by

$$P = F(\gamma - 1)E/\overline{V} \tag{1}$$

where F is the burn fraction ($0 \leqslant F \leqslant 1.0$), γ is a material constant, and E is the internal energy per initial unit volume. The relative volume is $\overline{V} = V/V_0$, where V and V_0 represent the current and initial element volumes, respectively. Other, more accurate expressions for the pressure can also be used, such as the JWL equation of state [8], if the appropriate material constants have been determined and are available.

The explosive is effectively initiated with the burn fraction, which is dependent on the time for the detonation wave to arrive and travel through the element, or the compressed state of the element. The burn fractions for these two conditions are

$$F = \frac{(t - t_s)D + b/2}{b} \tag{2a}$$

Contributed by the Applied Mechanics Division for publication in the JOURNAL OF APPLIED MECHANICS.

Discussion on this paper should be addressed to the Editorial Department, ASME, United Engineering Center, 345 East 47th Street, New York, N. Y. 10017, and will be accepted until June 1, 1981. Readers who need more time to prepare a Discussion should request an extension from the Editorial Department. Manuscript received by ASME Applied Mechanics Division, April, 1980; final revision, July, 1980.

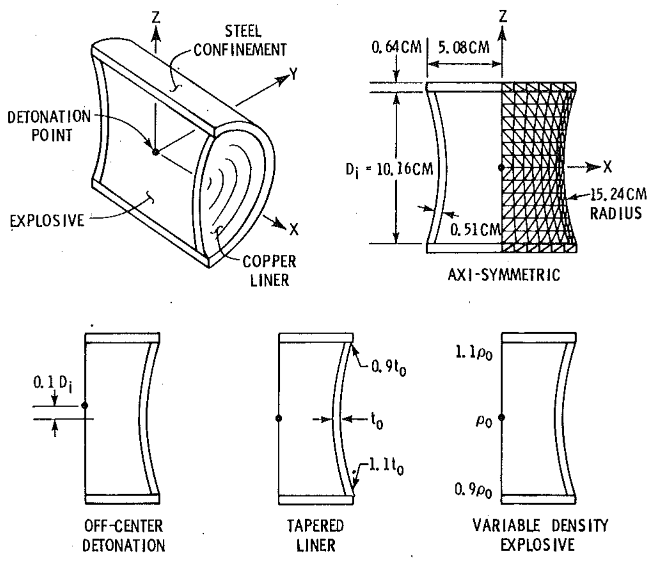

Fig. 1 **Geometric definition of the axisymmetric case and the three asymmetric cases**

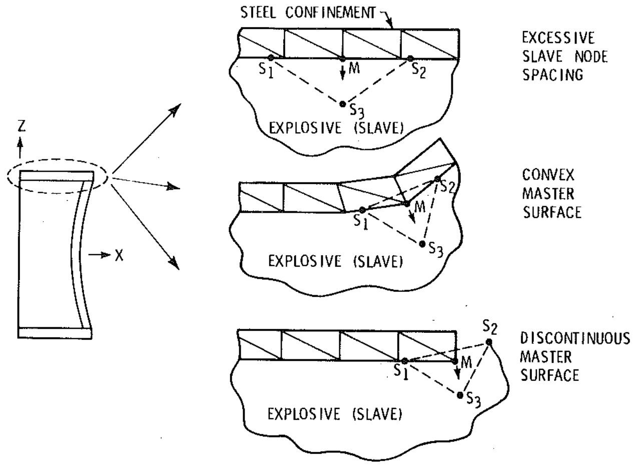

Fig. 2 **Potential sliding surface problems associated with omission of the second pass**

$$F = \frac{1-\bar{V}}{1-V_{CJ}} \qquad (2b)$$

In equation (2a), t is the current time and t_s is the time required for the detonation wave to reach the center of the element when traveling at the detonation velocity, D. A reference distance, $b = 2V_0^{1/3}$, is used to spread the wave front over a limited number of elements. Equation (2b) gives the burn fraction in terms of the compressed state, where $V_{CJ} = \gamma/(\gamma+1)$ is the Chapman-Jouquet relative volume. This allows a converging detonation wave to travel at a velocity greater than D. The maximum value of F from equations (2a) and (2b) is selected, if it is within the limits, $0 \leqslant F \leqslant 1.0$. If F is negative or greater than unity, then F is set to 0 or 1.0, respectively.

Sliding Surfaces. Since the explosive gas expands significantly and eventually vents at the intersection of the liner and the confinement shell, it is necessary to allow for sliding to occur between the explosive and the confinement shell. For the explosive-metal interface, the formulation is based on a double-pass approach. For the first pass, the metal is designated as the master surface and the explosive is designated as the slave surface. After the equations of motion are applied to the nodes of both surfaces in the usual manner, each slave node is checked to determine if it has passed through the master surface. Before this check is made, it is necessary to search through the master surface until the proper triangular plane (tetrahedral side) is identified. These "search routines" can be very complicated and will be described later.

If the slave node is found to pass through a triangular plane on the master surface, it is brought back to the surface of the plane and the normal velocities of the slave node and the three master nodes are adjusted. The adjusted velocities are obtained by conserving linear momentum normal to the plane, and angular momenta about the two axes contained in the plane. The fourth imposed condition is that the normal velocity of the slave node is equal to the normal velocity of the master plane at the slave node position. The formulations for the velocity adjustments are given in reference [6]. The velocity match is often altered as subsequent slave nodes are processed since each master node can be affected by more than one slave node. Therefore, the process must sometimes be repeated to provide an acceptable velocity match throughout the interface.

The second pass consists of redefining the explosive as the master surface and the metal as the slave surface. This insures that there is no intrusion of the metal material into the explosive material as could occur if the spacing of the explosive nodes was significantly larger than that of the metal nodes, or if the metal surface was convex toward the explosive. The double-pass approach also allows the expanding explosive to slide off the end of the metal surfaces without the use of artificial extension surfaces.

Fig. 2 shows some of the problems which occur if the second pass is omitted. For illustrative purposes, these conditions are shown in two dimensions only; the x-z plane at $y = 0$. The inner surface of the steel confinement shell is the master surface and the outer surface of the explosive is the slave surface. The common phenomenon associated with each of these conditions is that the master material intrudes into the slave material. The upper portion of Fig. 2 shows excessive slave node spacing; the distance between adjacent slave nodes S_1 and S_2 is significantly greater than the spacing of the associated master nodes. The result is that master node M is not directly resisted by either of the slave nodes. Due to the intensity of these loading conditions, the material tends to flow along the path of least resistance. In this case, node M would probably move into the slave material, the grid would overlap, and the computation would soon become meaningless.

A similar situation exists when the master surface is convex toward the slave surface. Generally this condition is not self-correcting; instead the master node continues to intrude, and slave nodes S_1 and S_2 remain on either side of the master node M. When the edge of the master surface is encountered, as shown in the lower portion of Fig. 2, slave node S_2 is no longer contained by the master surface and rapidly expands, effectively leaving master node M intruding into the slave material. Improper treatment of this area has been shown to lead to erroneous results [4].

All of these undesirable conditions can be corrected by using a double-pass approach. Since the second pass consists of interchanging the master and slave surfaces, node M becomes a slave node and is therefore placed back on the new master surface defined by nodes S_1 and S_2. As a result, it is no longer possible for one material on the interface to intrude into the other material.

The preceding discussion regarding the placement of the slave node into the master surface, and the subsequent adjustment of nodal velocities, has been for a specified slave node and the three corresponding master nodes which define the master surface at the slave node location. The identification of the appropriate triangular master plane for a specified slave node can be a very complex process, however.

There are two types of search routines; specialized and generalized. The specialized routines require much less computer time and should be used whenever possible. They can generally be used if the initial and deformed geometry of the master surface can be expressed as a single valued function of any two principal coordinates (i.e., any line parallel to the third principal axis must not pass through the master surface at more than one point). Under these conditions, the master

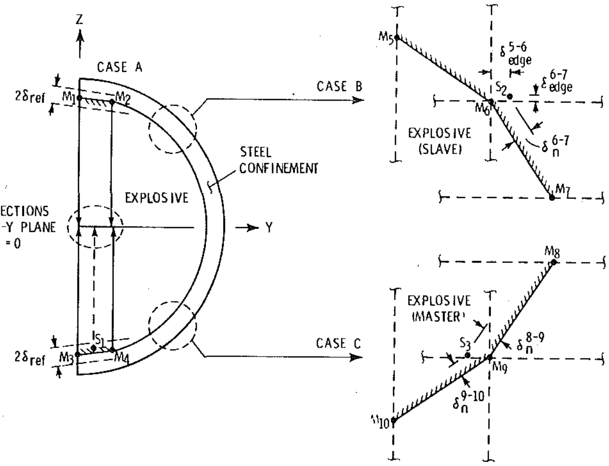

Fig. 3 Some examples of the search routine logic

surface projects onto a principal plane as an arrangement of triangles with no crossover of one triangle onto another. Then the projection of each slave node is checked to determine if it falls within the triangular projection of any master plane. As soon as a master triangle is found, the search is discontinued since the slave node can be associated with no other master triangle. The check for containment within the triangle is done by determining the distance from the slave node projection to each of the three lines of the master triangle projection. If all three distances are positive, then the slave node is contained within the triangle [9]. (This requires a specified sign convention and consistent designation of the three master lines.) This specialized approach can be used for many projectile-target impact problems [6, 9]. It can also be used for the sliding interface between the liner and explosive as shown in Fig. 1; this interface can be projected onto the y-z plane, where x is a single-valued function of y and z.

For the interface between the explosive and cylindrical steel confinement, however, the generalized approach must be used. Before stating a general rule for finding the proper master triangle, several definitions are required. δ_n is the normal distance between the slave node and the master plane. $\delta_{ref} = V_{ref}\Delta t$ where Δt is the integration time increment and V_{ref} is an input velocity (positive) which is greater than any relative velocity difference expected in the simulation. δ_{ref} is then a positive reference distance greater than the relative movement of any two nodes during one integration cycle. Another distance, δ_{edge}, is the distance between the slave node projection and the projection of one line of a master triangle. Since all projections cannot be made onto the same principal plane for the generalized approach, the principal plane selected is that plane which is most nearly parallel to the master plane. This can be readily determined from the normal direction cosines of the master triangle.

The selection is now based on the following: If a slave node is contained in the triangular projection (onto a principal plane) of one or more master surface triangles, and if it is close to the triangular plane, $\delta_n < \delta_{ref}$, then the master plane closest to the slave node is selected. If the slave node projection is not within any master triangular projections but is close normally to at least one triangular plane, $\delta_n < \delta_{ref}$, and if the distance from the slave node projection to the master triangular projection is small, $\delta_{edge} < \delta_{ref}$, then the master triangle with the smallest δ_{edge} is selected.

Fig. 3 shows examples of the search logic. Again, for clarity, the illustrations are shown in two dimensions only, the y-z plane at $x = 0$. Case A demonstrates the importance of the reference distance, δ_{ref}. For this case the explosive is the master surface, and it is desired to determine which master triangle (line in two dimensions) slave node S_1 should be associated with. The triangle containing master nodes M_1 and M_2 is projected onto the x-y plane since it is more nearly parallel to this plane. (The absolute value of the direction cosine in the z-direction is greater than those in the x and y-direction.) It can be seen that slave node S_1 falls within the projection of M_1 and M_2 on the x-y plane. However, the normal distance, δ_n, is significantly greater than δ_{ref} so the triangular plane containing nodes M_1 and M_2 is not the proper plane. The master plane containing nodes M_3 and M_4 also projects onto the x-y plane and contains the projection of the slave node. Since δ_n is less than δ_{ref}, this is the proper plane. Slave node S_1 is therefore placed onto the master triangle containing nodes M_3 and M_4, and the velocities are adjusted as described in reference [6].

Cases B and C show special instances which can arise when adjacent master triangles are projected onto different planes. In Case B, the explosive is the slave material and slave node S_2 has crossed over the master surface. The triangular plane containing master nodes M_5 and M_6 is projected onto the x-y plane and the triangular plane containing master nodes M_6 and M_7 is projected onto the x-z plane. Neither projection contains slave node S_2. Since the normal and edge distances are less than δ_{ref}, and since δ^{6-7}_{edge} is less than δ^{5-6}_{edge}, then the slave node is correctly associated with the triangular plane containing master nodes M_6 and M_7.

In Case C the explosive is the master material. Here, slave node S_3 is contained within the projections of two different planes. In addition, the normal distance to the two planes is less than δ_{ref}. Therefore, slave node S_3 is correctly associated with the triangular plane containing master nodes M_9 and M_{10} since it is closer normally to that plane; $\delta^{9-10}_n < \delta^{8-9}_n$.

Results

The preceding explosive and sliding surface options have been incorporated into the EPIC-3 code [6] such that numerical solutions can be obtained for the four different configurations in Fig. 1. The steel confinement and copper liner have plastic flow stresses of 0.35 GPa and 0.48 GPa, respectively. The octol explosive is represented by $\gamma = 2.85$, $E = 8860$ J/cm^3, $\rho_0 = 1.80$ g/cm^3, and $D = 8377$ m/s. For the sliding interfaces between the explosive and metal parts, the explosive is slave for the first pass and master for the second pass. The finite-element model contains 1288 nodes and 4392 tetrahedral elements. The coarse grid was selected to hold the computer time within acceptable levels. Each of the four conditions requires about 3 hr of CPU time on a Honeywell 6080 computer. The coarse grid, together with the simple Gamma law for the explosive, is not adequate to accurately simulate all the details of the problem. It does, however, show the relative magnitude of the various three-dimensional effects.

The dynamic formations of the various configurations are shown in Fig. 4. The cross-sectional results are at the x-z plane of symmetry at $y = 0$. The y-z plane at $x = 0$ is also a plane of symmetry, and the asymmetric conditions are relative to the z-axis. The axisymmetric condition at the top of Fig. 4 is included to provide a reference point for the other three conditions. It also provides a check for the sliding surface formulation. Even though this problem is essentially symmetric about the x axis, the sliding surface procedure is not inherently symmetric; when there is node to node contact on a sliding surface, the adjustments to the two nodes must be made in a direction normal to one of the triangular master planes which contains the master node. Since the selected triangular plane is the first one (which contains the slave node) encountered in the search, and since the triangular planes are not ordered in a symmetric manner, the symmetric slave nodes are not necessarily adjusted in a symmetric manner. The high degree of symmetry in the results indicates that this condition is probably self-correcting.

The initial cross section for the axisymmetric case is shown in Fig. 1. The first deformed shape in Fig. 4 is shown at 35 μs after detonation. The explosive has expanded significantly and is venting between the steel confinement and the copper liner. It can be seen that there is no intrusion of one material into another on the sliding interfaces, and that the upper and lower portions are essentially symmetric. A more detailed check indicates the velocities at the top and bottom edges of the liner are 1719 m/s and 1715 m/s, respectively. At 35 μs, the explosive has a negligible effect on the liner and is therefore removed from the simulation. The dynamic formation of the liner is shown from 50 μs to 200 μs after which there is limited plastic flow and the basic

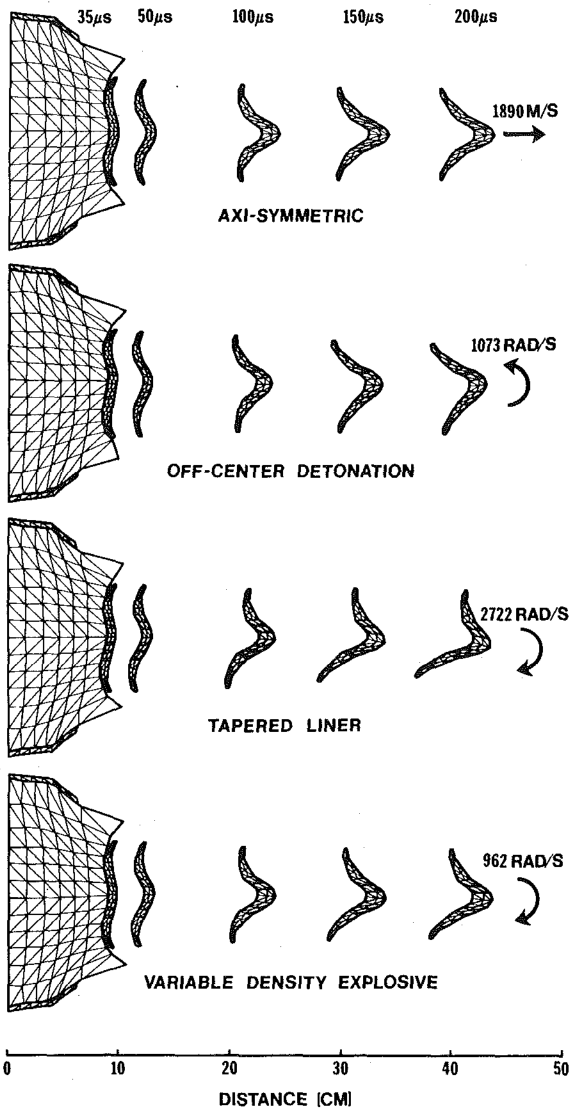

Fig. 4 Cross-sectional views of the dynamic formations

shape of the liner has been established. The axial velocity of 1890 m/s is essentially identical for all four conditions. A further check on the sliding surface formulation is provided by noting the low vertical off-axis velocity of 0.4 m/s and rotational velocity of 35 rad/s.

The second condition considers an off-center detonation where the explosive is detonated at a point 1.06 cm above the center line. During the initial stages of the response, the explosive pressure first reaches the upper portion of the liner and the liner achieves a clockwise rotational velocity of 4840 rad/s at 7.6 μs. Since this causes the upper portion of the liner to move away from the explosive at a faster rate than the lower portion, the explosive pressure is relatively decreased at the top and increased at the bottom. The increased pressure at the bottom eventually causes the final rotational velocity to be counterclockwise; 1073 rad/s at 200 μs. The effect of rotation is particularly significant for fragments where the length is much greater than the diameter, since the effect on the target is dependent on the orientation at the time of impact.

The next condition considers the effect of a tapered liner where the thickness varies linearly from 0.9 t_0 at the top to 1.1 t_0 at the bottom. The total mass of the tapered liner is equal to that of the constant thickness liners. This condition results in a significant rotational velocity of 2722 rad/s. At a linear velocity of 1890 m/s, the resulting rotation is 1.44 rad/m.

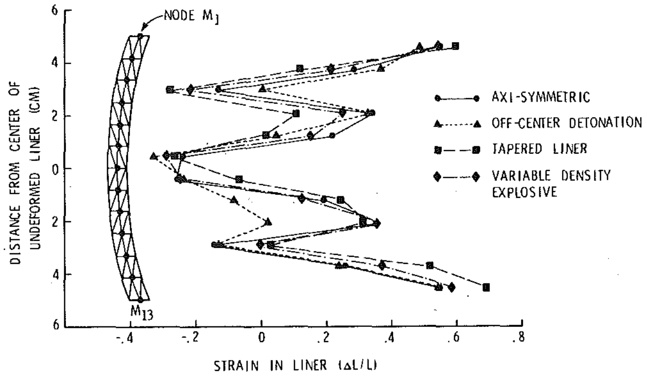

Fig. 5 One-dimensional, center-line strains, from node M_1 to node M_{13}, at the plane of symmetry, 200 μs after detonation

The final condition demonstrates the effect of a variable density in the explosive. It varies linearly from 1.1 ρ_0 at the top to 0.9 ρ_0 at the bottom. The total amount of explosive energy is equal to that of the other conditions. As expected, the denser explosive imparts a higher velocity to the upper portion of the liner and the resulting angular velocity is 962 rad/s.

Fig. 5 gives an indication of the relative distortions in the deformed liners. The internal strain distributions are important inasmuch as they can be used to give an indication of fracture; if the fragment breaks into several pieces, the effect on the target can be significantly altered. The one-dimensional strain along the center row of nodes, from node M_1 to M_{13}, is shown as a function of the initial liner geometry. The strains are plotted at the midpoints of the adjacent nodes. The same general pattern exists for all four conditions.

Several additional comments should be made about the computed results. First, the asymmetric conditions are generally more severe than would be expected in actual devices. An approximation would be to linearly interpolate the results for less severe asymmetric conditions. An additional numerical solution for a tapered liner with a ±5 percent variation indicates the rotational velocity of the liner is 53 percent of the velocity achieved with the ±10 percent variation shown in Fig. 4. This appears to indicate that the results could be interpolated. However, more solutions should be obtained to determine if this is true for the other conditions.

The rotational results are presented in terms of angular velocities for clarity. It is the angular momentum, however, which is conserved from 35 μs to 200 μs. Therefore, if the rotational inertia is significantly increased, as it would be for a long slender fragment, the rotational velocity would decrease accordingly. Vertical off-axis velocities were also experienced for the final three conditions. Generally, they were very low; 21 m/s, 4 m/s, and 9 m/s (all downward) for the off-center detonation, tapered liner and variable density explosive, respectively.

Referring back to the axisymmetric condition, it was previously stated that the results were essentially symmetric on the x-z plane of symmetry at $y = 0$. This symmetry condition does not exist as accurately around the periphery, however. Fig. 6 shows a three-dimensional view of the axisymmetric condition. It can be seen that jagged edges exist on the venting explosive at intervals of $\pi/4$ rad. This effect also occurs to a much lesser degree on the expanding confinement shell. This is due to the change in the orientation of the elements at these points, which is required to represent an expanding grid from the center of the device. This effect would probably be significantly reduced with a finer grid.

Another factor, relating to the sliding surface approach, is the accuracy of the velocity match between the explosive and metal portions of the device. It was previously stated that the velocity match between a slave node and the master surface could be altered as subsequent slave nodes were processed. For the results presented herein, a second velocity matching iteration is included for the first pass only. Fig. 7 shows a comparison of the normal velocities, at the interface of the

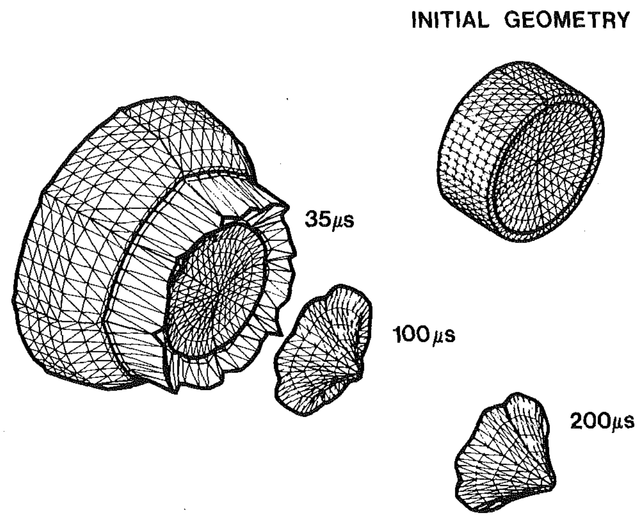

Fig. 6 Three-dimensional view of the axisymmetric dynamic formation

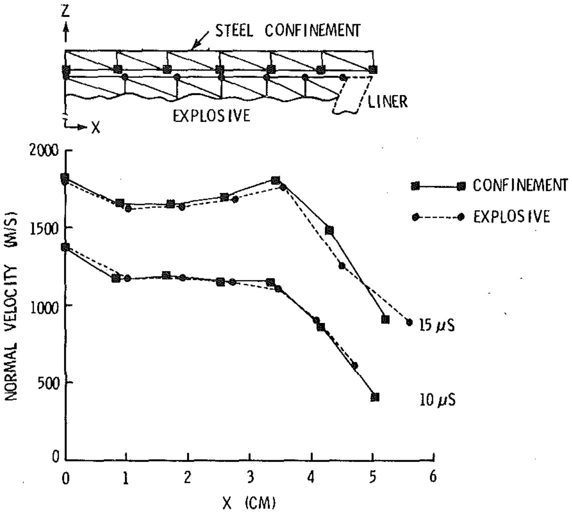

Fig. 7 Normal velocities at the explosive-confinement interface for the axisymmetric condition

explosive and confinement shell, for the axisymmetric condition. Since the detonation wave does not arrive at the confinement shell until about 6 μs, the confinement is rapidly accelerated between 6 μs and 10 μs. There is very little acceleration after 15 μs. It can be seen that the velocity matches are generally good. A part of the velocity difference at 15 μs may be due to the fact that the interface is no longer a straight line, but rather two curved surface, and the normal direction is taken as an estimated average of the two surfaces.

Summary

A numerical technique has been presented for three-dimensional problems involving explosive-metal interaction. Included is a description of an approach which can be used to obtain solutions for complex sliding surfaces. Numerical results are presented for an explosive device which accelerates a metal liner known as a self-forging fragment. The three-dimensional effects of off-center detonation, asymmetric liner thickness, and asymmetric explosive density are determined. For the conditions examined, the angular velocity of the liner is the most sensitive to the three-dimensional variations.

Acknowledgments

This work was funded by a Honeywell Independent Development Program. The many helpful discussions with D. J. Vavrick (Honeywell) are also appreciated; especially important was his concept of the double-pass approach.

References

1 Hermann, J. W., Randers-Pehrson, G., and Berus, E. R., "Experimental and Analytic Investigations of Self-Forging Fragments for the Defeat of Armor at Extremely Long Standoff," *Proceedings of the Third International Symposium on Ballistics,* Karlsruhe, Germany, Mar. 1977.

2 Carleone, J., Chou, P. C., and Simpson, R., "A Synthesis Method for Modern Warhead Design," *Proceedings of the Fourth International Symposium on Ballistics,* Monterey, Calif., Oct. 1978.

3 Hallquist, J. O., "A Numerical Treatment of Sliding Surfaces and Impact," *Computational Techniques for Interface Problems,* AMD, Vol. 30, ASME, eds., Park, K. C., and Gantling, D. K., 1979.

4 Werne, R. W., Jandrisevits, R. A., and Hanner, D. M., "An Advanced Analytical and Experimental Investigation of the Hydrodynamic Performance of a Misnay-Schardin Warhead," *Proceedings of the Fifth International Symposium on Ballistics,* Toulouse, France, Apr. 1980.

5 Chou, P. C., Carleone, J., and Karpp, R. R., "Criteria for Jet Formation From Impinging Shells and Plates," *Journal of Applied Physics,* Vol. 47, No. 7, July 1976, pp. 2975–2981.

6 Johnson, G. R., Colby, D. C., and Vavrick, D. J., "Three-Dimensional Computer Code for Dynamic Response of Solids to Intense Impulsive Loads," *International Journal for Numerical Methods in Engineering,* Vol. 14, No. 12, 1979, pp. 1865–1871.

7 Wilkins, M. L., "Calculation of Elastic-Plastic Flow," *Methods in Computational Physics 3,* eds., Alder, B., Fernback, S., and Rotenberg, M., Academic Press, New York, 1964, pp. 211–263.

8 Lee, E. L., Hornig, H. C., and Kury, J. W., "Adiabatic Expansion of High Explosive Detonation Products," UCRL-50422, Lawrence Livermore Laboratory, University of California, Livermore, May 1968.

9 Johnson, G. R., "Three-Dimensional Analysis of Sliding Surfaces During High Velocity Impact," ASME JOURNAL OF APPLIED MECHANICS, Vol. 44, No. 4, Dec. 1977, pp. 771–773.

V. A. Lubarda
Department of Mechanical Engineering,
University of Titograd,
Titograd, Yugoslavia
Student Mem. ASME

E. H. Lee
Professor,
Division of Applied Mechanics,
Department of Mechanical Engineering,
Stanford University,
Stanford, Calif. 94305
Fellow ASME

A Correct Definition of Elastic and Plastic Deformation and Its Computational Significance[1]

The plastic part of an elastic-plastic deformation is that remaining when the stress, and hence the elastic strain, is reduced to zero. Elastic deformation is that produced in this purely plastically deformed material by the action of stresses up to yield. The associated exact finite-deformation kinematics shows the almost universal assumption that the total rate of deformation is the sum of elastic and plastic rates to be in error. An incremental elastic-plastic theory is developed using the nonlinear kinematics. The theory is contrasted with that in common use and anomalies in the latter are discussed.

1 Introduction

The kinematics of elastic-plastic deformation at finite strain was incorporated into elastic-plastic constitutive relations by means of the matrix analysis of sequential deformations [1–3]. The configuration of a body in its undisturbed reference state at uniform temperature θ_0 is specified by the Cartesian position coordinates $\mathbf{X} = (X_1, X_2, X_3)$ of the body's material points. After loading beyond the elastic limit the body takes on the configuration $\mathbf{x}$ at time t given by the mapping

$$\mathbf{x} = \mathbf{x}(\mathbf{X}, t) \tag{1}$$

For elastic-plastic analysis the deformation is appropriately expressed in terms of the deformation gradient matrix

$$\mathbf{F}(\mathbf{X}, t) = \partial\mathbf{x}/\partial\mathbf{X}, \quad (F_{iJ} = \partial x_i/\partial X_J) \tag{2}$$

In order to define appropriate variables in which to express elastic-plastic analysis, the body is considered to be destressed and reduced to the initial temperature θ_0 at time t thus releasing the thermoelastic strains. The configuration is then specified by the mapping

$$\alpha = \alpha(\mathbf{X}, t) \tag{3}$$

Since after elastic-plastic deformation a body is commonly left in a state of residual stress when loads are removed and the temperature is reduced to the base value, destressing may require the body to be divided into infinitesimal elements so that the mapping (3) may then be discontinuous and not one-one [3, 4]. However a local "deformation gradient" $\mathbf{F}^p(\mathbf{X}, t)$ can be defined in each element which specifies the deformation after the macroscopic stress, and hence the thermoelastic strain, has been removed. $\mathbf{F}^p$ thus expresses the plastic deformation which has taken place. It corresponds directly to the deformation which would be associated with the migration of dislocations through unstressed crystal lattices according to the physical theory of plasticity. It also corresponds directly to the method of measuring the onset of plasticity through a proof stress test which determines the loss of reversibility to zero strain, and hence of purely elastic behavior, when the stress is cycled back to zero.

A similar local deformation gradient $\mathbf{F}^e$ specifies the mapping from the unstressed plastically deformed configuration α, (3), to the elastically-plastically deformed configuration $\mathbf{x}$, (1), and constitutes the elastic deformation gradient. Since $\boldsymbol{\alpha}$ is not in general a continuous one-one mapping, $\mathbf{F}^e(\mathbf{X}, t)$ is, like $\mathbf{F}^p$, a point function and not the partial derivative $\partial\mathbf{x}/\partial\boldsymbol{\alpha}$ (which usually does not exist).

The configurations of a material element in the neighborhoods of $\mathbf{X}$, $\boldsymbol{\alpha}(\mathbf{X}, t)$ and $\mathbf{x}(\mathbf{X}, t)$ are related since the sequence of transformations $\mathbf{X} \rightarrow \boldsymbol{\alpha}(\mathbf{X}, t)$ followed by $\boldsymbol{\alpha}(\mathbf{X}, t) \rightarrow \mathbf{x}(\mathbf{X}, t)$ is equivalent to the mapping $\mathbf{X} \rightarrow \mathbf{x}(\mathbf{X}, t)$, so that the chain rule determines

$$\mathbf{F}(\mathbf{X}, t) = \mathbf{F}^e(\mathbf{X}, t)\mathbf{F}^p(\mathbf{X}, t) \tag{4}$$

This expresses a simple but generally noncommutative coupling between elastic and plastic deformation.

But plasticity is an incremental or flow-type phenomenon so that increments or rates of deformation must be incorporated into the formulation of the theory. The gradient of the particle velocity

$$\mathbf{v} = \partial\mathbf{x}/\partial t|_{\mathbf{X}} \tag{5}$$

in the current configuration at time t is given by

$$\frac{\partial\mathbf{v}}{\partial\mathbf{x}} = \frac{\partial\mathbf{v}}{\partial\mathbf{X}}\frac{\partial\mathbf{X}}{\partial\mathbf{x}} = \dot{\mathbf{F}}\mathbf{F}^{-1} = \mathbf{L} \tag{6}$$

where $\dot{\mathbf{F}} = \partial\mathbf{F}/\partial t|_{\mathbf{X}}$. $\mathbf{L}$ can be decomposed into its symmetric part $\mathbf{D}$

---

[1] Dedicated to the memory of Suresh Chandra who was studying this problem before his untimely death.

Contributed by the Applied Mechanics Division for publication in the JOURNAL OF APPLIED MECHANICS.

Discussion on this paper should be addressed to the Editorial Department, ASME, United Engineering Center, 345 East 47th Street, New York, N. Y. 10017, and will be accepted until June 1, 1981. Readers who need more time to prepare a Discussion should request an extension from the Editorial Department. Manuscript received by ASME Applied Mechanics Division, March, 1980; final revision, August, 1980.

(the rate of deformation, velocity strain or stretching tensor) and its antisymmetric part $\mathbf{W}$ (the spin tensor):

$$\mathbf{L} = \mathbf{D} + \mathbf{W} \tag{7}$$

Substituting (4) into (6) gives

$$\mathbf{L} = \dot{\mathbf{F}}\mathbf{F}^{-1} = \dot{\mathbf{F}}^{e}\mathbf{F}^{e^{-1}} + \mathbf{F}^{e}\dot{\mathbf{F}}^{p}\mathbf{F}^{p^{-1}}\mathbf{F}^{e^{-1}} = \mathbf{L}^{e} + \mathbf{F}^{e}\mathbf{L}^{p}\mathbf{F}^{e^{-1}} \tag{8}$$

in which $\mathbf{L}^{e} = \dot{\mathbf{F}}^{e}\mathbf{F}^{e^{-1}}$ corresponds to the velocity gradient of the purely elastic deformation, and $\mathbf{L}^{p} = \dot{\mathbf{F}}^{p}\mathbf{F}^{p^{-1}}$ corresponds to the velocity gradient of the purely plastic deformation.

Equation (8) clearly demonstrates, as was pointed out in [3], that in general for strain rates expressed by $\mathbf{D}$, $\mathbf{D}^{e}$, and $\mathbf{D}^{p}$ (the symmetric parts of $\mathbf{L}$, $\mathbf{L}^{e}$, and $\mathbf{L}^{p}$)

$$\mathbf{D} \neq \mathbf{D}^{e} + \mathbf{D}^{p} \tag{9}$$

Relation (9) with an *equality* sign, or equivalently by multiplying by Δt to obtain strain increments,

$$\Delta\epsilon = \Delta\epsilon^{e} + \Delta\epsilon^{p} \tag{9a}$$

is the almost universal assumption in finite-element elastic-plastic computer codes and as a basis for incremental measurements of elastic-plastic material characteristics. For a recent reiteration and elaboration of the rate summability concept, see Nemat-Nasser [14]. This anomaly is examined in [4] where it is shown that the adoption of (9*a*) implies that certain *elastic* strain increments contribute terms then categorized as *plastic*. In the present paper we show that a careful development based on the kinematics expressed in (8) generates a new incremental theory, using the finite-strain elasticity constitutive relation, which exhibits the appropriate structure and symmetry properties to be incorporated into Hill's rate-potential, finite-deformation, variational principle [5] and hence into finite-element computer codes.

We shall assume isotropic elastic and plastic response to stress throughout the deformation and invariant elastic properties since these generate a relatively transparent analysis which is sufficient to contrast with the commonly accepted approach. Such isotropy implies that the plastic strain rate, based on normality with an isotropic yield surface, and the Euler or Almansi elastic strain have the same principal directions as the stress tensor.

It has been pointed out [3] that the component deformation gradients $\mathbf{F}^{e}$ and $\mathbf{F}^{p}$ are not uniquely defined because arbitrary local material element rotations in the unstressed state give alternate unstressed configurations. For analytical convenience, and with no basic loss of generality, we take the elastic deformation gradient $\mathbf{F}^{e}$, associated with destressing, to be rotation free and hence given by $\mathbf{V}^{e}$, a symmetric matrix.

$$\mathbf{F}^{e} = \mathbf{V}^{e} \tag{10}$$

(8) then takes the form

$$\mathbf{L} = \dot{\mathbf{V}}^{e}\mathbf{V}^{e^{-1}} + \mathbf{V}^{e}(\mathbf{D}^{p} + \mathbf{W}^{p})\mathbf{V}^{e^{-1}} = \dot{\mathbf{V}}^{e}\mathbf{V}^{e^{-1}} + \mathbf{V}^{e}\mathbf{D}^{p}\mathbf{V}^{e^{-1}} + \mathbf{V}^{e}\mathbf{W}^{p}\mathbf{V}^{e^{-1}} \tag{11}$$

and since $\mathbf{V}^{e}$ has the same principal directions as the elastic Euler strain, and hence also the same principal directions as stress *and* $\mathbf{D}^{p}$, the multiplications in $\mathbf{V}^{e}\mathbf{D}^{p}\mathbf{V}^{e^{-1}}$ are commutative so that, taking symmetric and antisymmetric parts, gives

$$\mathbf{D} = \mathbf{D}^{e} + \mathbf{D}^{p} + (\mathbf{V}^{e}\mathbf{W}^{p}\mathbf{V}^{e^{-1}})_{S} \tag{12}$$

$$\mathbf{W} = \mathbf{W}^{e} + (\mathbf{V}^{e}\mathbf{W}^{p}\mathbf{V}^{e^{-1}})_{A} \tag{13}$$

where the subscripts S and A indicate the symmetric and antisymmetric parts, respectively.

Thus, in rate form, the elastic-plastic coupling appears to be more involved than the deformation gradient relation (4). An interpretation of the significance of (12) is presented in [4]. The last term in (12) expresses a rate of strain contribution associated with elastic destressing, followed by rotation and elastic restressing, although it appears as a contribution associated with $\mathbf{L}^{p}$, and constitutes a residual strain increment following application and removal of a stress increment [4]. This may appear to be artificially associated with plastic flow because of the choice (10), but the additional strain-rate term, which contributes an increment of residual strain, arises from rotation of the body relative to the stress tensor and would still appear if the choice (10) had not been made. The theory must be sufficiently flexible to incorporate arbitrary rotation with elastic-plastic deformation if it is to be used as a vehicle for finite-element implementation. As explained in [4], such an elastic residual strain increment has commonly been categorized as contributing to plasticity.

Instead of utilizing the first term on the right-hand-side of (8) to give the elastic strain-rate $\mathbf{D}^{e}$, the approach developed in this paper is to combine it with the last term in (12) to yield a more cogent separation of elastic and plastic effects. Moreover use of the exact kinematic relation (12) eliminates anomalies associated with *hypothesising* an equality sign in (9), i.e., that the total strain-rate is the sum of elastic and plastic strain-rates.

2 The Elastic-Plastic Constitutive Relation

First, let us consider elastic response to stress. Since, without loss of generality, we define elastic deformation by the strain recovery on destressing without rotation, $\mathbf{F}^{e} = \mathbf{V}^{e}$, (10), and using the Truesdell-Noll notation [6 p. 52] the right and left Cauchy-Green tensors, $\mathbf{C}^{e}$ and $\mathbf{B}^{e}$ respectively, are equal

$$\mathbf{C}^{e} = \mathbf{F}^{e^{T}}\mathbf{F}^{e} = (\mathbf{V}^{e})^{2} = \mathbf{F}^{e}\mathbf{F}^{e^{T}} = \mathbf{B}^{e} \tag{14}$$

Thus the stress deformation relation for an isotropic thermoelastic material (equation (18) of [3] or equation (84.11) of [6]) takes the form

$$\boldsymbol{\tau} = 2\mathbf{C}^{e}\frac{\partial\psi}{\partial\mathbf{C}^{e}} \tag{15}$$

where $\boldsymbol{\tau}$ is the Kirchoff stress (det ($\mathbf{F}^{e}$) times the Cauchy stress) and ψ is the free energy per unit undeformed volume (equal to $\rho_0\psi$ as defined in [3]). The deduction of (15) depends on the fact that, for an isotropic body, $\mathbf{V}^{e}$, $\mathbf{C}^{e}$ and $\partial\psi/\partial\mathbf{C}^{e}$ all have the same principal axes so that products of the matrices are commutative.

Since the incremental or flow-type structure of the plasticity law demands that the elastic-plastic relation appear in rate form, (15) must be expressed in terms of the velocity gradients developed in the previous section.

$$\dot{\mathbf{C}}^{e} = \dot{\mathbf{V}}^{e}\mathbf{V}^{e} + \mathbf{V}^{e}\dot{\mathbf{V}}^{e} = (\mathbf{V}^{e}\dot{\mathbf{V}}^{e})^{T} + \mathbf{V}^{e}\dot{\mathbf{V}}^{e} = 2(\mathbf{V}^{e}\dot{\mathbf{V}}^{e})_{S} \tag{16}$$

so that

$$\begin{aligned}\mathbf{D}^{e} &= (\dot{\mathbf{V}}^{e}\mathbf{V}^{e^{-1}})_{S} = (\mathbf{V}^{e^{-1}}\mathbf{V}^{e}\dot{\mathbf{V}}^{e}\mathbf{V}^{e^{-1}})_{S} \\ &= \mathbf{V}^{e^{-1}}(\mathbf{V}^{e}\dot{\mathbf{V}}^{e})_{S}\mathbf{V}^{e^{-1}} = \frac{1}{2}\mathbf{V}^{e^{-1}}\dot{\mathbf{C}}^{e}\mathbf{V}^{e^{-1}}\end{aligned} \tag{17}$$

Thus the elastic terms in (12) can be rewritten as

$$\begin{aligned}\mathbf{D}^{e} + (\mathbf{V}^{e}\mathbf{W}^{p}\mathbf{V}^{e^{-1}})_{S} &= \frac{1}{2}\mathbf{V}^{e^{-1}}\dot{\mathbf{C}}^{e}\mathbf{V}^{e^{-1}} + \mathbf{V}^{e^{-1}}(\mathbf{V}^{e}\mathbf{V}^{e}\mathbf{W}^{p})_{S}\mathbf{V}^{e^{-1}} \\ &= \frac{1}{2}\mathbf{V}^{e^{-1}}[\dot{\mathbf{C}}^{e} - \mathbf{W}^{p}\mathbf{C}^{e} + \mathbf{C}^{e}\mathbf{W}^{p}]\mathbf{V}^{e^{-1}}\end{aligned} \tag{18}$$

by making use of the antisymmetry of W^{p}. The expression in square brackets is the Jaumann or corotational derivative ($\overset{\triangledown}{\ }$), [7, p. 402] of $\mathbf{C}^{e}$ for axes rotating with spin $\mathbf{W}^{p}$, i.e.,

$$\overset{\triangledown}{\mathbf{C}}{}^{e} = \dot{\mathbf{C}}^{e} - \mathbf{W}^{p}\mathbf{C}^{e} + \mathbf{C}^{e}\mathbf{W}^{p} \tag{19}$$

and (12) becomes

$$\mathbf{D} = \mathscr{D}^{e} + \mathbf{D}^{p} \tag{20}$$

where

$$\mathscr{D}^{e} = \frac{1}{2}\mathbf{V}^{e^{-1}}\overset{\triangledown}{\mathbf{C}}{}^{e}\mathbf{V}^{e^{-1}} \tag{21}$$

Thus the rate-of-deformation or stretching tensor $\mathbf{D}$ of the elastic-plastic deformation can be expressed as the sum of an elastic component involving the Jaumann rate of $\mathbf{C}^e$ (effectively a term involving the rate of finite elastic strain) and the plastic rate-of-deformation tensor, $\mathbf{D}^p$. This provides a basis for writing the elastic-plastic constitutive relation in incremental form.

Taking the Jaumann derivative with spin $\mathbf{W}^p$ of the elastic constitutive relation (15) gives

$$\overset{\triangledown}{\boldsymbol{\tau}} = 2\overset{\triangledown}{\mathbf{C}}{}^e \frac{\partial \psi}{\partial \mathbf{C}^e} + 2\mathbf{C}^e \left[\left(\frac{\partial^2 \psi}{\partial \mathbf{C}^{e^2}} : \mathbf{C}^e\right) + \frac{\partial^2 \psi}{\partial \theta \partial \mathbf{C}^e}\, \dot{\theta}\right] \tag{22}$$

where the colon, :, denotes the trace of the matrix product. In component form this becomes, for isothermal response with which this paper is mainly concerned

$$\overset{\triangledown}{\tau}_{ij} = \left[2\delta_{i\alpha}\left(\frac{\partial \psi}{\partial C^e}\right)_{\beta j} + 2C^e_{ik}\left(\frac{\partial^2 \psi}{\partial C^{e2}}\right)_{kj\alpha\beta}\right] \overset{\triangledown}{C}{}^e_{\alpha\beta} \tag{23}$$

and substituting for $\mathbf{C}^e$ from (21) gives

$$\overset{\triangledown}{\tau}_{ij} = 4\left[V^e_{im}V^e_{n\beta}\left(\frac{\partial \psi}{\partial C^e}\right)_{\beta j} + C^e_{ik}V^e_{\alpha m}V^e_{n\beta}\left(\frac{\partial^2 \psi}{\partial C^{e2}}\right)_{kj\alpha\beta}\right] \mathcal{D}^e_{mn} \tag{24}$$

or in concise notation

$$\overset{\triangledown}{\tau}_{ij} = \tilde{\Pi}_{ijmn}\mathcal{D}^e_{mn}, \qquad \overset{\triangledown}{\boldsymbol{\tau}} = \tilde{\boldsymbol{\Pi}}(\boldsymbol{\mathcal{D}}^e) \tag{25}$$

Inversion gives

$$\boldsymbol{\mathcal{D}}^e = \tilde{\boldsymbol{\Lambda}}^e(\overset{\triangledown}{\boldsymbol{\tau}}) \tag{26}$$

The plastic rate of deformation or velocity strain, $\mathbf{D}^p$, is given by the plastic-potential, time-independent, hardening law [3, equation (40)]

$$\mathbf{D}^p = \frac{1}{h}\left(\frac{\partial f}{\partial \boldsymbol{\tau}} : \dot{\boldsymbol{\tau}} + \frac{\partial f}{\partial \theta}\dot{\theta}\right)\frac{\partial f}{\partial \boldsymbol{\tau}} \tag{27}$$

where $f = g(\boldsymbol{\tau}) - c = 0$ is the yield function, g being on isotropic scalar function for isotropic hardening, and c a scalar function of temperature, θ, and history of plastic deformation. h is also a scalar function of plastic deformation history and temperature.

Since f is a scalar function of $\boldsymbol{\tau}$, the first term in the parenthesis in (27), being a part of $\dot{f}$, will not be changed by replacing $\dot{\boldsymbol{\tau}}$ by another tensor time derivative, such as $\overset{\triangledown}{\boldsymbol{\tau}}$. Thus (27) can be written

$$\mathbf{D}^p = \frac{1}{h}\left(\frac{\partial f}{\partial \boldsymbol{\tau}} : \overset{\triangledown}{\boldsymbol{\tau}} + \frac{\partial f}{\partial \theta}\dot{\theta}\right)\frac{\partial f}{\partial \boldsymbol{\tau}} \tag{28}$$

For the remainder of the development we will restrict ourselves to isothermal deformation ($\dot{\theta} = 0$), and write (28) in the form

$$D^p_{ij} = \left(\frac{1}{h}\frac{\partial f}{\partial \tau_{ij}}\frac{\partial f}{\partial \tau_{mn}}\right)\overset{\triangledown}{\tau}_{mn} = \Lambda^p_{ijmn}\overset{\triangledown}{\tau}_{mn}, \quad \mathbf{D}^p = \boldsymbol{\Lambda}^p(\overset{\triangledown}{\boldsymbol{\tau}}) \tag{29}$$

Combining (20), (26), and (29) gives

$$\mathbf{D} = (\tilde{\boldsymbol{\Lambda}}^e + \boldsymbol{\Lambda}^p)(\overset{\triangledown}{\boldsymbol{\tau}}) = \tilde{\boldsymbol{\Lambda}}(\overset{\triangledown}{\boldsymbol{\tau}}) \tag{30}$$

a rate-type law for elastic-plastic material. The operator $\tilde{\boldsymbol{\Lambda}}$ is a function of the current state which depends on the stress and the history of deformation. Inversion of (30) gives

$$\overset{\triangledown}{\boldsymbol{\tau}} = \tilde{\mathcal{L}}(\mathbf{D}) \tag{31}$$

3 Objectivity and Symmetry Properties

In order to contrast the elastic-plastic kinematic relations (9) (with an equality sign) and (20), we examine the relevant transformation characteristics of quantities involved under rotation of the current configuration by the proper orthogonal transformation $\mathbf{Q}(t)$

$$\mathbf{x}^* = \mathbf{Q}\mathbf{x} \tag{32}$$

The deformation gradient changes to

$$\mathbf{F}^* = \mathbf{Q}\mathbf{F} \tag{33}$$

Since elastic destressing is considered to occur without rotation, each element of the unstressed configuration must be subjected to the same rotation, $\mathbf{Q}(t)$, as the current configuration and this constraint must be introduced into the objectivity requirements. Thus

$$\mathbf{F}^{p*} = \mathbf{Q}\mathbf{F}^p \tag{34}$$

and

$$\mathbf{V}^{e*} = \mathbf{Q}\mathbf{V}^e\mathbf{Q}^T \tag{35}$$

It is clear that (33)–(35) are consistent with (4) and (10). Using (33)–(35) it can be readily shown that the following transformations arise:

$$\mathbf{D}^* = \mathbf{Q}\mathbf{D}\mathbf{Q}^T \tag{36}$$

$$\mathbf{D}^{p*} = \mathbf{Q}\mathbf{D}^p\mathbf{Q}^T \tag{37}$$

$$\mathbf{C}^{e*} = \mathbf{Q}\mathbf{C}^e\mathbf{Q}^T \tag{38}$$

$$\dot{\mathbf{C}}^{e*} = \mathbf{Q}\dot{\mathbf{C}}^e\mathbf{Q}^T + \dot{\mathbf{Q}}\mathbf{C}^e\mathbf{Q}^T + \mathbf{Q}\mathbf{C}^e\dot{\mathbf{Q}}^T \tag{39}$$

$$\mathbf{C}^{e*} = \mathbf{Q}\mathbf{C}^e\mathbf{Q}^T \tag{40}$$

$$\mathbf{D}^{e*} = \mathbf{Q}\mathbf{D}^e\mathbf{Q}^T + \frac{1}{2}\mathbf{Q}(\mathbf{V}^e\dot{\mathbf{Q}}^T\mathbf{Q}\mathbf{V}^{e^{-1}} + \mathbf{V}^{e^{-1}}\mathbf{Q}^T\dot{\mathbf{Q}}\mathbf{V}^e)\mathbf{Q}^T \tag{41}$$

$$\boldsymbol{\mathcal{D}}^{e*} = \mathbf{Q}\boldsymbol{\mathcal{D}}^e\mathbf{Q}^T \tag{42}$$

It is clear that (20) is objective since $\mathbf{D}$, $\boldsymbol{\mathcal{D}}^e$, and $\mathbf{D}^p$ all transform in the same way, whereas the common assumption of additive elastic and plastic strain rates; i.e., (9) with an equality sign, cannot be objective since $\mathbf{D}^e$ transforms differently from the other two terms.

It is important to examine the symmetry of the operators $\tilde{\Lambda}_{ijmn}$ (30) and $\tilde{\mathcal{L}}_{ijmn}$ (31) to check that the structure of the constitutive relation generates a rate-potential function [5] and hence can be incorporated into Hill's variational principle valid for evaluating solutions of problems involving finite deformation.

Equation (30) expresses $\tilde{\boldsymbol{\Lambda}}$ as the sum of elastic and plastic operators $\tilde{\boldsymbol{\Lambda}}^e$ and $\boldsymbol{\Lambda}^p$, and we examine these parts independently.

For isothermal isotropic elastic response the Helmholtz free energy, ψ, is a function of I_1, I_2, and I_3 the principal invariants of the Cauchy-Green deformation tensor $\mathbf{C}^e$:

$$I_1 = \mathrm{tr}\,(\mathbf{C}^e), \quad I_2 = [(\mathrm{tr}\,\mathbf{C}^e)^2 - \mathrm{tr}\,(\mathbf{C}^{e^2})]/2, \quad I_3 = \det \mathbf{C}^e \tag{43}$$

where tr stands for trace. The derivatives of ψ in (22) are then

$$\frac{\partial \psi}{\partial C^e_{ij}} = \frac{\partial \psi}{\partial I_1}\delta_{ij} + \frac{\partial \psi}{\partial I_2}(I_1\delta_{ij} - C^e_{ij}) + \frac{\partial \psi}{\partial I_3}I_3C^{e-1}_{ij} \tag{44}$$

and

$$\begin{aligned}\frac{\partial^2 \psi}{\partial C^e_{ij}\partial C^e_{\alpha\beta}} &= \left[\frac{\partial^2 \psi}{\partial I_1^2}\delta_{\alpha\beta} + \frac{\partial^2 \psi}{\partial I_1 \partial I_2}(I_1\delta_{\alpha\beta} - C^e_{\alpha\beta}) + \frac{\partial^2 \psi}{\partial I_1 \partial I_3}I_3C^{e-1}_{\alpha\beta}\right]\delta_{ij} \\ &+ \left[\frac{\partial^2 \psi}{\partial I_2 \partial I_1}\delta_{\alpha\beta} + \frac{\partial^2 \psi}{\partial I_2 \partial I_2}(I_1\delta_{\alpha\beta} - C^e_{\alpha\beta}) + \frac{\partial^2 \psi}{\partial I_1 \partial I_3}I_3C^{e-1}_{\alpha\beta}\right](I_1\delta_{ij} - C^e_{ij}) \\ &+ \left[\frac{\partial^2 \psi}{\partial I_3 \partial I_1}\delta_{\alpha\beta} + \frac{\partial^2 \psi}{\partial I_3 \partial I_2}(I_1\delta_{\alpha\beta} - C^e_{\alpha\beta}) + \frac{\partial^2 \psi}{\partial I_3 \partial I_3}I_3C^{e-1}_{\alpha\beta}\right]I_3C^{e-1}_{ij} \\ &+ \frac{\partial \psi}{\partial I_2}(\delta_{\alpha\beta}\delta_{ij} - \delta_{i\alpha}\delta_{j\beta}) + \frac{\partial \psi}{\partial I_3}(I_3C^{e-1}_{\alpha\beta}C^{e-1}_{ij} - I_3C^{e-1}_{ik}\delta_{k\alpha}\delta_{l\beta}C^{e-1}_{lj})\end{aligned} \tag{45}$$

Substitution of (44) and (45) into (24) gives the operator $\tilde{\Pi}_{ijmn}$, (25), and term-by-term examination establishes the symmetry

$$\tilde{\Pi}_{ijmn} = \tilde{\Pi}_{mnij} \tag{46}$$

The variables τ_{ij} and $\mathcal{D}^e_{mn}$ are both symmetric in their suffixes, this property of the former being confirmed by deduction from (21), (24), (44), and (45). This, in combination with (46), permits the constitutive relation (25) to be formulated so that

$$\tilde{\Pi}_{ijmn} = \tilde{\Pi}_{jimn} = \tilde{\Pi}_{ijnm} \tag{47}$$

In view of the symmetry (46), and regarding (25) as a matrix transformation of a vector with subscript (mn), to one with subscript (ij), inversion to (26) yields a symmetric inverse matrix $\tilde{\boldsymbol{\Lambda}}^e$. This combined with the symmetry of τ_{ij} and $\mathcal{D}^e_{mn}$ establishes the symmetry relations

$$\tilde{\Lambda}^e_{ijkl} = \tilde{\Lambda}^e_{klij} = \tilde{\Lambda}^e_{jikl} = \tilde{\Lambda}^e_{ijlk} \tag{48}$$

It is immediately clear that the plastic operator, $\boldsymbol{\Lambda}^p$, (29), exhibits the same symmetries, and hence also the elastic-plastic operator $\tilde{\boldsymbol{\Lambda}}$, (30). Again the symmetries are preserved by the matrix inversion of (30) to produce the operator $\tilde{\mathcal{L}}$, (31).

4 An Appropriate Variational Formulation

The symmetries established in the previous section guarantee the existence of a rate-potential function [5, 8] and hence lead to application of Hill's variational principle for velocity fields which is valid for finite deformation. Sequential application and time integration over the period of deformation permits the history of the deformation and stress distributions to be evaluated.

However, substitution of (31) into the variational formulation would involve unnecessary complexity since the Jaumann derivative of stress, $\check{\boldsymbol{\tau}}$, involves the spin tensor $\mathbf{W}^p$ (equation (19)), which cannot be simply expressed in terms of the velocity field as is evident from (11). In contrast the total spin $\mathbf{W}$ is simply the antisymmetric part of the velocity gradient. Incorporation of the Jaumann derivative based on the total spin is therefore more simply expressed and yields a convenient variational-principal structure for the determination of the velocity field.

To this end we define the Jaumann derivative associated with the total spin $\mathbf{W}$,

$$(\,^{\circ}\,) = (\,^{\cdot}\,) - \mathbf{W}(\ ) + (\ )\mathbf{W} \tag{49}$$

The corresponding differentiation of the elastic constitutive relation (15) yields

$$\mathring{\tau}_{ij} = 2\left[\delta_{im}\frac{\partial\psi}{\partial C^e_{nj}} + C^e_{i\alpha}\left(\frac{\partial^2\psi}{\partial C^{e2}}\right)_{\alpha jmn}\right]\mathring{C}^e_{mn} \tag{50}$$

where

$$\mathring{\mathbf{C}}^e = \mathbf{C}^e - \mathbf{W}\mathbf{C}^e + \mathbf{C}^e\mathbf{W} \tag{51}$$

Manipulation of this relation, by substituting from (13)

$$\mathbf{W} = (\dot{\mathbf{V}}^e\mathbf{V}^{e^{-1}})_A + (\mathbf{V}^e\mathbf{W}^p\mathbf{V}^{e^{-1}})_A \tag{52}$$

yields, after some algebraic manipulation

$$\mathring{\mathbf{C}}^e = \boldsymbol{\mathcal{D}}^e\mathbf{C}^e + \mathbf{C}^e\boldsymbol{\mathcal{D}}^e \tag{53}$$

$\mathcal{D}^e$ being defined in (21). When this is substituted into (50) we have

$$\mathring{\tau}_{ij} = 2\left[\delta_{i\alpha}\left(\frac{\partial\psi}{\partial C^e}\right)_{\beta j} + C^e_{ik}\left(\frac{\partial^2\psi}{\partial C^{e2}}\right)_{kj\alpha\beta}\right] \times (\delta_{\alpha m}C_{n\beta} + C_{\alpha m}\delta_{\beta n})\mathcal{D}^e_{mn} \tag{54}$$

and inversion and combination with the plastic strain-rate operator (29) according to (20) gives

$$\mathbf{D} = (\boldsymbol{\Lambda}^e + \boldsymbol{\Lambda}^p)\,\mathring{\boldsymbol{\tau}} = \boldsymbol{\Lambda}(\mathring{\boldsymbol{\tau}}) \tag{55}$$

where $\boldsymbol{\Lambda}^e$ is the inverse operator to that in (54). Inversion of (55) gives

$$\mathring{\boldsymbol{\tau}} = \mathcal{L}(\mathbf{D}) \tag{56}$$

On the basis of (54), (44), and (45) it can be shown that the operator $\mathcal{L}$ exhibits the same symmetry properties established in the previous section for operator $\tilde{\mathcal{L}}$ in (31). Thus the operator $\mathcal{L}$ can be expressed in rate-potential form and so incorporated into Hill's variational principle [5].

In order to include convection influences associated with finite deformation in a simple and complete manner, Hill's variational principle involves the unsymmetric nominal stress T_{Ji} (Piola-Kirchhoff I) and the gradient of the actual material velocity in the deformed configuration with respect to the reference position coordinates $\mathbf{X}$. The variational principle for the velocity field $\mathbf{v}$, (5), takes the form

$$\int_{V_0}\dot{T}_{Ji}\,\delta\left(\frac{\partial v_i}{\partial X_J}\right)dV_0 - \int_{V_0}\dot{b}_i\delta v_i dV_0 - \int_{S_0}\dot{f}_i\delta v_i dS_0 = 0 \tag{57}$$

b_i being the body force per unit reference volume, f_i the surface traction per unit reference area, and the superposed dot indicates time derivative. The rate of change of stress is expressed in terms of the rate-potential function E by the relation

$$\dot{T}_{Ji} = \frac{\partial E}{\partial(\partial v_i/\partial X_J)} \tag{58}$$

Thus, to incorporate directly the constitutive relation in the form (56) into (57) and (58), $\mathbf{D}$ being the symmetric part of the velocity gradient in the current configuration, the current configuration must be chosen as the reference configuration, and $\dot{T}_{Ji}$ expressed in terms of the rate of Kirchhoff stress, $\dot{\boldsymbol{\tau}}$, defined with respect to the initial configuration. The velocity distribution is thus evaluated at time t and hence the increments of displacement in the time interval t to $(t + \Delta t)$. The new configuration is then used as the reference state for evaluating the deformation during the next time-step. Iteration is used to improve the accuracy of the sequential procedure, and stresses are determined by integrating the constitutive relation as the deformation proceeds.

Now the Piola-Kirchhoff I stress is given in terms of the Kirchhoff stress (see, for example, [8] with the notation $\mathbf{s}$ for $\mathbf{T}$ and $J\overset{c}{\boldsymbol{\sigma}} = \overset{c}{\boldsymbol{\tau}}$ for $\boldsymbol{\tau}$) by

$$\mathbf{T} = \mathbf{F}^{-1}\boldsymbol{\tau} \tag{59}$$

For the reference state coincident with the current state at time t

$${}^t\mathbf{F}(t) = \mathbf{I} \tag{60}$$

the unit matrix. Differentiating (59) with respect to time in the interval t to $t + \Delta t$, using (49) and (60), then gives at time t

$${}^t\dot{\mathbf{T}} = {}^t\boldsymbol{\tau} + {}^t\boldsymbol{\tau}\mathbf{D} - \mathbf{D}\,{}^t\boldsymbol{\tau} - {}^t\boldsymbol{\tau}\mathbf{L} \tag{61}$$

where the superscript t indicates that these stresses are defined with the configuration at time t as reference state. But the Kirchhoff stress in (56) is based on the unstressed reference state of density ρ_0, and is defined, in terms of the Cauchy stress $\boldsymbol{\sigma}$ at some arbitrary time, by

$$\boldsymbol{\tau} = \frac{\rho_0}{\rho}\boldsymbol{\sigma} \tag{62}$$

whereas in (60) and (61) the configuration at time t is the reference state, and in the time interval t to $t + \Delta t$

$${}^t\boldsymbol{\tau} = \frac{\rho(t)}{\rho}\boldsymbol{\sigma} = \frac{\rho(t)}{\rho_0}\frac{\rho_0}{\rho}\boldsymbol{\sigma} = \frac{\rho(t)}{\rho_0}\boldsymbol{\tau} \tag{63}$$

Substituting into the variational principle (57) with $\mathbf{X} = \mathbf{x}(t)$ and incorporating (56) then yields after some manipulation

$$\int_V \frac{\rho(t)}{\rho_0}[\mathcal{L}_{ijmn}D_{mn}\delta D_{ij} + \tau_{ij}(-2D_{kj}\delta D_{ik} + L_{kj}\delta L_{ki})]dV - \int_V \dot{b}_i\delta v_i dV - \int_S \dot{f}_i\delta v_i dS = 0 \tag{64}$$

where b_i and f_i are per unit volume and area, respectively, in the configuration at time t. The formulation of the variational principle in terms of the Kirchhoff stress is essentially that presented by McMeeking and Rice [9] for the small elastic strain case except for the density ratio term which was not included and may not be important in that case.

The variational principle (64) forms a convenient basis for the generation of finite-element computer codes, many of which are in successful operation for small elastic strains, for example [9–11].

5 Finite Elastic-Plastic Deformation With Small Elastic Strain

Many problems involving the elastic-plastic deformation of metals may fall within the scope of a special case of the theory developed in this paper, that of finite deformation with small elastic strain. Then the squares of elastic strain components can be neglected. The elastic strain tensor can be defined as the Lagrange strain

$$\boldsymbol{\epsilon}^e = (\mathbf{C}^e - \mathbf{I})/2 \tag{65}$$

The Helmholtz free energy for isothermal deformation takes the form of the classical strain energy for infinitesimal strain

$$\psi = (\lambda \epsilon^e_{ii} \epsilon^e_{jj} + 2\mu \epsilon^e_{ij} \epsilon^e_{ji})/2 \tag{66}$$

Substitution of (65) into (66) yields

$$\psi = [\lambda(C^e_{ii}C^e_{jj} - 6C^e_{ii} + 9) + 2\mu(C^e_{ij}C^e_{ji} - 2C^e_{ii} + 3)]/8 \tag{67}$$

Since in (54) $\mathcal{D}^e$, which involves a time derivative of $\boldsymbol{\epsilon}^e$, is considered a first-order small term, analysis to first-order permits zero-order substitution of factors and hence $\mathbf{C}^e$ to be replaced by $\mathbf{I}$. $\mathcal{D}^e$ can then be replaced by $\mathbf{D}^e$, and (54) becomes

$$\mathring{\tau}_{ij} = 4 \left[\delta_{im} \left(\frac{\partial \psi}{\partial C^e} \right)_{ij} + \left(\frac{\partial^2 \psi}{\partial C^{e2}} \right)_{ijmn} \right] D^e_{mn} \tag{68}$$

Differentiation of (67) shows that the first derivative of ψ is of order ϵ, and can be neglected compared with the second derivative, so that (68) becomes

$$\mathring{\tau}_{ij} = (\lambda \delta_{ij} \delta_{mn} + 2\mu \delta_{im} \delta_{nj}) D^e_{mn} \tag{69}$$

Inversion gives

$$D^e_{ij} = \frac{1}{2\mu} (\delta_{im}\delta_{jn} - \frac{\lambda}{3\lambda + 2\mu} \delta_{ij}\delta_{mn}) \mathring{\tau}_{mn} \tag{70}$$

Substitution into (20) with the plasticity law (29) then yields

$$D_{ij} = \left[\frac{1}{2\mu} (\delta_{im}\delta_{jn} - \frac{\lambda}{3\lambda + 2\mu} \delta_{ij}\delta_{mn}) + \frac{1}{h} \frac{\partial f}{\partial \tau_{ij}} \frac{\partial f}{\partial \tau_{mn}} \right] \mathring{\tau}_{mn} \tag{71}$$

which can be inverted to give

$$\mathring{\tau}_{ij} = 2\mu \left[\delta_{i\alpha}\delta_{j\beta} + \frac{\lambda}{2\mu} \delta_{\alpha\beta}\delta_{ij} - \frac{1}{\dfrac{h}{2\mu} + \dfrac{\partial f}{\partial \tau_{mn}} \dfrac{\partial f}{\partial \tau_{mn}}} \frac{\partial f}{\partial \tau_{ij}} \frac{\partial f}{\partial \tau_{\alpha\beta}} \right] D_{\alpha\beta} \tag{72}$$

the operator on the right-hand side being the corresponding $\mathcal{L}$. The development following (69) parallels that given in [9] using different elastic moduli. If in certain problems, for example, stability analyses, a more precise formulation is needed, it may be possible to include higher-order terms in an approximation for the elastic-plastic operator $\mathcal{L}$, (56).

6 Discussion

This paper presents a rate or incremental formulation of the finite-deformation, elastic-plastic theory developed in [3]. The fact that in [3] the elastic constitutive relation was left in total elastic deformation form, rather than in rate form, limited utilization of the theory and application has been restricted to shock-wave analysis in which, by symmetry, principal directions of stress remained fixed in the body. This permits the use of logarithmic or natural strain which generates additivity of both elastic and plastic strain and strain-rates [12, 13]. However, this approach is not possible for arbitrary loading with rotation and the present contribution removes this restriction.

The present theory is based on exact nonlinear kinematics of elastic and plastic deformation. The latter is the deformation the body would exhibit if the macroscopic stress, and hence elastic strain, were maintained at zero while the remaining deformation proceeds. In the case of migration of dislocations, for example, increments of this plastic deformation are directly related to the specifics of the activity of such atomic mechanisms and are not coupled with the elastic strain to which the body is in fact continuously subjected. This is in contrast with an increment of irreversible or residual strain under maintained stress, which depends on the elastic strain because of the elastically deformed material lattice quite apart from the influence of rotation already considered. The elastic deformation is that due to stress acting on the purely plastically deformed material. The exact nonlinear kinematics logically directs the development of the theory including the appropriate stress and strain variables which arise.

The current commonly adopted elastic-plastic theory appears to have grown from a foundation of infinitesimal deformation kinematics which sets rates (or increments) of total strain as the sum of elastic and plastic contributions, using the rate-type law for the plastic strain and the derivative of the classical elasticity law for the elastic contribution. Combining such kinematics and constitutive laws yields a linear stress-rate strain-rate relation with stress and history variables as coefficients. In order to preserve objectivity (or from a more elementary standpoint, to permit rigid-body rotation to correspond to zero stress rate) the Jaumann corotational stress rate is selected for the elastic-plastic rate law. While the final rate law developed is objective, the components from which it was constructed either are not objective or do not correctly express the physical entities they purport to represent. It seems to us that this explains the anomalies which appear in the currently accepted elastic-plastic theory when it is subjected to careful scrutiny.

Perhaps some comments are in order to clarify the concept that the residual strain increment, left after addition and removal of a stress increment $\Delta\boldsymbol{\sigma}$, on a body in which the stress $\boldsymbol{\sigma}$ is maintained, contains an elastic part. Increments of stress and deformation about a state of maintained stress can be analyzed in terms of the rate of deformation $\mathbf{D}$ defined in (11) and (12). During the loading increment, elastic and plastic deformation increments can arise and all the terms in (12) are likely to be nonzero. The simplest unloading assumption for the stress increment $-\Delta\boldsymbol{\sigma}$ is to reverse the sign of $\dot{\mathbf{V}}^e$, the elastic deformation rate, and introduce no additional spin. Then the last term in (12) is zero for unloading, and the value of that term times Δt during the loading $\Delta\boldsymbol{\sigma}$ will be retained as a residual or irreversible strain increment, although it is independent of the plastic *flow* occurring during the loading increment [4]. Of course, the spin tensor W^p associated with the elastic-plastic loading increment could be reversed and incorporated into the elastic unloading increment, in which case the irreversible increment of deformation associated with W^p would become reversible. However this might be difficult to arrange in practice since in the loading increment the plastic strain will normally dominate and superposing the spin W^p on elastic unloading is likely to dominate the deformation process in unloading. In any event, to include spin in the unloading which defines plastic strain, and to have to devise a prescription for such spin, is likely to serve no useful purpose and would complicate the analysis compared with that corresponding to the choice (10), of unloading without rotation. Quite apart from the unloading question, it was already shown in [3] that the power expended by the deformation rate associated with the last term in (12) is zero, in contrast to that due to D^p, so that the former term was shown to be physically associated with elastic deformation even though it does not involve a change in the elastic deformation $\mathbf{V}^e$.

From the standpoint of application, the small elastic strain theory developed in the previous section, which results in essentially the formulation currently adopted in many computer codes valid for finite deformation, can be expected to be satisfactory for the majority of problems of metal deformation. Equation (18) shows that the plastic spin associated Jaumann derivative of the elastic Cauchy-Green tensor, $\mathbf{C}^e$, is a good approximation to the elastic contribution to the strain rate, which includes the effects of both the rate of change of stress and the rotation of the body. Equation (22) shows that this is associated directly with the same derivative of stress, and (13) indicates that the total spin will generally be a close approximation to the spin $\mathbf{W}^p$, so that the Jaumann derivative based on total spin will be a good approximation to that based on W^p. The present new formulation will permit a more accurate version of the theory to be developed if needed for particular problems.

It should perhaps be pointed out that, although the concept of the definition of plastic deformation as that remaining when the macroscopic stress, and hence elastic deformation, is reduced to zero is stressed in this paper, the general structure of the theory presented can encompass the situation when a Bauschinger effect involves reverse plastic flow on unloading before zero stress is reached. In this case there need be no particular difficulty in devising a Helmholtz free-energy function for the elastic range. The application of incremental theory involves only rates or increments of strain and not a prescription of total elastic or plastic strain. Formally one could define the plastic strain to correspond to zero stress evaluated from the elastic law even though this state cannot be reached without additional plastic flow. The utilization of this artificial unstressed state provides no impediment to evaluating stresses according to elastic or elastic-plastic theory where the corresponding physical behavior is occurring.

Acknowledgment

The results presented in this paper were obtained in the course of research sponsored by the U. S. Army Research Office under Grant No. DAAG29-77-G-0126 to Stanford University. The authors gratefully acknowledge this support.

References

1 Lee, E. H., "Elastic-Plastic Waves of One-Dimensional Strain," *Proceedings, 5th U. S. National Congress on Applied Mechanics*, ASME, 1966, pp. 405–420.

2 Lee, E. H., and Liu, D. T., "Finite-Strain Elastic-Plastic Theory Particularly for Plane Wave Analysis," *Journal of Applied Physics*, Vol. 38, 1967, pp. 19–27.

3 Lee, E. H., "Elastic-Plastic Deformation at Finite Strains," ASME JOURNAL OF APPLIED MECHANICS, Vol. 36, 1969, pp. 1–6.

4 Lee, E. H., and McMeeking, R. M., "Concerning Elastic and Plastic Components of Deformation," *International Journal of Solids and Structures*, Vol. 16, 1980, pp. 715–721.

5 Hill, R., "Some Basic Principles in the Mechanics of Solids Without a Natural Time," *Journal of the Mechanics and Physics of Solids*, Vol. 7, 1959, pp. 209–225.

6 Truesdell, C., and Noll, W., "The Nonlinear Field Theories of Mechanics," *Handbuck der Physik*, Band III/3, Springer-Verlag, 1965.

7 Malvern, L. E., *Introduction to the Mechanics of a Continuous Medium*, Prentice-Hall, Englewood Cliffs, N. J., 1969.

8 Lee, E. H., "Stress Analysis of Metal Forming Processes," *Engineering Plasticity: Theory of Metal Forming Processes*, ed., Lippmann, H., Springer-Verlag, 1978.

9 McMeeking, R. M., and Rice J. R., "Finite-Element Formulations for Problems of Large Elastic-Plastic Deformation," *International Journal of Solids and Structures*, Vol. 11, 1975, pp. 601–616.

10 Lee, E. H., Mallett, R. L., and Yang, W. H., "Stress and Deformation Analysis of the Metal Extrusion Process," *Comp. Meth. in Appl. Mech. Engg.*, Vol. 10, 1977, pp. 339–353.

11 Lee, E. H., Mallett, R. L., and McMeeking, R. M., "Stress and Deformation Analysis of Metal Forming Processes," *Numerical Modeling of Manufacturing Processes*, PVP-PB-025, eds./ Jones, R. F., Jr., Armen, H., and Fong, J. T., ASME, 1977, pp. 19–33.

12 Lee, E. H., and Wierzbicki, T., "Analysis of the Propagation of Plane Elastic-Plastic Waves at Finite Strain," ASME JOURNAL OF APPLIED MECHANICS, Vol. 34, 1967, pp. 931–936.

13 Germain, P., and Lee, E. H., "On Shock Waves in Elastic-Plastic Solids, *Journal of the Mechanics and Physics of Solids*, Vol. 21, 1973, pp. 359–382.

14 Nemat-Nasser, S., "Decomposition of Strain Measures and Their Rates in Finite Deformation Elastoplasticity," *International Journal of Solids and Structures*, Vol. 15, 1979, pp. 155–166.

G. J. Weng

Associate Professor,
Department of Mechanics
and Materials Science,
Rutgers University,
New Brunswick, N. J. 08903
Mem. ASME

Self-Consistent Determination of Time-Dependent Behavior of Metals

Though Kröner's self-consistent model is not fully consistent in the elastic-plastic deformation of polycrystals, it is found to be perfectly consistent in the time-dependent deformation of such materials. Hill's model, on the other hand, should be used with a modified constraint tensor containing the elastic moduli of the matrix in that case. Kröner's model is supplemented with a physically consistent constitutive equation for the slip system; these, together with Weng's inverse method, form the basis of a self-consistent determination of time-dependent behavior of metals. The kinematic component of the latent hardening law and the residual stress introduced in more favorably oriented grains are the two major driving forces for recovery and the Bauschinger effect in creep. The proposed method was applied to predict the creep and recovery strains of a 2618-T61 Aluminum alloy under pure shear, step and nonradial loading. The predicted results are seen to be in generally good agreement with the test data.

Introduction

Since Eshelby's classic paper [1] on the stress field of an ellipsoidal inclusion was published in 1957, its results have been widely used to predict various mechanical behavior of materials. One of its most important applications was developed into the "self-consistent model" for polycrystalline plasticity, which was originally introduced by Kröner [2] and subsequently applied by Budiansky and Wu [3]. Kröner's model, then, offered a promising approach to account for the complicated grain interaction. Later, Hill [4] reexamined the structure of self-consistent scheme, and found that Kröner's model was not entirely consistent, in that the decreasing constraint power of the matrix in plastic flow was not considered. Hill then proposed a more rigorous self-consistent scheme, which was characterized by a constraint tensor. The constraint tensor depends on the tangent moduli, instead of the elastic moduli of the matrix in elastic-plastic deformation. Ever since, Hill's model has become perhaps the most highly regarded, and has been successfully applied by Hutchinson [5], and recently combining Kröner's "explicit" spirit by Berveiller and Zaoui [6], among others.

Prompted by the success of self-consistent model in plasticity, Brown [7] first attempted to extend it to study the creep behavior of metals. Recognizing that Kröner's model was computationally easier than Hill's, he adopted the former model. Hutchinson [8] later also applied Hill's model to estimate the steady creep rate of a polycrystal from that of its constituents. The derivations of Brown and Hutchinson have provided many significant results. Hutchinson's results are particularly useful for the estimate of long-time creep.

It should be pointed out, at this stage, that both Kröner's and Hill's models were originally proposed for the study of time-independent plastic deformation of polycrystalline solids; they were not intended for the time-dependent creep problems. If the self-consistent models are to be extended to study the latter problems their applicability, in their given form, should be critically examined. In fact, upon examination it becomes evident that Kröner's model then becomes entirely consistent and that, while Hill's concept of constraint tensor still remains valid, its value should be given in a modified form. The crux of the matter is that, creep, unlike plastic deformation, is a truely "stress-free" process in the sense of Eshelby, because the creep strain rate, at any generic state, depends only on the current stress and deformation history and is *independent* of the stress rate. The latter independence obviously does not hold in plasticity, and this leads to the presence of tangent moduli in Hill's constraint tensor. This subtle point appears to have not been realized. Brown used Kröner's model but wrote: "Hill (1965) has shown that this model has certain limitations, since the pronounced directional weaknesses in the constraint of an already-yielded aggregate are disregarded. The present work suffers from the same limitations." Such limitations simply did not exist. Brown's results were less time-dependent than what he experimentally showed, because he used the steady state power law for the slip system to begin with. Hutchinson's formulation on the other hand is not affected by this consequence, since his objective was on the time-independent, steady-state creep rate of the aggregate.

A separate, yet equally plausible approach to derive the inelastic constitutive relations of polycrystals has been pursued by Lin [9], by means of his "equivalent body force." This concept was originally introduced for plasticity, and later applied to study the creep behavior of metals by Lin, et al. [10], and Weng [11]. Considering both transient and steady creep of the crystal, Lin, et al., derived the polycrystal

---

Contributed by the Applied Mechanics Division of THE AMERICAN SOCIETY OF MECHANICAL ENGINEERS, for presentation at the 1981 Joint ASME/ASCE Applied Mechanics, Fluids Engineering, and Bioengineering Conference, University of Colorado, Boulder, Colo., June 22-27, 1981.

Discussion on this paper should be addressed to the Editorial Department, ASME, United Engineering Center, 345 East 47th Street, New York, N. Y. 10017, and will be accepted until June 1, 1981. Readers who need more time to prepare a Discussion should request an extension from the Editorial Department. Manuscript received by ASME Applied Mechanics Division, April, 1980; final revision, July, 1980. Paper No. 81-APM-11.

properties from single crystal creep data. A two-step inverse method was proposed in [11]: first, the single crystal properties are derived from polycrystal data, and then these properties are used to predict the creep behavior of the same polycrystal under other required loading conditions. The derived single crystal properties account for the effect of grain boundaries and therefore are *in situ,* and the predicted polycrystal results can be compared directly with experiments.

In this paper we apply Kröner's self-consistent model and Weng's inverse method to study the time-dependent behavior of metals. A more physically consistent constitutive equation than those used in previous studies will also be introduced to account for the active and latent hardening of slip systems. Our consideration will be restricted to the temperature range below half the melting point (T_m), so that crystallographic slip is the main source of creep deformation. Since the elastic property of the grain for most structural metals is fairly isotropic, such an isotropy will be assumed. For highly anisotropic crystals Eshelby's "equivalent inclusion" could be introduced to obtain the additional inhomogeneous stress. Within the scope of small deformation grain rotation will be neglected.

Self-Consistent Determination of Creep: A Stress-Free Strain Problem

Kröner's self-consistent relation was given in [2], and rederived by Budiansky and Wu in [3]. However, by applying Eshelby's solution more directly the result could be so easily derived that it is tempting and revealing to reconsider it here.

Consider an ellipsoidal inclusion (grain) embedded in an infinitely extended matrix (aggregate). The stress and creep strain of the inclusion are denoted by σ and ϵ^c, while those of the aggregate are specified by the corresponding barred (averaging) quantities $\bar{\sigma}$ and $\bar{\epsilon}^c$. When the matrix and inclusion undergo the stress-free incremental strains $d\bar{\epsilon}^c$ and $d\epsilon^c$, respectively, the self-consistent scheme can be formulated by the two-step process:

1 Let the matrix and inclusion deform with the given amounts separately without constraint. To bring the deformed inclusion into the deformed matrix compatibly we apply

$$d\sigma_1 = \mathcal{L}(d\bar{\epsilon}^c - d\epsilon^c), \tag{1}$$

on the inclusion, where $\mathcal{L}$ is its elastic moduli tensor.

2 To remove the unwanted layer of surface force we apply a surface traction characterized by $d\sigma^* = -d\sigma_1$ on the interface. Then Eshelby's result shows that the additional stress induced in the inclusion, denoted by $d\sigma_2$, is given by

$$d\sigma_2 = \mathcal{L}\mathbf{S}(d\epsilon^c - d\bar{\epsilon}^c), \tag{2}$$

where Eshelby's $\mathbf{S}$ matrix, when multiplied by the effective stress-free strain increment, gives rise to the constraint local strain increment of the inclusion.

Thus, at the end of operation the induced stress increment in the inclusion is the sum of $d\sigma_1$ and $d\sigma_2$, i.e.

$$d\sigma = -\mathcal{L}(\mathbf{I} - \mathbf{S})(d\epsilon^c - d\bar{\epsilon}^c), \tag{3}$$

where $\mathbf{I}$ is the fourth-rank identity tensor. When the inclusion is spherical, equation (3) can be written as

$$d\sigma = -2\mu(1-\beta)(d\epsilon^c - d\bar{\epsilon}^c), \tag{4}$$

where μ is the shear modulus, and $\beta = 2(4-5\nu)/15(1-\nu)$, ν being Poisson's ratio. Equation (4) is the familiar Kröner's self-consistent relation. Since $\beta < 1$, the stress in more favorably oriented grains, characterized by $d\epsilon^c > d\bar{\epsilon}^c$, is relieved during this incremental process; conversely it is increased in less favorably oriented grains.

Suppose that during this incremental deformation the aggregate is further loaded with $d\bar{\sigma}$. Then, with the assumed elastic isotropy we have

$$\begin{aligned} d\sigma - d\bar{\sigma} &= -\mathcal{L}(\mathbf{I} - \mathbf{S})(d\epsilon^c - d\bar{\epsilon}^c) \\ &= -2\mu(1-\beta)(d\epsilon^c - d\bar{\epsilon}^c). \end{aligned} \tag{5}$$

Since the difference between the total strain of the grain and of the aggregate is given by $\mathbf{S}(d\epsilon^c - d\bar{\epsilon}^c)$, Hill's constraint tensor $\mathbf{L}^*$, in view of (5), is seen to satisfy

$$\mathbf{L}^*\mathbf{S} = \mathcal{L}(\mathbf{I} - \mathbf{S}), \tag{6}$$

instead of his original form $\mathbf{L}^*\mathbf{S} = \mathbf{L}(\mathbf{I} - \mathbf{S})$, $\mathbf{L}$ being the tangent moduli of the matrix under elastic-plastic deformations and $\mathbf{S}$ interpreted in this context. Evidently $\mathbf{L} = 0$ in a constant-stress creep test; the constraint power of the matrix would have vanished if Hill's original relation had been used.

Equation (5) provides the self-consistent variation of internal stress in the grain for each incremental process; the average of $d\sigma$ over all grain orientations gives rise to $d\bar{\sigma}$, and so does $d\epsilon^c$ to $d\bar{\epsilon}^c$. This equation can be used to calculate the time-dependent behavior of metals from those of its constituents, or vice versa.

Constitutive Equations of Single Crystals and Polycrystals

The self-consistent model provides a proper connection between the deformations of a grain and its aggregate. In order to use it to determine the time-dependent behavior of the aggregate, however, it needs to be supplemented with a physically consistent constitutive equation for the grain. Below $T_m/2$ creep in metal crystals is primarily caused by dislocation glide, during which their interactions, intersections and structural changes lead to active and latent hardening in slip systems. The creep rate of a slip system thus decreases even under a constant stress, until a steady state is reached. The steady creep rate of a slip system in general can be described by the power function of its resolved shear stress τ; so can its initial creep rate. The decrease of the transient creep rate, on the other hand, should be described in accordance with a proper theory of work hardening. For simplicity Taylor's isotropic hardening law [12] was used in [11]. This law offers a reasonable approximation under radial loading. But since it is in direct contradiction with the observed Bauschinger effect in crystals (for example, see Buckley and Entwistle [13]), it tends to result in an underestimate for creep strains under recovery, reversed loading or other nonradial loading. Recently, Weng [14] analyzed the nature of some dominant hardening mechanisms in metal crystals and found that, though dislocation tangles, jogs, forest cutting and "cell" structure primarily lead to the isotropic hardening in slip systems, the hardening behavior caused by dislocation pile-ups and dislocation rings encircling dispersions is kinematic instead. A mixed hardening law, which incorporates both isotropic and kinematic hardening, and is characterized by the "degree of isotropy in work hardening α," was proposed. Using this hardening law as the basis for the transient creep rate $\dot{\gamma}_t{}^c$, and again employing the power function for the steady creep rate $\dot{\gamma}_s{}^c$, we write the following constitutive relation for the ith slip system:

$$\overset{(i)}{\dot{\gamma}}_s{}^c = \kappa\overset{(i)}{\tau}{}^{\lambda}, \tag{7}$$

$$\overset{(i)}{\dot{\gamma}}_t{}^c = \eta\left\{\zeta\overset{(i)}{\tau}{}^{\lambda} - \left[\alpha\sum_j\left|\overset{(j)}{\gamma}_t{}^c\right| + (1-\alpha)\sum_j\cos\overset{(i,j)}{\theta}\cos\overset{(i,j)}{\phi}\,\overset{(j)}{\gamma}_t{}^c\right]\right\}, \tag{8}$$

where $\overset{(i,j)}{\theta}$ is the angle between the slip directions of the ith and jth slip systems, $\overset{(i,j)}{\phi}$ between their slip plane normals, and κ, λ, η, and ζ are four other single crystal constants. Both α and λ are dimensionless and κ, ζ, and η are in the units of $(\text{stress})^{-\lambda}$ $(\text{time})^{-1}$, $(\text{stress})^{-\lambda}$, and $(\text{time})^{-1}$, in turn. The total creep rate of a slip system $\dot{\gamma}^c$ is the sum of its transient and steady components. It is evident from (8) that the creep rate of a slip system decreases in accordance with the mixed hardening law, with $\alpha = 1$ and 0 corresponding to the isotropic and kinematic hardening, respectively. The kinematic nature associated with $\alpha = 0$ has been fully discussed in [15]. A constitutive equation like that given in [11] was found insensitive to recovery due to the overwhelming dependence of creep rate on τ, even with the isotropic hardening law replaced by the mixed hardening law.

To assist the determination of these five constants from the tensile creep data of its polycrystal, it is helpful to introduce similar constitutive equations for its creep behavior. We write the steady and transient creep rates $\dot{\bar{\epsilon}}_s{}^c$ and $\dot{\bar{\epsilon}}_t{}^c$, respectively, as

$$\dot{\bar{\epsilon}}_s{}^c = a\bar{\sigma}^b, \tag{9}$$

$$\dot{\bar{\epsilon}}_t{}^c = c(d\bar{\sigma}^b - \bar{\epsilon}_t), \tag{10}$$

where the four parameters a, b, c, and d can be easily determined from two tensile creep curves.

Comparison of equations (7), (8) to (9), (10) indicates that the nature of κ, λ, η, and ζ are similar to those of a, b, c, and d, in turn. The corresponding parameter of α for the polycrystal is not present in (10), which under pure tension does not require any specific hardening law. These five constants, each possessing a distinctive property, can be determined from two tensile, constant-stress creep and one recovery curves of the polycrystal.

Derivation of Single Crystal Properties From the Tensile Data of Its Polycrystal

Consider a polycrystalline aggregate, consisted of randomly oriented, equally sized single crystals. When the elastic anisotropy of each grain is neglected, the creep rate of the aggregate is simply the average of the creep rates of its constituent grains. In terms of rectangular components,

$$\dot{\bar{\epsilon}}_{ij}{}^c = \{\dot{\epsilon}_{ij}{}^c\}, \tag{11}$$

where $\{\ \}$ denotes the average taken over all crystal orientations. This notation will be used in the remainder of this paper.

The creep rate of a grain, on the other hand, depends on the slip rate of its slip systems. We allow at any instant every slip system to be active. This removes the single-slip restriction placed in [11], and appears to be more physically consistent. Consequently

$$\dot{\epsilon}_{ij}{}^c = \sum_k \overset{(k)}{\nu_{ij}} \overset{(k)}{\dot{\gamma}}{}^c, \tag{12}$$

where ν_{ij} is the symmetric part of the dyad $b_i n_j$, b_i and n_j being the slip direction and slip plane normal, respectively, of a slip system. The superscript k refers to the kth system, and the sum includes all systems in the grain. This summation convention is implicit throughout the paper and unless ambiguity might arise, the indicator k will be dropped for brevity.

Furthermore, the creep rate of a slip system, following (7) and (8), is a function of its resolved shear stress, which is related to the local stress in the grain by

$$\overset{(k)}{\tau} = \overset{(k)}{\nu_{ij}}\sigma_{ij}. \tag{13}$$

The local stress at time t is calculated following the self-consistent relation (5) with $d\epsilon_{ij}{}^c = \dot{\epsilon}_{ij}{}^c dt$, dt being the time increment.

We now consider the following quantities for the derivation of single crystal constants from the tensile properties of its polycrystal:

1 **Initial Creep Rate.** From equations (9) and (10) it is given by

$$\dot{\bar{\epsilon}}_0{}^c = (a + cd)\bar{\sigma}^b. \tag{14}$$

On the other hand from (11)–(13), (7) and (8), it can also be written as

$$\dot{\bar{\epsilon}}_0{}^c = (\kappa + \eta\zeta)\{\Sigma\nu_{11}{}^{\lambda+1}\}\bar{\sigma}^\lambda. \tag{15}$$

Comparison of (14) and (15) leads to

$$\lambda = b, \tag{16}$$

$$\kappa + \eta\zeta = \frac{a + cd}{\{\Sigma\nu_{11}{}^{b+1}\}}. \tag{17}$$

2 **Steady Creep Rate.** The steady creep rate of the aggregate under tension is given by equation (9). Also, by means of equations (11)–(13) and (7)

$$\dot{\bar{\epsilon}}_s{}^c = \kappa\{\Sigma\nu_{11}\tau_s{}^b\}, \tag{18}$$

where τ_s is the resolved shear stress of a slip system at steady state. Its value is not known *a priori*, but can be estimated approximately. In a tensile creep test, though the local stress field in each grain can be triaxial, its predominant component is still the tensile component. Thus neglecting the other components, we have $\tau_s \approx \nu_{11}\sigma_s$, where σ_s is the said component at steady state, which is heterogeneous throughout the aggregate and whose value in each grain depends on its orientation. We write

$$\overset{(k)}{\sigma_s} = \overset{(k)}{p}\bar{\sigma}, \tag{19}$$

for the kth grain, subject to the constraint

$$\{p\} = 1, \tag{20}$$

for self-consistency. The value of p for each grain thus characterizes the departure of its local tensile stress from the uniformly applied aggregate stress $\bar{\sigma}$. Then equation (18) becomes

$$\dot{\bar{\epsilon}}_s{}^c = \kappa\{\Sigma\nu_{11}{}^{b+1}p^b\}\bar{\sigma}^b. \tag{21}$$

We further note that at steady state $d\sigma = 0$ for each grain. Consequently from equation (4) $d\epsilon^c = d\bar{\epsilon}^c$. Since the creep rate in every grain is now equal to that of the aggregate, the averaging bracket in (21) can be deleted. Then, from equations (9) and (21), we arrive at

$$p = \left(\frac{a}{\kappa\Sigma\nu_{11}{}^{b+1}}\right)^{1/b}, \tag{22}$$

for each grain. Substitution of this relation into the constraint (20) yields

$$\kappa = a\left\{\frac{1}{(\Sigma\nu_{11}{}^{b+1})^{1/b}}\right\}^b. \tag{23}$$

3 **Initial Decreasing Rate of the Creep Rate.** From equations (9) and (10) it is given by

$$\left.\frac{d\dot{\bar{\epsilon}}^c}{d\bar{\epsilon}^c}\right|_{t=0} = -\frac{c^2 d}{a + cd}. \tag{24}$$

On the other hand consider the limiting process

$$\left.\frac{d\dot{\bar{\epsilon}}^c}{d\bar{\epsilon}^c}\right|_{t=0} = \lim_{\Delta t\to 0} \left.\frac{\Delta\{\dot{\epsilon}^c\}}{\Delta\{\epsilon^c\}}\right|_{t=0}.$$

From (12) we write $\Delta\{\dot{\epsilon}^c\} = \{\sum_i \overset{(i)}{\nu_{11}}\Delta\overset{(i)}{\dot{\gamma}}{}^c\}$. The variation of $\overset{(i)}{\dot{\gamma}}{}^c$, or $\Delta\overset{(i)}{\dot{\gamma}}{}^c$, in view of (7) and (8), depends on $\Delta\overset{(j)}{\tau}$ and $\Delta\overset{(j)}{\gamma_t}{}^c$ for all j. When the aggregate is under a changing, or sinusoidal stress, these factors are equally important. But in a constant-stress creep test, the former factor is less important than the latter. Thus

$$\Delta\overset{(i)}{\dot{\gamma}}{}^c \approx \sum_j \frac{\partial\overset{(i)}{\dot{\gamma}}{}^c}{\partial\overset{(j)}{\gamma_t}{}^c}\Delta\overset{(j)}{\gamma_t}{}^c;$$

consequently from (7) and (8)

$$\Delta\overset{(i)}{\dot{\gamma}}{}^c \approx -\eta\sum_j [\alpha + (1-\alpha)\cos\overset{(i,j)}{\theta}\cos\overset{(i,j)}{\phi}]\Delta\overset{(j)}{\gamma_t}{}^c. \tag{25}$$

Furthermore with $\Delta\gamma_t{}^c = \dot{\gamma}_t{}^c\Delta t$, (8), (13), and (16) we arrive at

$$\Delta\{\dot{\epsilon}^c\}_{t=0} \approx -\eta^2\zeta \times\left\{\sum_i \overset{(i)}{\nu_{11}}\sum_j [\alpha + (1-\alpha)\cos\overset{(i,j)}{\theta}\cos\overset{(i,j)}{\phi}]\overset{(j)}{\nu_{11}}{}^b\right\}\bar{\sigma}^b\Delta t. \tag{26}$$

On the other hand from (15) and (16)

$$\Delta\{\epsilon^c\}_{t=0} = (\kappa + \eta\zeta)\{\Sigma\nu_{11}{}^{b+1}\}\bar{\sigma}^b\Delta t. \tag{27}$$

Then, from equations (24), (26), (27) and (17), we find

$$\eta^2\zeta\left\{\sum_i \overset{(i)}{\nu_{11}}\sum_j [\alpha + (1-\alpha)\cos\overset{(i,j)}{\theta}\cos\overset{(i,j)}{\phi}]\overset{(j)}{\nu_{11}}{}^b\right\} = c^2 d. \tag{28}$$

Combining equations (28), (17), and (23), we finally have

$$\eta\left\{\sum_{i}^{(i)}\nu_{11}\sum_{j}\left[\alpha+(1-\alpha)\overset{(i,j)}{\cos\theta}\,\overset{(i,j)}{\cos\phi}\right]\overset{(j)}{\nu_{11}}{}^{b}\right\}$$

$$=\frac{c^2d}{\dfrac{a+cd}{\{\Sigma\nu_{11}{}^{b+1}\}}-a\left\{\dfrac{1}{(\Sigma\nu_{11}{}^{b+1})^{1/b}}\right\}^{b}}. \tag{29}$$

Equations (16), (17), (23), and (29) provide four equations for the five constants κ, λ, η, ζ, and α. The additional information can be obtained from the recovery curve. Since the degree of isotropy in work hardening α exists within the range $0 \leq \alpha \leq 1$, we may adopt the iterative process first by assuming $\alpha = 1$ (isotropic hardening), to derive the values of the remaining four parameters so that the two tensile creep curves can be well simulated. Next, we use these five constants to calculate the recovery curve. The calculated recovery strain is usually too small under the assumption of isotropic hardening. We then reduce the value of α to increase the kinematic component, and repeat the same process, until the two tensile creep curves and the recovery curve are accurately simulated. The corresponding values of these five parameters then can be used to predict the behavior of metals under desired loading conditions.

It should be pointed out that, due to the complicated nature of creep deformation in a polycrystalline solid, the foregoing equations can only provide the starting values for the iterative scheme. Since the stress relaxation in more favorably oriented grains under higher tensile stress is greater than that under lower stress, the actual value of λ is always greater than b.

Prediction of Creep, Recovery, and the Bauschinger Effect of an Aluminum Alloy

The lattice of an aluminum crystal is face-centered-cubic; it has four {111} slip planes and three ⟨110⟩ slip directions on each plane. The polycrystal model used here consists of 75 different crystal orientations, which were constructed with the aid of stereographic projections in the standard triangle to simulate the three-dimensional isotropy. Its isotropy, as measured by the generated creep strain components, has a maximum deviation from perfect isotropy of less than 4 percent. In this section we use the method outlined earlier to, first, derive the five single crystal constants from two tensile creep and one recovery curve of its polycrystal, and then use these constants to predict the creep, recovery, and the Bauschinger effect of the same polycrystal.

The experimental data of Blass and Findley [16], Findley and Lai [17, 18] on a 2618-T61 Aluminum alloy, tested at 200°C, will be used for derivation and for comparison. The two tensile creep curves were tested at $\bar{\sigma} = 119.5$ MPa (17.33 ksi) and 193.1 MPa (28 ksi) and the recovery curve taken following the creep at $\bar{\sigma} = 119.5$ MPa. The test data were given in terms of total strain. Since, as stated by Findley and Lai, there was no plastic deformation in these tests, the creep strains can be obtained from the total strain minus the elastic strain, with the Young's modulus $E = 65.0$ GPa (3.57×10^6 psi) [17]. The constant-stress creep tests lasted for 2 hr and the recovery 30 min. The creep and recovery data for these three loading conditions are shown as open circles in Fig. 1. These two creep curves were found to be representable by equations (9) and (10) with $a = 4.33 \times 10^{-11}$, $b = 3.82$, $c = 9.14 \times 10^{-2}$, and $d = 1.09 \times 10^{-8}$, where stress, strain, and strain rate were in the units of MPa, 10^{-4} m/m, and 10^{-4} m/m/min, respectively.

We used equations (16), (17), (23), and (29), and the iterative method outlined to derive the values of single crystal constants. The results are $\kappa = 2.52 \times 10^{-10}$, $\lambda = 4.12$, $\eta = 0.10$, $\zeta = 1.09 \times 10^{-7}$, and $\alpha = 0.28$, where stress and time are again expressed in terms of MPa and min, respectively. The calculated theoretical curves are also shown in Fig. 1; the experimental data are seen to be well simulated. In the numerical scheme the transient rate of a slip system was assumed to vanish when the parenthesis term in equation (8) became negative.

Four distinctively different loading conditions are available from the test data for comparison. These are:

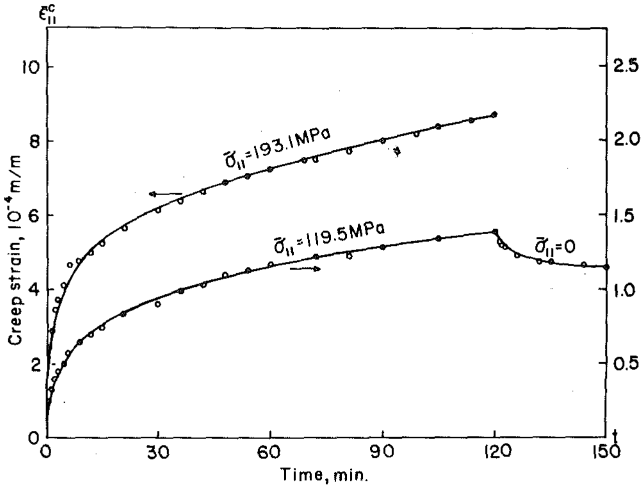

Fig. 1 Derivation of single crystal constants from tensile creep and recovery curves of a 2618-T61 Aluminum alloy

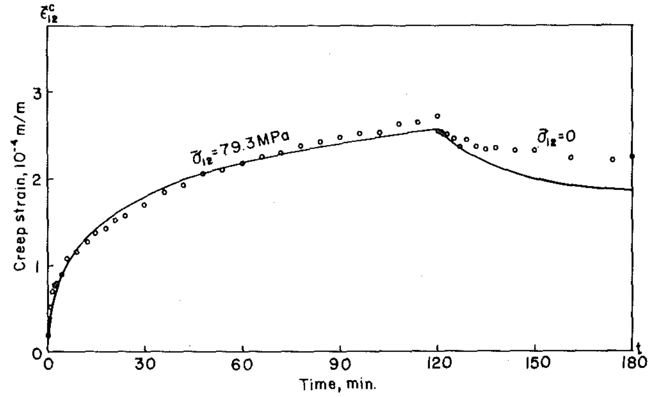

Fig. 2 Creep and recovery of a 2618-T61 Aluminum alloy under pure shear

(*i*) Creep under constant shear stress at $\bar{\sigma}_{12} = 79.3$ MPa (11.5 ksi) for 2 hr, followed by recovery for 1 hr.

(*ii*) Creep and recovery under axial step loading: first creep under $\bar{\sigma}_{11} = 137.9$ MPa (20 ksi) for 2 hr, followed by recovery for 30 min, and then creep under reloading at $\bar{\sigma}_{11} = 193.1$ MPa (28 ksi) for another 1.5 hr.

(*iii*) Creep under step and nonradial loading: first creep under $\bar{\sigma}_{12} = 99.3$ MPa (14.4 ksi) for 45 min, then step down to $\bar{\sigma}_{12} = 70.3$ MPa (10.2 ksi) for 15 min, and finally, creep under superimposed $\bar{\sigma}_{11} = 122$ MPa (17.7 ksi) for another 45 min. This program involves combined loading.

(*iv*) To examine the Bauschinger effect in creep, an opposite shear at $\bar{\sigma}_{12} = 99.3$ MPa (14.4 ksi) was further imposed for 45 min at the end of recovery in (*ii*) (the actual experimental test lasted for 1 hr). On the other hand the first part of creep data in (*iii*) under the same stress was replotted for comparison.

The complete creep strain history for these four loading conditions are shown in Figs. 2–5, in which the experimental data are given as open circles and the theoretical predictions expressed by the curves. In view of the extremely complicated behavior of metals under combined stress and step loading the agreement between the theory and experiments is seen to be generally good. In Fig. 2 creep strains predicted by the theory are fairly close to the test data, and the recovery, as evidenced by both the theoretical and experimental results, is far from complete after 1 hr. From the test data the recovered strain was about 0.50×10^{-4} m/m at the end; the theory on the other hand predicted the value 0.75×10^{-4} m/m. In Fig. 3 under axial step loading the theoretical results are very close to the experimental ones. In Fig. 4 though the theory slightly overestimates the creep strain during the

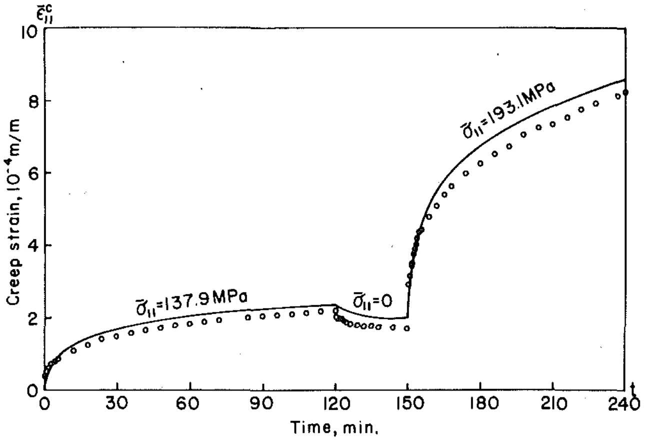

Fig. 3 Creep and recovery of a 2618-T61 Aluminum alloy under axial step loading

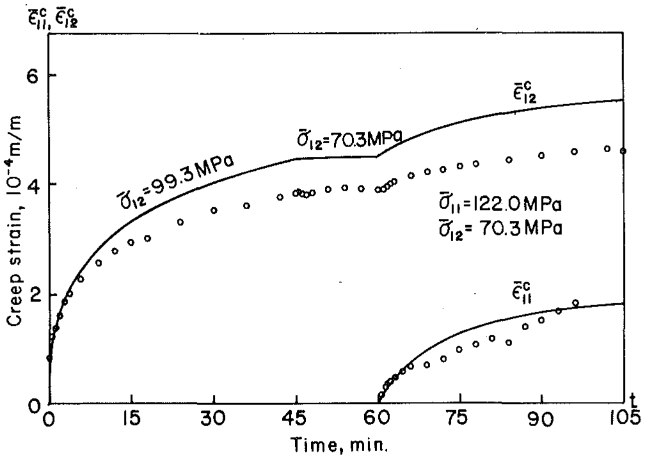

Fig. 4 Creep of a 2618-T61 Aluminum alloy under step shear and non-radial loading

first 45 min, the creep strains produced during the second and third stages of loading are in very good agreement with experiments. Finally, in Fig. 5, the creep strain under $G3$ was produced following a creep and recovery test in the opposite loading direction, while that under $E1$ was obtained without prior creep. The creep strain under $G3$ is seen to be far greater than its corresponding part under $E1$ from both theory and experiment. Although the theory in one case underestimates the creep strain by about 8 percent and in the other overestimates it by 15 percent, the directional Bauschinger effect in creep deformation is vividly disclosed.

Conclusions

In this paper we examined the applicability of Kröner's and Hill's self-consistent models, and found that, while Kröner's model was not entirely consistent in plasticity, it is fully consistent in creep. Hill's model, on the other hand, should be used with a modified constraint tensor, containing the elastic moduli, instead of the tangent moduli of the matrix.

Kröner's model was supplemented with a physically consistent constitutive equation for the slip system, which was based on a hardening law proposed by Weng. This law involves both isotropic and kinematic components in the latent hardening of slip systems, and is characterized by the degree of isotropy in working hardening. The kinematic component of the hardening law and the residual stress developed in more favorably oriented slip systems are the two major driving forces for recovery and the Bauschinger effect of the aggregate. Taylor's isotropic hardening law was found inadequate for the prediction of such behavior.

Kröner's self-consistent model, the proposed constitutive equation, and Weng's inverse method form the basis of the study of time-dependent behavior of metals. This method is in the most general form, and can be used to predict creep, recovery, and the Bauschinger effect under varying and combined stress.

We employed the proposed method to predict the time-dependent behavior of a 2618-T61 Aluminum alloy. The test data of Blass and Findley, and Findley and Lai were used for derivation and for comparison. First, the single crystal constants were derived from two tensile creep curves and one recovery curve of its aggregate. These constants were then used to calculate the creep and recovery strains of the same polycrystal under pure shear, axial step loading, and step and nonradial loading. The predicted results were seen to be in generally good agreement with experiments.

Acknowledgment

This work was supported by the National Science Foundation, Solid Mechanics Program, through Grant ENG 78-09738. The development of the isotropic, face-centered-cubic polycrystal model by Mr. C. R. Chiang is gratefully acknowledged.

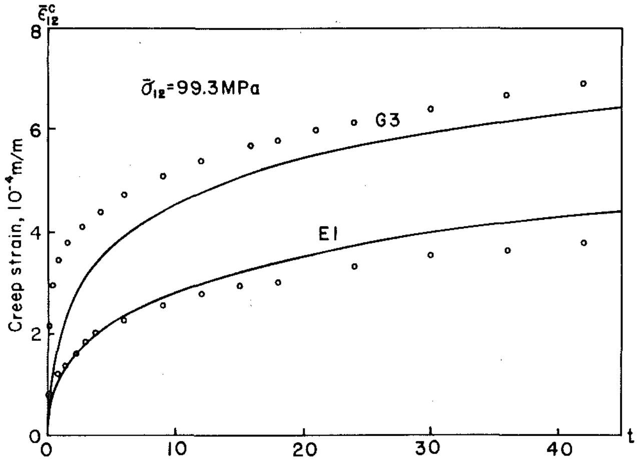

Fig. 5 The Bauschinger effect of a 2618-T61 Aluminum alloy in creep deformation

References

1 Eshelby, J. D., "The Determination of the Elastic Field of an Ellipsoidal Inclusion, and Related Problems," *Proceedings of the Royal Society*, London, Series A, Vol. 241, 1957, pp. 376–396.

2 Kröner, E., "Zur Plastischen Verformung des Vielkristalls," *Acta Metallurgica*, Vol. 9, 1961, pp. 155–161.

3 Budiansky, B., and Wu, T. T., "Theoretical Prediction of Plastic Strains of Polycrystals," *Proceedings, 4th U. S. National Congress of Applied Mechanics*, 1962, pp. 1175–1185.

4 Hill, R., "Continuum Micro-Mechanics of Elastoplastic Polycrystals," *Journal of the Mechanics and Physics of Solids*, Vol. 13, 1965, pp. 89–101.

5 Hutchinson, J. W., "Elastic-Plastic Behavior of Polycrystalline Metals and Composites," *Proceedings of the Royal Society*, London, Series A, Vol. 319, 1970, pp. 247–272.

6 Berveiller, M., and Zaoui, A., "An Extension of the Self-Consistent Scheme to Plastically Flowing Polycrystals," *Journal of the Mechanics and Physics of Solids*, Vol. 26, 1979, pp. 325–344.

7 Brown, G. M., "A Self-Consistent Polycrystalline Model for Creep Under Combined Stress States," *Journal of the Mechanics and Physics of Solids*, Vol. 18, 1970, pp. 367–381.

8 Hutchinson, J. W., "Bounds and Self-Consistent Estimates for Creep of Polycrystalline Materials," *Proceedings of the Royal Society*, London, Series A, Vol. 348, 1976, pp. 101–127.

9 Lin, T. H., "Physical Theory of Plasticity," *Advances in Applied Mechanics*, Vol. 11, ed., Yih, C. S., Academic Press, New York, 1971, pp. 256–312.

10 Lin, T. H., Yu, C. L., and Weng, G. J., "Derivation of Polycrystal Creep Properties From the Creep Data of Single Crystals," ASME JOURNAL OF APPLIED MECHANICS, Vol. 44, 1977, pp. 73–78.

11 Weng, G. J., "A Physically Consistent Method for the Prediction of Creep Behavior of Metals," ASME JOURNAL OF APPLIED MECHANICS, Vol. 46, 1979, pp. 800–804.

12 Taylor, G. I., "Plastic Strain in Metals," *Journal of the Institute of Metals,* Vol. 62-1, 1938, pp. 307–324.

13 Buckley, S. N., and Entwistle, K. M., "The Bauschinger Effect in Super-Pure Aluminum Single Crystals and Polycrystals," *Acta Metallurgica,* Vol. 4, 1954, pp. 352–361.

14 Weng, G. J., "Dislocation Theories of Work Hardening and Yield Surfaces of Single Crystals," *Acta Mechanica,* Vol. 37, 1980, pp. 217–230.

15 Weng, G. J., "Kinematic Hardening Rule in Single Crystals," *International Journal of Solids and Structures,* Vol. 15, 1979, pp. 861–870.

16 Blass, J. J., and Findley, W. N., "Short-Time, Biaxial Creep of an Aluminum Alloy With Abrupt Changes of Temperature and State of Stress," ASME JOURNAL OF APPLIED MECHANICS, Vol. 38, 1971, pp. 489–501.

17 Findley, W. N., and Lai, J. S., "Creep and Recovery of 2618 Aluminum Alloy Under Combined Stress With a Representation by a Viscous-Viscoelastic Model," ASME JOURNAL OF APPLIED MECHANICS, Vol. 45, 1978, pp. 507–514.

18 Lai, J. S., and Findley, W. N., "Creep of 2618 Aluminum Under Step Stress Changes Predicted by a Viscous-Viscoelastic Model," ASME JOURNAL OF APPLIED MECHANICS, Vol. 47, 1980, pp. 21–26.

W. N. Findley
Professor of Engineering,
Division of Engineering,
Brown University,
Providence, R. I. 02912
Fellow ASME

J. S. Lai
Professor of Civil Engineering,
School of Civil Engineering,
Georgia Institute of Technology,
Atlanta, Ga. 30332

Creep of 2618 Aluminum Under Side-Steps of Tension and Torsion and Stress Reversal Predicted by a Viscous-Viscoelastic Model

Combined tension and torsion creep experiments are reported in which (A) *one stress component was increased or decreased while the other remained constant;* (B) *one stress component was removed while the other remained constant;* (C) *torsion was partially or fully reversed with or without simultaneous constant tension. Among the observed features of the experimental results were the following: when one stress component was removed the creep from the other component was unaffected; upon small reductions in stress there was no recovery-type behavior; and when torsion was fully reversed, all prior strain was wiped out. A nonlinear viscous-viscoelastic model was used for which the material constants were derived from constant-stress creep and recovery data and previously reported. This model, together with certain necessary modifications, was used to compute the creep resulting from the complex stress histories described. Most features of the experimental results were predicted reasonably well by the modified theory.*

Introduction

The creep behavior of metals under changing stress—especially changes in state of combined stress and stress reversal—has received little experimental observation. Mathematical expressions employed, such as strain hardening or viscoelastic models, usually are unable to describe the detail of creep behavior under changes such as in the foregoing. References to prior work in this area are given in [1, 2].

In a previous paper [1] the authors described a viscous-viscoelastic model in which the strain was resolved into five components: elastic ϵ^e; time-independent plastic ϵ^p; positive nonrecoverable (viscous) ϵ^v(pos); negative nonrecoverable (viscous) ϵ^v(neg); and recoverable (viscoelastic) ϵ^{ve} components. From creep and recovery experiments under combined tension and torsion, the time and stress dependence of these components were evaluated for constant stresses. In [3] constitutive relations for changes in stress state were developed and their predictions were compared with actual creep behavior in simple stress states (uniaxial tension or pure torsion) under step changes in stress.

In the present paper, results of combined tension and torsion experiments with time-dependent stress histories including side step changes in tension and torsion and stress reversal in torsion are reported. Predictions of the experimental results are also presented using the constants determined in [1] and the constitutive relations derived in [3], with some modifications. The last two experiments discussed in the following were reported in [4] as tests E and G.

Material and Specimens

An aluminum forging alloy 2618-T61 was employed in these experiments. Specimens were taken from the same lot of 63.5 mm (2½ in.) dia forged rod as used in [1, 3] and the same lot as specimens D–H in [4]. Specimens were thin-walled tubes having outside diameter, wall thickness, and gage length of 25.4, 1.52, and 101.6 mm (1., 0.060, and 4. in.), respectively. A more complete description of material and specimens is given in [1].

Experimental Apparatus and Procedure

The conbined tension and torsion creep machine used for these experiments was described in [5] and briefly in [1]. The temperature control and measurement employed was described in [1, 4]. Stress was produced by applying dead weights at the end of levers. The shearing stress and tensor shearing strain reported were computed at midwall thickness of the specimen. The gage length employed was measured

---

Contributed by the Applied Mechanics Division of THE AMERICAN SOCIETY OF MECHANICAL ENGINEERS, for presentation at the 1981 Joint ASME/ASCE Applied Mechanics, Fluids Engineering, and Bioengineering Conference, University of Colorado, Boulder, Colo., June 22–27, 1981.

Discussion on this paper should be addressed to the Editorial Department, ASME, United Engineering Center, 345 East 47th Street, New York, N. Y. 10017, *and will be accepted until June 1, 1981. Readers who need more time to* prepare a Discussion should request an extension from the Editorial Department. Manuscript received by ASME Applied Mechanics Division, July, 1979; *final revision, August, 1980.* Paper No. 81-APM-8.

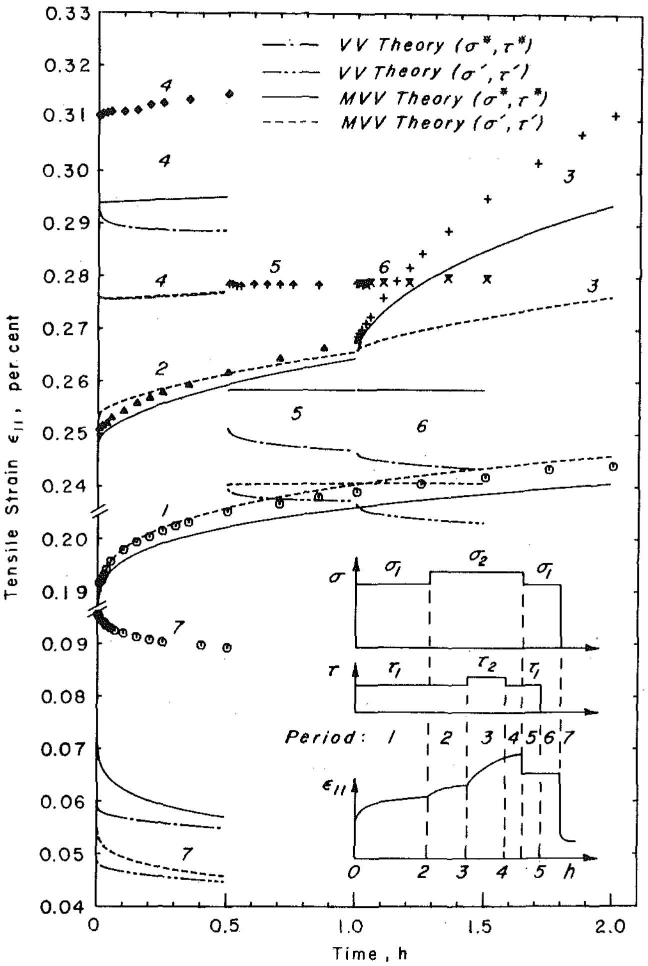

Fig. 1(*a*) **Tensile strain for combined tension and torsion creep of 2618-T61 Al at 200°C under side-steps of loading, unloading, and recovery. Where the *VV* theory is not shown it is the same as the *MVV* theory. Numbers indicate periods on insert. σ_1 = 119.5 MPa (17.33 ksi); σ_2 = 143.4 MPa (20.8 ksi); τ_1 = 69.0 MPa (10 ksi); and τ_2 = 82.7 MPa (12 ksi).**

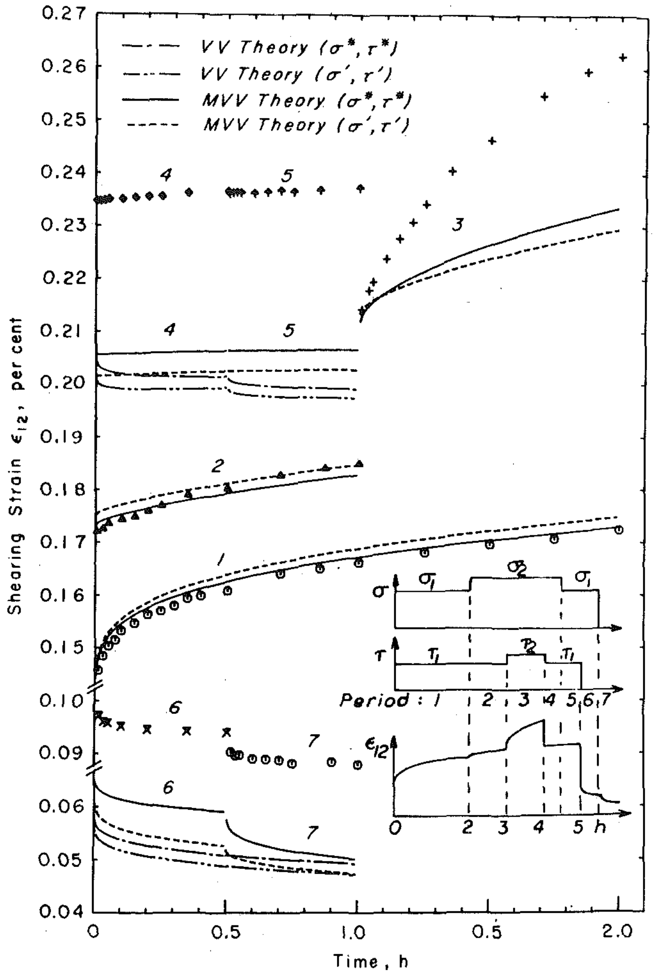

Fig. 1(*b*) **Shearing strain for combined tension and torsion creep of 2618-T61 Al at 200°C under side-steps of loading, unloading, and recovery. Where the *VV* theory is not shown it is the same as the *MVV* theory. Numbers indicate periods on insert. σ_1 = 119.5 MPa (17.33 ksi); σ_2 = 143.4 MPa (20.8 ksi); τ_1 = 69.0 MPa (10 ksi); and τ_2 = 82.7 MPa (12 ksi).**

at room temperature and no correction was made for thermal expansion. The weights were applied by hand at the start of a test by lowering them quickly (in less than 10 sec) but without shock. The time of the start of the test was taken to be the instant at which the load was fully applied. In the present experiments changes in loading were made at intervals during the creep tests. The load changes were accomplished by hand in the same manner. Strain was recorded at the following intervals following a load change: every 0.01*h* to 0.05*h*; every 0.02*h* to 0.1*h*; every 0.05*h* to 0.5*h*; every 0.1*h* to 1.0*h*; and every 0.2*h* to 2.0*h*. All experiments discussed in this paper were performed at 200 ± 0.6°C (392°F).

Experimental Results

Three combined tension and torsion creep experiments are shown in Figs. 1–3. Each experiment consisted of multiple steps of stress changes in tension or torsion alone and simultaneous changes in tension and torsion.

Fig. 1 shows results of a combined tension and torsion experiment in which there was a step increase in tension σ in period 2 with no change in torsion τ. In period 3, there was a step increase in torsion τ, with no change in tension σ. Subsequent periods involved partial unloading, first in torsion, then in tension, followed by recovery first in torsion, then in tension.

Fig. 2 shows the results of the series of changes in stress state during creep for the portion of test *E* conducted at 200°C as reported in [4]. In period 1, Fig. 2(*b*), there was pure torsion and in step 2 the torsion was partially unloaded. In period 3, tension was added with no change in torsion. In period 4, the torsion was removed with no change in the tension. In period 5, the tensile stress was increased and in period 6, the tensile stress was decreased back to that of period 4. In period 7, negative torsion was added with no change in tension.

Reversals of torsion were performed as part of experiments shown in Figs. 2 and 3. In Fig. 2 (*b*) following recovery in torsion in periods 4, 5, and 6 the shearing stress was partially reversed in period 7 to a negative value less than the maximum positive value in period 1, while the tensile stress remained constant at a level less than its maximum. In Fig. 3, the first reversal of torsion was preceded by positive torsion then recovery at zero stress. In periods 3, 4, and 5, stress reversals were performed in pure torsion. In period 6, a partial stress reversal occurred. In period 7, tension was added at constant torsion. Periods 8, 9, and 10 included stress reversals in torsion while the tension remained constant.

Discussion of Results

Among the features of the results of these creep tests the following may be noted at this point:

1 (*A*) When σ was increased while τ remained constant in Fig. 1, period 2, there was a small increase in creep rate with a slight primary-type character (a positive creep rate decreasing with time).

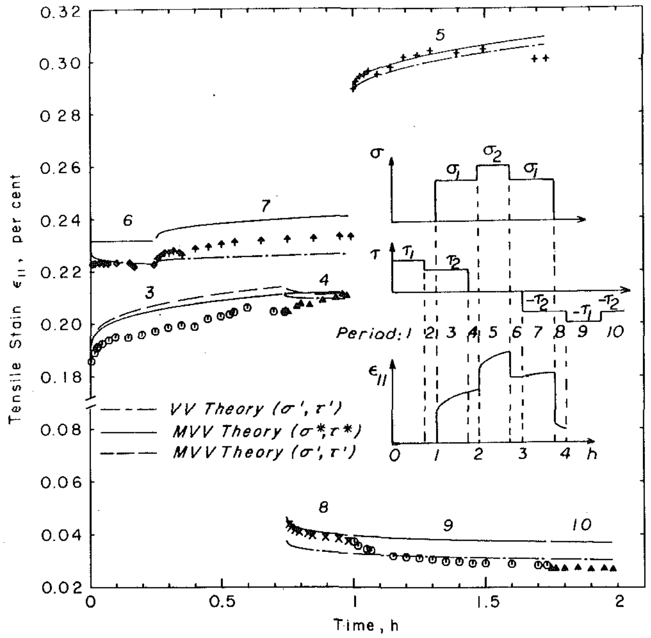

Fig. 2(*a*) Tensile strain for combined tension and torsion creep of 2618-T61 Al at 200°C under side-steps, partial, and complete reversal of torsion. Where the *VV* theory is not shown it is the same as the *MVV* theory. Numbers indicate periods on insert. σ_1 = 122.0 MPa (17.7 ksi); σ_2 = 172.4 MPa (25 ksi); τ_1 = 99.3 MPa (14.4 ksi); and τ_2 = 70.3 MPa (10.2 ksi).

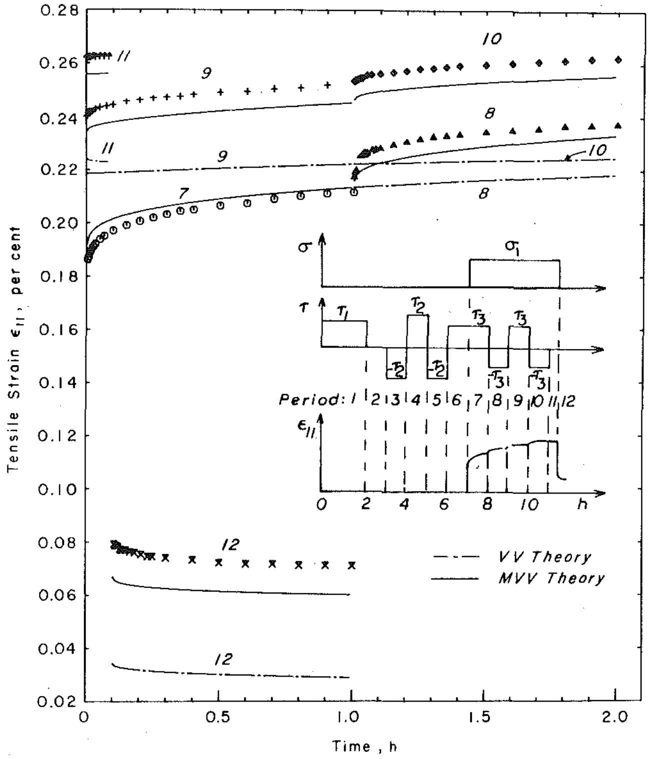

Fig. 3(*a*) Tensile strain for combined tension and torsion creep of 2618-T61 Al at 200°C under stress reversals in torsion with and without tensile stress. Where the *VV* theory is not shown it is the same as the *MVV* theory. Numbers indicate periods on insert. σ_1 = 122.0 MPa (17.7 ksi); τ_1 = 79.3 MPa (11.5 ksi); τ_2 = 99.3 MPa (14.4 ksi); and τ_3 = 70.3 MPa (10.2 ksi).

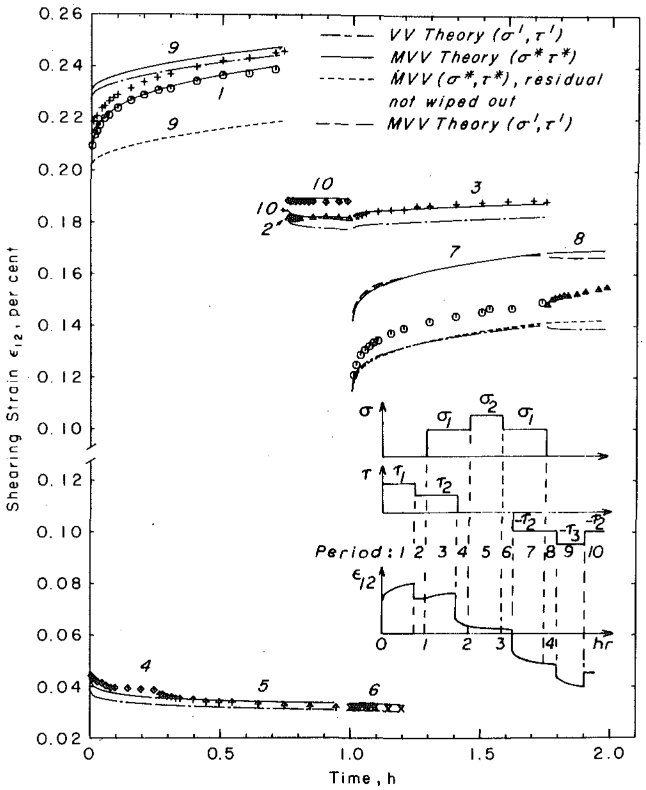

Fig. 2(*b*) Shearing strain for combined tension and torsion creep of 2618-T61 Al at 200°C under side-steps, partial, and complete reversal of torsion. Where the *VV* theory is not shown it is the same as the *MVV* theory. Numbers indicate periods on insert. σ_1 = 122.0 MPa (17.7 ksi); σ_2 = 172.4 MPa (25 ksi); τ_1 = 99.3 MPa (14.4 ksi); and τ_2 = 70.3 MPa (10.2 ksi).

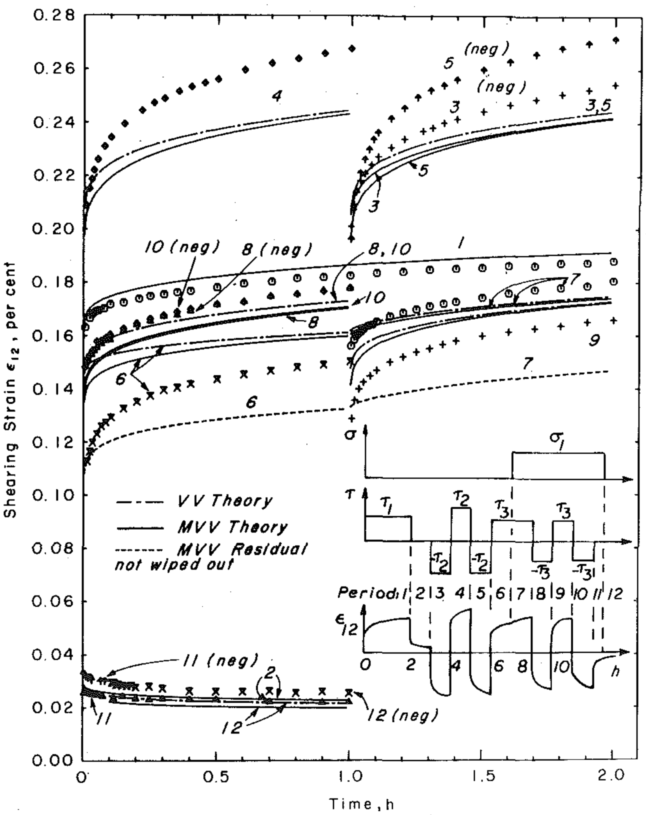

Fig. 3(*b*) Shearing strain for combined tension and torsion creep of 2618-T61 Al at 200°C under stress reversals in torsion with and without tensile stress. Where the *VV* theory is not shown it is the same as the *MVV* theory. Numbers indicate periods on insert. σ_1 = 122.0 MPa (17.7 ksi); τ_1 = 79.3 MPa (11.5 ksi); τ_2 = 99.3 MPa (14.4 ksi); and τ_3 = 70.3 MPa (10.2 ksi).

1 (*B*) However, when τ was increased while σ remained constant in Fig. 1, period 3, there was a large increase in creep rate with some primary-type characteristics.

2 (*A*) When τ was reduced while σ remained constant in Fig. 1, period 4, there was a large reduction in creep rate but no recovery-type behavior (negative creep rate decreasing with time).

2 (*B*) However, when σ was reduced while τ remained constant in Fig. 1, period 5, there was a small reduction in tensile creep rate, no change in torsion creep rate and no recovery-type behavior.

3 (*A*) On removal of one stress component to zero, time-dependent recovery occurred in the strain associated with the removed component, as in Fig. 1(*a*), period 7, Fig. 1(*b*), period 6, Fig. 2(*a*), period 8, Fig. 2(*b*), period 4, Fig. 3(*a*), period 12, and Fig. 3(*b*), period 11.

3 (*B*) However, as noted in item 2, there was no time-dependent recovery-type behavior resulting from the moderate reductions of stress, as noted in item 2 and in Fig. 2(*a*), period 6 and Fig. 2(*b*), periods 2 and 10.

4 When one stress component was removed to zero while the other remained constant no change occurred in the behavior of the strain component associated with the constant stress component as shown in Fig. 1(*a*), period 6, Fig. 2(*a*), period 4, Fig. 2(*b*), period 8, and Fig. 3(*a*), period 11.

5 On reversal of torsion stress new primary-type creep was observed in the shearing strain. The magnitudes of shearing creep strain and creep rate were similar, but the rates were somewhat larger, at each stress reversal; see Fig. 2(*b*), period 7, Fig. 3(*b*), periods 4, 5, 9, 10. The similarity of magnitudes meant that all prior strain was wiped out at each stress reversal.

6 Constant tension stress in the presence of reversing torsion stress showed a second primary-type tensile creep on the first reversal of torsion, which was about the same as that on the first loading. On subsequent reversals of torsion smaller primary-type tensile creep was observed at each stress reversal; see Fig. 3(*a*).

Constitutive Equations for Creep Under Combined Tension and Torsion

In the following the constitutive equations determined for the material under consideration in [1, 3] were used to predict the creep behavior resulting from the stress histories described in the preceeding sections. Some modifications of the theories are described which better predict some of the observed behavior described in the foregoing.

In [3] it was shown that creep of 2618 Aluminum at 200°C under combined tension and torsion could be described adequately by the following relation:

$$\epsilon_{ij}(t) = \epsilon^{e}_{ij} + \epsilon^{p}_{ij} + \epsilon^{v}_{ij}(t) + \epsilon^{ve}_{ij}(t), \tag{1}$$

where ϵ^{e}_{ij}, ϵ^{v}_{ij}, and ϵ^{ve}_{ij} represent the time-independent elastic strain, time-dependent nonrecoverable (viscous) strain, and time-dependent recoverable (viscoelastic) strain, respectively, and the time-independent plastic strain ϵ^{p}_{ij} was zero in the present experiments. ϵ^{v}_{ij} was further resolved into positive and negative parts because of its nonrecoverable feature. Without separate positive and negative parts $\dot{\epsilon}^{v}$ would be zero upon stress reversal because it is nonrecoverable. The elastic modulus E_0, shear modulus G_0, and Poisson's ratio ν for the material at 200°C as reported in [1, 3] are given in Table 1. The constitutive relations for $\epsilon^{v}_{ij}(t)$ and $\epsilon^{ve}_{ij}(t)$ under constant stresses and time-dependent stresses as proposed in [1, 3] are reviewed in the following.

Constant Stress. Under constant stress, the components ϵ^{v} and ϵ^{ve} under combined tension σ and torsion τ were represented by the following equations:

$$\epsilon^{ve}_{11}(t) = \left(\frac{R}{1+R}\right) F[(\sigma-\sigma'),(\tau-\tau')]t^{n}, \tag{2}$$

$$\epsilon^{ve}_{12}(t) = \left(\frac{R}{1+R}\right) G[(\sigma-\sigma'),(\tau-\tau')]t^{n}, \tag{3}$$

Table 1 Constants for equations (2)-(11) using σ', τ' for F_4^+, G_3^+, G_4^+

$F_1^+ = 6.084 \times 10^{-12}$, per Pa-h^n (0.004195, % per ksi-h^n)

$F_2^+ = -7.431 \times 10^{-20}$, per Pa^2-h^n (-0.0003533, % per ksi^2-h^n)

$F_3^+ = 7.596 \times 10^{-28}$, per Pa^3-h^n (0.0000249, % per ksi^3-h^n)

$\sigma^* = 9.143 \times 10^{7}$, Pa (13.26, ksi)

$G_1^+ = 7.170 \times 10^{-12}$, per Pa-h^n (0.004944, % per ksi-h^n)

$G_2^+ = 2.703 \times 10^{-28}$, per Pa^3-h^n (0.00000886, % per ksi^3-h^n)

$\tau^* = 4.571 \times 10^{7}$, Pa (6.630, ksi)

$F_4^+ = 1.0491 \times 10^{-28}$, per Pa^3-h^n (0.000003439, % per ksi^3-h^n)

$F_5^+ = 0$

$G_3^+ = -4.020 \times 10^{-20}$, per Pa^2-h^n (-0.0001911, % per ksi^2-h^n)

$G_4^+ = 9.222 \times 10^{-28}$, per Pa^3-h^n (0.00003023, % per ksi^3-h^n)

Note: $n = 0.270$
$R = 0.55$
$E_0 = 6.5 \times 10^{4}$ MPa (9.43×10^{6} psi)
$G_0 = 2.45 \times 10^{4}$ MPa (3.57×10^{6} psi)
$\nu = 0.321$

$$\epsilon^{v}_{11}(t) = \left(\frac{1}{1+R}\right) F[(\sigma-\sigma'),(\tau-\tau')]t^{n}, \tag{4}$$

$$\epsilon^{v}_{12}(t) = \left(\frac{1}{1+R}\right) G[(\sigma-\sigma'),(\tau-\tau')]t^{n}. \tag{5}$$

The nonlinear functions F and G in (2)–(5) were derived from a third-order multiple integral representation [1, 6, 7], where for constant stress

$$F(\sigma-\sigma', \tau-\tau') = F_1(\sigma-\sigma') + F_2(\sigma-\sigma')^2 + F_3(\sigma-\sigma')^3 + F_4(\sigma-\sigma')(\tau-\tau')^2 + F_5(\tau-\tau')^2 \tag{6}$$

$$G(\sigma-\sigma', \tau-\tau') = G_1(\tau-\tau') + G_2(\tau-\tau')^3 + G_3(\sigma-\sigma')(\tau-\tau') + G_4(\sigma-\sigma')^2(\tau-\tau'), \tag{7}$$

and σ', τ' are the components of stress corresponding to a creep limit which may be taken to have a Tresca form defined as follows:

$$\begin{gathered}(\sigma')^2 + 4(\tau')^2 = (\sigma^*)^2 = (2\tau^*)^2,\\ \sigma'/\sigma = \tau'/\tau,\end{gathered} \tag{8}$$

and σ^* and τ^* are the creep limits in pure tension and pure torsion, respectively. The coefficients F_i, G_i, and constants σ^*, τ^*, R, and n are values determined from constant combined tension-torsion creep tests reported earlier [1] and shown in Table 1. The values reported in [1] for F_4, G_3, and G_4 were incorrect. They should have been as shown in Table 1.

Another possible representation for creep under combined tension and torsion is to use (2)–(7) with the apparent creep limit defined as fixed values σ^* and τ^* for tensile components and torsion components of stress, respectively instead of (8). This change required computing new values of F_4^+, G_3^+, and G_4^+. The best estimates of these three values from the available test data are shown in Table 2.

Predictions of the creep behaviors based on these two different respresentations, variable creep limit σ' and τ', and fixed creep limit σ^* and τ^*, are presented in this paper. It must be noted that when the components of the creep limit are variable (σ', τ') every change in

Table 2 Constants for equations (2)–(11) using σ^*, τ^* for F_4^+ and G_3^+

F_1^+ , F_2^+ , F_3^+ , σ^* , G_1^+ , G_2^+ , τ^* , n and R are the same as in Table I.

$F_4^+ = 6.214 \times 10^{-27}$ per $\mathrm{Pa}^3\text{-}\mathrm{h}^n$ (0.0002037, % per $\mathrm{ksi}^3\text{-}\mathrm{h}^n$)

$F_5^+ = 0$

$G_3^+ = 1.562 \times 10^{-19}$ per $\mathrm{Pa}^2\text{-}\mathrm{h}^n$ (0.0007424, % per $\mathrm{ksi}^2\text{-}\mathrm{h}^n$)

$G_4^+ = 0$

combination of stress requires a change in σ', τ' in accordance with (8). For fixed creep limits σ^*, τ^* no change is needed, however.

Time-Dependent Stress. The modified superposition principle (MSP) derived as a simplification of the multiple integral representation was shown in [3] to describe the time-dependent recoverable (viscoelastic) strain reasonably well. Under a continuously varying stress σ, the strain response ϵ^{ve} under the modified superposition assumption can be represented for nonlinear behavior by

$$\epsilon_{ij}^{ve}(t) = \int_0^t \frac{\partial}{\partial\sigma(\xi)} f_{ij}[\bar{\sigma}(\xi), \bar{\tau}(\xi), t - \xi]\dot{\bar{\sigma}}(\xi)d\xi, \tag{9}$$

where $f_{ij}(\sigma, t)$ represents a nonlinear time-dependent creep function such as (2) and (3) for ϵ_{11}^{ve} and ϵ_{12}^{ve}, respectively, and where $\bar{\sigma}(t) = \sigma(t) - \sigma'(t)$ and $\bar{\tau}(t) = \tau(t) - \tau'(t)$.

For a series of m step changes in stress as employed in the present work, (9) becomes as follows for ϵ_{12}^{ve} for example:

$$\begin{aligned}\epsilon_{12}^{ve}(t) = \left(\frac{R}{1+R}\right)\{G(\bar{\sigma}_1, \bar{\tau}_1)[t^n - (t - t_1)^n] + \ldots \\ + G(\bar{\sigma}_{m-1}, \bar{\tau}_{m-1})[(t - t_{m-2})^n - (t - t_{m-1})^n] \\ + G(\bar{\sigma}_m, \bar{\tau}_m)(t - t_{m-1})^n\}, \quad t_{m-1} < t. \end{aligned} \tag{9a}$$

For the time-dependent nonrecoverable (viscous) strain component ϵ^v, it was shown in [3] that the strain-hardening theory reasonably represented the behavior of this strain component under a time-dependent stress input. The strain-hardening theory for ϵ_{11}^v and ϵ_{12}^v can be represented by the following equations:

$$\epsilon_{11}^v(t) = \frac{1}{1+R}\left[\int_0^t \{F[\bar{\sigma}(\xi), \bar{\tau}(\xi)]\}^{1/n} d\xi\right]^n, \tag{10}$$

$$\epsilon_{12}^v(t) = \frac{1}{1+R}\left[\int_0^t \{G[\bar{\sigma}(\xi), \bar{\tau}(\xi)]\}^{1/n} d\xi\right]^n. \tag{11}$$

Equations (10) and (11) were derived from (4) and (5), respectively, using the strain-hardening concept as in [1, 3].

For a series of m step changes in stress, as employed in the present paper, (11) for example becomes as follows:

$$\begin{aligned}\epsilon_{12}^v(t) = \left(\frac{1}{1+R}\right)\{[G(\bar{\sigma}_1, \bar{\tau}_1)]^{1/n}(t_1) + [G(\bar{\sigma}_2, \bar{\tau}_2)]^{1/n}(t_2 - t_1) \\ + [G(\bar{\sigma}_3, \bar{\tau}_3)]^{1/n}(t - t_2)\}^n, \quad t_2 < t. \end{aligned} \tag{11a}$$

Viscous-Viscoelastic (*VV*) Theory. The total strain following a time-dependent stress history was found according to (1) by adding to the elastic strain corresponding to the stresses existing at the time of interest the ϵ^{ve} given by (9) and the ϵ^v given by (10) or (11) for axial strain or shear strain.

Modified Viscous-Viscoelastic (*MVV*) Theory. In [3] it was found that the observed characteristics of creep behavior of the material under partial unloading were not properly predicted by the *VV* theory. It was found, however, that the *MVV* theory proposed in [3] described the creep behavior of the material under partial unloading more closely than the *VV* theory. In the following the *MVV* theory, which will be used also in this paper, is reviewed. The basic difference between the *MVV* and the *VV* theories is in the treatment of the creep limits for the recoverable strain ϵ^{ve}. These differences in treatment are illustrated in Fig. 4.

1 For the *nonrecoverable strain* component, the strain-hardening rule was employed. Upon reduction of stress from σ_A to a current stress σ_B, Fig. 4(a), the strain rate $\dot{\epsilon}^v$ continued at the reduced (decreasing) rate prescribed by the strain-hardening rule, (10) and (11), as shown in Fig. 4(a), unless the current stress σ_C equaled or was less than the creep limit σ^* (or σ'). When $\sigma_C \leq \sigma^*$ (or σ'), $\dot{\epsilon}^v$ was zero as prescribed by (10) and (11); see Fig. 4(a).

2 Upon *reloading* from a stress σ_C below to a stress σ_D above the creep limit, the nonrecoverable strain rate $\dot{\epsilon}^v$ resumed at the rate prescribed by (10) and (11) but as though there had been no interval t_x for which $\sigma_C \leq \sigma^*$ (or σ'); see Fig. 4(c).

3 For the *recoverable strain* component ϵ^{ve} on *partial unloading* the recoverable strain rate $\dot{\epsilon}^{ve}$ became and remained zero for all reductions of stress from σ_A to σ_B, as shown in Fig. 4(b) unless the total change in stress from the highest stress $\sigma_{\max}$ [$= \sigma_A$ in Fig. 4(b)] previously encountered to the current stress σ_C exceeded in magnitude the creep limit σ^* (or σ'). That is,

$$\dot{\epsilon}^{ve} = 0 \quad \text{when} \quad (\sigma_A - \sigma_B) \leq |\sigma^*| \quad (\text{or } \sigma'), \tag{12}$$

$$\dot{\epsilon}^{ve} \neq 0 \quad \text{when} \quad (\sigma_A - \sigma_C) > |\sigma^*| \quad (\text{or } \sigma'). \tag{13}$$

Equation (12) can be considered as meaning that for a small unloading the recoverable strain component was "frozen." Equation (13) indicates that if the change in stress was greater than $|\sigma^*|$ or $|\sigma'|$ then recovery would occur followed eventually by creep; see Fig. 4(b).

4 Upon *increasing the stress* to $\sigma_D(\sigma_D \geq \sigma_A)$ following a period t_x (a dead zone) for which $(\sigma_{\max} - \sigma_B) < \sigma^*$ (or σ') and $\dot{\epsilon}^{ve} = 0$ as discussed in 3 in the foregoing the recoverable strain component ϵ^{ve} continued to creep in accordance with the viscoelastic behavior (9) as though the period t_x never occurred; see Fig. 4(c). In computing the behavior for situations described in 2, 3, and 4, it was thus necessary to introduce a time shift in equation (9), (10) or (11) to eliminate the appropriate period t_x when ϵ^{ve} was "frozen." Thus the new time t' subsequent to a period $t_x = (t_c - t_a)$ becomes $t' = t - (t_c - t_a)$, where t is the real time and t_a, t_c are the times when σ_B and σ_D were applied.

5 When *recoverable and nonrecoverable strain* components are *considered together* two special circumstances arise. Consider that the stress decreases from the highest value σ_A to a lower value σ_B. If $\sigma_A > 2\sigma^*$ and $\sigma^* \leq \sigma_B \leq (\sigma_A - \sigma^*)$ then there is creep occurring from ϵ^v and recovery from ϵ^{ve}. However, if $\sigma_A < 2\sigma^*$ and $(\sigma_A - \sigma^*) < \sigma_B < \sigma^*$ then there is neither creep nor recovery, $\dot{\epsilon}^v = \dot{\epsilon}^{ve} = 0$.

6 When one *stress component decreased while the other remained constant* the recoverable strain component ϵ^{ve} was treated as follows. The material behavior in such situations (such as Fig. 1, period 5) suggested that reducing or removing one stress component, say τ, while the other component, say σ, remained constant affected the strain as follows. The strain corresponding to mixed stress components behaved as though these mixed components had suffered a small stress reduction. That is, the strain, say ϵ_{11}, associated with the mixed stress components, say $\sigma\tau^2$, became constant. The strain, say ϵ_{11}, associated with the pure stress terms, say σ, σ^2, σ^3 which were unchanged, continued as though nothing had happened.

Thus the following computations based on the (*MVV*) theory were used for decreasing side steps.

For example, in Fig. 1(a), period 4, the strain components corresponding to $\sigma\tau^2$ and τ^2 remained constant at their values just prior to the stress change, while the strain corresponding to σ, σ^2, σ^3 continued uninterrupted. Again in Fig. 1(a), period 6, the strain components corresponding to $\sigma\tau^2$ and τ^2 remained constant while the strain corresponding to σ, σ^2, σ^3 continued uninterrupted (in this case they were also constant). For ϵ_{12}^{ve} in Fig. 1(b), period 4, there was no change from the value just preceding the stress change because the $G(\sigma, \tau)$ terms, see (7), decreased and the shear stress decrease was less

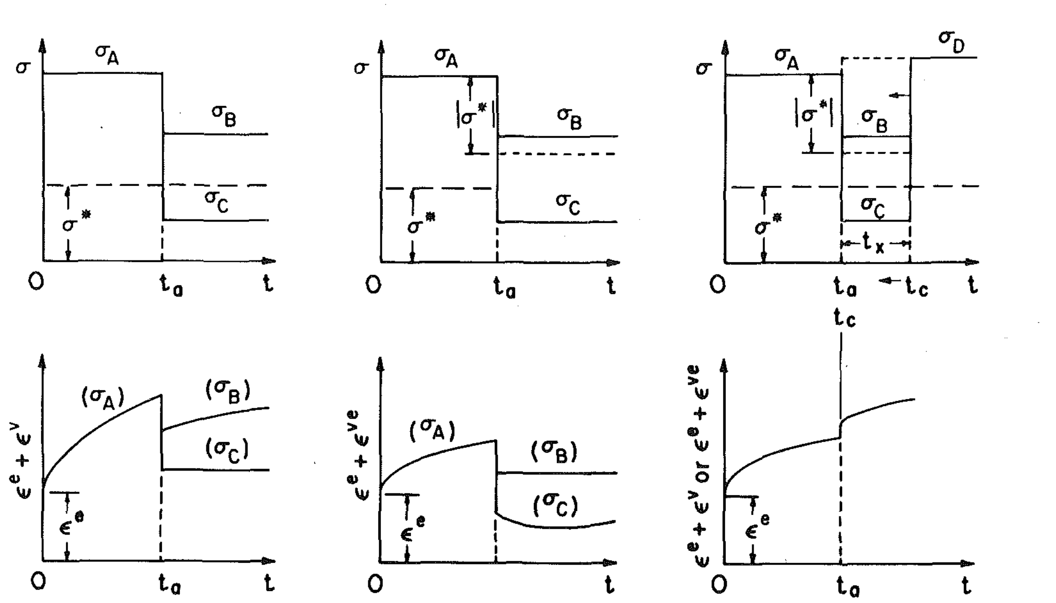

(a) Nonrecoverable Strain, Partial Unloading at t_a: $\sigma_B < \sigma^*$, $\dot{\epsilon}^v > 0$, $\sigma_C \leq \sigma^*$, $\dot{\epsilon}^v = 0$,

(b) Recoverable Strain, ϵ^{ve}; Partial Unloading at t_a: $\sigma_A - \sigma_C \leq |\sigma^*|$, $\dot{\epsilon}^{ve} = 0$, $\sigma_A - \sigma_B > |\sigma^*|$, $\dot{\epsilon}^{ve} \neq 0$.

(c) Reloading, at t_c; Nonrecoverable Strain, ϵ^v; $\sigma_C \leq \sigma^* < \sigma_D$. Time t_c Shifted. Recoverable Strain, ϵ^{ve}; $\sigma_D > \sigma_A > \sigma_C$, $\sigma_A - \sigma_C \leq |\sigma^*|$, Time t_c Shifted.

Fig. 4 Illustration of the role of the creep limit σ^* in partial unloading and reloading. ***Note corrections:*** **In (*b*) interchange σ_B and σ_C in equations; In (*c*) for recoverable strain change σ_C to σ_B in equations.**

than the creep limit. Similarly, in Fig. 1, period 5, there was no further change in ϵ_{11}^{ve} or ϵ_{12}^{ve}. This is consistent with 3 described previously. Recovery of ϵ_{11} in Fig. 1(*a*), period 7, was computed as though σ, σ^2, σ^3 terms recovered from the end of period 4 and $\sigma\tau^2$ and τ^2 terms recovered as from the end of period 3. For ϵ_{12}^{ve} in Fig. 1(*b*), period 6, the strain was computed by considering recovery from τ, τ^3 terms as though it started at the end of period 3, while the strain for $\sigma\tau$, $\sigma^2\tau$ terms remained constant. In Fig. 1(*b*), period 7, recovery continued from τ, τ^3 terms and recovery from the $\sigma\tau$, $\sigma^2\tau$ terms started as though from the end of period 3.

Predictions for Side Steps and Recovery

Both the *VV* theory and *MVV* theory just described were used to predict the creep behavior of the material under side steps and recovery experiments as shown in Fig. 1 and in Fig. 2, periods 1–6. In applying the constitutive relations for the predictions, both the variable creep limit, σ' and τ' (8) and the fixed creep limits σ^* and τ^* and their corresponding constants as shown, respectively, in Tables 1 and 2 were utilized. The results of the predictions are shown in Figs. 1 and 2.

In general the *MVV* theory using fixed creep limits (σ^*, τ^*) yielded the best comparison with the test data. It correctly described the constant creep rate observed in Fig. 1, periods 4, 5, Fig. 1(*a*), period 6, Fig. 2(*a*), period 6, and Fig. 2(*b*), periods 2 and 10, whereas, the *VV* theory showed pronounced recovery-type behavior in these periods. Also the recovery in Fig. 1, period 7 was correctly described by the *MVV* theory, but not in Fig. 1(*a*), period 7 by the *VV* theory.

The continuing creep observed in one component when the stress of the other component was removed was best described by the *MVV* theory, as shown in Fig. 2(*a*), period 4, Fig. 2(*b*), period 8, and Fig. 3(*a*), period 11; whereas the *VV* theory showed a recovery.

Comments on Fig. 1, Period 3. The marked difference between the predicted and the observed strains in the third period of Fig. 1 might be a manifestation of material nonlinearity under combined stress not accounted for in the third-order theory. The possibility of employing a fifth-order was explored. Additional appropriate higher-order terms were added to (6) and (7). This approach did not yield any significant improvement.

As reported in [1] combined tension and torsion tests XI and XII performed at the same stresses yielded a markedly higher creep rate from XI than XII. In [1], Test XI was omitted from the analysis from which the solid lines in Fig. 1 were predicted. Repeating the computations using an average of the results for XI and XII did not yield any overall improvements.

Predictions for Stress Reversals

Straightforward application of the concepts that a portion of the creep of metals is nonrecoverable and strain hardening suggests that reversal of stress should cause no further change in the nonrecoverable ϵ^v component of strain. The fact that considerable changes were observed, as shown in Fig. 3, was the reason that ϵ^v was resolved into two parts ϵ_{pos}^v and ϵ_{neg}^v in the present investigation. It was considered that positive and negative stresses would produce independent creep responses, the sum of which would be the resulting creep. Also it appeared that the nonrecoverable strain ϵ^v accumulated prior to reversal of stress was entirely wiped out on completely reversing the stress.

In Fig. 3(*b*) the dot-dash lines were computed using the *VV* theory with Table 2 and considering *all* prior strain wiped out upon reversal of stress. The solid lines (*MVV* theory) were computed considering that the nonrecoverable strain only was wiped out upon reversal of stress and the recoverable strain was computed in the usual manner, by equation (9*a*). Fig. 3(*b*) shows that the solid lines describe the character of the observed creep for complete stress reversal very well for periods 3, 4, 5, 8, 9, and 10, except for increasing creep rates in periods 3, 4, 5, and a shift in period 9.

The dotted lines in Fig. 3(*b*), periods 6 and 7, for which there was a partial reversal of stress, were computed by not wiping out the nonrecoverable strain at the end of period 6. The difference between the solid and dotted lines in periods 6 and 7 indicate the magnitude of the strain wiped out in arriving at the solid line. Comparing the solid and dotted lines with the test data for periods 6 and 7 suggests that the nonrecoverable strain was not wiped out at the start of period 6 (which was an incomplete stress reversal). It also suggests that during periods 6 and 7 the prior nonrecoverable strain was gradually wiped out, resulting in the increased rate shown.

The fact that the creep rate in Fig. 3(*b*), period 5, was not reduced, as would be expected from strain hardening as a result of the prior negatively stressed period 3, is proably due to the fact that the prior nonrecoverable strain was in fact wiped out (i.e., recovered). Thus there was no residual strain and hence no strain hardening.

The recovery in periods 11 and 12 was computed in the same manner as just described, with excellent results.

The torsion in Fig. 2(*b*), period 7, was not completely reversed. Again, as in period 6 of Fig. 3(*b*), the creep behavior suggested that the residual strain from period 6 was not wiped out during partial reversal of stress but was gradually reduced resulting in an increased creep rate. Thus the actual creep started at the dotted line and moved toward the solid line in Fig. 2(*b*), periods 7 and 8. In period 9, the torsion was increased so that it was then fully reversed. Fig. 2(*b*) shows both the *VV* and *MVV* theories for period 9 with the residual strain wiped out. Also shown as a dotted line is the *MVV* theory with the residual strain not wiped out. It appears that the actual data continued in period 9 to complete wiping out the residual strain by the end of period 9.

Predictions for Tension in the Presence of Reversing Torsion. In Fig. 3(*a*), periods 7–10, tension was added to the existing torsion (reversed in each period). The observed tensile strain ϵ_{11} in these periods showed small primary-type responses added at each reversal of torsion. The *VV* theory (9) and (10) were used first to treat the stress states in periods 7–11. Since ϵ_{11} is an even function of τ, reversing τ was equivalent to a continuous stressing of $\sigma = \sigma_1$, $\tau = \tau_3$. This approach yielded a continuous creep of ϵ_{11} as shown by the dot-dash lines in Fig. 3(*a*). Clearly, this is an inadequate description of the behavior except for period 7.

Observing that on reversal of shear (torsion) stress in the presence of tension the principal stresses changed direction markedly it was likely that a different set of active elements (slip planes and dislocations) would be involved for positive versus negative shear stress. Thus virgin-type behavior of ϵ^v would be involved in the axial strain resulting from the first reversal of stress, as also observed for the corresponding shear strain component in Fig. 3(*b*). In subsequent reversals only the mixed stress terms would be involved in ϵ^v.

Thus, for the *MVV* theory in Fig. 3(*a*), periods 7–10, the nonrecoverable creep ϵ^v_{11} was computed as follows by separating ϵ^v_{11}(pos) from ϵ^v_{11}(neg). ϵ^v_{11}(pos) was computed from τ_3 in periods 7 and 9 and zero stress in periods 8 and 10. All stress terms contributed virgin-type creep in period 7. In periods 8–10, the pure tension component of creep continued without interruption. In periods 8 and 10 the creep for mixed stress term $\sigma\tau^2$ remained constant; while in period 9 a new virgin-type creep due to $\sigma\tau^2$ was added (it was new because of the prior reversal of $\sigma\tau^2$). The creep for ϵ^v_{11}(neg) was computed in the same manner starting with creep from all stress terms in period 8. The ϵ^{ve}_{11} creep was continuous through periods 7–10 since τ had an even power in (6). The sum of all these components yielded the solid line in Fig. 3(*a*), which compares well with the experiment except that the strain at the start of period 8 was too small.

Recovery Following Stress Reversals. Recovery in Fig. 3, periods 11 and 12, was determined for the *MVV* theory as follows: In Fig. 3(*b*), period 11, ϵ^{ve}_{12} for τ, τ^3 recovered as from the end of period 10; ϵ^{ve}_{12} for $\sigma\tau$, $\sigma^2\tau$ remained constant. In period 12 ϵ^{ve}_{12} for τ, τ^3 continued to recover and ϵ^{ve}_{12} for $\sigma\tau$, $\sigma^2\tau$ recovered as though from the end of period 10. This produced the slight dip in the *MVV* theory between periods 11 and 12, as also observed in the data. In Fig. 3(*a*), period 12, ϵ^{ve}_{11} for σ, σ^2, σ^3 recovered as from the end of period 11 and ϵ^{ve}_{11} for $\sigma\tau^2$ recovered as though from the end of period 10.

Results and Conclusions

Analysis of results of nonlinear creep of 2618 aluminum under combined tension and torsion stress states and under varying stress history including step changes of one stress component while another component remained constant and reversal of shearing stress showed that the viscous-viscoelastic (*VV*) theory with certain modifications (*MVV*) theory predicted most of the features of the observed creep behavior quite well.

Among the conclusions are the following:

1 The behavior may be represented by resolving the time-dependent strain into recoverable and nonrecoverable components having the same time-dependence.

2 The material behaved as though there was a creep limit such that only very small creep occurred unless the stress was greater than a limiting value having fixed values σ^*, τ^* for tensile stress and shear stress components, respectively.

3 On partial unloading, the material behaved as though the nonrecoverable strain component ϵ^v continued to creep in accordance with strain hardening unless the stress became less than the creep limit; whereas the recoverable strain component ϵ^{ve} remained constant unless the decrease (change) in stress exceeded the magnitude of the creep limit.

4 On reloading following an interval t_x of partial unloading involving no further change in ϵ^{ve} the component ϵ^{ve} resumed creeping as though the interval t_x did not exist.

5 An increase in tension under constant torsion was well represented by the theory but a subsequent increase in torsion at constant tension was not as well represented.

6 Reduction of one stress component while the other remained constant required treating the pure stress and mixed stress terms separately. The strains associated with the mixed stress terms remained constant, whereas the strain behavior associated with the pure stress remained unchanged.

7 Removal of one of two stress components during creep was observed to have no effect on creep associated with the other stress component. This was partially accounted for by considering that the ϵ^{ve} strain associated with the mixed stress terms remained constant until both stress components were zero.

8 On partial or complete reversal of stress the nonrecoverable strain component ϵ^v behaved as though the reverse stress was applied to a virgin material.

9 If the stress was partially reversed the prior residual strain resulting from ϵ^v remained. However, if the stress component was completely reversed the residual strain from the nonrecoverable strain component ϵ^v appeared to be completely recovered (wiped out).

10 The axial creep resulting from cycles of reversed torsion in the presence of constant tension consisted of: continuous recoverable creep; plus continuous nonrecoverable creep from the first application of positive torsion and also from the first application of negative torsion associated with pure tension terms only; plus new virgin creep associated with the mixed tension-torsion stress terms at each reversal of torsion.

Acknowledgment

This work was supported by the Office of Naval Research and the Army Research Office, Research Grant No. DAAG29-78-G-0185. The material was contributed by the Aluminum Company of America. The authors are grateful to: U. W. Cho, for helpful discussions and recomputation of theory; R. M. Reed, for performing one experiment; and M. C. Gingrich and P. Orzechowski, for typing the manuscript.

References

1 Findley, W. N., and Lai, J. S., "Creep and Recovery of 2618 Aluminum Alloy Under Combined Stress with a Representation by a Viscous-Viscoelastic Model," ASME JOURNAL OF APPLIED MECHANICS, Vol. 45, Sept. 1978, pp. 507–514.

2 Findley, W. N., Cho, U. W. and Ding, J. L., "Creep of Metals and Plastics Under Combined Stresses—A Review," ASME *Journal of Engineering Materials and Technology,* Vol. 101, 1979, pp. 365–368.

3 Lai, J. S., and Findley, W. N., "Creep of 2618 Aluminum Under Step Stress Changes Predicted by a Viscous-Viscoelastic Model," ASME JOURNAL OF APPLIED MECHANICS, Vol. 47, Mar. 1980, pp. 21–26.

4 Blass, J. J., and Findley, W. N., "Short-Time Biaxial Creep of an Aluminum Alloy With Abrupt Changes of Temperature and State of Stresses," ASME JOURNAL OF APPLIED MECHANICS, Vol. 38, June 1971, pp. 489–501.

5 Findley, W. N., and Gjelsvik, A., "A Biaxial Testing Machine for Plasticity, Creep or Relaxation Under Variable Principal-Stress Ratios," *Proceedings of the American Society for Testing and Materials,* Vol. 62, 1962, pp. 1103–1118.

6 Green, A. E., and Rivlin, R. S., "The Mechanics of Nonlinear Materials With Memory, Part I," *Archive for Rational Mechanics and Analysis*, Vol. 1, 1957, p. 1.

7 Findley, W. N., Lai, J. S., and Onaran, K., *Creep and Relaxation of Nonlinear Viscoelastic Materials,* North-Holland Publishers, Amsterdam, 1976.

D. Kujawski[1]
E. Krempl
Professor of Mechanics.
Fellow ASME

Department of Mechanical
Engineering, Aeronautical Engineering,
and Mechanics,
Rensselaer Polytechnic Institute,
Troy, N. Y. 12181

The Rate (Time)-Dependent Behavior of Ti-7Aℓ-2Cb-1Ta Titanium Alloy at Room Temperature Under Quasi-Static Monotonic and Cyclic Loading

Uniaxial tests using a servocontrolled testing machine and strain measurement at the gage length were performed on a high-strength, low-ductility Titanium alloy. Tests involved monotonic and cyclic loadings with strain rates between 2×10^{-8} *to* 10^{-3} s^{-1}, *stress rates from* 10^{-1} *to* 10^2 *MPa* s^{-1}, *repeated changes in strain rates, and short-term relaxation and creep tests. The inelastic behavior is strongly rate-dependent. Ratchetting is shown to increase as the stress rate decreases. No strain-rate history effect was found. A unique stress-strain curve is ultimately reached for a given strain rate irrespective of prior history as long as only positive stresses are imposed. In the plastic range the relaxation drop in a given time period depends only on the strain rate preceding the test and is independent of the actual stress and strain.*

Introduction

Stress-strain curves obtained under dynamic conditions (at strain rates above 10 s^{-1}) can lie significantly above static stress-strain curves obtained at static strain rates (order 10^{-2} s^{-1} or less). Frequently, in the case of static test results, no specific strain rate is reported with the implication that rate (time)-dependence[2] prevails for static loading conditions. This assumption is also made in "static" plasticity theories. However static stress-strain curves can be obtained at loading rates which differ by several orders of magnitude, and rate-dependence may be present within the static strain-rate range. Indeed this has been demonstrated in the case of several metals [1–3] tested at room temperatures. For AISI Type 304 Stainless Steel we have found significant room-temperature rate-dependence manifested in loading-rate sensitivity of the yield and flow stresses at different static strain (stress) rates, and in creep and relaxation behavior. AISI Type 304 Stainless Steel exhibits low-yield strength and high ductility. The Titanium alloy used in this study has high-yield strength and considerably less ductility than AISI Type 304 Stainless Steel.

In materials science plastic flow is considered a rate process [4] and relaxation experiments are performed at room temperature [5, 6] using specially equipped universal testing machines.

In viscoplasticity, some constitutive theories assume the existence of a quasistatic or equilibrium stress-strain curve [7–11] characteristic of the rate-independent portion of material response. In some cases [7–9] dynamic-rate dependence is recognized and an equilibrium stress-strain curve is used which is obtained from static tests where loading rates are not specified.

The purpose of this study is to examine in a qualitative way the loading rate-dependence of the stress-strain curves, the creep and relaxation behavior of this high-strength, low-ductility material using the method of servocontrolled mechanical testing. This method is frequently used in fracture mechanics and low-cycle fatigue testing but has not been employed for the determination of material properties for constitutive equation development. It is ideally suited for this purpose since it permits the accurate measurement of the material response at various loading rates through the use of feedback principles.

---

[1] Permanent address—Institute of Basic Machine Design, ul. Narbutta 84, 02-524 Warszawa, Poland.

[2] Rate (time)-dependence encompasses loading rate-sensitivity, creep, and relaxation.

Contributed by the Applied Mechanics Division of THE AMERICAN SOCIETY OF MECHANICAL ENGINEERS, for presentation at the 1981 Joint ASME/ASCE Applied Mechanics, Fluids Engineering, and Bioengineering Conference, University of Colorado, Boulder, Colo., June 22–27, 1981.

Discussion on this paper should be addressed to the Editorial Department, ASME, United Engineering Center, 345 East 47th Street, New York, N. Y. 10017, and will be accepted until June 1, 1981. Readers who need more time to prepare a Discussion should request an extension from the Editorial Department. Manuscript received by ASME Applied Mechanics Division, January, 1980; final revision, July, 1980. Paper No. 81-APM-7.

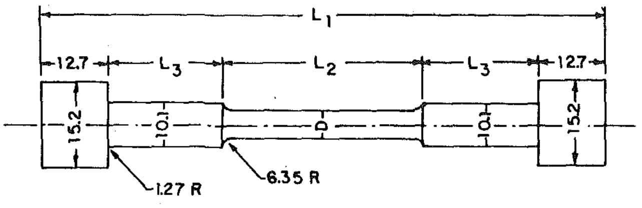

SPECIMEN	L_1	L_2	L_3	D
B1, B3, T1, T3	121.92	20.32	38.1	6.35
B2, B4, B5, T4, T5	120.65	44.45	25.4	7.62

ALL DIMENSIONS IN MILLIMETERS

Fig. 1 Specimens used in this study

Material and Specimens

The Ti-7Aℓ-2Cb-1Ta alloy was donated by the Naval Research Laboratory and was identified by the NRL Code T89. Blanks of approximately 20 × 20 × 120 mm were cut from the top (Label T) and bottom (Label B) of a 3-in. (76.2 mm) thick plate. The longest side of the blanks was perpendicular to the direction of rolling. To equilibrate texture effects the blanks were subjected to a beta-anneal heat-treatment of ½ hr at 2000°F in vacuum and subsequent cooling to room temperature in helium at a rate approximating air cooling. Two different types of specimens shown in Fig. 1 were machined from the heat-treated blanks. The specimens with the short-gage length were used for the cyclic experiments. A total of nine specimens were tested.

Testing Equipment and Procedure

All specimens were tested at room temperature in an MTS servocontrolled tension-torsion system with dual ramp function generator. The test results were recorded on an XY-recorder. Displacement was in all cases measured by an MTS clip-on extensometer clamped on the gage length and converted to engineering strain and strain rate using standard methods. Engineering stresses based on the original cross section are used throughout this study.

In the following we refer to stress (strain) control, creep and relaxation. In actuality the load (displacement) is controlled. During creep the load is kept constant and during relaxation the displacement in the gage length is held fixed.

The clip-on extensometer together with the function generator and the servocontrolled system enable an accurate strain control which is not possible with conventional testing machines. By simply changing the command signal stress control can be achieved in the servocontrolled test system. The reported test data represent real material behavior. The strain measurement on the gage length together with the servocontrol (feedback) system and the frequencies used in this study insure that *no testing machine bias* enters into the recorded data.

Test Results

Behavior for Positive Stress. *Influence of Loading Rate.* Test results of three different specimens B2, B5, and T5 are depicted in Fig. 2. Specimen B2 was loaded under stress control at 69 MPa s^{-1}. Repeated loadings and unloadings with strain-rate changes were used in the tests with specimens B5 (full line) and T5 (dashed line).

The stress-strain behavior is initially linear with slope E on all loadings starting at points O, D, F, and F_1. At stresses larger than 450 MPa the effects of rate become noticeable and are significant in the

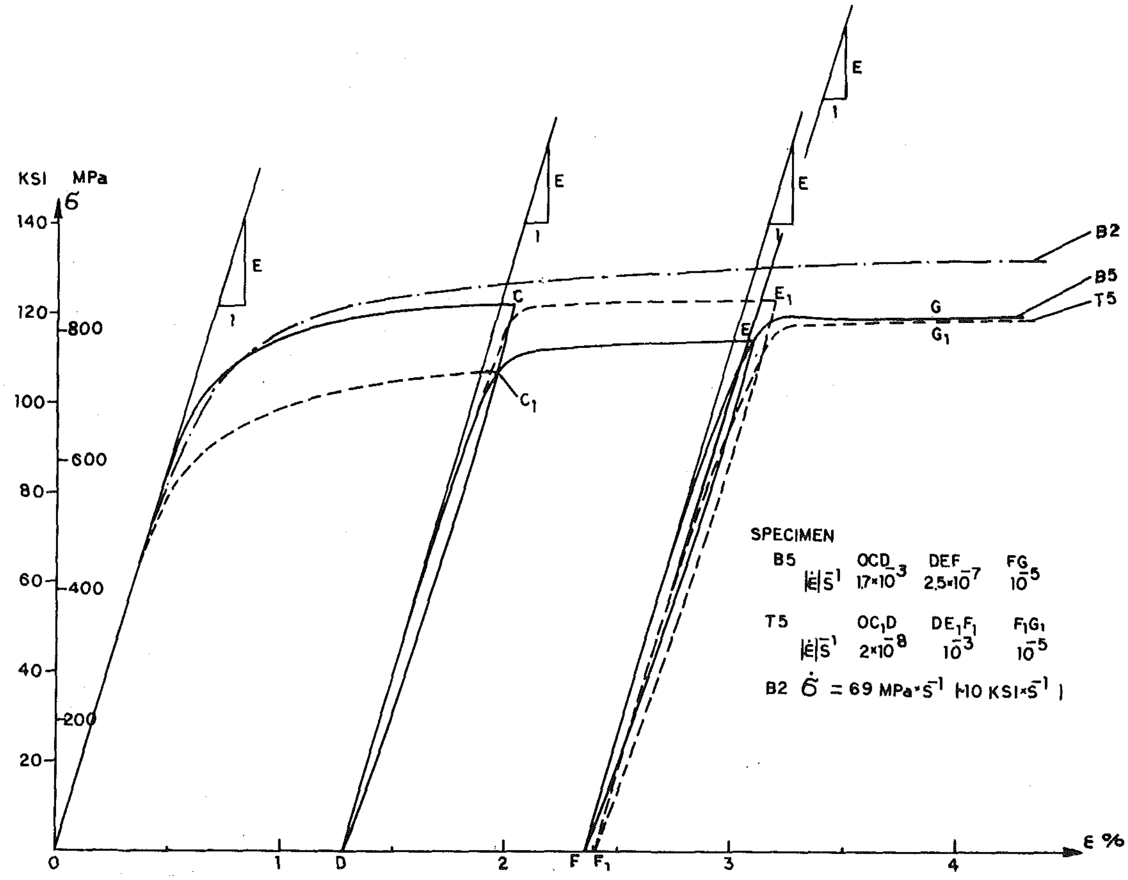

Fig. 2 The effect of loading rate and type of control on the stress-strain diagram of three different specimens; no strain-rate history effect is observed

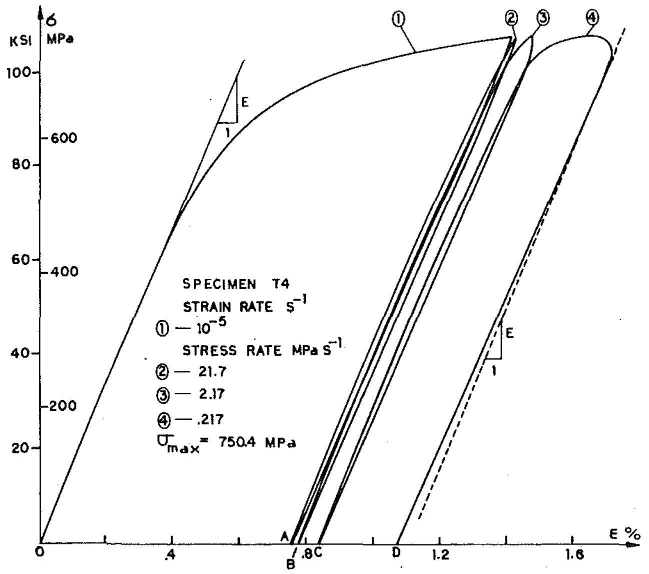

Fig. 3 Effect of type of loading and loading rate on unloading behavior; the amount of ratchet strain (strain accumulation) increases with a decrease in stress rate

Table 1 Rate-dependence of 0.2 percent offset yield strength σ_y

Specimen No.	$\dot{\varepsilon}$ s^{-1}	$\dot{\sigma}$ MPa s^{-1}	σ_y MPa
B1	10^{-4}		738
B2		69	764
B4	10^{-4}		730
B5	1.7×10^{-3}		763
T1	10^{-4}		725
T4	10^{-5}		675
T5	2×10^{-8}		632

plastic range.[3] Also the 0.2 percent yield strength is dependent on rate as seen in Fig. 2.

Table 1 shows the variation of the 0.2 percent offset yield strength with loading rate. The difference between the yield strength at the slowest (2×10^{-8} s^{-1}) and fastest (1.7×10^{-3} s^{-1}) strain rate is 21 percent or 131 MPa. The yield strengths for three different specimens determined at the same strain rate (10^{-4} s^{-1}) differ at the most by 13 MPa or 2 percent. We see that the scatter is not very large and that the influence of rate is very noticeable in the range of static strain rates.

The initial unloading behavior starting at points C, C_1, E, and E_1 is not linear elastic. The slope is initially larger than the elastic modulus and continuously decreases as the stress decreases. At zero stress the unloading slope is less than the elastic modulus (see also Fig. 3). The initial slope on reloading is equal to the modulus of elasticity and a small hysteretic loop develops as shown in Fig. 2.

In the plastic range the stress-strain curves obtained at different strain rates are equidistant. The stress-strain diagram for specimen B2 obtained under stress control, however, shows a somewhat higher slope at a given strain level than the others.

For specimens B5 and T5 which were subjected to a different strain-rate history up to points F and F_1, respectively, the same strain rate of 10^{-5} s^{-1} was used in the final loading starting at F and F_1 and the two curves ultimately coincide within normal scatter.

Although specimens B5 and T5 underwent different strain and strain-rate histories, their final stress-strain curves coincide when loaded with the same final strain rate. We observe that the material can forget the prior history and that a strain-rate history effect [12–14] is absent. Note added in proof: Extension of the graph beyond C for

---

[3] Plastic range is the region of the stress-strain curve in which the tangent modulus changes very little and is small compared to the elastic modulus.

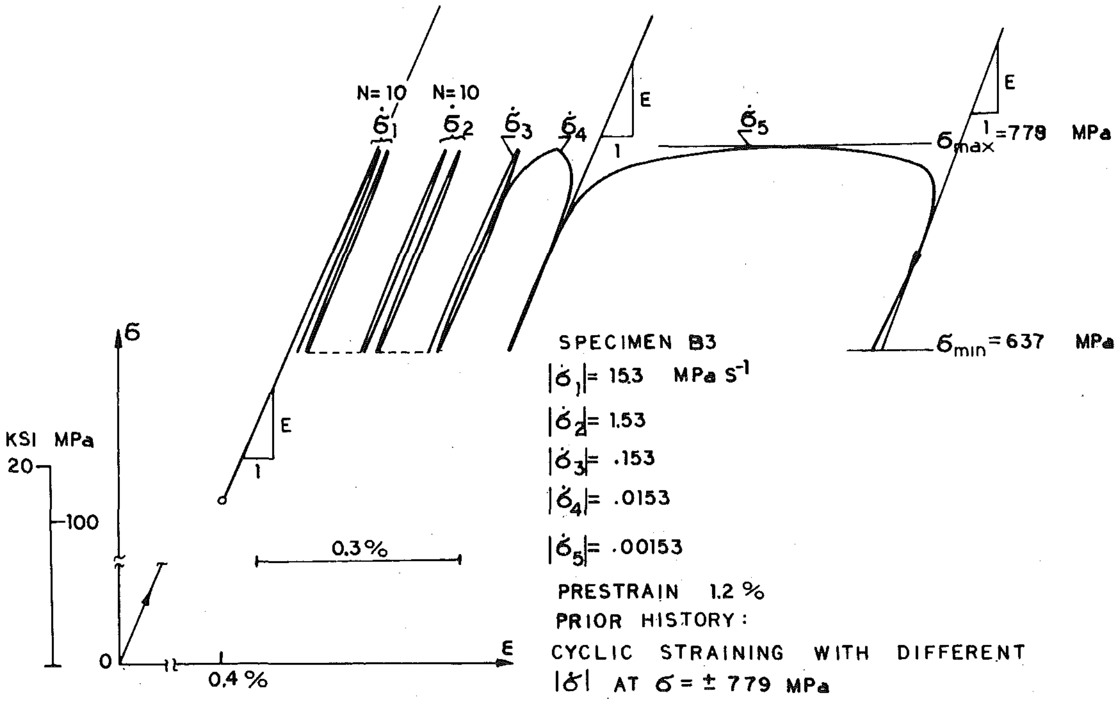

Fig. 4 Effect of stress rate on ratchet strain for partial unloading; at $|\dot{\sigma}_1|$ and $|\dot{\sigma}_2|$ 10 cycles were performed with only one cycle at the other stress rates; the two dashed horizontal lines indicate a translation made for ease in interpreting the graph; they have no physical significance

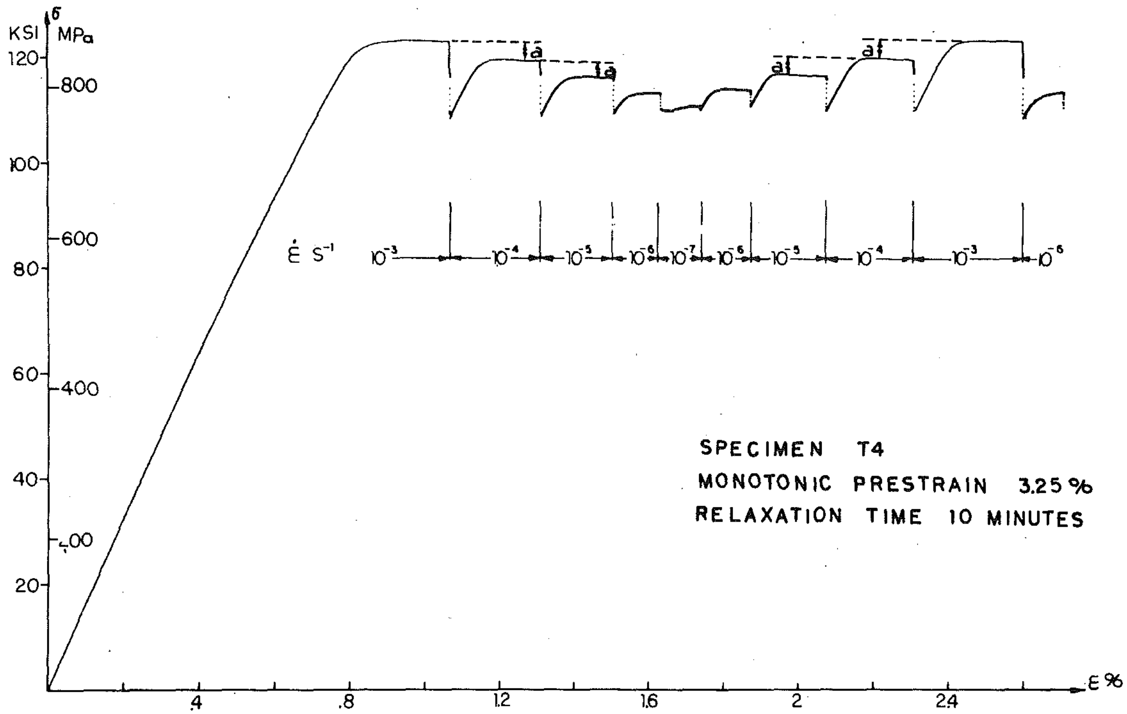

Fig. 5 Relaxation and strain-rate change-stress change behavior; after completion of a 10 min relaxation test loading was continued at the indicated strain rate; the distances $\Delta\sigma$ are examples of the stress changes reported in Table 2

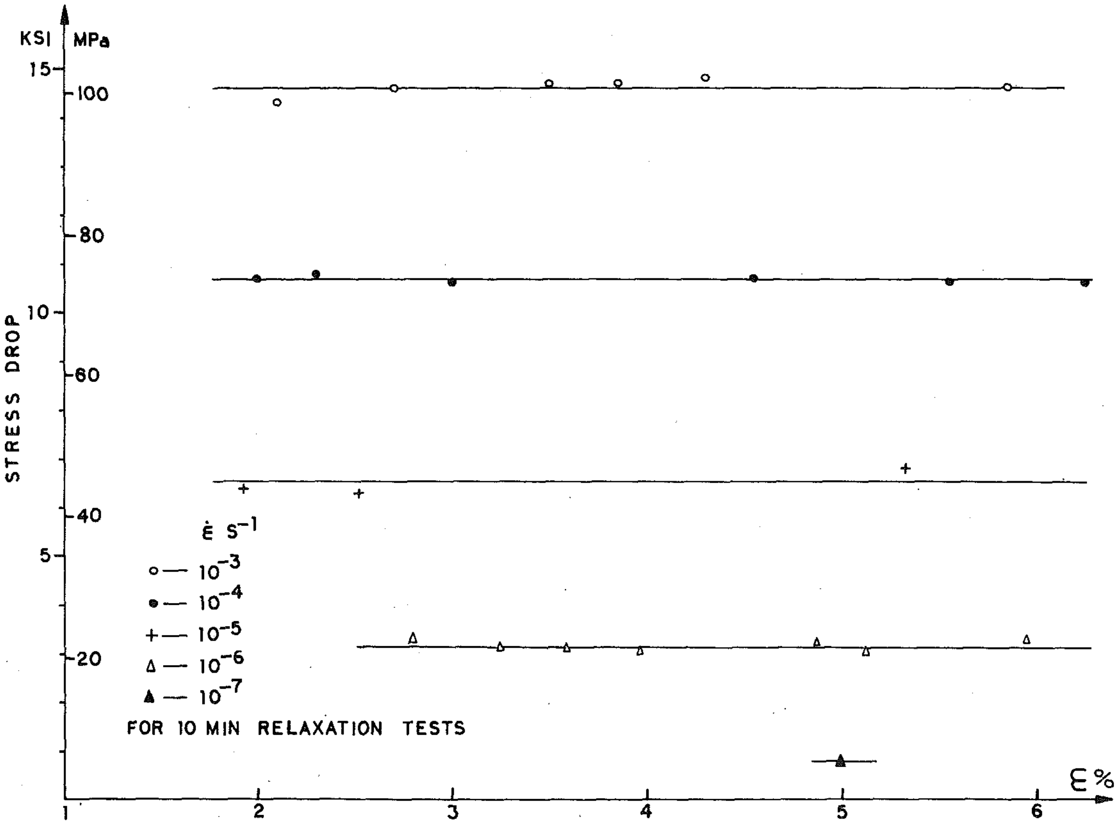

Fig. 6 Stress drops during 10 min relaxation tests obtained with specimens B4, B5, T4; although each specimen was subjected to a different history, the relaxation behavior depends only on strain rate prior to the start of the relaxation test

specimen B5 and comparison with DE_1 also implies the absence of a strain-rate history effect.

Figs. 3 and 4 further demonstrate the effect of loading rate. In Fig. 3 specimen T4 was first loaded and unloaded to zero stress at a strain rate of $10^{-5}\,s^{-1}$; see curve (1) 0A. At point A a stress controlled loading was started right away. During one loading and unloading cycle the absolute value of the stress rate was kept constant; however, each new cycle (points B and C) was started with a tenfold reduced stress rate without changing the maximum stress; see curves (2), (3), and (4). It is evident that the stress rate has a significant effect on the ratchet strain (distances AB, BC, CD) accumulated during one cycle. This ratchet strain is caused by a "creep deformation" allowed by the stress control at stress levels approaching the maximum stress of the cycle.[4] This creeping is negligible at a stress rate of 21.7 MPa s^{-1} but becomes significant at 0.217 MPa s^{-1}. The stress controlled (2), (3), (4) and the strain controlled (1) unloading curves display significant differences. The former show initial negative slopes not found for (1). For curve (2) the negative slope is not pronounced since not enough time is available for "creep" to develop during initial unloadings.

Fig. 4 is intended to illustrate the effect of "creeping out" further. In this test only partial loading and unloading is performed between $\sigma_{\max}$ and $\sigma_{\min}$ and the stress rate is varied by four orders of magnitude. At $|\dot{\sigma}_5|$ the cycle took 51.42 hr for completion. It is important to note that the *maximum stress equals* the *maximum stress obtained during prior loading.*

We see that stress rate has a significant effect on the ratchet strain accumulated in one cycle. It is of course very strongly dependent on stress level. Fig. 4 implies that insignificant ratchet strain would have developed at a stress of 690 MPa at $|\dot{\sigma}_5|$, since the stress-strain curves corresponding to this loading rate are almost linear up to this stress level. Also the evidence in Figs. 3 and 4 suggests that the ratchet strains measured at $\sigma_{\min}$ in Fig. 4 are approximately equal to the one measured at $\sigma = 0$.

Relaxation Behavior for Positive Stresses in the Plastic Range. The relaxation behavior of this material in the *plastic range* is shown in Fig. 5 which depicts stress drops in 10 min and subsequent reloading at various strain rates. It is evident that the total stress drop and therefore the relaxation rate depends on the strain rate preceding the relaxation tests. For a given strain rate the total stress drop is further independent of the strain at the start relaxation test. In other tests started at strains below the ones used in Fig. 5 we found that the stress drop is also independent of the initial stress. The validity of these statements is demonstrated in Fig. 6 where the stress drops in 10 min relaxation of three different specimens are plotted versus total strain. We know from Fig. 2 that a unique stress-strain curve is associated with a given strain rate. Consequently the stress drops shown in Fig. 6 are also independent of the stress at the start of the relaxation test.

The data in Figs. 5 and 6 permit the following statement:

In the plastic range where the modulus is nearly constant and much less than the elastic modulus, the stress drop in a given period of time depends only on the strain-rate preceding the relaxation test. It is independent of the stress and strain at the start of the relaxation test.

Fig. 5 shows that the stress-strain curve eventually returns to a level characteristic of the particular strain rate. The material forgets the prior history if only relaxation during loading periods are involved. Instead of performing relaxation during loading, in the test corresponding to Fig. 7 a relaxation period was introduced after partial unloading where the modulus is close to the elastic one. Compared

---

[4] Such creeping motions are impossible in displacement control.

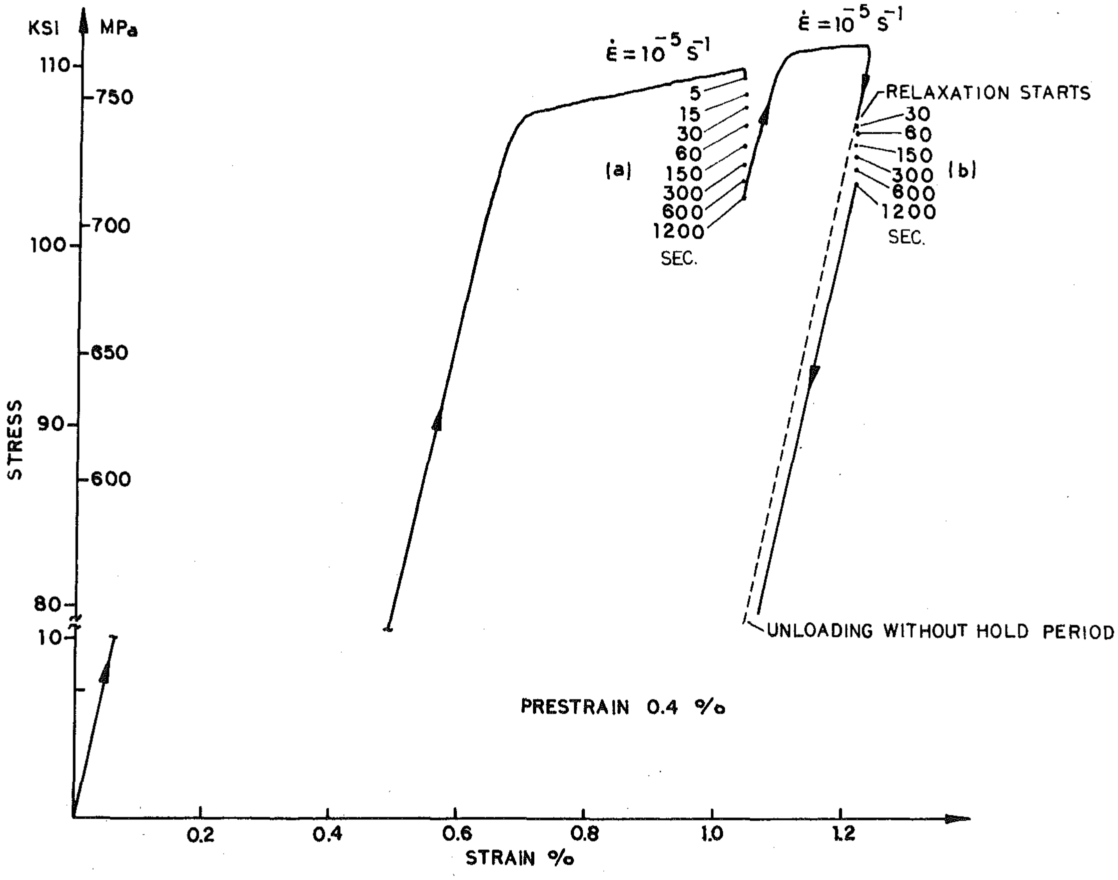

Fig. 7 Relaxation periods of 20 min during Loading (*a*) and unloading below the maximum stress level (*b*); the relaxation period (*b*) causes a displacement of the stress-strain curve to the right

to (*a*) the relaxation at (*b*) occurs at a reduced rate. Upon continued unloading the stress-strain curve does not return to the assumed original unloading curve (dashed in Fig. 7). Rather it is displaced to the right. In this case the prior relaxation history is not forgotten.

Stress Change During Strain-Rate Changes. Figs. 2 and 5 indicate that there exists at every strain a stress level characteristic of a given strain rate. Available data involving frequent relaxation periods and strain-rate changes such as shown in Fig. 5 were analyzed by determining at a given strain the characteristic stress level for a strain rate of 10^{-6} and 10^{-3} s^{-1}. The tests include cycling between the strain rates; see Fig. 9 of [1]. The results are shown in Fig. 8. It is seen that the stress level differences are independent of strain and prior history for positive stresses.

Reversed Cyclic Loading. *Strain Control.* Completely reversed strain controlled cyclic loading was performed at a strain range of $\Delta\epsilon = 1.6$ percent (B1) and 2.4 percent (T1), respectively. After some initial hardening followed by softening the stress range is observed to be almost constant. This Ti-alloy exhibits cyclically neutral behavior.

After the steady cyclic behavior was reached the effect of strain rate on the hysteresis loop was studied by changing the strain rate at suitable cycle intervals. At each strain rate two or three cycles were recorded before the next strain rate change was initiated. Both step-up and step-down changes in strain rate were performed.

After each change in strain rate a different hysteresis loop developed. The transition from one loop to the next was accomplished

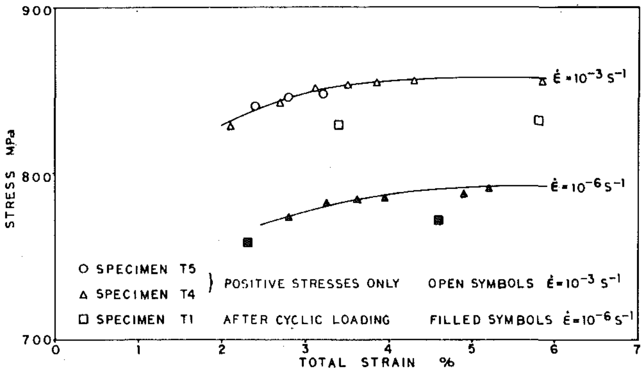

Fig. 8 Stress values characteristic of a given strain rate versus strain for three different specimens; each specimen was subjected to frequent relaxation and strain-rate changes as demonstrated in Fig. 5; although the stress levels are different for the cyclically preloaded specimen the stress level differences for the same strain rates are equal; see also Table 2

Table 2 Strain-rate change—stress change behavior

Strain Rate Change From s^{-1}	To	Corresponding Stress Change* MPa Zero-to-Tension Loading Specimen T4	After Cyclic** Loading Specimen T1
10^{-3}	10^{-4}	24.9	24.8
10^{-3}	10^{-5}	45.8	47.6
10^{-3}	10^{-6}	65.6	63.7
10^{-3}	10^{-7}	82.1	79.7
10^{-4}	10^{-5}	20.9	19.5
10^{-6}	10^{-6}	40.8	37.2
10^{-5}	10^{-6}	19.4	17.7

[*] Stress change is obtained from the xy-records by an extrapolation of the respective stress-strain diagrams. An example of such an extrapolation is given in Figure 5.

[**] About 60 cycles at ± 1.2%.

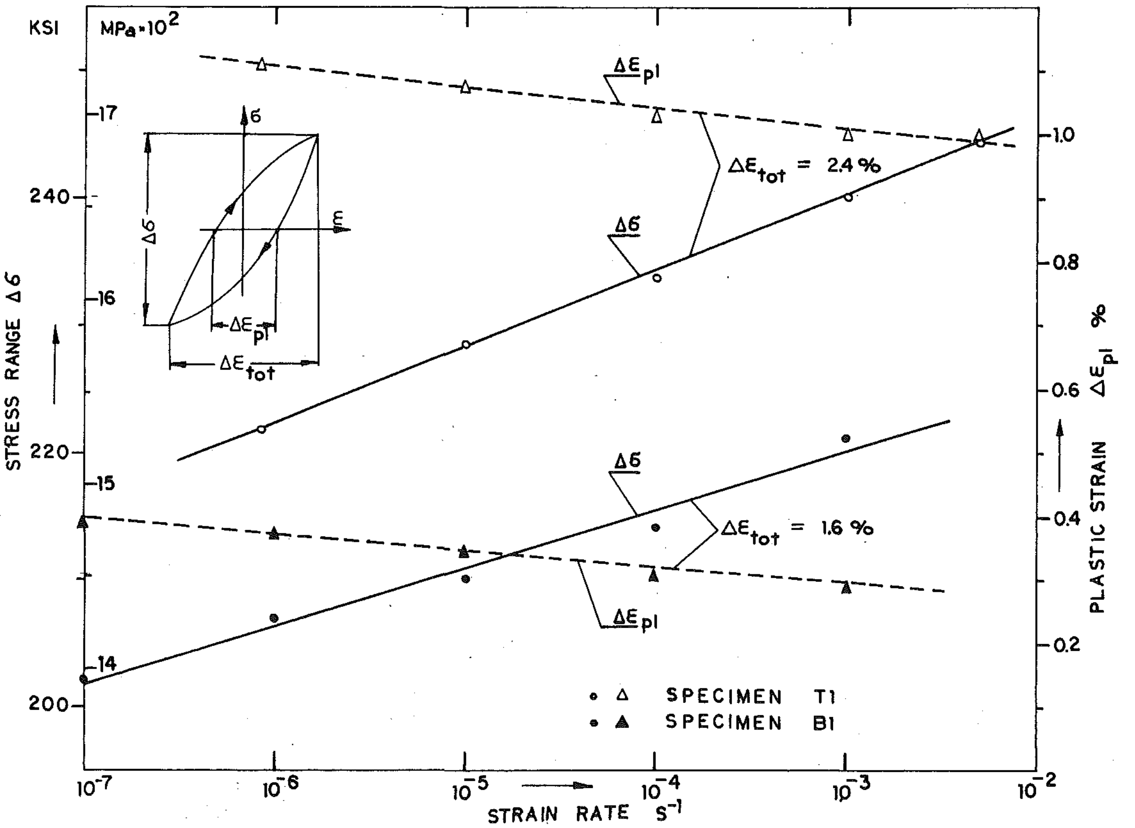

Fig. 9 The influence of strain rate on the stress range and the width of the hysteresis loop at zero stress for a strain range of 2.4 and 1.6 percent; transitions from loops obtained at various strain rates are reversible

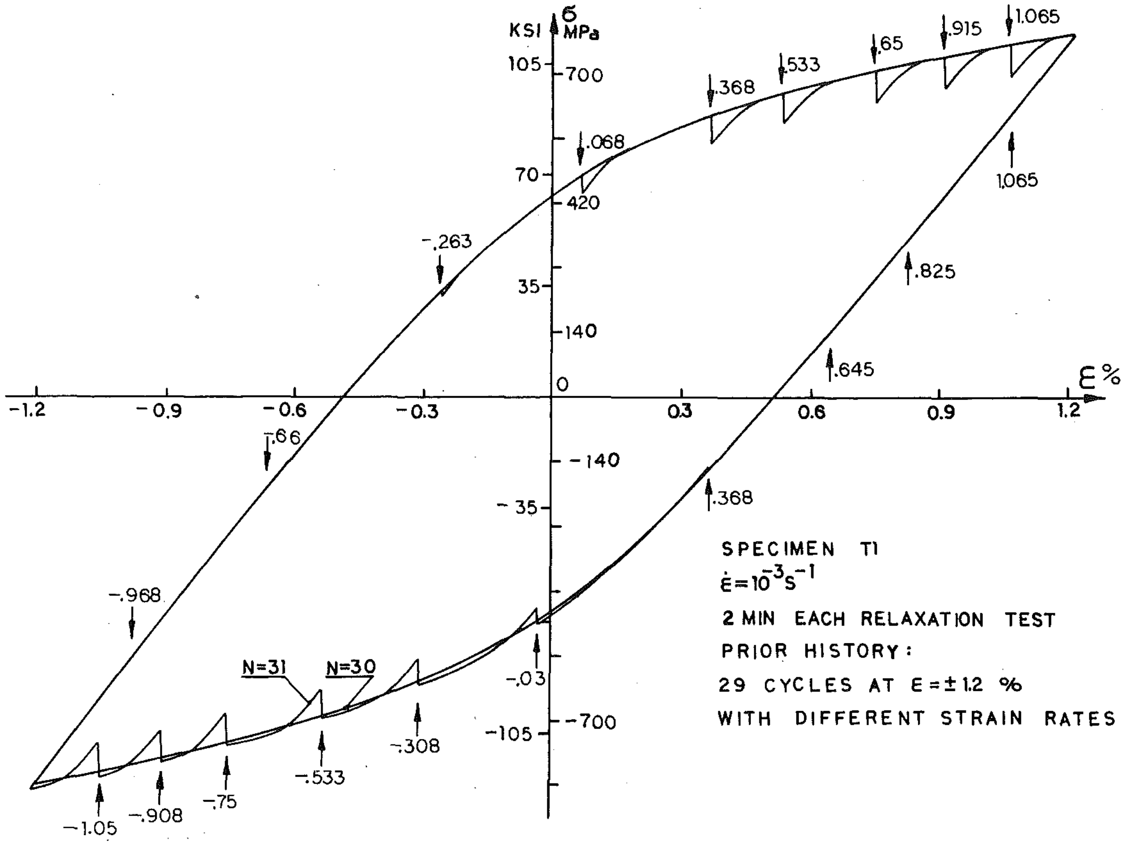

Fig. 10 Strain-controlled test at $\Delta\epsilon = 2.4$ percent with 2 min relaxation periods commencing at each arrow and subsequent loading at $|\dot{\epsilon}| = 10^{-3}$ s^{-1}; almost elastic behavior is observed in the nearly straight portions of the loop

within less than 0.05 percent strain and was fully reversible, e.g., after a step-up test from 10^{-6} to 10^{-3} s^{-1} followed by a step-down test to 10^{-6} s^{-1} the two hysteresis loops for 10^{-6} s^{-1} coincided within experimental accuracy.

An increase in strain rate results in an increase in stress range and a decrease in the width of the loop at zero stress. The results are shown in Fig. 9. For a change in three orders of magnitude in strain rate the corresponding stress range changes are 95 MPa or 7 percent and 125 MPa or 11 percent at $\Delta\epsilon = 1.6$ percent, and $\Delta\epsilon = 2.4$ percent, respectively. The line for $\Delta\sigma$ at $\Delta\epsilon = 2.4$ percent has a higher slope than the one for $\Delta\epsilon = 1.6$ percent. The plastic strain range (dashed lines in Fig. 9) decreases with increasing strain rate.

Fig. 10 illustrates how "inelasticity is distributed" around the hysteresis loop. The arrows with the numbers indicate the strains at which a 2 min relaxation test was introduced. At the end of these tests loading resumed at a strain rate of 10^{-3} s^{-1}. It is seen that no relaxation occurs in 2 min in the nearly straight portions of the loop and that relaxation increases gradually as the slope decreases. The initial slope at the commencement of each loading following relaxation is very close to the modulus of elasticity. After the relaxation periods the stress-strain curve returns to the original hysteresis loop. (No relaxation periods are introduced *right after unloading* as was done in Fig. 7.) The relaxation periods are forgotten. (The differences in the compression part of Fig. 10 are probably due to continued small cycle-dependent changes.)

Load (Stress) Control. Specimen B3 was used to perform stress-controlled loading with 2 min constant load creep periods ($\dot{\sigma} = 0$) as indicated by the arrows on the right of Fig. 11.

Starting from the origin the specimen was loaded to a maximum load and then unloaded to zero stress at point A, the end of Section (1). Section (2) starts at A and ends at B where loading compression and subsequent reloading in tension followed. Section (3) terminates at point C.

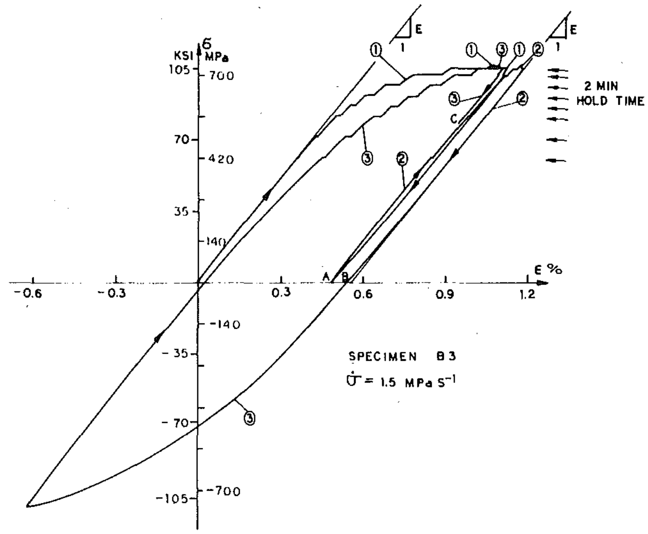

Fig. 11 Load controlled loading; at the stress levels corresponding to the arrows on the right 2 min creep periods are introduced during *every* loading and unloading; creep develops gradually and is more pronounced on loading than on unloading

On loading ($\dot{\sigma} > 0$) creep develops gradually and in a nonlinear fashion. (Although the highest and lowest stress levels at which creep tests were performed differ by less than a factor of two, the respective creep strains accumulated in 2 min differ by much more than a factor of two.) We also note that at the same stress level creep is less during unloading than during loading. This can be seen at the two highest stress levels of each of Sections (1), (2), and (3). Indeed no creep was found at all at the low stress levels during unloading. Also the creep

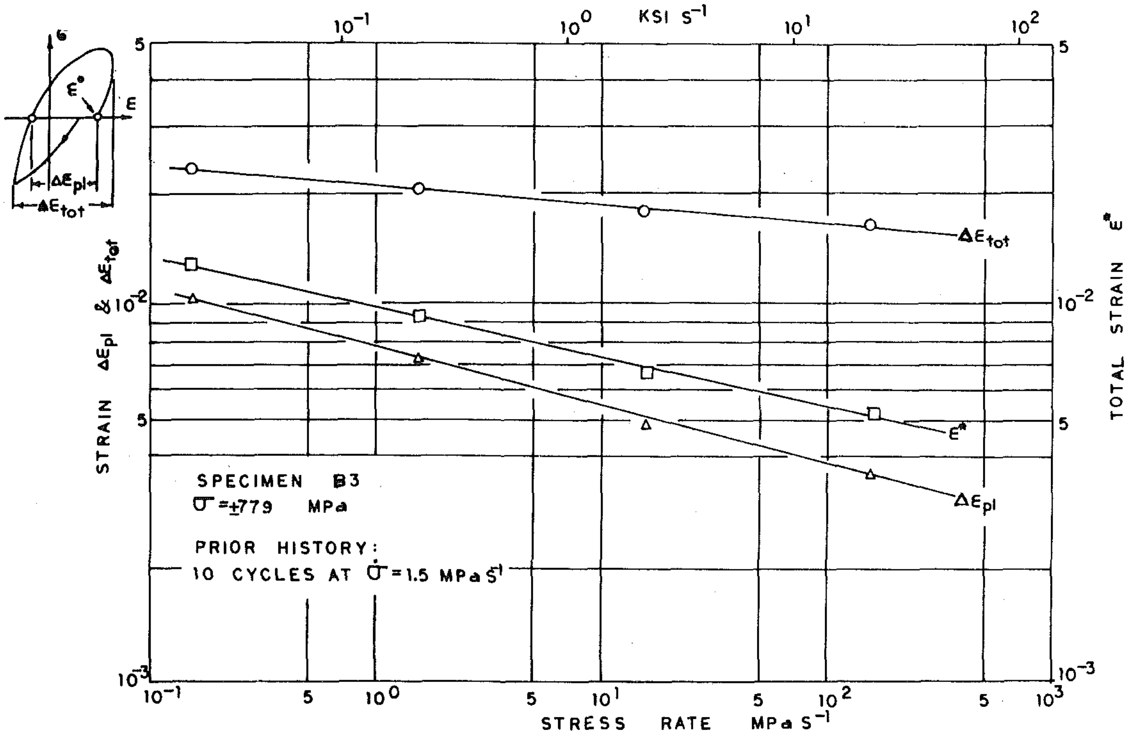

Fig. 12 Load controlled loading; continuation of test in Fig. 11; the influence of loading rate on the total strain range, the plastic strain range and the strain reached during unloading from tension; the movement of the loop toward increasing strain ϵ^* is permanent

strains during loading are at the same stress level different for sections (1), (2), and (3). Creep is least developed for Section (2).

After the tests shown in Fig. 11 the maximum stress was increased to ±779 MPa and uninterrupted cycling continued for 10 cycles at 1.5 MPa s^{-1}. Then after completion of one cycle the stress rate was *consecutively decreased* at zero stress going into compression and the changes in the hysteresis loop were observed, specifically the strains at zero stress. Fig. 12 shows that the loop shifted toward positive strains (ϵ^* increases as the stress rate was decreased), and that both the width at zero load ($\Delta\epsilon_{pl}$) and the total width ($\Delta\epsilon_{tot}$) increased with decreasing rate. We also note that $\Delta\epsilon_{pl}$ increases much faster than $\Delta\epsilon_{tot}$.

The movement of the hysteretic loop to the right is probably due to a higher maximum true stress in tension than in compression. (We use load control.) The movement is permanent. An increase of stress rate will narrow the loop; it will, however, continue to move toward positive strains. The original position of the loop, in contrast to strain cycling, will not be obtained when the stress rate returns to the same value after an excursion to low or high stress rates.

Discussion

The results of this study show clearly that the inelastic deformation of this high-strength, low-ductility Ti-alloy is rate dependent. The rate-dependence is basically logarithmic; the loading rates must be changed by an order of magnitude to get a significant change in the stress-strain behavior.

Both the elastic and inelastic behavior of this material is very consistent and very well reproducible. The modulus of elasticity (the slope at the stress-strain origin), for example, was determined on nine specimens to be 117 GPa ± 1 Gpa. Further, the results in Figs. 6, 8, and Table 1 permit the comparison of results obtained with different specimens.

This study is qualitative in nature and demonstrates that at the loading rates used in this study plastic flow is basically rate-dependent and that loading rate-sensitivity, creep, and relaxation are closely related. The results suggest a number of qualitative conclusions important for constitutive equation development.

No Strain-Rate History Effect (SRHE). The results shown in Figs. 2, 5, 8 and others demonstrate that prior history can be "forgotten." When the material is stressed into the plastic range.[5] a unique stress-strain curve is ultimately obtained for a given positive strain rate provided the prior history consisted only of positive stresses. We do not observe a SRHE [12–14]. These results are in agreement with our findings for AISI Type 304 Stainless Steel [1, 2] but are at variance with results obtained in dynamic plasticity [12–14] where strain rates in excess of 10^{-1} s^{-1} are involved.

We have not found dynamic plasticity experiments with strain-rate changes on AISI Type 304 SS and on *this Ti-alloy*. We do not know whether these metals exhibit a SHRE in dynamic plasticity. However, a very important difference between dynamic plasticity tests and our tests is in the strain rates and in the experimental equipment. The servocontrolled testing machine insures that the strain rate is always maintained at the specified value. Such assurance is not always available in dynamic plasticity experiments.

Inelasticity Is Rate-Dependent. At the loading rates used in this study inelasticity[6] is rate-dependent. As the loading rate is decreased the flow stress decreases (Figs. 2 and 5). Relaxation behavior is tied to loading rate. A decrease in loading rate causes a decrease in the stress drop in a given time in a relaxation test (Figs. 5 and 6).

It is therefore not unreasonable to assume the existence of an equilibrium stress-strain curve [7–9, 15–17] obtained at very slow loading rates. Creep and relaxation tests started from points on this curve will not cause any time-dependent accumulation of strain and stress, respectively. The results of this study suggest that the equilibrium stress-strain curve must be below the stress-strain curve of

---

[5] Fig. 7 shows that relaxation right after unloading ($\dot\epsilon < 0$) can cause a permanent shift of the unloading curve. Also changes in stress rate during stress-controlled cycling can cause a permanent shift of the hysteresis loop; see the discussion related to Fig. 12. In these cases prior history is not forgotten.

[6] Inelasticity denotes deviations from linear elasticity.

$\dot{\epsilon} = 10^{-8}\,s^{-1}$. In [17] the curve corresponding to $\dot{\epsilon} = 10^{-12}\,s^{-1}$ was taken as the equilibrium stress-strain curve.

Relaxation and Strain Rate-Stress Change Behavior. For positive strain rates and as long as the loading history involves only positive stresses the flow stresses and the relaxation behavior are directly related. After an initial transient period a flow stress characteristic of a given strain rate is reached (Figs. 2, 5, and 8). Relaxation rates observed in tests started from the flow stress in the plastic range depend only on the strain rate preceding the relaxation test. The sole dependence of the relaxation rate on previous strain rate ceases to be true when the slope of the σ-ϵ diagram preceding the relaxation test is different from the slope characteristic for the plastic range (Fig. 7; in Fig. 10 all relaxation tests start from a curve with $\dot{\epsilon}$ = constant; the relaxation drops are different.).

A dependence of the flow stress on prior history is shown in Fig. 8 for specimen T1 which underwent prior strain cycling at $\Delta\epsilon = 2.4$ percent. After about 60 cycles the specimen was unloaded from tension to zero load. A regular tensile test with repeated strain-rate changes involving increases and decreases in strain rates was then started. The flow stress for the T1 specimen is less than for specimens T4 and T5; see Fig. 8. Table 2, however, demonstrates that the stress level difference between the flow stress at various strain rates before and after cyclic loading is equal within the accuracy of the extrapolation used in getting the data.

Cyclic loading changes the stress level characteristic of a given strain rate. The strain rate-stress change behavior remains unaltered.

In the experiments of AISI Type 304 Stainless Steel [1] which undergoes considerable cyclic hardening both the stress level and the stress level difference were altered.

Unloading and Reloading Behavior. Figs. 2–5, 7, 10, and 11 show that inelastic behavior is observed at and below the prior maximum stress level. This is especially true for Figs. 7, 10, and 11. Figs. 10 and 11 also indicate that inelasticity develops differently in loading and unloading.

In the unloading leg, beginning at some stress level *below the maximum stress* (see Fig. 7), a nearly rate-independent linear behavior is observed which in this material extends to and beyond the zero stress axis. It appears therefore that during unloading a region of almost elastic behavior is present akin to the behavior obtained at the origin upon initial loading.

The observed creep behavior in Fig. 11 is at variance with creep theories which assume that creep rate depends only on creep strain and stress. It can be explained by requiring that the creep rate depends on overstress [15–17].

The type of control influences the unloading behavior considerably. When a low stress rate is used "creeping out" is observed during unloading, which can be considerable (Figs. 4 and 3). No such creep effect is possible in strain control. Constitutive theories should account for this bias between stress and strain control.

Comparison With Experiments on AISI Type 304 Stainless Steel. Although AISI Type 304 SS is a low-strength, high-ductility material, its inelastic behavior [1, 2] is similar to this high-strength, low-ductility Ti-alloy.[7] The stress levels are quite different in the two cases; however, the relaxation, the strain rate-stress change behavior and the unloading behavior are qualitatively the same. These findings suggest that the viscoplastic model based on total strain and overstress [15–19] is capable of qualitatively reproducing the observed behavior.

Acknowledgment

This research was supported by the National Science Foundation and the Office of Naval Research. The heat-treated Ti-blanks were donated by the Naval Research Laboratory through T. W. Crooker. Helpful comments of Drs. Y. Asada and E. P. Cernocky are appreciated. Mr. V. Kallianpur helped in the preparation of the manuscript.

References

1 Krempl, E., "An Experimental Study of Room-Temperature Rate-Sensitivity, Creep and Relaxation of AISI Type 304 Stainless Steel," *Journal of the Mechanics and Physics of Solids,* Vol. 27, 1979, pp. 363–375.

2 Kujawski, D., Kallianpur, V., and Krempl, E., "Uniaxial Creep, Cyclic Creep and Relaxation of AISI Type 304 Stainless Steel at Room Temperature," *Journal of the Mechanics and Physics of Solids,* Vol. 28, 1980, pp. 129–148.

3 Baron, H. G., "Stress-Strain Curves of Some Metals and Alloys, at Low Temperatures and High Rates of Strain," *Journal of the Iron and Steel Institute,* 1956, pp. 354–365.

4 Kocks, U. S., Argon, A. S., and Ashby, M. F., "Thermodynamics and Kinetics of Slip," *Progress in Materials Science,* Vol. 19, 1975.

5 Argon, A. S. ed., *Constitutive Equations in Plasticity,* The MIT Press, Cambridge, 1975.

6 Yamada, H., and Li, C. Y., "Stress Relaxation and Mechanical Equation of State in Austenitic Stainless Steels," *Met. Trans.,* Vol. 4, 1973, p. 2133.

7 Malvern, L. E., "The Propagation of Longitudinal Waves of Plastic Deformation in a Bar of Material Exhibiting a Strain Rate Effect," ASME JOURNAL OF APPLIED MECHANICS, Vol. 18, 1951, pp. 203–208.

8 Perzyna, P., "The Constitutive Equation for Rate-Sensitive Plastic Materials," *Quarterly of Applied Mathematics,* Vol. 20, 1963, pp. 321–332.

9 Eisenberg, M. A., Lee, C. W., and Phillips, A., "Observations on the Theoretical and Experimental Foundations of Thermoplasticity," *International Journal of Solids and Structures,* Vol. 13, 1977, pp. 1239–1255.

10 Cristescu, N., "A Procedure for Determining the Constitutive Equations for Materials Exhibiting Both Time-Dependent and Time-Independent Plasticity," *International Journal of Solids and Structures,* Vol. 8, 1972, pp. 511–530.

11 Cristescu, N., *Dynamic Plasticity,* North Holland, 1967.

12 Klepaczko, J., "Thermally Activated Flow and Strain-Rate History Effect for Some Polycrystalline fcc Metals," *J. Mat. Sci. Eng.,* Vol. 18, 195, pp. 121–135.

13 Nicholas, T., "Strain-Rate and Strain-Rate-History Effects in Several Metals in Torsion," *Experimental Mechanics,* Vol. 11, 1971, pp. 370–374.

14 Campbell, J. D., and Briggs, T. L.: "Strain-Rate History Effects in Polycrystalline Molybdenum and Niobium," *J. Less Common Metals,* Vol. 40, 1975, pp. 235–250.

15 Cernocky, E. P., and Krempl, E., "A Nonlinear Uniaxial Integral Constitutive Equation Incorporating Rate Effects, Creep, and Relaxation," *International Journal of Non-Linear Mechanics,* Vol. 14, 1979, pp. 183–203.

16 Cernocky, E. P. and Krempl, E., "A Theory of Viscoplasticity Based on Infinitesimal Total Strain," *Acta Mechanica:* Vol. 36, 1980, pp. 263–289.

17 Liu, M. C. M., and Krempl, E., "A Uniaxial Viscoplastic Model Based on Total Strain and Overstress:," *Journal of the Mechanics and Physics of Solids,* Vol. 27, 1979, pp. 377–391.

18 Cernocky, E. P., and Krempl, E., "A Theory of Thermoviscoplasticity Based on Infinitesimal Total Strain," *International Journal of Solids and Structures,* Vol. 16, 1980, pp. 723–741.

19 Cernocky, E. P., and Krempl, E., "A Theory of Thermoviscoplasticity for Uniaxial Mechanical and Thermal Loading," to appear *Journal de Méchanique Appliquée.*

---

[7] All tests with the Ti-alloy were terminated at strains of approximately 7 percent. Small cracks were usually observed around this strain. Strains greater than 40 percent are needed for Type 304 SS before necking starts.

W. D. Webster, Jr.

Assistant Professor,
Department of Mechanical Engineering,
General Motors Institute,
1700 W. Third Avenue,
Flint, Mich. 48502
Assoc. Mem. ASME

An Isoparametric Finite Element With Nodal Derivatives

A finite element using the nodal point values of the first partial derivatives of the unknown function with respect to the coordinates to increase the order of the resulting interpolating polynomial is formulated as an isoparametric element. The shape functions in local coordinates are given and then to satisfy requirements for the transformation of derivatives are modified for use with the global coordinates. Examples of a cantilever beam, a curved cantilever beam, and a flat bar with a hole demonstrate the high-order capabilities of the element. The advantages of the element over other isoparametric elements are discussed.

Introduction

Most of the higher-order finite elements in use are constructed by the addition of nodes. If the interpolation polynomials known as shape functions can be defined so as to express the desired function, typically displacement, in terms of the nodal values of the function, the element is generally usable. Another technique used to develop a higher-order element is to express the desired function in terms of the nodal values of the partial derivatives of the function with respect to the coordinates in addition to those of the function [1–3].

The former procedure is usually preferred in that the same shape functions can also be used to describe the mapping from local to global coordinates. When finite elements are so constructed, using one set of shape functions, the element is called isoparametric [4]. Isoparametric elements have the distinct property that each node defines a point in space as well as a value for the desired function.

The latter procedure has used other techniques to describe the mapping from local to global coordinates [5–7]. This can result in subparametric or superparametric elements in that either extra nodes for defining the geometry or a different order of interpolation function for the geometry or both are utilized. The element described herein uses derivatives to achieve higher-order interpolating functions and also maintains the concept of isoparametric elements.

Theoretical Development

The two-dimensional quadilateral element (Figs. 1 and 2) has four corner nodes. At each node, two displacement components and their

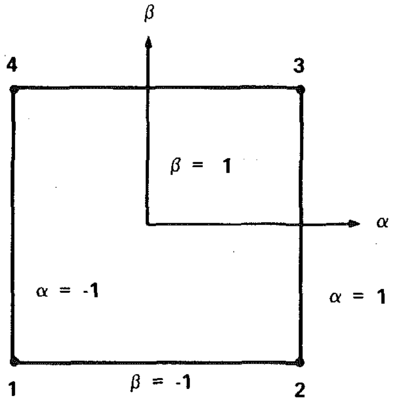

Fig. 1 Quadilateral shaped element in local coordinate system

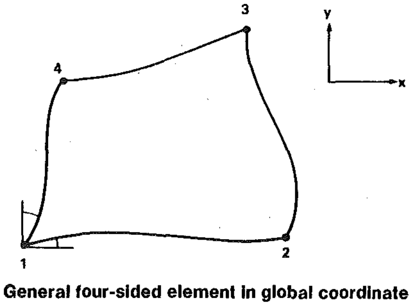

Fig. 2 General four-sided element in global coordinate system

---

Contributed by the Applied Mechanics Division of THE AMERICAN SOCIETY OF MECHANICAL ENGINEERS, for presentation at the 1981 Joint ASME/ASCE Applied Mechanics, Fluids Engineering, and Bioengineering Conference, University of Colorado, Boulder, Colo., June 22–27, 1981.

Discussion on this paper should be addressed to the Editorial Department, ASME, United Engineering Center, 345 East 47th Street, New York, N.Y. 10017, and will be accepted until June 1, 1981. Readers who need more time to prepare a Discussion should request an extension from the Editorial Department. Manuscript received by ASME Applied Mechanics Division, December, 1979; final revision, May, 1980. Paper No. 81-APM-1.

first partial derivatives with respect to the local coordinates (U, U_α, U_β, V, V_α, V_β) are defined thus, allowing a total of six generalized displacements. The shape functions defining the displacements (U and V) in terms of the nodal point values of displacement and the first partial derivatives with respect to the local coordinates are developed using matrix inversion [8] in conjunction with a Taylor series expansion [9]. The interpolating polynomial functions for the displacements expressed in the generalized coordinates a_i and b_i are

$$U = a_0 + a_1\alpha + a_2\beta + a_3\alpha^2 + a_4\alpha\beta + a_5\beta^2 + a_6\alpha^3 + a_7\alpha^2\beta + a_8\alpha\beta^2 + a_9\beta^3 + a_{10}\alpha^3\beta + a_{11}\alpha\beta^3 \quad (1a)$$

and

$$V = b_0 + b_1\alpha + b_2\beta + b_3\alpha^2 + b_4\alpha\beta + b_5\beta^2 + b_6\alpha^3 + b_7\alpha^2\beta + b_8\alpha\beta^2 + b_9\beta^3 + b_{10}\alpha^3\beta + b_{11}\alpha\beta^3 \quad (1b)$$

The generalized coordinates are found by evaluating the polynomial and its first derivatives at each of the four nodes, and then inverting the resulting simultaneous equations. Substituting into equation (1) and grouping terms according to the 12 nodal displacements and derivatives results in the following shape functions:

For U and V:

$$N_i = \frac{1}{8}(1 + \alpha_0)(1 + \beta_0)(2 + \alpha_0 - \alpha^2 + \beta_0 - \beta^2); \quad i = 1, 4, 7, 10 \quad (2a)$$

For U_α and V_α:

$$N_i = -\frac{1}{8}(1 + \alpha_0)(1 + \beta_0)(1 - \alpha^2)\alpha_i; \quad i = 2, 5, 8, 11 \quad (2b)$$

For U_β and V_β:

$$N_i = -\frac{1}{8}(1 + \alpha_0)(1 + \beta_0)(1 - \beta^2)\beta_i; \quad i = 3, 6, 9, 12 \quad (2c)$$

where

$$\alpha_0 = \alpha\alpha_i \quad \beta_0 = \beta\beta_i$$

and

$$\alpha_i = \pm 1 \quad \beta_i = \pm 1.$$

The displacements are expressed in terms of the nodal displacements and derivatives in local coordinates by

$$U = [N]\begin{Bmatrix} \{u\}_1 \\ \{u\}_2 \\ \{u\}_3 \\ \{u\}_4 \end{Bmatrix} \quad (3a)$$

and

$$V = [N]\begin{Bmatrix} \{v\}_1 \\ \{v\}_2 \\ \{v\}_3 \\ \{v\}_4 \end{Bmatrix} \quad (3b)$$

where

$$\{u\}_i = \begin{Bmatrix} U \\ U_\alpha \\ U_\beta \end{Bmatrix}_i \quad i = 1, 2, 3, 4 \quad (3c)$$

and

$$\{v\}_i = \begin{Bmatrix} V \\ V_\alpha \\ V_\beta \end{Bmatrix}_i \quad i = 1, 2, 3, 4 \quad (3d)$$

Since the values of the first derivatives of the displacements with respect to the global coordinates differ from those of the first derivatives of the displacements with respect to the local coordinates, it is necessary to modify the shape functions derived in local coordinates in order that the global nodal displacements and their first partial derivatives with respect to the global coordinates can be used. Thus

$$N_i^* = C_i(N_i) \quad i = 1, 2, \ldots, 12 \quad (4)$$

where N_i^* is the modified shape function and C_i defines the transformation on the original shape function N_i. For the displacements

$$C_i(N_i) = N_i \quad i = 1, 4, 7, 10. \quad (5)$$

For the shape functions associated with the derivatives of the displacements the chain rule gives

$$U_\alpha = \frac{\partial U}{\partial \alpha} = \frac{\partial U}{\partial x}\frac{\partial x}{\partial \alpha} + \frac{\partial U}{\partial y}\frac{\partial y}{\partial \alpha} = U_x\frac{\partial x}{\partial \alpha} + U_y\frac{\partial y}{\partial \alpha} \quad (6a)$$

and

$$U_\beta = \frac{\partial U}{\partial \beta} = \frac{\partial U}{\partial x}\frac{\partial x}{\partial \beta} + \frac{\partial U}{\partial y}\frac{\partial y}{\partial \beta} = U_x\frac{\partial x}{\partial \beta} + U_y\frac{\partial y}{\partial \beta} \quad (6b)$$

The partial derivatives of the global coordinates with respect to the local coordinates are evaluated by isolating the element boundaries that intersect at the nodal point associated with the given shape function. For example, at nodal point 1 the boundaries are defined in local coordinates by $\beta = -1$ and by $\alpha = -1$ (Fig. 1) and correspondingly in global coordinates by $y = F(x)$ and $x = G(y)$, respectively, where F and G are third-order polynomials.

For $\beta = -1$, the global abscissa of the boundary can be expressed (nonuniquely) in terms of the local coordinates by

$$x = \frac{x_2 - x_1}{2}\alpha + \frac{x_2 + x_1}{2}. \quad (7)$$

(This expression is chosen since it is identical to the x-α relationship for a curve-side boundary of an isoparametric element if the boundary is formed by nodes having evenly spaced global abscissa.)

Taking the derivative of x with respect to α gives

$$\frac{\partial x}{\partial \alpha} = \frac{h_2}{2} \quad (8)$$

where

$$h_2 = x_2 - x_1.$$

Since the global ordinate of the boundary is defined as a third-order polynomial in terms of the global abscissa, the chain rule gives

$$\frac{\partial y}{\partial \alpha} = \frac{\partial y}{\partial x}\frac{\partial x}{\partial \alpha} = F'(x)\frac{\partial x}{\partial \alpha}. \quad (9)$$

Substituting (8) into (9) gives

$$\frac{\partial y}{\partial \alpha} = \frac{h_2}{2}F'(x). \quad (10)$$

Similarly, for $\alpha = -1$, using the global ordinate of the boundary gives

Nomenclature

B = strain-displacement transformation matrix

C_i = transformation on shape functions

D = stress-strain transformation matrix

F, G = third-order polynomial functions

h = vertical or horizontal projection of an element side

K = stiffness matrix

N_i = shape function

N_i^* = modified shape function

U, V = displacements

x, y = global coordinates

α, β = local coordinates

$$\frac{\partial y}{\partial \beta} = \frac{h_3}{2}, \quad (11)$$

where

$$h_3 = y_4 - y_1$$

Thus

$$\frac{\partial x}{\partial \beta} = \frac{h_3}{2} G'(y). \quad (12)$$

Substituting equations (6), (8), (10), (11), and (12) for each of the four nodes into equation (3) results in the following modified shape functions for the derivatives:

$$C_i(N_i) = \frac{h_i}{2} N_i + \frac{h_{i+1}}{2} F'(x_j) N_{i+1} \qquad i = 2, 5, 8, 11; \qquad j = (i+1)/3 \quad (13a)$$

$$C_i(N_i) = \frac{h_i}{2} N_i + \frac{h_{i-1}}{2} G'(y_k) N_{i-1} \qquad i = 3, 6, 9, 12; \qquad k = i/3. \quad (13b)$$

where $h_2 = h_5 = x_2 - x_1, h_6 = h_9 = y_3 - y_2, h_8 = h_{11} = x_3 - x_4, h_3 = h_{12} = y_4 - y_1$.

The displacements can now be expressed in terms of the nodal displacements and derivatives in global coordinates by

$$U = [N^*] \begin{Bmatrix} \{u^*\}_1 \\ \{u^*\}_2 \\ \{u^*\}_3 \\ \{u^*\}_4 \end{Bmatrix} \quad (14a)$$

and

$$V = [N^*] \begin{Bmatrix} \{v^*\}_1 \\ \{v^*\}_2 \\ \{v^*\}_3 \\ \{v^*\}_4 \end{Bmatrix} \quad (14b)$$

where

$$\{u^*\}_i = \begin{Bmatrix} U \\ U_x \\ U_y \end{Bmatrix}_i \quad i = 1, 2, 3, 4 \quad (14c)$$

and

$$\{v^*\}_i = \begin{Bmatrix} V \\ V_x \\ V_y \end{Bmatrix}_i \quad i = 1, 2, 3, 4. \quad (14d)$$

If the element is isoparametric, then the shape functions given by (2) must also transform the geometry from local to global coordinates. For nodal point 1, using equations (8) and (11) and the chain rule for the coordinates gives

$$x_\alpha = \frac{\partial x}{\partial \alpha} = \frac{\partial x}{\partial x}\frac{\partial x}{\partial \alpha} = \frac{h_2}{2} x_x \quad (15a)$$

and

$$y_\beta = \frac{\partial y}{\partial \beta} = \frac{\partial y}{\partial y}\frac{\partial y}{\partial \beta} = \frac{h_3}{2} y_y \quad (15b)$$

Substituting equation (15) for each of the four nodes into equation (3) where now the displacements are replaced by the coordinates results in the following modified shape functions:

For Coordinates:

$$C_i(N_i) = N_i \quad i = 1, 4, 7, 10 \quad (16a)$$

For Derivatives:

$$C_i(N_i) = \frac{h_i}{2} N_i \quad i = 2, 3, 5, 6, 8, 9, 11, 12 \quad (16b)$$

The partial derivatives of the coordinates of the boundaries with respect to the global coordinates at the nodal points must be defined values just as the coordinates are defined values. Again examining nodal point 1 and the boundaries defined by $\alpha = -1$ and $\beta = -1$. For $\beta = -1$,

$$x_x = \frac{\partial x}{\partial x} = 1 \quad (17)$$

and

$$y_x = \frac{\partial y}{\partial x} = F'(x) \quad (18)$$

For $\alpha = -1$,

$$x_y = \frac{\partial x}{\partial y} = G'(y) \quad (19)$$

and

$$y_y = \frac{\partial y}{\partial y} = 1. \quad (20)$$

The geometry of the element is now given by

$$X = [N^*] \begin{Bmatrix} \{x\}_1 \\ \{x\}_2 \\ \{x\}_3 \\ \{x\}_4 \end{Bmatrix} \quad (21a)$$

and

$$Y = [N^*] \begin{Bmatrix} \{y\}_1 \\ \{y\}_2 \\ \{y\}_3 \\ \{y\}_4 \end{Bmatrix} \quad (21b)$$

where

$$\{x\}_i = \begin{Bmatrix} x_i \\ 1 \\ G'(y_i) \end{Bmatrix} \quad i = 1, 2, 3, 4 \quad (21c)$$

and

$$\{y\}_i = \begin{Bmatrix} y_i \\ F'(x_i) \\ 1 \end{Bmatrix} \quad i = 1, 2, 3, 4. \quad (21d)$$

$x_i, y_i, G'(y_i)$, and $F'(x_i)$ are specified values for each node of the element.

Stiffness Matrix

The stiffness matrix is developed using the classical approach

$$[K] = \int [B]^T [D][B] dV \quad (22)$$

where $[K]$ is the stiffness matrix, $[B]$ is the strain-displacement transformation matrix, $[D]$ is the stress-strain transformation matrix, and V is the volume of the region. A procedure for evaluating this integral is given in reference [10].

Element Performance

Case 1. A cantilever beam (Fig. 3) is subjected to a concentrated load at the free end. A one element model is sufficient to give excellent results for the displacements and stresses. Since the partial derivatives of the displacements with respect to the coordinates can be con-

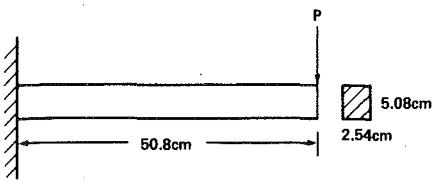

$E = 2.068 \times 10^{11}$ Pa

$v = .3$

$G = \frac{E}{2(1+v)}$

$P = 44{,}482$N

$I = 27.74\text{cm}^4$

$S_p = \frac{PL^3}{3EI} + \frac{PL}{AG}$

$\sigma = \frac{MY}{I}$

	S_p(cm)	Δ(%)	σ_{max}(MPa)	Δ(%)
Theory	3.4087	–	2068.44	–
One Element	3.4056	.09	2039.10	1.42

Fig. 3 Cantilever beam with a concentrated end load

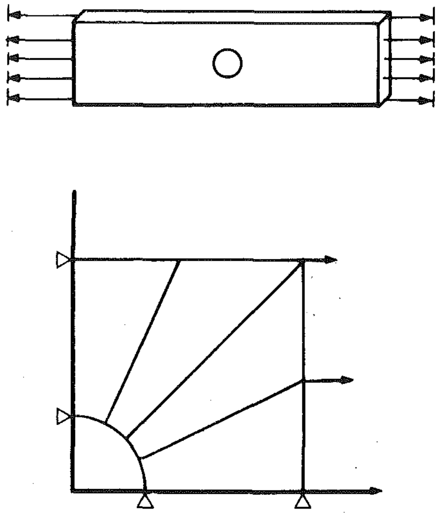

Fig. 5 Flat bar with hole with uniform axial loading

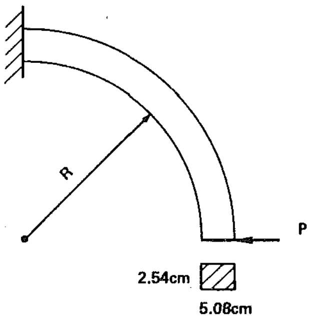

$E = 2.068 \times 10^{11}$ Pa $R = 25.4$cm

$v = .3$

$G = \frac{E}{2(1+v)}$

$P = 44{,}482$N

$I = 27.74\text{cm}^4$

$S_p = \frac{\pi PR^3}{4EI} + \frac{\pi PR}{4AG} + \frac{\pi PR}{4AE}$

$\sigma = \frac{M}{AR}(1 + \frac{1}{Z}\frac{Y}{R+Y})$

	S_p(cm)	Δ(%)	σ_{max}(MPa)	Δ(%)
Theory	1.00942	–	1107.75	–
Two Elements	.99974	.96	1089.04	1.69

Fig. 4 Curved cantilever beam with a concentrated end load

$K = \frac{\sigma_{max}}{P/A}$

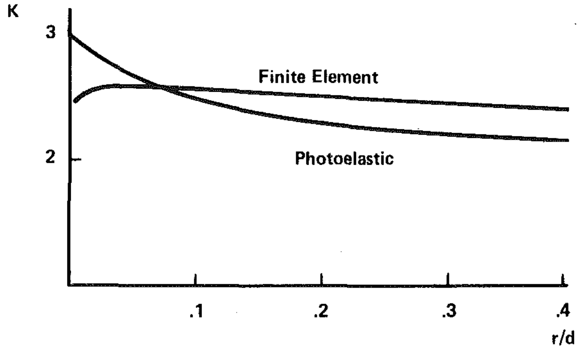

Fig. 6 Stress concentration factor

strained or freed at the nodal points, the problem of the Poisson effects at the cantilever support is overcome with this element.

Case 2. A curved cantilever beam (Fig. 4) is subjected to a concentrated load at the free end. A two element model gives very good results. The geometry of the element is approximated by a third-order polynomial on the boundaries. Expanding the equation for the curve of the beam into a Taylor series gives

$$y = R_i \sin\theta - h\cot\theta + \frac{h^2}{2R_i \sin^3\theta} - \frac{h^3\cos\theta}{2{R_i}^2\sin^5\theta} \tag{23}$$

where h is the distance from the starting point of the element side. For $\theta = 90°$, the curve is best approximated by a quadratic. Thus, when specifying the coordinate derivatives for noncubic boundaries, attention must be paid to the resulting polynomial curve. Unjudicious specification of nodal derivatives could result in undesirable S-shaped boundaries.

Case 3. A flat bar with a circular hole (Fig. 5) is subjected to a uniform axial stress at the ends. The stress concentration factors found using a four element model are compared to those found photoelastically by Frocht [11] for several variations in geometry (Fig. 6). The element performed well except in the area of the discontinuity of the stress concentration factor as would be expected.

Conclusion

When compared to the four node quadilateral isoparametric element, the isoparametric element with derivatives described gives higher-order accuracy for rectangular and quadilateral elements but requires no additional input. For curved-side boundaries only are the two slopes at each node given in equations (10) and (12) required as extra input. This allows much flexibility in describing the boundary elements while maintaining the ease of input for the internal quadilateral elements. Continuity of stress and strain is maintained at the nodes. Thus displacements and stresses are specified at the same points, the nodes. Additional information such as rotations, normal strains, and shear strains is also available at the nodes. This method is easily extended to the three-dimensional case.

It should be noted, however, that elements that use nodal derivatives suffer the disadvantage of not being suitable for those cases where strain discontinuities exist at element interfaces. For example, material or thickness changes would require special treatment of the derivative degrees of freedom at the interface nodes.

References

1 Zienkiewicz, O. C., et al., "Iso-Parametric and Associated Element Families for Two- and Three-Dimensional Analysis," *Finite Element Methods in Stress Analysis,* TAPIR, Technical University of Norway, Trondheim, 1969.

2 Felippa, C. A., and Clough, R. W., "The Finite Element Method in Solid Mechanics," *Numerical Solution of Field Problems in Continuum Physics, SIAM-AMS Proceedings,* Vol. 2, American Mathematical Society, Providence, R.I., 1970, pp. 222–225.

3 William, K., "Finite Element Analysis of Cellular Structures," PhD Dissertation, University of California, Berkeley, 1969.

4 Irons, B. M., and Zienkiewicz, O. C., "The Iso-Parametric Element System—A New Concept in Finite Element Analysis," Conf. Recent Advances in Stress Analysis, J.B.C.S.A., Royal Aero, Soc., London, 1968.

5 Chacour, S., "Danuta,' A Three-Dimensional Finite Element Program Used in the Analysis of Turbomachinery," ASME *Journal of Basic Engineering*, Vol. 94, 1972, pp. 71–77.

6 Dawe, D. J., "Parallelogrammic Elements in the Solution of Rhombic Cantilever Plate Problems," *Journal of Strain Analysis*, Vol. I, No. 3, 1966, pp. 223–229.

7 Davis, R. L., and Webster, W. D., Jr., "Application of the Finite Element Method to Extrusion Processes," *SME NAMRC Proceeding*, 1978.

8 Huebner, K. H., *The Finite Element Method for Engineers*, Wiley, New York, 1975, pp. 136–138.

9 Webster, W. D., "Shape Functions Derived by Taylor Series," *Proceedings, Third Engineering Mechanics Division Specialty Conference*, 1979, pp. 33–36.

10 Zienkiewicz, O. C., *The Finite Element Method in Engineering Science*, McGraw-Hill, London, 1971.

11 Frocht, Max M., "Factors of Stress Concentration Photoelastically Determined," ASME TRANS., Vol. 57, 1935, p. A-67.

J. H. Prevost
Assistant Professor,
Department of Civil Engineering,
Princeton University,
Princeton, N. J. 08544

T. J. R. Hughes[1]
Associate Professor,
Department of Structural Mechanics,
California Institute of Technology,
Pasadena, Calif. 91125
Mem. ASME

Finite-Element Solution of Elastic-Plastic Boundary-Value Problems

It is demonstrated that elastic-plastic failure states may be captured in finite-element models by employing (1) the elastic-plastic material stiffness to form the global stiffness, (2) reduced/selective integration techniques to alleviate mesh "locking" due to incompressibility, and (3), in the case of symmetrical configurations, an imperfection in the form of a weak element.

Introduction

It is the objective of the theory of plasticity to offer a mathematical description of the mechanical behavior of rate-independent materials in the plastic range. The theory follows the well-established precedent set by the theory of elasticity. Its recent popularity stems from its extreme versatility and accuracy in modeling real engineering material behavior. The origin of the theory dates back to a series of papers by Tresca in the 1860's in which he proposed the maximum shear stress criterion for the yielding of metals. The actual formulation of the theory was made by Saint Venant and Levy in 1870, Prandtl in 1924, and Reuss in 1930. References to early works on the subject may be found in [4].

Early works in plasticity only dealt with the simplest class of plastic materials, viz., isotropic elastic-perfectly plastic materials. In that case, the behavior of the real material is idealized by assuming that it behaves like a linear isotropic elastic solid until the shear stress reaches a critical intensity defined by the yield criterion, after which it flows plastically. Although this theory is the simplest, no general analytical method could then be developed for solving general boundary-value problems involving an isotropic elastic-perfectly plastic solid body. Until recently, exact solutions had only been obtained for trivial problems which are one-dimensional or ones which involve proportional loading conditions. The recent development of numerical techniques such as the finite-element method has now rendered possible, in principle, the solution of any properly posed boundary-value problem in continuum mechanics. Numerous numerical solutions for elastic-plastic problems have thus been proposed in the recent literature. However, it appears that many of these solutions are deficient

1 In not converging toward a limit load (when such a limit load exists) but rather rising steadily and attaining values far in excess of the true limit load.

2 In not exhibiting localization of deformation phenomena when such localizations should occur.

The fact that the numerical solution does not exhibit a limit load or too high a limit load, indicates that the computed stiffness is larger than it should be and/or does not become singular when it should. A possible cause for this was pointed out in [11] and is related to the fact that special care must be taken in the numerical formulation in order to be able to handle the incompressible plastic flow which takes place at failure. New techniques have now been devised to deal successfully with incompressibility constraint requirements [7]. However, even when using these techniques, numerical solutions have not seemed capable of capturing localization phenomena, thus prompting several investigators [5, 15], to devise special purpose finite-element procedures.

It is the purpose of this paper to:

1 Investigate the ingredients necessary to capture failure states accurately by numerical methods.

2 To demonstrate that limit loads and localization phenomena can be captured successfully by finite-element models.

For simplicity, attention in this presentation is restricted to small strains/deformations only. As for notation, boldface letters denote vectors, second-order and fourth-order tensors in three dimensions.

Preliminaries

The form of the plasticity equations first proposed by Melan [10] in 1938 is given as follows:

$$\mathbf{d}^P = \langle L \rangle \mathbf{P} \tag{1}$$

in which $\mathbf{d}$ = symmetric part of the velocity gradient; $\mathbf{P}$ = dimen-

---

[1] Presently, Associate Professor of Mechanical Engineering, Division of Applied Mechanics, Stanford University, Stanford, Calif. 94305.

Contributed by the Applied Mechanics Division of THE AMERICAN SOCIETY OF MECHANICAL ENGINEERS, for presentation at the 1981 Joint ASME/ASCE Applied Mechanics, Fluids Engineering, and Bioengineering Conference, University of Colorado, Boulder, Colo., June 22–27, 1981.

Discussion on this paper should be addressed to the Editorial Department, ASME, United Engineering Center, 345 East 47th Street, New York, N. Y. 10017, and will be accepted until June 1, 1981. Readers who need more time to prepare a Discussion should request an extension from the Editorial Department. Manuscript received by ASME Applied Mechanics Division, February, 1980; final revision, September, 1980. Paper No. 81-APM-17.

sionless symmetric second-order tensor normalized in such a way that $\mathbf{P}{:}\mathbf{P} = 1$ and such that $\mathbf{P}$ gives the direction of plastic deformations; and a superscript p is used to denote plastic rate of deformations. In equation (1), L is the loading function,

$$L = \frac{1}{H'}\mathbf{Q}{:}\dot{\mathbf{t}} \qquad (2)$$

in which H' = plastic modulus; $\dot{\mathbf{t}}$ = material rate of Cauchy stress; $\mathbf{Q}$ = dimensionless symmetric second-order tensor normalized in such a way that $\mathbf{Q}{:}\mathbf{Q} = 1$ and such that $\mathbf{Q}$ is the outer normal to the yield surface in stress space; and the symbol $\langle\,\rangle$ denotes the MacCauley's bracket, viz., $\langle L \rangle = L$ if $L \geq 0$, otherwise $\langle L \rangle = 0$. For a plastic hardening case, $H' > 0$, whereas $H' < 0$ for a softening case. When $H' = 0$, a perfectly plastic case is obtained.

Before proceeding any further, it is of importance to note that, as a consequence of the normality rule the plastic fourth-order flexibility tensor is equal to the outer product of the two second-order tensors $\mathbf{P}$ and $\mathbf{Q}$. The plasticity equations alone are therefore singular, and cannot be inverted to yield a purely plastic material stiffness. In order to be able to derive such a stiffness, the material's elasticity must also be taken into account. It is a fundamental assumption of the theory of plasticity that the total rate of deformation tensor in the plastic range may be decomposed into the sum of elastic and plastic rates of deformation.

In order to be able to separate the contributions of the elastic and plastic properties in the total deformation, it is commonly assumed that the elasticity of the material is isotropic and linear. Anisotropic and nonlinear effects are assumed to be due to the material's plasticity. The resulting elastic-plastic flexibility tensor is nonsingular and can be inverted to yield the material's stiffness as

$$\dot{\mathbf{t}} = \mathbf{C}{:}\mathbf{d} = \mathbf{E}{:}\mathbf{d} - \frac{\mathbf{E}{:}\mathbf{P}}{H' + \mathbf{Q}{:}\mathbf{E}{:}\mathbf{P}}\mathbf{Q}{:}\mathbf{E}{:}\mathbf{d} \qquad (3)$$

in which

$$E_{abcd} = \Lambda\delta_{ab}\delta_{cd} + G(\delta_{ac}\delta_{bd} + \delta_{ad}\delta_{bc}) \qquad (4)$$

denotes the elasticity tensor; and Λ, G = Lamé's constants. Note that when $\mathbf{P} \neq \mathbf{Q}$ (i.e., a nonassociative plastic flow rule is used), the $\mathbf{C}$ tensor does not exhibit the major symmetry and therefore leads to a nonsymmetric stiffness matrix. On the other hand, when $\mathbf{P} = \mathbf{Q}$ (i.e., an associative plastic flow rule is used), the $\mathbf{C}$ tensor possesses the major symmetry and leads to a symmetric stiffness matrix. For the simple case of an isotropic elastic-plastic material which yields according to the von Mises criterion [4], viz.,

$$\tfrac{3}{2}\,\mathbf{s}{:}\mathbf{s} - k^2 = 0 \qquad (5)$$

where $\mathbf{s} = \mathbf{t} - \frac{1}{3}$ trace $(\mathbf{t})\mathbf{I}$ = deviatoric stress tensor, equation (3) simplifies to

$$\dot{\mathbf{t}} = 2G\mathbf{d} + \Lambda(\mathrm{trace}\ \mathbf{d})\mathbf{I} - 2G\,\frac{2G/H'}{1 + 2G/\mathrm{H}'}\,\frac{3}{2k^2}\,\mathbf{s}(\mathbf{s}{:}\mathbf{d}) \qquad (6)$$

for an associative plastic flow rule.

Limit Load

A state of failure is reached when deformations start to occur under constant surface tractions. For the elastic-plastic solid body to eventually reach such a state, the material stiffness must be singular, i.e.,

$$\mathbf{C}{:}\mathbf{d} = \mathbf{0} \qquad (7)$$

must possess a nontrivial solution, so that the global stiffness of the solid body may be singular.

Assuming $\mathbf{Q}{:}\mathbf{E}{:}\mathbf{P} \neq 0$, it may be seen that the material elastic-plastic stiffness is singular if $H' = 0$. This follows by showing that

$$\mathbf{X}{:}\mathbf{C}{:}\mathbf{X} = 0 \qquad (8)$$

where $\mathbf{X}$ is a nonzero, symmetric second-order tensor. Taking $\mathbf{X} = \mathbf{Q}$, equation (3) yields

$$\mathbf{Q}{:}\mathbf{C}{:}\mathbf{Q} = H'\,\frac{\mathbf{Q}{:}\mathbf{E}{:}\mathbf{Q}}{H' + \mathbf{Q}{:}\mathbf{E}{:}\mathbf{P}} \qquad (9)$$

which is zero if $H' = 0$.

It is therefore apparent that if the correct limit state is to be detected by the numerical solution, it is helpful to use the elastic-plastic material stiffness rather than any other algorithmically convenient stiffness to form the global stiffness (as in initial-stress-type methods). However, to advance the solution into the post-bifurcation regime requires algorithmic strategies which are not considered herein.

Localization Phenomena

The basic theoretical principles for understanding the localization phenomenon are contained in references [1–3, 8, 14, 16], where it is shown that its existence in elastic-plastic solids is contingent upon the loss of ellipticity of the velocity equations of equilibrium, i.e., localization is to occur when [3]

$$\det\,(\mathbf{n}\cdot\mathbf{C}\cdot\mathbf{n}) = 0 \qquad (10)$$

in which det = determinant, and $\mathbf{n}$ = unit vector, whose orientation defines a characteristic curve for the equations of continuing equilibrium $(C_{abcd}v_{c,d})_{,a} = 0$, where $\mathbf{v}$ = spatial velocity. For an elastic-plastic material, equation (10) imposes that [14]

$$\frac{H'}{2G} = 2\mathbf{n}\cdot\mathbf{P}\cdot\mathbf{Q}\cdot\mathbf{n} - (\mathbf{n}\cdot\mathbf{P}\cdot\mathbf{n})(\mathbf{n}\cdot\mathbf{Q}\cdot\mathbf{n}) - \mathbf{P}{:}\mathbf{Q}$$

$$- \frac{\Lambda}{\Lambda + 2G}\,[(\mathbf{n}\cdot\mathbf{P}\cdot\mathbf{n}) - \mathrm{trace}\ \mathbf{P}][(\mathbf{n}\cdot\mathbf{Q}\cdot\mathbf{n}) - \mathrm{trace}\ \mathbf{Q}] \qquad (11)$$

It is of importance to note that the plasticity equations of equilibrium are the ones which lose ellipticity. This again suggests that if localization phenomena are to be captured by the numerical solution, it is helfpul to use the elastic-plastic material stiffness rather than any other algorithmically convenient stiffness.

Numerical Examples

In the following sections, a number of examples are presented which demonstrate that both limit loads and localization phenomena in elastic-plastic solid bodies may be accurately captured by a finite-element solution of the velocity equations of equilibrium. For that purpose, the finite-element code DIRT [6] is used. Elastic-plastic equations lead directly to the definition of tangent stiffness matrix (see, e.g., [9]), and an incremental predictor-corrector-type algorithm is adopted [6]. The element and material model libraries are modularized and may be easily expanded without alteration of the main code. The present element library contains a two-dimensional element with plane stress/plane strain options, and a three-dimensional element. Full finite deformation effects may be accounted for. A contact element is also available for two and three-dimensional analysis. The present material library contains a linear elastic model and various elasto-plastic and soil models. Some features which are available in the program are

- Both symmetric and nonsymmetric matrix equation solvers.
- Reduced/selective integration procedures, for effective treatment of incompressibility constraints [7].

In the following calculations, the four node bilinear isoparametric element was used with the standard selective integration scheme [6, 7].

1 **Localization of Deformations Into Shear Bands.** Numerical results which illustrate the phenomenon of localization of deformation into shear bands for a rectangular block constrained to plane deformations and subjected to tension in one direction are presented hereafter.

In order to make the study quite specific, the material is modeled as an incompressible isotropic elastic-plastic Prandtl-Reuss material (equation 6)). Fig. 1(a) shows the two-dimensional finite-element representation of the tensile specimen. The grid consists of 171 bilinear isoparametric rectangular elements. The specimen length-to-width ratio is equal to two, and 9 elements are placed across the

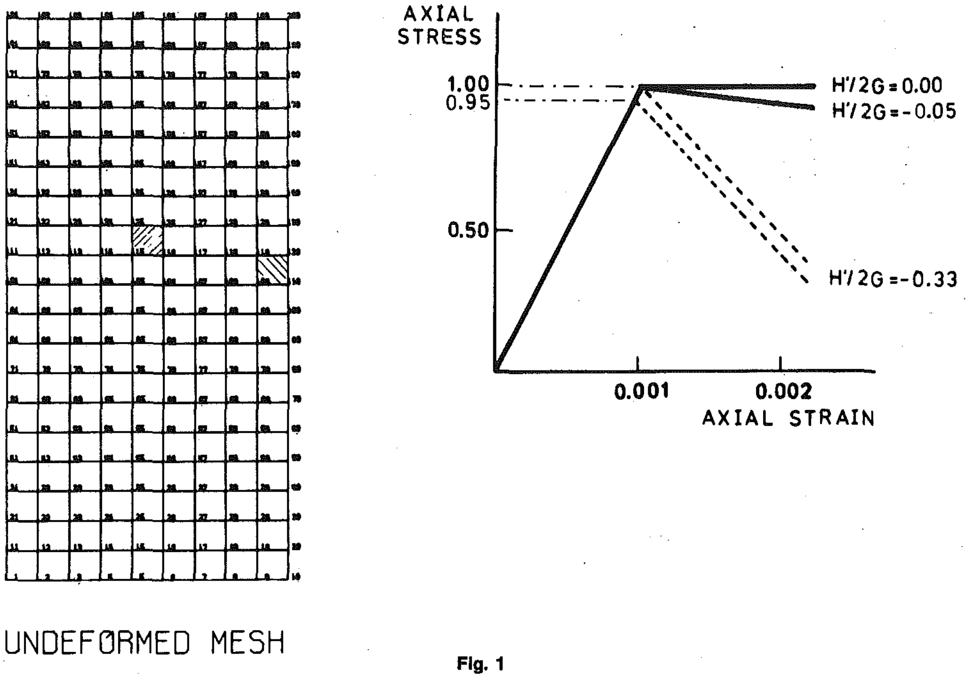

Fig. 1

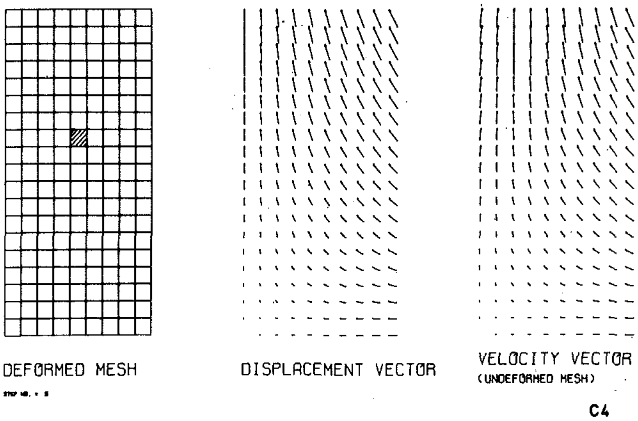

Fig. 2(*a*)

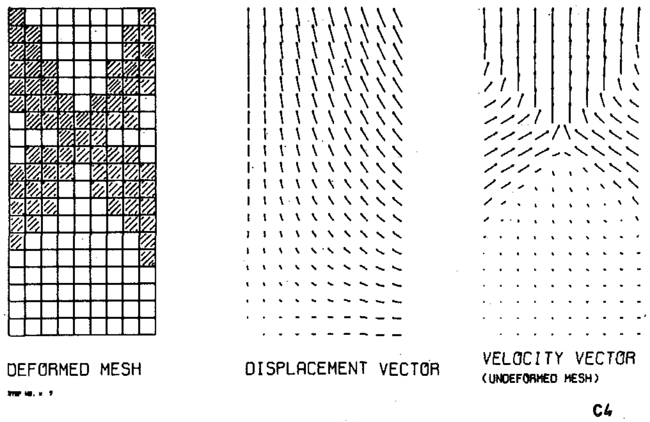

Fig. 2(*b*)

width. Uniform longitudinal end displacements are prescribed, and no shearing tractions are applied. The lower left corner of the specimen is fixed, and the loading is accomplished by imposing increments of displacement at the upper end of the specimen.

For the particular case of the Prandtl-Reuss material, loss of ellipticity of the velocity equations of equilibrium in the small deformation regime is achieved simply by selecting a plastic modulus less or equal to zero. The best numerical results were obtained for $H' < 0$, and in the following $H'/2G = -0.048$. The corresponding angle for the plane of localization is then 38.7°. The assumed stress-strain curve is shown in Fig. 1(*b*).

In a first attempt to obtain localization, both the material properties and the end displacements were taken as uniform. These conditions resulted in smooth and continuously varying deformation patterns well into the softening range, but no localization occurred because of the symmetry of the loading, geometry, and homogeneity of the material properties. This result may be interpreted by recalling that the loss of ellipticity is a necessary but not a sufficient condition for localization. Some type of nonuniformity (perturbation) is necessary

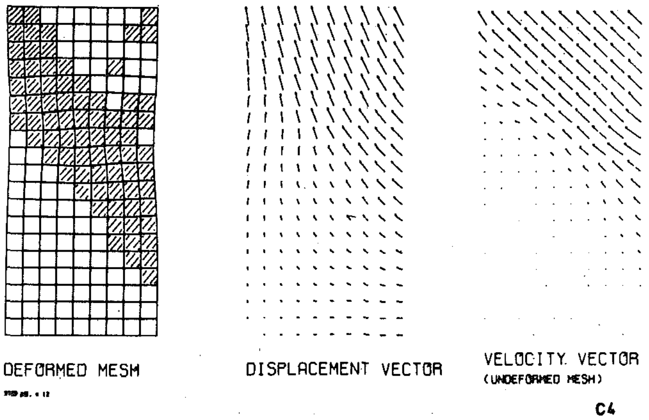

Fig. 2(*c*)

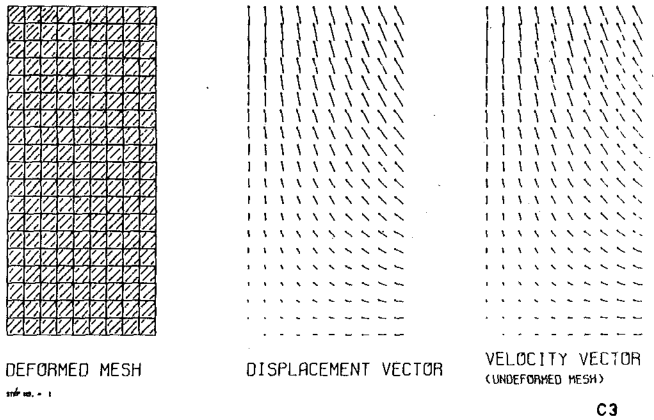

Fig. 3(*a*)

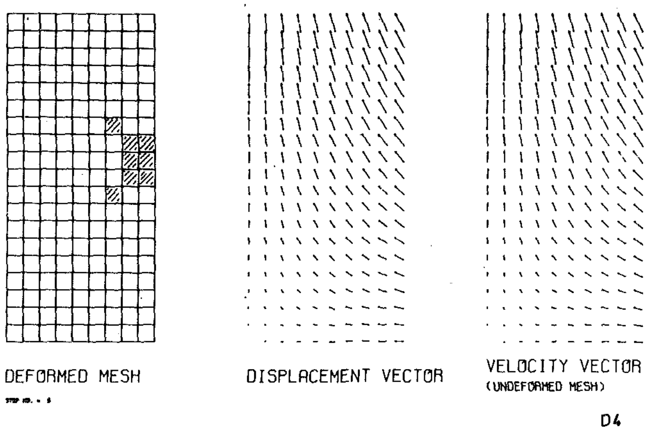

Fig. 4(*a*)

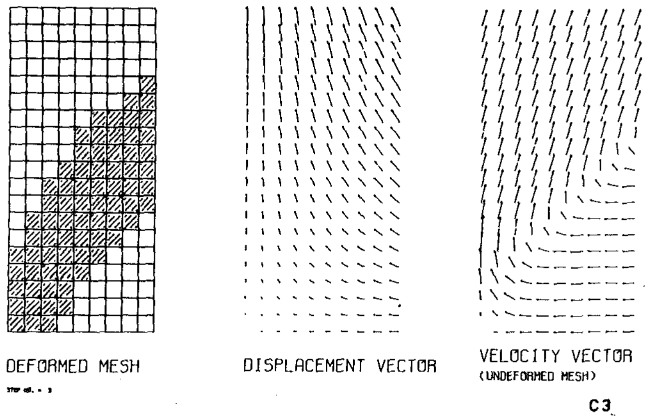

Fig. 3(*b*)

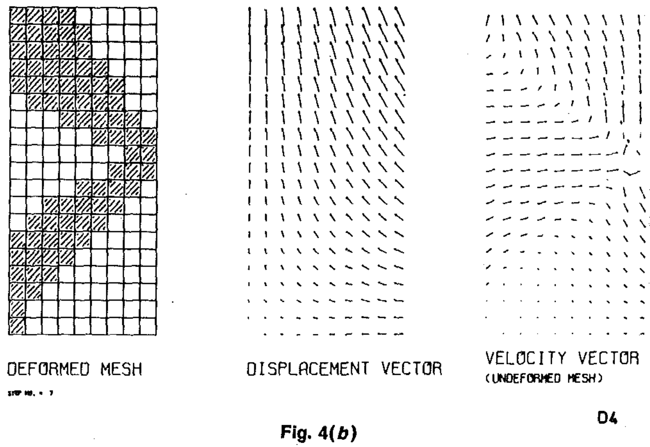

Fig. 4(*b*)

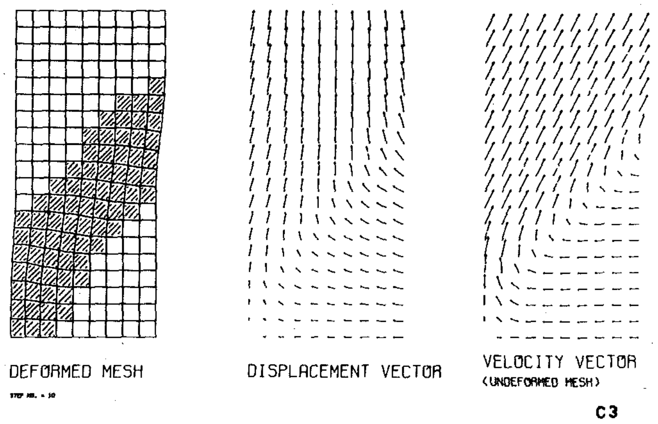

Fig. 3(*c*)

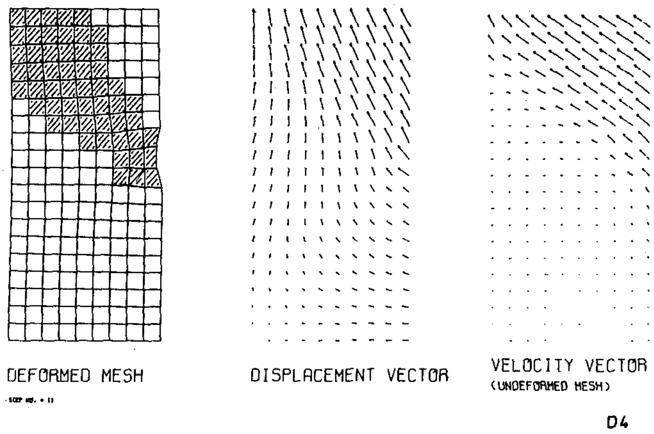

Fig. 4(*c*)

in order to trigger the phenomenon. In the following, localization is achieved by introducing a weak element which plays the role of a local "imperfection" in the material properties. This element is located either at the center (series C) or at the side (series D) of the specimen as shown in Fig. 1, and its plactic modulus is such that $H'/2G = -1/3$. Typical results are shown in Figs. 2–5. The spreading of the plastic zone is indicated by a shaded area. In both Figs. 2 and 3, the imperfection is located at the center of the specimen. In Fig. 2 it has a yield strength 5 percent smaller than the surrounding material. In Fig. 2(*a*) the axial strain = 0.099 percent, and only the weak element has yielded. Upon further loading, localization occurs and as shown in Fig. 2(*b*) (axial strain = 0.101 percent) results in a very symmetrical pattern. This pattern was found to remain stable upon further loading and the specimen failed by necking. In Fig. 2(*c*) (axial strain = 0.150 percent) a slight nonuniformity in the end displacements was introduced to break this symmetry. This was achieved by making the upper right-hand corner longitudinal displacement 1 percent larger than the remaining. By comparing Figs. 2(*b*) and 2(*c*), it is apparent that as a result, some elements unloaded and one shear band emerged. Note that the angle of the slip line is close to the predicted value 38.7°). In Fig. 3, the imperfection has the same strength as its surrounding. In Fig. 3(*a*), the axial strain = 0.100 percent, and all the elements have yielded. In Figs. 3(*b*) and 3(*c*), the axial strain = 0.103 percent and 0.120 percent, respectively. Note that the localization

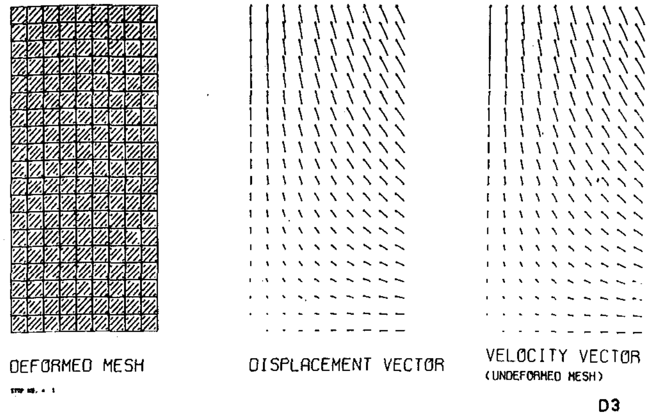

Fig. 5(*a*)

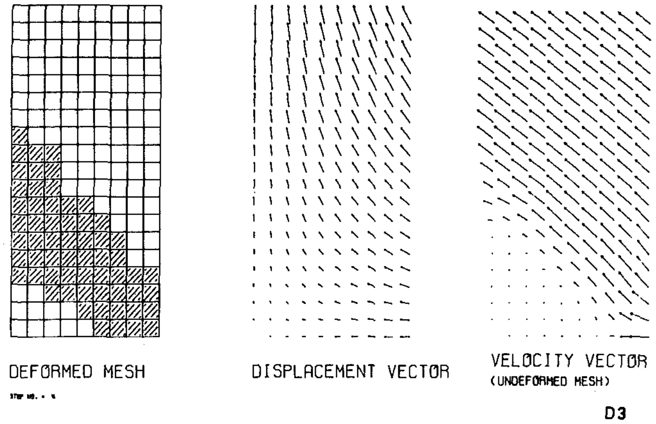

Fig. 5(*b*)

pattern is very different from the one found in Fig. 2. Again this is stable, and the subsequent failure of the specimen is illustrated by Fig. 3(*c*). In both Figs. 4 and 5, the imperfection is located at the side of the specimen. In Fig. 4 it has a yield strength 5 percent smaller than the surrounding material. In Fig. 4(*a*), the axial strain = 0.099 percent. Upon further loading, localization takes place and leads to the formation of two symmetrical slip lines as shown in Fig. 4(*b*) (axial strain = 0.101 percent). However, this configuration is not stable, and upon further loading, only one shear band remains as shown in Fig. 4(*c*) (axial strain = 0.140 percent). In Fig. 5 the imperfection has the same strength as its surrounding and this leads directly to one shear band as shown in Fig. 5(*b*) (axial strain = 0.102 percent). Again, note that for all cases, the angle of the slip line is very close to the predicted value (38.7°).

2 Failure States. In order to demonstrate that finite-element solutions can capture failure states accurately, i.e., both limit loads and localization phenomena, numerical results for the classical punch problem [4, 12, 13] are presented.

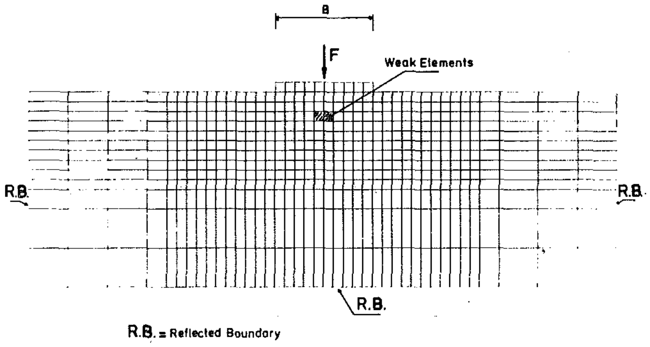

Fig. 6

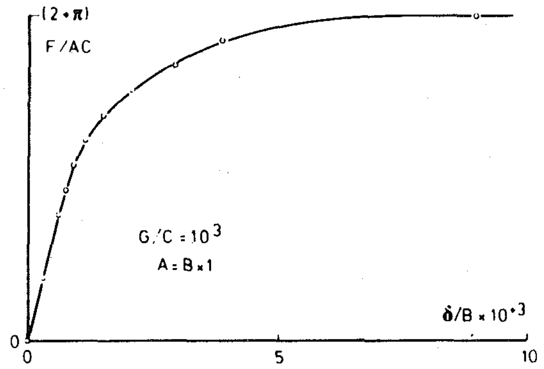

Fig. 7

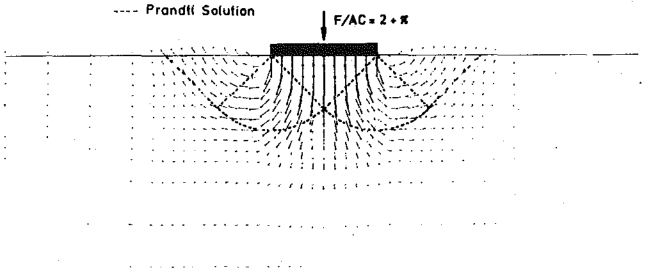

Fig. 8

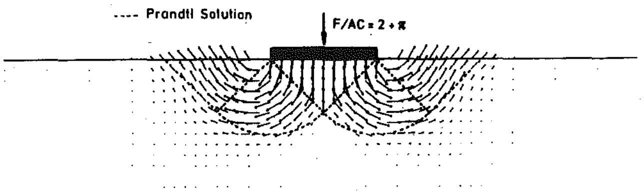

Fig. 9

The material is the classical incompressible isotropic elastic-perfectly plastic Prandtl-Reuss material (equation (6) in which $H' = 0$) and Fig. 6 shows the two-dimensional finite-element representation of the problem geometry and the notation. The punch is represented by a strip of elements ten-thousand times stiffer than the supporting medium. Loading is achieved by the centered vertical force F. the computed load-displacement curve is shown in Fig. 7, where $c = k/\sqrt{3}$ = simple shear strength. Note that the failure load is very accurately captured by the numerical solution. Fig. 8 shows the computed velocity field at failure when the medium is initially perfectly homogeneous. Note that again localization could not occur because of the symmetry of the loading, geometry and homogeneity of the material properties. Fig. 9 shows the computed velocity at failure when a small inhomogeneity has been introduced by placing two weak elements ($H'/2G = -1/3$) in the line of the foundation as shown in Fig. 6. The load-displacement curve in that case remains identical to the one obtained for the homogeneous deposit. However, note that at failure in that case, localization of the deformations takes place and the computed velocity field very accurately follows the classical slip line solution [13].

Summary and Conclusions

It is shown in this paper that finite-element models of elastic-plastic boundary-value problems can accurately represent failure states when the elastic-plastic material stiffness is used to form the global stiffness, and reduced/selective integration techniques are used to alleviate mesh locking due to incompressibility. In order to trigger the localization of the deformations at failure in symmetric problems, and capture the correct slip line field, a local material imperfection is used in the form of a weak element. However, it is of interest to note that the use of such local imperfections seems to be necessary only for symmetric problems. As shown for instance in [17], finite-element models capture failure states accurately without any such perturbations in nonsymmetric problems.

Acknowledgments

Computer time was provided by Princeton University Computer Center and the California Institute of Technology Computer Center.

References

1 Hadamard, J., "Lecons sur la Propagation des Ondes et les Equations de l'Hydrodynamique," Paris, Chapter 6, 1903.

2 Hill, R., "A General Theory of Uniqueness and Stability in Elastic-Plastic Solids," *Journal of the Mechanics and Physics of Solids*, Vol. 6, 1958, pp. 236–249.

3 Hill, R., "Acceleration Waves in Solids," *Journal of the Mechanics and Physics of Solids*, Vol. 10, 1962, pp. 1–16.

4 Hill, R., *The Mathematical Theory of Plasticity*, Oxford University Press, London, 1950, p. 355.

5 Hodge, P. G., and van Rij, H. M., "A Finite-Element Model for Plane Strain Plasticity," ASME JOURNAL OF APPLIED MECHANICS, Vol. 46, No. 3, pp. 536–542.

6 Hughes, T. J. R., and Prevost, J. H., "DIRT II—A Nonlinear Quasi-Static Finite-Element Analysis Program," California Institute of Technology, Pasadena, Calif., Aug. 1979.

7 Malkus, D. S., and Hughes, T. J. R., "Mixed Finite-Element Methods—Reduced and Selective Integration Techniques: A Unification of Concepts," *Computer Methods in Applied Mechanics and Engineering*, Vol. 15, No. 1, 1978, pp. 63–81.

8 Mandel, J., "Conditions de Stabilite et Postulate de Drucker," in *Rheology and Soil Mechanics*, eds., Karavtchenko, J., and Sirieys, P. M., Springer-Verlag, 1966, pp. 58–68.

9 McMeeking, R. M., and Rice, J. R., "Finite-Element Formulation for Problems of Large Elastic-Plastic Deformation," *International Journal of Solids and Structures*, Vol. 11, 1975, pp. 601–616.

10 Melan, E., "Zur plastizität des zäumlichen kontinuums," *Ingenieur-Archive*, Vol. 9, 1938, pp. 116–126.

11 Nagtegaal, J. C., Parks, D. M., and Rice, J. R., "On Numerically Accurate Finite-Element Solutions in the Fully Plastic Range," *Computer Methods in Applied Mechanics and Engineering*, Vol. 4, 1974, pp. 153–177.

12 Prager, W., and Hodge, P. G., *Theory of Perfectly Plastic Solids*, Dover Publications, New York, 1968, p. 264.

13 Prandtl, L., "Uber die Haerte plasticher Koerper," *Goettinger Nachr. Math-Pshys.*, K1 1920, 1920, pp. 74–85.

14 Rice, J. R., "The Localization of Plastic Deformations," in *Theoretical and Applied Mechanics, Proceedings*, 14th IUTAM Congress, Delft, The Netherlands, North Holland Publishing Co., 1976, pp. 207–220.

15 van Rij, H., and Hodge, P. G., "A Slip Model for Finite-Element Plasticity," ASME JOURNAL OF APPLIED MECHANICS, Vol. 45, No. 3, 1978, pp. 527–532.

16 Thomas, T. Y., *Plastic Flow and Fracture in Solids*, Academic Press, Inc., 1961.

17 Prevost, J. H., Hughes, T. J. R., and Cohen, M. F., "Analysis of Gravity Offshore Structure Foundations," *Journal of Petroleum Technology*, Feb., 1980, pp. 199–209.

R. L. Smith[2]
Research Associate.

S. L. Phoenix
Associate Professor.
Assoc. Mem. ASME

Sibley School of Mechanical
and Aerospace Engineering,
Cornell University,
Ithaca, N. Y. 14853

Asymptotic Distributions for the Failure of Fibrous Materials Under Series-Parallel Structure and Equal Load-Sharing[1]

Asymptotic distributions are obtained for both the strength and the time to failure of a fibrous material for which mild bonding or friction exists between fibers. The analysis is based on the chain-of-bundles probability model, and equal load sharing is assumed for the nonfailed fiber elements in each bundle. Asymptotic results are obtained for the difficult but useful case where k, the number of bundles in the chain, grows very rapidly with respect to n, the number of fibers in each bundle. For both strength and time to failure, a classical extreme value distribution is found to be the asymptotic distribution, and the parameters are given in terms of certain fiber properties. The results apply to long, flexible fibrous structures such as yarns and cables.

1 Introduction

The fibrous materials of interest in this paper are long and flexible, and consist of strong fibers aligned in parallel. Very mild bonding or friction exists between fibers, as would be the case in long flexible cables, or in yarns with low twist. When an axial load is applied to the material, fibers break in a random manner, and the total load is distributed across the unfailed fibers according to some load-sharing mechanism. We will assume that the statistical failure characteristics of a single fiber are known for any given time varying load, and our problem is to determine the corresponding characteristics for the fibrous material.

Because of the mild bonding or friction between fibers, a broken fiber becomes fully inoperative only over a region which is small relative to the total material length; indeed, the fiber is capable of supporting almost all its original load at only a short distance from the break. It is this localization of the effects of failure which is responsible for the high strength of such materials. Thus we model the material as a chain of k statistically and structurally independent bundles with n fibers in each bundle as shown in Fig. 1. The length δ of each bundle is the length of this ineffective region for a broken fiber.

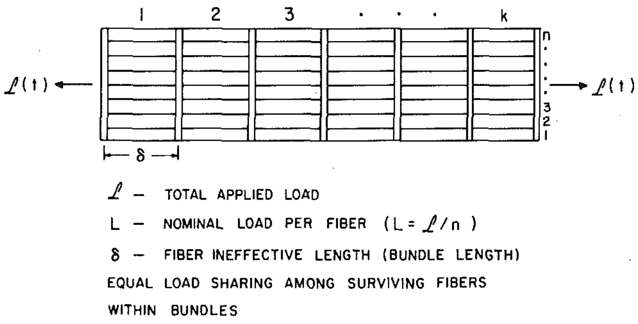

Fig. 1 Series-parallel model for the failure of a fibrous material in the form of a chain of k bundles with n fiber elements per bundle; failure of the material occurs with the failure of the weakest bundle

For each bundle, we will assume the simplest load sharing rule which is *equal load-sharing;* that is, at any time the total load is distributed equally over all unfailed fibers, with the failed fibers carrying no load. This assumption is most appropriate for a bundle of straight, parallel fibers of equal length in which there is no physical contact among the fibers, but we make this assumption in the present case of mild bonding or friction between fibers. However, in the case of stiff composite materials where the fibers are encased in a matrix material thus causing the bonding among fibers to be much stronger, this as-

---

[1] This research was supported by the United States Department of Energy under Contract DE-AC02-76 ERO 4027.

[2] Presently, Department of Mathematics, Imperial College of Science and Technology, London SW7 2BZ, England.

Contributed by the Applied Mechanics Division for publication in the JOURNAL OF APPLIED MECHANICS.

Discussion on this paper should be addressed to the Editorial Department, ASME, United Engineering Center, 345 East 47th Street, New York, N. Y. 10017, and will be accepted until June 1, 1981. Readers who need more time to prepare a Discussion should request an extension from the Editorial Department. Manuscript received by ASME Applied Mechanics Division, January, 1980; final revision, August, 1980.

sumption of equal load sharing must be replaced by what is called *local* load-sharing. In this case, the mechanics of fiber/matrix interactions comes into play, and the load redistribution is concentrated on fibers which are immediate neighbors to the failed fibers, while more distant fibers in the lateral direction remain unaffected. The mathematical analysis for this case proceeds in a very different direction from that considered here. For further discussion, the reader is referred to Harlow and Phoenix [1–4]. Here, all analysis will be under the equal load-sharing rule.

The early work on the model of this paper was performed in classic studies by Daniels [5] in the static case, and Coleman [6–9] in the time-dependent case. Daniels and Coleman obtained important asymptotic results for certain cases involving *single* bundles of increasing size n, and recently Phoenix [10, 11] has extended the asymptotic results in the broader time-dependent framework proposed by Coleman [9]. The latter paper [11] of Phoenix ties together the models of Coleman and Daniels, these being distinct for the most part; Daniels' static model is actually *not* a special case of the time-dependent model on which Coleman performed the bulk of his work.

In this paper, we obtain asymptotic distributions for both the *strength* and the *time to failure* of the fibrous material; that is, of the chain-of-bundles. The results will be asymptotic as both n the number of fibers and k the number of bundles increase indefinitely together, but most important, we seek results for the most useful and difficult case where k increases *rapidly* with respect to n. The fibrous material is thus long and slender, as yarns and cables typically are.

We begin with a brief description of the three versions of the model that we consider. These versions differ with respect to the assumptions made about the failure of a single fiber. The first model is based on that of Daniels for static strength, ignoring fatigue. The remaining models are all extensions of Coleman's model for time to failure incorporating fiber fatigue. In each case, we summarize earlier asymptotic results for *single* bundles. As bundle size n increases, an asymptotic normal distribution occurs for both single bundle strength and time to failure in fatigue, and we give the distribution parameters.

Next, we focus on the analytical difficulties in determining the asymptotic distribution for the strength or time to failure of the *chain* of k bundles, as both k and n increase. Since failure of the chain occurs when the *weakest* bundle fails, the problem becomes one in the realm of the asymptotic theory of extreme order statistics, wherein the *lower tails* of the bundle distributions dominate in importance. Now, on the one hand, we have classic, asymptotic results in extreme value theory which would apply under the normal distribution for the k variates. On the other hand, we have *asymptotic* normal distributions for bundle failure as $n \to \infty$, the *exact* distributions being essentially unknown. The key question is "As $n \to \infty$, under what conditions on the increasing of k with respect to n may we replace the (unknown) *exact* distributions for bundle failure with the corresponding (known) *asymptotic* distributions in this extreme value analysis?"

To further understand the nature of these difficulties, we discuss certain ramifications of the central limit theorem, paying particular attention to the *rates* of convergence of the asymptotic distributions to the exact distributions, both in an absolute sense and in a relative sense. We will see that it is the *relative* error in their respective lower tails that is important, and this draws us into the framework of large deviations theory as developed by Cramér and Petrov [12]. We will quote certain relevant results for later use.

Next, we focus on the Poisson limit law to gain a deeper understanding of certain technical aspects of the extreme value analysis, and to introduce the key asymptotic distributions which ultimately arise for the failure of the fibrous material.

Finally, we obtain the main asymptotic results of the paper. It is found that both the *strength* and *failure time* of the fibrous material have an asymptotic distribution function of the form $1 - \exp\{-\exp[(y - b_n)/a_n]\}$ where the parameters a_n and b_n are given explicitly in each case. To a large extent, this form is a consequence of the *equal load-sharing* assumption and the asymptotic normality it yields for bundle strength. Elaboration on certain technical details, which are required in the light of the preliminary discussion, are reported elsewhere by Smith [13, 14]. We conclude with an example which reveals some practical ramifications of the main results. We also discuss some additional results obtained by other authors. In particular, the calculations of Gücer and Gurland [15], whose model is actually the chain-of-bundles model in Daniels' static setting take on a new strength as we now justify certain steps in their analysis.

2 The Series-Parallel Model and Earlier Results

To reiterate, the fibrous material is a parallel structure of n fibers, and is partitioned into a series of k short sections or bundles of length δ. Thus the material is viewed as a chain of k bundles with n fiber elements per bundle, and its total length is $l = k\delta$.

A *total* load $\mathcal{L}$ is applied in tension along the axis of the structure, and in general this load will be time varying. But to compare results for different bundle sizes n, we speak in terms of the *applied* load $L = \mathcal{L}/n$, so that L is the nominal load per fiber in the bundle. In the static case, we focus on the strength which is the largest load L that the structure supports, and in the time-dependent case, we focus on the time to failure given the load L as a function of time. The k bundles are structurally and statistically independent, and failure of the fibrous material occurs when the first bundle fails.

At any time, the nonfailed fiber elements in each bundle share the total load $\mathcal{L}$ equally, and failed elements carry no load; earlier, this was referred to as the *equal load-sharing rule*. Thus, if i of the n fiber elements in a bundle have failed, each surviving element supports the higher load $nL/(n - i)$ rather than the nominal value L.

2.1 The Static Strength of Single Bundles. We now consider the static case, and summarize Daniels' asymptotic results for a single bundle [5]. If the individual fiber strengths are denoted by $X_1, X_2, \ldots, X_n$, and we let $X_{(1)} \leqq X_{(2)} \leqq \ldots \leqq X_{(n)}$ be these strengths arranged in increasing order, then the bundle will support the load L if $L \leqq X_{(1)}$ or $nL/(n-1) \leqq X_{(2)}$ or ... or $nL \leqq X_{(n)}$; if none of these inequalities are satisfied, the bundle will fail. Thus the *bundle strength* L_n^* is given by

$$L_n^* = \max\left\{X_{(1)}, \left(\frac{n-1}{n}\right)X_{(2)}, \ldots, \left(\frac{1}{n}\right)X_{(n)}\right\}. \tag{1}$$

The distribution function of L_n^*, which we denote by $F_n^*(x) = \Pr\{L_n^* \leqq x\}$, is desired under the assumption that the fiber strengths $X_1, \ldots, X_n$ are independent random variables with common distribution function $F(x)$, $x \geqq 0$. While no compact expression was found for $F_n^*(x)$ for large n, Daniels showed that the bundle strength L_n^* is asymptotically normally distributed with known parameters. One verion of his result is as follows [13]:

Theorem 2.1. Assume $F(x)$, $x \geqq 0$ is continuous with $F(0) = 0$ and $\int_0^\infty x^2 dF(x) < \infty$. Let

$$\mu^* = \sup\{x[1 - F(x)]: \quad x \geqq 0\}, \tag{2}$$

that is, μ^* is the maximum value achieved by the function $x[1 - F(x)]$ as $x \geqq 0$ is increased indefinitely. Also, let x^* be the value of x where this maximum is attained, and assume x^* is unique and positive. Finally, let

$$\sigma^* = x^*[F(x^*)(1 - F(x^*))]^{1/2}. \tag{3}$$

Then for all real z

$$F_n^*(\mu^* + n^{-1/2}\sigma^* z) \to \Phi(z) \tag{4}$$

as $n \to \infty$ where $\Phi(z) = (2\pi)^{-1/2}\int_{-\infty}^{z} \exp(-t^2/2)dt$ is the standard normal distribution function with mean zero and variance one.

Thus the bundle strength L_n^* is asymptotically normally distributed with mean μ^* and standard deviation $\sigma^*/\sqrt{n}$. The asymptotic mean μ^* is easily appreciated upon considering a very large bundle. If the load in each surviving fiber is x, the fraction of surviving fibers is $1 - F(x)$, and thus, the applied load L is approximately $x[1 - F(x)]$. Maximizing $x[1 - F(x)]$ by varying $x \geqq 0$ will approximately yield the bundle strength L_n^*, since the standard deviation $\sigma^*/\sqrt{n}$ is small for large n. Later, we will see that the convergence implied by (4) is insufficient for our purposes.

2.2 The Time to Failure of Single Bundles. The model of the previous section is appropriate only when fiber fatigue does not occur to any appreciable extent. In this section, we discuss the time to failure of single bundles where the fibers fatigue under load. To do this, some mathematical model is needed for the probability distribution for failure of a single fiber under an arbitrary load history $l(t)$, $t \geqq 0$. We concentrate on a class of models proposed by Coleman [6–9]; these have shown remarkable agreement with the experimental behavior of a variety of materials.

In the simplest model [7, 8], the probability that a surviving fiber under current load l fails in the next infinitesimal time interval of length δt is given by $\kappa(l)\delta t + o(\delta t)$ where the function $\kappa(x)$, the so-called *breakdown rule,* is some positive and increasing function of $x \geqq 0$. Then, the distribution for the failure time T of a single fiber subjected to the load history $l(t)$, $t \geqq 0$ is given by

$$P\{T \leqq t\} = 1 - \exp\left\{-\int_0^t \kappa(l(s))ds\right\}, \quad t \geqq 0. \tag{5}$$

The simplicity of this model stems from the fact that the *hazard rate* for the fiber at time t is simply $\kappa(l(t))$, and does not depend on the load history prior to time t. In fact, under the constant load $l > 0$, the foregoing distribution function reduces to the exponential distribution with constant hazard rate $\kappa(l)$. These facts simplify the analysis for bundles because of this "memoryless property."

Consider now a single bundle of n fibers subjected to the constant load $L > 0$ (total load $\mathcal{L} = nL$). At first, each fiber bears the load L, but after $j - 1$ fibers have failed, the load on each survivor has increased to $nL/(n - j + 1)$ according to the equal load-sharing rule. Thus the hazard rate for the time $Y_{n,j}$, which is the time between the $(j - 1)$th and the jth failure, is simply the number of surviving fibers multiplied by the hazard rate for one fiber, that is,

$$\lambda_{n,j} = (n - j + 1)\kappa(nL/(n - j + 1)). \tag{6}$$

Consequently, the distribution of $Y_{n,j}$ is given by the exponential distribution

$$P\{Y_{n,j} \leqq t\} = 1 - \exp\{-\lambda_{n,j}t\}, \quad t \geqq 0 \tag{7}$$

for $1 \leqq j \leqq n$, and moreover, the random variables $Y_{n,1}, Y_{n,2}, \ldots, Y_{n,n}$ are independent because of the memoryless feature. The time to failure T_n of the bundle is simply the sum

$$T_n = \sum_{j=1}^{n} Y_{n,j}. \tag{8}$$

The function $\kappa(x)$ is often taken to be the *power law breakdown rule*

$$\kappa(x) = (x/l_0)^\rho, \tag{9}$$

where l_0 and ρ are positive constants, and $\rho \geqq 1$ is assumed. Not only are the fatigue features realistic under this rule, but the analysis for bundles under time-varying loads is simplified greatly, as we see shortly.

Under this power law breakdown rule (9), we have $\lambda_{n,j} = (L/l_0)^\rho n^\rho (n - j + 1)^{-\rho+1}$. Since $Y_{n,j}$ follows the exponential distribution (7), it has mean $\lambda_{n,j}^{-1}$ and variance $\lambda_{n,j}^{-2}$, so that the mean and variance of T_n are, respectively,

$$\begin{aligned} E[T_n] &= \sum_{j=1}^{n} \lambda_{n,j}^{-1} \\ &= (L/l_0)^{-\rho} n^{-1} \sum_{j=1}^{n} [(n - j + 1)/n]^{\rho-1} \\ &\to (L/l_0)^{-\rho} \int_0^1 x^{\rho-1} dx \quad (\text{as } n \to \infty) \\ &= \rho^{-1}(l_0/L)^\rho, \end{aligned} \tag{10}$$

and

$$\begin{aligned} n \operatorname{Var}[T_n] &= n \sum_{j=1}^{n} \lambda_{nj}^{-2} \\ &= (L/l_0)^{-2\rho} n^{-1} \sum_{j=1}^{n} [(n - j + 1)/n]^{2\rho-2} \end{aligned} \tag{11}$$

$$\begin{aligned} &\to (L/l_0)^{-2\rho} \int_0^1 x^{2\rho-2} dx \quad (\text{as } n \to \infty) \\ &= (2\rho - 1)^{-1}(l_0/L)^{2\rho}. \end{aligned} \tag{11}$$

(*Cont.*)

Because the bundle failure time T_n is the sum of the independent random variables $Y_{n,1}, \ldots, Y_{n,n}$, we may apply the Liapunov form of the Central Limit theorem for sums of independent, nonidentically distributed random variables (Chung [16, page 200]) to obtain the asymptotic distribution of T_n. The result is that $(T_n - E[T_n])/\sqrt{\operatorname{Var}[T_n]}$ converges in distribution to a normal random variable with mean zero and variance one. Alternatively, T_n is asymptotically normally distributed with mean $\rho^{-1}(l_0/L)^\rho$ and standard deviation $(l_0/L)^\rho n^{-1/2}(2\rho - 1)^{-1/2}$.

While (5) has permitted straightforward analysis, the implication of exponentially distributed life for a fiber under constant load is not realistic in most situations. To alleviate this difficulty, Coleman [9] proposed the more general model for the time to failure of a single fiber

$$P\{T \leqq t\} = G\left(\int_0^t \kappa(l(s))ds\right), \quad t \geqq 0. \tag{12}$$

where $G(y)$, $y \geqq 0$ is an arbitrary probability distribution function satisfying $G(0) = 0$. Thus, under constant load l, any distribution for fiber life is possible; (5) is the special case $G(y) = 1 - e^{-y}$, $y \geqq 0$. The difficulty is that under this model, the times $Y_{n,1}, \ldots, Y_{n,n}$ between fiber failures in the bundle are no longer independent, and the foregoing arguments do not hold; however, under very general assumptions, Phoenix [10] has recently demonstrated the asymptotic normality of T_n in this case too, and has discussed extensively the computation of the asymptotic mean and variance. These results also apply to time-dependent load histories $L(t)$, $t \geqq 0$ (for instance, linearly increasing or cyclic loads) provided the power law breakdown rule (9) is assumed.

We state some of these asymptotic results for bundles under the more general form (12) for single fibers. We make some further technical assumptions which are somewhat more restrictive than in Phoenix [10] but which are required later:

(A1) $G(x)$, $x \geqq 0$ is a continuous distribution function with $G(0) = 0$ and $\int_0^\infty e^{zx} dG(x) < \infty$ for some $z > 0$.

(A2) $\kappa(x)$, $x \geqq 0$ is continuous, increasing and unbounded with $\kappa(x) > 0$ for all $x > 0$. Furthermore, for each fixed $\lambda > 0$, the function

$$\Psi(x;\lambda) = \begin{cases} 1/\kappa(\lambda/(1 - x)), & 0 \leqq x < 1 \\ 0, & x = 1 \end{cases} \tag{13}$$

has a bounded, continuous second derivative on $[0, 1]$.

(A3) The bundle load program $L(t)$, $t \geqq 0$ is a continuously differentiable function of t, and satisfies $L(t) > 0$ for $t > 0$ and $\int_0^\infty L(t)^\rho dt = +\infty$ for fixed $\rho > 0$.

For the loading of the bundle, we consider two cases:

Case 1: Constant load program $L(t) \equiv \mathbf{L} > 0$.

Case 2: Arbitrary load program $L(t)$ in conjunction with the power law breakdown rule $\kappa(x) = (x/l_0)^\rho$, $l_0 > 0$ and $\rho \geqq 2$, and with $L(t)$ satisfying Assumption (A3).

Next, let $g(t)$, $0 \leqq t < 1$ be the right-continuous inverse of the distribution function $G(y)$, $y \geqq 0$, that is $g(t) = \inf\{y : G(y) > t\}$. (Essentially, $g(t)$ is the value g satisfying $G(g) = t$. For example, the inverse of $G(y) = 1 - e^{-y}$, $y \geqq 0$ is $g(t) = \log[1/(1 - t)]$.) For $\lambda > 0$ define

$$\mu^\#(\lambda) = -\int_0^1 \Psi'(t;\lambda)g(t)dt, \tag{14}$$

and

$$\sigma^\#(\lambda) = \left[2\int_0^1 \int_0^t s(1 - t)\Psi'(s;\lambda)\Psi'(t;\lambda)dg(s)dg(t)\right]^{1/2} \tag{15}$$

where $\Psi' = d\Psi/dt$. Finally, let

$$F_n^{\#}(t) = \Pr\{T_n \leqq t\} \tag{16}$$

be the distribution function for the time to bundle failure T_n given the load program $L(t)$, $t \geqq 0$. Our result is as follows:

Theorem 2.2 For Case 1 let $t_b = \mu^{\#}(\mathbf{L})$ and $\sigma_b = \sigma^{\#}(\mathbf{L})$. For Case 2, define t_b and σ_b by $\int_0^{t_b} L(s)^\rho ds = \mu^{\#}(1)$ and $\sigma_b = L(t_b)^{-\rho}\sigma^{\#}(1)$, respectively. Then, for all real z

$$F_n^{\#}(t_b + n^{-1/2}\sigma_b z) \rightarrow \Phi(z) \tag{17}$$

as $n \rightarrow \infty$ where $\Phi(z)$ is the standard normal distribution function with mean zero and variance one.

Thus the bundle time to failure T_n is asymptotically normally distributed with mean t_b and standard deviation $\sigma_b/\sqrt{n}$, a result which parallels Theorem 2.1 for the static case. The formulas for t_b and σ_b are in a slightly different form from those in Phoenix [10], but are equivalent nevertheless. See Phoenix [17] for further applications of the above asymptotic results. In particular, for linearly increasing loads $L(t) = L_0 t$, $t \geqq 0$ where $L_0 > 0$ is the loading rate, an asymptotic normal distribution is again found for bundle strength L_n^* but the asymptotic mean and variance now depend on the loading rate L_0. We point out that Daniels' static model is *not* a special case.

We have obtained asymptotic normality for the strength and failure time of single bundles. The key question is *"How close are the asymptotic and exact distributions as n increases?"* For *single* bundles, such error bounds are useful. But when considering asymptotic results for long chains of bundles, an error analysis is crucial particularly in the lower tails of the respective asymptotic and exact distributions.

3 Proximity of Exact and Asymptotic Distributions for Bundle Failure

We begin by considering some ramifications of the *Central Limit theorem.* This theorem states that if $S_n = (X_1 + \ldots + X_n)/n$ where $X_1, X_2, \ldots$ are independent and identically distributed random variables with common mean μ and variance σ^2, then $\mathcal{S}_n = \sqrt{n}(S_n - \mu)/\sigma$ has an asymptotic normal distribution as $n \rightarrow \infty$, with mean *zero* and variance *one.* Symbolically, if $F_n(x) = P\{S_n \leqq x\}$, $x \geqq 0$ denotes the distribution function of S_n, then this result may be written as

$$F_n(\mu + n^{-1/2}\sigma z) \rightarrow \Phi(z) \quad \text{as} \quad n \rightarrow \infty \tag{18}$$

for any real number z. (Notice the similarity with Theorems 2.1 and 2.2. The quantity S_n is analogous to L_n^* and to T_n.)

This theorem is of great practical importance because it allows one to obtain a quick and accurate approximation of the distribution function $F_n(x)$, $x \geqq 0$ whenever n is reasonably large. The exact computation of $F_n(x)$ is typically laborious, however the Central Limit theorem suggests the approximation

$$F_n(x) \doteqdot \Phi(\sqrt{n}(x - \mu)/\sigma) \tag{19}$$

which is easily used since tables for the normal function $\Phi(x)$ are widely available.

We now discuss two problems associated with the approximation (19). The first concerns the *rate of convergence* in an absolute sense. We know that the error is small when n is large, but how fast does the error approach zero as $n \rightarrow \infty$? How large must n be for the approximation to reach a desired level of accuracy? These questions are answered by the *Berry-Esseen theorem* which we now state.

Berry-Esseen Theorem. Suppose, in addition to the aforementioned assumptions for the Central Limit theorem, we have $\rho = E[|X_i - \mu|^3] < \infty$. Then

$$|F_n(\mu + n^{-1/2}\sigma z) - \Phi(z)| < 3\rho\sigma^{-3}n^{-1/2} \tag{20}$$

for all n and real z.

A proof is given in Feller [12, page 542].

Thus the Berry-Esseen theorem gives an explicit upper bound on the difference between the exact distribution function and its normal approximation uniformly in all z. It turns out that the explicit formula (20) is not often used in practice because it tends to *overestimate* the actual error considerably. But the most important feature of the result is that, as $n \rightarrow \infty$, the error decreases to zero at the rate $n^{-1/2}$. The key question is: "Will a similar rate of decrease occur for the normal approximations to the distribution functions for the failure of single bundles?" In practice, the normal approximation is widely used for n as small as 30 or 40, though of course, this depends on the use to which the approximation is to be put as we now see.

The second kind of problem associated with the approximation (19) is not resolved by the Berry-Esseen theorem. This problem concerns *events of very small probability.* In such situations, the knowledge that the absolute error is small may be of little use. As an example, consider a chain consisting of k links. Let $Y_1, \ldots, Y_k$ be the strengths of the links, and assume these to be independent and identically distributed random variables with common distribution function $G(y)$, $y \geqq 0$. The strength of the chain is $M_k = \min\{Y_1, \ldots, Y_k\}$, and has the distribution function

$$G_k(y) = 1 - [1 - G(y)]^k, \quad y \geqq 0. \tag{21}$$

Now suppose we want the median strength of the chain, that is, the load m^* for which $G_k(m^*) = 1/2$. According to (21), this reduces to wanting the load m^* for which $G(m^*) = 1 - (\frac{1}{2})^{1/k} \simeq 0.693/k$ when k is large. If $k = 10{,}000$, m^* must solve $G(m^*) = 0.0000693$, the right-hand side of which is a very small number. Now, if we only have an *approximation* for $G(y)$, say $\tilde{G}(y)$, and we know $|G(y) - \tilde{G}(y)| < 0.001$ for all y, this is not useful when $k = 10{,}000$ because the *relative error* in estimating $G(y)$ is $0.001/0.0000693 = 14.4$ which is very high; we would be prone to making large errors in estimating the median strength m^* when using $\tilde{G}(y)$. But for one link ($k = 1$) the relative error is $0.001/(1/2) = 0.002$, and an estimate of the median strength m^* of *one* link is likely to be quite accurate. Obviously the situation worsens as k increases, and thus, accuracy further into the lower tail of $G(y)$ is required. In this example, which is at the heart of the matter in this paper, the Berry-Esseen theorem is of no help because it only deals with absolute error while we are really concerned with relative error.

Cramér-Petrov Theorem. The analytical tool for studying relative error in situations where the normal distribution approximates the true distribution, is the *large deviations theory* developed by Cramér and Petrov. A convenient formulation of the problem is as follows: Given a sequence $z_1, z_2, \ldots, z_n, \ldots$ of positive numbers (which we denote by $\{z_n\}$), under what conditions is it true that

$$F_n(\mu - n^{-1/2}\sigma z_n)/\Phi(-z_n) \rightarrow 1 \tag{22}$$

as $n \rightarrow \infty$? For $\{z_n\}$ bounded there is no problem, but if $z_n \rightarrow \infty$ (and thus $-z_n \rightarrow -\infty$) then both the numerator and denominator in (22) tend to zero.

In the case of the Central Limit theorem, the main result is as follows. Assume that Cramér's condition holds, that is, that the moment generating function of X_i, $E[\exp(sX_i)]$, is finite for all s in some interval $(-A, A)$, where $A > 0$. (This assumption implies that all moments of X_i are finite, so it is a much stronger assumption than those made previously.) Then (22) holds if $n^{-1/6}z_n \rightarrow 0$. For a proof see Feller [12, page 548].

In terms of the approximation (19), this implies that when n is large, the *relative* error in the approximation is small, provided that $|(\sqrt{n}(x - \mu)/\sigma)|$ is small compared to $n^{1/6}$. It turns out that Cramér's condition is important. Although it can be relaxed in some instances, some condition is required guaranteeing that the tails of the distribution function $F(x)$ for the X_i decay exponentially fast. Indeed, if the tails of $F(x)$ decrease only polynomially fast, then the same is true of $F_n(x)$, and (22) will be false for any sequence z_n which increases as fast as any positive power of n. This happens, for instance, whenever X_i has only finitely many moments.

3.1 Error Bounds for the Asymptotic Distribution for Bundle Strength. According to Theorem 2.1, we have asymptotic normality for the strength of a single Daniels' bundle. In light of the foregoing discussion, it is meaningful to ask whether analogues of the Berry-Esseen theorem and the Cramér-Petrov theorem on large deviations hold for the strength of a single Daniels' bundle. The answer is affirmative, and we now present the results.

Let $q(t)$, $0 \leqq t < 1$ denote the right-continuous inverse of $F(x)$, $x \geqq 0$, that is, $q(t) = \inf\{x{:}\, F(x) > t\}$. Let $\mu(t) = q(t)(1-t)$ and assume $\mu(t)$ attains its maximum at a unique point t^* as t is increased from zero to one. Evidently, $\mu(t^*) = \mu^*$ as defined by (2) and $t^* = F(x^*)$. We assume

(B1) $q(t)$ is nondecreasing on $[0, 1)$, $q(0) = 0$ and $\int_0^1 q^2(t)dt < \infty$.

(B2) There exist points $t_0 < t^* < t_1$ such that $\mu(t)$ is strictly increasing on $[t_0, t^*]$, strictly decreasing on $[t^*, t_1]$ and its supremum over all t not in $[t_0, t_1]$ is strictly less than μ^*.

(B3) $\mu(t)$ is three times, continuously differentiable on a neighborhood of t^*, and $\mu''(t^*)$ is strictly negative.

These assumptions differ slightly from those for Theorem 2.1. If $\mu''(t^*) = 0$ in (B3) but some higher derivative of $\mu(t)$ is negative at $t = t^*$, the results we give later are false, but analogous results do exist. We do not consider this case since (B3) (and the other assumptions) are almost always satisfied in practice.

Under assumptions (B1)–(B3), we have the following results:

Theorem 3.1 There exists a constant $K > 0$ such that

$$|F_n^*(\mu^* + n^{-1/2}\sigma^* z) - \Phi(z)| < Kn^{-1/6} \tag{23}$$

where all quantities are as in Theorem 2.1.

The constant K depends on the distribution function $F(x)$, $x \geqq 0$ for fiber strength, but is independent of n and z.

Theorem 3.2 Assume $\{z_n, n \geqq 1\}$ is a sequence of positive numbers such that $z_n \to \infty$, and $n^{-1/6}z_n \to 0$. Then

$$F_n^*(\mu^* - n^{-1/2}\sigma^* z_n)/\Phi(-z_n) \to 1 \tag{24}$$

as $n \to \infty$ where all quantities are as in Theorem 2.1.

The proofs of these results are given in Smith [13].

Notice that Theorem 3.1 is analogous to the Berry-Esseen theorem discussed earlier except that the rate of convergence is only $n^{-1/6}$ rather than $n^{-1/2}$. This happens to be the best rate possible, that is, (23) would be false if $n^{-1/6}$ were replaced by any function of n tending to zero faster than $n^{-1/6}$. This slow rate of convergence has been confirmed by some exact calculations using a recursive formula (See Fig. 4.1 in Harlow and Phoenix [1]), and will be seen also in an example that we discuss later. However, the proof of Theorem 3.1 suggests an improved approximation which leads to a considerable reduction in error as compared with the normal approximation of Theorem 2.1. Using this approximation, it is possible to compute $F_n^*(x)$ within acceptable error bounds for n only moderately large. Further details are given in Smith [13].

Theorem 3.2 is analogous to the Cramér-Petrov theorem discussed earlier, though we have not needed Cramér's condition. We mention that analogous theorems for the *upper* tails of $F_n(x)$ and $F_n^*(x)$ exist where for example $(1 - F_n^*(\mu^* + n^{-1/2}\sigma^* z_n))/(1 - \Phi(z_n)) \to 1$ as $n \to \infty$. In this case Crámer's condition *is* needed.

3.2 Error Bounds for the Asymptotic Distribution for Time to Bundle Failure. According to Theorem 2.2, we have asymptotic normality for the time to failure of a bundle under Coleman's assumptions. We have an analog for the Cramér-Petrov theorem, this being crucial in the chain-of-bundles setting. The theorem is as follows:

Theorem 3.3. Let $\{z_n, n \geqq 1\}$ be a sequence of positive numbers satisfying $z_n \to \infty$ and $n^{-1/6+\epsilon}z_n \to 0$ for some $\epsilon > 0$. Under the assumptions of Theorem 2.2

$$F_n^{\#}(t_b - n^{-1/2}\sigma_b z_n)/\Phi(-z_n) \to 1 \tag{25}$$

as $n \to \infty$.

For a proof see Smith [14].

As for an analog to the Berry-Esseen theorem, Spencer [18] has obtained a result, under assumptions similar to ours, which indicates that the rate of convergence in this time-dependence case is $O(n^{-1/2})$ rather than $O(n^{-1/6})$ as in Theorem 3.1 for the static case. This can only improve the accuracy of our later results.

Having now obtained the key theorems (Theorems 3.2 and 3.3), we now proceed with a discussion of extreme value theory to introduce key concepts that will be used in obtaining asymptotic results for a long chain of bundles.

4 The Poisson Limit Law and the Main Extreme Value Distribution

Suppose in the static case we have 800 bundles in a long chain, each one of which has a probability $p = 0.001$ of failing under given load L, independently of all the others. (In our earlier notation, $F_n^*(L) = p = 0.001$ and $k = 800$.) What is the probability that the chain-of-bundles will support L, that is, that there are no bundles which fail under load L? What is the probability that there are at most two bundles with strength less than L?

This kind of problem is commonly handled using the *Poisson Limit theorem* which, after the Central Limit theorem, is probably the best-known limit theorem. Now the mean number of bundles that fail under L is $kp = 0.8$, and the distribution of the *number* of such bundles N is approximately the *Poisson distribution*

$$P\{N = j\} = \frac{e^{-\lambda}\lambda^j}{j!}, \quad j = 0, 1, 2, \ldots \tag{26}$$

with mean $\lambda = kp = 0.8$. Hence, the answers to the previous two questions are approximately $e^{-0.8} = 0.4493$ and $e^{-0.8}(1 + 0.8 + (0.8)^2/2) = 0.9526$, respectively, so that rare failure for a single bundle turns into a substantial chance of failure for the chain.

Poisson Limit Theorem. If one has k independent experiments, each resulting in "failure" with probability p and success otherwise, and if $k \to \infty$ and $p \to 0$ in such a way that $pk \to \lambda$ for some fixed $0 < \lambda < \infty$, then the distribution of the number of failures converges to the Poisson distribution with mean λ.

In particular, the probability that there is at least one failure (which corresponds to the failure of our chain-of-bundles) converges to $1 - e^{-\lambda}$. The proof of this theorem can be found in any introductory textbook on probability.

The Poisson Limit theorem is used in studying the asymptotic distribution of extreme values. Suppose $X_1, X_2, X_3, \ldots$ are independent and identically distributed random variables with common distribution function $F(x)$, and let $M_k = \min\{X_1, \ldots, X_k\}$. (This is the situation of the chain model associated with (21).) We seek the limit distribution of M_k; that is, we seek constants $a_k > 0$, b_k real and a limit distribution function $H(z)$ such that

$$P\{M_k \leqq a_k z + b_k\} \to H(z) \quad \text{as} \quad k \to \infty \tag{27}$$

for each real z.

Suppose we can find constants a_k, b_k, and a function $V(z)$ such that

$$kF(a_k z + b_k) \to V(z) \quad \text{as} \quad k \to \infty. \tag{28}$$

Now if we define "failure on the ith experiment" as the event $\{X_i \leqq a_k z + b_k\}$ for $1 \leqq i \leqq k$, then the conditions of the Poisson Limit theorem hold, and the distribution of the *number* of "failures" converges to the Poisson distribution with mean $V(z)$. In particular

$$P\{M_k \leqq a_k z + b_k\} = 1 - e^{-V(z)}. \tag{29}$$

Thus, in the foregoing chain-of-bundles example, the role of λ is played by $V(z)$ (for z fixed), and p is $F_n^*(a_k z + b_k)$ which diminishes to satisfy $pk \to \lambda$ as $k \to \infty$ if $a_k > 0$ and b_k are properly selected. But the new aspect is that the *same* $a_k > 0$ and b_k must work for all z.

Here are two examples with important ramifications in the strength of materials.

1 Suppose the distribution function $F(x)$, $x \geqq 0$ satisfies $F(0) = 0$ and $F(x) \sim cx^\rho$ as $x \to 0$ from above, where $c > 0$ and $\rho > 0$. Take $b_k = 0$ and $a_k = (kc)^{-1/\rho}$. Then, for any $z > 0$, we have $kF(a_k z + b_k) \to z^\rho$ as $k \to \infty$ while for $z \leqq 0$, we automatically have $F(a_k z + b_k) \equiv 0$. Hence (28) holds with

$$V(z) = \begin{cases} z^\rho, & z > 0 \\ 0, & z \leqq 0, \end{cases} \tag{30}$$

and (27) holds with

$$H(z) = \begin{cases} 1 - e^{-z^{\rho}}, & z > 0 \\ 0, & z \leqq 0. \end{cases} \tag{31}$$

The distribution function (31) is known as *the Weibull distribution.* For example, the strength of a single fiber may be viewed as the strength of the weakest of a large number of short segments of the fiber. For this reason, the strength of single fibers is often successfully modeled using a two parameter Weibull distribution.

2 Let $F(x)$, $-\infty < x < \infty$ be the normal distribution function $\Phi(x)$, $-\infty < x < \infty$, and define

$$\alpha_k = (2 \log k)^{-1/2} \tag{32}$$

and

$$\beta_k = (\log \log k + \log (4\pi))(8 \log k)^{-1/2} - (2 \log k)^{1/2}. \tag{33}$$

Then we have the following important result.

Theorem 4.1. For each real z,

$$k\Phi(\alpha_k z + \beta_k) \to e^z \quad \text{as} \quad k \to \infty, \tag{34}$$

where α_k and β_k are given by (32) and (33), respectively. Thus $P\{M_k \leqq \alpha_k z + \beta_k\} \to H(z)$ where

$$H(z) = 1 - \exp(-\exp z), \quad -\infty < z < \infty. \tag{35}$$

The proof of this theorem is given in Galambos [19, pages 65–67], and hinges on the lower tail result

$$\Phi(x) = (-\sqrt{2\pi}x)^{-1} \exp(-x^2/2)(1 + r(x))$$

for the normal distribution function where $r(x) \to 0$ as $x \to -\infty$. This example is very important for the later developments. Many other aspects of extreme value theory, including Gnedenko's characterization of all possible extreme value distributions, are discussed in the recent book by Galambos [19].

5 Main Asymptotic Distributions for the Chain-of-Bundles

On the one hand, we have asymptotic normal distributions for the strength and failure time of large, single bundles as stated in Theorems 2.1 and 2.2, respectively. On the other hand, we have the extreme value distribution associated with the smallest of a large sample of independent and identically distributed normal random variables, as stated in Theorem 4.1. Since the failure of the chain-of-bundles occurs with the failure of the weakest bundle, we would have the desired asymptotic distribution in Theorem 4.1 if the *true* distributions for bundle failure could be replaced by the *asymptotic* normal distributions, respectively.

Intuitively, a simple replacement should work provided k, the chain length, does not increase too quickly as a function of n, the bundle size. But for our results to be useful in applications, we must have k increase *rapidly* with respect to n. It turns out that the large deviations theory associated with the Cramér-Petrov theorem of Section 3 is crucial to the resolution of this problem.

For definiteness, fix a sequence $k(1), k(2), \ldots, k(n), \ldots$ of positive integers tending to infinity. We denote this sequence by $\{k(n)\}$, and seek the limiting distribution of the strength and time to failure of the chain of bundles as $n \to \infty$.

5.1 Asymptotic Results for Static Strength. Let L^*_{n1}, $L^*_{n2}, \ldots, L^*_{nk}$ be the strengths of k independent bundles as described in Section 2.1. We seek the limit distribution of $M^*_{nk(n)}$ as $n \to \infty$ where $M^*_{nk} = \min\{L^*_{n1}, L^*_{n2}, \ldots, L^*_{nk}\}$. Thus n and k tend to infinity simultaneously following the sequence $\{k(n)\}$. In the light of the discussion of Section 4, it suffices to find constants $a^*_n > 0$, b^*_n real and a function $V(z)$ such that

$$k(n)F^*_n(a^*_n z + b^*_n) \to V(z) \tag{36}$$

where $F^*_n(x)$, $x \geqq 0$ is recalled to be the distribution function for the strength of a *single* bundle.

Combining the approximation

$$F^*_n(x) \doteq \Phi(\sqrt{n}(x - \mu^*)/\sigma^*), \quad x \geqq 0 \tag{37}$$

(see (4)) with (34) suggests the following: Define $a^*_n = \alpha_{k(n)}\sigma^* n^{-1/2}$ and $b^*_n = \mu^* + \beta_{k(n)}\sigma^* n^{-1/2}$ where $\alpha_{k(n)}$ and $\beta_{k(n)}$ are as in (32) and (33), respectively. Then we conjecture that (36) holds with $V(z) = e^z$, $-\infty < z < \infty$. Upon comparing (36) with (34), we see that the necessary and sufficient condition for our conjecture to be verified is that as $n \to \infty$,

$$F^*_n(a^*_n z + b^*_n)/\Phi(\alpha_{k(n)}z + \beta_{k(n)}) \to 1. \tag{38}$$

But (38) is just (24) of Theorem 3.2 with $z_n = -(\alpha_{k(n)}z + \beta_{k(n)})$.

Since z_n is the same order of magnitude as $(\log k(n))^{1/2}$, and Theorem 3.2 assumed $n^{-1/6}z_n \to 0$, it is sufficient that $n^{-1/3} \log k(n) \to 0$. Putting all the pieces together, we have the following result:

Theorem 5.1. Assume conditions (B1)–(B3) hold and that $n^{-1/3} \log k(n) \to 0$ as $n \to \infty$. Let

$$a^*_n = \sigma^*(2n \log k(n))^{-1/2} \tag{39}$$

and

$$b^*_n = \mu^* + n^{-1/2}\sigma^*[(\log \log k(n) + \log (4\pi))(8 \log k(n))^{-1/2} - (2 \log k(n))^{1/2}], \tag{40}$$

where μ^* and σ^* are defined by (2) and (3), respectively. Then, for all real z, the distribution function for the strength of the chain-of-bundles, satisfies

$$P\{M^*_{nk(n)} \leqq a^*_n z + b^*_n\} \to 1 - \exp(-\exp(z)) \tag{41}$$

as $n \to \infty$.

Theorem 5.1 gives the limiting distribution for the strength of our series-parallel model of the fibrous material under a broad range of sequences $\{k(n)\}$. In particular, *k may be increased as any power of n,* and thus, will hold for long thin structures. Note that under the assumptions of Theorem 5.1, the strength of the fibrous material converges stochastically to the asymptotic mean strength μ^* of a single bundle as bundle size n increases. (Crudely speaking, the material strength approaches a constant as the variability in strength shrinks to zero.) On the other hand, if $k(n) \to \infty$ too rapidly, we would expect that the strength of the fibrous material would converge stochastically to zero. This has been shown by Harlow, Smith, and Taylor [20] who compute the limiting distributions as $k \to \infty$ for n fixed. The two results together represent extreme cases.

5.2 Asymptotic Results for Time to Failure. Let T_{n1}, $T_{n2}, \ldots, T_{nk}$ be the failure times of k independent bundles as described in Section 2.2. We seek the limit distribution of $M^{\#}_{nk(n)}$ as $n \to \infty$ where $M^{\#}_{nk} = \min\{T_{n1}, T_{n2}, \ldots, T_{nk}\}$. Thus n and k tend to infinity together simultaneously following the sequence $\{k(n)\}$.

The analysis here is analogous to that in the previous section for static failure, with $F^{\#}_n(t)$ in place of $F^*_n(x)$, t_b, and σ_b in place of μ^* and σ^*, respectively, and Theorem 3.3 in place of Theorem 3.2. The only difference is $n^{-1/6+\epsilon}z_n \to 0$ for some $\epsilon > 0$ is assumed in Theorem 3.3 so that $n^{-1/3+2\epsilon} \log k(n) \to 0$ is sufficient. We thus have the following result:

Theorem 5.2. Assume conditions (A1)–(A3) hold, and that $n^{-1/3+2\epsilon} \log k(n) \to 0$ as $n \to \infty$ for some $\epsilon > 0$. Let

$$a^{\#}_n = \sigma_b(2n \log k(n))^{-1/2}, \tag{42}$$

and

$$b^{\#}_n = t_b + n^{-1/2}\sigma_b[(\log \log k(n) + \log (4\pi))(8 \log k(n))^{-1/2} - (2 \log k(n))^{1/2}], \tag{43}$$

where t_b and σ_b are as defined in Theorem 2.2. Then for all real z, the distribution function for the time to failure of a chain-of-bundles under load history $L(t)$, $t \geqq 0$ satisfies

$$P\{M^{\#}_{nk(n)} \leqq a^{\#}_n z + b^{\#}_n\} \to 1 - \exp(-\exp(z)), \tag{44}$$

as $n \to \infty$.

Theorem 5.2 gives the limiting distribution for the failure time of the fibrous material under a variety of load histories $L(t)$, $t \geqq 0$ and a broad range of sequences $\{k(n)\}$. In particular k may be increased as *any* power of n. Here, the failure time of the fibrous material converges stochastically to the asymptotic mean t_b of a single bundle as $n \to \infty$. But if $k(n) \to \infty$ too rapidly, we would expect the time to failure to converge stochastically to zero. This has been shown by Harlow, Smith, and Taylor [20] under the simplest model of Coleman (5). They compute limiting distributions as $k \to \infty$ for n fixed. Corresponding results under the more general model (12) are not yet available. The two results together would represent extreme cases.

Recently, Borges [21] has studied the time to failure model in great detail under the simpler assumptions (5) for single fibers. By making corrections for the deviation from normality, his results extend those given here. In particular, he assumes $n^{-1} \log k(n)$ so that the chain length k is permitted to grow even faster relative to bundle size n than in our case. Unfortunately, Borges results are quite difficult to use, and thus, we will not present them here.

6 Comments on Applications

In the static case, the distribution function for the strength of the fibrous material may be approximated as

$$P\{M^*_{nk} \leqq x\} \doteq 1 - \exp\{-\exp[(x - b^*_n)/a^*_n]\}, \quad x \geqq 0, \qquad (45)$$

where a^*_n and b^*_n are given by (39) and (40), respectively, and $k(n)$ is just k, the number of bundles in the chain. (This amounts to a restatement of Theorem 5.1.)

In earlier work, Coleman [22] argued that the strength of single fibers is naturally modeled by the Weibull distribution

$$F(x) = 1 - \exp\{-\delta(x/x_0)^\gamma\}, \quad x \geqq 0 \qquad (46)$$

where δ is the fiber length, and the positive constants x_0 and γ are the *scale* (under $\delta = 1$) and *shape* parameters, respectively. He also obtained μ^* and σ^* of Theorem 1.1, and showed how the asymptotic mean strength μ^* for a single bundle diminishes as the variability in fiber strength increases ($\gamma \to 0$). At the same time, μ^* diminishes in proportion to $\delta^{-1/\gamma}$ as the fiber element length δ increases. We have shown here that for large k and large n, the strength of the fibrous material is approximately μ^*. But the question arises: "How close is the asymptotic distribution (45) to the true distribution function for M^*_{nk}, the strength of the fibrous material?"

An Example. To answer the aforementioned question, we consider a long fibrous cable under Coleman's framework, and let $H^*_{k,n}(x)$ be the distribution function for the cable strength. We let $x_\delta = x_0\delta^{-1/\gamma}$ so that x_δ is the true scale parameter of the Weibull distribution (46) for the fiber strength. The mean fiber strength is $x_\delta\Gamma(1 + 1/\gamma)$ which is numerically very close to x_δ for typical γ. In our example, we let the chain length $k = 10{,}000$, take $n = 10$ and 50, and assume $\gamma = 10$. Thus the cable is very long and slender, and has fibers with a coefficient of variation of strength of about 12 percent.

Now if the number of fibers n were very large, the strength of the cable would be $\mu^* = x_\delta\gamma^{-1/\gamma}\exp\{-1/\gamma\} = 0.719\, x_\delta$, or about 72 percent of the strength of the fiber elements. But for these fairly small values of n of 10 and 50, the exact cable distribution function $H^*_{k,n}(x)$ and its asymptotic approximation (45) appear as in Fig. 2 where the scaling is such that (45) plots as a straight line. The graphs of the exact distribution were obtained using a recursive formula for $F^*_n(x)$ as originally developed by Daniels [5]. (See Harlow and Phoenix [1] for further discussion. Numerical instabilities make it almost impossible to obtain results for n significantly larger than 50, thus underscoring the value of asymptotic results.) Notice that for $n = 50$ the true median strength of the cable is $0.635x_\delta$ which is considerably less than μ^*. The asymptotic formula (45) predicts the slightly lower value 0.593 x_δ. Notice also the greatly reduced variability in cable strength for larger n.

Fig. 2 indicates that $n = 50$ is still quite small for application of the asymptotic distribution (45); fortunately, the predictions are conservative. It turns out that the rather slow rate of convergence in increasing n is tied to that of (23) in Theorem 3.1 where the error decays as $n^{-1/6}$. Smith [13] has developed an improved approximation which uses new constants $\hat{b}_n$ in place of b^*_n. These perform much better for moderate n, though they are much more difficult to calculate.

We remark that changes in k by two orders of magnitude have little effect on the character of the results in Fig. 2, as our analysis would suggest. However, decreasing γ does reduce the relative accuracy somewhat for these values of n. Gücer and Gurland [15] have graphed various estimates of the median strength in this setting as k, n, and γ change, and we urge the reader to consult their work for further insight in applications.

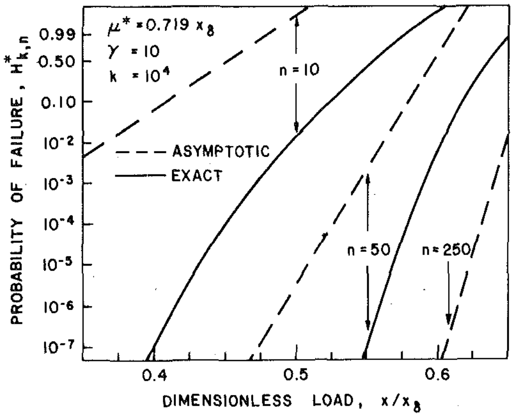

Fig. 2 Comparison of exact and asymptotic distributions for the strength of a long fibrous cable; a Weibull distribution is assumed for fiber strength

In the time-dependent case, the distribution function for the time to failure of the fibrous material, under a given load history $L(t)$, $t \geqq 0$, may be approximated as

$$P\{M^\#_{nk} \leqq t\} \doteq 1 - \exp\{-\exp[(t - b^\#_n)/a^\#_n]\}, \quad t \geqq 0 \qquad (47)$$

where $a^\#_n$ and $b^\#_n$ are given by (42) and (43), respectively. (This amounts to a restatement of Theorem 5.2.) We would expect (47) to perform better in the time-dependent case than (45) did in the static case, as revealed in Fig. 2.

For applications, we refer the reader to Phoenix [10, 17] for useful formulas for computing t_b and σ_b of Theorem 2.2. Otherwise, the general behavior is analogous to that for the static case above, and Gücer and Gurland's graphs [15] may be used with "time" in place of "strength."

References

1 Harlow, D. G., and Phoenix, S. L., "The Chain-of-Bundles Probability Model for the Strength of Fibrous Materials I: Analysis and Conjectures," *Journal of Composite Materials*, Vol. 12, 1978, pp. 195–214.

2 Harlow, D. G., and Phoenix, S. L., "The Chain-of-Bundles Probability Model for the Strength of Fibrous Materials II: A Numerical Study of Convergence," *Journal of Composite Materials*, Vol. 12, 1978, pp. 314–334.

3 Harlow, D. G., and Phoenix, S. L., "Probability Distributions for the Strength of Composite Materials I: Two-Level Bounds" *International Journal of Fracture*, to appear.

4 Harlow, D. G., and Phoenix, S. L., "Probability Distributions for the Strength of Composite Materials II: A Convergent Sequence of Tight Bounds," *International Journal of Fracture*, to appear.

5 Daniels, H. E., "The Statistical Theory of Strength of Bundles of Threads," *Proceedings of the Royal Society*, London, Series A, Vol. 183, 1945, pp. 405–435.

6 Coleman, B. D., "Time-Dependence of Mechanical Breakdown Phenomena," *Journal of Applied Physics*, Vol. 27, 1956, pp. 862–866.

7 Coleman, B. D., "A Stochastic Process Model for Mechanical Breakdown," *Transactions of the Society of Rheology*, Vol. 1, 1957, pp. 153–168.

8 Coleman, B. D., "Time-Dependence of Mechanical Breakdown in Bundles of Fibers III: The Power Law Breakdown Rule," *Transactions of the Society of Rheology*, Vol. 2, 1958, pp. 195–218.

9 Coleman, B. D., "Statistics and Time-Dependence of Mechanical Breakdown in Fibers, *Journal of Applied Physics*, Vol. 29, 1958, pp. 968–983.

10 Phoenix, S. L., "The Asymptotic Time to Failure of a Mechanical System of Parallel Members," *SIAM Journal on Applied Mathematics*, Vol. 34, 1978, pp. 227–246.

11 Phoenix, S. L., "The Asymptotic Distribution for the Time to Failure of a Fiber Bundle," *Advances in Applied Probability*, Vol. 11, 1979, pp. 153–187.

12 Feller, W., *An Introduction to Probability Theory and Its Applications*, Vol. 2, Wiley, New York, 1971.

13 Smith, R. L, "The Asymptotic Distribution of the Strength of a Series-

Parallel System With Equal Load-Sharing," *Annals of Probability,* to appear.

14 Smith, R. L. "Limit Theorems for the Reliability of Series-Parallel Load-Sharing Systems," PhD thesis, May 1979, Cornell University, Ithaca, N.Y.

15 Gücer, D. E., and Gurland, J., "Comparison of the Statistics of Two Fracture Modes," *Journal of the Mechanics and Physics of Solids,* Vol. 10, 1962, pp. 365–373.

16 Chung, K., *A Course in Probability Theory,* Academic Press, New York, 1974.

17 Phoenix, S. L., "Stochastic Strength and Fatigue of Fiber Bundles," *International Journal of Fracture,* Vol. 14, 1978, pp. 327–344.

18 Spencer, F. W., "An Application of Weak Convergence Theory of the Study of the Stochastic Failures in Parallel Mechanical Systems," PhD thesis, Aug. 1978, Cornell University, Ithaca, N.Y.

19 Galambos, J., *The Asymptotic Theory of Extreme Order Statistics,* Wiley, New York, 1978.

20 Harlow, D. G., Smith, R. L., and Taylor, H. M., "The Asymptotic Distribution of Certain Long Composite Cables," Technical Report No. 384, 1978, School of Operations Research and Industrial Engineering, Cornell University, Ithaca, N.Y.

21 Borges, W. S., "Extreme Value Theory in Triangular Arrays With an Application to the Reliability of Fibrous Materials," PhD thesis, May 1978, Cornell University, Ithaca, N.Y.

22 Coleman, B. D., "On the Strength of Classical Fibres and Fibre Bundles, *Journal of the Mechanics and Physics of Solids* Vol. 7, 1958, pp. 60–70.

R. B. King
Research Assistant.

G. Herrmann
Professor and Chairman.
Fellow ASME

Division of Applied Mechanics,
Department of Mechanical Engineering,
Stanford University,
Stanford, Calif. 94305

Nondestructive Evaluation of the J and M Integrals

The usefulness of two conservation integrals, the so-called J and M integrals, in fracture mechanics is reviewed. A method for experimental evaluation of these quantities by direct determination of the values of their integrands at various points along a contour is presented, and contrasted with "compliance" methods which have been used to evaluate J. This technique has been applied to three different specimen configurations, and the experimental results compare favorably with theoretical predictions.

Introduction

The usefulness of the J integral in fracture mechanics is well known. Recently it has been pointed out by Freund [1] that another conservation integral, the M integral, is also of practical importance. This paper deals with the experimental evaluation of the J and M integrals by direct measurement of the terms in their integrands.

The definition and physical significance of the J and M integrals have been discussed elsewhere [1, 2] and will be summarized here. For a plane problem of an elastic solid containing a crack, the J integral is defined as

$$J = \int_c (Wn_1 - t_k u_{k,1})ds \tag{1}$$

where

c = a contour surrounding the crack tip
W = the strain-energy density
u_k = the displacement vector
t_k = the traction vector defined by the outward normal to c
$t_k = \sigma_{jk} n_j$

J is applicable to nonlinear elastic solids and to elastoplastic solids which can be treated as nonlinear elastic (deformation theory of plasticity) [2]. Another conservation integral, the M integral, is defined as

$$M = \oint_c (Wx_i n_i - t_k u_{k,i} x_i)ds \tag{2}$$

where c is now a closed curve.

While it has been previously stated that M is restricted in applicability to linear elastic solids [2], a more recent rederivation of M indicates it remains valid in nonlinear solids [3]. J and M are interpreted physically as energy release rates: if c encloses the tip of a crack oriented along the x_1-axis, then J represents the energy release rate with respect to translation of the tip of the crack in the x_1-direction; if c completely encloses a crack or other flaw in a solid, then M represents the energy release rate associated with self-similar expansion of the flaw [2].

The J integral is useful in fracture mechanics because it can be shown to be equal to the crack extension force G_{I}, and hence obeys Irwin's relationship (stated here for plane stress and Mode I deformation)

$$J = G_{\mathrm{I}} = \frac{1}{E}(K_{\mathrm{I}}^2) \tag{3}$$

Even in cases of general yielding, so long as no unloading occurs, comparison of the value of J determined in a body of a certain material versus the critical value of J (J_{Ic}) for that material, is a useful fracture criterion [4]. The usefulness of the M integral in crack problems stems from the fact that M can be shown to be proportional to J by using path-independence arguments [1]. For instance, consider an interior crack in a body with origin of coordinates centered on the crack (Fig. 1). Since M is path-independent, its value around any path c_2 will be the same as that around c_1. The straight segments of c_1 along the crack faces contribute nothing to M because they are radial segments ($x_i n_i = 0$) which are traction free. The remainder of c_1 is composed of vanishingly small arcs around the tips of the crack. For the small arc c_r around the right tip, the contribution to M is

$$\int_{c_r} (Wan_1 - t_k u_{k,1} a)\, ds = aJ$$

The arc around the left tip made the same contribution, hence the total value of M is

$$M = 2aJ$$

Thus knowledge of M permits evaluation of J. The M integral can be evaluated in cases where J is inconvenient or inapplicable (i.e., if there is loading on the crack faces).

Contributed by the Applied Mechanics Division of THE AMERICAN SOCIETY OF MECHANICAL ENGINEERS, for presentation at the 1981 Joint ASME/ASCE Applied Mechanics, Fluids Engineering, and Bioengineering Conference, University of Colorado, Boulder, Colo., June 22–27, 1981.

Discussion on this paper should be addressed to the Editorial Department, ASME, United Engineering Center, 345 East 47th Street, New York, N.Y. 10017, and will be accepted until June 1, 1981. Readers who need more time to prepare a Discussion should request an extension from the Editorial Department. Manuscript received by ASME Applied Mechanics Division, April, 1980; final revision, July, 1980. Paper No. 81- APM-2.

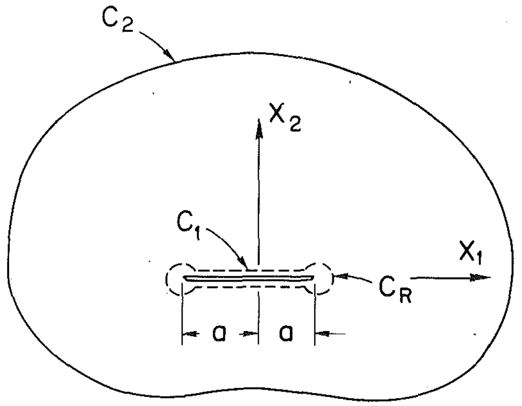

Fig. 1 *M* **integral contours for an interior crack**

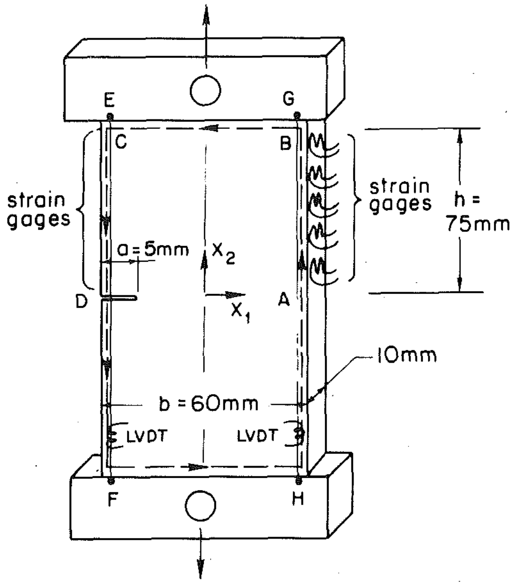

Fig. 2 **Schematic of edge cracked panel used for** *J* **integral experiment**

Techniques for Experimentally Evaluating *J* and *M*

The customary technique for measuring the J integral is the well-known Begley and Landes compliance method which takes advantage of the physical interpretation of J as an energy release rate [4]. Denoting the total mechanical energy of a specimen under load containing a crack by E, if E is measured twice for the same load, once for a specimen with crack length a, and again for an identical specimen but with crack length $a + \Delta a$, then J is given by

$$J = \frac{-\Delta E}{\Delta a}$$

which can be shown to be given by the area between the load versus displacement curves for the two crack lengths. Alternatively, if E is measured for several different crack lengths, J is given by the negative of the slope of a plot of E versus a. Recently it has been shown [5] that for certain specimen configurations the J integral can be determined from a load displacement curve for a single crack length. In contrast with the technique described in the foregoing this method could be called "nondestructive" because it requires only a single specimen of fixed crack length.

An alternative nondestructive technique is presented here for evaluating both the J and M integrals. The method makes direct use of the definition of J (or M) as a contour integral and involves experimental evaluation of the integrand at various points along a contour and then determination of the integral by numerical integration. In general, determination of the integrand of J or M involves knowledge of all the components in the $x_1 - x_2$ plane of the stress and rotation tensors (or, equivalently, of the displacement gradient tensor). Determination of all these quantities experimentally would be difficult. However, as will be shown below, in special cases with proper choice of the contour c, the integrands of J and M simplify considerably, so that they can be experimentally evaluated using strain gages and displacement transducers. The authors have successfully applied this technique on three specimen geometries.

While the experimental results to be discussed have been restricted to Linear Elastic Fracture Mechanics, the method used should be applicable for evaluating J or M in nonlinear elastic and elastoplastic cases (subject to the restrictions on validity of J and M in such situations). If any yielding takes place along the contour c, the strain gages employed must be capable of tracing the plastic deformation.

Examples

The first configuration considered was an edge-cracked panel, a schematic of which is shown in Fig. 2. The value of the J integral for such a specimen when subjected to remote uniaxial tension was determined experimentally. The contour chosen for evaluation of the J integral followed the vertical edges of the specimen and then proceeded horizontally adjacent to the shoulders. Because of symmetry, the value of the J integral for the entire contour is equal to twice the value of J along path $ABCD$. Along the traction-free vertical edges, the second term in the integrand vanishes and the only nonzero component of stress is σ_{22}. Hence the strain-energy density W is given by

$$W = \tfrac{1}{2} E \epsilon_{22}{}^2 \quad \text{(in plane stress}^1\text{)} \tag{6}$$

and denoting by J_v the contribution to J of the vertical edges,

$$J_v = \int_0^h \frac{E}{2} \epsilon_{22/x_1=b}{}^2 \, dx_2 - \int_h^0 \frac{E}{2} \epsilon_{22/x_1=-b}{}^2 \, dx_2 \tag{7}$$

Assuming the value of σ_{yy} along the horizontal paths is constant and equal to the far-field stress σ, and denoting by J_h the contribution of one of the horizontal portions of the contour, leads to

$$J_h = - \int_b^{-b} (\sigma_{12}\epsilon_{11} + \sigma u_{2,1}) \, dx_1 \tag{8}$$

Assuming the shear stress near the shoulder to be sufficiently small, such that the first term may be neglected, we can write

$$J_h = -\sigma \int_b^{-b} u_{2,1} dx_1 = \sigma u_2 \big|{}_{-b}^{b} \tag{9}$$

The J integral is given by $J = 2(J_h + J_v)$.

The specimen used in this experiment was made of Aluminum 6061-T6, and the dimensions are shown in Fig. 2. Five strain gages were placed along each of the vertical edges AB and DC, and the displacement between points E and F and G and H was measured using two linear variable differential transformers (LVDT's). The specimen was placed in a hydraulic testing machine using pin grips, and a tensile load of 42000 N was applied. The measured value of J was 1.54 N/mm (J_H contributed 90 percent of this). Using the handbook value of the stress-intensity factor for this configuration [6], and relation (3) leads to the theoretical value $J = 1.49$ N/mm. The experimentally determined value of J agrees with this within 3 percent.

A second experiment involved evaluation of the M integral for a specimen containing an edge crack into which a wedge was forced. A schematic of the specimen is shown in Fig. 3. For the case of an edge crack in an infinite body, the M integral was evaluated for such a

---

[1] A plane state of stress will be assumed here in evaluating the integrand of J or M because thin specimens are used. It is known, of course, that, in the immediate vicinity of the crack tip, the state of stress is triaxial and if anything is closer to plane strain. This leads to a paradox in applying the Irwin relation, which is discussed in reference [6].

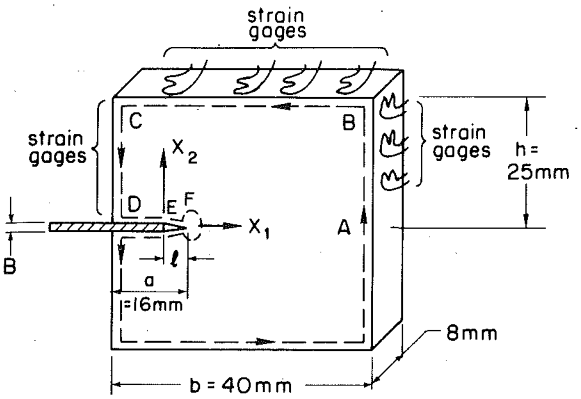

Fig. 3 Schematic of specimen with wedged open crack used for *M* integral experiment

loading arrangement by Freund [1], and his reasoning is followed here. For the entire closed contour shown in Fig. 3, the conservation law $M = 0$ applies. The portions of the contour along the crack face make no contribution to M: for small crack opening these are very nearly radial segments, and path EF is traction-free, while on path DE the tangential component of traction is zero and the normal component of displacement is zero. The factor x_i in the integrand makes it nonsingular at the end of the wedge (point E), hence there is no contribution from a vanishingly small arc at the origin. A small arc at F contributes $-lJ$. Denoting the contribution of the portion of the edges of the specimen by M_0, applying the conservation law $M = 0$ gives

$$M_0 - lJ = 0 \tag{10}$$

Experimental determination of M_0 will thus permit evaluation of the J integral. Since the edges are traction-free M_0 is given by

$$M_0 = \int_0^h \frac{E}{2} \epsilon_{22}{}^2 (b - a + l)\, dx_2 + \int_{l-a}^{b-a+l} \frac{E}{2} \epsilon_{11}{}^2 h dx_1 + \int_0^h \frac{E}{2} \epsilon_{22}{}^2 (a - l)\, dx_2 \tag{11}$$

For the case of an infinite body containing a semi-infinite crack which is forced open a distance B, Freund has determined the theoretical value of M_0 to be (in plane stress) [1]

$$M_0 = \frac{EB^2}{8\pi} \tag{12}$$

M_0 for a finite body is approximated by adding a correction which is derived in Appendix 1.

For the actual experiment a specimen of Aluminum 6061-T6 was used, Fig. 3. The specimen differed from the theoretical model used in that the crack was machined so that it was initially slightly open (to permit installation of the wedge) and was forced open further by the wedge. A steel wedge was used which was rammed in place using a hydraulic hand press. The difference, B, between the crack opening distances before and after insertion of the wedge was measured using a traveling microscope. A total of 10 strain gages were mounted along the edges $ABCD$.

The value of M determined from the strain gage readings was 195.8 Newtons. Applying the measured value of $B (B = 0.00535$ in.) to the theoretical solution for the infinite case and the finiteness correction, led to a theoretical value for M of 223.6 N, with which the experimental value is in agreement within approximately 12 percent. The discrepancy is probably due to deviation of the specimen geometry from the theoretical model used, and the approximate nature of the finiteness correction.

In the third specimen configuration considered, the M integral was evaluated for a center-cracked panel under uniaxial tension, a diagram of which is shown in Fig. 4. The contour chosen follows vertically along the edges of the specimen and horizontally a slight distance away from the shoulders. By symmetry it is only necessary to evaluate one quadrant. Thus

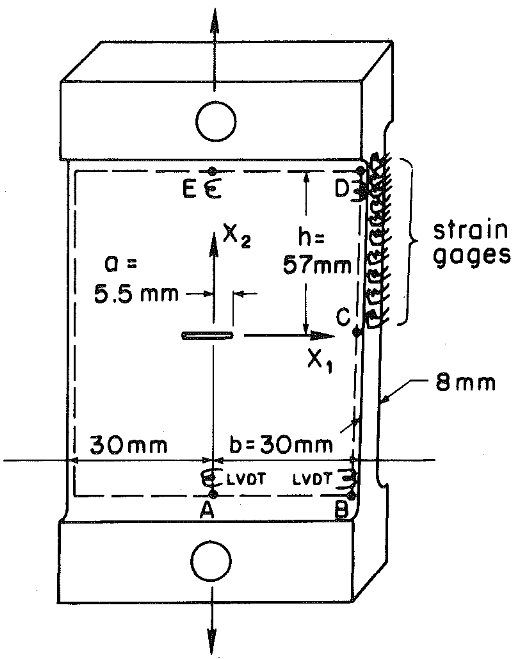

Fig. 4 Schematic of center cracked panel used for *M* integral experiment

$$M = 4(M_{AB} + M_{BC}) \tag{13}$$

where M_{AB} and M_{BC} are the contributions to M of paths AB and BC, respectively. On the traction-free vertical edge BC, $W = (E/2)\epsilon_{22}{}^2$ and $x_i n_i = b$, so

$$M_{BC} = \frac{bE}{2} \int_0^h \epsilon_{22}{}^2\, dx_2 \tag{14}$$

The contribution to M along the horizontal path AB is given by

$$M_{AB} = \int_0^b \left\{ \frac{1}{2} (\sigma_{11}{}^2 - \sigma_{22}{}^2 + 2(1 + \nu)\, \sigma_{12}{}^2)\, h + \frac{x_1}{E} (\sigma_{12}\sigma_{11} - \nu\sigma_{12}\sigma_{22}) - \sigma_{12}u_{1,2}h + x_1\sigma_{22}u_{1,2} \right\} dx_1 \tag{15}$$

Since path AB is near the shoulder, σ_{yy} may be assumed constant, but it is not obvious whether any further simplifying assumptions are justified. Consequently the importance of the various terms in M_{AB} was investigated by making use of the solution for an infinite cracked panel under remote uniaxial tension. The M integral was evaluated for a large rectangular path in the infinite plate, chosen to simulate the contour used in our finite specimen. This investigation is presented in Appendix 2, where it is shown that the contributions of terms containing σ_{11} and σ_{12} are negligible, and if a quadratic variation with x is assumed for u_2, the result for M_{AB} is

$$M_{AB} = \frac{-hb\sigma^2}{E} + \frac{4\sigma b}{3} [u_2(b, h) - u_2(0, h)] \tag{16}$$

A specimen of Aluminum 6061-T6, the dimensions of which are shown in Fig. 4, was used for the experiment. Ten strain gages were mounted on the vertical edge BC and displacement transducers (LVDT's) were placed between points B, D and A, E as shown in Fig. 4. The specimen was placed in a hydraulic testing machine and loaded in tension to 30000 N. The experimental value of the M integral was found to be 11.52 N. The theoretical value for M was found, using

$$M = 2aJ = 2a \frac{K_I{}^2}{E},$$

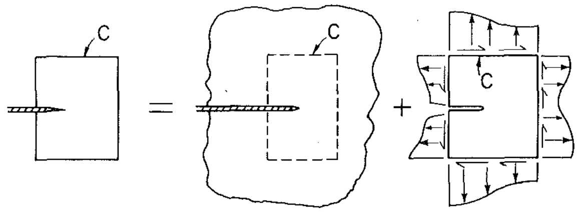

Fig. 5 Theoretical correction for finiteness of specimen with wedged open crack

to be 11.23 N. The measured value agrees with the theoretical value within 3 percent.

Conclusions

It has been shown that for certain special specimen geometries, by convenient choice of contours, the J and M integrals simplify sufficiently to permit experimental evaluation of the terms in their integrands, although it has been seen that care must be exercised in making simplifying assumptions regarding the terms in the integrand (as was especially true for the center-cracked panel). Experimental values of J and M thus determined agree well with corresponding theoretical values, so this appears to be a viable technique for nondestructive experimental evaluation of the J and M integrals.

Acknowledgment

This research was supported in part by AFOSR F49620-79-C-0217 and Electric Power Research Grant RP-609-1 to Stanford University. The authors are most grateful to Professors D. M. Barnett of Stanford University and Stephen Burns of the University of Rochester, N.Y., for many valuable discussions with regard to the contents of this paper.

References

1 Freund, L. B., "Stress-Intensity Factor Calculations Based on a Conservational Integral," *International Journal of Solids and Structures,* Vol. 14, 1978, pp. 241–250.

2 Budiansky, B., and Rice, J. R., "Conservation Laws and Energy Release Rates," ASME JOURNAL OF APPLIED MECHANICS, Vol. 40, 1973, pp. 201–203.

3 Herrmann, A. G., "Material Momentum Tensor and Path-Independent Integrals of Fracture Mechanics," to be published.

4 Begley, J. A., and Landes, J. D., "The *J* Integral as a Fracture Criterion," *Fracture Toughness, Proceedings of the 1971 National Symposium on Fracture Mechanics,* Part II, ASTM STP-514, 1972, pp. 1–20.

5 Rice, J. R., Paris, P. C., and Merkle, J. G., "Some Further Results of *J*-Integral Analysis and Estimates," *Progress in Flaw Growth and Fracture Toughness Testing, Proceedings of the 1972 National Symposium on Fracture Mechanics,* ASTM STP-536, 1973, pp. 231–245.

6 Tada, H., *The Stress Analysis of Cracks Handbook,* Del Research Corp., 1973.

7 Cottrell, A. H., *Dislocations and Plastic Flow in Crystals,* Oxford, Clarendon Press, 1953.

8 Eftis, J., Subramonian, N., and Liebowitz, H., "Crack Border Stress and Displacement Equations Revisited," *Engineering Fracture Mechanics,* Vol. 9, 1977, pp. 189–210.

APPENDIX 1

Approximation for the *M* Integral for a Panel Containing an Edge Crack Into Which a Wedge Is Forced

The state of stress in a finite body containing an edge crack may be obtained by adding to the stresses in the infinite body those due to a solution which removes the tractions along the rectangular contour c (Fig. 5). If the distance l is sufficiently small, these tractions should be approximately the same as those caused in the infinite body by an edge dislocation of Burger's vector $B\mathbf{e}_2$ where $\mathbf{e}_2$ is a unit vector parallel to the x_2 coordinate axis. The elasticity solution for such an edge dislocation is given in terms of the Airy's stress function ϕ as

$$\phi = \frac{-EB}{4\pi} x_1 \ln r \text{ [7]} \tag{17}$$

where r is the radius measured from the end of the dislocation. It is desired to determine the effect of the tractions on c corresponding to ϕ on $k_{\rm I}$ and $k_{\rm II}$. The normal component of traction can be expressed as the superposition of a symmetric part (tensile load), an antisymmetric part (bending), and a self-equilibrating part. The effect of the latter will decay with distance from the edge according to Saint-Venant's principle and hence should have little effect on $k_{\rm I}$. The former two are found by determining the force and moment to which the tractions are statically equivalent. The effect of the shear component of traction on $k_{\rm II}$ is estimated by determining a statically equivalent constant shear loading. Only the horizontal edges need be considered: the normal component of traction on the vertical edges is by symmetry statically equivalent to pure tensile loading, which does not contribute to $k_{\rm I}$ because it is parallel to the crack. For any two-dimensional curve c, statically equivalent forces and moments can be expressed as follows:

$$F_1 = \int_c T_1 ds = \frac{\partial \phi}{\partial_{x_2}}\bigg|_S^F \tag{18}$$

$$F_2 = \int_c T_2 ds = -\frac{\partial \phi}{\partial_{x_1}}\bigg|_S^F \tag{19}$$

$$M_3 = \int_c \mathbf{r} \times \mathbf{T} ds = \left[\phi - x_1 \frac{\partial \phi}{\partial_{x_1}} - x_2 \frac{\partial \phi}{\partial_{x_2}}\right]\bigg|_S^F \tag{20}$$

where S and F denote the initial and terminal points of the curve c. Making use of (17)–(20), the result for the case at hand is

$$\text{Tensile load} = F_2 = \frac{EB}{4\pi}\left[\ln\left(\frac{\sqrt{a^2+h^2}}{\sqrt{(b-a)^2+h^2}}\right) + \frac{a^2}{a^2+h^2} - \frac{(b-a)^2}{(b-a)^2+h^2}\right] \tag{21}$$

$$\text{Shear load} = F_1 = \frac{-EB}{4\pi}\left[\frac{ah}{\sqrt{a^2+h^2}} + \frac{(b-a)h}{\sqrt{(b-a)^2+h^2}}\right] \tag{22}$$

$$\text{Moment} = M_3 = \frac{EB}{4\pi}(c+d) \tag{23}$$

Knowing these, $k_{\rm I}$ and $k_{\rm II}$ can be determined from a handbook [6], and the correction to M_0 is given by

$$\Delta M_0 = lJ = l\left(\frac{1}{E}\right)(k_{\rm I}{}^2 + k_{\rm II}{}^2) \tag{24}$$

APPENDIX 2

Evaluation of the *M* Integral for a Large Rectangular Path in an Infinite Body Containing a Crack

The solution for an infinite plate containing a crack under remote uniaxial tension will be employed in the form presented by Eftis, et al. [8]. For symmetric loadings the stresses and displacements are given by

$$\sigma_{xx} = 2 \operatorname{Re} \phi'(z) - 2y \operatorname{Im} \phi''(z) + B$$

$$\sigma_{yy} = 2 \operatorname{Re} \phi'(z) + 2y \operatorname{Im} \phi''(z) - B$$

$$\sigma_{xy} = -2 \operatorname{Re} \phi''(z)$$

$$u_x = \frac{1}{2\mu}\{(k-1) \operatorname{Re} \phi(z) - sy \operatorname{Im} \phi'(z) + Bx\}$$

$$u_y = \frac{1}{2\mu}\{(k+1) \operatorname{Im} \phi(z) - zy \operatorname{Re} \phi'(z) - By\}$$

where $\phi(z)$ is a standard Kolosoff-Mushkelishvili potential function, B is a real constant, and $k = (3-\nu)/(1-\nu)$ in plane stress and $3-4\nu$ in plane strain. The solution to uniaxial tension of an infinite cracked panel is given by

$$\phi(z) = \frac{\sigma}{2}\sqrt{z^2-a^2} - \frac{\sigma}{4}z, \quad B = \frac{-\sigma}{z}$$

In order to apply this solution to determine M for a large rectangular contour, the solution is expanded for large values of r/a. Terms of order a^2/r^2 must be kept or all information about the crack would be lost. The result for stresses, displacements, and displacement gradients is

$$\sigma_{xx} = \frac{\sigma a^2}{r^6}\left(\frac{x^4}{2} - \frac{y^4}{2} - 3x^2y^2\right)$$

$$\sigma_{yy} = \sigma + \frac{\sigma a^2}{r^6}\left(\frac{x^4}{2} - \frac{3y^4}{2} + 3x^2y^2\right)$$

$$\sigma_{xy} = \frac{\sigma a^2}{r^6}(x^3y - 3xy^3)$$

$$u_x = \frac{1}{2\mu}\left\{(k-3)\frac{\sigma}{4}x + \frac{\sigma a^2}{4r^4}[(-k+1)\,x^3 + (-k+5)\,xy^2]\right\}$$

$$u_y = \frac{1}{2\mu}\left\{(k-1)\frac{\sigma}{4}y + \frac{\sigma a^2}{4r^4}[(k-1)\,x^2y + (k+3)y^3]\right\}$$

$$u_{x,y} = \frac{1}{2\mu}\frac{\sigma a^2}{r^6}[(k+3)x^3y + (k-5)xy^3]$$

$$u_{y,x} = \frac{1}{4\mu}\frac{\sigma a^2}{r^6}[(-k+1)x^3y + (-k+7)xy^3]$$

The M integral is given by

$$M = 2(M_{AB} + M_{BC})$$

where paths AB and BC are shown in Fig. 6. Expanding the general experession for M, in plane stress

$$M_{AB} = 2\int_0^b \frac{1}{2E}(\sigma_{xx}{}^2 - \sigma_{yy}{}^2 + 2(H\nu)\,\sigma_{xy}{}^2)\,h$$
$$\left. + \frac{x}{E}(\sigma_{xy}\sigma_{xx} - \nu\sigma_{xy}\sigma_{yy}) - \sigma_{xy}u_{x,y}h + x\sigma_{yy}u_{y,x}\right\}dx$$

$$M_{BC} = 2\int_0^h \left\{\frac{1}{2E}(\sigma_{yy}{}^2 - \sigma_{xx}{}^2 + 2(1-\nu)\,\sigma_{xy}{}^2)\,b - \frac{y}{E}\sigma_{xy}\sigma_{yy}\right.$$
$$\left. + \frac{y\nu}{E}\sigma_{xy}\sigma_{xx} - y\sigma_{xx}u_{x,y} - b\sigma_{xy}u_{x,y}\right\}dy$$

The following terms are of order higher than a^2/r^2 and may be neglected:

$$\sigma_{xx}{}^2,\ \sigma_{xy}{}^2,\ \sigma_{xy}\sigma_{xx},\ \sigma_{xy}u_{x,y},\ \sigma_{xy}u_{y,x} \quad \text{and} \quad \sigma_{xx}u_{x,y}$$

Substituting the expanded expressions for stresses and displacements, and integrating to determine $M_{AB} + M_{BC}$, the only contribution to the final result is from

$$2\int_0^h \frac{-y\sigma_{xy}\sigma_{yy}}{E}\,dy = \frac{2\sigma^2a^2}{E}\left[\tan^{-1}\frac{h}{b} - \frac{b^3h + 2bh^3}{(b^2+h^2)^2}\right]$$

and

$$2\int_0^h x\sigma_{yy}u_y dx = \frac{2\sigma^2a^2}{E}\tan^{-1}\frac{b}{h}$$

It turns out that the term

$$\frac{-2\sigma^2a^2}{E}\left(\frac{b^3h + 2bh^3}{(b^2+h^2)^2}\right)$$

is cancelled by other terms. Thus

$$M = 2(M_{AB} + M_{BC}) = \frac{4\sigma^2a^2}{E}\left(\tan^{-1}\frac{h}{b} + \tan^{-1}\frac{b}{h}\right) = \frac{2\pi\sigma^2a^2}{E}$$

which is equal to the correct value for M in plane stress,

$$M = 2aJ = 2a\frac{k_I{}^2}{E} = \frac{2a(\sigma\sqrt{\pi a})^2}{E} = \frac{2\pi\sigma^2a^2}{E}$$

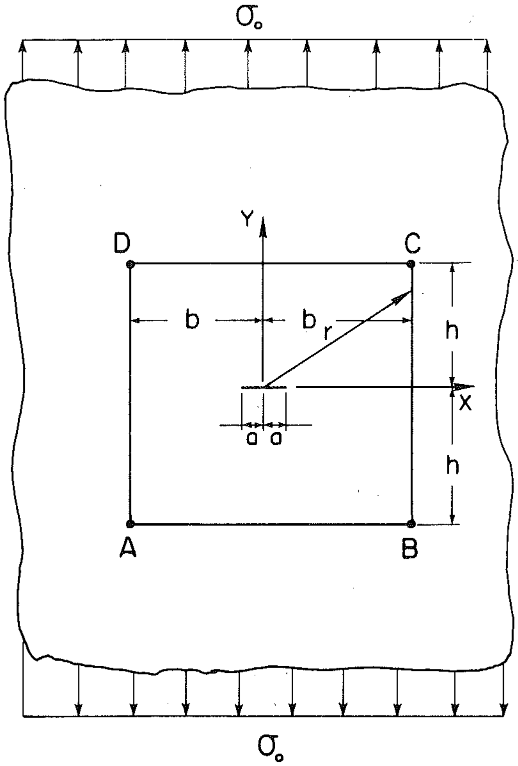

Fig. 6 Contour for theoretical evaluation of the *M* integral in infinite cracked panel

If all terms which are negligible for large values of r/a are omitted, M_{AB} becomes

$$M_{AB} \cong \frac{hb\sigma^2}{E} + 2\sigma\int_0^b \left(xu_{y,x} - \frac{\nu x}{E}\sigma_{XY}\right)dx$$

Now

$$\int_0^b xu_{y,x}\,dx = xu_y|_0^b - \int_0^b u_y dx$$
$$= bu_y(b,h) - \int_0^b u_y dx$$

If it is assumed that u_y and σ_{xy} vary quadratically with x, then

$$\int_0^b u_y dx \cong \frac{b}{3}(u_y(b,h) + 2u_y(0,h)$$

and

$$\int_0^b x\sigma_{xy}dx = \frac{b^2}{4}(\sigma_{xy}(b,h) + \sigma_{xy}(0,h)$$

After substituting numerical values, the M integral was determined for the large rectangular path in an infinite plate using these approximations, and was found to agree within 1 percent of the exact value, so these appear to be good approximations. In addition it was found that the contribution of the σ_{xy} term was negligible, and the result for M_{AB} is

$$M_{AB} = \frac{-hb\sigma^2}{E} + \frac{4\sigma b}{E}[u_y(b,h) - u_y(0,h)]$$

K. Vijayakumar[1]
Research Scientist.

S. N. Atluri
Regents' Professor of Mechanics.
Mem. ASME

Center for the Advancement
of Computational Mechanics,
School of Civil Engineering,
Georgia Institute of Technology,
Atlanta, Ga. 30332

An Embedded Elliptical Crack, in an Infinite Solid, Subject to Arbitrary Crack-Face Tractions

In this paper, following a critical assessment of earlier work of Green and Sneddon, Segedin, Kassir, and Sih (who obtained solutions for specific cases of normal loading on the crack face and the cases of constant and linear shear distribution on the crack face), Shah and Kobayashi (whose work is limited to the case of third-order polynomial distribution of normal loading on the crack face), and Smith and Sorensen (whose work is limited to the case of a third-order polynomial variation of shear loading on the crack face), a general solution is presented for the case of arbitrary normal as well as shear loading on the faces of an embedded elliptical crack in an infinite solid. The present solution is based on a generalization of the potential function representation used by Shah and Kobayashi. Expressions for stress-intensity factors near the flaw border, as well as for stresses in the far-field, for the foregoing general loadings, are given.

1 Introduction

The problem of a flat elliptical crack embedded in an infinite solid, of linear elastic material, has attracted much attention in the literature due to its fundamental role in the studies of fracture susceptibility of (embedded or surface) flawed, three-dimensional, engineering structures. When the solid is subjected to uniform tension at infinity, perpendicular to the plane of the crack (or, equivalently, when the crack face is subjected to uniform pressure, in the complementary problem), Green and Sneddon [1] have solved the problem using the known gravitational potential for a uniform elliptical disk. The case of uniform shear loading along the crack face was treated by Kassir and Sih [2], who obtained an exact solution in terms of two harmonic functions which, as in the tension problem [1], are constant multiples of the aforementioned gravitational potential. Kassir and Sih [2] have also derived expressions for the stress field near the crack border as well as for the stress-intensity factors.

Several investigations reported later were primarily concerned with the generalization of the work in [1] for the cases of the crack surface subjected to various degrees of polynomial pressure distribution normal to the crack surface. The first such generalization was contained in a procedure suggested by Segedin [3] who proposed the use of certain type of ellipsoidal harmonics, and their partial derivatives, which satisfy the Laplace equation. These potential functions were later used by Kassir and Sih [4] in expressing solutions for both the problems of the crack surface (*i*) under normal load [4, equation 3.24, p. 80] and (*ii*) under shear loads [4, equation 3.50, p. 86]. However, the contributions of these potentials employed in [4] to each stress component at the crack surface are not linearly independent polynomial functions and hence, one has to make a judicious choice of the potential functions for each degree of polynomial loading individually. By making such judicious choices, without, however, indicating a general procedure for such choices, Kassir and Sih [4] have presented exact solutions for some higher-order homogeneous polynomial loadings normal to the crack face, but limited their analysis to a torsional load in the case of shear loading on the crack face.

Prior to the work of [4] (what appears to us) a more logical choice of the potentials as given in [3] was made by Shah and Kobayashi [5] in representing the solution for the problem of the crack surface under arbitrary normal load. Though not explicitly stated in [5], the choice in [5] can be seen to be such that the individual contributions of the potential functions to the normal stress component on the crack surface are linearly independent, and moreover, form a complete set of polynomials. Shah and Kobayashi [5] have limited their analysis to a third-degree polynomial pressure distribution normal to the crack face, stating that the work involved in deriving the appropriate expressions for the chosen potentials was exhorbitant.

In the present paper, because of the previously stated linear independency and completeness of the contributions to stress components, at the crack surface, of the potentials, and due to the analytical convenience they afford, the potentials chosen by Shah and Kobayashi [5] are used to represent solutions *for both the problems of crack surface under arbitrary* (*i*) *normal and* (*ii*) *shear loading.* It is

---

[1] Research Scientist, on leave from the Indian Institute of Science, Bangalore, India.

Contributed by the Applied Mechanics Division for publication in the JOURNAL OF APPLIED MECHANICS.

Discussion on this paper should be addressed to the Editorial Department, ASME, United Engineering Center, 345 East 47th Street, New York, N. Y. 10017, and will be accepted until June 1, 1981. Readers who need more time to prepare a Discussion should request an extension from the Editorial Department. Manuscript received by ASME Applied Mechanics Division, May, 1980; final revision, August, 1980.

demonstrated to be possible to derive general solutions for arbitrary (normal as well as tangential) crack face tractions. Such general solutions are obtained for stress-intensity factors along the crack periphery for both the cases of (*i*) arbitrary applied normal stress distribution; and (*ii*) arbitrary applied shear stress distribution, on the crack face.

For the sake of completeness, the Trefftz's formulation [6] for a plane surface of discontinuity is first briefly sketched. This is followed by the treatment of the foregoing problem of an embedded elliptical crack in an infinite solid. The presentation of the algebraic details of the analysis is kept to a minimum in the interest of clarity as well as reasons of space.

2 Trefftz's Formulation for a Plane Surface of Discontinuity

Let u_α $(\alpha = 1, 2, 3)$ and $\sigma_{\alpha\beta}(\alpha,\beta = 1, 2, 3)$ denote displacements and stresses, respectively, in a homogeneous, isotropic linear elastic solid. The stress-displacement relations are, by Hooke's law,

$$\sigma_{\alpha\beta} = G\left(u_{\alpha,\beta} + u_{\alpha,\beta} + \frac{2\nu}{1-2\nu}\,\delta_{\alpha\beta}u_{\gamma,\gamma}\right) \tag{1}$$

where G and ν are the shear modulus and Poisson's ratio to the material, respectively. The Navier displacement equations of equilibrium in the absence of body forces are

$$u_{\beta,\beta\alpha} + (1-2\nu)u_{\alpha,\beta\beta} = 0 \tag{2}$$

in rectangular Cartesian coordinates $x_\alpha(\alpha = 1, 2, 3)$. In the foregoing the notations, $(\ )_{,\alpha} = \partial(\ )/\partial x_\alpha$; and $(\ )_{,\alpha\beta} = \partial^2(\ )/\partial x_\alpha \partial x_\beta$ have been employed.

Let R be a region of discontinuity in the plane $x_3 = 0$ such that, after deformation, the material inside R breaks up with free upper and lower surfaces, and remains continuous outside R. To deal with such a problem it is convenient to consider its complementary problem in which the surface of region of discontinuity is subjected to arbitrary transactions $\sigma_{3\alpha}$.

It is well known [7] that the solution for the aforementioned problem can be expressed in terms of four harmonic functions ψ and $\phi_\alpha(\alpha = 1, 2, 3)$ in the form

$$u_\alpha = \phi_\alpha + x_3\psi_{,\alpha} \tag{3}$$

so that the equations (2) are satisfied if

$$\phi_{\alpha,\alpha} + (3-4\nu)\psi_{,3} = 0 \tag{4}$$

The stress components in terms of ϕ_α and ψ are

$$\sigma_{\alpha\beta} = G\Big[\phi_{\alpha,\beta} + \phi_{\beta,\alpha} + \delta_{\alpha 3}\psi_{,\beta} + \delta_{\beta 3}\psi_{,\alpha} + 2x_3\psi_{,\alpha\beta} + \delta_{\alpha\beta}\frac{2\nu}{1-2\nu}(\phi_{\gamma,\gamma} + \psi_{,3})\Big] \tag{5}$$

The boundary conditions along the surface of the region of discontinuity are given by

$$\sigma_{33}^{(0)} = \frac{2G}{1-2\nu}\left[\nu(\phi_{1,1} + \phi_{2,2}) + (1-\nu)(\phi_3 + \psi)_{,3}\right] \tag{6a}$$

$$\sigma_{3\alpha}^{(0)} = G[\phi_{\alpha,3} + (\phi_3 + \psi)_{,\alpha}], \quad \alpha = 1,2 \tag{6b}$$

inside the region R in the plane $x_3 = 0$, wherein, the notation $\sigma_{\alpha\beta}^{(0)}$ is used for a prescribed quantity.

The problem is further simplified by expressing ψ and ϕ_α in the form

$$\psi = \nabla . \hat{f} = f_{\alpha,\alpha} \tag{7}$$

$$\phi_1 = (1-2\nu)(f_{1,3} + f_{3,1}) - (3-4\nu)f_{1,3} \tag{8a}$$

$$\phi_2 = (1-2\nu)(f_{2,3} + f_{3,2}) - (3-4\nu)f_{2,3} \tag{8b}$$

and

$$\phi_3 = -(1-2\nu)(f_{1,1} + f_{2,2}) - 2(1-\nu)f_{3,3} \tag{8c}$$

Then, the governing equations, namely,

$$\psi_{,\alpha\alpha} = 0, \quad \phi_{\alpha,\beta\beta} = 0, \; \phi_{\alpha,\alpha} + (3-4\nu)\psi_{,3} = 0$$

for ψ and ϕ_α are satisfied in the three functions $f_\alpha(\alpha = 1, 2, 3)$ are harmonic. The stress components $\sigma_{\alpha\beta}$ in terms of $f_\alpha(\alpha = 1, 2, 3)$ are given by

$$\sigma_{11} = 2G[f_{3,11} + 2\nu f_{3,22} - 2f_{1,31} - 2\nu f_{2,32} + x_3(\nabla . \hat{f})_{,11}] \tag{9a}$$

$$\sigma_{22} = 2G[f_{3,22} + 2\nu f_{3,11} - 2f_{2,32} - 2\nu f_{1,31} + x_3(\nabla . \hat{f})_{,22}] \tag{9b}$$

$$\sigma_{12} = 2G[(1-2\nu)f_{3,12} - (1-\nu)(f_{1,32} + f_{2,13}) + x_3(\nabla . \hat{f})_{,12}] \tag{9c}$$

$$\sigma_{33} = 2G[-f_{3,33} + x_3(\nabla . \hat{f})_{,33}] \tag{9d}$$

$$\sigma_{31} = 2G[-(1-\nu)f_{1,33} + \nu(f_{1,11} + f_{2,21}) + x_3(\nabla . \hat{f})_{,13}] \tag{9e}$$

$$\sigma_{32} = 2G[-(1-\nu)f_{2,33} + \nu(f_{1,12} + f_{2,22}) + x_3(\nabla . \hat{f})_{,23}] \tag{9f}$$

The boundary conditions (6) to be satisfied inside the region R in the plane $x_3 = 0$ take the much simpler forms

$$\sigma_{33}^{(0)} = -2Gf_{3,33} \tag{10a}$$

$$\sigma_{3\alpha}^{(0)} = -2G[(1-\nu)f_{\alpha,33} - \nu(f_{1,1\alpha} + f_{2,2\alpha})], \quad \alpha = 1, 2 \tag{10b}$$

in which the boundary condition for f_3 is uncoupled from f_1 and f_2.

It is to be noted that only the symmetric components of f_α with respect to the plane $x_3 = 0$ need to be considered for satisfying the boundary conditions (10). If the solid is of infinite extent in all directions and the stress components decay to zero as one moves toward infinity, then the solutions $f_\alpha(\alpha = 1, 2, 3)$ are harmonic functions symmetric in x_3. In such a case, the problem governing f_3 is independent of the problem governing f_1 and f_2. Kassir and Sih [4] have denoted the former as a symmetric problem and the later one as a skew-symmetric problem.

3 Embedded Elliptical Crack in an Infinite Solid

Let the region of discontinuity be bounded by an ellipse

$$\frac{x_1^2}{a_1^2} + \frac{x_2^2}{a_2^2} = 1, \quad a_1^2 > a_2^2 \tag{11}$$

in the plane $x_3 = 0$. The foregoing geometry of the crack surface is more conveniently described in an ellipsoidal coordinate system. The necessary ellipsoidal coordinates $\xi_\alpha(\alpha = 1, 2, 3)$ are the roots of the cubic equation

$$\omega(\xi) = 0 \tag{12}$$

where

$$\omega(\xi) = 1 - \frac{x_1^2}{a_1^2 + \xi} - \frac{x_2^2}{a_2^2 + \xi} - \frac{x_3^2}{\xi} \tag{13}$$

They are connected to the Cartesian coordinates x_α by the relations [8]

$$a_1^2(a_1^2 - a_2^2)x_1^2 = (a_1^2 + \xi_1)(a_1^2 + \xi_2)(a_1^2 + \xi_3) \tag{14a}$$

$$a_2^2(a_2^2 - a_1^2)x_2^2 = (a_2^2 + \xi_1)(a_2^2 + \xi_2)(a_2^2 + \xi_3) \tag{14b}$$

$$a_1^2a_2^2x_3^2 = \xi_1\xi_2\xi_3 \tag{14c}$$

where

$$-a_1^2 \le \xi_1 \le -a_2^2 \le \xi_2 \le 0 \le \xi_3 < \infty \tag{14d}$$

The expression for $\omega(\xi)$ in equation (13) may be written in the alternate form

$$\omega(\xi) = P(\xi)/Q(\xi) \tag{15}$$

where

$$P(\xi) = (\xi - \xi_1)(\xi - \xi_2)(\xi - \xi_3) \tag{16a}$$

$$Q(\xi) = \xi(\xi + a_1^2)(\xi + a_2^2) \tag{16b}$$

The partial derivatives of ξ_α with respect of x_β required later are given[2] by

$$\partial_\beta^1 \xi_\alpha = \frac{2x_\beta Q(\xi_\alpha)}{(a_\beta^2 + \xi_\alpha)P'(\xi_\alpha)} \tag{17}$$

in which, for $\beta = 3$, a_3 is zero. In the foregoing, the following notation is used: ∂_β^n indicates the nth partial derivative w.r.t. x_β and P' indicates the derivative of P w.r.t. ξ.

The elliptic boundary (11) in the plane $x_3 = 0$ corresponds to the curve $\xi_3 = 0$, $\xi_2 = 0$. The crack surface itself namely, the region inside ellipse (11) in the plane $x_3 = 0$ is given in a simple manner by the surface $\xi_3 = 0$.

The boundary conditions (10) may also be expressed in ellipsoidal coordinates. From practical considerations, however, it is useful to describe the distribution of the applied loads $\sigma_{3\alpha}^{(0)}$ in Cartesian coordinates. Moreover, the potentials are required to be symmetric with respect to the plane $x_3 = 0$. It is obviously difficult to meet this requirement in ellipsoidal coordinate system.

From previous considerations, it is convenient to carry out the analysis by a judicious use of both Cartesian and ellipsoidal coordinate systems.

Basic Potentials V_n ($n = 1, 2, \ldots$). Basic potentials useful for the analysis were suggested by Segedin [3]. They are of the form

$$V_n = \int_{\xi_3}^{\infty} [\omega(s)]^n \frac{ds}{\sqrt{Q(s)}}, \quad n = 1, 2, \ldots \tag{18}$$

(In fact, the function V_n is known to be harmonic for all real values of $n \geq 0$ [9]. It is symmetric in each x_α since $\omega(s)$ and ξ_3 are symmetric in x_α.)

To examine the suitability of the functions in equation (18) for the analysis of crack surface under arbitrary loading, we first consider the contribution of V_n to the stress components along the crack surface.

By direct differentiation of the expression for V_n with respect to x_α, we have

$$\begin{aligned}\partial_\alpha^1 V_n &= \frac{\partial}{\partial x_\alpha} \int_{\xi_3}^{\infty} \omega^n(s) \frac{ds}{\sqrt{Q(s)}} \\ &= \int_{\xi_3}^{\infty} \partial_\alpha^1 \omega^n \frac{ds}{\sqrt{Q(s)}} - \left[\frac{\omega^n(s)}{\sqrt{Q(s)}}\right]_{s=\xi_3} \partial_\alpha^1 \xi_3 \\ &= n \int_{\xi_3}^{\infty} \rho_\alpha x_\alpha \omega^{n-1} \frac{ds}{\sqrt{Q(s)}} - \left[\frac{\omega^n(s)}{\sqrt{Q(s)}}\right]_{s=\xi_3} \partial_\alpha^1 \xi_3 \quad \text{(no sum on } \alpha)\end{aligned} \tag{19}$$

in which

$$\begin{aligned}\rho_\alpha &= -2/(a_\alpha^2 + s), \quad \alpha = 1, 2 \\ &= -2/s, \quad \alpha = 3\end{aligned} \tag{20}$$

The second term on the right-hand side of equation (19) is zero since $\omega(\xi_3) = 0$. Hence

$$\partial_\alpha^1 V_n = n \int_{\xi_3}^{\infty} \rho_\alpha x_\alpha \omega^{n-1} \frac{ds}{\sqrt{Q(s)}}, \quad n = 1, 2, \ldots \text{ (no sum on } \alpha)$$

Differentiating again with respect to x_β we get from equation (21),

$$\partial_\beta^1 \partial_\alpha^1 V_n = n \int_{\xi_3}^{\infty} \rho_\alpha [(n-1)\rho_\beta x_\alpha x_\beta + \delta_{\alpha\beta}\omega] \omega^{n-2} \frac{ds}{\sqrt{Q(s)}}, \quad n \geq 2 \tag{21}$$

$$= -\left[\frac{\rho_\alpha x_\alpha}{\sqrt{Q(s)}}\right]_{s=\xi_3} \partial_\beta^1 \xi_3 + \delta_{\alpha\beta} \int_{\xi_3}^{\infty} \frac{\rho_\alpha ds}{\sqrt{Q(s)}}, \quad n = 1 \tag{22}$$

Along the crack surface $\xi_3 = 0$, i.e., the region inside the ellipse (11) in the plane $x_3 = 0$, one obtains from equations (22), for $\alpha, \beta = 1, 2$, in view of equation (17), that

$$\begin{aligned}[\partial_\beta^1 \partial_\alpha^1 V_n]_{\xi_3=0} &= n(n-1) \int_0^{\infty} \rho_\alpha \rho_\beta x_\alpha x_\beta [\omega^{n-2}]_{x_3=0} \frac{ds}{\sqrt{Q(s)}} \\ &\quad + n\delta_{\alpha\beta} \int_0^{\infty} \rho_\alpha [\omega^{n-1}]_{x_3=0} \frac{ds}{\sqrt{Q(s)}}, \quad n = 1, 2, \ldots (\alpha, \beta = 1, 2)\end{aligned} \tag{23}$$

In the case of the derivative $\partial_3^2 V_n$, the expressions (22) contain singular terms. In the limit $\xi_3 \to 0$, however, it can be shown that

$$\lim_{\xi_3 \to 0} [\partial_3^2 V_n] = -[(\partial_1^2 + \partial_2^2)V_n]_{\xi_3=0} \tag{24}$$

as it should be since V_n satisfies the Laplace equation.

It can be seen that the expressions in equations (23) and (24) are polynomials in x_1 and x_2. However, since the functions

$$[\omega^n]_{x_3=0}, \quad n = 1, 2, 3 \ldots \infty \tag{25}$$

are polynomials in x_1^2 and x_2^2, the aforementioned polynomials in equations (23) and (24) do not form a complete set to represent an arbitrary function of the varibles x_1 and x_2. Hence, if the functions f_α in the problem are represented as linear combinations of V_n ($n = 1, 2, \ldots \infty$), one cannot obtain arbitrary distributions of $\sigma_{3\alpha}$ ($\alpha = 1, 2, 3$) along the crack surface. That is, the functions V_n($n = 1, 2, \ldots \infty$) do not form a complete set to represent solutions f_α for an arbitrary loading along the crack surface.

Complete Set of Potentials F_{kl} ($k,l = 0, 1, 2, \ldots$). Let each component of the applied load $\sigma_{3\alpha}^{(0)}$ be a polynomial of degree M in x_1 and x_2. Then the number of linearly independent terms in each component is $\frac{1}{2}(M + 1)(M + 2)$. Hence, to represent the solution for each f_α, one has to find the same number of linearly independent harmonic functions of the type V_n such that a linear combination of their polynomial contributions to the tractions along the crack surface match with the given polynomial distributions of applied loads exactly. For this purpose, we consider the functions of the type

$$\partial_1^k \partial_2^l V_n = \frac{\partial^{k+l} V_n}{\partial x_1^k \partial x_2^l} \tag{26}$$

first suggested by Segedin [3] and later used by Shah and Kobayashi [5] and Kassir and Sih [4], and Smith and Sorensen [6]. It can be easily shown [3] that the aforementioned partial derivatives of V_n are harmonic for $k + l < n$ with polynomial contributions of degree $2n - k - l - 2$ to the tractions along the crack surface. These functions would be suitable for the analysis if the integers, k, l, n are restricted by the relations

$$2(k + l + 1) \leq 2n \leq M + k + l + 2 \tag{27}$$

However, the number of functions corresponding to the integers k, l, n satisfying the relations (27) are more than $\frac{1}{2}(M + 1)(M + 2)$ for $M \geq 2$. As such, the aforegoing polynomial contributions of these functions are not linearly independent for $M \geq 2$.

In the symmetric problem, wherein only f_3 is nonzero, Shah and Kobayashi [5] have chosen the required set of functions for representing f_3 by taking $n = k + l + 1$ ($\leq M + 1$) and varying $k + l$ from 0 to M. They have, however, limited their work to $M = 3$ from practical considerations such as exhorbitant work involved in obtaining and using partial derivatives (26) in the analysis.[3] Kassir and Sih [4] have considered some specific (incomplete) homogeneous polynomial loadings up to the degree $M = 6$; thus the results in [4] are inadequate for the solution of a problem of crack face pressure of an arbitrary polynomial variation even of degree 6. In retrospect it appears that for each loading Kassir and Sih [4] have chosen a suitable combination

---

[2] Note that

$$\frac{\partial \omega(\xi_\alpha)}{\partial x_\beta} = \frac{-2x_\beta}{a_\beta^2 + \xi_\alpha} + \left[\frac{\partial \omega(\xi)}{\partial \xi}\right]_{\xi=\xi_\alpha} \frac{\partial \xi_\alpha}{\partial x_\beta} = 0 \quad \text{and} \quad P(\xi_\alpha) = 0$$

[3] One of the reviewers has brought to our attention the efforts of Broekhoven in extending the results of [5] in the case of $M = 4$ in the symmetric problem. Upon further literature search the authors found reference [18], wherein Broekhoven mentions such effort, but no detailed results are given.

of k, l, n satisfying conditions (27) but no general procedure for the choice was indicated in [4].

In the case of shear loading, Kassir and Sih [2] have considered the problem of crack surface under constant shear for which the solutions for f_1 and f_2, which only are nonzero, are constant multiples of V_1. Later [4], they have also obtained solutions for the problem of crack surface under torsional load.

Smith and Sorensen [6] have considered a complete cubic-polynomial load tangentical to the crack face leading to a (20 × 20) matrix equation. They have not, however, presented in [6] the expressions for the matrix elements. The problem of torsional load, as a special case of their analysis [6], was treated in detail and variation of the stress-intensity factors along the crack border were presented in graphical form in [6]. From the previous observations, it can be seen that, for high-order polynomial shear loadings, no solutions were reported until now in the literature, even though the solutions for f_1 and f_2 can be obtained in terms of a suitable set of functions (26).

In the present paper, Shah and Kobayashi's representation [5] for the solution is extended to the general case of arbitrary loading by expressing the solutions f_α ($\alpha = 1, 2, 3$) in the form

$$f_\alpha = \sum_k \sum_l C_{\alpha,k,l} F_{kl} \tag{28}$$

where, by definition,

$$F_{kl} = \partial_1^k \partial_2^l V_{k+l+1} \tag{29}$$

and $C_{\alpha,k,l}$ are unknown constants to be determined from the analysis.

Partial Derivatives of F_{kl}

By successive differentiation, it can be shown that, since $\omega(\xi_3) = 0$,

$$F_{kl} = \int_{\xi_3}^{\infty} \partial_1^k \partial_2^l \omega^{k+l+1} \frac{ds}{\sqrt{Q(s)}} \tag{30}$$

and

$$\partial_\beta^1 F_{kl} = \int_{\xi_3}^{\infty} \partial_\alpha^1 \partial_1^k \partial_2^l \omega^{k+l+1} \frac{ds}{\sqrt{Q(s)}}, \quad \alpha = 1, 2, 3 \tag{31}$$

Differentiating both sides of equation (31) with respect to x_β, we obtain the second-order partial derivatives of F_{kl} required for the evaluation of stress components along the crack face in the form

$$\partial_\beta^1 \partial_\alpha^1 F_{kl} = F_{kl\beta\alpha}^0 + F_{kl\beta\alpha}^1 \quad (\alpha, \beta = 1, 2, 3) \tag{32}$$

in which

$$\begin{aligned} F_{kl\beta\alpha}^0 &= -[\partial_\alpha^1 \partial_1^k \partial_2^l \omega^{k+l+1}/\sqrt{Q(s)}]_{s=\xi_3}\, \partial_\beta^1 \xi_3 \\ &= (k+l+1)! \frac{x_1^k x_2^l x_\alpha x_\beta}{(\xi_3 - \xi_1)(\xi_3 - \xi_2)} [\rho_1^k \rho_2^l \rho_\alpha \rho_\beta \sqrt{Q(s)}]_{s=\xi_3} \end{aligned} \tag{33}$$

and

$$F_{kl\beta\alpha}^1 = \int_{\xi_3}^{\infty} \partial_\beta^1 \partial_\alpha^1 \partial_1^k \partial_2^l\, \omega^{k+l+1} \frac{ds}{\sqrt{Q(s)}} \tag{34}$$

In the foregoing ( )! denotes the factorial of the respective quantity. The derivation of expression (33) is given in Appendix of the presented paper.

Expressions for Boundary Errors. To satisfy boundary conditions (10), it is necessary to evaluate only the derivatives

$$\partial_\alpha^1 \partial_\beta^1 F_{kl}, \alpha, \beta = 1,2; \quad \text{and} \quad \partial_3^1 \partial_3^1 F_{kl}$$

along the crack surface $\xi_3 = 0$. The former three derivatives along the crack surface are given by

$$[\partial_\alpha^1 \partial_\beta^1 F_{kl}]_{\xi_3=0} = [F_{kl\alpha\beta}^1]_{\xi_3=0} \quad \alpha, \beta = 1, 2 \tag{35}$$

since

$$[F_{kl\alpha\beta}^0]_{\xi_3=0} = 0, \quad \alpha, \beta = 1, 2 \tag{36}$$

In the evaluation of the derivative $\partial_3^1 \partial_3^1 F_{kl}$ along the crack surface $\xi_3 = 0$, however, both F^0 and F^1 terms are singular at $\xi_3 = 0$ but it can be shown that their sum remains finite, as stated by Shah and Kobayashi [5] and tends to the regular (finite) component of F_{kl33}^1 as ξ_3 tends to zero, i.e.,

$$[\partial_3^1 \partial_3^1 F_{kl}]_{\xi_3=0} = \text{finite component of} \lim_{\xi_3 \to 0} [F_{kl33}^1] \tag{37}$$

Alternatively, we have

$$\partial_3^1 \partial_3^1 F_{kl} = -[\partial_1^1 \partial_1^1 + \partial_2^1 \partial_2^1] F_{kl}$$

so that

$$[\partial_3^1 \partial_3^1 F_{kl}]_{\xi_3=0} = -[F_{kl11}^1 + F_{kl22}^1]_{\xi_3=0} \tag{38}$$

which is finite for each k and l. The foregoing expression (38) was used earlier by Kassir and Sih [4].

Substituting the series (28) in equations (10) and using equations (35) and (37) or (38), one obtains

$$\sigma_{33}^{(0)} + 2G \sum_k \sum_l C_{3,k,l} [\partial_3^1 \partial_3^1 F_{kl}]_{\xi_3=0} = 0 \tag{39a}$$

and

$$\begin{aligned} \sigma_{3\alpha}^{(0)} + 2G \sum_k \sum_l [(1+\nu)\partial_3^1 \partial_3^1 F_{kl} C_{\alpha,k,l} \\ - \nu(C_{1,k,l} F_{kl1\alpha}^1 + C_{2,k,l} F_{kl2\alpha}^1)]_{\xi_3=0}, \quad {\scriptstyle \alpha=1,2} \end{aligned} \tag{39b}$$

The left-hand side expressions of the foregoing equations may be considered as expressions for boundary errors. Applying any known principle of nullification of errors such as least squares, collocation, power series expansion, Fourier series expansion, it is in principle possible to obtain a sufficient number of linear algebraic equations for the determination of the parameters $C_{\alpha,k,l}$.

Polynomial Load Distributions. If the distribution of applied loads $\sigma_{3\alpha}^{(0)}(\alpha = 1, 2, 3)$ along the crack surface are finite-order polynomials in x_1 and x_2, it is possible to obtain exact solutions by using power series expansion of the boundary errors and equating the coefficient of each power term of the series of zero. For this purpose, one needs the polynomial series expansion of the derivatives F_{kl} in equations (39). Such expansions are available, until now, for the first few values of $k + l$ only [3–6] as discussed earlier. Here, the necessary expansions for a general value of $k + l$ are derived and they are given in the following (however, for the sake of clarity and conciseness, the tedious algebraic details are omitted):

(*i*) $\alpha, \beta = 1, 2$:

$$\begin{aligned} [\partial_\alpha^1 \partial_\beta^1 F_{kl}]_{\xi_3=0} &= \sum_{p=p_0}^{k+l+1} \sum_{q=q_0}^{p} (-1)^p \frac{(k+l+1)!}{(k+l+1-p)!} \frac{(2p-2q)!}{(p-q)!} \frac{(2q)!}{q!} \\ &\times \frac{x_1^{2p-2q-k'}}{(2p-2q-k')!} \frac{x_2^{2q-l'}}{(2q-l')!} \int_0^\infty \frac{ds}{(a_1^2+s)^{p-q}(a_2^2+s)^q \sqrt{Q(s)}} \end{aligned} \tag{40}$$

in which

$$k' = k + \delta_{1\alpha} + \delta_{1\beta}, \quad l' = l + \delta_{2\alpha} + \delta_{2\beta}$$

$$p_0 = \text{integer value of } (k' + l' + 1)/2$$

and

$$q_0 = \text{integer value of } (l' + 1)/2$$

The integral in equation (40) can be evaluated in terms of complete *elliptic integrals of the first and second kinds.*

(*ii*) $\alpha = \beta = 3$:

The expression for $[\partial_3^1 \partial_3^1 F_{kl}]_{\xi_3=0}$ may be obtained from equations (38) and (40). If equation (37) is used, it takes the following form:

$$\begin{aligned} [\partial_3^1 \partial_3^1 F_{kl}]_{\xi_3=0} &= \text{finite component of} \lim_{\xi_3 \to 0} F_{kl33}^1 \\ &= \sum_{p=p_0}^{k+l+1} \sum_{q=q_0}^{p-1} (-1)^p \frac{(k+l+1)!}{(k+l+1-p)!} \frac{(2p-2-2q)!}{(p-1-q)!} \frac{(2q)!}{q!} \end{aligned} \tag{41}$$

$$\times \frac{x_1^{2p-2-2q-k}}{(2p-2-2q-k)!} \frac{x_2^{2q-l}}{(2q-l)!} J \tag{41 (Cont.)}$$

in which

$p_0 = 1 +$ integer value of $(k + l + 1)/2$

$q_0 =$ integer value of $(l + 1)/2$

and

$$J = \text{finite part of} \lim_{\xi_3 \to 0} \int_{\xi_3}^{\infty} \frac{2ds}{s(a_1^2+s)^{p-1-q}(a_2^2+s)^q \sqrt{Q(s)}} \tag{42}$$

Crack Surface Under Normal Load. Let the normal load $\sigma_{33}^{(0)}$ along the crack surface in the symmetric problem be expressed in the form

$$\sigma_{33}^{(0)} = \sum_{i=0}^{1} \sum_{j=0}^{1} \sum_{m=0}^{M} \sum_{n=0}^{m} A_{3,m-n,n}^{(i,j)} x_1^{2m-2n+i} x_2^{2n+j} \tag{43}$$

so that the values of i, j specify the symmetries of the load with respect to the axes of the ellipse.

The solution for the function f_3 in terms of the potentials F_{mn} is assumed in the form

$$f_3 = \sum_{i=0}^{1} \sum_{j=0}^{1} \sum_{k=0}^{M} \sum_{l=0}^{k} C_{3,k-l,l}^{(i,j)} F_{2k-2l+i,2l+j} \tag{44}$$

In the foregoing, for purposes of clarity, a potential such as F_{mn} is represented as $F_{2k-2l+i,2l+j}$; thus it is to be understood that m and n take the values $(2k-2l+i)$ and $(2l+j)$, respectively.

The aforementioned expressions for $\sigma_{33}^{(0)}$ and f_3 are substituted in the boundary condition (10*a*). The polynomial expansion of the second-order derivative of each of the potentials F's is obtained from equation (41). The coefficients of like power terms on both sides of equation (10*a*) are equated to each other leading to the following set of linear algebraic equations for the determination of the parameters C's:

$$\frac{(-1)^{m+i+j}}{(2m-2n+i)!(2n+j)!} \sum_{\mathrm{k=m}}^{\mathrm{M}} \sum_{\mathrm{l=0}}^{\mathrm{k}} (-1)^k I_3^{(i,j)} J_3^{(i,j)} C_{3,k-l,l}^{(i,j)} = \left(\frac{1}{2G}\right) A_{3,m-n,n}^{(i,j)}, \quad \begin{matrix} m = 0, 1, 2 \ldots M \\ n = 0, 1, 2 \ldots m \end{matrix} \tag{45}$$

in which

$$I_3^{(i,j)} = \frac{(2k+i+j+1)!}{(k-m)!} \frac{[2(k-l+m-n+i)]!}{(k-l+m-n+i)!} \frac{[2(n+l+j)]!}{(n+l+j)!} \tag{46}$$

and

$$J_3^{(i,j)} = \text{finite part of} \lim_{\xi_3 \to 0} \times \int_{\xi_3}^{\infty} \frac{2}{s(a_1^2+s)^{k-l+m-n+i}(a_2^2+s)^{l+n+j}} \frac{ds}{\sqrt{Q(s)}} \tag{47}$$

The foregoing equations (45) may be solved in successive steps as outlined as follows:

(*i*) From the $M + 1$ equations corresponding to $m = M, n = 0, 1, 2, \ldots M$, solve for the $M + 1$ coefficients

$$C_{3,M-l,l}^{(i,j)}, \quad l = 0, 1, 2, \ldots M$$

(*ii*) Substitute the values of coefficients obtained in step (*i*), in the M equations corresponding to $m = M - 1, n = 0, 1, 2, \ldots M - 1$. Solve these M equations for the M coefficients

$$C_{3,M-1-l,l}^{(i,j)}, \quad l = 0, 1, 2, \ldots M - 1$$

(*iii*) Continue the process solving, at the $(M + 1 - r)$th step, the $r + 1$ equations corresponding to $m = r, n = 0, 1, 2, \ldots r$ for the $r + 1$ coefficients

$$C_{3,r-l,l}^{(i,j)}, \quad l = 0, 1, 2, \ldots r$$

and taking values of $r = M - 2, M - 3, \ldots 1, 0$ in succession.

It may be mentioned here that Shah and Kobayashi [5] have confined their work to $M = 1$ in each of the symmetric groups $(i, j) = (0, 0)$ $(0, 1)$, and $(1, 0)$ and to $M = 0$ in the case of doubly antisymmetric loading corresponding to $(i, j) = (1, 1)$. Kassir and Sih [4] have considered homogeneous polynomial loadings corresponding to $M = 1$, 2, 3 in the doubly symmetric group $(i, j) = (0, 0)$ and to $M = 1$ in the two groups $(i, j) = (0, 1), (1, 0)$. Solutions in [4] were obtained, however, by using combinations of F_{kl} different from those given in equation (44) except in the case of $M = 1$ in the $(0, 0)$ group.

Crack Surface Under Shear Load. As in the symmetric problems, the applied shear load components $\sigma_{3\alpha}^{(0)}$ $(\alpha = 1, 2)$ in the skew-symmetric problem may be taken in the form

$$\sigma_{3\alpha}^{(0)} = \sum_{i=0}^{1} \sum_{j=0}^{1} \sum_{m=0}^{M} \sum_{n=0}^{m} A_{\alpha,m-n,n}^{(i,j)} x_1^{2m-2n+i} x_2^{2n+j} \tag{48}$$

and the solutions for f_α may be assumed in the form

$$f_\alpha = \sum_{i=0}^{1} \sum_{j=0}^{1} \sum_{k=0}^{M} \sum_{l=0}^{k} C_{\alpha,k-l,l}^{(i,j)} F_{2k-2l+i,2l+j} \tag{49}$$

in which the upper value for k is dependent on α, i, j, and M.

Due to the skew-symmetric nature, the problem decomposes into the following two problems denoted by $P_1(\alpha, \beta, M)$ and $P_2(\alpha, \beta, M)$, $\alpha \neq \beta$:

(*i*) *Problem* $P_1(\alpha, \beta, M)$: $\sigma_{3\alpha}^{(0)}$ is symmetric and $\sigma_{3\beta}^{(0)}$ is antisymmetric in both x_1 and x_2.

(*ii*) *Problem* $P_2(\alpha, \beta, M)$: $\sigma_{3\alpha}^{(0)}$ is symmetric in x_1 and antisymmetric in x_2; $\sigma_{3\beta}^{(0)}$ is antisymmetric in x_1 and symmetric in x_2.

In each of the just mentioned two problems, the expressions taken for the load components, the series assumed for the solutions, and the derived linear algebraic equations governing the coefficients C's are given as follows:

(*i*) *Problem* $P_1(\alpha, \beta, M)$:

$$\sigma_{3\alpha}^{(0)} = \sum_{m=0}^{M} \sum_{n=0}^{m} A_{\alpha,m-n,n}^{(0,0)} x_1^{2m-2n} x_2^{2n} \tag{50}$$

$$\sigma_{3\beta}^{(0)} = x_1 x_2 \sum_{m=0}^{M-1} \sum_{n=0}^{m} A_{\beta,m-n,n}^{(1,1)} x_1^{2m-2n} x_2^{2n} \tag{51}$$

where

$$\sigma_{3\beta}^{(0)} = 0 \quad \text{for} \quad M = 0 \tag{52}$$

$$f_\alpha^{(0,0)} = \sum_{k=0}^{M} \sum_{l=0}^{k} C_{\alpha,k-l,l}^{(0,0)} F_{2k-2l,2l} \tag{53}$$

$$f_\beta^{(1,1)} = \sum_{k=0}^{M-1} \sum_{l=0}^{k} C_{\beta,k-l,l}^{(1,1)} F_{2k-2l+1,2l+1} \tag{54}$$

where

$$f_\beta^{(1,1)} = 0 \quad \text{for} \quad M = 0 \tag{55}$$

$$\left(\frac{1}{2G}\right) A_{\alpha,m-n,n}^{(0,0)} = \frac{(-1)^m}{(2m-2n)!(2n)!} \Bigg[\sum_{k=m}^{M} \sum_{l=0}^{k} (-1)^k \{(1-\nu) I_3^{(0,0)} J_3^{(0,0)} - \nu I_\alpha^{(0,0)} J_\alpha^{(0,0)}\} C_{\alpha,k-l,l}^{(0,0)} - \nu \sum_{k=m-1}^{M-1} \sum_{l=0}^{k} (-1)^{k-1} I_{12}^{(1,1)} J_{12} \times C_{\beta,k-l,l}^{(1,1)} \Bigg], \quad \begin{matrix} m = 0, 1, 2 \ldots M \\ n = 0, 1, 2 \ldots m \end{matrix} \tag{56a}$$

$$\left(\frac{1}{2G}\right) A_{\beta,m-n,n}^{(1,1)} = \frac{(-1)^m}{(2m-2n+1)!(2n+1)!} \Bigg[\sum_{k=m}^{M-1} \sum_{l=0}^{k} (-1)^k \{(1-\nu) I_3^{(1,1)} J_3^{(1,1)} - \nu I_\beta^{(1,1)} J_\beta^{(1,1)}\} C_{\beta,k-l,l}^{(1,1)} - \nu \sum_{k=m+1}^{M} \sum_{l=0}^{k} (-1)^{k-1} \times I_{12}^{(0,0)} J_{12} C_{\alpha,k-l,l}^{(0,0)} \Bigg] \quad \begin{matrix} m = 0, 1, 2 \ldots M-1 \\ n = 0, 1, 2, 3 \ldots m \end{matrix} \tag{56b}$$

in which

$$I_\alpha^{(i,j)} = \frac{(2k+i+j+1)!}{(k-m)!} \frac{[2(k-l+m-n+i+\delta_{1\alpha})]!}{(k-l+m-n+i+\delta_{1\alpha})!} \times \frac{[2(n+l+j+\delta_{2\alpha})]!}{(n+l+j+\delta_{2\alpha})!} \quad (\alpha = 1, 2) \tag{57a}$$

$$I_{12}^{(i,j)} = \frac{(2k+i+j+1)!}{(k-m+i+j-1)!} \frac{[2(k-l+m-n+1)]!}{(k-l+m-n+1)!} \frac{[2(l+n+1)]!}{(l+n+1)!} \tag{57b}$$

$$J_\alpha^{(i,j)} = \int_0^\infty \frac{1}{(a_1^2+s)^{k-l+m-n+i+\delta_{1\alpha}}(a_2^2+s)^{l+n+j+\delta_{2\alpha}}} \frac{ds}{\sqrt{Q(s)}} \qquad (\alpha = 1, 2) \tag{58a}$$

$$J_{12} = \int_0^\infty \frac{1}{(a_1^2+s)^{k-l+m-n+1}(a_2^2+s)^{l+n+1}} \frac{ds}{\sqrt{Q(s)}} \tag{58b}$$

In the particular case of $M = 0$, we have

$$\sigma_{3\alpha}^{(0)} = A_{\alpha,0,0}^{(0,0)}, \quad \sigma_{3\beta}^{(0)} = 0$$

$$f_\alpha^{(0,0)} = C_{\alpha,0,0}^{(0,0)} F_{00}, \quad f_\beta^{(1,1)} = 0, \quad \alpha \neq \beta = 1, 2 \tag{59}$$

The equations (56) reduce to

$$2G[(1-\nu)I_3^{(0,0)}J_3^{(0,0)} - \nu\, I_\alpha^{(0,0)}J_\alpha^{(0,0)}]C_{\alpha,0,0}^{(0,0)} = A_{\alpha,0,0}^{(0,0)} \tag{60}$$

so that, in the case of constant shear, the solutions $f_\alpha^{(0,0)}$ $(\alpha = 1, 2)$ are constant multiples of F_{00}.

As in the symmetric problem equations (56) may be solved in successive steps by solving first for the $(2M + 1)$ coefficients

$$C_{\alpha,M-l,l}^{(0,0)}, \quad l = 0, 1, 2 \ldots M$$

and

$$C_{\beta,M-1-l,l}^{(1,1)}, \quad l = 0, 1, 2 \ldots M - 1$$

from the $(2M + 1)$ equations consisting of $M + 1$ equations of (56*a*) for $m = M$, $n = 0, 1, 2 \ldots M$ and M equations of (56*b*) for $m = M - 1$, $n = 0, 1, 2 \ldots M - 1$.

(*ii*) *Problem* $P_2(\alpha, \beta, M)$:

$$\sigma_{3\alpha}^{(0)} = x_2 \sum_{m=0}^{M} \sum_{n=0}^{m} A_{\alpha,m-n,n}^{(0,1)} x_1^{2m-2n} x_2^{2n} \tag{61}$$

$$\sigma_{3\beta}^{(0)} = x_1 \sum_{m=0}^{M} \sum_{n=0}^{m} A_{\beta,m-n,n}^{(1,0)} x_1^{2m-2n} x_2^{2n} \tag{62}$$

$$f_\alpha^{(0,1)} = \sum_{k=0}^{M} \sum_{l=0}^{k} C_{\alpha,k-l,l}^{(0,1)} F_{2k-2l,2l+1} \tag{63a}$$

$$f_\beta^{(1,0)} = \sum_{k=0}^{M} \sum_{l=0}^{k} C_{\beta,k-l,l}^{(1,0)} F_{2k-2l+1,2l} \tag{63b}$$

$$\begin{aligned}\left(\frac{1}{2G}\right) A_{\alpha,m-n,n}^{(0,1)} &= \frac{(-1)^{m+1}}{(2m-2n)!(2n+1)!} \\ &\times \sum_{k=m}^{M} \sum_{l=0}^{k} (-1)^k \{[(1-\nu)I_3^{(0,1)}J_3^{(0,1)} - \nu\, I_\alpha^{(0,1)}J_\alpha^{(0,1)}] \\ &\qquad \times C_{\alpha,k-l,l}^{(0,1)} - \nu\, I_{12}^{(1,0)} J_{12} C_{\beta,k-l,l}^{(1,0)}\}\end{aligned} \tag{64a}$$

$$\begin{aligned}\left(\frac{1}{2G}\right) A_{\beta,m-n,n}^{(1,0)} &= \frac{(-1)^{m+1}}{(2m-2n+1)!(2n)!} \\ &\times \sum_{k=m}^{M} \sum_{l=0}^{k} (-1)^k \{[(1-\nu)\, I_3^{(1,0)}J_3^{(1,0)} - \nu\, I_\beta^{(1,0)}J_\beta^{(1,0)}] \\ &\qquad \times C_{\beta,k-l,l}^{(1,0)} - \nu\, I_{12}^{(0,1)} J_{12} C_{\alpha,k-l,l}^{(0,1)}\} \\ m &= 0,1,2\ldots M \\ n &= 0,1,2\ldots m\end{aligned} \tag{64b}$$

As in the previous problem, equations (64) may be solved in successive steps by solving first for the $2(M + 1)$ coefficients

$$C_{\alpha,M-l,l}^{(0,1)}, \quad C_{\alpha,M-l,l}^{(1,0)}, \quad l = 0, 1, 2 \ldots M$$

from the $2(M + 1)$ equations corresponding to $m = M$, $n = 0, 1, 2 \ldots M$.

It is to be noted that, in the case of arbitrary polynomial loading, the integer M in the summation in equation (48) can assume different values $M(\alpha, i, j)$ for different combinations of α, i, and j. In such a case, we define, for $\alpha \neq \beta = 1, 2$,

$$M_{1\alpha} = \max\,[M(\alpha, 0, 0), M(\beta, 1, 1) + 1],$$

and

$$M_{2\alpha} = \max\,[M(\alpha, 0, 1), M(\beta, 1, 0)] \tag{65}$$

Then the solution of the skew-symmetric problem for arbitrary polynomial loading is given by a linear sum of the solutions of the four problems

$$P_1(\alpha, \beta, M_{1\alpha}), \quad P_2(\alpha, \beta, M_{2\alpha}), \quad \alpha \neq \beta = 1, 2 \tag{66}$$

Stress-Intensity Factors k_α $(\alpha = 1, 2, 3)$. Kassir and Sih [2] have shown that in the vicinity of the periphery of an elliptical crack on the plane $x_3 = 0$, the ellipsoidal coordinates become

$$\xi_1 = -(a_1^2 \sin^2\theta + a_2^2 \cos^2\theta) \tag{67a}$$

$$\xi_2 = 0 \tag{67b}$$

$$\xi_3 = 2a_1a_2r(a_1^2 \sin^2\theta + a_2^2 \cos^2\theta)^{-1/2} \tag{67c}$$

where r is the radial distance normal to the crack border in the plane $x_3 = 0$, and θ is the angle in the parametric equations of the ellipse

$$x_1 = a_1 \cos\theta \quad \text{and} \quad x_2 = a_2 \sin\theta \tag{68}$$

The normal and tangential components σ_{n3}, σ_{t3} near the border of the elliptical crack (where n and t are directions normal and tangential to the crack border in the plane $x_3 = 0$) in the plane $x_3 = 0$ are given by the relations

$$\sigma_{n3} = \sigma_{31} \cos\beta + \sigma_{32} \sin\beta \tag{69a}$$

$$\sigma_{t3} = -\sigma_{31} \sin\beta + \sigma_{32} \cos\beta \tag{69b}$$

where β, the angle between the outward normal of the crack border (in the plane $x_3 = 0$) and x_1-axis, is related to θ by the equations

$$\cos\beta = a_2 \cos\theta/\sqrt{A}\,, \quad \sin\beta = a_1 \sin\theta/\sqrt{A} \tag{70}$$

$$A = a_1^2 \sin^2\theta + a_2^2 \cos^2\theta \tag{71}$$

The stress-intensity factors k_α are defined as

$$K_1 = \lim_{r\to 0} [(2\pi r)^{1/2}\sigma_{33}]_{\xi_2=0} \tag{72a}$$

$$K_2 = \lim_{r\to 0} [(2\pi r)^{1/2}\sigma_{n3}]_{\xi_2=0} \tag{72b}$$

and

$$K_3 = \lim_{r\to 0} [(2\pi r)^{1/2}\sigma_{t3}]\xi_{\xi_2=0} \tag{72c}$$

From equations (67), (69)–(72), the expressions for K_α take the following forms:

$$K_1 = \left(\frac{\pi}{a_1a_2}\right)^{1/2} A^{1/4} \lim_{\xi_3\to 0} [\xi_3^{1/2}\sigma_{33}]_{\xi_2=0} \tag{73a}$$

$$\begin{aligned}K_2 = \left(\frac{\pi}{a_1a_2}\right)^{1/2} A^{-1/4} \Big\{ & a_2 \cos\theta \lim_{\xi_3\to 0} [\xi_3^{1/2}\sigma_{31}]_{\xi_2=0} \\ & + a_1 \sin\theta \lim_{\xi_3\to 0} [\xi_3^{1/2}\sigma_{32}]_{\xi_2=0}\Big\}\end{aligned} \tag{73b}$$

and

$$\begin{aligned}K_3 = \left(\frac{\pi}{a_1a_2}\right)^{1/2} A^{-1/4} \Big\{ & a_2 \cos\theta \lim_{\xi_3\to 0} [\xi_3^{1/2}\sigma_{32}]_{\xi_2=0} \\ & - a_1 \sin\theta \lim_{\xi_3\to 0} [\xi_3^{1/2}\sigma_{31}]_{\xi_2=0}\Big\}\end{aligned} \tag{73c}$$

From equations (9*d*)–(9*f*), we have

$$\lim_{\xi_3\to 0} [\xi_3^{1/2}\sigma_{33}]_{\xi_2=0} = -2G \lim_{\xi_3\to 0} [\xi_3^{1/2}f_{3,33}]_{\xi_2=0} \tag{74}$$

and

$$\lim_{\xi_3\to 0}[\xi_3^{1/2}\sigma_{3\alpha}]_{\xi_2=0} = -2G \lim_{\xi_3\to 0}$$

$$\times [\xi_3^{1/2}[\{(1-\nu)f_{\alpha,33} - (f_{\alpha,\alpha\alpha} + f_{\beta,\beta\alpha})\}]_{\xi_2=0} \quad \alpha \neq \beta = 1, 2 \quad (75)$$

Since the solutions for f_α are linear combinations of potentials F_{kl}, one needs the following quantities for evaluating the right-hand side expressions in equations (74) and (75).

$$G_{33}^{kl} = \lim_{\xi_3\to 0}[\xi_3^{1/2}\partial_3^2 F_{kl}]_{\xi_2=0}$$

$$= \lim_{\xi_3\to 0}[\xi_3^{1/2}(F^0_{kl33} + F^1_{kl33})]_{\xi_2=0}$$

$$= -(-2)^{k+l+2}(k+l+1)!\,\frac{\cos^k\theta\,\sin^l\theta}{a_1^{k+1}a_2^{l+1}} \quad (76)$$

$$G_{\alpha\beta}^{kl} = \lim_{\xi_3\to 0}[\xi_3^{1/2}\partial_\beta^1\partial_\alpha^1 F_{kl}]_{\xi_2=0}$$

$$= \lim_{\xi_3\to 0}[\xi_3^{1/2}F^0_{kl\alpha\beta}]_{\xi_2=0}$$

$$= \left(\frac{1}{A}\right)(-2)^{k+l+2}(k+l+1)!\,\frac{\cos^k\theta\,\sin^l\theta}{a_1^{k-1}a_2^{l-1}}\,\frac{x_\alpha x_\beta}{a_\alpha^2 a_\beta^2},$$

$$\alpha, \beta = 1, 2 \quad (77)$$

where $x_\alpha x_\beta$ are given by equation (68).

By using equations (74), (75), series solutions obtained for f_α, and the equations (76) and (77), the stress-intensity factors K_α are evaluated from equations (73). The expressions for K_α thus obtained are given next.

***(i)* Symmetric Problem.** From equations (44), (73*a*), (74), and (76), the expression for the stress-intensity factor K_1 is obtained as

$$K_1 = -2G\left(\frac{\pi}{a_1a_2}\right)^{1/2} A^{1/4}\sum_{i=0}^{1}\sum_{j=0}^{1}\sum_{k=0}^{M}\sum_{l=0}^{k} G_{33}^{2k-2l+i,2l+j}C_{3,k-l,l}^{(i,j)}$$

$$= 8G\left(\frac{\pi}{a_1a_2}\right)^{1/2} A^{1/4}\sum_{i=0}^{1}\sum_{j=0}^{1}\sum_{k=0}^{M}\sum_{l=0}^{k}(-2)^{2k+i+j}(2k+i+j+1)!$$

$$\times\frac{1}{a_1a_2}\left(\frac{\cos\theta}{a_1}\right)^{2k-2l+i}\left(\frac{\sin\theta}{a_2}\right)^{2l+j} C_{3,k-l,l}^{(i,j)} \quad (78)$$

***(ii)* Skew-Symmetric Problem.** The solutions for f_1 and f_2 in this problem are linear sums of the solutions of the problems P_1 and P_2 which take the form

$$f_1 = \sum_{i=0}^{1}\sum_{j=0}^{1} f_1^{(i,j)} = \sum_{i=0}^{1}\sum_{j=0}^{1}\sum_{k=0}^{M}\sum_{l=0}^{k} C_{1,k-l,l}^{(i,j)} F_{2k\text{-}2l+i,2l+j}$$

and

$$f_2 = \sum_{i=0}^{1}\sum_{j=0}^{1} f_1^{(1-i,1\text{-}j)} = \sum_{i=0}^{1}\sum_{j=0}^{1}\sum_{k=0}^{M}\sum_{l=0}^{k} C_{2,k-l,l}^{(1-i,1-j)} F_{2k-2l+1-i,2l+1-j} \quad (79)$$

The stress-intensity factors K_2 and K_3 corresponding to the foregoing series solutions (79) are given by

$$K_2 = 8G\left(\frac{\pi}{a_1a_2}\right)^{1/2} A^{-1/4}\frac{1}{a_1a_2}[H_1a_2\cos\theta + H_2a_1\sin\theta], \quad (80a)$$

$$K_3 = 8G\left(\frac{\pi}{a_1a_2}\right)^{1/2} A^{-1/4}(1-\nu)\frac{1}{a_1a_2}[H_2a_2\cos\theta - H_1a_1\sin\theta]$$

$$(80b)$$

in which

$$H_1 = \sum_{i=0}^{1}\sum_{j=0}^{1}\sum_{k=0}^{M}\sum_{l=0}^{k}(-2)^{2k+i+j}(2k+i+j+1)!\left(\frac{\cos\theta}{a_1}\right)^{2k-2l+i}$$

$$\times\left(\frac{\sin\theta}{a_2}\right)^{2l+j} C_{1,k-l,l}^{(i,j)} \quad (81)$$

and

$$H_2 = \sum_{i=0}^{1}\sum_{j=0}^{1}\sum_{k=0}^{M}\sum_{l=0}^{k}(-2)^{2k+2-i-j}(2k+3-i-j)!\left(\frac{\cos\theta}{a_1}\right)^{2k-2l+1-i}$$

$$\times\left(\frac{\sin\theta}{a_2}\right)^{2l+1-j} C_{2,k-l,l}^{(1-i,1-j)} \quad (82)$$

4 Concluding Remarks

In the foregoing we have presented a general solution for the problem of an infinite linear elastic solid containing a flat elliptical crack, whose faces are subjected to an *arbitrary* polynomial variation of *normal* as well as *tangential* tractions. This represents a generalization of the cited earlier works of other authors [1–6]. The expressions for the three-modes of stress-intensity factors, K_1, K_2, and K_3 along the flaw border, for the considered general loading, are given. The expressions for the stresses in the far-field for the considered problem of arbitrary loading on the crack face, are given in Appendix of the present paper.

One of the most pressing needs in applied fracture mechanics is the accurate and cost-effective evaluation of stress-intensity factors along the border of embedded or surface flaws in complex structural geometries such as aircraft attachment lugs, nuclear reactor pressure-vessel-nozzle junctions, etc. The shapes of these flaws are often assumed, to a first approximation, as elliptical or part-elliptical. In solving these complex practical problems, several approaches such as, the Schwartz-Neuman alternating technique [10, 11], the boundary-integral equation technique [12], and singularity-finite-element methods [13, 14] have been reported in literature. It is generally recognized [15] that even though the alternating technique may be the simplest and most cost-effective technique, the results obtained so far through this technique are not as accurate as those obtained through the finite element and boundary-integral-equation approaches.

In the alternating technique, as applied to the problem of cracks in finite solids, two solutions are needed, generally. One of these solutions is for stresses in the uncracked finite body at the location of the considered crack, and the other solution is for the problem of an infinite body with a crack whose faces are subject to arbitrary normal as well as shear traction components. For cracks in complex finite bodies, such as described earlier, the first solution previously mentioned, would in general lead to a rather complex stress-field at the location of the considered crack. Because of the limitation of the available analytical results for the second solution discussed in the foregoing [1–6], the stress-fields of the aforementioned first problem were always approximated by polynomials of order ≤3 in the use of the alternating technique [10, 11]. Since this limitation has been overcome in the present paper, the results of the present paper may effectively be employed in devising a more accurate and cost-effective alternating-solution technique for analyzing complex, flawed, structural geometries. The results of our efforts in this direction will be reported shortly.

Acknowledgments

This work has been supported by the U.S. National Science Foundation under Grant No. ENG-76-16418. The authors express their appreciation to Clifford J. Astill for his encouragement. The authors thank Ms. M. Eiteman for her patience in typing this manuscript.

References

1 Green, A. E., and Sneddon, I. N., "The Distribution of Stress in the Neighborhood of a Flat Elliptical Crack in an Elastic Solid," *Proceedings of the Cambridge Philosophical Society,* Vol. 46, 1950, pp. 159–163.

2 Kassir, M. K., and Sih, G. C., "Three-Dimensional Stress Distribution Around an Elliptical Crack Under Arbitrary Loadings," ASME JOURNAL OF APPLIED MECHANICS, Vol. 33, 1966, pp. 601–611.

3 Segedin, C. M., "Some Three-Dimensional Mixed Boundary-Value Problems in Elasticity," Report 67-3, Department of Aeronautics and Astronautics, College of Engineering, University of Washington, June 1967, 35 pp.

4 Kassir, M. K., and Sih, G. C., "Three-Dimensional Crack Problems," *Mechanics of Fracture,* ed., Sih, G. C., Vol. 2, Noordhoff International Publishing, 1975.

5 Shah, R. C., and Kobayashi, A. S., "Stress-Intensity Factor for an Elliptical Crack Under Arbitrary Normal Loading," *Engineering Fracture Mechanics*, Vol. 3, 1971, pp. 71–96.

6 Smith, F. W., and Sorensen, D. R., "The Elliptical Crack Subjected to Nonuniform Shear Loading," ASME JOURNAL OF APPLIED MECHANICS, Vol. 41, 1974, pp. 502–509.

7 Trefftz, E., *Handbuch der Physik*, Vol. 6, Springer-Verlag, Berlin, 1928, p. 92.

8 Wittaker, E. T., and Watson, G. N., *Modern Analysis*, Cambridge, London, 1962.

9 Bateman, H., *Partial Differential Equations of Mathematical Physics*, Cambridge, London, 1959.

10 Kobayashi, A. S., Enetanya, A. N., and Shah, R. C., "Stress-Intensity Factors for Elliptical Cracks," *Prospects of Fracture Mechanics*, eds., Sih, G. C., van Elst, H. C., and Broek, D., Noordhoff Int. Publ., 1975, pp. 525–544.

11 Sorensen, D. R., and Smith, F. W., "Semielliptical Surface Cracks Subjected to Shear Loading," *Pressure Vessel Technology, Part II* (Materials and Fabrication), *Proceedings*, Vol. 3, ICPVT, Tokyo, ASME, N.Y., 1977, pp. 545–551.

12 Heliot, J., Labbens, R., and Pellissier-Tannon, A., "Semi-Elliptical Cracks in a Cylinder Subjected to Stress Gradients," *Fracture Mechanics*, ASTM STP 677, 1979, pp. 341–364.

13 Atluri, S. N., and Kathiresan, K., "3D Analyses of Surface Flaws in Thick-Walled Reactor Pressure-Vessels Using Displacement-Hybrid Finite-Element Method," *Nuclear Engineering & Design*, Vol. 51, No. 2, 1979, pp. 163–176.

14 Atluri, S. N., "Higher-Order, Special, and Singular Finite Elements," Chapter 4, *State-of-the-Art Surveys in Finite Element Methods*, eds., Noor, A. K., and Pilkey, W., ASME, N.Y., 1980, 80 pp., to appear.

15 "A Critical Evaluation of Numerical Solutions to the 'Bench Mark' Surface Flaw Problem," ed., McGowan, J. J., [Editorial Committee: S. N. Atluri, A. S. Kobayashi, R. C. Labbans, J. J. McGowan, J. C. Newman, Jr., C. W. Smith, and F. W. Smith], Society for Experimental Stress Analyses, 1980, 51 pages, to appear.

16 Shah, R. C., and Kobayashi, A. S., "Stress-Intensity Factors for an Elliptical Crack Approaching the Surface of Semi-Infinite Solid," Boeing Company Document No. D-180-14494-1, 1971.

17 Quinlan, P. M., Private communication, Sept. 1979.

18 Broekhoven, M. J. G., and van de Ruijtenbeck, M. G., "Fatigue Crack Extension Nozzle Junctions; Comparison of Analytical Approximations With Experimental Data," Paper G4/7, *Trans. of 3rd Int. Conf. on Struct. Mech. in Reactor Technology*, Vol. 3, Part G, compiled by Jaeger, T. A., CECA, CEE, CEEA, Luxemborg, 1975.

APPENDIX

We consider here evaluation of potentials F_{kl} and their partial derivatives required for calculating displacements and stress components at a point away from the crack surface.

Earlier, Shah and Kobayashi [5] have derived, for values of $k + l$ up to 3 expressions for F_{kl} and their partial derivatives up to second-order in terms of incomplete elliptic integrals and Jacobian elliptic functions. In a subsequent investigation [16], they have also obtained expressions for some third-order partial derivatives of F_{kl} required in the evaluation of stress components σ_{22}, σ_{12}, and σ_{23} in the symmetric problem. It appears that, in deriving the aforementioned expressions, they have expressed the power term ω^{k+l+1} as a polynomial in x_α^2 ($\alpha = 1, 2, 3$) and carried out necessary differentiations. Kassir and Sih [4] have, however, adopted the chain rule of differentiation involving total derivatives with respect fo ω and obtained expressions in a slightly different form for their potentials and partial derivatives up to second-order in the analyses of both symmetric and skew-symmetric problems.

In the present paper, we derive the necessary expressions for a general potential F_{kl} and its partial derivatives by both the aforementioned procedures. For this purpose, it is convenient to consider the required partial derivatives of F_{kl} as a sum $(H_0 + H_1)$ of an integrated component H_0 and an integral H_1 of the form

$$H_1 = \int_{\xi_3}^{\infty} \partial_1^{k_1} \partial_2^{l_1} \partial_3^{m_1} \omega^{k+l+1} \frac{ds}{\sqrt{Q(s)}} \tag{83}$$

Then the component H_0 and the form of H_1 in F_{kl} and its partial derivatives are as listed as follows:

(*i*) F_{kl}:

$$H_0 = 0$$

and

$$k_1 = k, \quad l_1 = l, \quad m_1 = 0 \quad \text{in} \quad H_1 \tag{84}$$

(*ii*) $\partial_\alpha^1 F_{kl}$:

$$H_0 = 0$$

and

$$k_1 = k + \delta_{1\alpha}, l_1 = l + \delta_{2\alpha}, m_1 = \delta_{3\alpha} \quad \text{in} \quad H_1 \tag{85}$$

(*iii*) $\partial_\beta^1 \partial_\alpha^1 F_{kl}$:

$$\begin{aligned} H_0 &= F^0_{kl\beta\alpha} \\ &= -\left[\partial_\alpha^1 \partial_1^k \partial_2^l \omega^{k+l+1} \frac{1}{\sqrt{Q(s)}}\right]_{s=\xi_3} \partial_\beta^1 \xi_3 \end{aligned} \tag{86}$$

$$k_1 = k + \delta_{1\alpha} + \delta_{1\beta}, \quad l_1 = l + \delta_{2\alpha} + \delta_{2\beta}$$

$$m_1 = \delta_{3\alpha} + \delta_{3\beta} \quad \text{in} \quad H_1 \tag{87}$$

(*iv*) $\partial_\gamma^1 \partial_\beta^1 \partial_\alpha^1 F_{kl}$:

$$H_0 = \frac{\partial}{\partial x_\gamma} F^0_{kl\beta\alpha} - \left[\partial_\beta^1 \partial_\alpha^1 \partial_1^k \partial_2^l \omega^{k+l+1} \frac{1}{\sqrt{Q(s)}}\right]_{s=\xi_3} \partial_\gamma^1 \xi_3 \tag{88}$$

$$k_1 = k + \delta_{1\alpha} + \delta_{1\beta} + \delta_{1\gamma}$$

$$l_1 = l + \delta_{2\alpha} + \delta_{2\beta} + \delta_{2\gamma}$$

and

$$m_1 = \delta_{3\alpha} + \delta_{3\beta} + \delta_{3\gamma} \quad \text{in} \quad H_1 \tag{89}$$

The integrand in equation (83) may be evaluated in two ways mentioned earlier. In the first procedure, the power term ν^{k+l+1} is expanded in terms of $x_\alpha^2 (\alpha = 1, 2, 3)$ and term-by-term differentiations are carried out. Then, we get

$$\begin{aligned} \partial_1^{k_1} \partial_2^{l_1} \partial_3^{m_1} \omega^{k+l+1} = (k + l + 1)! \sum_{p=0}^{k+l+1} \sum_{q=0}^{p} \sum_{r=0}^{q} \frac{(-1)^p}{(k + l + 1 - p)!} \\ \times \frac{(2p - 2q)!}{(p - q)!} \frac{(2q - 2r)!}{(q - r)!} \frac{(2r)!}{r!} \frac{x_1^{2p-2q-k_1}}{(2p - 2q - k_1)!} \frac{x_2^{2q-2r-l_1}}{(2q - 2r - l_1)!} \\ \times \frac{x_3^{2r-m_1}}{(2r - m_1)!} \frac{1}{(a_1^2 + s)^{p-q} (a_2^2 + s)^{q-r} s^r} \end{aligned} \tag{90}$$

Substitution of the foregoing expression in equation (83) leads to an expression for H_1 containing integrals of the type

$$J_{pqr} = \int_{\xi_3}^{\infty} \frac{1}{(a_1^2 + s)^{p-q} (a_2^2 + s)^{q-r} s^r} \frac{ds}{\sqrt{Q(s)}} \tag{91}$$

The aforementioned integrals can be evaluated in terms of incomplete elliptic integrals of the first and second kinds and Jacobian elliptic functions.

The expression in (90) can also be used in (86) and (88) for the evaluation of the integrated parts H_0. However, much simpler expressions for these integrated parts are derived from the second procedure described in the following.

In adopting the second procedure involving chain rule of differentiation, we note that

$$\begin{aligned} \partial_\alpha^i \omega^{k+l+1} &= \sum_{p=0}^{I} A_p^{(i)} \rho_\alpha^p (\partial_\alpha^1 \omega)^{i-2p} \frac{d^{i-p} \omega^{k+l+1}}{d\omega^{i-p}} \\ &= (k + l + 1)! \sum_{p=0}^{I} A_p^{(i)} \rho_\alpha^{i-p} x_\alpha^{i-2p} \frac{\omega^{k+l+1+2p-i}}{(k + l + 1 + 2p - i)!} \end{aligned} \tag{92}$$

in which $A_p^{(i)}$ are integer constants and

$$I = I(i/2) = \text{integer value of } i/2 \tag{93}$$

The previous form for a partial derivative of the power term was recognized earlier by Quinlan [17]. The integer constants $A_p^{(i)}$ ($p = 1, 2, \ldots I$) for values of i up to 10 were also obtained by him by carrying out successive differentiations. By differentiating both sides of equation (92) with respect to x_α, however, we obtain the following recurrence relations among the coefficients $A_p^{(i)}$:

$$A_0^{(0)} = 1, \quad A_0^{(i+1)} = A_0^{(i)}$$

$$A_p^{(i+1)} = A_p^{(i)} + (i - 2p + 2) A_{p-1}^{(i)}, \quad p = 1, 2, \ldots I \tag{94}$$

and

$$A_{l+1}^{(i+1)} = A_l^{(i)} \quad \text{when} \quad I\left(\frac{i+1}{2}\right) = I\left(\frac{i}{2}\right) + 1 \qquad (94)\ (Cont.)$$

Using the form for a partial derivative of the power term, we get

$$\partial_1^{k_1}\partial_2^{l_1}\partial_3^{m_1}\omega^{k+l+1} = (k+l+1)! \sum_{p=0}^{k_1} \sum_{q=0}^{l_1} \sum_{r=0}^{m_1} A_p^{(k_1)} A_q^{(l_1)}$$
$$\times A_r^{(m_1)} \rho_1^{k_1-p} \rho_2^{l_1-q} \rho_3^{m_1-r} x_1^{k_1-2p} x_2^{l_1-2q} x_3^{m_1-2r} \frac{\omega^N}{N!} \qquad (95)$$

where

$$N = k + l + 1 + p + q + r - k_1 - l_1 - m_1. \qquad (96)$$

By substituting the foregoing expression (95) in equation (83), one gets an alternate expression for H_1 involving integrals of the type

$$J = \int_{\xi_3}^{\infty} \frac{\omega^N}{(a_1^2+s)^{k_1-p}(a_2^2+s)^{l_1-q} s^{m_1-r}} \frac{ds}{\sqrt{Q(s)}} \qquad (97)$$

which are relatively complicated in comparison with the integrals in equation (91).

However, in view of the property $\omega(\xi_3) = 0$, the form (95) is convenient for finding the integrated components H_0 in equations (86) and (88). The contributions of terms in (95) to H_0 are from terms corresponding to $N = 0$. Hence, we get the following simple expressions for the integrated components in the second and third-order partial derivatives of F_{kl}:

$$F_{kl\beta\alpha}^0 = (k+l+1)! \frac{x_1^k x_2^l x_\alpha x_\beta}{(\xi_3 - \xi_1)(\xi_3 - \xi_2)} [\rho_1^k \rho_2^l \rho_\alpha \rho_\beta \sqrt{Q(s)}]_{s=\xi_3} \qquad (98)$$

The expression for H_0 in (88) is obtained as

$$H_0 = \frac{\partial}{\partial x_\gamma} F_{kl\beta\alpha}^0 + \frac{(k+l+1)!}{(\xi_3-\xi_1)(\xi_2-\xi_1)} \sqrt{Q(\xi_3)} \left\{ \rho_1^{k_1}\rho_2^{l_1}\rho_3^{m_1}\rho_\gamma \right.$$
$$\left. \times x_1^{k_1} x_2^{l_1} x_3^{m_1} x_\gamma \left[\frac{(k_1-1)k_1}{2\rho_1 x_1^2} + \frac{(l_1-1)l_1}{2\rho_2 x_2^2} + \frac{(m_1-1)m_1}{2\rho_3 x_3^2} \right] \right\}_{s=\xi_3} \qquad (99)$$

in which k_1, l_1, and m_1 are given by equations (87).

The partial derivative of $F_{kl\beta\alpha}^0$ in (99) may be obtained from the expression (98) by treating ξ_α ($\alpha = 1, 2, 3$) as functions of x_α ($\alpha = 1, 2, 3$).

Substituting the foregoing second and third-order partial derivatives of F_{kl} appropriately into equations (9*a*)–(9*f*), the expression for *each of the six stress components in the far-field can easily be written* down. These lengthy expressions are omitted here for the sake of conciseness and clarity.

K. Tanaka[1]
T. Mura
Professor Civil Engineering,
Mem. ASME

Materials Research Center and
Department of Civil Engineering,
The Technological Institute,
Northwestern University,
Evanston, Ill. 60201

A Dislocation Model for Fatigue Crack Initiation

The slip band formed in a grain on the material surface is a preferential site for crack initiation during low strain fatigue of polycrystalline metals. The forward and reverse plastic flow within the slip band is modeled in the present study by dislocations with different signs moving on two closely located layers, and it is assumed that their movement is irreversible. Based on the model, the monotonic buildup of dislocation dipoles piled up at the grain boundary is systematically derived using the theory of continuously distributed dislocations. This buildup is associated with the progress of extrusion or intrusion. The number of stress cycles up to the initiation of a crack of the grain size order is defined as the cycle when the stored strain energy of accumulated dislocations reaches a critical value. The relation between the initiation life and the plastic strain range derived theoretically is in agreement with a Coffin-Manson type law, and that between the fatigue strength and the grain size is expressed in an equation of the Petch type.

Introduction

The initiation of fatigue cracks is one of the most important stages in the fatigue fracture processes of metals. A large number of metallographic observations has been carried out to elucidate the micromechanisms responsible for crack initiation. The state of the art is described in two recent excellent review articles by Grosskreutz [1] and Laird and Duquette [2]. The site of crack initiation varies depending on the microstructures of the material involved and types of applied stresses. Among possible sites of crack initiation, the slip band is preferential one for pure, single-phase metals and some polyphase metals under a low strain cycling [1, 2]. The cyclic strain is concentrated along the slip band and the extrusion or intrusion is accompanied with it.

Most of the models proposed to account for the formation of extrusions or intrusions are based on Mott's assumption [3] that dislocations move along different paths in the slip bands under forward and reverse loadings. These models, however, are rather qualitative and fail to yield any systematic, quantitative way to evaluate the monotonic buildup or ratcheting of plastic deformation by a cyclic loading. One exception is the model proposed by Lin and Ito [4]. They considered two thin slices closely located in a grain on the specimen surface, with one part sliding during forward loading and the other part sliding during reverse loading. To make this mode of deformation possible, they assumed a special field for the internal stress. Such an initial stress is not always expected in reality.

In the present paper, a more reasonable model for early fatigue damage is proposed. The plastic deformation within the slip band is modeled by two adjacent layers of dislocation pileups. Each layer has a different sign. A systematic buildup of accumulation of dislocation dipoles is derived under the assumption of the irreversible dislocation motion. The model can also yield a Coffin-Manson type law for crack initiation and the Petch-type equation for the grain size dependency of fatigue strength.

Model and Analysis

Model of Damage Accumulation. In the fatigue of smooth specimens of polycrystalline materials, a slip band crack is expected to nucleate in a grain on the surface which has a high value of cyclic shear stress resolved from the applied stress on the slip plane in the slip direction. Under a uniaxial stress, the resolved shear stress becomes maximum when the normal of the slip plane and the slip direction are inclined at 45 deg to the stress axis. Figs. 1 and 2 illustrate two extreme cases of the most favorably oriented grains located on the surface. Fig. 1 is the section perpendicular to the specimen surface. The slip plane is perpendicular to the sheet face and the slip direction is in it. Fig. 2 is a picture of the section parallel to the surface inside the specimen. The slip plane is perpendicular to the specimen surface and the slip direction is on the specimen surface. In the following discussion, the former case is denoted as the case of orientation A and the latter one as that of orientation B.

The dislocations generated in a most favorably oriented grain under the tensile stress are piled up against the grain boundary. In Figs. 1 and 2, the dislocation pileups on layer I are made under tension. The dislocations in Fig. 1 are created at the surface of the specimen and moved to the interior of a grain. The dislocations in Fig. 2 are created inside a grain and move to the grain boundary. The back stress caused

---

[1] On leave from Department of Engineering Science, Kyoto University, Kyoto, Japan.

Contributed by the Applied Mechanics Division of THE AMERICAN SOCIETY OF MECHANICAL ENGINEERS, for presentation at the 1981 Joint ASME/ASCE Applied Mechanics, Fluids Engineering, and Bioengineering Conference, University of Colorado, Boulder, Colo., June 22-27, 1981.

Discussion on this paper should be addressed to the Editorial Department, ASME, United Engineering Center, 345 East 47th Street, New York, N. Y. 10017, and will be accepted until June 1, 1981. Readers who need more time to prepare a Discussion should request an extension from the Editorial Department. Manuscript received by ASME Applied Mechanics Division, May, 1980; *final revision, July, 1980.* Paper No. 81-APM-3.

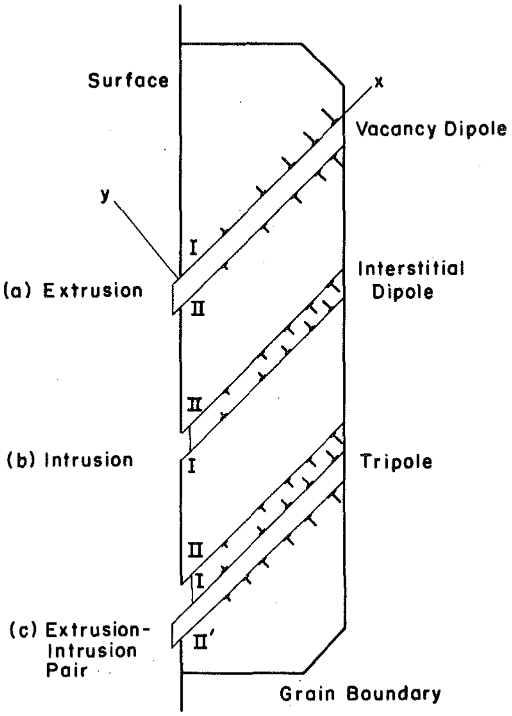

Fig. 1 Dislocation motion in a most favorably oriented grain (Case *A* orientation) and the formation of extrusion and intrusion by dislocation accumulation

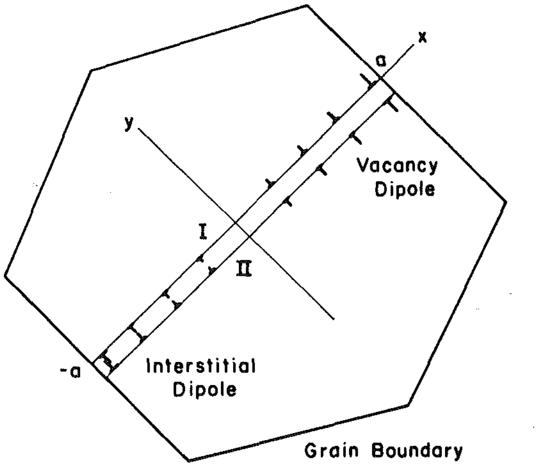

Fig. 2 Dislocation motion in a most favorably oriented grain (Case *B* orientation)

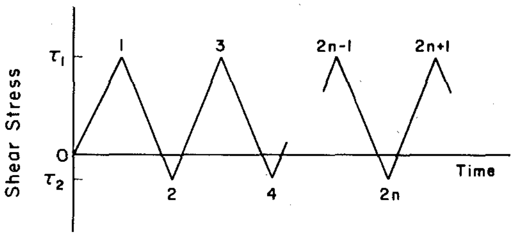

Fig. 3 Applied shear stress pattern

by pileup dislocations is negative in the vicinity of pileup layer I. Therefore, the reverse plastic flow is expected to take place near the layer during subsequent reverse loading.

If the dislocations piled up on layer I move in the opposite direction under reverse loading, there is no accumulation of dislocations, so no fatigue fracture takes place. In the following model, it is assumed that the dislocations formed by previous forward loading are irreversible and that the reverse plastic flow is taken up by the motion of dislocations with the opposite sign on the other slip plane which is located very close to the previous one. The basis for the assumption of irreversible dislocation motion as an extreme case will be discussed later. The dislocation pileups made under reverse loading are those on layer II shown in Figs. 1 and 2. The pileups of negative dislocations on layer II cause a positive back stress on layer I. This back stress enhances the pileup of positive dislocations during the next stage of forward loading. In this way, the accumulation of dislocation dipoles is amplified with the number of stress cycles. In the case of orientation *A*, extrusion, intrusion, or an extrusion-intrusion pair is monotinically built up as illustrated in Fig. 1. For a general case, the dislocation accumulation is accompanied by surface roughening because the slip direction is not parallel to the specimen surface. In the case of orientation *B*, the specimen surface is not roughened by dislocation accumulation.

In the following sections, the progress of dislocation accumulation will be calculated by using the theory of continuously distributed dislocations. The calculation is carried out in two-dimensional cases and the material is assumed to be isotropic. By considering long-life fatigue, the slip band is isolated and the distance between two neighboring layers is negligible compared with the length of pileup layers.

Dislocation Accumulation for the Case of Double Pileup. The cyclic shear stress on the primary slip plane in a most favorably oriented grain is shown in Fig. 3, where τ_1 is the maximum stress and τ_2 is the minimum stress in one cycle. The calculation will first be made for Case *B* shown in Fig. 2. The Cartesian coordinates x, y are used as indicated in the figure. The grain size is $2a$.

Under the first loading of stress τ_1 greater than the frictional stress k, the dislocation distribution with density $D_1(x)$ is produced on layer I. By assuming k to be constant, the equilibrium condition of dislocations inside layer I is expressed as

$$\tau_1{}^D + \tau_1 - k = 0, \tag{1}$$

where $\tau_1{}^D$ is the dislocation stress (back stress) given by

$$\tau_1{}^D = A \int_{-a}^{a} D_1(x')dx'/(x - x'). \tag{2}$$

The domain of the dislocation distribution is $-a < x < a$ and

$$A = Gb/2\pi(1 - \nu), \tag{3}$$

where b is the Burgers vector, G the shear modulus, and ν Poisson's ratio.

Equation (1) can be solved with the use of the inversion formula of Muskhelishvili under the condition of the unbounded density at two tips of the pileup $x = \pm a$ [5]. The dislocation density $D_1(x)$ is

$$\begin{aligned} D_1(x) &= \frac{1}{\pi^2 A} \frac{1}{(a^2 - x^2)^{1/2}} \int_{-a}^{a} (a^2 - x'^2)^{1/2} \frac{\tau_1 - k}{x - x'} dx' \\ &= (\tau_1 - k)x/\pi A(a^2 - x^2)^{1/2}. \end{aligned} \tag{4}$$

The total number of dislocations between $x = 0$ and a is

$$N_1 = \int_0^a D_1(x)dx = (\tau_1 - k)a/\pi A. \tag{5}$$

The plastic displacement $\phi(x)$ caused by the motion of dislocations generated at $x = 0$ is

$$\phi(x) = \int_x^a bD(x')dx' \tag{5a}$$

where $\phi(\pm a) = 0$.
The total plastic displacement γ_1 in $-a \leq x \leq a$ is

$$\gamma_1 = \int_{-a}^{a} \phi(x)dx = \int_{-a}^{a} bD_1(x)xdx = (\tau_1 - k)ba^2/2A. \tag{6}$$

The multiplication of the number of pileup layers in a unit area by the γ_1 value yields the macroscopic plastic strain. For simplicity, γ_1 is called the plastic strain. The stored energy of dislocations per unit thickness of the specimen is

$$U_1 = -\tfrac{1}{2}\int_{-a}^{a} \tau_1{}^D \phi(x)dx$$

$$= -\int_{-a}^{a} \tau_1{}^D bD_1(x)xdx/2 = \gamma_1(\tau_1 - k)/2. \qquad (7)$$

According to the present model, the reverse loading from the stress τ_1 to τ_2 causes the dislocations with a negative sign piling up on layer II, instead of the dislocations moving in the reverse direction on layer I. By denoting the density of dislocation piled up on layer II as $D_2(x)$ and the back stress due to $D_2(x)$ by $\tau_2{}^D$, the equilibrium condition in layer II is expressed as

$$\tau_2{}^D + \tau_1{}^D + \tau_2 + k = 0, \qquad (8)$$

where the friction stress k is acting on the motion of netative dislocations. The distance between layers I and II is assumed to be very small compared with the pileup length. Then, $\tau_1{}^D$ on layer II can be regarded as the same as on Layer I. Substitution of equation (1) into equation (8) yields

$$\tau_2{}^D - (\Delta\tau - 2k) = 0, \qquad (9)$$

where $\Delta\tau = \tau_1 - \tau_2$. Only when $\Delta\tau$ is larger than $2k$ can the dislocations on layer II be generated from $x = 0$ and pile up at $x = \pm a$. The dislocation density $D_2(x)$, the total number of dislocations N_2 between $x = 0$ and a, and the plastic strain γ_2 are obtained from equation (9) in a similar way. These are

$$\left.\begin{aligned} D_2(x) &= -(\Delta\tau - 2k)x/\pi A(a^2 - x^2)^{1/2} \\ N_2 &= -(\Delta\tau - 2k)a/\pi A \\ \gamma_2 &= -(\Delta\tau - 2k)ba^2/2A. \end{aligned}\right\} \qquad (10)$$

The values of N_2 and γ_2 are negative. The stored energy of dislocations $D_2(x)$ is the positive value

$$U_2 = -\gamma_2(\Delta\tau - 2k)/2. \qquad (11)$$

The pileup of negative dislocations on layer II causes a positive back stress on layer I. This back stress enhances the pileup of dislocations on layer II during the subsequent reverse loading.

The increment of dislocation $D_k(x)$, the dislocation number N_k, the plastic strain increment γ_k, the back stress increment $\tau_k{}^D$, and the stored energy U_k at the kth step of the forward and reverse loading processes are obtained in a similar manner. They are

$$D_k(x) = (-1)^{k+1}\Delta D(x), \quad N_k = (-1)^{k+1}\Delta N, \quad \gamma_k = (-1)^{k+1}\Delta\gamma$$

$$\tau_k{}^D = (-1)^{k+1}(2k - \Delta\tau), \quad U_k = \Delta U \qquad (12)$$

where

$$\begin{aligned} \Delta\tau &= \tau_1 - \tau_2 \\ \Delta D(x) &= (\Delta\tau - 2k)x/\pi A(a^2 - x^2)^{1/2} \\ \Delta N &= (\Delta\tau - 2k)a/\pi A \\ \Delta\gamma &= (\Delta\tau - 2k)ba^2/2A \\ \Delta U &= \Delta\gamma(\Delta\tau - 2k)/2. \end{aligned} \qquad (13)$$

The index k takes $2n$ at the minimum stress after n-cycles and $2n + 1$ at the maximum stress after n-cycles.

Stress Distribution and Strain Energy at the Maximum Stress After *n*-Cycles. The total density of dislocations $D_I(x)$ piled up on layer I, their number N_I and stored strain energy U_I are given as the sum of the increments of the corresponding values made during each loading stage. They are

$$D_I(x) = \sum_{n=0}^{n} D_{2n+1}(x) = D_1(x) + n\Delta D(x) \qquad (14)$$

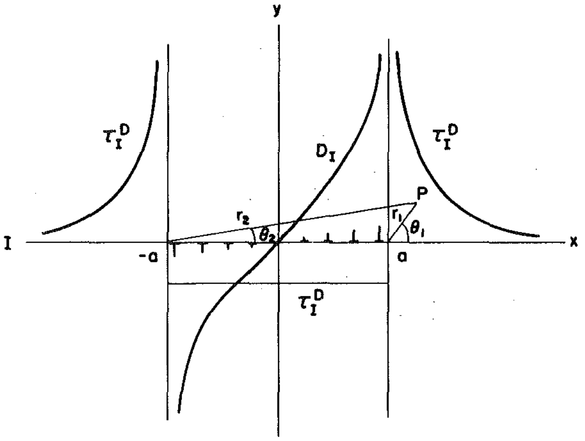

Fig. 4 Dislocation distribution on layer I and its stress distribution for the case of double pileup

$$N_I = \sum_{n=0}^{n} N_{2n+1} = N_1 + n\Delta N \qquad \begin{matrix}(14)\\(Cont.)\end{matrix}$$

$$U_I = \sum_{n=0}^{n} U_{2n+1} = U_1 + n\Delta U.$$

The corresponding values for dislocation pileup on layer II are

$$\begin{aligned} D_{II}(x) &= \sum_{n=1}^{n} D_{2n}(x) = -n\Delta D(x) \\ N_{II} &= \sum_{n=1}^{n} N_{2n} = -n\Delta N \\ U_{II} &= \sum_{n=1}^{n} U_{2n} = n\Delta U. \end{aligned} \qquad (15)$$

The stress field after n-cycles can be given as the sum of three components: the applied stress, the internal stresses due to the dislocation pileups on layers I and II. From equations (4), (13), and (14), the dislocation density $D_I(x)$ is given as

$$D_I(x) = T_I x/\pi A(a^2 - x^2)^{1/2} \qquad (16)$$

where

$$T_I = \tau_1 - k + n(\Delta\tau - 2k). \qquad (17)$$

The aforementioned dislocation distribution is the same as the distribution of crack dislocations for a crack with length $2a$ subjected to the shear stress T_I [6]. The stress field due to the pileup dislocation density $D_I(x)$ is identical to that due to the crack. Fig. 4 shows the shear stress distribution on $y = 0$, together with the dislocation distribution. The stress intensification takes place only near the tips of the pileup. The singular terms of the stress field in the vicinity of the right-hand tip of the pileup are expressed as [6, 7]

$$\begin{aligned} \sigma_{xx}{}^{D_I} &= -\frac{K_I}{(2\pi r_1)^{1/2}}\sin\frac{\theta_1}{2}\left(2 + \cos\frac{\theta_1}{2}\cos\frac{3\theta_1}{2}\right) \\ \sigma_{yy}{}^{D_I} &= \frac{K_I}{(2\pi r_1)^{1/2}}\sin\frac{\theta_1}{2}\cos\frac{\theta_1}{2}\sin\frac{3\theta_1}{2} \\ \sigma_{xy}{}^{D_I} = \tau_I{}^D &= \frac{K_I}{(2\pi r_1)^{1/2}}\cos\frac{\theta_1}{2}\left(1 - \sin\frac{\theta_1}{2}\sin\frac{3\theta_1}{2}\right) \end{aligned} \qquad (18)$$

where K_I is the stress-intensity factor given by

$$K_I = T_I\sqrt{\pi a} = [(\tau_1 - k) + n(\Delta\tau - 2k)]\sqrt{\pi a}. \qquad (19)$$

The stress field due to the dislocation pileup on layer II is identical to that caused by a crack under the negative shear stress

$$T_{II} = -n(\Delta\tau - 2k). \qquad (20)$$

The stress-intensity factor is

$$K_{\mathrm{II}} = T_{\mathrm{II}}\sqrt{\pi a} = -n(\Delta\tau - 2k)\sqrt{\pi a}. \qquad (21)$$

In low-strain, long-life fatigue, the values of T_{I} and K_{I} are nearly equal to the negative values of T_{II} and K_{II}, because the term $\tau_1 - k$ becomes negligible compared with the term $n(\Delta\tau - 2k)$ near crack initiation.

Dislocation Accumulation for the Cases of Single Pileups. If the dislocation source is at the grain boundary in Case B shown in Fig. 2, only positive dislocations are generated on layer I under forward loading and negative ones on layer II under reverse loading. The equilibrium equation (1) is now solved under the condition that the density is bounded at $x = -a$ and unbounded at $x = a$. The density $D_1(x)$ is

$$D_1(x) = (\tau_1 - k)(a + x)^{1/2}/\pi A(a - x)^{1/2}. \qquad (22)$$

The total number of dislocations is given by

$$N_1 = (\tau_1 - k)a/A. \qquad (23)$$

This is equal to the ledge of the grain boundary formed in dislocation generation, when it is multipled by the Burgers vector. Since the dislocation source is at $x = -a$, the plastic strain γ_1 is calculated as

$$\gamma_1 = \int_{-a}^{a} bD(x)(x + a)dx = 3(\tau_1 - k)ba^2/2A. \qquad (24)$$

Equation (22) can be rewritten as

$$D_1(x) = (\tau_1 - k)x/\pi A(a^2 - x^2)^{1/2} + (\tau_1 - k)a/\pi A(a^2 - x^2)^{1/2}. \qquad (25)$$

The first term is equal to equation (4) and the second term is the distribution for unstressed pileup of positive dislocations with the number N_1. The stored energy of the latter distribution is given by Hirth and Lothe [8] as $(N_1{}^2\, b/2A)\ \ln\,(2R/a)$, where R is the outer cutoff radius of the dislocation stress field. Therefore, the stored strain energy is

$$U_1 = C\gamma_1(\tau_1 - k)/2 \qquad (26)$$

where

$$C = 1/3[1 + 2\ln\,(2R/a)]. \qquad (27)$$

The dislocation accumulation in the subsequent stages is expressed by equations (12) with the following substitution:

$$\Delta D(x) = (\Delta\tau - 2k)(a + x)^{1/2}/\pi A(a - x)^{1/2}, \qquad \Delta N = (\Delta\tau - 2k)a/A$$

$$\Delta\gamma = (\Delta\tau - 2k)3ba^2/2A, \quad \Delta U = C\Delta\gamma(\Delta\tau - 2k)/2. \qquad (28)$$

Equations (14) and (15) can be used as expressions for the dislocation accumulation after n-cycles. The dislocation density on layer I is

$$D_{\mathrm{I}}(x) = T_I(a + x)^{1/2}/\pi A(a - x)^{1/2} \qquad (29)$$

where T_{I} is given by equation (17). The stresses, $\sigma_{xx}{}^{D_{\mathrm{I}}}$, $\sigma_{yy}{}^{D_{\mathrm{I}}}$, and $\sigma_{xy}{}^{D_{\mathrm{I}}} = \tau_I{}^D$, due to $D_{\mathrm{I}}(x)$, can be calculated by adding the stresses caused by each dislocation. The stresses are calculated to be

$$\sigma_{xx}{}^{D_{\mathrm{I}}} = -\frac{T_{\mathrm{I}}}{\sqrt{r_1}}\left\{\frac{ay}{r_1\sqrt{r_2}}\cos\left(\frac{3\theta_1 + \theta_2}{2}\right) + 2\sqrt{r_2}\sin\left(\frac{\theta_1 - \theta_2}{2}\right)\right\}$$

$$\sigma_{yy}{}^{D_{\mathrm{I}}} = \frac{T_{\mathrm{I}}}{\sqrt{r_1}}\left(\frac{ay}{r_1\sqrt{r_2}}\right)\cos\left(\frac{3\theta_1 + \theta_2}{2}\right) \qquad (30)$$

$$\sigma_{xy}{}^{D_{\mathrm{I}}} = \frac{T_{\mathrm{I}}}{\sqrt{r_1}}\left\{\sqrt{r_2}\cos\left(\frac{\theta_1 - \theta_2}{2}\right) - \frac{ay}{r_2\sqrt{r_1}}\sin\left(\frac{3\theta_1 + \theta_2}{2}\right)\right\} - \tau$$

where (r_1, θ_1) and (r_2, θ_2) are the coordinates shown in Fig. 4. By expanding the foregoing equation near the right-hand tip of the pileup, it can be seen that this stress field also has a singularity similar to the shear crack stress field. The stress-intensity factor is given by

$$K_{\mathrm{I}} = 2T_{\mathrm{I}}\sqrt{\pi a} = 2[\tau_1 - k + n(\Delta\tau - 2k)]\sqrt{\pi a}. \qquad (31)$$

Similarly, the stress-intensity factor for the stress field due to the pileup dislocations on layer II is

$$K_{\mathrm{II}} = 2T_{\mathrm{II}}\sqrt{\pi a} = -2n(\Delta\tau - 2k)\sqrt{\pi a}. \qquad (32)$$

The analysis of Case A, of single pileup from the surface, shown in Fig. 1 is complicated because of the image force of the free surface. The exact solution cannot be obtained in a closed form. Two approximations will be considered.

The solutions for Case B of double pileup could be used by regarding one half of the pipeup as imaginary. In this approximation, the right-hand side of the double pileup in Fig. 2 corresponds to a vacancy dipole pileup with the extrusion shown in Fig. 1(a), while the left-hand side corresponds to an interstitial dipole pileup with the intrusion shown in Fig. 1(b). The amounts of intrusion and extrusion are obtained by multiplying the total number of dislocations with the Burgers vector. A second approximation can be given by regarding the length of a single pileup in an infinite plate as the length of the slip band emanated from the surface. The former approximation is expected to yield the lower bound of the solution and the latter, its upper bound.[2] The extrusion-intrusion pair can be formed when the negative dislocation motion takes place on two layers adjacent to layer I as shown in Fig. 1(c).

Crack Initiation. There are three ways for an embryonic crack to be formed in dislocation pileup accumulated under cyclic stress. A large tensile stress built up between two layers at the top of the pileups of vacancy dipoles shown in Figs. 1 and 2 could become large enough to create the nucleus of a crack. Since the densities of pileup dislocation on two layers are about the same for long-life fatigue, except for the sign, the tensile stress σ_{xx} at $x = a$ and at half the distance between two layers is given as follows using equations (18), (19), and (21):

$$\sigma_{xx} = \sigma_{xx}{}^{D_{\mathrm{I}}} + \sigma_{xx}{}^{D_{\mathrm{II}}} = 3\sqrt{a}\, n(\Delta\tau - 2k)/\sqrt{2h} \qquad (33)$$

where h is the distance between two layers. The number of stress cycles for the formation of a crack embryo is given from the aforementioned equation by assuming that the crack is nucleated when σ_{xx} becomes the theoretical strength. For Case A shown in Fig. 1, embryonic cracks are formed inside the material at the grain boundary of the surface grain where the vacancy dipoles are piled up. The site of crack nucleation is on the surface at the grain boundary in Case B in Fig. 2.

Formation of intrusion causes the stress concentration under the applied stress, and it can also be regarded as the crack embryo. The depth of intrusion equals the total number of accumulated dislocations, $N_{\mathrm{I}} = N_{\mathrm{II}} = n\Delta N$, multiplied by the Burgers vector. It increases in each cycle and is $n\ b\Delta N$ after n-cycles. Equation (13) or (28) can be used as an approximation for ΔN in the case of orientation A. The third possible site is the ledge left at the grain boundary when the dislocation source is at the grain boundary in the case of orientation B. The size of the ledge is equal to $n\ b\Delta N$ where ΔN is given by equation (28). In the previous two cases, it is rather difficult to determine the define length of time for the formation of an embryonic crack.

The following growth of a crack embryo will take place along the slip bands. Fig. 5 illustrates two types of initiation and growth of cracks. The condition of the growth of the crack embryo will be treated from the viewpoint of energy balance. If the stored strain energy due to dislocations accumulated after n-cycles becomes equal to the surface energy, the layers of dislocation dipoles can be transformed into a free surface. The life of the crack initiation n_c is now defined as the number of stress cycles when the following energy condition is satisfied:

$$U = U_{\mathrm{I}} + U_{\mathrm{II}} = 2n_c\Delta U = 4\ a w_s \qquad (34)$$

---

[2] The stress-intensity factor for the surface crack with length a under shear stress τ is $1.12\ \tau\sqrt{\pi a}$ [7]. The first approximation yields $\tau\sqrt{\pi a}$ as the stress-intensity factor, while the second approximation yields $1.41\ \tau\sqrt{\pi a}$.

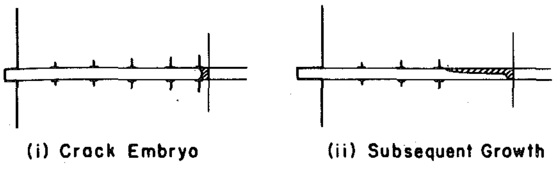

(i) Crack Embryo (ii) Subsequent Growth

(a) Crack initiation from vacancy dipoles or extrusion

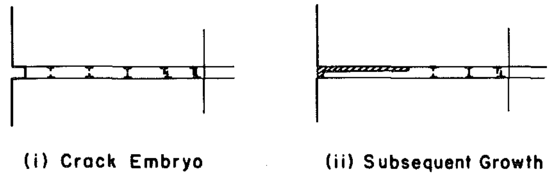

(i) Crack Embryo (ii) Subsequent Growth

(b) Crack initiation from intrusion

Fig. 5 Two types of crack initiation; (*a*) Crack initiation from vacancy dipoles or extrusion, (*i*) crack embryo, (*ii*) subsequent growth; (*b*) Crack initiation from intrusion, (*i*) crack embryo, (*ii*) subsequent growth

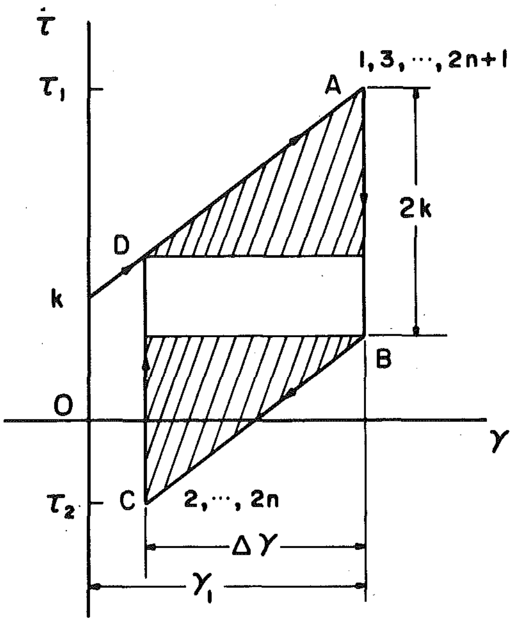

Fig. 6 Stress-strain hysteresis loop

for Case B with the pileup length $2a$. The value of w_s is the specific fracture energy for a unit area. The right-hand side of the equation is $2\,aw_s$ for Case A. For a double pileup case, n_c is

$$n_c = 4\,aw_s/(\Delta\tau - 2k)\Delta\gamma$$

$$= 2bw_s a^3/A(\Delta\gamma)^2 \qquad (35)$$

$$= 8\,Aw_s/ba(\Delta\tau - 2k)^2 \qquad (36)$$

where equation (13) is used in the derivation. For the case of a single pileup of orientation A, w_s is substituted by w_s/C in the foregoing equations. For general cases, including the single pileup for orientation B, the previous equations are applicable with a minor change of the coefficient.

Discussion

A most striking advantage of the present model is that the progress of the ratcheting of a plastic deformation in the slip band can be calculated in each forward and reverse loading. The irreversibility of dislocation motion in two neighboring layers as assumed in the model can be realized if the friction stress against the dislocation motion is higher in the reverse direction than in the forward direction by a small amount. Only when the dislocation sources are located very close to each other, the dislocation accumulation can take place as calculated in the previous chapter. For the case of an isolated dislocation source, the dislocation motion on a single plane becomes reversible because no positive back stress is produced by the dislocations on a secondary layer. In the real situation, the motion of dislocations will be irreversible or reversible depending on a statistical distribution of dislocation sources.

Two neighboring layers considered in the model can be regarded as the zone of strain localization such as the persistent slip bands found in low strain fatigue. Several experiments have been reported on the slip movement under cyclic stress and most of them indicated a certain irreversibility of plastic deformation. Keith and Gilman [9] observed in their etch pit study in lithium fluoride crystals that dislocation movements were irreversible under cyclic stressing except for the small motion of dislocation loops. More macroscopically, Charsley and Desvaux [10, 11] found that a partial reversal of the tensile slip steps and extrusion-type or intrusion-type slip steps occurred during compression, but no total reversal was seen in single crystals with wavy and planar slip modes. Their observations substantiate partly the assumption of the present model.

The slip step within the persistent slip bands in copper single crystals was observed by Finney and Laird [12] with the interferometric technique. In their observations, the macroscopic strain carried out by the persistent slip bands was reversible; only at the finest distribution of slip within the band was the deformation not strictly reversible. The macroscopic behavior of the cyclic stress-strain hysteresis of the slip band derived from the present model is shown in Fig. 6. In the first forward loading up to τ_1, the material hardens linearly with the plastic strain according to equation (6) or (24). During the next reverse loading, the stress-strain relation follows the *ABC* path shown in the figure. The amount of plastic strain range $\Delta\gamma$ is a linear function of the stress range subtracted by twice the friction stress as given by equation (13) or (28). The subsequent forward and reverse loadings result in the closed hysteresis loop *CDABC* of stress and strain. The hysteresis loop is macroscopically reversible, which agrees with the finding by Finney and Laird [12] or more generally with the hysteresis loop found at the saturation stage of the fatigue process.

Although the irreversibility of dislocation motion as assumed in the present model has not yet been fully rationalized, either experimentally or theoretically, the success in evaluating the ratcheting deformation and the reasonable estimate of crack initiation life given as follows will make the irreversibility assumption acceptable as an extreme case. Obviously, further studies are required on the dislocation motion under cyclic stressing.

The energy criterion for crack initiation gives a direct correspondence to the Coffin-Manson relation. From equation (35), we have

$$n_c(\Delta\gamma)^2 = 2\,bw_s a^3/A. \qquad (37)$$

The right-hand term is a material parameter which is independent of the applied stress. Coffin [13] and Manson [14] originally found the life law for complete fracture of smooth specimens under high strain cycling. Later, a similar law was confirmed to be valid for low-strain and long-life fatigue [15]. The life up to the initiation of the crack on the grain size order was about 50 percent of the total life without respect to the stress amplitude in long-life fatigue [16]. Therefore, the Coffin-Manson relation seems to be valid for the initiation of crack in long-life fatigue, with which the present model is concerned. The strain energy of dislocations is accumulated in the same amount in each forward and reverse loading except the first loading. The amount of stored energy does not correspond to the total area of the hysteresis loop, but only to the shaded area shown in Fig. 6. The energy corresponding to the remaining area of the loop is the dissipated work against the friction stress. Martin [17] derived the Coffin-Manson relation about 20 years ago by regarding the segment of the plastic

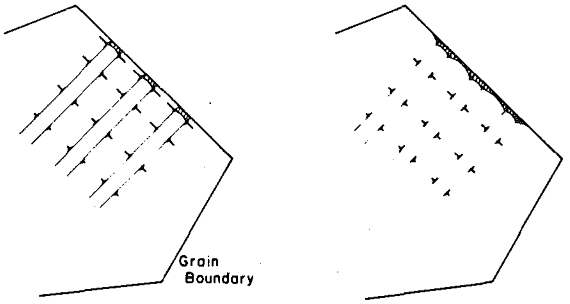

(a) Crack Embryo (b) Subsequent Growth

Fig. 7 Grain boundary crack initiated by stacked pileups of vacancy dipoles; (a) crack embryo, (b) subsequent growth

work associated with work hardening as accumulating damage. The present model gives a clear interpretation of his accumulating damage as the dislocation strain energy stored in the material by the irreversible motion of dislocations.

The initiation life expressed by equation (36) in terms of stresss can be rewritten as

$$\Delta\tau = 2k + (8\,Aw_s/bn_c)^{1/2}a^{-1/2}. \tag{38}$$

Since the length $2a$ is the grain size, the previous equation is of the Petch type for constant initiation life. The Petch-type relation has been reported for the long-life fatigue of several metals [16, 18].

The value of w_s consists of the surface energy and the plastic fracture work. Because no reliable data have been reported on the Coffin-Manson type and the Petch-type equations for crack initiation, the exact estimate of w_s is difficult. The following equation of the Petch type is reported by Taira and others [16] for the endurance limit for low carbon steel:

$$\sigma_e = 114 + 0.329/\sqrt{d} \tag{39}$$

where σ_e (MPa) is the stress amplitude of the endurance limit and d (meters) is the grain size. By using $E = 2.1 \times 10^5$ MPa, $\nu = 0.3$, $n_c = 10^6$ and $d = 2a$, the value of w_s estimated from equations (38) and ((39) is 3.8×10^5 N/m. This is much larger than the surface energy of iron, so the plastic fracture work is predominant.

Among the three possible sites for the formation of an embryonic crack, which site to operate is greatly dependent upon the material involved. The relaxation zone which may occur at the pileup tip in the vicinity of grain boundaries reduces the stress concentration and prolongs the time of embryonic crack formation in the cases of orientation A and B. This concurs with the fact that internal cracks are rarely observed beneath the extrusions [1, 2]. For general cases, screw dislocation movement is superimposed on the edge dislocation motion and the intrusion and extrusion are formed in the slip band, shortening the initiation life of a crack embryo. In the fatigue of a copper single crystal, Ebner and Backofen [19] observed the difficulty of crack initiation when the primary slip direction is parallel to the specimen surface such as in the grain with orientation B. However, such an observation has not been reported with respect to polycrystalline materials.

If the materials contain inclusions, the slip motion can be blocked by the inclusions and the crack can be initiated at the inclusions [1]. This type of crack initiation can also be analyzed using the present model of dislocation accumulation combined with a proper fracture criterion.

When the applied stress or strain is relatively high, the slip deformation is rather uniform within a grain, and the grain boundary becomes a preferential site for crack initiation. The stacking of slip bands which contain the pileups of dislocation dipoles can give an explanation of the grain boundary cracking. Fig. 7 illustrates the situation. Several embryonic cracks are made along the grain boundary by the stacking of pileups of vacancy dipoles, and are connected to a boundary crack under the action of the tensile stress normal to the bounary. Under even higher strain, the deformation is almost uniform within a grain and then a single slip band or its stacking may no longer be appropriate for expressing the deformation in a grain. The cubical dependence of the right-hand term of the Coffin-Manson type equation (37) on the grain size will disappear. The micromechanics of inclusions will be a tool in treating the deformation of a single grain in the plastically deformed polycrystalline matrix [20]. Nonetheless, in this case the model of monotonic builtup plastic deformation under cyclic stress will play an essential role as an elementary process.

An application of the present model and its refinement will be made in the future in each particular case of materials and testing conditions.

A phenomenological approach by Zarka, et al., [21] can also derive conditions for the cyclic ratcheting.

Conclusions

With regard to the plastic flow within the slip band in a most favorably oriented grain in low strain fatigue, the assumption of the irreversibility of dislocation motion yields a systematic increase in the amount of pileups of dislocation dipoles under cyclic loading. Forward loading causes a pileup of dislocations with a positive sign on one layer; the reverse flow is taken up by the dislocations with a negative sign moving on subsequent layers which are located very close to the first layer. The ratcheting deformation takes place with the help of the back stress due to dislocations made in a previous loading stage. While the macroscopic stress-strain hysteresis follows the saturated closed loop, the pileup of dislocation dipoles and the surface roughening are monotonically increased in quantity. The theoretical analysis of the model for two-dimensional cases, using the continuously distributed dislocation theory, yielded an exact assessment of the accumulation of dislocations together with the cyclic stress-strain behavior.

Several possible sites for the formation of the crack embryo were examined based on the stress distribution of accumulated dislocations and on the geometrical irregularities of the surface and the grain boundary. The sites are at the tip of the pileup of vacancy dipoles, the intrusion, and the ledge of the grain boundary. The material properties were expected to affect which site to operate. The time of the initiation of a crack of the grain size order was determined as the time when the stored energy of accumulated dislocations reaches a critical value. The relation between the initiation life thus determined and the plastic strain range is in agreement with the Coffin-Manson law, and that between the grain size and the fatigue strength is expressed in the functional form of the Petch type. Finally, several possible applications of the present model were suggested in relation to the other modes of fatigue crack initiation.

Acknowledgments

This work was supported by the National Science Foundation through the Materials Research Center of Northwestern University under Grant No. The authors are pleased to acknowledge discussions with Prof. Morris E. Fine of Northwestern University.

References

1 Grosskreutz, J. C., "The Mechanisms of Metal Fatigue," *physica status solidi*, (b), Vol. 47, 1971, pp. 359–396.

2 Laird, C., and Duquette, D. J., "Mechanisms of Fatigue Crack Nucleation," *Corrosion Fatigue*, eds. Devereux, O. F., McEvily, A. J., and Staehle, R. W., NACE 2, 1972, pp. 88–117.

3 Mott, N. E., "A Theory of the Origin of Fatigue Cracks," *Acta Metallurgica*, Vol. 6, 1958, pp. 195–197.

4 Lin, T. H., and Ito, Y. M., "Mechanics of Fatigue Crack Nucleation Mechanism," *Journal of the Mechanics and Physics of Solids*, Vol. 17, 1969, pp. 511–523.

5 Head, A. K., and Louat, N., "The Distribution of Dislocations in Linear Arrays," *Australian Journal of Physics*, Vol. 8, 1955, pp. 1–7.

6 Bilby, B. A., and Eshelby, J. D., "Dislocations and the Theory of Fracture," *Fracture*, ed., Liebowitz, H., Vol. 1, 1968, pp. 99–182.

7 Tada, H., Paris, P. C., and Irwin, G. R., *The Stress Analysis of Cracks Handbook*, Del Research Corporation, 1973, p. 1.3 and 2.29.

8 Hirth, J. P., and Lothe, J., "Dislocation Pileups," *Theory of Dislocations*, McGraw-Hill, New York, 1968, pp. 694–718.

9 Keith, R. E., and Gilman, J. J., "Progress Report on Dislocation Behavior in Lithium Fluoride Crystals During Cyclic Loading," ASTM Special Technical Publications, No. 237, 1959, pp. 3–20.

10 Charsley, P., and Desvaux, M. P. E., "The Behavior of Copper—12 Percent Aluminum Under Simple Reversed Stresses," *Materials Science and Engineering*, Vol. 4, 1969, pp. 211–220.

11 Desvaux, M. P. E., and Charsley, P., "Slip Lines on Pure Copper Deformed in Tension and Compression," *Materials Science and Engineering*, Vol. 4, 1969, pp. 221–230.

12 Finney, J. M., and Laird, C., "Slip Localization in Cyclic Deformation of Copper Single Crystals," *Philosophical Magazine*, Vol. 31, 1975, pp. 339–366.

13 Coffin, L. F., "A Study of the Effects of Cyclic Thermal Stresses on Ductile Metals," ASME TRANS., Vol. 76, 1954, pp. 931–950.

14 Manson, S. S., "Behavior of Materials Under Conditions of Thermal Stress," NACA, TN, 2933, 1954.

15 Lukáš, P., Klesnil, M., and Polák, J., "High Cycle Fatigue Life of Metals," *Materials Science and Engineering*, Vol. 15, 1974, pp. 239–245.

16 Taira, S., Tanaka, K., and Hoshina, M., "Grain Size Effect on Crack Nucleation and Growth in Long-Life Fatigue of Low-Carbon Steel," ASTM Special Technical Publications, No. 675, 1979, pp. 135–173.

17 Martin, D. E., "An Energy Criterion for Low-Cycle Fatigue," ASME *Journal of Basic Engineering*, Vol. 83, 1961, pp. 565–571.

18 Thompson, A. W., and Backofen, W. A., "The Effect of Grain Size on Fatigue," *Acta Metallurgica*, Vol. 19, 1971, pp. 597–606.

19 Ebner, M. L., and Backofen, W. A., "Fatigue of Single Crystals of Copper," *Transactions AIME*, Vol. 215, 1959, pp. 510–520.

20 Mura, T., and Mori, T., "Applications of Micromechanics," *Micromechanics*, Baifu-kan, Tokyo, 1975, pp. 149–170.

21 Zarka, J., Engel, J. J., and Inglebert, G., "On a Simplified Inelastic Analysis of Structures," *Nuclear Engineering Design*, Vol. 57, 1980, pp. 333–368.

G. M. L. Gladwell

Professor,
Solid Mechanics Division,
Department of Civil Engineering,
University of Waterloo,
Waterloo, Ontario N21 3G1,
Canada

The Contact Problem for a Rigid Inclusion Pressed Between Two Dissimilar Elastic Half Planes

Paper concerns the plane-strain problem of a rigid, thin, rounded inclusion pressed between two isotropic elastic half planes with different elastic constants. Required to find the extents of the contact regions between each plane and the inclusion, and the contact stress distributions. The governing integral equations are solved approximately by using Chebyshev expansions. Numerical results are presented.

Introduction

The plane-strain problem which will be studied is shown in Fig. 1. Two elastic half planes with shear moduli and Poisson's ratios μ_i, ν_i $(i = 1, 2)$, respectively, are pressed together by a pressure which at infinity is given by $\tau_{yy} = -p_0$. A rigid obstacle, symmetrical in x but not necessarily in y, lies between the two half planes. It is assumed that the contacts between the two half planes, and between the obstacle and each half plane, are all frictionless. It is required to find the extents of the contact regions and the displacement and stress fields.

The problem for two identical half planes was solved in closed form by Alblas [1]. The corresponding problem for two identical *layers* was solved by Alblas [2]; both problems were solved by Gladwell [3, 4] by using Chebyshev polynomial representations.

Formulation

Boundary values of displacements, stresses, etc., for $y = 0^{\pm}_{-}$ will be labeled 1, 2, respectively. The profiles of the obstacle for $y = 0^{\pm}_{-}$ may then be taken as $y = \pm f_i(x)$ where, for infinitesimal elasticity theory, there is no loss of generality if one assumes that

$$f_i(x) = d_i - x^2/(2r_i). \qquad (1)$$

If $p_i(x) \equiv -\tau^{(i)}_{yy}\,(x,\,0)$, the boundary conditions on $y = 0$ may be written

$$-\infty < x < \infty, \quad \tau^{(i)}_{xy}\,(x,\,0) = 0, i = 1, 2, \qquad (2)$$

$$\left.\begin{aligned} c_i \le |x| \le l,\ & p_i(x) = 0, \qquad i = 1,2,\\ |x| \ge l,\ & p_1(x) = p_2(x), \end{aligned}\right\} \qquad (3)$$

$$\left.\begin{aligned} &|x| \le c_i, v_i(x) = (-)^{i-1} f_i(x),\ i = 1,2,\\ &|x| \ge l,\ v_1(x) = v_2(x) \end{aligned}\right\} \qquad (4)$$

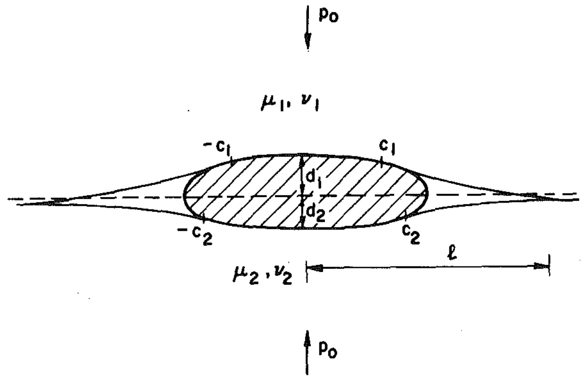

Fig. 1 **A rigid obstacle is pressed between two dissimilar half planes**

In addition there are the conditions at infinity

$$\tau^{(i)}_{xx}\,(x,\,y) = 0 = \tau^{(i)}_{xy}\,(x,\,y), \quad \tau^{(i)}_{yy}\,(y,\,y) = -p_0 \ \ as \ \ (x^2 + y^2) \to \infty, \qquad (5)$$

the equilibrium conditions on the obstacle

$$P \equiv \int_{-c1}^{c1} p_1(x)dx = \int_{-c_2}^{c2} p_2(x)dx, \qquad (6)$$

and the condition of compression in the contact regions, namely,

$$-\infty < x < \infty, \quad p_i(x) \ge 0, \quad i = 1, 2. \qquad (7)$$

The solution for each half plane may be obtained as the superposition of two fields. The first corresponds to a uniform stress field in the y-direction, namely, $\tau^{(i)}_{yy}\,(x,\,y) = -p_0$, for which

$$2\mu_i u_i(x,\,y) = \nu_i p_0 x, \quad 2\mu_i v_i(x,\,y) = -(1 - \nu_i) p_0 y. \qquad (8)$$

The second may be expressed in terms of Fourier cosine transforms. Thus, if $v_i(x)$, $p_i(x)$ are the combined fields then (Sneddon [5, p. 457]) on the x-axis

---

Contributed by the Applied Mechanics Division for publication in the JOURNAL OF APPLIED MECHANICS.

Discussion on this paper should be addressed to the Editorial Department, ASME, United Engineering Center, 345 East 47th Street, New York, N. Y. 10017, and will be accepted until June 1, 1981. Readers who need more time to prepare a Discussion should request an extension from the Editorial Department. Manuscript received by ASME Applied Mechanics Division, March, 1980; final revision, July, 1980.

$$v_i(x) = (-)^{i-1}\vartheta_i\, \mathcal{F}_c[\xi^{-1}P_i(\xi); x] \tag{9}$$

$$p_i(x) - p_0 = \mathcal{F}_c[P_i(\xi); x] \tag{10}$$

where $\vartheta_i = (1 - \nu_i)/\mu_i$. It is convenient to work with displacement derivatives; then

$$v_i'(x) = (-)^i\vartheta_i\, \mathcal{F}_s[P_i(\xi); x] \tag{11}$$

and equations (4) may be replaced by

$$\left.\begin{array}{l} |x| \le c_i, v_i'(x) = (-)^{i-1}f_i'(x), \quad i = 1, 2, \\ |x| \ge l, \;\; v_1'(x) = v_2'(x), \end{array}\right\} \tag{12}$$

provided that the compatibility equation

$$v_1(l) \equiv f_1(c_1) + \int_{c_1}^{l} v_1'(x)dx = -f_2(c_2) + \int_{c_2}^{l} v_2'(x)dx \equiv v_2(l) \tag{13}$$

is satisfied.

If the common contact pressure for $|x| \ge l$ is denoted by $q(x)$, then equations (3) and (10) yield

$$\mathcal{F}_c[P_i(\xi); x] = \begin{cases} p_i(x) - p_0, & |x| \le c_i, \\ -p_0, & |c_i| < |x| < l, \\ q(x) - p_0, & |x| \ge l. \end{cases} \tag{14}$$

But (Lowengrub [6]) if

$$\mathcal{F}_c[F(\xi); x] = f(x), \quad -\infty < x < \infty \tag{15}$$

then

$$\mathcal{F}_s[F(\xi); x] = -\frac{1}{\pi}\int_{-\infty}^{\infty}\frac{f(t)dt}{t - x} \tag{16}$$

provided that $f(x)$ is an even function of x. Thus

$$\mathcal{F}_s[P_i(\xi); x] = -\frac{1}{\pi}\int_{-c_i}^{c_i}\frac{p_i(\xi) - p_0}{\xi - x}d\xi + \frac{1}{\pi}\int_{L_i}\frac{p_0 d\xi}{\xi - x} - \frac{1}{\pi}\int_{L}\frac{q(\xi) - p_0}{\xi - x}d\xi, \tag{17}$$

where $L_i = (-l, -c_i) \cup (c_i, l)$ and $L = (-\infty, -l) \cup (l, \infty)$. This representation for $\mathcal{F}_s[P_i(\xi); x]$, when linked to equations (12), yields three integral equations of Cauchy type, one on each of $(-c_i, c_i)$ and one on L. In principle it is possible to solve for either q or p_1, p_2 in terms of p_1, p_2 or q, respectively, but not only are the integral equations so obtained extremely complicated but also it is still necessary to satisfy the side conditions (6), (7), and (13). An approximate solution seems preferable.

Chebyshev Polynomial Solution

An appropriate representation for $p_i(x)$, an even function of x with $(c_i^2 - x^2)^{1/2}$ behavior at $\pm c_i$, is

$$p_i(x) = p_0(1 - x^2/c_i^2)^{1/2}\sum_{n=1}^{N} a_n^{(i)}\, U_{2n-2}(x/c_i) \tag{18}$$

where $U_n(x)$ is the Chebyshev polynomial of the second kind. The integrals in (17) involving $p_i(\xi)$ may be evaluated explicitly by using the result (Gladwell [3])

$$R_n(t) \equiv -\frac{1}{\pi}\int_{-1}^{1}\frac{(1 - \tau^2)^{1/2}U_{n-1}(\tau)d\tau}{\tau - t} = \begin{cases} T_n(t), & |t| \le 1, \\ [t - \operatorname{sign}(t)(t^2 - 1)^{1/2}]^n, & |t| > 1, \end{cases} \tag{19}$$

where $T_n(t)$ is the Chebyshev polynomial of the first kind. Thus

$$\frac{1}{\pi}\int_{-c_i}^{c_i}\frac{p_i(\xi)d\xi}{\xi - x} = -p_0\sum_{n=1}^{N} a_n^{(i)}\, R_{2n-1}(x/c_i). \tag{20}$$

The contact stress $q(x)$ is an even function of x, with $(x^2 - l^2)^{1/2}$ behavior near $x = l+$ and with limiting value p_0 as $x \to \infty$. A suitable representation is

$$q(x) = p_0(1 - t^2)^{1/2} + p_0 t(1 - t^2)^{1/2}\sum_{n=1}^{N} b_n U_{2n-1}(t), \tag{21}$$

where $t = l/x$. The integrals involving $q(x)$ in (17) may then be transformed into those of type (19), leading to

$$v_i'(x) = (-)^{i-1}\vartheta_i p_0\left\{R_1(t) + t\sum_{n=1}^{N} b_n R_{2n}(t) - \sum_{n=1}^{N} a_n^{(i)}\, R_{2n-1}(x/c_i)\right\}. \tag{22}$$

Thus equations (12) become

$$\vartheta_i p_0\left\{R_1(t) + t\sum_{n=1}^{N} b_n R_{2n}(t) - \sum_{n=1}^{N} a_n^{(i)}\, T_{2n-1}(x/c_i)\right] = f_1'(x), \tag{23}$$

where $i = 1, 2$ and $|x| \le c_i$, and

$$\vartheta_1'\left\{T_1(t) + t\sum_{n=1}^{N} b_n T_{2n}(t) - \sum_{n=1}^{N} a_n^{(1)}\, R_{2n-1}(x/c_1)\right\} = -\vartheta_2\left\{T_1(t) + t\sum_{n=1}^{N} b_n T_{2n}(t) - \sum_{n=1}^{N} a_n^{(2)}\, R_{2n-1}(x/c_2)\right. \tag{24}$$

where $|x| \ge l$, i.e., $|t| \le 1$.

The functions $R_1(t)$, $tR_{2n}(t)$ in (23), and the functions $t^{-1}R_{2n-1}(x/c_i)$ in equation (24) are well behaved in the intervals $|x| \le c_i$ and $|x| \ge l$, respectively, and may therefore be represented in their respective intervals by Chebyshev polynomial series. In (23) write $x = c_i\tau$, then $t = l/x = 1/(k_i\tau)$ where $k_i = c_i/l$, and we use the approximations

$$R_1(t) = R_1[1/(k_i\tau)] = \sum_{m=1}^{N} e_m^{(i)}\, T_{2m-1}(\tau) \tag{25}$$

$$tR_{2n}(t) = [1/(k_i\tau)]R_{2n}[1/(k_i\tau)] = \sum_{m=1}^{N} d_{m,2n}^{(i)}\, T_{2m-1}(\tau) \tag{26}$$

so that, on equating the coefficients of $T_{2m-1}(\tau)$ on each side of (23) we find

$$e_m^{(i)} + \sum_{n=1}^{N} d_{m,2n}^{(i)}\, b_n - a_m^{(i)} = -S_i\delta_{m,1}, \tag{27}$$

where $i = 1, 2$; $m = 1, 2, \ldots N$ and

$$f_i'(x)/(\vartheta_i p_0) = -x/(r_i\vartheta_i p_0) = -S_i\tau, \quad S_i = c_i/(r_1\vartheta_i p_0). \tag{28}$$

Equation (24) is treated in the same way; now $x/c_i = l/(c_i t) = 1/(k_i t)$ and

$$\begin{aligned}(1/t)R_{2n-1}(x/c_i) &= [k_i/(k_i t)]R_{2n-1}(1/(k_i t)) \\ &= k_i\sum_{m=1}^{N+1\,\prime} d_{m,2n-1}^{(i)}\, T_{2m-2(t)} \\ &= k_i\left\{\tfrac{1}{2}\, d_{1,2n-1}^{(i)} + \sum_{m=1}^{N} d_{m+1,2n-1}^{(i)}\, T_{2m}(t)\right\}. \end{aligned} \tag{29}$$

The prime in the foregoing summation indicates that the first term is halved. The use of this approximation in (24) leads to

$$\vartheta_1\left\{2 - k_1\sum_{n=1}^{N} d_{1,2n-1}^{(1)}\, a_n^{(1)}\right\} = -\vartheta_2\left\{2 - k_2\sum_{n=1}^{N} d_{1,2n-1}^{(2)}\, a_n^{(2)}\right\} \tag{30}$$

$$\vartheta_1\left\{b_m - k_1\sum_{n=1}^{N} d_{m+1,2n-1}^{(1)}\, a_n^{(1)}\right\} = -\vartheta_2\left\{b_m - k_2\sum_{n=1}^{N} d_{m+1,2n-1}^{(2)}\, a_n^{(2)}\right\} \tag{31}$$

for $m = 1, 2, \ldots N$.

The solution procedure is now straightforward. We suppose that ϑ_1, ϑ_2, or sufficiently $\vartheta_2/\vartheta_1 = \Gamma$, and k_1, k_2 (satisfying $0 < k_i < 1$) have been chosen. Equations (30) and (31) yield

$$1 = \tfrac{1}{2}\sum_{n=1}^{N}\{\lambda_1 d_{1,2n-1}^{(1)}\, a_n^{(1)} + \lambda_2 d_{1,2n-1}^{(2)}\, a_n^{(2)}\} \tag{32}$$

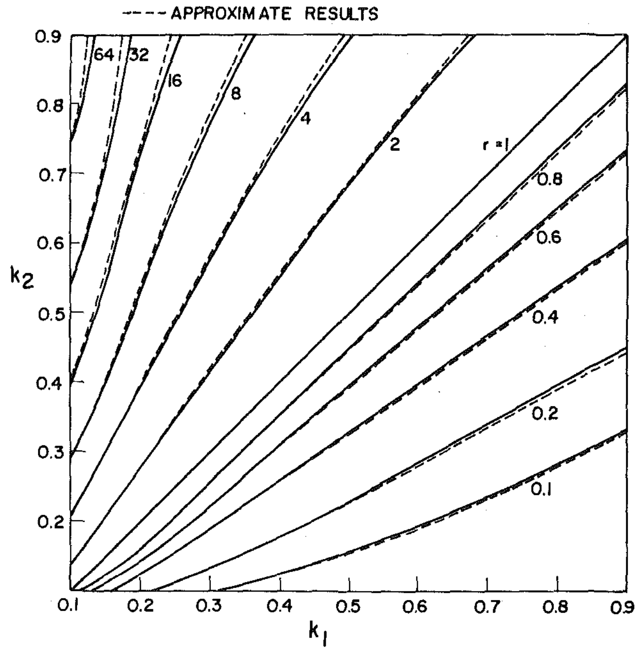

Fig. 2 Contours of $\Gamma = \gamma_2/\gamma_1$ for given values of k_1, k_2

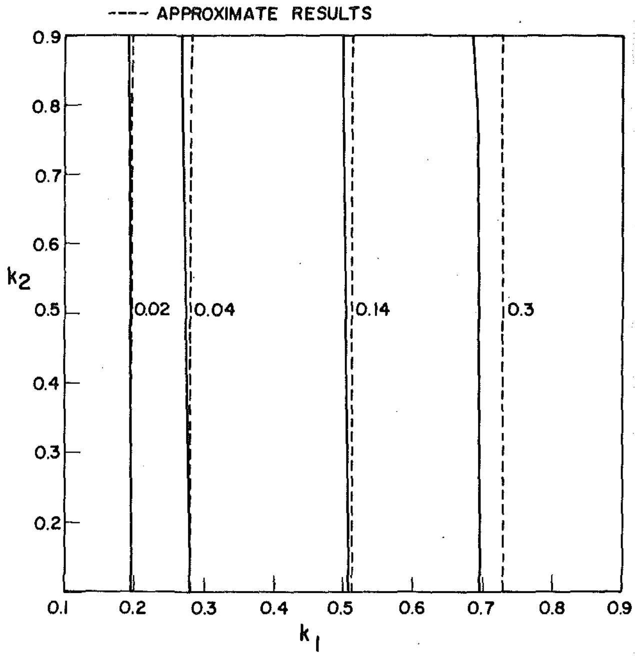

Fig. 3 Contours of $\vartheta_1 p_0 r/l$ for given values of k_1, k_2

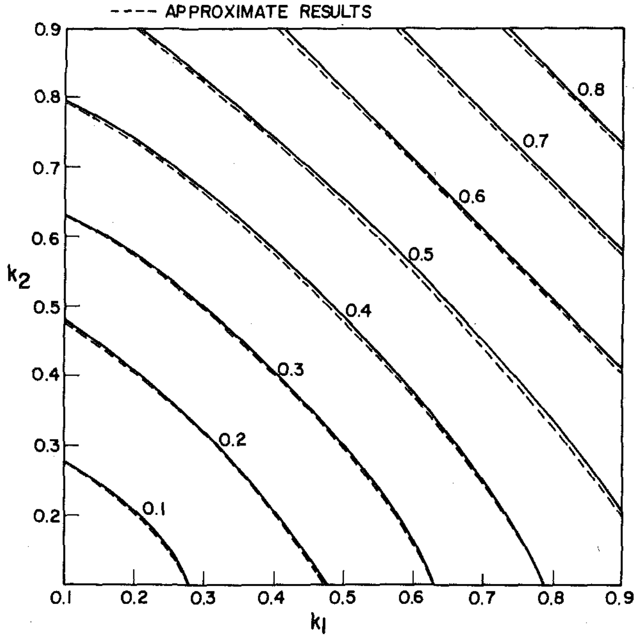

Fig. 4 Contours of $r(d_1 + d_2)/l^2$ for given values of k_1, k_2

$$b_m = \sum_{n=1}^{N} \{\lambda_1 d^{(1)}_{m+1,2n-1}\, a^{(1)}_n + \lambda_2 d^{(2)}_{m+1,2n-1}\, a^{(2)}_n\} \tag{33}$$

where $\lambda_i = k_i\vartheta_i/(\vartheta_1 + \vartheta_2)$. Multiply the first term in (27) by the right-hand side of (32) and substitute (33) for b_m in the second term. The result is $2N$ equations for the $2N$ coefficients $a^{(1)}_n$, $a^{(2)}_n$. Assuming (on physical grounds) that the homogeneous equations with $S_1 = 0 = S_2$ have only the trivial solution, we may write the solution of the homogeneous equations in the form

$$a^{(i)}_m = \sum_{j=1}^{2} A^{(i)}_{m,j}\, S_j. \tag{34}$$

When $p_i(x)$ is given by (18), the equilibrium equation (6) becomes

$$2P/(\pi l p_0) = k_1 a^{(1)}_1 = k_2 a^{(2)}_1. \tag{35}$$

Thus, on using (34), we find

$$k_1 \sum_{j=1}^{2} A^{(1)}_{1,j}\, S_j = k_2 \sum_{j=1}^{2} A^{(2)}_{1,j}\, S_j \tag{36}$$

which, since k_1, k_2 are known, is an equation for S_1/S_2. Once S_1/S_2 is known, the values of S_1 and S_2 separately may be found by substituting the expressions (34) for $a^{(1)}_n$, $a^{(2)}_n$ in equation (32). At this stage all the coefficients $a^{(1)}_n$, $a^{(2)}_n$, b_n are known; after verifying that the contact pressures are compressive, there remains one final equation, the compatibility equation (13) which may be written

$$d_1 + d_2 = \frac{c_1^2}{2r_1} + \frac{c_2^2}{2r_2} - \int_{c_1}^{l} v_1'(x)dx + \int_{c_2}^{l} v_2'(x)dx. \tag{35}$$

This equation yields $d_1 + d_2$ in terms of known quantities.

Numerical Results

For the case of two identical half planes, Alblas [1] found that

$$\frac{\vartheta p_0 r}{l} = \frac{2}{\pi}[K - E] \tag{36}$$

where K, E are the complete elliptic integrals with arguments $k = k_1 = k_2$, and

$$\frac{2rd}{l^2} = \frac{2}{\pi}[E'(E - K) + k^2KK']. \tag{37}$$

All the figures refer to the particular case in which the obstacle is symmetrical, so that $r_1 = r_2$. Fig. 2 shows the contours of Γ for given values of k_1, k_2; Fig. 3 shows those of $\vartheta_1 p_0 r/l$ and Fig. 4 shows those of $r(d_1 + d_2)/l^2$. These results were computed as follows. Define $T_i = k_i/S_i = \vartheta_i p_0 r_i/l$. If $r_1 = r_2$ then $T_2/T_1 = \vartheta_2/\vartheta_1 = \Gamma$. For given values of k_1, k_2, an arbitrary value of $\Gamma = \gamma^{(0)}$ was chosen, and T_1, T_2 were computed as described in the section, "Chebyshev Polynomial Solution." The value of $T_2/T_1 = \Gamma^{(1)}$ was computed and the calculation was repeated with $\Gamma = \Gamma^{(1)}$. It was found in practice that T_2/T_1 was most insensitive to the chosen value of Γ so that two steps of the iteration were always sufficient to yield the value of Γ appropriate to those k_1, k_2 and $r_1 = r_2$. For $k_1 = k_2$ the results were compared to those of equations (36) and (37). It was found that $N = 5$ was adequate for $k \le 0.5$ and $N = 9$ was adequate for $0.6 \le k \le 0.9$.

Figs. 5 and 6 show the contact pressure and normal displacement

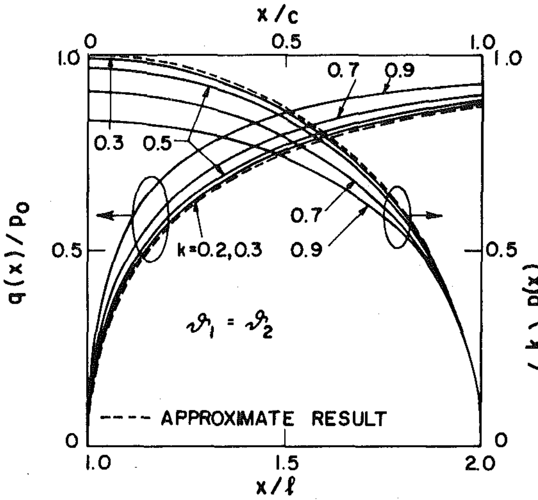

Fig. 5 The scaled contact pressure when $\vartheta_1 = \vartheta_2$

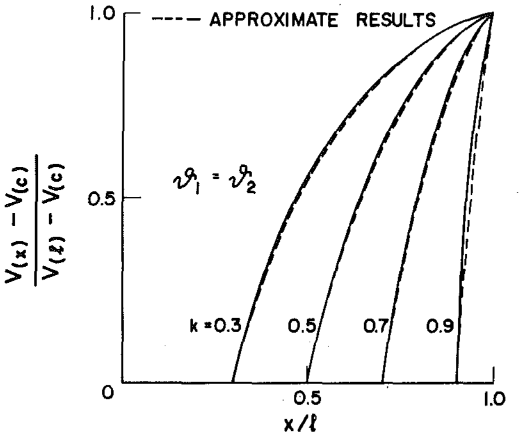

Fig. 6 The normal displacement on the free boundary when $\vartheta_1 = \vartheta_2$

on the free boundary when $\vartheta_1 = \vartheta_2$. Figs. 7 and 8 show the corresponding quantities when $\vartheta_1 \neq \vartheta_2$.

Comparison With a First Approximation

The numerical results show that for small k_1, k_2 the contact pressures are approximately given by the first terms in (18) and (21). Thus, to a first approximation,

$$p_i(x) = p_0 a_1^{(i)} (1 - x^2/c_i^2)^{1/2}, \quad q(x) = p_0(1 - l^2/x^2)^{1/2}, \tag{38}$$

$$v_i'(x) = (-)^{i-1} \vartheta_i p_0 \{R_1(l/x) - a_1^{(i)} R_1(x/c_i)\}. \tag{39}$$

Now equations (23) and (24) give

$$\vartheta_i p \{R_1(l/x) - a_1^{(i)} (x/c_i)\} = -x/r_i, \quad |x| \leq c_i, \tag{40}$$

$$\vartheta_1 \{l/x - a_1^{(1)} R_1(x/c_1)\} = -\vartheta_2 \{l/x - a_1^{(2)} R_1(x/c_2)\}, \; |x| \geq l. \tag{41}$$

Now $R_1(t) = t - (t^2 - 1)^{1/2} \simeq 1/(2t)$ to the first-order approximation, so that

$$\vartheta_i p_0(1/2 - a_1^{(i)}/k_i) = -l/r_i, \tag{42}$$

$$(\vartheta_1 + \vartheta_2) = (\vartheta_1 k_1 a_1^{(1)} + \vartheta_2 k_2 a_1^{(2)})/2: \tag{43}$$

But equation (35) gives $k_1 a_1^{(1)} = k_2 a_1^{(2)}$ so that $k_1 a_1^{(i)} = 2$ and equation (23) gives

$$\vartheta_i p_0 l(1/2 - 2/k_i^2) = -1/r_i. \tag{44}$$

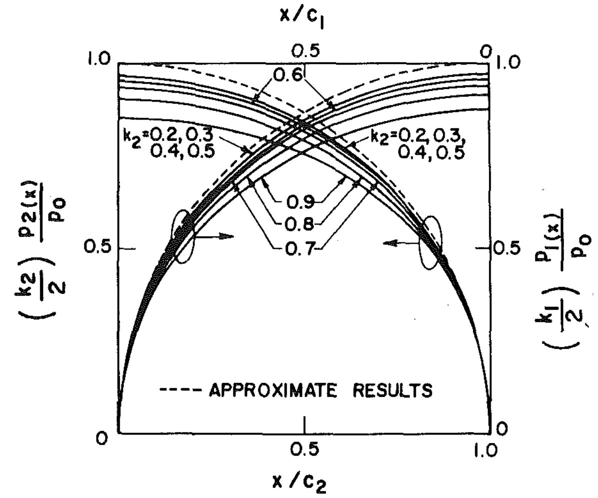

Fig. 7 The scaled contact pressures on the obstacle when $k_1 = 0.5$

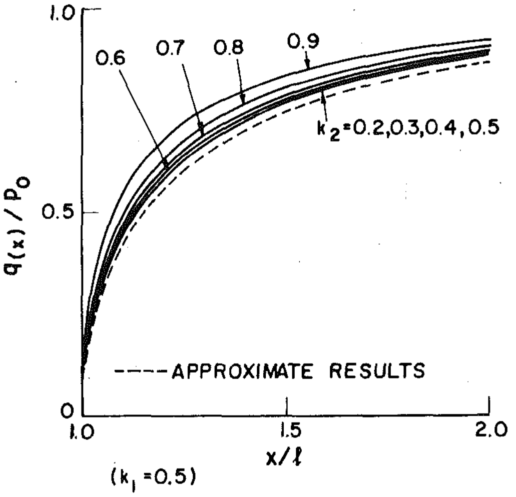

Fig. 8 The scaled exterior contact pressure when $k_1 = 0.5$

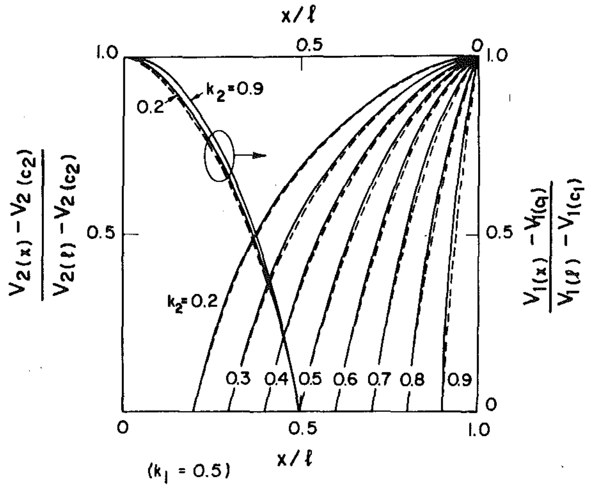

Fig. 9 The normal displacements on the free boundaries when $k_1 = 0.5$

If the obstacle is symmetrical then

$$\frac{\vartheta_2}{\vartheta_1} = \frac{\dfrac{4}{k_1^2} - 1}{\dfrac{4}{k_2^2} - 1}, \quad \frac{\vartheta_1 p_0 r}{l} = \frac{2}{\dfrac{4}{k_1^2} - 1}. \tag{45}$$

The compatibility equation becomes

$$d_1 - \frac{c_1^2}{2r_1} + \vartheta_1 p_0 \int_{c_1}^{l} \left\{ R_1\left(\frac{l}{x}\right) - a_1^{(1)} R_1\left(\frac{x}{c_1}\right)\right\} dx + d_2 - \frac{c_2^2}{2r_2} + \vartheta_2 p_0 \int_{c_2}^{l} \left\{ R_1\left(\frac{l}{x}\right) - a_1^{(2)} R_1\left(\frac{x}{c_2}\right)\right\} dx = 0, \tag{46}$$

which yields, when $r_1 = r_2$,

$$\frac{(d_1 + d_2)r}{l^2} = \frac{k_1^2 + k_2^2}{2} - \frac{2k_1^2}{4 - k_1^2} T_1 - \frac{2k_2^2}{4 - k_2^2} T_2, \tag{47}$$

where

$$T_j = u_j - u_j^{-1} + \ln k_j - 2 \ln u_j, \quad u_j = 1 + (1 - k_j^2)^{1/2}. \tag{48}$$

The results obtained from this approximation are shown on all the graphs and it is clear that they in general show excellent agreement with the computed results. The contact pressure is not particularly closely approximated but it is still very closely proportional to $(1 - x^2/c_i^2)^{1/2}$.

References

1 Alblas, J. B., "On the Two-Dimensional Contact Problem of a Rigid Cylinder, Pressed Between Two Elastic Half Planes," *Mechanics Research Communications*, Vol. 1, 1974, pp. 15–20.

2 Alblas, J. B., "On the Two-Dimensional Contact Problem of a Rigid Cylinder Pressed Between Two Elastic Layers," *The Mechanics of the Contact Between Deformable Bodies*, de Pater, A. D., and Kalker, J. J., eds., Delft University Press, 1975, pp. 110–126.

3 Gladwell, G. M. L., "The Contact Problem for a Rigid Cylinder Pressed Between Two Elastic Layers," ASME JOURNAL OF APPLIED MECHANICS, Vol. 44, No. 1, Mar. 1977, pp. 36–40.

4 Gladwell, G. M. L., "A Note on a Three-Part Contact Problem, Chebyshev Polynomials and Elliptic Integrals," *International Journal of Engineering Science*, Vol. 18, 1980, pp. 61–67.

5 Sneddon, I. N., *Fourier Transforms*, McGraw-Hill, New York, 1951.

6 Lowengrub, M., "Stress Distribution Due to a Griffith Crack at the Interface of an Elastic Half Plane and a Rigid Foundation," *International Journal of Engineering Science*, Vol. 11, 1973, pp. 477–488.

J. G. Simmonds

Professor,
Department of Applied Mathematics
and Computer Science,
University of Virginia,
Charlottesville, Va. 22901
Mem. ASME

Exact Equations for the Large Inextensional Motion of Elastic Plates[1]

The governing equations for plates that twist as they deform are reduced to 14 differential equations, first-order in a single space variable and second-order in time. Many of the equations are the same as for statics. Nevertheless, the extension to dynamics is nontrivial because the natural coordinates to use to describe the deformed, developable midsurface are not Lagrangian. The plate is assumed to have two curved, stress-free edges, one built-in straight edge, and one free straight edge acted upon by a force and a couple. There are 7 boundary conditions at the built-in end and 7 at the free end.

Introduction

Helicopter blades, aircraft wings, and inflatable buildings are examples of thin-walled structures that undergo large elastic deflections. If shell theory is used to model the large motions of such structures, then, except for rubberlike materials, the midsurface deformation must be nearly *inextensional.* This is because the strains will be small compared to the rotations. The degree to which inextensionality approximates the actual kinematic state depends on the geometric boundary conditions, the nature of the external loads, and the distance along the midsurface to an edge. Fortunately, the error in an inextensional solution can be assessed *a posteriori* and used, if need be, as an outer solution in a singular perturbation analysis of the original problem. Indeed, even if plastic flow occurs, it may be reasonable to assume that the major portion of the shell is in a state of elastic, inextensional deformation.

The theory of large, inextensional motions of elastic shells is virtually undeveloped. For example, it is only within the last year that exact *static* equations have been derived for simplest, nontrivial case imaginable, namely, the inextensional bending of an end-loaded cantilevered plate [1, 2].

Nowadays, large computer codes are used to solve special cases of the equations of motion of nonlinear shell theory. In developing new codes of greater generality, it would seem desirable to incorporate near inextensionality *explicitly.* Otherwise, most of the computational effort may be consumed in generating displacement fields that produce small extensional strains.

As a first step in this direction we derive herein exact equations of motion for an elastic, inextensional plate that twists as it deforms. The plate is assumed to be bounded by two straight edges and two curved ones. One straight edge is built-in and the other may be acted upon by a force and a couple. The curved edges are stress-free. Inertial and distributed external loads act over the deformed midplane of the plate. We shall use the notation of [1, 2] and, for conciseness, refer to these two papers extensively.[2] We introduce a slight change, however, to simplify the dynamic analysis: in what follows it is the *left* end of the plate that is built-in and the *right* end that is free.

The deformed midplane of the plate is a moving developable surface and thus of the form [1]

$$\mathbf{y}(\alpha,\eta,t) = \mathbf{x}(\alpha,t) + \eta\mathbf{u}(\alpha,t). \tag{1}$$

Here α is the angle that the generators in the developed midplane make with the built-in edge, $\mathbf{x}$ is the position of the line $\mathcal{B}$ that bisects the built-in edge and is orthogonal to the generators, η is distance along a generator from $\mathcal{B}$, and $\mathbf{u}$ is a unit vector along a generator; see Figs. 1 and 2 of [1].

The dynamic extension of the static equations developed in [1, 2] is nontrivial because the natural set of coordinates to describe a developable surface, α and η, are not material (Lagrangian) coordinates. Consequently, whereas 7 equation suffice for static problems, 14 are needed in dynamic ones. Seven boundary conditions are known at the built-in end ($\alpha = 0$), and 7 at the free end ($\alpha = \hat{\alpha}$). Numerical solutions of these equations will be considered in a later paper.

---

[1] This work was supported by the National Science Foundation under Grant MOS-73-08659A02.

Contributed by the Applied Mechanics Division for publication in the JOURNAL OF APPLIED MECHANICS.

Discussion on this paper should be addressed to the Editorial Department, ASME, United Engineering Center, 345 East 47th Street, New York, N. Y. 10017, and will be accepted until June 1, 1981. Readers who need more time to prepare a Discussion should request an extension from the Editorial Department. Manuscript received by ASME Applied Mechanics Division, April, 1980.

[2] We take this opportunity to correct a minor error in [2]: in equations (15) and (65) replace sin γ by cos γ.

Vector Equations of Motion

The first step is to add inertial loads to the force and moment equilibrium equations in [1] and to switch from the independent variable ξ, that measures distance along $\mathcal{B}$, to α. Primes and dots are used in [1, 2] to denote differentiation with respect to ξ and α, respectively. These two operations are related by $\rho(\ )' = (\ )^{\cdot}$, where ρ is the geodesic radius of $\mathcal{B}$. Let $\mathbf{y}^{**}$ denote the acceleration with respect to an inertial frame of a particle on the deformed midsurface. Equation (69) of [1] then implies the following equation of conservation of linear momentum:

$$\mathbf{F}^{\cdot} + \mathbf{Q} = \mathbf{P}^{(1)}, \tag{2}$$

where, from (67) of [1],

$$\mathbf{Q} = \int (\rho - \eta)\mathbf{p}d\eta \tag{3}$$

and

$$\mathbf{P}^{(1)} = \int (\rho - \eta)m\mathbf{y}^{**}d\eta. \tag{4}$$

Here m is the mass/area of the undeformed midplane. We recall that $\int$ is short for $\int_{\eta-}^{\eta+}$, where η_+ and η_- denote the (unknown) distances along a generator to the curved edges; see Fig. 1 of [1].

For a plate that twists as it deforms, it seems best to take moments with respect to the point $\mathbf{x} + \rho\mathbf{u}$ on the edge of regression of the deformed midplane. Thus, from equations (70) of [1] and (12) of [2], we obtain the following equation of conservation of angular momentum:

$$\mathbf{M}^{\cdot} + \mathbf{u} \times (\rho^{\cdot}\mathbf{F} + \mathbf{P}^{(2)} - \mathbf{L}) = \mathbf{0}, \tag{5}$$

where

$$\mathbf{L} = \int (\rho - \eta)^2\mathbf{p}d\eta \tag{6}$$

and

$$\mathbf{P}^{(2)} = \int (\rho - \eta)^2 m\mathbf{y}^{**}d\eta. \tag{7}$$

Acceleration and Inertial Load Vectors

Let x and y denote the Cartesian coordinates of a particle in the undeformed (= developed) midplane. The position $\mathbf{y}$ of the particle during the motion may be regarded as a function of x, y, and t. By definition,

$$\mathbf{y}^* \equiv \mathbf{y}_t(x,y,t), \tag{8}$$

where $(\ )_t = \partial(\ )/\partial t$. In the developed midplane we have, from Fig. 1 of [2], the following relations between the coordinates (x,y) and (α,η):

$$x = p(\alpha,t)\cos\alpha + r(\alpha,t)\sin\alpha - \eta\sin\alpha \tag{9}$$

$$y = p(\alpha,t)\sin\alpha - r(\alpha,t)\cos\alpha + \eta\cos\alpha. \tag{10}$$

Here p is the perpendicular distance in the developed midplane from the center of the built-in edge to the generator α = constant, and r is the distance along this generator from $\mathcal{B}$ to the foot of the perpendicular; see Fig. 1 and equation (95) of [2]. Thus α and η are functions of x, y, and t, even though we cannot express this dependence explicitly. From (1) and (8),

$$\begin{aligned}\mathbf{y}^* &= \mathbf{y}_\alpha(\alpha,\eta,t)\alpha_t + \mathbf{y}_\eta(\alpha,\eta,t)\eta_t + \mathbf{y}_t(\alpha,\eta,t)\\ &= \alpha_t(\mathbf{x}^{\cdot} + \eta\mathbf{u}^{\cdot}) + \eta_t\mathbf{u} + \mathbf{x}_t + \eta\mathbf{u}_t.\end{aligned} \tag{11}$$

But

$$\mathbf{x}^{\cdot} = \rho\mathbf{t}, \quad \mathbf{x}(0,t) = \mathbf{0}, \tag{12}$$

where $\mathbf{t}$ is a unit tangent to $\mathcal{B}$, and from equations (3) and (4) of [2], $\mathbf{t}^{\cdot} = \mathbf{u} + \lambda\mathbf{m}$ and $\mathbf{u}^{\cdot} = -\mathbf{t}$, where $\mathbf{m} = \mathbf{t} \times \mathbf{u}$ and λ is the torsion/curvature ratio of the edge of regression. Thus

$$\mathbf{y}^* = \alpha_t(\rho - \eta)\mathbf{t} + \eta_t\mathbf{u} + \mathbf{x}_t + \eta\mathbf{u}_t. \tag{13}$$

We now express α_t and η_t in terms of p_t and r_t. Differentiating both sides of (9) and (10) with respect to t and noting from equations (54) and (55) of [2] that

$$p^{\cdot} = \rho - r, \quad p(0,t) = 0, \quad r^{\cdot} = p, \quad r(0,t) = 0, \tag{14, 15}$$

we have

$$0 = [\alpha_t(\rho - \eta) + p_t]\cos\alpha + (r_t - \eta_t)\sin\alpha \tag{16}$$

$$0 = [\alpha_t(\rho - \eta) + p_t]\sin\alpha - (r_t - \eta_t)\cos\alpha. \tag{17}$$

Hence

$$(\rho - \eta)\alpha_t = -p_t, \quad \eta_t = r_t, \tag{18, 19}$$

and (13) reduces to

$$\mathbf{y}^* = -p_t\mathbf{t} + r_t\mathbf{u} + \mathbf{x}_t + \eta\mathbf{u}_t. \tag{20}$$

Inextensionality implies that, in general, the geodesic curvature of $\mathcal{B}$ does *not* vanish with the deformation, and, thus, neither do p or r. More precisely, from Fig. 1 of [2], we have

$$\int_0^\alpha \rho(\beta,t)\mathbf{T}(\beta)d\beta + r(\alpha,t)\mathbf{U}(\alpha) - p(\alpha,t)\mathbf{T}(\alpha) = \mathbf{0}. \tag{21}$$

Here

$$\mathbf{T}(\alpha) = \mathbf{i}\cos\alpha + \mathbf{j}\sin\alpha, \quad \mathbf{U}(\alpha) = -\mathbf{i}\sin\alpha + \mathbf{j}\cos\alpha \tag{22, 23}$$

are unit vectors, tangent and normal, respectively, to $\mathcal{B}$ in the developed midplane, and $\mathbf{i}$ and $\mathbf{j}$ are fixed unit vectors, $\mathbf{i}$ pointing into the plate and tangent to $\mathcal{B}$ at the built-in edge and $\mathbf{j}$ lying along the built-in edge.

To obtain well-conditioned differential equations, i.e., to avoid situations in which groups of relatively large terms must add to nearly zero, we introduce in place of $\mathbf{x}$ the new dependent variable

$$\mathbf{z} = \mathbf{x} + r\mathbf{u} - p\mathbf{t}. \tag{24}$$

Clearly, in view of (21), $\mathbf{z}$ *does* vanish with the deformation. From (12), (14), (15) and equations (3) and (4) of [2], it follows that $\mathbf{z}$ satisfies the differential equation and boundary condition

$$\mathbf{z}^{\cdot} = -p\lambda\mathbf{m}, \quad \mathbf{z}(0,t) = \mathbf{0}. \tag{25}$$

In terms of $\mathbf{z}$, (20) reads

$$\mathbf{y}^* = \mathbf{z}_t + p\mathbf{t}_t + (\eta - r)\mathbf{u}_t. \tag{26}$$

Again using the chain rule, $(\ )^* = (\ )_\alpha\alpha_t + (\ )_\eta\eta_t + (\ )_t$, and noting the differential equations for $\mathbf{t}$, $\mathbf{u}$, p, r, and $\mathbf{z}$, we obtain

$$\mathbf{y}^{**} = \lambda(\rho - \eta)^{-1}p_t{}^2\mathbf{m} + \mathbf{z}_{tt} + p\mathbf{t}_{tt} + (\eta - r)\mathbf{u}_{tt}. \tag{27}$$

Let

$$I_n = \int (\rho - \eta)^n m d\eta, \quad n = 0,1,2,3, \tag{28}$$

and assume, for simplicity, that m is constant. With the aid of equation (21) of [2] we have

$$I_n = m\int_\delta^{\delta(1+\mu)} \sigma^n d\sigma = m\delta^{n+1}[(1 + \mu)^{n+1} - 1]/(n + 1). \tag{29}$$

(The geometrical meaning of δ and μ may be found in Fig. 1 of [2]). Inserting (27) into (4) and (7), we obtain for the inertial terms that appear in (2) and (5),

$$\mathbf{P}^{(\nu)} = I_{\nu-1}\lambda p_t{}^2\mathbf{m} + I_\nu(\mathbf{z}_{tt} + p\mathbf{t}_{tt}) + J_{\nu+1}\mathbf{u}_{tt}, \quad \nu = 1,2, \tag{30}$$

where

$$J_{\nu+1} = (\rho - r)I_\nu - I_{\nu+1} = qI_\nu - I_{\nu+1}, \tag{31}$$

the second form of $J_{\nu+1}$ coming from equations (52) and (95) of [2].

The Dynamic Finite Rotation Vector

In [1], Libai and the author introduced a finite rotation vector $\mathbf{r}$ to describe the position of the triad $(\mathbf{t},\mathbf{u},\mathbf{m})$ with respect to the triad $(\mathbf{i},\mathbf{j},\mathbf{k})$, where $\mathbf{k} = \mathbf{i} \times \mathbf{j}$. In dynamic problems it is convenient to introduce the vector $\mathbf{s}$ that measures the rotation of $(\mathbf{t},\mathbf{u},\mathbf{m})$ relative to the triad

$(\mathbf{T},\mathbf{U},\mathbf{k})$. The reason is to obtain well-conditioned equations. Although the triad $(\mathbf{T},\mathbf{U},\mathbf{k})$ rotates, recall that $\mathbf{T}$ and $\mathbf{U}$ depend on α only and $\mathbf{k}$ is constant. Thus, if the deformation is small, so will be $\mathbf{s}$.

For conciseness, set $(\mathbf{t},\mathbf{u},\mathbf{m}) = (\mathbf{u}_1,\mathbf{u}_2,\mathbf{u}_3)$, $(\mathbf{T},\mathbf{U},\mathbf{k}) = (\mathbf{U}_1,\mathbf{U}_2,\mathbf{U}_3)$, and $(\mathbf{i},\mathbf{j},\mathbf{k}) = (\mathbf{e}_1,\mathbf{e}_2,\mathbf{e}_3)$. Then in terms of $\mathbf{s}$ [3]

$$\mathbf{u}_i = \mathbf{U}_i + [\mathbf{s} \times \mathbf{U}_i + \tfrac{1}{2}\mathbf{s} \times (\mathbf{s}. \times \mathbf{U}_i)]Q \equiv s_{ij}\mathbf{U}_j, \tag{32}$$

where

$$Q = (1 + \tfrac{1}{4}\mathbf{s}\cdot\mathbf{s})^{-1}. \tag{33}$$

In (32) $i = 1,2,3$, a repeated index is summed from 1 to 3, and the s_{ij} are elements of a proper orthogonal (rotation) matrix. Note that $s_{ij}s_{kj} = \delta_{ik}$, the Kronecker delta. As $-\mathbf{s}$ inverts the transformation that sends the triad $(\mathbf{u}_1,\mathbf{u}_2,\mathbf{u}_3)$ into $(\mathbf{U}_1,\mathbf{U}_2,\mathbf{U}_3)$, it follows that $\mathbf{s}$ has the representations

$$\mathbf{s} = s_i\mathbf{u}_i = s_i\mathbf{U}_i. \tag{34}$$

Substituting (34) into (32), we obtain the well-known representation [3]

$$\begin{aligned} s_{ij} &= (1 - \tfrac{1}{2}Qs_ks_k)\delta_{ij} + (\epsilon_{ijk}s_k + \tfrac{1}{2}s_is_j)Q \\ &\equiv \delta_{ij} + t_{ij}, \end{aligned} \tag{35}$$

where ϵ_{ijk} is the permutation symbol.

To derive differential equations for the components of $\mathbf{s}$, consider first the Frenet equations for the $\mathbf{u}_i$'s. From (97) and (98) of [1]

$$\mathbf{u}_i^{\cdot} = \rho\boldsymbol{\omega} \times \mathbf{u}_i, \tag{36}$$

where

$$\rho\boldsymbol{\omega} = -\lambda\mathbf{u}_2 + \mathbf{u}_3. \tag{37}$$

On the other hand, from (32),

$$\mathbf{u}_i^{\cdot} = s_{ij}^{\cdot}\mathbf{U}_j + s_{ij}\mathbf{U}_j^{\cdot}. \tag{38}$$

It follows from $s_{ij}s_{kj} = \delta_{ij}$ and (32) that

$$s_{ij}^{\cdot}\mathbf{U}_j = s_{ij}^{\cdot}s_{kj}\mathbf{u}_k = \tfrac{1}{2}(s_{ij}^{\cdot}s_{kj} - s_{ij}s_{kj}^{\cdot})\mathbf{u}_k. \tag{39}$$

But the coefficients of the $\mathbf{u}_k$'s in (39) are elements of a skew matrix. Hence there exists a vector $\rho\boldsymbol{\Omega}$ such that

$$s_{ij}^{\cdot}\mathbf{U}_j = \rho\boldsymbol{\Omega} \times \mathbf{u}_i. \tag{40}$$

Furthermore, from (22) and (23),

$$s_{ij}\mathbf{U}_j^{\cdot} = s_{ij}\mathbf{k} \times \mathbf{U}_j = \mathbf{k} \times \mathbf{u}_i. \tag{41}$$

Inserting (40) and (41) into (38) and comparing the resulting equation with (36) we see that

$$\rho\boldsymbol{\omega} = \rho\boldsymbol{\Omega} + \mathbf{k}. \tag{42}$$

Now the relation between $\mathbf{r}$ and $\boldsymbol{\omega}$, as expressed by equation (108) of [1], is precisely the same as that between $\mathbf{s}$ and $\boldsymbol{\Omega}$, i.e.,

$$s_i'\mathbf{u}_i = \boldsymbol{\Omega} + \tfrac{1}{2}\mathbf{s} \times \boldsymbol{\Omega} + \tfrac{1}{4}(\boldsymbol{\Omega}\cdot\mathbf{s})\mathbf{s}. \tag{43}$$

Adding initial conditions, setting $(\quad)' = \rho(\quad)^{\cdot}$, replacing $\rho\boldsymbol{\Omega}$ by $\rho\boldsymbol{\omega} - \mathbf{k}$, and noting from (32) that

$$\mathbf{k} = \mathbf{U}_3 = \mathbf{u}_3 + [\mathbf{u}_3 \times \mathbf{s} + \tfrac{1}{2}\mathbf{s} \times (\mathbf{s} \times \mathbf{u}_3)]Q, \tag{44}$$

we obtain the following component form of (43):

$$s_1^{\cdot} = s_2 + \tfrac{1}{2}\lambda s_3 - \tfrac{1}{4}\lambda s_2 s_1, \quad s_1(0,t) = 0 \tag{45}$$

$$s_2^{\cdot} = -\lambda - s_1 - \tfrac{1}{4}\lambda s_2^2, \quad s_2(0,t) = 0 \tag{46}$$

$$s_3^{\cdot} = -\tfrac{1}{2}\lambda s_1 - \tfrac{1}{4}\lambda s_2 s_3, \quad s_3(0,t) = 0. \tag{47}$$

Components of the Inertial Loads

Let $\mathcal{V} = \partial/\partial t$. Then from (32) and (35)

$$\mathcal{V}(\mathbf{u}_i) = \mathcal{V}(t_{ij})\mathbf{U}_j = s_{kj}\mathcal{V}(t_{ij})\mathbf{u}_k, \tag{48}$$

where $\mathcal{V}(t_{ij})$ is to be computed in terms of the s_i's from (35). Likewise,

$$\mathcal{V}^2(\mathbf{u}_i) = s_{kj}\mathcal{V}^2(t_{ij})\mathbf{u}_k. \tag{49}$$

Further, let

$$\mathbf{z} = z_i\mathbf{U}_i. \tag{50}$$

Then

$$\mathcal{V}^2(\mathbf{z}) = \mathcal{V}^2(z_i)\mathbf{U}_i = s_{ji}\mathcal{V}^2(z_i)\mathbf{u}_j. \tag{51}$$

Inserting (49) and (51) into (30), we obtain

$$\mathbf{p}^{(\nu)} = \{\delta_{3i}I_{\nu-1}A + s_{ij}[I_\nu B_j + J_{\nu+1}\mathcal{V}^2(t_{2j})]\}\mathbf{u}_i \equiv P_i'^{(\nu)}\mathbf{u}_i, \tag{52}$$

where

$$A = \lambda[\mathcal{V}(p)]^2, \quad B_j = \mathcal{V}^2(z_j) + p\mathcal{V}^2(t_{1j}). \tag{53, 54}$$

Component Form of (25)

Insert (32) with $i = 3$ and (50) into (25) to obtain

$$z_i^{\cdot}\mathbf{U}_i = -z_i\mathbf{U}_i^{\cdot} - p\lambda s_{3i}\mathbf{U}_i. \tag{55}$$

As noted in (41), $\mathbf{U}_i^{\cdot} = \mathbf{k} \times \mathbf{U}_i$ which, since $\mathbf{U}_3^{\cdot} = \mathbf{k}^{\cdot} = \mathbf{0}$, is equivalent to the statement $\mathbf{U}_\alpha^{\cdot} = \epsilon_{\alpha\beta}\mathbf{U}_\beta$, where $\epsilon_{\alpha\beta}$ is the two-dimensional permutation symbol. Thus the component form of (25) is

$$z_1^{\cdot} = z_2 - p\lambda s_{31}, \quad z_1(0,t) = 0 \tag{56}$$

$$z_2^{\cdot} = -z_1 - p\lambda s_{32}, \quad z_2(0,t) = 0 \tag{57}$$

$$z_3^{\cdot} = -p\lambda s_{33}, \quad z_3(0,t) = 0. \tag{58}$$

Component Form of the Equations of Motion

Set

$$\mathbf{F} = F_i\mathbf{u}_i. \tag{59}$$

Then, with (52) and equations (3)–(5) of [2], (2) implies that

$$F_1^{\cdot} = F_2 + \lambda F_3 + P_1^{(1)}, \quad F_1(0,t) = ? \tag{60}$$

$$F_2^{\cdot} = F_1 + P_2^{(1)}, \quad F_2(0,t) = ? \tag{61}$$

$$F_3^{\cdot} = -\lambda F_1 + P_3^{(1)}, \quad F_3(0,t) = ? \tag{62}$$

For simplicity, assume that there are no distributed external loads $(\mathbf{p} = 0)$. Insert (52) and (59) into (5) and, as in [2], set

$$\mathbf{M} = M_t\mathbf{t} + T_u\mathbf{u} + M_m\mathbf{m} \tag{63}$$

to obtain the scalar equations

$$M_t^{\cdot} - T_u - \lambda M_m + \rho^{\cdot}F_3 + P_3^{(2)} = 0 \tag{64}$$

$$T_u^{\cdot} + M_t = 0 \tag{65}$$

$$M_m^{\cdot} + \lambda M_t - \rho^{\cdot}F_1 - P_1^{(2)} = 0. \tag{66}$$

It may be verified immediately that equations (16)–(49) of [2] are unchanged, save $P\cos\phi$ is to be replaced by F_3 wherever it appears.

Nondimensionalization

All variables that appear in both the static and dynamic equations are nondimensionalized by equations (59)–(63) of [2]. The new variables that appear in the dynamic equations are scaled and nondimensionalized as follows:

$$(z_\alpha,z_3) = \epsilon L(\epsilon\bar{z}_\alpha,\bar{z}_3), \quad \alpha = 1,2 \tag{67}$$

$$(F_\alpha,P_\alpha^{(1)},F_3,P_3^{(1)}) = (\epsilon D/L)(\epsilon\bar{F}_\alpha,\epsilon\bar{P}_\alpha,\bar{F}_3,\bar{P}_3), \tag{68}$$

$$(P_\alpha^{(2)},P_3^{(2)}) = \epsilon D(\epsilon\bar{P}_\alpha^{(2)},\bar{P}_3^{(2)}) \quad (s_\alpha,s_3) = \epsilon(\bar{s}_\alpha,\epsilon\bar{s}_3), \tag{69}$$

$$(s_{\alpha3},s_{3\alpha}) = (t_{\alpha3},t_{3\alpha}) = \epsilon(\bar{s}_{3\alpha},\bar{s}_{\alpha3}), \quad (t_{\alpha\beta},t_{33}) = \epsilon^2(\bar{t}_{\alpha\beta},\bar{t}_{33}) \tag{70}$$

$$A = (\epsilon D/mL^2)\bar{A}, \quad (B_\alpha,B_3) = (\epsilon D/mL^3)(\epsilon\bar{B}_\alpha,\bar{B}_3) \tag{71}$$

$$I_n, J_n = mL^{n+1}(\bar{I}_n, \bar{J}_n), \quad t = L^2(m/D)^{1/2}\bar{t}. \tag{72}$$

In these equations $\epsilon = PL/D$, where P is a measure of the vertical force at the built-in edge, L is a typical length of the plate, and D is the bending stiffness.

If we drop overbars then of the equations needed in what follows, only (35), (45)–(47), (52) for $i = 3$, and (62) and (64) change form; (45)–(47), (62), and (64) are given by (82)–(84), (90), and (91), respectively; (35) breaks down into

$$s_{\alpha\beta} = \delta_{\alpha\beta} + \epsilon^2 t_{\alpha\beta}, \quad s_{33} = 1 + \epsilon^2 t_{33} \tag{73, 74}$$

$$t_{\alpha\beta} = [\epsilon_{\alpha\beta} s_3 + \tfrac{1}{2} s_\alpha s_\beta - \tfrac{1}{2}(s_\gamma s_\gamma + \epsilon^2 s_3^2)\delta_{\alpha\beta}]Q \tag{75}$$

$$s_{\alpha 3} = t_{\alpha 3} = (\epsilon_{\beta\alpha} s_\beta + \tfrac{1}{2}\epsilon^2 s_\alpha s_3)Q \tag{76}$$

$$s_{3\alpha} = t_{3\alpha} = (\epsilon_{\alpha\beta} s_\beta + \tfrac{1}{2}\epsilon^2 s_\alpha s_3)Q \tag{77}$$

$$t_{33} = -\tfrac{1}{2} s_\alpha s_\alpha Q, \tag{78}$$

where

$$Q = [1 + \tfrac{1}{4}\epsilon^2(s_\alpha s_\alpha + \epsilon^2 s_3^2)]^{-1}, \tag{79}$$

and (52) implies that $P_3^{(\nu)}$ takes the form

$$P_3^{(\nu)} = I_{\nu-1}A + s_{33}[I_\nu B_3 + J_{\nu+1}\mathcal{V}^2(t_{23})] + \epsilon^2 s_{\alpha 3}[I_\nu B_\alpha + J_{\nu+1}\mathcal{V}^2(t_{2\alpha})]. \tag{80}$$

The Complete Set of Dimensionless, Dynamic Differential Equations

Scattered throughout [2] and the present paper are differential equations for the unknowns l_+, $\mathbf{s} = s_i\mathbf{U}_i$, $\mathbf{z} = z_i\mathbf{U}_i$, $\mathbf{F} = F_i\mathbf{u}_i$, M_t, M_m, λ, and μ. These are equivalent to a set of 14 scalar equations and are listed next together with the known or unknown values of the 14 dependent variables at $\alpha = 0$. These equations contain a number of auxiliary quantities that, ultimately, can be expressed in terms of α, the 14 dependent variables, or prescribed load and geometric parameters. To avoid too much rewriting, we have preceded each differential equation with a pair of braces containing information giving, first, the source of the differential equation, and second, the equations that define the auxiliary variables. Thus, for example, {(56)–(58); [(51), 2], (74), (77)–(79)} means that the differential equations are (56)–(58) of the present paper and that the auxiliary variables on their right sides are defined by equation (51) of [2] and (74) and (77)–(79), of the present paper. Equations for the angles $\beta_\pm$ and $\gamma_\pm$ can be found in terms of l_+ once the equations $y = f_\pm(x)$ for the curved edges of the undeformed midplane have been specified. (For example, for a quadrilateral plate, these angles are constants with $\beta_\pm = \gamma_\pm$.)

In these equations there are 7 unknown boundary conditions at the built-in edge $\alpha = 0$. Six of these represent the unknown components of the force and moment vectors. The seventh, $\mu(0,t)$, represents a measure of the distance from the center of the built-in edge to the edge of regression. At the free end, $\alpha = \hat{\alpha}$, there are also 7 boundary conditions: the force and moment must be prescribed and $\delta\mu$ must be equal to dimensionless length of the free edge.

{[(41), 2]; [(33), 2]}

$$l_+^{\cdot} = \delta \sec(\alpha - \beta_+)\cos(\gamma_+ - \beta_+), \quad l_+(0,t) = 0. \tag{81}$$

{(45)–(47)}

$$s_1^{\cdot} = s_2 + \tfrac{1}{2}\epsilon^2\lambda(s_3 - \tfrac{1}{2}s_1 s_2), \quad s_1(0,t) = 0 \tag{82}$$

$$s_2^{\cdot} = -\lambda - s_1 - \tfrac{1}{4}\epsilon^2 s_2^2, \quad s_2(0,t) = 0 \tag{83}$$

$$s_3^{\cdot} = -\tfrac{1}{2}\lambda s_1 - \tfrac{1}{4}\epsilon^2 s_2 s_3, \quad s_3(0,t) = 0 \tag{84}$$

{(56)–(58); [(51), 2], (74), (77)–(79)}

$$z_1^{\cdot} = z_2 - p\lambda s_{31}, \quad z_1(0,t) = 0 \tag{85}$$

$$z_2^{\cdot} = -z_1 - p\lambda s_{32}, \quad z_2(0,t) = 0 \tag{86}$$

$$z_3^{\cdot} = -p\lambda s_{33}, \quad z_3(0,t) = 0 \tag{87}$$

{(60)–(62); [(33), (51), 2], (29), (31), (52)–(54), (73)–(79)}

$$F_1^{\cdot} = F_2 + \lambda F_3 + P_1^{(1)}, \quad F_1(0,t) = ? \tag{88}$$

$$F_2^{\cdot} = -F_1 + P_2^{(1)}, \quad F_2(0,t) = ? \tag{89}$$

$$F_3^{\cdot} = -\epsilon^2\lambda F_1 + P_3^{(1)}, \quad F_3(0,t) = ? \tag{90}$$

{(64), (66); [(26), (33), (44), (49), (68), 2], (29), (31), (52)–(54), (73)–(79)}

$$M_t^{\cdot} = \lambda[\epsilon^2 M_m - \ln(1 + \mu)] - \rho^{\cdot} F_3 - P_3^{(2)}, \quad M_t(0,t) = ? \tag{91}$$

$$M_m^{\cdot} = -\lambda M_t + \rho^{\cdot} F_1 + P_1^{(2)}, \quad M_m(0,t) = ? \tag{92}$$

{[(46), (66), 2]; [(48), (49), 2]}[3]

$$\lambda^{\cdot} = [(1 + \tfrac{1}{2}\mu)M_t + \delta(1 + \mu)F_3 - \lambda\mu A]/E,$$

$$\lambda(0,t) = -T_u(0,t)/\ln[1 + \mu(0,t)] = ? \tag{93^4}$$

$$\mu^{\cdot} = (1 + \mu)\{[(\mu A - (\delta/\lambda)(1 + \mu)F_3]\ln(1 + \mu) - \mu M_t/\lambda\}/E, \quad \mu(0,t) = ? \tag{94}$$

Conclusions

Although we have ended with a relatively large number of equations, it must be emphasized that they involve only *one* spatial variable. This is a consequence of incorporating explicitly the constraint of inextensionality. Also these equations apply to plates of essentially *any* planform.

In a subsequent paper we intend to compute numerically the motion of a skewed quadrilateral plate that is subjected, at its free end, to a static dead load that is then released suddenly.

References

1 Simmonds, J. G., and Libai, A., "Exact Equations for the Inextensional Deformation of Cantilevered Plates," ASME JOURNAL OF APPLIED MECHANICS, Vol. 46, 1979, pp. 631–636.

2 Simmonds, J. G., and Libai, A., "Alternate Exact Equations for the Inextensional Deformation of Arbitrary, Quadrilateral, and Triangular Plates," ASME JOURNAL OF APPLIED MECHANICS, Vol. 46, 1979, pp. 895–900.

3 Beatty, M., "Vector Analysis of Finite Rotations," ASME JOURNAL OF APPLIED MECHANICS, Vol. 44, 1977, pp. 501–502.

---

[3] Recall that $P\cos(\epsilon\phi)$ is to be replaced by F_3 in equation (68) of [2].

[4] This equation replaces (65).

Y. Takeuti
Professor.
Mem. ASME

T. Furukawa
Postgraduate Student.

Department of Mechanical Engineering,
University of Osaka Prefecture,
Mozu, Sakai, 591, Japan

Some Considerations on Thermal Shock Problems in a Plate

Manson has given a well-known conventional approach to thermal shock problems in a plate. In his investigation, however, the inertia term and the thermomechanical coupling term were neglected in the governing field equations. As a result, the treatment became quasi-static, and then it was inadequate to model thermal shock problems having a steep time-gradient in the thermal and mechanical fields. In the present paper, we examine a rigorous treatment to find the exact solution for thermal shock problems in a plate when the following two effects are taken into account:

(*a*) *Dynamic treatment due to the presence of an inertia term.*
(*b*) *A coupled thermal stress problem in the presence of a thermoelastic coupling term.*

Thus we can determine the significance of these effects on the thermal stress distribution when a sudden change of temperature occurs.

1 Introduction

When thermal stresses are generated by a sudden change in temperature, this is called a thermal shock problem. In Manson's well-known approach [1] on this subject, the conventional treatise for thermal shock problems in a plate under an unsteady-state temperature field, rests on the assumption that the inertia term may be neglected in the governing equation of motion, and that the thermoelastic coupling term may be neglected in the heat-conduction equation. This hypothesis, based on the quasi-static process, is known to yield useful results in practical engineering applications without significant errors.

Strictly speaking, however, in a conventional analysis such as Manson's, time enters only as a parameter in transient thermal and mechanical problems. It is evident that the quality of approximation must depend both upon the size of the relevant intrinsic inertia or coupling parameter and on the nature of time variations inherent in the temperature distribution. In particular, if the temperature field exhibits sufficiently steep time-gradients, dynamic effects disregarded in the traditional treatment of the problem may become significant. When the inertia term is taken into account, the character of the problem is considerably altered.

Moreover, if presence of a thermoelastic coupling is taken into account, an exact analysis would require the simultaneous determination of stress and temperature distributions.

In order to check Manson's theory, the present paper has considered both effects separately for the thermal shock problem in a plate, and we have learned which effect is most significant for determining thermal stress distribution.

From an analytical point of view, the effect of the coupling term appears in the heat conduction equation, and the effect of the inertia term appears in the mechanical field equation. Therefore, it is an important and interesting problem that the treatments are individually pursued for the uncoupled dynamic problem and for the quasi-static coupled problem when the boundary and initial conditions used in a plate are the same as those of Manson's problem.

From our results, it seems more important to consider the coupling term rather than the inertia term for ordinary metals.

2 Dynamic Thermal Stresses in a Plate

In this section, first we limit consideration to the uncoupled dynamic problem of thermoelasticity.

The inertia term has been taken into account in several thermoelastic investigations since the appearance of Danilovskaya's [2] and Mura's [3] original papers. Most papers deal with the problems of infinite or semi-infinite regions, and present only the first wave of the thermoelastic stresses. Only Singh and Puri's papers [4, 5] deal with the dynamic thermal stresses in a plate with finite width. However, their investigations found solutions for cases having an infinitely large heat-transfer coefficient in a surrounding liquid, and obtained only the components of thermal stresses normal to the boundary (σ_{xx}). As for thermal shock problems, the component of stress normal to the section (σ_{yy}) is greater and the solution for this stress component is

---

Contributed by the Applied Mechanics Division for publication in the JOURNAL OF APPLIED MECHANICS.

Discussion on this paper should be addressed to the Editorial Department, ASME, United Engineering Center, 345 East 47th Street, New York, N.Y. 10017, and will be accepted until June 1, 1981. Readers who need more time to prepare a Discussion should request an extension from the Editorial Department. Manuscript received by ASME Applied Mechanics Division, October, 1979; final revision, July, 1980.

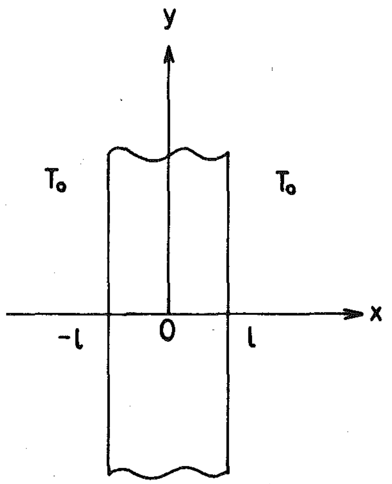

Fig. 1 Boundary conditions on a plate

more important. Moreover, in Puri's work, numerical results were not given, so we cannot imagine any of the characteristic behavior of a thermal stress distribution due to the dynamic effect.

As shown in Fig. 1, an infinitely long plate with width $2l$ is suddenly heated by liquid at the high temperature T_0.

The uncoupled heat-conduction equation is given by

$$\kappa T_{,xx} = T_{,t} \tag{1}$$

in which the comma denotes partial differentiation with respect to a variable and T is the temperature change, κ is the thermal diffusivity, and t is time.

For the sake of convenience, we introduce the following dimensionless quantities:

$$X = x/l,\ Y = y/l,\ Z = z/l,\ T_D = T/T_0,\ t_D = \kappa t/l^2,\ H = hl \tag{2}$$

where h is the relative surface heat-transfer coefficient. Upon substitution of these in equation (1), we have

$$T_{D,XX} = T_{D,t_D} \tag{3}$$

The initial and the boundary conditions can be written in the nondimensional forms

$$T_D(X, 0) = 0 \quad \text{at} \quad t_D = 0 \tag{4}$$

$$T_{D,X} \pm H(T_D - 1) = 0 \quad \text{at} \quad X = \pm 1 \tag{5}$$

Applying the Laplace transform over time, denoted by a bar, the system of the heat-conduction equations is reduced to

$$\overline{T}_{D,XX} = p\,\overline{T}_D \tag{6}$$

$$\overline{T}_{D,X} \pm H(\overline{T}_D - p^{-1}) = 0 \quad \text{at} \quad X = \pm 1 \tag{7}$$

where p is a parameter of the Laplace transform.
It follows from equations (6) and (7) that

$$\overline{T}_D = \frac{H \cosh(\sqrt{p}X)}{p(\sqrt{p}\sinh\sqrt{p} + H\cosh\sqrt{p})} \tag{8}$$

Inverting the Laplace transform, we obtain the temperature solution

$$T_D = 1 - 2\sum_{n=1}^{\infty} \frac{\sin\omega_n \cos(\omega_n X)}{\omega_n + \sin\omega_n \cos\omega_n} e^{-\omega_n^2 t_D} \tag{9}$$

where ω_n are the positive roots of the equation

$$\omega_n \tan\omega_n = H \tag{10}$$

The one-dimensional thermoelastic equilibrium equation with the inertia term can be expressed as

$$u_{,xx} - v_p^{-2}u_{,tt} = \{(1+\nu)/(1-\nu)\}\alpha T_{,x} \tag{11}$$

where u is the displacement component in the x-direction, ν is Poisson's ratio, E is Young's modulus, ρ is the density, α is the linear thermal expansion coefficient, and

$$v_p^2 = (1-\nu)E/\{(1+\nu)(1-2\nu)\rho\}$$

For the present problem, the stress components can be expressed in the dimensionless forms

$$\begin{aligned}
\sigma_{XX} &= \{(1-\nu)/(1-2\nu)\}\{u_{D,X} + \nu(C_{1D}+C_{2D})/(1-\nu) - T_D\} \\
\sigma_{YY} &= \{(1-\nu)/(1-2\nu)\}\{\nu(u_{D,X}+C_{2D})/(1-\nu) + C_{1D} - T_D\} \\
\sigma_{ZZ} &= \{(1-\nu)/(1-2\nu)\}\{\nu(u_{D,X}+C_{1D})/(1-\nu) + C_{2D} - T_D\}
\end{aligned} \tag{12}$$

where

$$\begin{aligned}
u_D &= u\{(1-\nu)/(1+\nu)l\alpha T_0\} \\
\{C_{1D}, C_{2D}\} &= \{(1-\nu)/(1+\nu)\alpha T_0\}\{c_1(t), c_2(t)\} \\
\{\sigma_{XX}, \sigma_{YY}, \sigma_{ZZ}\} &= \{(1-\nu)/E\alpha T_0\}\{\sigma_{xx}, \sigma_{yy}, \sigma_{zz}\}
\end{aligned} \tag{13}$$

and $c_1(t)$ and $c_2(t)$ are the normal strain in the y and z-directions, respectively, to be determined by the boundary conditions. It follows from equations (11) and (13) that

$$u_{D,XX} - V^{-2}u_{D,t_Dt_D} = T_{D,X} \tag{14}$$

where

$$V = v_p l/\kappa$$

Now we assume that the initial conditions are given by

$$u_D(X, 0) = 0, \quad C_{1D}(0) = C_{2D}(0) = 0 \tag{15}$$

Applying the Laplace transform to equation (14) with conditions (15), it follows that

$$\overline{u}_{D,XX} - (p^2/V^2)\overline{u}_D = \overline{T}_{D,X} \tag{16}$$

Substituting equation (8) into (16), the solution of $\overline{u}_D$ is therefore,

$$\overline{u}_D = A\sinh\left(\frac{pX}{V}\right) + \frac{H\sinh(\sqrt{p}X)}{(1-p/V^2)p\sqrt{p}\,(\sqrt{p}\sinh\sqrt{p} + H\cosh\sqrt{p})} \tag{17}$$

where A is an integral constant.

Applying the Laplace transform to the first equation of (12) with the conditions of (15), we have

$$\overline{\sigma}_{XX} = \frac{1-\nu}{1-2\nu}\left\{\frac{p}{V}A\cosh\frac{pX}{V} + \frac{H\cosh\sqrt{p}X}{V^2(1-p/V^2)(\sqrt{p}\sinh\sqrt{p} + H\cosh\sqrt{p})} + \frac{\nu}{1-\nu}(\overline{C}_{1D} + \overline{C}_{2D})\right\} \tag{18}$$

For the traction-free surface, the normal stresses must vanish at the boundaries

$$\overline{\sigma}_{XX} = 0 \quad \text{at} \quad X = \pm 1. \tag{19}$$

Substituting equation (18) into equation (19) we obtain

$$\frac{p}{V}A\cosh(p/V) + \frac{H\cosh\sqrt{p}}{V^2(1-p/V^2)(\sqrt{p}\sinh\sqrt{p} + H\cosh\sqrt{p})} + \frac{\nu}{1-\nu}(\overline{C}_{1D} + \overline{C}_{2D}) = 0 \tag{20}$$

The remaining boundary condition is given for the following three end conditions:

(i) The displacements are not restrained in either the y and z-directions

$$\int_{-1}^{1}\overline{\sigma}_{YY}dX = \int_{-1}^{1}\overline{\sigma}_{ZZ}dX = 0 \tag{21}$$

(*ii*) The displacement is restrained in the z-direction (or y) only

$$\int_{-1}^{1} \bar{\sigma}_{YY} dX = 0, \quad \overline{C}_{2D} = 0 \tag{22}$$

(*iii*) The displacements are restrained in both directions

$$\overline{C}_{1D} = \overline{C}_{2D} = 0 \tag{23}$$

By using the foregoing conditions of equations (20)–(23), A, $\overline{C}_{1D}$, and $\overline{C}_{2D}$ can be determined, and then the subsidiary solution of $\bar{u}_D$ can be obtained. Thus, applying the Laplace inversion formulas with the theorem of residue, the final expression of u_D can be expressed as

$$\begin{aligned} u_D = \xi_k X - 2 \sum_{n=1}^{\infty} & \frac{e^{-\omega_n{}^2 t_D} \sin \omega_n}{(1 + \Omega_n V^{-1})(\omega_n + \sin \omega_n \cos \omega_n)} \\ & \times \left[\frac{\sin \omega_n X}{\omega_n} + \left\{ \Omega_n \cos \omega_n - \eta_k \left(\frac{1-2\nu}{1-\nu} V + \Omega_n \right) \frac{\sin \omega_n}{\omega_n} \right\} \right. \\ & \left. \times \frac{\sinh \Omega_n X}{\omega_n{}^2 (1 - \eta_2 \eta_k \Omega_n{}^{-1} \tanh \Omega_n) \cosh \Omega_n} \right] \\ & - 2H \sum_{n=1}^{\infty} \{ (K_k I_k - L_k G_k) \cos (V p_{nk} t_D) \\ & + (K_k G_k + L_k I_k) \sin (V p_{nk} t_D) \} \sin p_{nk} X \end{aligned} \tag{24}$$

in which the subscripts k to η are used to indicate the foregoing boundary conditions of equations (21)–(23), and then η_k is taken as follows:

$$\eta_1 = 2\nu, \quad \eta_2 = \nu/(1-\nu), \quad \eta_3 = 0, \tag{25}$$

and

$$\begin{aligned} & \xi_1 = (1-\nu)/(1+\nu), \quad \xi_2 = 1 - \nu, \quad \xi_3 = 1, \quad \Omega_n = \omega_n{}^2 V^{-1}, \\ & A_k = \alpha_{nk} D_k + H \cos \alpha_{nk}, \quad B_k = \alpha_{nk} E_k + H \tanh \alpha_{nk} \sin \alpha_{nk}, \\ & K_k = (p_{nk} A_k V^{-1} - B_k)[(1 + p_{nk}{}^2 V^{-2}) \\ & \qquad \times (A_k{}^2 + B_k{}^2)\{p_{nk}{}^2 - \eta_2 \eta_k (1 - \eta_2 \eta_k)\} \sin p_{nk}]^{-1}, \\ & L_k = (A_k + p_{nk} B_k V^{-1}) K_k / (p_{nk} A_k V^{-1} - B_k), \\ & \qquad D_k = \tanh \alpha_{nk} \cos \alpha_{nk} - \sin \alpha_{nk}, \\ & I_k = p_{nk} V^{-1} \cos \alpha_{nk} - (\eta_k / 2\alpha_{nk}) \{ p_{nk} E_k V^{-1} \\ & \qquad + (1 - 2\nu) D_k / (1 - \nu) \} \\ & G_k = -p_{nk} V^{-1} \tanh \alpha_{nk} \sin \alpha_{nk} + (\eta_k / 2\alpha_{nk}) \\ & \qquad \times \{ (1 - 2\nu) E_k / (1 - \nu) - p_{nk} D_k / V \}, \\ & E_k = \tanh \alpha_{nk} \cos \alpha_{nk} + \sin \alpha_{nk}, \quad \alpha_{nk} = \sqrt{p_{nk} V / 2} \end{aligned} \tag{26}$$

where p_{nk} are the positive roots of the equation

$$\cos p_{nk} - (\eta_2 \eta_k \sin p_{nk}) p_{nk}{}^{-1} = 0 \tag{27}$$

In a similar way, after the inversions, coefficients C_{1D} and C_{2D} can be uniquely determined.

Substituting the foregoing results into equation (12), the complete expressions for thermal stresses are

$$\begin{aligned} \sigma_{XX} = \frac{1-\nu}{1-2\nu} & \sum_{n=1}^{\infty} \\ & \times \frac{2 \sin \omega_n \cdot e^{-\omega_n{}^2 t_D}}{(1 + \Omega_n V^{-1})(\omega_n + \sin \omega_n \cos \omega_n)\{1 - \eta_2 \eta_k \tanh \Omega_n / \Omega_n\}} \\ & \times \left[\eta_k \left(\frac{1-2\nu}{1-\nu} + \frac{\Omega_n}{V} \right) \left\{ \frac{\cosh \Omega_n X}{\cosh \Omega_n} - 1 \right\} \frac{\sin \omega_n}{\omega_n} \right. \\ & + (\cos \omega_n - \cos \omega_n X) \frac{\eta_2 \eta_k \tanh \Omega_n}{V} \\ & \left. + \{ \cos \omega_n X - (\cosh \Omega_n X \cos \omega_n) / \cosh \Omega_n \} \Omega_n V^{-1} \right] \\ & + 2H \{ (1-\nu)/(1-2\nu) \} \sum_{n=1}^{\infty} \{ (K_k I_k - L_k G_k) \cos p_{nk} V t_D \end{aligned} \tag{28}$$

$$\begin{aligned} & + (K_k G_k + L_k I_k) \sin p_{nk} V t_D \} \\ & \qquad \times (\phi_k \cos p_{nk} - \cos p_{nk} X) p_{nk} \end{aligned} \tag{28}$$

(Cont.)

$$\begin{aligned} \sigma_{YY} = \frac{1-\nu}{1-2\nu} & \sum_{n=1}^{\infty} \\ & \times \frac{2 \sin \omega_n \cdot e^{-\omega_n{}^2 t_D}}{(1 + \Omega_n V^{-1})(\omega_n + \sin \omega_n \cos \omega_n)\{1 - (\eta_2 \eta_k \tanh \Omega_n) \Omega_n{}^{-1}\}} \\ & \times \left[\left(\frac{1-2\nu}{1-\nu} + \frac{\Omega_n}{V} \right) \left\{ \eta_2 \eta_k \frac{\cosh \Omega_n X}{\cosh \Omega_n} - \phi_k \right\} \right. \\ & \times \frac{\sin \omega_n}{\omega_n} + (\phi_k \cos \omega_n - \eta_k \cos \omega_n X)(\eta_2 \tanh \Omega_n)/V \\ & + \Omega_n V^{-1} \{ \cos \omega_n X - \nu \cosh \omega_n X \cos \omega_n / (1-\nu) \cosh \Omega_n \} \\ & \left. + \{ (1-2\nu)/(1-\nu) \} \{ 1 - \eta_2 \eta_k \tanh \Omega_n / \Omega_n \} \cos \omega_n X \right] \\ & + 2H \{ (1-\nu)/(1-2\nu) \} \eta_2 \sum_{n=1}^{\infty} \{ (K_k I_k - L_k G_k) \cos p_{nk} V t_D \\ & + (K_k G_k + L_k I_k) \sin p_{nk} V t_D \} \times (\phi_k \sin p_{nk} - p_{nk} \cos p_{nk} X) \\ & + (\phi_k - \phi_1) \end{aligned} \tag{29}$$

where $\phi_1 = 1$, $\phi_2 = 1$, $\phi_3 = 0$.

For the sake of brevity, the expression of σ_{ZZ} is omitted here.

It is obvious from equations (28) and (29) that thermal stresses can be represented as the sum of the term decaying exponentially with time and the term oscillating as a pulse with time.

Numerical Results

Numerical calculations based upon the foregoing derivations were carried out for the first end Condition (*i*). In our computations we adopt the following values as material constants:[1]

$$\nu = 1/3, \quad H = 10, \quad V = 100$$

In evaluating the eigenvalues in equations (10) and (27), we found 50 terms by Newton's approximation technique. The calculation of the stresses was truncated at 50 terms, and it was successful enough to obtain convergence. Figs. 2 and 3 show the variations in thermal stresses on the normal section with thickness for several dimensionless times. Figs. 4 and 5 show the variations in stresses at the middle section and at the boundary surface with dimensionless time. Throughout the figures, the classical solutions are plotted as dotted lines.

The maximum value of σ_{XX} occurs at the middle surface of the plate. However, since the maximum σ_{YY} or σ_{ZZ} is much larger than the maximum σ_{XX}, it is very important to find σ_{YY} and σ_{ZZ}.

3 Coupled Thermal Stresses in a Plate

Next, we consider only the effect of the coupling term for the same problem in a plate.

For coupled thermal stress problems, there have been several approximate solutions for a short time period in the works of Hetnarski and others [6–8]. However, they only treated the problems for the infinite or semi-infinite region, and for limited time of heating. Therefore, there has been no rigorous solution for the plate with a finite thickness for the whole time period.

As was noted earlier in this paper, in a precise analysis of thermal shock problems, the treatment requires simultaneous determination of temperature and deformation due to the possibility of a large coupling parameter or a large volumetric strain velocity. For the present case, the corrected heat-conduction equation can be written as

$$T_{D,XX} - T_{D,t_D} = \delta (u_{D,X} + C_{1D} + C_{2D})_{,t_D} \tag{30}$$

---

[1] We use exaggerated value for V to find a particular behavior of the stress propagation due to the dynamic effect; see Table 1.

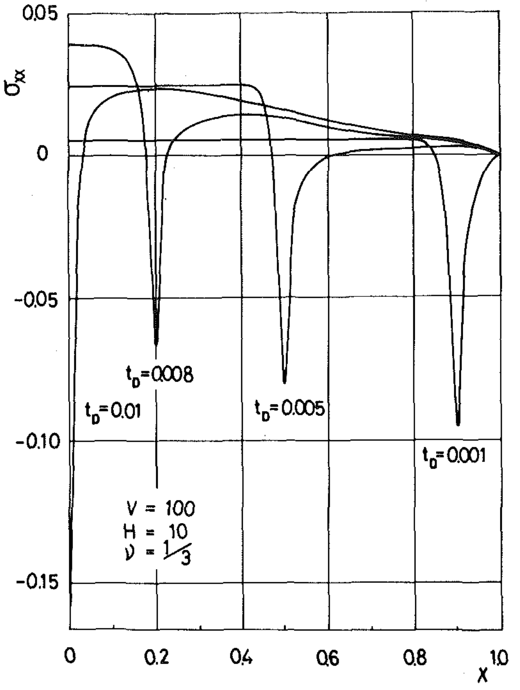

Fig. 2 Dynamic thermal stress distribution of σ_{XX} in cross-sectional direction for very short time

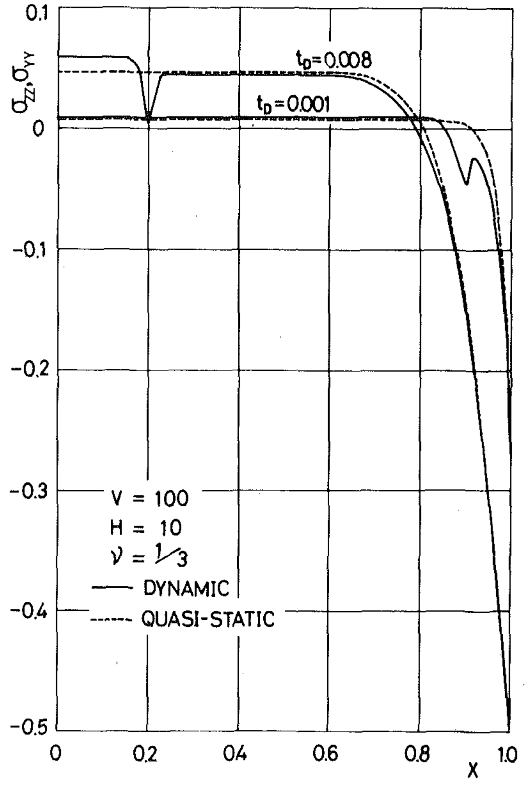

Fig. 3 Dynamic thermal stress distribution of σ_{YY} in cross-sectional direction

where δ is the coupling parameter

$$\delta = \frac{(1+\nu)E\alpha^2 T^*}{(1-\nu)(1-2\nu)\rho c_\nu} \tag{31}$$

The equation of equilibrium is given by

$$u_{D,XX} = T_{D,X} \tag{32}$$

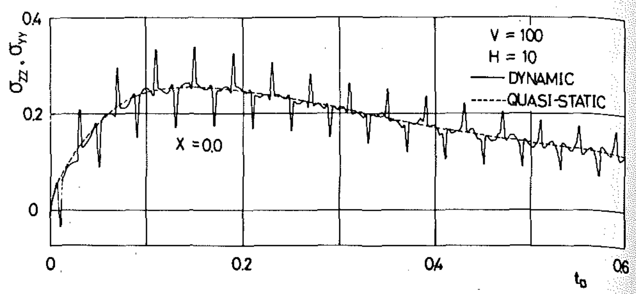

Fig. 4 Propagation of dynamic thermal stresses σ_{YY} in the middle plane of the plate

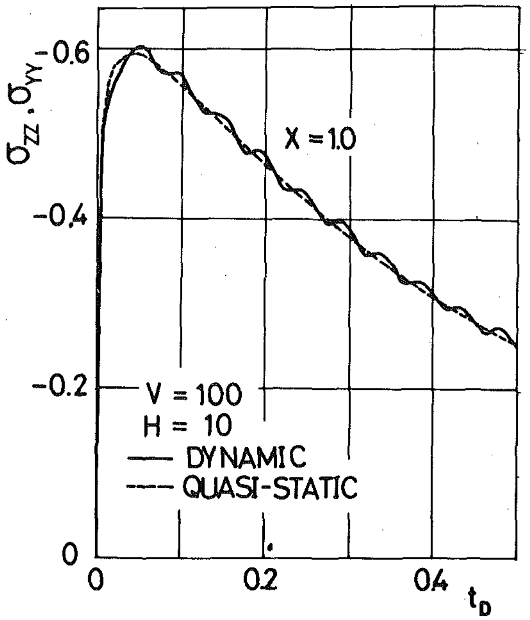

Fig. 5 Dynamic thermal stresses variation of σ_{YY} on the surface with time

Applying Laplace transforms to equations (30) and (32), we obtain

$$\overline{u}_{D,XX} = \overline{T}_{D,X} \tag{33}$$

$$\overline{T}_{D,XX} - p\overline{T}_D = \delta p(\overline{u}_{D,X} + \overline{C}_{1D} + \overline{C}_{2D}) \tag{34}$$

Solving the foregoing two equations simultaneously, we obtain

$$\overline{T}_D = A\cosh qX - \{\delta/(1+\delta)\}(\overline{C}_{1D} + \overline{C}_{2D} + D) \tag{35}$$

$$\overline{u}_D = (A\sinh qx/q - \delta X(\overline{C}_{1D} + \overline{C}_{2D})/(1+\delta) + DX/(1+\delta) \tag{36}$$

where A and D are integral constants, and $q = \sqrt{(1+\delta)p}$.

Substituting the results of equations (35) and (36) into equations (12), we have

$$\begin{aligned}
\overline{\sigma}_{XX} &= \nu\{\overline{C}_{1D} + \overline{C}_{2D} + (1-\nu)D/\nu\}/(1-2\nu) \\
\overline{\sigma}_{YY} &= -A\cosh qX + \frac{\{1-\nu+(2-3\nu)\delta\}\overline{C}_{1D}}{(1-2\nu)(1+\delta)} \\
&\quad + \frac{\{\nu+(1-\nu)\delta\}(\overline{C}_{2D}+D)}{(1-2\nu)(1+\delta)} \\
\overline{\sigma}_{ZZ} &= -A\cosh qX + \frac{\{\nu+(1-\nu)\delta\}(\overline{C}_{1D}+D)}{(1-2\nu)(1+\nu)} \\
&\quad + \frac{\{1-\nu+(2-3\nu)\delta\}\overline{C}_{2D}}{(1-2\nu)(1+\nu)}
\end{aligned} \tag{37}$$

Unknown constants A, $\overline{C}_{1D}$, $\overline{C}_{2D}$, and D can be determined by the conditions of equations (7), (19), and (21)–(23).

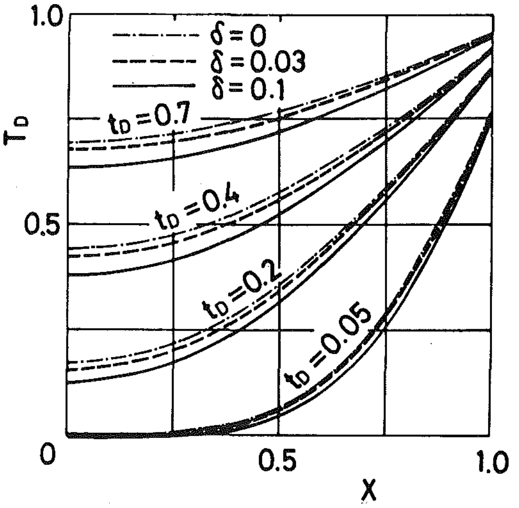

Fig. 6 Coupled temperature variation in the cross-sectional direction for the Boundary Condition (*I*)

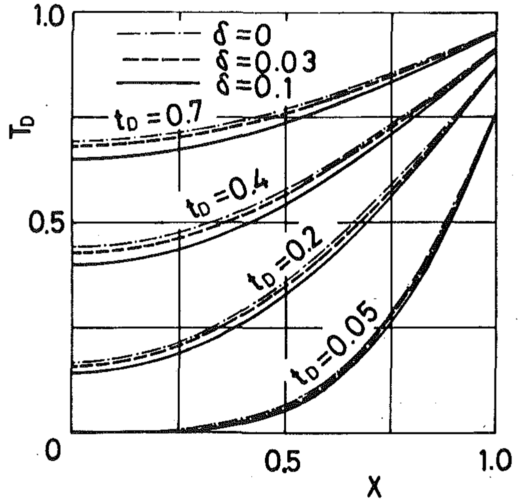

Fig. 7 Coupled temperature variation in the cross-sectional direction for the Boundary Condition (*III*)

It follows that the subsidiary solution can be expressed as

$$\bar{T}_D = A(\cosh qX - R\sinh q/q)$$

$$\bar{u}_D = A(\sinh qX/q - PX\sinh q/q)$$

$$\bar{\sigma}_{XX} = 0 \qquad (38)$$

$$\bar{\sigma}_{YY} = A(-\cosh qX + Q\sinh q/q)$$

$$\bar{\sigma}_{ZZ} = A(-\cosh qX + S\sinh q/q)$$

where

$$A = (H/p)(q\sinh q + H\cosh q - HR\sinh q/q)^{-1}$$

P, Q, R, and S are to be taken for each boundary conditions of (*i*)–(*iii*), respectively

$$(i)\ P = 2\{\nu + (1-\nu)\delta\}/\{1+\nu+3(1-\nu)\delta\},\quad Q = 1,$$

$$R = 2(1-2\nu)\delta/\{1+\nu+3(1-\nu)\delta\},\quad S = 1,$$

$$(ii)\ P = \{\nu + (1-\nu)\delta\}/\{1+2(1-\nu)\delta\},\quad Q = 1, \qquad (39)$$

$$R = (1-2\nu)\delta/\{1+2(1-\nu)\delta\},\quad S = P,$$

$$(iii)\ P = Q = R = S = 0$$

Applying the theorem of residue and inverting the transforms, we obtain

$$T_D = 1 - \sum_{n=1}^{\infty} B_n\{\cos(\omega_n X) - (R\sin\omega_n)/\omega_n\}e^{-\omega_n{}^2 t_D/(1+\delta)} \qquad (40)$$

$$u_D = \xi X - \sum_{n=1}^{\infty} B_n\{\sin(\omega_n X)/\omega_n - (P\sin\omega_n)X/\omega_n\}e^{-\omega_n{}^2 t_D/(1+\delta)} \qquad (41)$$

$$\sigma_{XX} = 0$$

$$\sigma_{YY} = -\eta - \sum_{n=1}^{\infty} B_n\{-\cos\omega_n X + (Q\sin\omega_n)/\omega_n\}e^{-\omega_n{}^2 t_D/(1+\delta)}$$

$$\sigma_{ZZ} = -\zeta - \sum_{n=1}^{\infty} B_n\{-\cos\omega_n X + (S\sin\omega_n)/\omega_n\}e^{-\omega_n{}^2 t_D/(1+\delta)} \qquad (42)$$

where ω_n are the nth positive roots of

$$H\omega_n\cos\omega_n - (\omega_n{}^2 + HR)\sin\omega_n = 0, \qquad (43)$$

and B_n, ξ, η, and ζ are given by the forms as

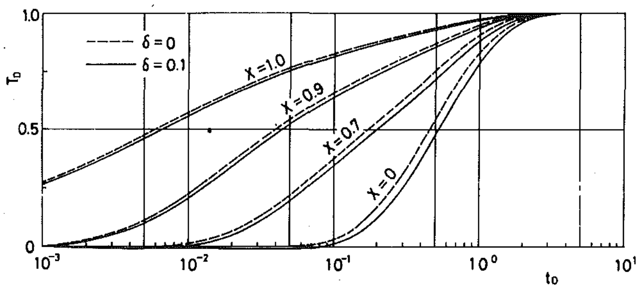

Fig. 8 Coupled temperature variation with times

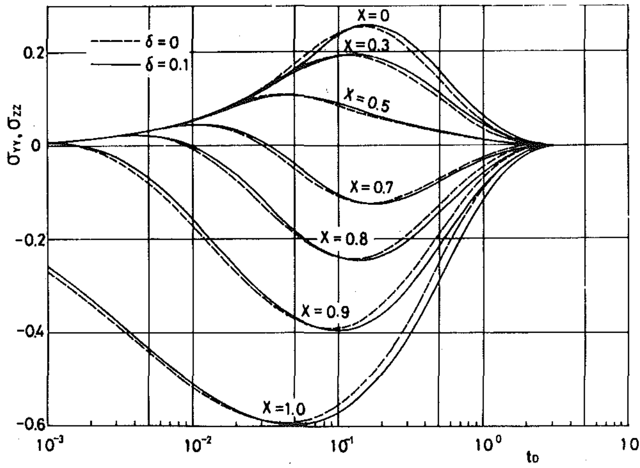

Fig. 9 Coupled thermal stress variations of σ_{YY} with time for Condition(*I*)

$$B_n = \frac{2\omega_n\sin\omega_n}{\omega_n{}^2 + \omega_n\sin\omega_n\cos\omega_n - 2R\sin^2\omega_n} \qquad (44)$$

$$\xi = (1-\nu)/(1+\nu),\quad \eta = \zeta = 0,\quad \text{for Condition } (i),$$

$$\xi = 1-\nu,\quad \eta = 0,\quad \zeta = 1-\nu,\quad \text{for Condition } (ii),$$

$$\xi = \eta = \zeta = 1,\quad \text{for Condition } (iii).$$

Numerical Results

The foregoing solutions will be illustrated numerically by the following values of material constants:

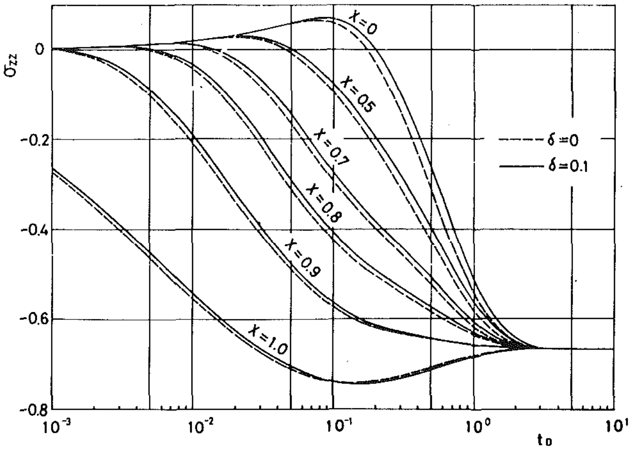

Fig. 10 Coupled thermal stress variations of σ_{zz} with time for Condition(*ii*)

Table 1 A glance at dynamic and coupling parameters

Fundamental equation:

(Dynamic) $u_{,xx} - \Gamma u_{,tt} = T_{,x}$ $(\Gamma = V^{-2})$ (14)

(Coupled) $T_{,xx} - T_{,t} = \delta(u_{,x} + c_1 + c_2)_{,t}$ (30)

Parameter	Materials		
	mild steel	aluminum	lead
Γ	3.74×10^{-18}	5.95×10^{-17}	7.23×10^{-18}
δ	0.0083	0.031	0.079

where $T = 293^{\circ}K$, $l = 10cm$

$$\nu = 1/3, \quad H = 10, \quad \delta = 0.1$$

The foregoing coupling parameter is representative of commercial alloys. For example, when $T^* = 293°K$ (20°C), typical values of the coupling parameter δ are

$$\text{aluminum alloy} = 0.031, \quad \text{lead} = 0.079.$$

Figs. 6–8 show temperature variations with thickness and dimensionless time when $\delta = 0.1, 0.03$, and 0 for the three boundary conditions. Figs. 9 and 10 show the thermal stress variations with the dimensionless time and thickness for the Condition (*i*) and (*ii*). In all the figures, the dotted lines express the results of uncoupled cases. It is obvious that there is a distinct difference between the coupled and the uncoupled treatment. As is seen in Figs. 9 and 10, one observes that the maximum stress at the surface must be decreased in the first short period of heating when the coupling effect is taken into account.

4 Conclusion

There have been a lot of papers which have dealt with coupled dynamic thermoelasticity. However, most of the papers solved only pure one-dimensional problems for an infinite or a semi-infinite region, and only σ_{XX} was obtained in their results. In engineering thermal shock problems, it is more important to consider the problem of a finite domain having moderate thickness, and to find the stress component σ_{YY} or σ_{ZZ} for the actual engineering problems, even if it is limited to one-dimensional treatment. Moreover, in industrial machine design, it is a truly important problem which effect is to be considered in calculation as well as being theoretically interesting.

This paper is divided in two parts, dealing, respectively, with inertia effects and thermoelastic coupling effects. First, we reconsidered results of the dynamic problems discussed in Section 2. The present exact analytical stress solution, which vanishes at time $t \to \infty$, is valid for the whole time interval, while Singh's solution is valid only for the short-time interval.

In general, the magnitude of this dynamic effect depends on the parameter $V = v_p l/\kappa$. In the case of $V = 100$, adopted in the present analysis, the dynamic effect is fairly large in stress distributions for σ_{xx}, σ_{yy}, and σ_{zz}. However, if we take $l = 1$ cm in computing for an actual steel, then the value of V becomes very large, that is, $V = 5.18 \times 10^6$. For this value, therefore, in actual problems, the corrections introduced in the foregoing from the present calculations are so small that the dynamic thermal stresses may be approximated closely by a quasi-static solution. In other words, the ratio of dynamic to quasi-static values of thermal stresses is unity for a large value of V, and hence the dynamic effects can be neglected in usual materials. Thus Manson's formula can be approximately justified when one considers the dynamic effect of thermal shock problems.

Now, let us consider the thermal shock problems in a plate when considering coupling thermoelastic problems in the absence of an inertia term. It appears from Figs. 6–9 that coupled solutions exhibit explicit differences between the coupled theory and classical ones in temperature and thermal stresses, even if computation is carried out for practical engineering materials. For the temperature solutions, for example, the ratio of coupled to uncoupled values is about 5 percent smaller for $\delta = 0.03$ and $t_D = 0.4$. This means that the coupling effect reduces temperature rise, and the thermal stresses are slightly relieved in the beginning of the thermal shock for the Boundary Conditions (*i*)–(*iii*). However, the thermal stresses become slightly larger than the uncoupled results after some time interval, due to the delay in temperature rise between the outer surface and the middle one. As a whole, the maximum thermal stress is larger in the case of the coupled theory. Therefore, it is necessary to modify Manson's uncoupled quasi-static formula.

In summary, as illustrated in Table 1, it should be pointed out that the coupling parameter in a fundamental heat-conduction equation eventually appears in value to effect the temperature distribution. Hence, we can guess that the dynamic parameter gives very small effect.

In conclusion, it is more important to consider the coupled effects than to consider the inertia effects for thermal shock problems because the coupling effects are much larger than the inertia effects for ordinary metals. In the usual case, inertia effects may disappear in pure thermal stress problems in contrast to the coupling effects which result in a small lag in the stress distribution.

References

1 Manson, S. S., *Thermal Stress and Low Cycle Fatigue*, McGraw-Hill, New York, 1966, pp. 273–311.

2 Danilovskaya, V. I., "Thermal Stresses in an Elastic Half-Space Due to a Sudden Heating of Its Boundary," (in Russian), *Prikladnaya Matematika i Mekhanika*, Vol. 14, 1950, pp. 316–318.

3 Mura, T., "Thermal Strain and Stresses in Transient State," *Proceedings of the 2nd Japan Congress on Applied Mechanics*, Vol. 2, 1952, pp. 9–12.

4 Singh, A., and Puri, P., "Dynamic Thermal Stresses in an Infinite Slab," *Arch. Mech. Stosw.*, Vol. 15, 1963, pp. 77–88.

5 Puri, P., "One-Dimensional Dynamic Problems of Thermoelasticity," *Arch. Mech. Stosw.*, Vol. 16, 1964, pp. 93–102.

6 Hetnarski, R., "Coupled One-Dimensional Thermal Shock Problem for Small Times," *Arch. Mech. Stosw.*, Vol. 13, 1961, pp. 295–305.

7 Hetnarski, R., "Solution of the Coupled Problem of Thermoelasticity in the Form of Series of Functions," *Arch. Mech. Stosw.*, Vol. 16, 1964, pp. 919–941.

8 Boley, B. A., and Tolins, I. S., "Transient Coupled Thermoelastic Boundary-Value Problems in the Half Space," ASME JOURNAL OF APPLIED MECHANICS, Vol. 29, 1962, pp. 637–644.

M. Hirao
Research Associate.

H. Fukuoka
Professor.

Faculty of Engineering Science,
Osaka University,
Toyonaka,
Osaka 560, Japan

K. Hori
Engineer,
Higashi-Fuji Laboratory,
Toyota Motor Co., Ltd.,
Shizuoka 410-11, Japan

Acoustoelastic Effect of Rayleigh Surface Wave in Isotropic Material

The acoustoelastic effect is investigated for the Rayleigh surface wave propagating in a homogeneous isotropic material. The initial deformations considered are uniform and nonuniform only in the direction of depth. The formulas for the velocity change versus the change in the applied static stress are derived in the first-order approximation. The result for the uniform case, reducing to that of Hayes and Rivlin, exhibits no dispersion and the velocity change proportional to the principal strains. To be noted is the result that the Rayleigh wave becomes dispersive under the nonuniform stress state, depending roughly on the product of the wave number and the characteristic depth over which the stress varies. The dispersion is remarkable for the relatively low frequency and diminishes as the frequency increases. The analytical results are verified by measurements with mild-steel samples on the basis of the sing-around technique.

1 Introduction

The relationship between the stress in solids and the characteristics of elastic wave propagation has been studied through the years as a branch of the nondestructive evaluation (NDE) of materials. One hopes to provide a new and powerful technique for the stress measurement by means of ultrasonics. The basis of study is the stress-induced change in the propagation velocity, which is referred to as acoustoelastic effect [1–5]. The property of this effect depends on the material nonlinearity and the type of wave propagated, including the directions of propagation and polarization. Linear relationship for the velocity change and the change in the applied static stress has been confirmed experimentally within the elastic region of most materials [1, 3, 5]; an exception is copper [5].

Main part of the experimental work reported up to now has been confined to the usage of ultrasonic bulk waves, i.e., longitudinal and transverse waves. By the bulk wave acoustoelasticity, the applied or residual stress averaged over the total path-length can be measured, provided that the second and third-order elastic constants and initial anisotropy are given in advance, and vice versa. One of the shortcomings of current bulk-wave usage is the inability to detect the through-wall stress distribution, for example, the residual stress in cold-rolled plate. In some applications, moreover, the knowledge of the surface stress is only required. The acoustoelasticity of the Rayleigh wave [6] is hopeful for such possible applications, although it has been long untried. The Rayleigh wave travels the free surface of solid half space and the depth of penetration into the solid is approximately one wavelength. Therefore, in the case of nonuniform stress state, the Rayleigh wave acoustoelasticity is expected to depend on the frequency. The main purpose of the present research is to verify this expectation by both analysis and experiment and discuss the property of this type of Rayleigh wave dispersion.

The Rayleigh wave acoustoelasticity was first analyzed by Hayes and Rivlin [7], together with that of the Love wave. For aluminum alloys, Martin [8] investigated the relative effects of stress and preferred grain orientation. Also, Adler, et al. [9], utilized the Rayleigh wave velocity change to measure the residual stress of circumferential welds in pipe. These works, however, restricted themselves to the case of uniform deformation, so that the Rayleigh wave dispersion due to stress application was neither discussed nor observed. In this paper, we shall first analyze the Rayleigh wave acoustoelasticity in the uniform case and present the experimental data from the uniaxial tensile loading. The velocity change shows good agreement between analysis and experiment. The formula for the nonuniform case is next derived, which shows the Rayleigh wave dispersion as a function of the degree of stress variation within the penetration depth. The experiment with the simple bending of plates, where the stress varies linearly with depth, supports the analytical result. In the experimental work, the transit time variation of the Rayleigh wave in the megahertz range is measured by the sing-around technique.

2 Basic Equations

We are concerned with the Rayleigh wave propagation on the free surface of a semi-infinite homogeneous isotropic material which is initially under static deformation. The theoretical foundation of this problem has been established on the basis of the second-order elasticity [4, 10] and here we will only outline the important results.

The infinitesimal displacement w_k superimposed on some given stress state is governed by [4]

$$\rho \frac{\partial^2 w_k}{\partial t^2} = \sigma_{lm} \frac{\partial^2 w_k}{\partial x_l \partial x_m} + \frac{\partial}{\partial x_l}\left(S_{klmn} \frac{\partial w_m}{\partial x_n}\right), \qquad (1)$$

Contributed by the Applied Mechanics Division for publication in the JOURNAL OF APPLIED MECHANICS.

Discussion on this paper should be addressed to the Editorial Department, ASME, United Engineering Center, 345 East 47th Street, New York, N. Y. 10017, and will be accepted until June 1, 1981. Readers who need more time to prepare a Discussion should request an extension from the Editorial Department. Manuscript received by ASME Applied Mechanics Division, February, 1980; final revision, August, 1980.

$$\begin{aligned}S_{klmn} = {} & \lambda\delta_{kl}\delta_{mn} + \mu(\delta_{km}\delta_{ln} + \delta_{kn}\delta_{lm}) \\ & + [(-\lambda + \nu_1)\delta_{kl}\delta_{mn} + (-\mu + \nu_2)(\delta_{km}\delta_{ln} + \delta_{kn}\delta_{lm})]e \\ & + 2(\lambda + \nu_2)(e_{kl}\delta_{mn} + e_{mn}\delta_{kl}) \\ & + 2(\mu + \nu_3)(e_{km}\delta_{ln} + e_{kn}\delta_{lm} + e_{lm}\delta_{kn} + e_{ln}\delta_{km}), \qquad (2)\end{aligned}$$

where $e = e_{kk}$, a Cartesian coordinate system $x_i (i = 1, 2, 3)$ specifies the position in the initial deformed state, ρ is the mass density, σ_{kl} the stress, and e_{kl} the strain in that state. There holds the generalized Hooke's law between σ_{kl} and e_{kl}. The second and third-order elastic constants are denoted by (λ, μ) and (ν_1, ν_2, ν_3), respectively. The latter characterizes the material nonlinearity in the first-order approximation. The fourth-order tensor $\mathbf{S}$, which carries the slight anisotropy due to the stress, can be considered as the elasticity tensor for the prestressed isotropic material. Since the acoustoelastic effect is discussed to the first-order, higher-order terms in the initial deformation gradients have been ignored. Hereafter, we employ summation convention for every repeated suffix unless otherwise mentioned.

Let us consider a solid half space occupying the region $x_2 \geqq 0$ and assume that the stress acting is uniform in the whole region or a function of the depth x_2 only. Moreover we take the coordinate axes so as to coincide with the principal directions of stress. Then, from the equilibrium equation and boundary condition, we have $\sigma_{kl} = 0$ for $k \neq l$ and $\sigma_{22} = 0$. When the Rayleigh wave propagates in the x_1-direction, the problem degenerates to two-dimensional and the displacement associated with the Rayleigh wave has the form

$$w_i = f_i(x_2) \exp [ik(x_1 - Vt)], \quad (i = 1, 2) \qquad (3)$$

and $w_3 = 0$ just as the classical treatment. The component w_3 corresponds to the SH mode which is also possible in the semi-infinite solid but now independent of the Rayleigh wave. In equation (3), k denotes the wave number, V the phase velocity, and $f_i (i = 1, 2)$ the amplitudes that depend on the depth.

One more assumption is that the path of the Rayleigh wave is along a straight line. Then, the boundary condition can be written in the following simple form [10]:

$$\sigma'_{kl}l_l + \sigma_{kl}l'_l = 0 \quad \text{at} \quad x_2 = 0, \qquad (4)$$

where

$$\sigma'_{kl} = -\sigma_{kl}\frac{\partial w_m}{\partial x_m} + \sigma_{km}\frac{\partial w_l}{\partial x_m} + \sigma_{lm}\frac{\partial w_k}{\partial x_m} + S_{klmn}\frac{\partial w_m}{\partial x_n}, \qquad (5)$$

and

$$l'_l = \frac{1}{2} l_l l_m l_n \left(\frac{\partial w_m}{\partial x_n} + \frac{\partial w_n}{\partial x_m}\right) - l_m \frac{\partial w_m}{\partial x_l}, \qquad (6)$$

are the increments owing to the displacement w_k, respectively, in the stress and the unit normal to the boundary surface. Making use of the fact that $\mathbf{l} = [0, -1, 0]^T$, $w_3 = 0$, and $w_i (i = 1, 2)$ is independent of x_3, we find the relevant boundary condition in terms of f_i

$$\left.\begin{aligned} Df_1 + if_2 = 0, \\ S_{1122}f_1 + S_{2222}Df_2 = 0, \end{aligned}\right\} \quad \text{at} \quad x_2 = 0, \qquad (7)$$

where $D \equiv d/d(kx_2)$. Since the particle motion by the Rayleigh wave is confined to the vicinity of the free surface, the amplitudes should decay with depth

Substitution of w_k into equation (1) leads to

$$\begin{aligned} & [D(S_{1212}D) - (\sigma_{11} + S_{1111}) + \mu V^2/V_T^2]f_1 \\ & \qquad + i[(S_{1212} + S_{1122})D + DS_{1212}]f_2 = 0, \\ & [D(S_{2222}D) - (\sigma_{11} + S_{1212}) + \mu V^2/V_T^2]f_2 \\ & \qquad + i[(S_{1212} + S_{1122})D + DS_{1122}]f_1 = 0, \qquad (8) \end{aligned}$$

where $V_T^2 = \mu/\rho$. By setting

$$\begin{aligned} f_1 &= -i[(S_{1212} + S_{1122})D + DS_{1212}]F, \\ f_2 &= [\mu V^2/V_T^2 - (\sigma_{11} + S_{1111}) + D(S_{1212}D)]F, \end{aligned} \qquad (9)$$

the first of equations (8) is automatically satisfied. Then, applying equations (9) to the second of equations (8), we have the fourth-order differential equation for F;

$$\begin{aligned} & [\mu V^2/V_T^2 - (\sigma_{11} + S_{1111}) + D(S_{1212}D)][\mu V^2/V_T^2 - (\sigma_{11} + S_{1212}) \\ & \qquad + D(S_{2222}D)]F + [(S_{1212} + S_{1122})D + DS_{1122}] \\ & \qquad\qquad \times [(S_{1212} + S_{1122})D + DS_{1212}]F = 0. \qquad (10) \end{aligned}$$

Equation (10) and boundary condition (7) are the basic equations for the following analysis.

3 Uniform Deformation

The acoustoelastic analysis for the uniform deformation and corresponding experimental data are to be presented in this section. The analytical result does not differ essentially from that of Hayes and Rivlin [7].

Analysis. When the initial deformation is uniform, equation (10) reduces to

$$\begin{aligned} & [\mu V^2/V_T^2 - (\sigma_{11} + S_{1111}) + S_{1212}D^2][\mu V^2/V_T^2 - (\sigma_{11} + S_{1212}) \\ & \qquad + S_{2222}D^2]F + (S_{1212} + S_{1122})^2 D^2 F = 0. \qquad (11) \end{aligned}$$

The general solution to this equation is

$$F = \sum_{i=1}^{4} A_i \exp(-m_i k x_2), \qquad (12)$$

where A's are the constants and m's are the real roots of the characteristic equation. Since F should tend zero as x_2 tends infinity, the two of the A's with $m < 0$ must vanish. Thus we obtain

$$F = \sum_{i=1}^{2} A_i \exp(-m_i k x_2), \qquad (13)$$

where $m_i > 0$ $(i = 1, 2)$.

On substituting equation (13), the boundary condition (7) yields a set of linear homogeneous equations for A_1 and A_2. From the condition that the solution be nontrivial, we have the frequency equation

$$\begin{aligned} & [S_{2222}\{\alpha - (\sigma_{11} + S_{1111})\} + S_{1122}{}^2]\{\alpha - (\sigma_{11} + S_{1212})\} \\ & \qquad = S_{1212}S_{2222}(\alpha - \sigma_{11})^2\{\alpha - (\sigma_{11} + S_{1111})\}, \qquad (14) \end{aligned}$$

for $\alpha \equiv \rho V^2$. In the derivation, the characteristic equation has been used to eliminate m_1 and m_2, and a degenerate case $m_1 = m_2$ has been omitted. The possible degenerate cases were fully discussed in [7]. The frequency equation (14) determines the Rayleigh wave (phase) velocity in uniformly deformed material as the function of the initial strains.

Since $\sigma_{22} = 0$, only two of the principal strains are independent with each other and the following convenient expression is assumed:

$$\alpha = \alpha_0 + \alpha_1 e_{11} + \alpha_2 e_{22}. \qquad (15)$$

Applying equation (15) to equation (14) and neglecting the higher-order terms in the strains, the expressions for the constants α's can be deduced. The resultant α's are, of course, exactly the same as those given by Hayes and Rivlin [7] with the formal difference of definition of elastic constants. To save space, they are not presented here. The relative velocity change is then given by

$$\Delta V/V_0 \equiv (V - V_0)/V_0 = (\alpha_1/2\alpha_0)e_{11} + (\alpha_2/2\alpha_0 - \mu/\lambda)e_{22}, \qquad (16)$$

where V_0 is the Rayleigh wave velocity in the natural state, being defined by $(\alpha_0/\rho_0)^{1/2}$, ρ_0 is the density in the natural state or

$$\begin{aligned} & (V_0/V_{T0})^6 - 8(V_0/V_{T0})^4 + 8[(3\lambda + 4\mu) \;/\; (\lambda + 2\mu)](V_0/V_{T0})^2 \\ & \qquad - 16(\lambda + \mu)/(\lambda + 2\mu) = 0. \qquad (17) \end{aligned}$$

In view of equation (16), the Rayleigh wave in the uniformly deformed material undergoes no dispersion as in the stress-free case. This property might be foreseen, since all the quantities appeared in the nondimensional form in the starting equations (7) and (11).

Determination of Elastic Constants. Throughout the present study, the specimens were machined from the rolled plate of mild steel (C; 0.17 percent, Si; 0.25 percent, Mn; 0.72 percent). They were tem-

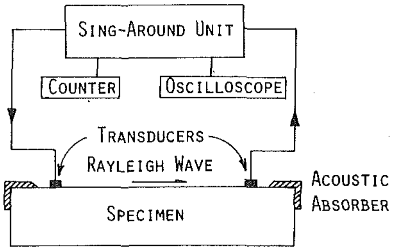

Fig. 1 **Measurement system based on the sing-around technique**

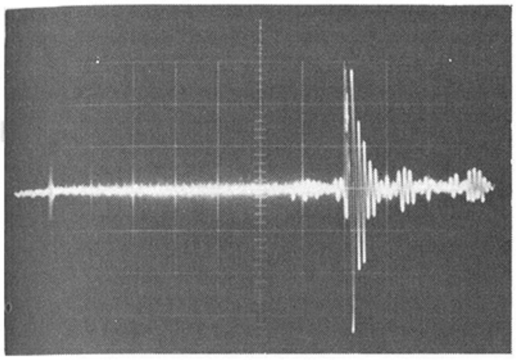

Fig. 2 **Rayleigh wave signal produced by 2MHz strip-type transducers [abscissa; 5 μsec/div, ordinate; 0.5 Volt/div]**

pered at 900°C for ¾ hr and subsequently air-cooled. The surfaces were finished by plane-grinding and mechanical-polishing.

To evaluate the coefficients of equation (16), five elastic constants and the density should be known. For this, the acoustoelastic effect of bulk waves was first measured on the 20mm-thickness tensile specimens, employing 5 MHz PZT transducers and the sing-around apparatus which will be explained in the following. The load was uniaxial tension up to 150MPa in stress and the path of the ultrasonics was taken to be normal to the load direction. The result of averaging several measurements is as follows: $\lambda = 10.74 \times 10^4$, $\mu = 8.19 \times 10^4$, $\nu_1 = -0.13 \times 10^5$, $\nu_2 = \nu_3 = -2.0 \times 10^5$ (all in unit of MPa) and $\rho_0 = 7.837 \times 10^3$ kg/m^3.

With these values of elastic constants and density, the coefficients α's are calculated to render

$$\Delta V/V_0 = -0.31e_{11} - 0.69e_{22}, \tag{18}$$

and $V_0 = 3.00 \times 10^3$m/sec. In the following experiment, the Rayleigh wave is propagated parallel to the direction of uniaxial tensile load. In this situation, we have $\Delta V/V_0 = -0.11e_{11}$ by substituting $e_{22} = -\sigma e_{11}$, σ being Poisson's ratio ($\sigma = 0.284$). Since the rate of the Rayleigh wave velocity change is very small, i.e., about a tenth part of the strain in the propagation direction, more care was required in the acoustoelastic experiment for the Rayleigh wave than that for the bulk waves. For comparison, the longitudinal and transverse waves polarized parallel and normal to the direction of uniaxial load underwent the relative velocity changes at the rates 0.32, 0.26, and −1.48, respectively; all three propagated normal to the load direction.

Experimental Result. The electronic equipments used for the Rayleigh wave acoustoelasticity is illustrated schematically in Fig. 1. An electronic pulse of 0.1 μsec width was sent out from the sing-around unit. The transmitting transducer converted it into the ultrasonic Rayleigh wave pulse. After traveling the specimen surface, the pulse reached the receiving transducer. Then, the Rayleigh wave was transformed back into the electronic pulse and fed back to the sing-around unit. This pulse was therein amplified to $+1.5V$ from the zero level through the auto-gain controller and after preselected delay time retriggered the pulse generator, thus circulating the closed loop.

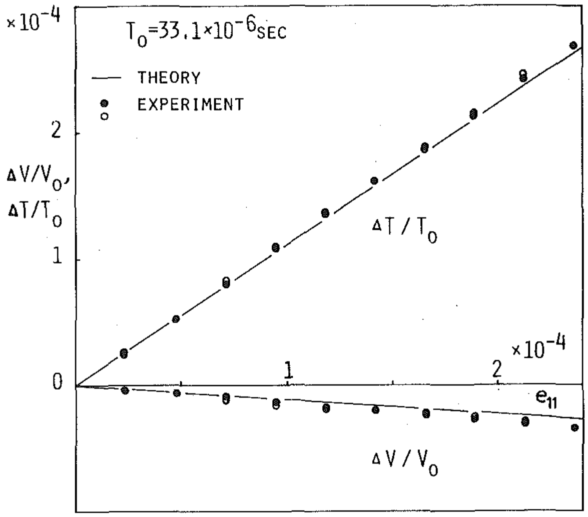

Fig. 3 **Relative variations of Rayleigh wave transit time and velocity versus the uniaxial tensile strain**

The trigger level was fixed to $0.5V$ in the present experiment. The counter, having a reference frequency of 10MHz, displayed the averaged period over 10^4 sing-around cycles. The oscilloscope and the testing machine completed the measurement system.

The Rayleigh wave was generated and received by a pair of thickness-mode 2MHz PZT ceramic strips, of 14mm length and 0.75mm width, attached in parallel on the specimen surface. The strip width corresponds to a half wavelength of the Rayleigh wave to be generated. Under this condition, optimum efficiency for Rayleigh wave excitation and reception could be achieved. This type of Rayleigh wave transducer was found to be superior in resulting a sharply rising signal to the wedge and comb transducers [6]. A disadvantage is the low tolerance of the ceramic strips to high loading, so that we set the load limit to be 50MPa in the surface stress. Fig. 2 shows the Rayleigh wave signal generated and received in this way.

In order to obtain the relative velocity change experimentally, the relation

$$\Delta V/V_0 = e_{11} - \Delta T/T_0, \tag{19}$$

was used, e_{11} being the surface strain in the propagation direction. The relative change in the transit time ($\Delta T/T_0$) was determined from the change in the sing-around period T, while e_{11} could be monitored by the strain gauge method. The typical result of the tensile experiment is shown in Fig. 3. The same specimens that were used to determine the elastic constants were tested and the strip-type transducers were spaced about 100mm apart. The straight lines are drawn according to the analytical result, i.e., $\Delta V/V_0 = -0.11e_{11}$ and $\Delta T/T_0 = 1.11e_{11}$. Data taken during the loading sequence are designated by solid circles and data during the unloading sequence by open circles. Within the tested range of strain, the Rayleigh wave velocity appears to vary linearly with the applied strain as predicted by the analysis based on the second-order elastic theory. Taking the low rate of change into account, the analytical and experimental results agree well with each other.

4 Nonuniform Deformation

The stress application to the material causes the slight change in the elastic properties and then in the response to the elastic wave propagation. As the consequence, the acoustoelastic phenomena do occur. When the initial deformation has a distribution in the direction of depth, the degree of change in the elastic properties also varies with depth. In this sense, the material subjected to such a deformation is qualitatively similar to the layered or stratified material, in which the Rayleigh wave is known to be dispersive. This section is devoted to the analytical and experimental verification of the natural expectation that the Rayleigh wave will be dispersive in the nonuniformly deformed material.

Analysis. As in the preceding section, the solution F is constructed so as to satisfy equation (10) and boundary condition (7) within the first-order approximation. Since the coefficients of equation (10) are no longer constant in this case, the calculation turns much complicated. Based on the smallness of initial strain, which is in the order 10^{-3} at most for mild steel, we shall seek the solution F in the perturbation scheme and assume the expansion

$$F = F^0 + F^1. \tag{20}$$

The zeroth-order solution F^0 corresponds to the classical one when the initial stress is absent, while the first-order solution F^1 denotes the small perturbation from it due to the initial stress, reflecting the acoustoelastic effect. The order of magnitude of F^1 relative to F^0 is that of the initial strain.

Substituting equation (20) into equation (10) and collecting the terms with the same order, the respective equations for F^0 and F^1 can be yielded. One for F^0 is

$$\{\kappa D^4 + [(\kappa+1)V_0^2/V_{T0}^2 - 2\kappa]D^2 + (V_0^2/V_{T0}^2 - \kappa)(V_0^2/V_{T0}^2 - 1)\}F^0 = 0, \tag{21}$$

from which we obtain

$$F^0 = \sum_{i=1}^{2} A_i \exp(-n_i k x_2), \tag{22}$$

where

$$n_1 = (1 - V_0^2/V_{T0}^2)^{1/2}, \quad n_2 = (1 - V_0^2/\kappa V_{T0}^2)^{1/2}, \tag{23}$$

and $\kappa = (\lambda + 2\mu)/\mu$. When the stress is removed, m_1 and m_2 of equation (13) reduce to n_1 and n_2. On the other hand, the equation for F^1 is inhomogeneous one with homogeneous part identical to the left-hand side of equation (21). By using the solution F^0 and then the integration, we have

$$\begin{aligned} F^1 = hk \sum_{i=1}^{2} A_i \Big[& n_2 e^{n_1 k x_2} \int_\infty^{x_2} R_i e^{-(n_i+n_1)kx_2} dx_2 - n_1 e^{n_2 k x_2} \\ & \int_\infty^{x_2} R_i e^{-(n_i+n_2)kx_2} dx_2 - n_2 e^{-n_1 k x_2} \int_0^{x_2} R_i e^{-(n_i-n_1)kx_2} \\ & \times dx_2 + n_1 e^{-n_2 k x_2} \int_0^{x_2} R_i e^{-(n_i-n_2)kx_2} dx_2 \Big], \end{aligned} \tag{24}$$

where $h = [2\kappa n_1 n_2 (n_1^2 - n_2^2)]^{-1}$. The explicit expression of $R_i (i = 1, 2)$ is presented in the Appendix.

The solution F thus constructed obeys the restriction that f_1 and f_2 should tend zero as x_2 tends infinity, irrespective of the external stress acting. Applying $F = F^0 + F^1$ to boundary condition (7), we obtain after tedious but straightforward computation

$$\begin{aligned} \sum_{i=1}^{2} \Big[& -\kappa n_2^2 - (\kappa-1)n_i^2 + z + U_{1i}^{(1)} \overline{e_{11}} + U_{1i}^{(2)} \overline{e_{22}} + V_{1i}^{(1)} \overline{De_{11}} \\ & + V_{1i}^{(2)} \overline{De_{22}} + W_{1i}^{(1)} \overline{D^2 e_{11}} + W_{1i}^{(2)} \overline{D^2 e_{22}} \\ & + h(\kappa-1)n_2\{(1+n_1^2)I_{i1} - 2n_1 n_2 I_{i2}\}\Big] A_i = 0, \\ \sum_{i=1}^{2} \Big[& -\{(\kappa-1)(\kappa-2) - \kappa^2 n_2^2 + \kappa n_i^2 + \kappa z\} n_i + U_{2i}^{(1)} \overline{e_{11}} \\ & + U_{2i}^{(2)} \overline{e_{22}} + V_{2i}^{(1)} \overline{De_{11}} + V_{2i}^{(2)} \overline{De_{22}} + W_{2i}^{(1)} \overline{D^2 e_{11}} + W_{2i}^{(2)} \overline{D^2 e_{22}} \\ & + h(\kappa-1)n_1 n_2 \{2I_{i1} - (1+n_1^2)I_{i2}\}\Big] A_i = 0, \end{aligned} \tag{25}$$

where

$$z \equiv 2\Delta V V_0/V_{T0}^2, \tag{26}$$

$$\begin{aligned} I_{ij} &= \int_0^\infty k R_i e^{-(n_i+n_j)kx_2} dx_2 \\ &= [n_i^2 - n_j^2 + \kappa(n_j^2 - n_2^2)](n_i + n_j)^{-1} z \\ &\quad + \sum_{l=1}^{2} \{-M_i^{(l)} \overline{e_{ll}} + [L_i^{(l)} + (n_i + n_j)M_i^{(l)}]E_{ij}^{(l)}\}, \end{aligned} \tag{27}$$

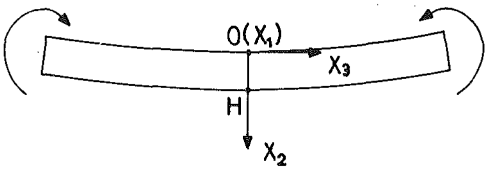

Fig. 4 Configuration of coordinate system for simple bending of plate; Rayleigh wave is propagated along x_1-axis

$$E_{ij}^{(l)} = \int_0^\infty k e_{ll} e^{-(n_i+n_j)kx_2} dx_2 \quad \text{(not summed on } l\text{)} \tag{28}$$

The bar over the strains and their derivatives indicates the values at the free surface $x_2 = 0$. Here recall that $\sigma_{22} = 0$ and e_{11} and e_{22} are independent with each other. For U's, V's, and W's, see the Appendix.

With the aid of equation (27), equations (25) can be written in the matrix form

$$(G_{ij} + a_{ij} z + b_{ij})A_j = 0, \tag{29}$$

where

$$G_{ij} = (\kappa - 1)\begin{bmatrix} -(1+n_1^2) & -2n_2^2 \\ 2n_1 & n_2(1+n_1^2) \end{bmatrix}, \tag{30}$$

$$a_{ij} = \begin{bmatrix} 1 + (\kappa-1)[(1+n_1^2)/(2n_1)^2 - n_2/(n_1+n_2)], & 1 + (\kappa-1)[1 - (1+n_1^2)/n_1(n_1+n_2)]/2\kappa \\ -\kappa n_1 + (\kappa-1)[1 - (1+n_1^2)n_1 - (n_1+n_2)]/2n_1, & -\kappa n_2 - (\kappa-1)[(n_1-n_2)^{-1} - (1+n_1^2)/4n_2]/\kappa \end{bmatrix}, \tag{31}$$

and b_{ij} is the linear combination of $\overline{e_{ll}}$, $\overline{De_{ll}}$, $\overline{D^2 e_{ll}}$ and $E_{ij}^{(l)}$ $(l = 1, 2;$ not summed). The nontrivial condition for A_i then requires

$$|G_{ij} + a_{ij} z + b_{ij}| = 0. \tag{32}$$

Note that z and the elements of **b** are of the order of the initial strains. Neglecting these small terms, we obtain the zeroth-order solution $|\mathbf{G}| = 0$, which leads to equation (17) and gives V_0. The variation of the phase velocity owing to the external stress is determined by the first-order solution as

$$z = -(G_{11}b_{22} + G_{22}b_{11} - G_{12}b_{21} - G_{21}b_{12})/(G_{11}a_{22} + G_{22}a_{11} - G_{12}a_{21} - G_{21}a_{12}). \tag{33}$$

Equation (33) defines z as the function of the principal strains, their derivatives up to the second-order evaluated at $x_2 = 0$, and also the integration over the half space. Since $D \equiv d/d(kx_2)$ and the integration (28) is involved there, z depends on k as well. Therefore the Rayleigh wave is dispersed in nonuniformly deformed material as opposed to the stress-free and uniformly stressed cases. The extent of the Rayleigh wave dispersion is roughly determined by the ratio of the wavelength to the characteristic depth over which the initial stress varies or, in other words, how abruptly the stress varies within the penetration depth. For a given stress state, the dispersion is remarkable for a relatively low frequency and diminishes as the frequency increases. It was numerically checked that, approaching to the high-frequency limit, the result of equation (33) is asymptote to that of equation (15) for the uniform case.

As an illustrating example, the foregoing formula was applied to the Rayleigh wave propagating the surface of the simply bent plate as shown in Fig. 4. In this situation, $\sigma_{11} = \sigma_{22} \doteq 0$ and the terms in k^{-1} do appear since the remaining stress component σ_{33} is the linear function of x_2. As a final result, we obtain

$$\Delta V/V_0 = (\beta_0 + \beta_1/kH)\overline{e_{11}}, \tag{34}$$

where H denotes the plate thickness. The constants β_0 and β_1 can be written in terms of (λ, μ) and (ν_1, ν_2, ν_3), although the expressions are much cumbersome. Using the elastic constants obtained previously,

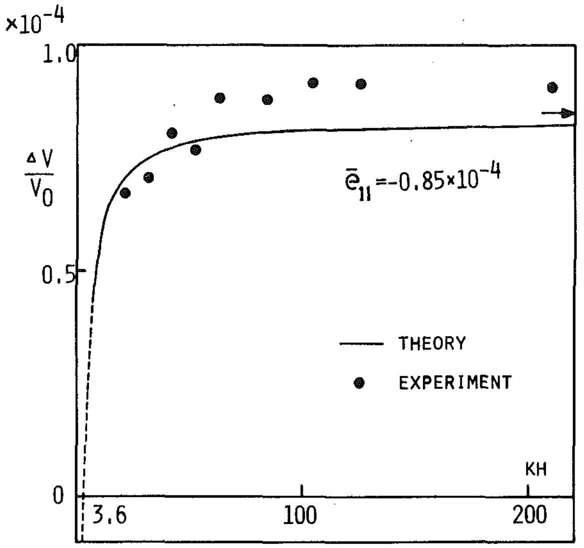

Fig. 5 Dispersion of Rayleigh wave propagating the surface of bent plates; theoretical curve is asymptote to $\Delta V/V_0 = 0.84 \times 10^{-4}$

they are evaluated as $\beta_0 = -0.99$ and $\beta_1 = 3.55$. Equation (34) implies that the phase velocity of the Rayleigh wave changes linearly with the initial strain and furthermore its rate of proportionality consists of the constant and $(kH)^{-1}$ terms. The latter term does cause the Rayleigh wave dispersion. It should be noted that the group velocity resulting from equation (34) is frequency-independent.

Experimental Result. In order to confirm equation (34) experimentally, mild-steel plates of 5, 10, 20mm thicknesses were simply bent. The Rayleigh wave was generated and received, as before, by the strip-type transducers whose resonance frequencies were nominally 2, 3, and 5MHz. They were transversely situated on the surface about 120mm apart. We thus obtain the data as to $\Delta V/V_0$ for nine different values of kH, ranging from 21 to 209.

In Fig. 5, the experimental result is compared with the theoretical curve according to equation (34). The plate thickness was much larger than the Rayleigh wave penetration depth, so that the elastic waves observed were completely Rayleigh waves. Otherwise, such guided waves that obey the Rayleigh-Lamb frequency equation will be produced. The theoretical curve for $kH < 2\pi$ is drawn with broken line, suggesting that the plate thickness is less than the wavelength.

Considering the experimental error, correspondence of the theoretical and experimental results is satisfactory. The slight disagreements could derive from some sources. First, the elastic constants may be inaccurate in a degree. Above all, the precise determination for the value of ν_1 was difficult, which has been the usual case [5]. An additional error source might be the anisotropy or texture developed during the rolling process and the specimen making. The anistropy has some distribution across the thickness, since the material underwent the inhomogeneous plastic deformation. Therefore it may affect the measurement of the Rayleigh wave dispersion due to the nonuniform stress state, although the relative order of magnitude to the acoustoelastic effect seems to be small in reality.

Concluding Remarks

The acoustoelastic theory has been developed to derive the approximate formulas for the Rayleigh wave velocity change induced by the stress. The corresponding experimental data were obtained on the mild-steel samples by using the sing-around apparatus. The result of the uniform case was essentially the same as the case of bulk waves in point of no dispersion and linear relationship between the changes in stress and velocity. The analysis for the nonuniform case revealed the Rayleigh wave dispersion due to the stress nonuniformity in the depthwise direction as well as the proportionality to the surface stress. The analytical result was supported by the experiment with the simple bending of plate. If the higher surface stress were available, the degree of dispersion could be enhanced to make the measurement easy and accurate. Unfortunately, however, the strip-type transducers prevented it because of the low tolerance to the high surface stress.

The acoustoelastic formula obtained in this paper allows the detailed prediction of the dispersion property for a known stress state. But it should be noted that the inverse does not hold in general, that is, the experimental data on the dispersion are not sufficient in themselves for the full estimation of the stress distribution.

Acknowledgment

The authors wish to thank Mr. Y. Kashima for his contribution of determining the elastic constants. They are also grateful to the reviewer for drawing attention to Martin's paper.

References

1 Hughes, D. S., and Kelly, J. L., "Second-Order Elastic Deformation of Solids," *Physical Review*, Vol. 92, 1953, pp. 1145–1149.

2 Toupin, R. A., and Bernstein, B., "Sound Waves in Deformed Perfectly Elastic Materials," *Journal of the Acoustical Society of America*, Vol. 33, 1961, pp. 216–225.

3 Crecraft, D. I., "The Measurement of Applied and Residual Stresses in Metals Using Ultrasonic Waves," *Journal of Sound and Vibration*, Vol. 5, 1967, pp. 173–192.

4 Tokuoka, T., and Iwashimizu, Y., "Acoustoelasticity," *Science of Machine*, Vol. 27, 1975, pp. 860–864 [in Japanese].

5 Fukuoka, H., and Toda, H., "Preliminary Experiment on Acoustoelasticity for Stress Analysis," *Archives of Mechanics*, Vol. 29, 1977, pp. 673–686.

6 Viktorov, I. A., *Rayleigh and Lamb Waves*, Plenum Press, New York, 1967.

7 Hayes, M., and Rivlin, R. S., "Surface Waves in Deformed Elastic Materials," *Archive of Rational Mechanics and Analysis*, Vol. 8, 1961, pp. 358–380.

8 Martin, G. B., "Rayleigh-Wave Velocity, Stress and Preferred Grain Orientation in Aluminum," *Nondestructive Testing International*, Vol. 32, 1974, pp. 199–203.

9 Adler, L., et al., "The Relationship Between Ultrasonic Rayleigh Waves and Surface Residual Stress," *Material Evaluation*, Vol. 35, 1977, pp. 93–96.

10 Eringen, A. C., and Şuhubi, E. S., *Elastodynamics*, Academic Press, New York, 1974.

APPENDIX

$$R_i(x_2) = [n_i^2 - n_1^2 + \kappa(n_i^2 - n_2^2)]z + \sum_{l=1}^{2} (L_i^{(l)} e_{ll} + M_i^{(l)} D e_{ll}), \quad (35)$$

where

$$\begin{aligned} L_i^{(1)} &= 2\kappa r_4 n_i^4 + 2[(V_0^2/V_{T0}^2 - 4)r_4 - \kappa(1 + 2r_4) - 1 - 2r_3]n_i^2 \\ &\quad + 2(1 + 2r_3 + 4r_4)n_1^2 + 2\kappa(1 + r_4)n_2^2, \\ M_i^{(1)} &= 2[(n_1^2 - \kappa n_i)^2 r_4 - (\kappa - 1)(r_3 + r_4)]n_i, \\ L_i^{(2)} &= [r_0(r_1 + 2r_2) + 4(r_3 + 2r_4) + \kappa(r_0 r_2 + 2r_4)]n_i^4 \\ &\quad + \{[(r_1 + 3r_2 - 1 - \kappa)r_0 + 4r_3 + 10r_4]V_0^2/V_{T0}^2 + 2\kappa(1 - r_0 r_2 - 2r_4) \\ &\quad + 2(1 - r_0 r_1 - 2r_0 r_2 - 2r_3 - 4r_4)\}n_2^2 \\ &\quad + [(r_1 + 2r_2 + V_0^2/V_{T0}^2)r_0 - 2]n_1^2 + \kappa(V_0^2/V_{T0}^2 - 2 + r_0 r_2 + 2r_4)n_2^2, \\ M_i^{(2)} &= -\{[(r_1 + 2r_2)r_0 + 4(r_3 + 2r_4)]n_i^2 + (r_0 r_2 + 2r_4)(\kappa n_i^2 + n_1^2) \\ &\quad + \kappa[(r_1 + 2r_2)r_0 + 4(r_3 + 2r_4)]n_2^2 \\ &\quad - (\kappa - 1)[(r_1 + r_2)r_0 + 2(r_3 + r_4)]\}n_i. \quad (36) \end{aligned}$$

In equations (25),

$$\begin{aligned} &U_{1i}^{(1)} = -2[1 + 2(r_3 + 2r_4) + r_3 n_i^2], \quad V_{1i}^{(1)} = 2(r_3 + r_4)n_i, \quad W_{1i}^{(1)} = -2r_4, \\ &U_{1i}^{(2)} = -(V_0^2/V_{T0}^2 - r_1 - 2r_2)r_0 - 2 - (r_0 r_1 + 2r_3)n_i^2, \\ &V_{1i}^{(2)} = [(r_1 + r_2)r_0 + 2(r_3 + r_4)]n_i, \quad W_{1i}^{(2)} = -r_0 r_2 - 2r_4, \\ &U_{2i}^{(1)} = 2\{[\kappa(1 + 3r_4) + 2(2r_3 + r_4)]n_1 - \kappa r_4 n_i^3\}, \\ &V_{2i}^{(1)} = 2[-\kappa(1 + 2r_3) + (2\kappa n_i^2 - 3\kappa - 2)r_4], \quad W_{2i}^{(1)} = -2\kappa r_4 n_i, \end{aligned} \quad (37)$$

$$\begin{aligned} \mathrm{U}_{2i}^{(2)} = -\{&\kappa[(r_1 - r_2 - V_0^2/V_{T0}^2)r_0 + 2(2r_3 + r_4)] \\ &- (r_0 r_2 + 2r_4)(2 + \kappa n_i^2) - 3(r_0 r_1 + 2r_3) + [(r_1 + 2r_2)r_0 \\ &+ 4(r_3 + 2r_4)](n_i^2 + n_2^2)\}n_i, \\ V_{2i}^{(2)} = (2\kappa n_i^2 &+ \kappa - 2)(r_0 r_2 + 2r_4) + \kappa[2 - (r_1 + 2r_2 + V_0^2/V_{T0}^2)r_0], \\ W_{2i}^{(2)} = -\kappa&(r_0 r_2 + 2r_4)n_i. \end{aligned} \tag{37}$$

(37)
(*Cont.*)

In the previous expressions,

$$r_0 = -2\mu/\lambda,\ r_1 = (-\lambda + \nu_1)/\mu, \quad r_2 = -1 + \nu_2/\mu,\ r_3 = (\lambda + \nu_2)/\mu, \quad r_4 = 1 + \nu_3/\mu. \tag{38}$$

A. N. Ceranoglu
Assistant Professor,
Bogazici University,
Istanbul, Turkey

Yih-Hsing Pao
Professor,
Department of Theoretical
and Applied Mechanics,
Cornell University,
Ithaca, N. Y. 14853
Mem. ASME

Propagation of Elastic Pulses and Acoustic Emission in a Plate

Part 1: Theory

Transient waves generated by a variety of dynamic nuclei of strains including a concentrated force, a single-couple, a double-force, a double-couple without moment, a center of rotation, and a center of explosion in an elastic plate are analyzed. Some of these sources, or a combination of them, could be used to model the dynamic process of material defects. The analysis is based on the generalized ray theory and Cagniard's method and the solutions are presented in terms of Green's dyadics for a plate.

1 Introduction

This investigation arose out of a need for a better understanding of the nature of the stress waves generated by defects upon their origination and expansion. It is known that whenever a material undergoes a plastic deformation or local failure, transient elastic waves are generated due to the rapid release of localized strain energy. Such radiation of elastic waves is known as acoustic emission in the field of nondestructive testing of materials [1]. In spite of a great number of research done on the subject, the mode or type of stress wave that dominates in the immediate vicinity of the source of acoustic emission is still unknown. This question cannot be answered unless the dynamic process of the source, and the propagation characteristics of the elastic wave are studied in detail.

In this paper we present several point source models which can be used in describing the mechanism of acoustic emission. The approach is analogous to the modeling of statical point defects in crystalline materials [2], and the mechanism of earthquakes in the field of geophysics [3]. It has been pointed out that the seismic radiation from an earthquake is likely to be connected with the solution of a problem of dislocation, that is, a sudden creation of discontinuities in either the displacement or the stress field across the fault surface. Burridge and Knopoff [4], have shown that such discontinuities can be replaced by a distribution of forces called equivalent body forces, which produce the same radiation when applied over the fault surface in the absence of the fault. They have also shown that while concentrated forces represent discontinuities in the traction field, self equilibrating forces, i.e., forces with zero resultant, can be used to model discontinuities in the displacement fields. An infinite isotropic elastic plate is chosen as the medium where transient waves due to point sources such as a single-force, a double-force, a single-couple, a double-couple without moment, a center of rotation, and a center of dilatation propagate. These sources, known also as nuclei of strains, or some combination of them can be used as equivalent body forces in modeling defects such as initiation and growth of cracks, voids, etc.

Transient response of an elastic plate is usually analyzed by Fourier synthesizing all normal modes, the theory of which was investigated by Lamb [5] and Pursey [6]. The Fourier synthesis can also be effected by applying the Laplace transform. The inversion of the Laplace transform usually involves a summation of residues which are infinite in number, hence, the accuracy of the final answer depends on the number of terms taken in the series.

As an alternative, we have chosen to use a method based on the generalized ray theory. In this theory, the total wave motion is decomposed into disturbances that travel along a multitude of ray-paths, each of which undergoes different number of reflections at the plate surfaces. Since the travel times along ray-paths with a large number of reflections are longer than those with a few reflections, only a finite number of rays are to be considered in each study. The solution thus obtained is exact from the onset of waves up to the time of arrival of the next generalized ray which is not included in the calculations. A review of the method was recently given by Pao and Gajewski [7]. In a half space, the ray-path undergoes, to the most, only one reflection at the surface. Hence, the results given in this paper also include solutions for the aforementioned point sources in a half space [3].

The development of the generalized ray theory goes back to 1939, when Cagniard [8] studied the transient waves in two homogeneous half spaces in contact. In his monumental work, he had shown that by going through a sequence of contour deformations and changes of integration variables, one can find the inverse Laplace transforms of the expressions for each ray. Details of this method related to transient waves in a plate will be given in Parts 2 and 3.

Generalized ray theory and Cagniard's method were first applied to study the wave propagation in elastic plates by Mencher [9] who used the Bromwich expansion to recast the normal mode solution into the form of summation of individual rays. His results were confined

---

Contributed by the Applied Mechanics Division of THE AMERICAN SOCIETY OF MECHANICAL ENGINEERS, for presentation at the 1981 Joint ASME/ASCE Applied Mechanics, Fluids Engineering, and Bioengineering Conference, University of Colorado, Boulder, Colo., June 22-27, 1981.

Discussion on this paper should be addressed to the Editorial Department, ASME, United Engineering Center, 345 East 47th Street, New York, N.Y. 10017, and will be accepted until June 1, 1981. Readers who need more time to prepare a Discussion should request an extension from the Editorial Department. Manuscript received by ASME Applied Mechanics Division, August, 1979. Paper No. 81-APM-4.

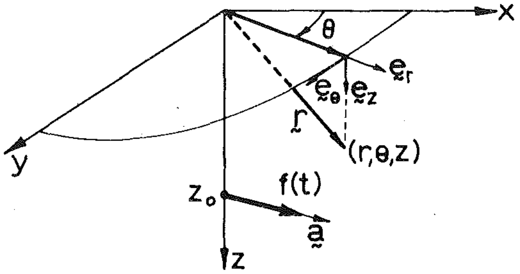

Fig. 1 Geometry of an oblique, concentrated force

to axisymmetric loading and epicentral response. Other works on axisymmetric problems were done by Knopoff [10], Davids [11], Miklowitz [12], and Pao, et al. [13]. Contributions on nonaxisymmetric plate problems were made by Pytel and Davids [14], and Davids and Lawhead [15] where they have considered shear impacts and oblique impacts. However, their results were all for the epicentral responses of the plate. Off-central results were given by Shmuely [16, 17] where he considered a line source on the surface of a plate. Mention should also be made of the works by Fulton and Sneddon [18], Scott and Miklowitz [19], Norwood [20], and Wu and Norwood [21] who have considered distributions of normal surface loads. In addition to a concentrated force, results for a double-force and a center of dilatation were also reported by Pao, et al. [13]. We note that a plate is a special case of a multilayered solid. A comprehensive study of transient waves in a multilayered medium based on the method of generalizated ray theory was made by Müller [22].

In this paper, the solution to nonaxisymmetric point sources such as a concentrated force, a double-force, a single-couple, a double-couple without moment, a center of rotation, and a center of dilatation will be presented using the generalized ray theory [3, 7]. The paper is divided into three parts. Part 1 presents the Laplace transformed solutions for the general response of a plate. All solutions are expressed in terms of Green's dyadics and their derivatives for a plate. In part 2 the details of the Cagniard's method for inverting the Laplace transforms of the epicentral response of the plate will be presented along with numerical calculations. Part 3 will be devoted to the general off-epicentral response of the plate.

2 Concentrated Force in an Elastic Medium

1 Green's Dyadic of Unbounded Medium. Consider a concentrated force of magnitude $f(t)$ acting at the point $(0, 0, z_0)$ along an arbitrary direction indicated by the unit vector **a** (Fig. 1). The solution for this problem is well known [3, 23]. For the purpose of applying this solution to analyze waves in a plate, we recast it in terms of displacement potentials ϕ, ψ, and χ in cylindrical coordinates (r, θ, z) [7, equation 6.11]. The displacements are related to these potentials through the relations

$$u_r = \frac{\partial\phi}{\partial r} + \frac{\partial^2\psi}{\partial r\partial z} + \frac{1}{r}\frac{\partial\chi}{\partial\theta}$$

$$u_\theta = \frac{1}{r}\frac{\partial\phi}{\partial\theta} + \frac{1}{r}\frac{\partial^2\psi}{\partial\theta\partial z} - \frac{\partial\chi}{\partial r} \tag{1}$$

$$u_z = \frac{\partial\phi}{\partial z} + \frac{\partial^2\psi}{\partial z^2} - \kappa^2\frac{\partial^2\psi}{\partial t^2}$$

while the stresses at a surface z = constant are given by

$$\tau_{zz} = \left(\frac{\kappa^2 - 2}{\kappa^2}\right)\frac{\partial^2\phi}{\partial t^2} + \frac{2}{\kappa^2}\frac{\partial}{\partial z}\left(\frac{\partial\phi}{\partial z} + \frac{\partial^2\psi}{\partial z^2} - \kappa^2\frac{\partial^2\psi}{\partial t^2}\right)$$

$$\tau_{rz} = \frac{1}{\kappa^2}\frac{\partial}{\partial r}\left(2\frac{\partial\phi}{\partial z} + 2\frac{\partial^2\psi}{\partial z^2} - \kappa^2\frac{\partial^2\psi}{\partial t^2}\right) + \frac{1}{\kappa^2}\frac{1}{r}\frac{\partial}{\partial\theta}\left(\frac{\partial\chi}{\partial z}\right) \tag{2}$$

$$\tau_{z\theta} = \frac{1}{\kappa^2}\frac{1}{r}\frac{\partial}{\partial\theta}\left(2\frac{\partial\phi}{\partial z} + 2\frac{\partial^2\psi}{\partial z^2} - \kappa^2\frac{\partial^2\psi}{\partial t^2}\right) - \frac{1}{\kappa^2}\frac{\partial}{\partial r}\left(\frac{\partial\chi}{\partial z}\right)$$

The potentials satisfy the wave equation of the type $c_i^2\nabla^2(\phi, \psi, \chi) = \partial^2(\phi, \psi, \chi)/\partial t^2$; where $c_i = c$ for ϕ, and $c_i = C$ for ψ and χ. The two wave speeds and their ratio κ are defined in equation (6).

Denote the Laplace transform of a time function $f(t)$ by $\bar{f}(s)$,

$$\bar{f}(s) = \int_0^\infty f(t)e^{-st}dt. \tag{3}$$

The Laplace transformed displacement potentials for the wave field generated by a concentrated force as shown in Fig. 1 are then given by [7]

$$\bar{\phi}_1(\mathbf{r}, s; \mathbf{a}) = a_z\bar{F}(s)\int_0^\infty S_p(\xi)e^{-s\eta|z-z_0|}J_0(s\xi r)\xi d\xi$$

$$+ a_r\bar{F}(s)\int_0^\infty S_p'(\xi)e^{-s\eta|z-z_0|}J_1(s\xi r)\xi d\xi$$

$$\bar{\psi}_1(\mathbf{r}, s; \mathbf{a}) = -a_z s^{-1}\bar{F}(s)\int_0^\infty S_v(\xi)e^{-s\zeta|z-z_0|}J_0(s\xi r)d\xi$$

$$- a_r s^{-1}\bar{F}(s)\int_0^\infty S_v'(\xi)e^{-s\zeta|z-z_0|}J_1(s\xi r)d\xi$$

$$\bar{\chi}_1(\mathbf{r}, s; \mathbf{a}) = -a_\theta\bar{F}(s)\int_0^\infty S_H(\xi)e^{-s\zeta|z-z_0|}J_1(s\xi r)d\xi. \tag{4}$$

In these equations

$$\bar{F}(s) = \bar{f}(s)/(4\pi\kappa^2\mu h^2) \tag{5}$$

and a_α $(\alpha = r, \theta, z)$ are the components of the unit vector **a** in cylinderical coordinates. The wave speeds c and C of the pressure (P) and shear (S) waves, respectively, are given by

$$c^2 = (\lambda + 2\mu)/\rho, \quad C^2 = \mu/\rho, \quad \kappa = c/C. \tag{6}$$

where λ and μ are the Lamé constants and ρ is the mass density of the material. The η and ζ are the slowness along the z-direction for the P and S-waves, respectively,

$$\eta = (\xi^2 + 1)^{1/2}, \quad \zeta = (\xi^2 + \kappa^2)^{1/2} \tag{7}$$

and ξ is the slowness in the radial direction. Note that h is any convenient length, introduced to normalize length, and the quantities given in equation (1)–(7) have been nondimensionalized while those given in reference [7] were in dimensional form. The quantities in this paper are related to those in reference [7] through the relations

$$(\xi, \eta, \zeta) = c(\xi^*, \eta^*, \zeta^*), \quad \eta^* = (\xi^{*2} + c^{-2})^{1/2},$$

$$\zeta^* = (\xi^{*2} + C^{-2})^{1/2}$$

$$r = r^*/h, \quad z = z^*/h, \quad u = u^*/h$$

$$(\phi, \chi) = h^{-2}(\phi^*, \chi^*), \quad \psi = \psi^* h^{-3}$$

$$t = ct^*/h, \quad s = s^*h/c$$

where the quantities with (*) are in dimensional form as given in reference [7].

For a concentrated force,

$$S_p = -\epsilon, \quad S_p' = -\xi/\eta$$

$$S_v = \xi/\zeta, \quad S_v' = \epsilon, \quad S_H = \kappa^2/\zeta \tag{8}$$

where the subscripts p and v pertain to the pressure waves and vertically polarized shear waves (SV-waves), while H denotes the horizontally polarized shear waves (SH-waves). These source functions together with others are tabulated in Table 1. In equation (8) and the table, ϵ is the directivity constant and it has the value ±1 according to whether the waves are propagating in the direction of $\pm z$-axis from the source.

Substituting equation (4) into (1), we obtain three displacements in Laplace transformed state. The component in the z-direction is

$$\bar{u}_z(\mathbf{r}, s; \mathbf{a}) = s\bar{F}(s)\left[a_z\int_0^\infty S_pD_{zp}e^{-s\eta|z-z_0|}J_0(s\xi r)\xi d\xi\right.$$

$$\left.+ a_r\int_0^\infty S_p'D_{zp}e^{-s\eta|z-z_0|}J_1(s\xi r)\xi d\xi\right] \tag{9}$$

Table 1 Source functions

SOURCE TYPE	FUNCTION	INTERIOR			ON SURFACE			$\bar{F}(s)$
		P ($j = 1$)	SV ($j = 2$)	SH ($j = H$)	P ($j = 1$)	SV ($j = 2$)	SH ($j = H$)	
Center of explosion	S_j^*	$1/\eta$	-	-	-	-	-	$\frac{M_o\bar{f}(s)}{4\pi\kappa^2\mu hs}$
Single force	S_j	$-\varepsilon$	ξ/ζ	κ^2/ζ	$\gamma 2\kappa^2(\xi^2+\zeta^2)/\Delta_r$	$-4\kappa^2\xi\eta/\Delta_r$	κ^2/ζ	$\frac{F_o\bar{f}(s)}{4\pi\kappa^2\mu h^2s^2}$
	S'_j	$-\xi/\eta$	ε		$4\kappa^2\xi\zeta/\Delta_r$	$-\gamma 2\kappa^2(\xi^2+\zeta^2)/\Delta_r$		
Single couple, Double force, & Double couple without moment	S_j	η	$-\varepsilon\xi$	κ^2/ζ	-	-	-	$\frac{M_o\bar{f}(s)}{4\pi\kappa^2\mu s^2h^3}$
	S'_j	$-\xi/\eta$	ε	$-\varepsilon\kappa^2$	-	-	-	
	S''_j	$\varepsilon\xi$	$-\zeta$	-	-	-	-	
	S'''_j	$-\varepsilon\xi$	ξ^2/ζ	-	-	-	-	
Center of rot.	$S_j^\dagger$	-	$-\kappa^2/\zeta$	$-\varepsilon\kappa^2$	-	-	-	
	$S_j^{\dagger\prime}$	-	-	κ^2/ζ	-	-	-	

$\varepsilon=\pm 1$ according to the direction the ray travels with respect to ± z-axis,
$\gamma=\pm 1$ whether the source is at $z=0$ or $z=1$ surfaces.
$\Delta_r = 4\xi^2\eta\zeta - (\xi^2+\zeta^2)^2$
$\eta^2 = \zeta^2+1, \ \zeta^2 = \xi^2+\kappa^2$
$\kappa^2 = (c/C)^2 = (\lambda+2\mu)/\mu$

h is the thickness of the plate which is taken as unity in the calculations, and $M_o = \lim(F_o\delta)$ as $\delta \to 0$. For a double force the same limit is denoted by D_o.

$$+ s\bar{F}(s)\left[a_z \int_0^\infty S_v D_{zv} e^{-s\zeta|z-z_0|} J_0(s\xi r)\xi d\xi \right.$$
$$\left. + a_r \int_0^\infty S'_v D_{zv} e^{-s\zeta|z-z_0|} J_1(s\xi r)\xi d\xi\right] \qquad (9)\ (Cont.)$$

where

$$D_{zp} = -\epsilon\eta, \quad D_{zv} = -\xi \qquad (10)$$

are the receiver functions associated with the displacement u_z. These receiver functions together with those for the radial and angular displacements are given in Table 2. Each term inside the brackets in equation (9) represents a single ray propagating the distance between the source and the receiver. The first term corresponds to the ray that propagates as a P-wave; it is characterized by the source functions (S_p, S'_p), receiver function D_{zp} and the phase function $\eta|z - z_0|$. The second term is for a ray traveling as a SV-wave and it is characterized by the functions (S_v, S'_v), D_{zv}, and $\zeta|z - z_0|$. Note that SH-waves do not contribute to the displacement in the z-direction. If each ray is denoted by $\bar{u}_{zj}(\mathbf{r}, s; \mathbf{a})$, then one can write equation (9) as

$$\bar{u}_z(\mathbf{r}, s, \mathbf{a}) = \sum_j^2 \bar{u}_{zj}(\mathbf{r}, s; \mathbf{a})$$

where

$$\bar{u}_{zj}(\mathbf{r}, s; \mathbf{a}) = s\bar{F}(s)\left[a_z \int_0^\infty S_j \Pi_{jj}^{n} D_{zj} e^{-sg_j(z,\xi)} J_0(s\xi r)\xi d\xi \right.$$
$$\left. + a_r \int_0^\infty S'_j \Pi_{jj}^{n} D_{zj} e^{-sg_j(z,\xi)} J_1(s\xi r)\xi d\xi\right]. \qquad (11)$$

Table 2 Receiver functions $D_{\alpha k}$; definitions and notations are given in Table 1

MODE		k	INTERIOR POINT	ON SURFACE
u_r u_θ	P	1	$-\xi$	$4\kappa^2\zeta\eta\xi/\Delta_r$
	SV	2	$-\varepsilon\zeta$	$-2\kappa^2\gamma\zeta(\xi^2+\zeta^2)/\Delta_r$
	SH	H	1	2
u_z	P	1	$-\varepsilon\eta$	$-2\kappa^2\gamma\eta(\xi^2+\zeta^2)/\Delta_r$
	SV	2	$-\xi$	$4\kappa^2\eta\zeta\xi/\Delta_r$
σ_{rz} $\sigma_{r\theta}$	P	1	$2\varepsilon\eta\zeta/\kappa^2$	0
	SV	2	$(\xi^2+\zeta^2)/\kappa^2$	0
	SH	H	$-\varepsilon\zeta/\kappa^2$	0
σ_{zz}	P	1	$(\xi^2+\zeta^2)/\kappa^2$	0
	SV	2	$2\varepsilon\xi\zeta/\kappa^2$	0

The index j indicates the mode of rays, $j = 1$ being the P-mode and $j = 2$ the SV-mode. The function Π_{jj}^{n} which is related to the reflection of rays in a half space is inserted at this point for later discussions. For an unbounded medium such as in equation (9), Π_{jj}^{n} equals 1. The $g_j(z, \xi)$ is the phase function of each ray and is given by

$$g_j(z, \xi) = \eta z_{pj} + \zeta z_{sj} \tag{12}$$

where z_{pj} and z_{sj} are the projections along the z-axis of the ray-path in P and S-modes, respectively. In an unbounded medium, for the P-ray we set $z_p = |z - z_0|$, $z_s = 0$; and for the S-ray, we set $z_p = 0$, $z_s = |z - z_0|$.

Note that the first integral in equation (11), after it is inversely transformed, represents the displacement u_z due to a concentrated force acting along the z-axis ($a_z = 1, a_r = a_\theta = 0$); it will be denoted by $\overline{G}_{zz}^{jj}$. The second integral is the displacement u_z due to a force applied along the radial direction ($a_z = 0$), and will be denoted by $\overline{G}_{zr}^{jj}$. In similar manner, one can define $\overline{G}_{rr}^{jj}$, $\overline{G}_{r\theta}^{jj}$, etc. Then the quantities $\Sigma\, \overline{G}_{\alpha\beta}^{jj}$, summed over all possible j's ($j = 1$ and 2 corresponding to P and SV-waves, respectively), plus $\overline{G}_{\alpha\beta}^{H}$ for the SH-wave are the components in cylindrical coordinates of the Laplace transformed Green's displacement dyadics $\overline{\mathbf{G}}(\mathbf{r}, s)$. Since they appear repeatedly in the ensuring calculation, we group all the components, together with $\nabla\overline{\mathbf{G}}$ which will be needed later, in the Appendixes A and B, respectively. In terms of the components of Green's dyadics, the displacement field in an infinite medium is

$$\overline{u}_\alpha(\mathbf{r}, s; \mathbf{a}) = \overline{F}(s) \sum_{j=1}^{2} [a_r\overline{G}_{\alpha r}^{jj} + a_\theta\overline{G}_{\alpha\theta}^{jj} + a_z\overline{G}_{\alpha z}^{jj}] + \overline{F}(s)[a_r\overline{G}_{\alpha r}^{H} + a_\theta\overline{G}_{\alpha\theta}^{H}] \tag{13}$$

where $j = 1$ pertains to a P-mode, and $j = 2$ a SV-mode. Note that for $\overline{\mathbf{G}}^{jj}$, four of the nine components, $\overline{G}_{r\theta}$, $\overline{G}_{\theta r}$, $\overline{G}_{\theta z}$, and $\overline{G}_{z\theta}$, vanish identically, and the only nonvanishing components of $\overline{\mathbf{G}}^{H}$ are $\overline{G}_{rr}^{H}$ and $\overline{G}_{\theta\theta}^{H}$.

2 Green's Dyadics for Half Space. Waves that originate at a point inside a half space behave just like those in an infinite medium until they reach a point on the boundary where they are reflected and refracted. Hence, the particular solutions obtained in the previous section represent incident waves on the boundary. Due to mode conversion, elastic waves of either P-mode or SV-mode when incident on a plane surface, will be reflected as two waves, one in each mode. However, the SH-waves reflect only as SH-waves. Following the approach of Spencer [24], we express the displacement potentials for the rays reflected by the surface $z = 0$ and propagating in the region $z \geq 0$ as

$$\begin{aligned}
\overline{\phi}^{(\text{ref})} = {} & \overline{F}(s)\left[a_z \int_0^\infty S_p R^{pp} e^{-s\eta(z+z_0)} J_0 \xi d\xi + a_r \int_0^\infty S_p' R^{pp} e^{-s\eta(z+z_0)} J_1 \xi d\xi\right] \\
& + \overline{F}(s)\left[a_z \int_0^\infty S_v R^{vp} e^{-s(\zeta z_0+\eta z)} J_0 \xi d\xi + a_r \int_0^\infty S_v' R^{vp} e^{-s(\zeta z_0+\eta z)} J_1 \xi d\xi\right] \\
\overline{\psi}^{(\text{ref})} = {} & s^{-1}\overline{F}(s)\left[a_z \int_0^\infty S_v R^{vv} e^{-s\zeta(z+z_0)} J_0 d\xi + a_r \int_0^\infty S_v' R^{vv} e^{-s\zeta(z+z_0)} J_1 d\xi\right] \\
& + s^{-1}\overline{F}(s)\left[a_z \int_0^\infty S_p R^{pv} e^{-s(\eta z_0+\zeta z)} J_0 d\xi + a_r \int_0^\infty S_p' R^{pv} e^{-s(\eta z_0+\zeta z)} J_1 d\xi\right] \\
\overline{\chi}^{(\text{ref})} = {} & \overline{F}(s) a_\theta \int_0^\infty S_H R^H e^{-s\zeta(z+z_0)} J_1 d\xi
\end{aligned} \tag{14}$$

For brievity, the argument $(s\xi r)$ of all Bessel functions are omitted in the foregoing. The phase functions in all integrals are changed by an additional term according to the mode of the reflected wave; the unknown functions R^{pp}, R^{vv}, R^{vp}, R^{pv}, and R^H which are called the generalized reflection coefficients at the free surface $z = 0$, can be determined by satisfying the boundary condition on this surface. The total field in the half space is then determined by combining results in equation (4) and (14)

$$(\overline{\phi}, \overline{\psi}, \overline{\chi}) = (\overline{\phi}_1, \overline{\psi}_1, \overline{\chi}_1) + (\overline{\phi}^{(\text{ref})}, \overline{\psi}^{(\text{ref})}, \overline{\chi}^{(\text{ref})}) \tag{15}$$

For a traction-free surface, the boundary conditions that must be satisfied by the total field are

$$\overline{\tau}_{zz}(r, \theta, 0, s) = \overline{\tau}_{zr}(r, \theta, 0, s) = \overline{\tau}_{z\theta}(r, \theta, 0, s) = 0 \tag{16}$$

The stresses are calculated from the potentials of the total field according to equation (2). It was stated by Chandra [25] and were also proven by Ceranoglu [26] that the last two boundary conditions are satisfied if the following reduced boundary conditions are satisfied:

$$2\frac{\partial\overline{\phi}}{\partial z} + 2\frac{\partial^2\overline{\psi}}{\partial z^2} - \kappa^2 s^2 \overline{\psi}\bigg|_{z=0} = 0, \quad \frac{\partial\overline{\chi}}{\partial z}\bigg|_{z=0} = 0. \tag{17}$$

Substitution of the potentials given by (15) into the boundary conditions yields

$$\begin{gathered}
R^{pp} = R^{vv} = [4\xi^2\eta\zeta + (\xi^2 + \zeta^2)^2]/\Delta_r \\
R^{pv} = -4\eta\xi(\xi^2 + \zeta^2)/\Delta_r, \quad R^{vp} = -4\zeta\xi(\xi^2 + \zeta^2)/\Delta_r \\
R^H = 1 \\
\Delta_r = 4\xi^2\eta\zeta - (\xi^2 + \zeta^2)^2
\end{gathered} \tag{18}$$

These reflection coefficients are the same as those for plane waves at a traction-free plane boundary.

In the half space occupying the region $z \leq h$ ($h > z_0$), expressions similar to those given by equation (14) can be written with the understanding that the reflection coefficients pertaining to the surface $z = h$ are used. The phase functions should be changed accordingly. Hence, following the same procedure, one obtains, for the half space $z \leq h$, the reflection coefficients at $z = h$ as

$$\begin{aligned}
R_{pp} = R_{vv} &= R^{pp} = R^{vv} \\
R_{pv} &= -R^{pv} \\
R_{vp} &= -R^{vp} \\
R_H &= 1
\end{aligned} \tag{19}$$

Thus, for reflection with mode conversion, the value of downward reflection coefficient is negative of the upward one.

One can now write the total displacement $\overline{u}_\alpha$ at a point inside the half space ($z \geq 0$)

$$\begin{aligned}
\overline{u}_\alpha(\mathbf{r}, s; \mathbf{a}) = {} & \overline{F}(s)\left\{\sum_{j=1}^{2} [a_r\overline{G}_{\alpha r}^{jj} + a_\theta\overline{G}_{\alpha\theta}^{jj} + a_z\overline{G}_{\alpha z}^{jj}]_1 + [a_r\overline{G}_{\alpha r}^{H} + a_\theta\overline{G}_{\alpha\theta}^{H}]_1\right\} \\
& + \overline{F}(s)\left\{\sum_{j=1}^{2}\sum_{k=1}^{2} [a_r\overline{G}_{\alpha r}^{jk} + a_\theta\overline{G}_{\alpha\theta}^{jk} + a_z\overline{G}_{\alpha z}^{jk}]_2 + [a_r\overline{G}_{\alpha r}^{H} + a_\theta\overline{G}_{\alpha\theta}^{H}]_2\right\} \\
& (\alpha = r, \theta, z)
\end{aligned} \tag{20}$$

The superscripts j, k (= 1, 2) for Green's dyadics indicate a P-mode ($j, k = 1$) or SV-mode ($j, k = 2$); and the superscript H indicates the SH-mode. The subscript 1 of all bracket denotes the first group of rays directly radiating from the source to a receiver. For this group we take $n = 1$, and $\Pi_{jj}^{n} = 1$ and $\Pi_{H}^{n} = 1$ in Green's dyadics (Appendixes A, B). The subscript 2 denotes the second group of rays which have been reflected once at the surface. For this group, we take $\Pi_{11}^{n} = R^{pp}$, $\Pi_{22}^{n} = R^{vv}$, $\Pi_{12}^{n} = R^{pv}$, $\Pi_{21}^{n} = R^{vp}$, and $\Pi_{H}^{n} = R^H = 1$ while $n = 2$.

There are, in general, eight rays in the evaluation of $\overline{u}_\alpha$ in a half space, two direct and four reflected P and SV-rays, plus one direct and one reflected SH-ray. For the convenience of future discussion, the previous result is symbolically expressed as

$$\overline{u}_\alpha(\mathbf{r}, s; \mathbf{a}) = \sum_{i=1}^{8} \overline{u}_{\alpha i}(\mathbf{r}, s; \mathbf{a}) \quad \alpha = r, \theta, z \tag{21}$$

The index i no longer pertains to P or SV-mode as in equation (20).

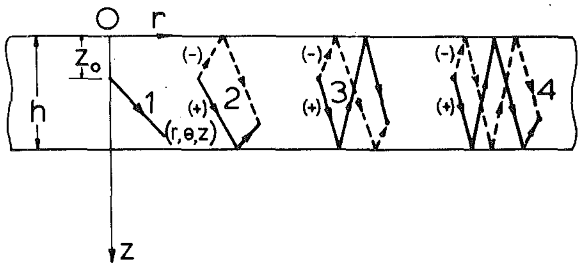

Fig. 2 Ray groups in a plate

3 **Green's Dyadics for a Plate.** In a plate, the waves generated at a point by the source can propagate along many different paths before they reach the receiver. Fig. 2 shows some of the possible rays. For example, along Path 1 there are two rays traveling the distance between the source and the receiver; the first is a P-wave and the second arriving at a later time is the S-ray. These two rays are the same as those rays propagating in an unbounded medium. The waves traveling along 2^+ or 2^- (+ or − denote the direction of the source segment of a particular ray, with respect to the z-axis) have been reflected by the boundaries once. Since a P or SV-wave gives rise to two waves while SH-waves gives rise to one SH-wave upon reflection by a plane surface, a total of $2^2 + 1 = 5$ rays will travel along each of the Path 2. Pp, Pv, Vv, Vp, and Hh are the five rays traveling along Path 2^-. The letters P, V, and H represent the P, SV, and SH-modes; the lower and upper case letters denote the downward ($+z$) and upward ($-z$) propagation directions, respectively, of the wave along each segment of the path. The number of rays traveling along the Path 3^+ is $2^3 + 1 = 9$, pPp, pPv, pVp, pVv, vVv, vVp, vPv, vPp, hHh. Each of these rays are identified by their source function $S_j(\xi)$, phase function $g_n(z, \xi)$, receiver function $D_{\alpha k}(\xi)$, and the product of the reflection coefficient function $\Pi^n_{ij}(\xi)$. For the rays along Paths 1, 2^-, and 3^+ these functions are tabulated in Table 3 where the thickness of the plate is taken as unity. The final solution of the plate problem can be written as

$$\bar{u}_\alpha(\mathbf{r}, s; \mathbf{a}) = \bar{F}(s) \sum_{n=1}^{\infty} \left\{ \sum_{j=1}^{2} \sum_{k=1}^{2} [a_r \bar{G}^{jk}_{\alpha r} + a_\theta \bar{G}^{jk}_{\alpha\theta} + a_z \bar{G}^{jk}_{\alpha z}]_n \right.$$
$$\left. + [a_r \bar{G}^{H}_{\alpha r} + a_\theta \bar{G}^{H}_{\alpha\theta}]_n \right\} \quad (22a)$$

The superscript j will represent the mode of the first segment (from the source) and k the last segment (to the receiver) for the nth ray in a plate. Although the double sum on j and k is from 1 to 2 (P or SV-mode) it implies 2 rays for $n = 1$; 4 rays for $n = 2$; 8 rays for $n = 3$; . . . etc. When all rays are arranged in a sequence, the previous result can be expressed symbolically as, like equation (21)

$$\bar{u}_\alpha(\mathbf{r}, s; \mathbf{a}) = \sum_{i}^{\infty} \bar{u}_{\alpha i}(\mathbf{r}, s; \mathbf{a}) \quad (\alpha = r, \theta, z) \quad (22b)$$

Since each ray has a distinct travel time, only a finite number of them are to be added when the inverse Laplace transform is completed.

4 **Surface Source and Receiver Functions.** The analysis so far was for a source and a receiver both located inside the elastic medium. The source and the receiver functions have to be modified as discussed in the following sections, if the source or receiver is situated on a traction-free surface. The final expressions are shown in Tables 1 and 2.

(a) Surface Source. Consider a half space ($z \geq 0$) with the source and receiver both buried inside. In general, both P and S-waves will be generated at the source location. The rays that arrive at the receiver are those that travel along the Paths 1 and 2^- (Fig. 2). Consider now the rays p, Pp, and Sp. As z_0 approaches zero, these three rays coalesce to form a single direct ray which will be called the P-ray. Hence, the three ray-integrals can now be combined to form one integral with a new source function, say, S^*_p, for the P-waves

$$S^*_p = S_p + S_p R^{pp} + S_v R^{vp}. \quad (23a)$$

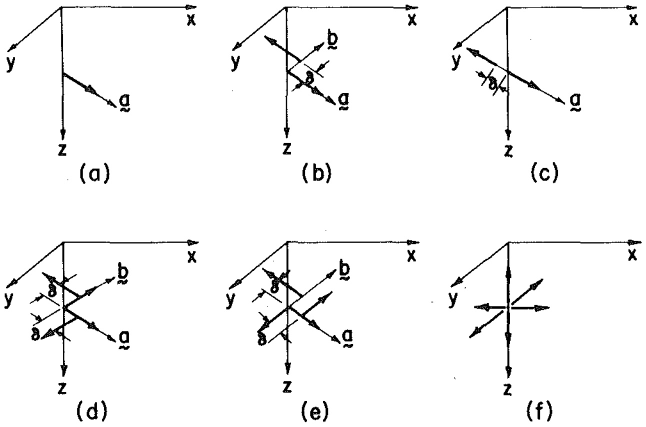

Fig. 3 Dynamic nuclei of strains; (*a*) Single-force; (*b*) Single-couple; (*c*) Double-force; (*d*) Double-couple without moment; (*e*) Center of rotation; (*f*) Center of explosion

In a similar manner, combination of the rays s, Ss, and Ps yields the surface source function for the SV-waves, S^*_v,

$$S^*_v = S_v + S_v R^{vv} + S_p R^{pv} \quad (23b)$$

The surface source function for the SH-waves is obtained by applying the limiting process to the h and Hh rays, yielding

$$S^*_H = S_H + S_H R^H = 2S_H \quad (23c)$$

Hence, if the source is located on the surface of the plate, all of the source functions have to be replaced by those given by equations (23).

(b) Surface Receiver. Expressions for the case of a surface receiver on $z = 0$ can be obtained in a similar manner. For the P-wave receiver function, one has to consider the rays P, Pp, and Ps. As z approaches zero, all of these three rays coalesce and once again the three integrals can be combined to one with a new receiver function, $D^*_{\alpha p}$

$$D^*_{\alpha p} = D_{\alpha p} + D_{\alpha p} R^{pp} + D_{\alpha v} R^{pv} \quad (24a)$$

In a similar way the SV-wave receiver function is obtained by combining three rays V, Vv, and Vp and the SH-wave receiver function by combining the H and Hh rays,

$$D^*_{\alpha v} = D_{\alpha v} + D_{\alpha v} R^{vv} + D_{\alpha p} R^{vp} \quad (24b)$$

$$D^*_{\alpha H} = D_{\alpha H} + D_{\alpha H} R^H = 2D_{\alpha H} \quad (24c)$$

If the receiver is at the surface $z = h$ of a plate and the source is either in the interior, or on the opposite side, we should replace the reflection coefficients in equation (24) by the corresponding ones R_{pp}, R_{pv}, R_{vv}, and R_{vp} as given by equation (19).

3 Other Point Sources in a Plate

Solutions for waves generated by other types of point sources such as a single-couple, a double-force, a double-couple without moment, a center of rotation, and a center of explosion can be all derived from that of a single concentrated force. These solutions are simply obtained by calculating the directional derivatives of the displacement field due to a concentrated force, equation (22). In an infinite medium, these point sources are called nuclei of strains, [23].

1 **Single Couple.** Configuration of two forces which result in a single-couple is shown in Fig. (3*b*). The unit vector **a** which denotes the direction of the concentrated force of magnitude F_0 forms an orthogonal triad with two other unit vectors **b** and **c** such that

$$\mathbf{c} = \mathbf{a} \times \mathbf{b} \quad (25)$$

The vector **c** then indicates the direction of the resultant moment.

Let $\bar{\mathbf{u}}_1$ denote the displacement field due to the force F_0 acting at the point $P_1(0, 0, z_0)$ and in the direction of vector **a**. Then

$$\bar{\mathbf{u}}_1(\mathbf{r}, s) = F_0\bar{\mathbf{u}}(\mathbf{r}, s; \mathbf{a}) \tag{26}$$

where the components of $\bar{\mathbf{u}}(\mathbf{r}, s; \mathbf{a})$ are those given by equation (22). Now, consider a second force of magnitude F_0 acting along the direction of the vector $-\mathbf{a}$ at a point P_2 which is δ units away from P_1 along the vector $\mathbf{b}$. Then the displacement field, $\bar{\mathbf{u}}_2$, due to this second force is given by

$$\bar{\mathbf{u}}_2(\mathbf{r}, s) = -F_0\mathbf{u}(\mathbf{r} - \delta\mathbf{b}, s; \mathbf{a}). \tag{27}$$

The total field due to these two forces is the sum of the individual fields, i.e., $\bar{\mathbf{u}}_1 + \bar{\mathbf{u}}_2$. In the limit as δ approaches zero, the two forces form a single-couple acting at the point $(0, 0, z_0)$ and the total field is given by

$$\bar{\mathbf{u}}^c(\mathbf{r}, s) = M_0(\mathbf{b}\cdot\nabla)\bar{\mathbf{u}}(\mathbf{r}, s; \mathbf{a}) \tag{28}$$

where

$$M_0 = \lim_{\delta\to 0}(F_0\delta); \quad \mathbf{b}\cdot\nabla = b_r\frac{\partial}{\partial r} + b_\theta\frac{1}{r}\frac{\partial}{\partial\theta} + b_z\frac{\partial}{\partial z}$$

Components of $\bar{\mathbf{u}}^c$ can be expressed in terms of $\overline{\mathcal{G}} = \nabla\bar{\mathbf{G}}$ or $\bar{\mathbf{G}}\nabla$ as listed in Appendix B.

$$\begin{aligned}
\bar{u}_z^c(\mathbf{r}, s) = \bar{F}(s)\sum_{n=1}^{\infty}\Bigg\{\sum_{j=1}^{2}\sum_{k=1}^{2}&\big[b_za_z\overline{\mathcal{G}}_{zzz}^{jk} + b_ra_r\overline{\mathcal{G}}_{zrr}^{jk} + b_za_r\overline{\mathcal{G}}_{zzr}^{jk}\\
&+ b_ra_z\overline{\mathcal{G}}_{zrz}^{jk} + b_\theta a_\theta\overline{\mathcal{G}}_{z\theta\theta}^{jk}\big]\Bigg\}_n\\
\bar{u}_r^c(\mathbf{r}, s) = \bar{F}(s)\sum_{n=1}^{\infty}\Bigg\{\sum_{j=1}^{2}\sum_{k=1}^{2}&\big[b_za_z\overline{\mathcal{G}}_{rzz}^{jk} + b_ra_r\overline{\mathcal{G}}_{rrr}^{jk} + b_\theta a_\theta\overline{\mathcal{G}}_{r\theta\theta}^{jk}\\
&+ b_za_r\overline{\mathcal{G}}_{rzr}^{jk} + b_ra_z\overline{\mathcal{G}}_{rrz}^{jk}\big]\\
&+ \big[b_ra_r\overline{\mathcal{G}}_{rrr}^{H} + b_\theta a_\theta\overline{\mathcal{G}}_{r\theta\theta}^{H} + b_za_r\overline{\mathcal{G}}_{rzr}^{H} + b_ra_z\overline{\mathcal{G}}_{rrz}^{H}\big]\Bigg\}_n\\
\bar{u}_\theta^c = \bar{F}(s)\sum_{n=1}^{\infty}\Bigg\{\sum_{j=1}^{2}\sum_{k=1}^{2}&\big[b_ra_\theta\overline{\mathcal{G}}_{\theta r\theta}^{jk} + b_\theta a_r\overline{\mathcal{G}}_{\theta\theta r}^{jk} + b_\theta a_z\overline{\mathcal{G}}_{\theta\theta z}^{jk} + b_za_\theta\overline{\mathcal{G}}_{\theta z\theta}^{jk}\big]\\
&+ \big[b_\theta a_r\overline{\mathcal{G}}_{\theta\theta r}^{H} + b_ra_\theta\overline{\mathcal{G}}_{\theta r\theta}^{H} + b_\theta a_z\overline{\mathcal{G}}_{\theta\theta z}^{H} + b_za_\theta\overline{\mathcal{G}}_{\theta z\theta}^{H}\big]\Bigg\}_n
\end{aligned} \tag{29}$$

where

$$\bar{F}(s) = M_0\bar{f}(s)/(4\pi\kappa^2\mu h^3) \tag{30}$$

The *SH*-waves, indicated by the superscript H of $\mathcal{G}$'s, contribute nothing to the $\bar{u}_z^c$ component. In an infinite medium, explicit expressions for $\mathbf{u}^c(x_i, t)$ in Cartesian components are given in reference [27, p. 40]. Upon the completion of the inverse Laplace transform as discussed in Parts 2 and 3, equation (29) yields the displacements due to a single couple in an infinite space ($n = 1$), a half space ($n = 1, 2$), as well as in a plate ($n = 1, 2, \ldots$).

2 Double-Force. Going through the derivation as explained in the previous subsection, one obtains the displacement field due to a double-force as shown in Fig. 3(c),

$$\bar{\mathbf{u}}^d(\mathbf{r}, s) = D_0(\mathbf{a}\cdot\nabla)\bar{\mathbf{u}}(\mathbf{r}, s; \mathbf{a})$$

$$D_0 = \lim_{\delta\to 0}(-F_0\delta) \tag{31}$$

Comparing equations (31) and (28), it is seen that the former is obtained from the latter by simply replacing b_r, b_θ, b_z by a_r, a_θ, a_z, respectively. In vector notation, the results are

$$\bar{\mathbf{u}}^d(\mathbf{r}, s) = \bar{\mathbf{u}}^c(\mathbf{r}, s)]_{\mathbf{b}=\mathbf{a}} \tag{32}$$

where in this case

$$\bar{F}(s) = D_0\bar{f}(s)/(4\pi\kappa^2\mu h^3) \tag{33}$$

Numerical results for a double-force in a half space were reported in reference [28].

3 Double-Couple Without Moment. Superposition of two single-couples with moments in opposite directions yields a point source known as the double-couple without moment, Fig. 3(d). From equation (28), the displacement field is given by

$$\bar{\mathbf{u}}^{dc}(\mathbf{r}, s) = M_0(\mathbf{b}\cdot\nabla)\bar{\mathbf{u}}(\mathbf{r}, s; \mathbf{a}) + M_0(\mathbf{a}\cdot\nabla)\bar{\mathbf{u}}(\mathbf{r}, s; \mathbf{b}) \tag{34}$$

The components of the displacement for each ray are then given by the relations

$$\begin{aligned}
\bar{u}_z^{dc}(\mathbf{r}, s) = \bar{F}(s)\sum_{n=1}^{\infty}\Bigg\{\sum_{j}^{2}\sum_{k}^{2}&\big[2b_za_z\overline{\mathcal{G}}_{zzz}^{jk} + 2b_ra_r\overline{\mathcal{G}}_{zrr}^{jk} + 2b_\theta a_\theta\overline{\mathcal{G}}_{z\theta\theta}^{jk}\\
&+ (b_za_r + a_zb_r)(\overline{\mathcal{G}}_{zrz}^{jk} + \overline{\mathcal{G}}_{zzr}^{jk})\big]\Bigg\}_n\\
\bar{u}_r^{dc}(\mathbf{r}, s) = \bar{F}(s)\sum_{n}^{\infty}\Bigg\{\sum_{j}^{2}\sum_{k}^{2}&\big[2b_za_z\overline{\mathcal{G}}_{rzz}^{jk} + 2b_ra_r\overline{\mathcal{G}}_{rrr}^{jk} + 2b_\theta a_\theta\overline{\mathcal{G}}_{r\theta\theta}^{jk}\\
&+ (b_za_r + a_rb_z)(\overline{\mathcal{G}}_{rzr}^{jk} + \overline{\mathcal{G}}_{rrz}^{jk})\big] + \big[2b_za_z\overline{\mathcal{G}}_{rzz}^{H} + 2b_ra_r\overline{\mathcal{G}}_{rrr}^{H}\\
&+ 2b_\theta a_\theta\overline{\mathcal{G}}_{r\theta\theta}^{H} + (b_za_r + a_rb_z)(\overline{\mathcal{G}}_{rzr}^{H} + \overline{\mathcal{G}}_{rrz}^{H})\big]\Bigg\}_n\\
\bar{u}_\theta^{dc}(\mathbf{r}, s) = \bar{F}(s)\sum_{n}^{\infty}\Bigg\{\sum_{j}^{2}\sum_{k}^{2}&\big[(b_ra_\theta + a_rb_\theta)(\overline{\mathcal{G}}_{\theta r\theta}^{jk} + \overline{\mathcal{G}}_{\theta\theta r}^{jk})\\
&+ (b_\theta a_z + a_\theta b_z)(\overline{\mathcal{G}}_{\theta z\theta}^{jk} + \overline{\mathcal{G}}_{\theta\theta z}^{jk})\big] + \big[(b_ra_\theta + a_rb_\theta)(\overline{\mathcal{G}}_{\theta r\theta}^{H} + \overline{\mathcal{G}}_{\theta\theta r}^{H})\\
&+ (b_\theta a_z + a_\theta b_z)(\overline{\mathcal{G}}_{\theta z\theta}^{H} + \overline{\mathcal{G}}_{\theta\theta z}^{H})\big]\Bigg\}_n
\end{aligned} \tag{35}$$

where $\bar{F}(s)$ is given by equation (30).

4 Center of Rotation. A center of rotation is obtained by superposing two single-couples with moments in the same direction, [23], configuration of the two single-couples being shown in Fig. 3(e).

$$\bar{\mathbf{u}}^{cr}(r, s) = M_0(\mathbf{b}\cdot\nabla)\bar{\mathbf{u}}(\mathbf{r}, s; \mathbf{a}) + M_0\,(\mathbf{a}\cdot\nabla)\bar{\mathbf{u}}(\mathbf{r}, s; -\mathbf{b}) \tag{36}$$

The vertical components of the displacement field is

$$\bar{u}_z^{cr}(\mathbf{r}, s) = \bar{F}(s)(b_ra_z - b_za_r)\sum_{n}^{\infty}\left\{\sum_{j}^{2}\sum_{k}^{2}(\overline{\mathcal{G}}_{zrz}^{jk} - \overline{\mathcal{G}}_{zzr}^{jk})\right\}_n \tag{37}$$

Substituting $\overline{\mathcal{G}}_{lmn}$'s from Appendix B into the foregoing expression, and also into those for $\bar{u}_\theta^{cr}$ and $\bar{u}_r^{cr}$ we find that these expressions can be written as

$$\begin{aligned}
\bar{u}_z^{cr}(\mathbf{r}, s) &= \bar{F}(s)c_\theta\left\{[\overline{\mathcal{G}}_{z\theta}^{\prime 2}]_{n=1} + \sum_{n=2}^{\infty}\left(\sum_{k=1}^{2}\overline{\mathcal{G}}_{z\theta}^{\prime k}\right)_n\right\}\\
\bar{u}_r^{cr}(\mathbf{r}, s) &= \bar{F}(s)c_\theta\left\{[\overline{\mathcal{G}}_{r\theta}^{\prime 2} + \overline{\mathcal{G}}_{r\theta}^{\prime H}]_{n=1} + \sum_{n=2}^{\infty}\left[\sum_{k=1}^{2}(\overline{\mathcal{G}}_{r\theta}^{\prime k} + \overline{\mathcal{G}}_{r\theta}^{\prime H})\right]\right\}\\
\bar{u}_\theta^{cr}(\mathbf{r}, s) &= \bar{F}(s)\Bigg\{c_z[\overline{\mathcal{G}}_{\theta z}^{\prime 2} + \overline{\mathcal{G}}_{\theta z}^{\prime H}]_{n=1} + c_r[\overline{\mathcal{G}}_{\theta r}^{\prime 2} + \overline{\mathcal{G}}_{\theta r}^{\prime H}]_{n=1}\\
&\quad + \sum_{n=2}^{\infty}\left[\sum_{k=1}^{2}(c_z\overline{\mathcal{G}}_{\theta z}^{\prime k} + c_r\overline{\mathcal{G}}_{\theta r}^{\prime k}) + c_z\overline{\mathcal{G}}_{\theta z}^{\prime H} + c_5\overline{\mathcal{G}}_{\theta r}^{\prime H}\right]_n\Bigg\}
\end{aligned} \tag{38}$$

where c_i are the components in cylindrical coordinates of the vector $\mathbf{c}$ given by equation (25), and the expressions for $\overline{\mathcal{G}}_{\alpha\beta}^{\prime k}$ are given in Appendix C. Note that only S-waves are emitted by the source, but rays with segments in P-mode are generated upon reflections.

5 Center of Explosion. The displacement field due to a center of explosion can be obtained by simply superposing three mutually orthogonal double forces. Hence, using the expressions derived for a double-force, one obtains after some simple manipulation, the following expressions for the displacement field:

$$\begin{aligned}
\bar{u}_z^{ce}(r, z, s) &= \bar{F}(s)\left[(\overline{\mathcal{G}}_{zz}^{*1})_{n=1} + \sum_{n=2}^{\infty}\left(\sum_{k=1}^{2}\overline{\mathcal{G}}_{zz}^{*k}\right)_n\right]\\
\bar{u}_r^{ce}(r, z, s) &= \bar{F}(s)\left[\left(\overline{\mathcal{G}}_{rr}^{*1}\right)_{n=1} + \sum_{n=2}^{\infty}\left(\sum_{k=1}^{2}\overline{\mathcal{G}}_{rr}^{*k}\right)_n\right]
\end{aligned} \tag{39}$$

where

$$(\overline{\mathcal{G}}_{zz}^{*k})_n = s^2\int_0^{\infty}S_1^*\Pi_{1k}^{n}D_{zk}e^{-sg_n}\xi J_0(s\xi r)d\xi$$

$$(\overline{\mathcal{G}}_{rr}^{*k})_n = s^2\int_0^{\infty}S_1^*\Pi_{1k}^{n}D_{rk}e^{-sg_n}\xi J_1(s\xi r)d\xi$$

$$S_1 = 1/\eta, \quad g_n = (z_p\eta + z_s\zeta)_n$$

Note that only P-waves are radiated at the source location while the segments in S-mode are generated upon reflection from the boundaries.

As shown in reference [7], the results for a center of explosion can be derived directly from the solution for an inhomogeneous equation for ϕ.

References

1 Spanner, J. C., *Acoustic Emission Techniques and Applications,* Intex Publishing Company, Evanston, Ill., 1974.

2 Eshelby, J. D., "The Continuum Theory of Lattice Defects," *Solid State Physics,* Vol. 3, 1956, pp. 70–144.

3 Aki, K., and Richards, P. G., *Quantitative Seismology-Theory and Methods,* Vols. 1 and 2, W. H. Freeman and Co., San Francisco, 1980, Chapters 4 and 14.

4 Burridge, R., and Knopoff, L., "Body Force Equivalents for Seismic Dislocations," *Bull. Seism. Soc. Am.,* Vol. 54, 1964, pp. 1875–1914.

5 Lamb, H., "On Waves in an Elastic Plate," *Proceedings of the Royal Society,* London, Series A, Vol. 93, 1917, pp. 114–128.

6 Pursey, H., "The Launching and Propagation of Elastic Waves in Plates," *Quarterly of Mechanics and Applied Mathematics,* Vol. 10, 1957, pp. 45–62.

7 Pao, Y. H., and Gajewski, R., "The Generalized Ray Theory and Transient Response of Layered Elastic Solids," *Physical Acoustics,* Vol. 13, Chapter 6, ed., Mason, W. P., Academic Press, New York, 1977.

8 Cagniard, L., *Reflection and Refraction of Progressive Seismic Waves,* McGraw-Hill, New York, 1962.

9 Mencher, A. L., "Epicentral Displacement Caused by Elastic Waves in an Infinite slab," *Journal of Applied Physics,* Vol. 24, 1953, pp. 1240–1246.

10 Knopoff, L., "Surface Motions of a Thick Plate," *Journal of Applied Physics,* Vol. 29, 1958, pp. 661–670.

11 Davids, N., "Transient Analysis of Stress-Wave Penetration in Plates," ASME JOURNAL OF APPLIED MECHANICS, Vol. 26, 1959, pp. 651–660.

12 Miklowitz, J., "Transient Compressional Waves in an Infinite Elastic Plate or Elastic Layer Overlying a Rigid Half Space," ASME JOURNAL OF APPLIED MECHANICS,Vol. 29, 1962, pp. 53–60.

13 Pao, Y. H., Gajewski, R., and Ceranoglu, A. N., "Acoustic Emission and Transient Waves in an Elastic Plate," *Journal of the Acoustical Society of America,* Vol. 65, 1979, pp. 96–105.

14 Pytel, A., and Davids, N., "Transient Analysis of Shear Impact," ASME JOURNAL OF APPLIED MECHANICS, Vol. 29, 1962, pp. 33–39.

15 Davids, N., and Lawhead, W., "Transient Analysis of Oblique Impact on Plates," *Journal of the Mechanics and Physics of Solids,* Vol. 13, 1965, pp. 199–212.

16 Shmuely, M., "Response of Plates to Transient Sources," *Journal of Sound and Vibration,* Vol. 4, 1974, pp. 491–506.

17 Shmuely, M., "Stress Wave Propagation in Plates Subjected to Transient Linear Source," *International Journal of Solids and Structures,* Vol. 11, 1975, pp. 679–691.

18 Fulton, J., and Sneddon, I. N., "The Dynamical Stress Produced in a Thick Plate by the Action of Surface Forces," *Proceedings, Glasg. Math. Ass.,* Vol. 3, 1958, pp. 153–163.

19 Scott, R. A., and Miklowitz, J., "Transient Nonaxisymmetric Wave Propagation in an Infinite Isotropic Elastic Plate," *International Journal of Solids and Structures,* Vol. 5, 1969, pp. 65–79.

20 Norwood, F. R., "Transient Response of an Elastic Plate to Loads With Finite Characteristic Dimensions," *International Journal of Solids and Structures,* Vol. 11, 1975, pp. 33–51.

21 Wu, J. H. H., and Norwood, F. R., "Transient Analysis of a Three-Dimensional Plate by the Ray Grouping Technique," *International Journal of Solids and Structures,* Vol. 13, 1977, pp. 1225–1238.

22 Müller, G., "Theoretical Seismograms for some Types of Point-Sources in Layered Media," *Zeitschrift für Geophysik,* Vol. 34, 1968, pp. 15–35.

23 Love, A. E. H., *A Treatise on the Mathematical Theory of Elasticity,* 4th ed., Dover Publications, New York, 1944.

24 Spencer, T. W., "The Method of Generalized Reflection and Transmission Coefficients," *Geophysics,* Vol. 25, 1960, pp. 625–641.

25 Chandra, U., "Theory of Head Waves for Focal Mechanism Studies," *Bulletin Seis. Soc. Am.,* Vol. 58, 1968, pp. 993–1019.

26 Ceranoglu, A. N., "Acoustic Emission and Propagation of Elastic Pulses in a Plate," PhD thesis, Cornell University, 1979.

27 Eringen, A. C., and Suhubi, E. S., *Elastodynamics, Vol. 2, Linear Theory,* Academic Press, New York, 1975.

28 Afandi, O. F., and Scott, R. A., "Excitation of an Elastic Half Space by a Time-Dependent Dipole, I and II," *International Journal of Solids and Structures,* Vol. 8, 1972, pp. 1145 and 1163.

29 Pardee, W. J., "Acoustic Emission and the Plate Green's Function," *Journal of Applied Physics,* Vol. 18, 1977, pp. 676–686.

30 Pao, Y. H., and Varatharajulu, V., "Huygens' Principle, Radiation Conditions, and Integral Formulas for the Scattering of Elastic Waves," *Journal of the Acoustical Society of America,* Vol. 59, 1976, pp. 1361–1371.

APPENDIX *A*

In this Appendix we list the components of the Laplace transformed Green's dyadic, $\overline{\mathbf{G}}(r, z, \theta, s)$, appearing in equation (13). For simplicity the limits of the integrals will be omitted with the understanding they all go from 0 to ∞. The index n for each component of $\overline{\mathbf{G}}$ indicates the number of segments of each ray path, the first superscript j identifying the mode (P or SV) of the first segment (from the source), and the second superscript k the mode of the last segment (to the receiver). The two subscripts, r, θ, or z are the indices for dyadic components. Thus $\overline{G}_{\alpha\beta}$ means the displacement component in the direction of α-coordinate that is generated by the β-component of the source.

***P* and *SV*-Components.** (j, k = 1 and 2 for P and SV-mode, respectively)

$$(\overline{G}^{jk}_{zz})_n = s \int S_j \Pi^n_{jk} D_{zk} e^{-sg_n} J_0(s\xi r)\xi d\xi$$

$$(\overline{G}^{jk}_{zr})_n = s \int S'_j \Pi^n_{jk} D_{zk} e^{-sg_n} J_1(s\xi r)\xi d\xi$$

$$(\overline{G}^{jk}_{z\theta})_n = 0$$

$$(\overline{G}^{jk}_{rr})_n = -s \int S'_j \Pi^n_{jk} D_{rk} e^{-sg_n} J_0(s\xi r)\xi d\xi + \frac{1}{r}\int S'_j \Pi^n_{jk} D_{rk} e^{-sg_n} J_1(s\xi r) d\xi$$

$$(\overline{G}^{jk}_{r\theta})_n = 0$$

$$(\overline{G}^{jk}_{rz})_n = s \int S_j \Pi^n_{jk} D_{rk} e^{-sg_n} J_1(s\xi r)\xi d\xi$$

$$(\overline{G}^{jk}_{\theta\theta})_n = -\frac{1}{r}\int S'_j \Pi^n_{jk} D_{\theta k} e^{-sg_n} J_1(s\xi r) d\xi$$

$$(\overline{G}^{jk}_{\theta r})_n = (\overline{G}^{jk}_{\theta z})_n = 0$$

where

$$g_n = (z_p\eta + z_s\zeta)_n,$$

z_p and z_s are the sums of vertical projections of all segments in P and S-modes, respectively, for a ray with n-segments. S_j and $D_{\alpha k}$ are the source and receiver functions which are given in Tables 1 and 2, respectively. Π^n_{jk} is the product of $(n-1)$ reflection coefficients for a ray with n-segments.

Note that, from Tables 1 and 2, the product $S'_j D_{zk}$ (for u_z) equals $S_j D_{rk}$ (for u_r). Hence $\overline{G}^{jj}_{zr}$ equals $\overline{G}^{jj}_{rz}$ for an unbounded medium ($\Pi_{jj} = 1$) as expected. This is also true for a surface force/surface receiver and buried force/buried receiver in a plate. However the equality does not hold for surface force/buried receiver or buried force/surface receiver combinations.

SH-Components.

$$(\overline{G}^H_{zz})_n = (\overline{G}^H_{zr})_n = (\overline{G}^H_{r\theta})_n = (\overline{G}^H_{z\theta})_n = \overline{G}^H_{\theta z})_n = (\overline{G}^H_{r\theta})_n = (\overline{G}^H_{\theta r})_n = 0$$

$$(\overline{G}^H_{rr})_n = \frac{1}{r}\int S_H \Pi^n_H D_{rH} e^{-sg_n} J_1(s\xi r) d\xi$$

$$(\overline{G}^H_{\theta\theta})_n = s \int S_H \Pi^n_H D_{\theta H} e^{-sg_n} J_0(s\xi r)\xi d\xi - \frac{1}{r}\int S_H \Pi^n_H D_{\theta H} e^{-sg_n} J_1(s\xi r) d\xi$$

Note that the SH-components only contribute to the rays that have all of their segments in S-mode, i.e., $z_{pn} = 0$, and $g_n = (\zeta z_H)_n$.

The inverse Laplace transform of each integral will be discussed in Part 2 of this series of papers for $r = 0$; and in Part 3 for $r > 0$. When the time function of the source is harmonic in the form of $\exp(-i\omega t)$ the preceding Green's dyadics $\overline{G}^{jk}_{\alpha\beta}$ are also the displacements for steady-state response if the parameter s is replaced by $i\omega$ [29].

APPENDIX *B*

In this Appendix the components of the third-order Green's tensor, $\overline{\mathcal{G}}$ which appears in the displacement field expressions for higher-order force systems as discussed in Section 3 are given.

P and SV-Components. (j, k = 1 and 2 for P and SV-modes, respectively)

$$(\overline{\mathcal{G}}^{jk}_{zzz})_n = s^2 \int \mathcal{S}_j \Pi^n_{jk} D_{zk} e^{-sg_n} J_0(s\xi r)\xi d\xi$$

$$(\overline{\mathcal{G}}^{jk}_{zrr})_n = s^2 \int \mathcal{S}'_j \Pi^n_{jk} D_{zk} e^{-sg_n} J_0(s\xi r)\xi^2 d\xi$$

$$-\frac{s}{r}\int \mathcal{S}'_j\Pi^n_j D_{zk}e^{-sg_n}J_1(s\xi r)\xi d\xi$$

$$(\overline{\mathcal{G}}^{jk}_{z\theta\theta})_n = \frac{s}{r}\int \mathcal{S}'_j\Pi^n_{jk}D_{zk}e^{-sg_n}J_1(s\xi r)\xi d\xi$$

$$(\overline{\mathcal{G}}^{jk}_{zzr})_n = s^2\int \mathcal{S}'''_j\Pi^n_{jk}D_{zk}e^{-sg_n}J_1(s\xi r)\xi d\xi$$

$$(\overline{\mathcal{G}}^{jk}_{zrz})_n = -s^2\int \mathcal{S}'''_j\Pi^n_{jk}D_{zk}e^{-sg_n}J_1(s\xi r)\xi d\xi$$

$$(\overline{\mathcal{G}}^{jk}_{zr\theta})_n = (\overline{\mathcal{G}}^{jk}_{z\theta r})_n = (\overline{\mathcal{G}}^{jk}_{zz\theta})_n = (\overline{\mathcal{G}}^{jk}_{z\theta z})_n = 0$$

$$(\overline{\mathcal{G}}^{jk}_{rrr})_n = s^2\int \mathcal{S}'_j\Pi^n_{jk}D_{rk}e^{-sg_n}J_1(s\xi r)\xi^2 d\xi$$

$$+\frac{s}{r}\int \mathcal{S}'_j\Pi^n_{jk}D_{rk}e^{-sg_n}J_0(s\xi r)\xi d\xi$$

$$-\frac{2}{r^2}\int \mathcal{S}'_j\Pi^n_{jk}D_{rk}e^{-sg_n}J_1(s\xi r)d\xi$$

$$(\overline{\mathcal{G}}^{ik}_{r\theta\theta})_n = -\frac{s}{r}\int \mathcal{S}'_j\Pi^n_{jk}D_{rk}e^{-sg_n}J_0(s\xi r)\xi d\xi$$

$$+\frac{2}{r^2}\int \mathcal{S}'_j\Pi^{n'}_{jk}D_{rk}e^{-sg_n}J_1(s\xi r)d\xi$$

$$(\overline{\mathcal{G}}^{jk}_{rzz})_n = s^2\int \mathcal{S}_j\Pi^n_{jk}D_{rk}e^{-sg_n}J_1(s\xi r)\xi d\xi$$

$$(\overline{\mathcal{G}}^{jk}_{rzr})_n = -s^2\int \mathcal{S}''_j\Pi^n_{jk}D_{rk}e^{-sg_n}J_0(s\xi r)\xi d\xi$$

$$+\frac{s}{r}\int \mathcal{S}''_j\Pi^n_{jk}D_{rk}e^{-sg_n}J_1(s\xi r)d\xi$$

$$(\overline{\mathcal{G}}^{jk}_{rrz})_n = s^2\int \mathcal{S}'''_j\Pi^n_{jk}D_{rk}e^{-sg_n}J_0(s\xi r)\xi d\xi$$

$$-\frac{s}{r}\int \mathcal{S}'''_j\Pi^n_{jk}D_{rk}e^{-sg_n}J_1(s\xi r)d\xi$$

$$(\overline{\mathcal{G}}^{jk}_{rr\theta})_n = (\overline{\mathcal{G}}^{jk}_{r\theta r})_n = (\overline{\mathcal{G}}^{jk}_{rz\theta})_n = (\mathcal{G}^{jk}_{r\theta z})_n = 0$$

$$(\mathcal{G}^{jk}_{\theta\theta r})_n = -\frac{s}{r}\int \mathcal{S}'_j\Pi^n_{jk}D_{\theta k}e^{-sg_n}J_0(s\xi r)\xi d\xi$$

$$+\frac{2}{r^2}\int \mathcal{S}'_j\Pi^n_{jk}D_{\theta k}e^{-sg_n}J_1(s\xi r)d\xi$$

$$(\overline{\mathcal{G}}^{jk}_{\theta\theta z})_n = \frac{s}{r}\int \mathcal{S}'''_j\Pi^n_{jk}D_{\theta k}e^{-sg_n}J_1(s\xi r)d\xi$$

$$(\overline{\mathcal{G}}^{jk}_{\theta r\theta})_n = (\overline{\mathcal{G}}^{jk}_{\theta\theta r})_n$$

$$(\overline{\mathcal{G}}^{jk}_{\theta z\theta})_n = -\frac{s}{r}\int \mathcal{S}''_j\Pi^n_{jk}D_{\theta k}e^{-sg_n}J_1(s\xi r)d\xi$$

$$(\overline{\mathcal{G}}^{jk}_{\theta\theta\theta})_n = (\overline{\mathcal{G}}^{jk}_{\theta rr})_n = (\overline{\mathcal{G}}^{jk}_{\theta zz})_n = (\overline{\mathcal{G}}^{jk}_{\theta rz})_n = (\overline{\mathcal{G}}^{jk}_{\theta zr})_n = 0$$

SH-Components.

$$(\overline{\mathcal{G}}^{H}_{z\alpha\beta})_n = 0 \qquad \alpha, \beta = r, \theta, z$$

$$(\overline{\mathcal{G}}^{H}_{rrr})_n = \frac{s}{r}\int \mathcal{S}_H\Pi^n_H D_{rH}e^{-sg_n}J_0(s\xi r)\xi d\xi$$

$$-\frac{2}{r^2}\int \mathcal{S}_H\Pi^n_H D_{rH}e^{-sg_n}J_1(s\xi r)d\xi$$

$$(\overline{\mathcal{G}}^{H}_{r\theta\theta})_n = (-\overline{\mathcal{G}}^{H}_{rrr})_n$$

$$(\overline{\mathcal{G}}^{H}_{rzr})_n = \frac{s}{r}\int \mathcal{S}'_H\Pi^n_H D_{rH}e^{-sg_n}J_1(s\xi r)d\xi$$

$$(\overline{\mathcal{G}}^{H}_{rrz})_n = (\overline{\mathcal{G}}^{H}_{rr\theta})_n = (\overline{\mathcal{G}}^{H}_{r\theta r})_n = (\overline{\mathcal{G}}^{H}_{r\theta z})_n = (\overline{\mathcal{G}}^{H}_{rz\theta})_n = (\overline{\mathcal{G}}^{H}_{rzz})_n = 0$$

$$(\overline{\mathcal{G}}^{H}_{\theta r\theta})_n = -s^2\int \mathcal{S}_H\Pi^n_H D_{\theta H}e^{-sg_n}J_1(s\xi r)\xi^2 d\xi - \overline{\mathcal{G}}^{H}_{rrr}$$

$$(\overline{\mathcal{G}}^{H}_{\theta\theta r})_n = -\frac{s}{r}\int \mathcal{S}_H\Pi^n_H D_{\theta H}e^{-sg_n}J_0(s\xi r)\xi d\xi$$

$$+\frac{2}{r^2}\int \mathcal{S}_H\Pi^n_H D_{\theta H}e^{-sg_n}J_1(s\xi r)d\xi$$

$$(\overline{\mathcal{G}}^{H}_{\theta z\theta})_n = s^2\int \mathcal{S}'_H\Pi^n_H D_{\theta H}e^{-sg_n}\xi J_0(s\xi r)d\xi$$

$$-\frac{s}{r}\int \mathcal{S}'_H\Pi^n_H D_{\theta H}e^{-sg_n}J_1(s\xi r)d\xi$$

$$(\overline{\mathcal{G}}^{H}_{\theta\theta\theta})_n = (\overline{\mathcal{G}}^{H}_{\theta\theta z})_n = (\overline{\mathcal{G}}^{H}_{\theta rr})_n = (\overline{\mathcal{G}}^{H}_{\theta rz})_n = (\overline{\mathcal{G}}^{H}_{\theta zr})_n = (\overline{\mathcal{G}}^{H}_{\theta zz})_n = 0$$

Once again the components due to SH-waves only contribute if all of the segments in a given ray are in S-mode, i.e., $z_p = 0$, $z_s = z_H$ in g_n.

In cylindrical coordinates r, θ, z, because four of the nine components of **G** ($G_{r\theta}, G_{\theta r}, G_{\theta z}, G_{z\theta}$) vanish identically, the nonvanishing components of $\boldsymbol{\mathcal{G}} = \nabla\mathbf{G}$ are the same as those of $\mathcal{G}^c = \mathbf{G}\nabla$, that is ($\alpha$, $\beta = r, \theta, z$),

$$\mathcal{G}_{r\alpha\beta} = \mathcal{G}^c_{\alpha\beta r} = \partial G_{\alpha\beta}/\partial r, \quad \alpha\beta \neq r\theta, \theta r, \theta z, z\theta,$$

$$\mathcal{G}_{z\alpha\beta} = \mathcal{G}^c_{\alpha\beta z} = \partial G_{\alpha\beta}/\partial z, \quad \alpha\beta \neq r\theta, \theta r, \theta z, z\theta,$$

$$\mathcal{G}_{\theta\alpha\beta} = \mathcal{G}^c_{\alpha\beta\theta}$$

where the four nonvanishing components of the last group are

$$\mathcal{G}_{\theta r\theta} = \mathcal{G}_{\theta\theta r} = (G_{rr} - G_{\theta\theta})/r$$

$$\mathcal{G}_{\theta\theta z} = G_{rz}/r, \quad \mathcal{G}_{\theta z\theta} = G_{zr}/r$$

The 14 nonvanishing components of the Laplace transform of $\boldsymbol{\mathcal{G}}^c$ are listed in this Appendix where the superscript c is dropped for convenience. Note that the Green's stress tensor is given by [27, 30]

$$\boldsymbol{\Sigma} = \lambda\mathbf{I}(\nabla\cdot\mathbf{G}) + \mu(\nabla\mathbf{G} + \mathbf{G}\nabla)$$

where **I** is the idem-factor. Hence the components of $\boldsymbol{\mathcal{G}}$ are useful in calculating Green's stress tensor.

APPENDIX *C*

The displacement field in terms of the third-order Green's tensor due to a center of rotation is given by equation (37). These equations can be written in a much simpler form by introducing the expressions

$$(\overline{\mathcal{G}}'^k_{z\theta})_n \equiv (\overline{\mathcal{G}}^{jk}_{zrz} - \overline{\mathcal{G}}^{jk}_{zzr})_n; \quad (\overline{\mathcal{G}}'^k_{r\theta})_n \equiv (\overline{\mathcal{G}}^{jk}_{rrz} - \overline{\mathcal{G}}^{jk}_{rzr})_n$$

$$(\overline{\mathcal{G}}'^k_{\theta z})_n \equiv (\overline{\mathcal{G}}^{jk}_{\theta\theta r} - \overline{\mathcal{G}}^{jk}_{\theta r\theta})_n; \quad (\overline{\mathcal{G}}'^k_{\theta r})_n \equiv (\overline{\mathcal{G}}^{jk}_{\theta z\theta} - \overline{\mathcal{G}}^{jk}_{\theta\theta z})_n$$

Substituting the expressions for $\overline{\mathcal{G}}^{jk}_{ilm}$ from Appendix B we get

P and SV Components.

$$(\overline{\mathcal{G}}'^k_{z\theta})_n = -s^2\int S^{\dagger}_2\Pi^n_{2k}D_{zk}e^{-sg_n}J_1(s\xi r)\xi d\xi$$

$$(\overline{\mathcal{G}}'^k_{\theta z})_n = \frac{s}{r}\int S^{\dagger}_2\Pi^n_{2k}D_{\theta k}e^{-sg_n}J_1(s\xi r)d\xi$$

$$(\overline{\mathcal{G}}'^k_{r\theta})_n = s^2\int S^{\dagger}_2\Pi^n_{2k}D_{rk}e^{-sg_n}J_0(s\xi r)\xi d\xi - (\overline{\mathcal{G}}'^k_{\theta z})_n$$

SH-Components.

$$(\overline{\mathcal{G}}'^H_{r\theta})_n = -\frac{s}{r}\int S^{\dagger}_H\Pi^n_H D_{rH}e^{-sg_n}J_1(s\xi r)d\xi$$

$$(\overline{\mathcal{G}}'^H_{\theta z})_n = s^2\int S^{\dagger}_H\Pi^n_H D_{\theta H}e^{-sg_n}J_1(s\xi r)\xi^2 d\xi$$

$$(\overline{\mathcal{G}}'^H_{\theta r})_n = s^2\int S^{\dagger}_H\Pi^n_H D_{\theta H}e^{-sg_n}J_0(s\xi r)\xi d\xi$$

$$-\frac{s}{r}\int S^{\dagger}_H\Pi^n_H D_{\theta H}e^{-sg_n}J_1(s\xi r)d\xi$$

In analogous to the case of center of explosion, the solutions for a center of rotation can also be obtained directly by assuming a proper body force potential for the rotational part of a body force and then solving the inhomogeneous equations for ψ and χ.

A. N. Ceranoglu
Assistant Professor,
Bogazici University,
Istanbul, Turkey

Yih-Hsing Pao
Professor,
Department of Theoretical
and Applied Mechanics,
Cornell University,
Ithaca, N. Y. 14853
Mem. ASME

Propagation of Elastic Pulses and Acoustic Emission in a Plate

Part 2: Epicentral Responses

In the first part of this paper expressions for Green's dyadics in terms of the generalized ray integrals for both unbounded and bounded media were given. In this part Cagniard's method is applied to obtain the transient response along the epicentral points of an elastic plate. Numerical results are shown for a concentrated force, a single-couple, a double force, a double-couple without moment and a center of rotation up to 10 transit time required for the longitudinal (P)-wave to cross the thickness of the plate.

4 Response of a Plate Along the Axis of the Source

General expressions for the displacement field due to different point sources were given in Part 1. These expressions are simplified considerably if one is interested in the response of the plate along the axis passing through the source, i.e., $r = 0$. Displacement fields, pertinent to the axial points are obtained by taking the limit of the foregoing expressions as r approaches zero. In the limit as $\alpha \rightarrow 0$ the following expressions are applied:

$$\lim_{\alpha \rightarrow 0} J_0(\alpha) = 1; \quad \lim_{\alpha \rightarrow 0} J_1(\alpha) = \alpha/2. \tag{40}$$

Applying the aforementioned limiting process to the components of the Green's tensor $\overline{G}_{mn}(r, z, s)$ and $\overline{\mathcal{G}}_{lmn}(r, z, s)$, one obtains the corresponding expressions at the points along the axis, $r = 0$, which are listed in Appendix *D*.

In what follows, we show how the inverse Laplace transform of these ray integrals for epicentral locations are computed exactly by applying the Cagniard's method. It is seen that, excluding the factor s or s^2, the integrals for each ray appearing both in $\overline{G}_{mn}(0, z, s)$ and $\overline{\mathcal{G}}_{lmn}(0, z, s)$, (see Appendix *D*) are all of the form

$$\overline{I}(z, s) = \int_0^\infty E(\xi)\xi e^{-sg(\xi, z)} d\xi \tag{41}$$

where $g(\xi, z) = \eta z_p + \zeta z_s$ is the phase function and $E(\xi)$ is an even function of ξ involving the source function, receiver function, and the product of the reflection coefficients. The indices j, k, H, etc., for a particular ray have been omitted. The factor of s or s^2 can be combined with the function $\overline{F}(s)$ which appears in the expressions for the displacement field due to an arbitrary time function. Hence, knowing the inverse Laplace transforms of the integrals of equation (41), one can obtain the complete solution through a convolution integral. The inversion of the integral $\overline{I}(z, s)$ will be carried out as discussed in the following.

Note that s, the Laplace transform parameter, appears only as a factor in the exponent of the integrand of $\overline{I}(z, s)$ and nowhere else in the integral. This permits an explicit determination of the Laplace inversion. If a new variable of integration, t, is introduced such that

$$t = g(\xi, z) = z_p \eta + z_s \zeta \tag{42}$$

the integration over the real variable ξ is then transformed into an integration over another real variable t. This is a one-to-one transformation over the interval $[0, \infty]$, and one can solve for ξ as a function of t, when z is specified,

$$\xi(t) = \frac{1}{|z_p - z_s|} \{t^2(z_p^2 + z_s^2)^2 - 2z_p z_s t[t^2 + (1 - \kappa^2)(z_s^2 - z_p^2)]^{1/2} + (z_p^2 - \kappa^2 z_s^2)(z_s^2 - z_p^2)\}^{1/2} \quad z_p \neq z_s \tag{43}$$

$$\xi(t) = \frac{1}{2z_p t}\{[t^2 - z_p^2(1 + \kappa^2)]^2 - 4z_p^4\kappa^2\}^{1/2} \quad z_p = z_s$$

Hence, equation (41) is transformed to

$$\overline{I}(z, s) = \int_{t_A}^\infty E[\xi(t)]\xi(t) \left(\frac{d\xi}{dt}\right) e^{-st} dt \tag{44}$$

where

$$\frac{d\xi}{dt} = \frac{\zeta\eta}{\xi(z_p\zeta + z_s\eta)} \tag{45}$$

and t_A, the value of t at $\xi = 0$, is the arrival time of a particular ray.

$$t_A = z_p + \kappa z_s \tag{46}$$

The lower limit of integration in equation (44) is changed to zero by introducing the Heaviside's step function

---

Contributed by the Applied Mechanics Division of THE AMERICAN SOCIETY OF MECHANICAL ENGINEERS, for presentation at the 1981 Joint ASME/ASCE Applied Mechanics, Fluids Engineering, and Bioengineering Conference, University of Colorado, Boulder, Colo., June 22–27, 1981.

Discussion on this paper should be addressed to the Editorial Department, ASME, United Engineering Center, 345 East 47th Street, New York, N. Y. 10017, and will be accepted until June 1, 1981. Readers who need more time to prepare a Discussion should request an extension from the Editorial Department. Manuscript received by ASME Applied Mechanics Division, August, 1979. Paper No. 81-APM-5.

$$\bar{I}(z, s) = \int_0^\infty \left\{ E\,[\xi(t)]\xi(t)\left(\frac{d\xi}{dt}\right)\mathrm{H}(t - t_A)\right\} e^{-st}{}_{dt} \qquad (47)$$

The aforementioned equation simply means that $\bar{I}(z, s)$ is the Laplace transform of the quantity inside the curly bracket, hence,

$$I(z, t) = E[\xi(t)]\xi(t)(d\xi/dt)\mathrm{H}(t - t_A) \qquad (48)$$

where $\xi(t)$ is given by equation (43).

As mentioned earlier, the coefficients of these integrals, $\bar{I}(s)$, appearing in the expressions for the displacement field are either $s\bar{F}(s)$ or $s^2\bar{F}(s)$, where $\bar{F}(s)$ involves the Laplace transform of the time function, $\bar{f}(s)$, for the source. From Table 2, it is seen that these coefficients in general can be written as $s^m\bar{f}(s)$. Now, from the convolution theorem

$$\begin{aligned}\mathcal{L}^{-1}[s^m\bar{f}(s)\bar{I}(s)] &= \frac{\partial^m}{\partial t^m}\int_0^t f(t-\tau)I(\tau)d\tau \\ &= \int_0^t f^{(m)}(t-\tau)I(\tau)d\tau + f^{(m-1)}(O)I(t) + \ldots \\ &\qquad + f(O)I^{(m-1)}(t) \qquad (49)\end{aligned}$$

where $\mathcal{L}^{-1}$ denotes the inverse Laplace transform operator and the superscript in parenthesis denotes the order of differentiation with respect to the argument. For a concentrated force, m equals 1 while for the other sources discussed in this paper, m equals 2.

Equations (48) and (49) give rise to the exact transient response for pulses traveling along a particular path from the source to any point on the z-axis passing through the source. The total response is obtained by summing up waves along all possible ray-paths as explained in the next section.

In the next section, we show numerical results for the epicentral responses of a plate excited by six types of buried sources, a single-force, a double-force, a single-couple, a double-couple without moment, a center of rotation, and a center of explosion, and also a surface force. The time function for the source is either a step function, or a parabolic ramp function. General responses due to an arbitrary time function can then be determined by a convolution integral as shown in equation (49). By measuring the general responses at the surface of a plate, it is also possible to determine the source time function by deconvolutions [31]. Hence, the exact step responses as shown in this paper will be useful to evaluate the time function of a source.

This inverse process of deconvolution is not only useful in characterizing the time function of a source, but also a powerful technique to calibrate a transducer [32]. The Lamb's solution for a half space has been applied to deconvolute a loading function [33], and to calibrate an ultrasonic transducer [34]. Experimentally, it is easier to do the calibration on a plate, than on a massive block which simulates a half space [35].

5 Numerical Results and Discussions of Responses at Epicenter

In a plate, the waves radiated at the source location travel along many different paths before they reach the receiver. Hence, the first step in the calculations is to sketch the possible ray-paths as shown in Fig. 2 and assign modes as P or S systematically to all segments of each ray. The vertical projections z_p and z_s of the segments in P and S-modes for the jth ray are then obtained. The arrival time, t_A, calculated from equation (46), is then compared with the maximum time of interest and if the former is less than the latter, the contribution due to this ray is calculated.

Excluding the source and the receiver segments, i.e., the first and the last segments of a given ray, let m_p and m_s be the number of segments traveled in P and S-modes, respectively. These $(m_p + m_s)$ *segments can be arranged in* $(m_p + m_s)!/(m_p!m_s!)$ *number of com*binations. Each possible configuration has a unique product of reflection coefficients, Π^n_{jk}. However, those rays that have the same total number of P to P and S to S reflections will have the same numerical value of Π^n_{jk}. This is because $R^{pp} = R_{pp}$, $R^{vv} = R_{vv}$, $R^{pv} = -R_{pv}$, and $R^{vp} = -R_{vp}$.

As an illustration, consider a ray with 10 segments ($n = 10$) where both the source and the receiver segments are in P-mode, $j, k = 1$, and let $m_p = 5$, $m_s = 3$. The total number of possible combinations is then $(5 + 3)!/(5!3!) = 56$. However, it does not mean that 56 different calculations are needed. These 56 rays can further be grouped into three subgroups with

$$\Pi^{(1)}_{11} = (R^{pp})^5(R^{vv})^2R^{vp}R_{pv}$$

$$\Pi^{(2)}_{11} = (R^{pp})^4(R^{vv})(R^{pv})^2R^{vp}R_{vp}$$

$$\Pi^{(3)}_{11} = (R^{pp})^3(R^{vp})^3(R_{pv})^3$$

In the first group, there are 6 rays with a value of $\Pi^{10}_{11} = \Pi^{(1)}_{11}$, in the second group 30 rays with $\Pi^{10}_{11} = \Pi^{(2)}_{11}$, and in the third group 20 rays with $\Pi^{10}_{11} = \Pi^{(3)}_{11}$. Since the source function, receiver function, phase function and the arrival time for all these rays are the same, the contribution due to these rays can be calculated at once with one integral, where

$$S_1\Pi^{10}_{11}D_{\alpha 1} = S_1[6\Pi^{(1)}_{11} + 30\Pi^{(2)}_{11} + 20\Pi^{(3)}_{11}]D_{\alpha 1}.$$

Hence, by choosing the proper source function, receiver function and forming the product Π^n_{jk}, the expressions for the rays are assembled for numerical evaluations. In the following numerical examples it was assumed that $\kappa^2 = 3$, corresponding to the case where the two Lamé constants are equal ($\lambda = \mu$).

1 **Concentrated Force.** The displacement fields at the epi-

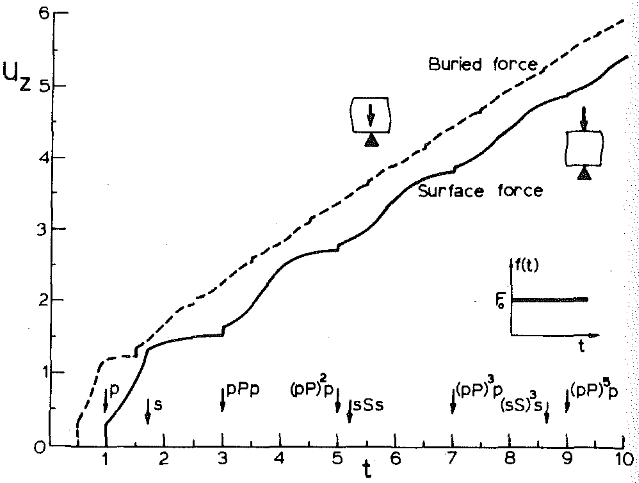

Fig 4 (*a*) Vertical force

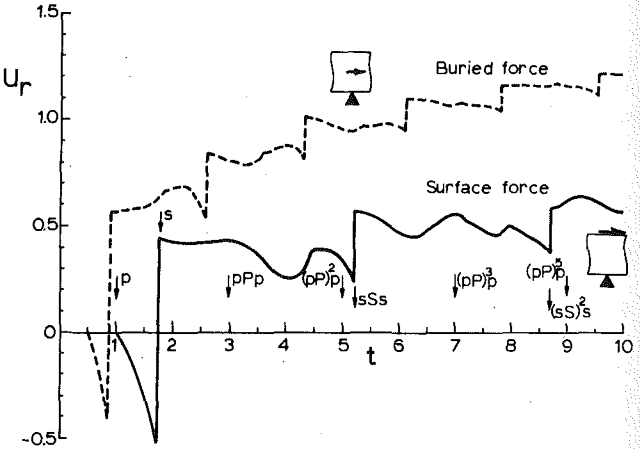

Fig 4 (*b*) Horizontal force

Fig. 4 Response of the surface $z = 1$ due to a concentrated force at $z_0 = 0$ and 1/2; ordinate is the normalized displacement $\pi\mu h^2 u_\alpha/F_0 a_\alpha (\alpha = r, z)$

Table 3 Parameters of the three groups of ray integrals for $\bar{u}_\alpha(z > z_0)$ in a plate due to a concentrated force at $z = z_0$

n	Ray	Source Function S_j					Receiver Function $D_{\alpha k}$					Product of Reflection Coefficients Π^n_{jk}	Phase Function g_n
		S_1	S_2	S_1'	S_2'	S_H	D_{z1}	D_{z2}	D_{r1}	D_{r2}	D_H		
1	p	-1	-	$-\xi/\eta$	-	-	$-\eta$	-	$-\xi$	-	-	1	$\eta(z-z_o)$
	s	-	ξ/ζ	-	1	-	-	$-\xi$	-	$-\zeta$	-	1	$\zeta(z-z_o)$
	h	-	-	-	-	κ^2/ζ	-	-	-	-	1	1	$\zeta(z-z_o)$
2	Pp	1	-	$-\xi/\eta$	-	-	$-\eta$	-	$-\xi$	-	-	R^{pp}	$\eta(z+z_o)$
	Pv	1	-	$-\xi/\eta$	-	-	-	$-\xi$	-	$-\zeta$	-	R^{pv}	$\eta z_o+\zeta z$
	Vv	-	ξ/ζ	-	-1	-	-	$-\xi$	-	$-\zeta$	-	R^{vv}	$\zeta(z+z_o)$
	Vp	-	ξ/ζ	-	-1	-	-	$-\eta$	$-\xi$	-	-	R^{vp}	$\zeta z_o+\eta z$
	Hh	-	-	-	-	κ^2/ζ	-	-	-	-	1	1	$\zeta(z+z_o)$
3	pPp	-1	-	$-\xi/\eta$	-	-	$-\eta$	-	$-\xi$	-	-	$R_{pp}R^{pp}$	$\eta(2+z+z_o)$
	pPv	-1	-	$-\xi/\eta$	-	-	-	$-\xi$	-	$-\zeta$	-	$R_{pp}R^{pv}$	$\eta(2-z_o)+\zeta z$
	pVp	-1	-	$-\xi/\eta$	-	-	$-\eta$	-	$-\xi$	-	-	$R_{pv}R^{vp}$	$\eta(1+z_oz)+\zeta$
	pVv	-1	-	$-\xi/\eta$	-	-	-	$-\xi$	-	$-\zeta$	-	$R_{pv}R^{vv}$	$\eta(1-z_o)+\zeta(1+z)$
	vVv	-	ξ/ζ	-	1	-	-	$-\xi$	-	$-\zeta$	-	$R_{vv}R^{vv}$	$\zeta(2+z-z)$
	vVp	-	ξ/ζ	-	1	-	$-\eta$	-	$-\xi$	-	-	$R_{vv}R^{vp}$	$\eta z+\zeta(2-z_o)$
	vPv	-	ξ/ζ	-	1	-	-	$-\xi$	-	$-\zeta$	-	$R_{vp}R^{pv}$	$\eta+\zeta(1-z_o+z)$
	vPp	-	ξ/ζ	-	1	-	$-\eta$	-	$-\xi$	-	-	$R_{vp}R^{pp}$	$\eta(1+z)+\zeta(1-z_o)$
	hHh	-	-	-	-	κ^2/ζ^2	-	-	-	-	1	1	$\zeta(2+z-z_o)$

central locations are calculated from equations (13) and (22) where the components of Green's dyadics $\overline{\mathbf{G}}(0, z, s)$ are listed in Appendix *D*. The value of m in equations (49) is 1 for a concentrated force. Hence, if $f(t)$ is taken to be Heaviside's step function, i.e., $f(t) = \mathrm{H}(t)$, then the only contribution in equation (49) comes from the term $f(0)I(t)$.

Fig. (4*a*) and (4*b*) show the response of a point on the surface $z = 1$ due to a buried ($z_0 = 0.5$) and a surface ($z_0 = 0$) force. The ordinate is the normalized displacement $\pi\mu h^2 u_\alpha/(F_0)$, $(\alpha = r, \theta, z)$, and the abcissa is the nondimensional time $t = ct^*/h$. The results in Fig. 4(*a*) are in complete agreement with those given by Knopoff [10], and Pao, et al. [13], and those in Fig. 4(*b*) are similar to those given by Davids [14] who calculated the response due to the incident wave generated by a shear impact on the plate. The vertical displacement, u_z, experiences jumps at the arrivals of the rays with all segments in the *P*-mode while the displacements u_r and u_θ have jumps at the arrivals of rays in *S*-mode. The magnitude of these jumps calculated from the corresponding rays by setting $t = t_A$ or $\xi = 0$, are

$$(\pi\mu h^2/F_0)[u_z(0, z, t_A)] = a_z/(\gamma\kappa^2 z_p)$$

$$(\pi\mu h^2/F_0)[u_\alpha(0, z, t_A)] = a_r/(\gamma z_s) \quad \alpha = r, \theta \tag{50}$$

where γ is 1 for a surface force and 2 for a buried force.

A total of 156 and 381 rays are calculated for surface and buried sources, respectively, in order to obtain the exact response up to $t = 10$. The arrival time of the *P*, *pPp*, *pPpPp*, . . . are indicated on the figure for the surface source.

2 Double-Force and Center of Explosion. Motion of a plate due to a buried double-force and a center of explosion for each ray are calculated from equations (32) and (39), respectively. The case of a vertical double-force and center of explosion were first studied by Pao, et al. [13]; some of their results are reproduced here for completeness.

Since a center of explosion is obtained by superposing three mutually orthogonal double-forces, it is expected that the response of a plate due to a vertical double-force be similar to that of a center of explosion. This is shown in Fig. 5 where three different time function, Heaviside's step function, a linear ramp function, and a parabolic ramp function are considered. Superposition principle for these ramp functions are given in Table 4. The rise time of the ramp functions were taken to be 0.4. It is seen that by introducing a finite rise time, the response signatures become smoother. The displacement field due to these two kinds of sources exhibit a delta function behavior at the arrivals of rays with all segments in *P*-mode, Fig. 5(*a*). A period equal to twice the travel time of a *P*-wave to cross the thickness of the plate, $T^* = 2h/c$, can be associated with these curves. This periodic behavior is due to the interference of those rays with $2m$ and $(2m + 1)$ reflections from the surfaces of the plate.

Table 4 Superposition formulas for time functions

Types	Rise time or duration	Function
Step	0	$H(t)$
Linear ramp	Δ	$f_1(t)H(t) - f_1(t-\Delta)H(t-\Delta)$
Triangular pulse	2Δ	$f_1(t)H(t) - 2f_1(t-\Delta)H(t-\Delta) + f_1(t-2\Delta)H(t-2\Delta)$
Parabolic ramp	2Δ	$f_2(t)H(t) - 2f_2(t-\Delta)H(t-\Delta) + f_2(t-2\Delta)H(t-2\Delta)$
Parabolic pulse	4Δ	$f_2(t)H(t) - 2f_2(t-\Delta)H(t-\Delta) + 2f_2(t-3\Delta)H(t-3\Delta)$ $- f_2(t-4\Delta)H(t-4\Delta)$

$f_1(t) = t \qquad f_2(t) = \frac{1}{2}t^2$

Responses due to a horizontal and an oblique double-force are shown in Fig. 6. These results have not been reported previously. Note that for a vertical double-force, Fig. 5, and for a horizontal double-force, Fig. 6(*a*), the only nonvanishing component of the displacement field is u_z, however, for an oblique orientation of the double-force, Fig. 6(*b*), both u_z and u_r are nonzero. This shows that the response for an

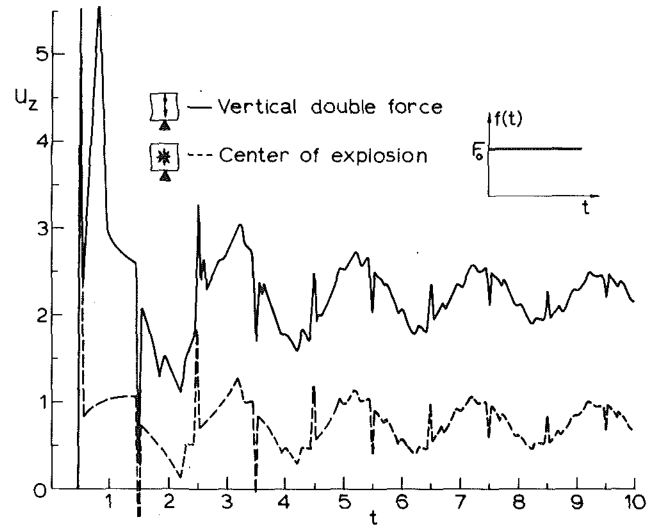

Fig. 5(*a*) Step time function

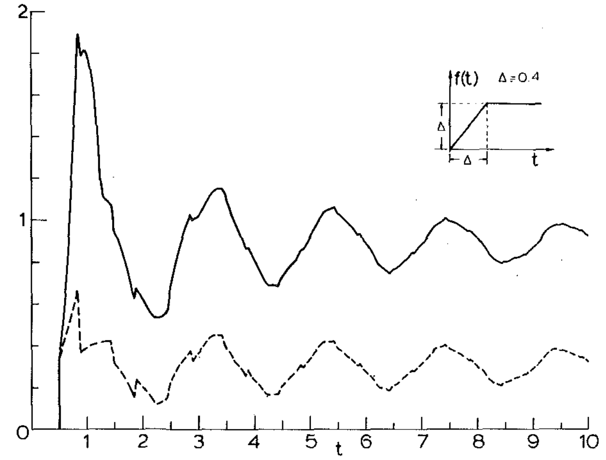

Fig. 5 (*b*) Linear ramp time function

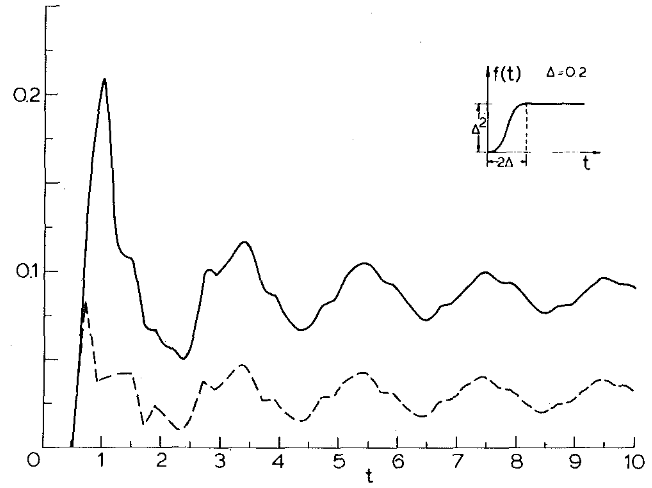

Fig. 5 (*c*) Parabolic ramp time function

Fig. 5 Epicentral response of the surface $z = 1$ due to a point source at $z_0 = 1/2$; the ordinate is the normalized nondimensional displacement $\pi\mu h^3 u_z/D_0$

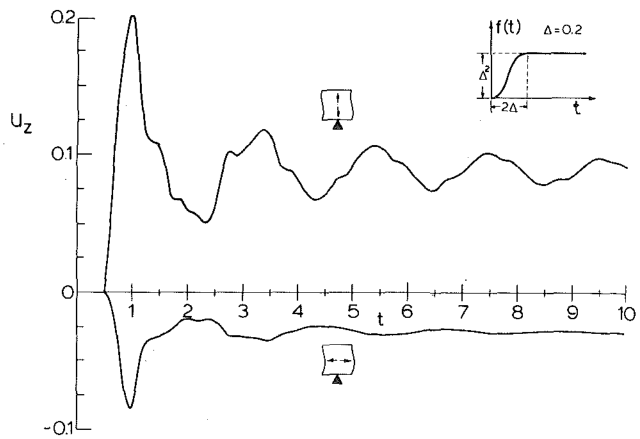

Fig. 6 (*a*) Vertical **a** = (0, 0, 1) and horizontal (1, 0, 0) double-force (u_r = 0)

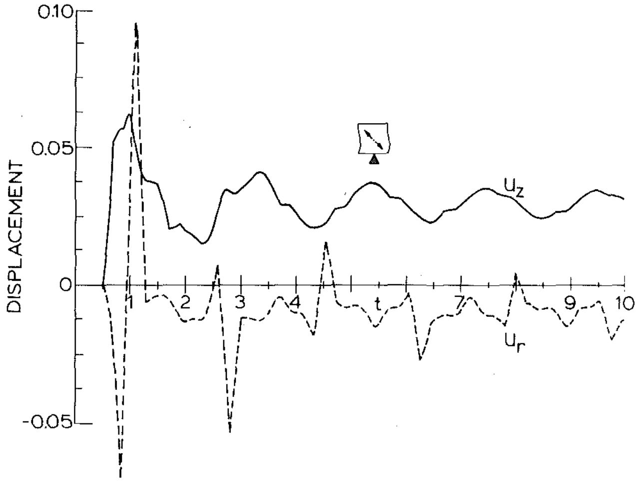

Fig. 6 (*b*) An oblique double-force, $\sqrt{2}$ **a** = (1, 0, 1)

Fig. 6 Epicentral response of the surface $z = 1$ due to three different orientations of a double-force at $z_0 = 1/2$; the ordinate is the normalized displacement $\pi\mu h^3 u_\alpha/D_0 (\alpha = r, z)$

oblique double-force cannot be obtained by adding vectorially the results due to two mutually perpendicular "components." This is due to the fact that the Green's function for a double force is a third rank tensor, $\mathcal{G}_{ijk}$, which is symmetric only with respect to the first two indices, i and j. Contrary to the vertical displacement which is nearly periodic with the period $2h/c$ ($T^* = 2$), the radial displacement has an oscillatory behavior with a period of $T^* = 2h/C$, and $c/C = \sqrt{3}$ in this case.

3 Single-Couple and Center of Rotation. Eventhough a single-couple is not a self equilibrating force system, it is known as Type I force system of Honda in geophysics, and has been used in modeling some of the earthquake mechanisms, [36]. Epicentral responses of the plate calculated from equations (29) are shown in Fig. 7 for three different orientations of the couple. In these figures the time-dependency of the source is a parabolic ramp function with a rise time of 0.4. The vertical displacement due to couples whose generating forces initially lie in a plane parallel or perpendicular to the surfaces of the plate vanishes (Fig. 7(*a*), however, it is nonzero for other orientations (Fig. 7(*b*). An interesting feature of the single-couple is observed when the generating forces, lying in a plane that contains the z-axis, and make an angle of $\pi/4$ with this axis. For such an orientation, there is no contribution to the radial displacement from those rays which originate as a P-wave. Similar to the double-force case, periods of $2h/c$ and $2h/C$ can be associated with the long-time behavior of the vertical and radial displacements, respectively.

Superposing two single couples, the moments being in the same direction and the generating forces along two orthogonal vectors, results in a force system known as the center of rotation. This source generates only S-waves at the source location, however, the P-waves

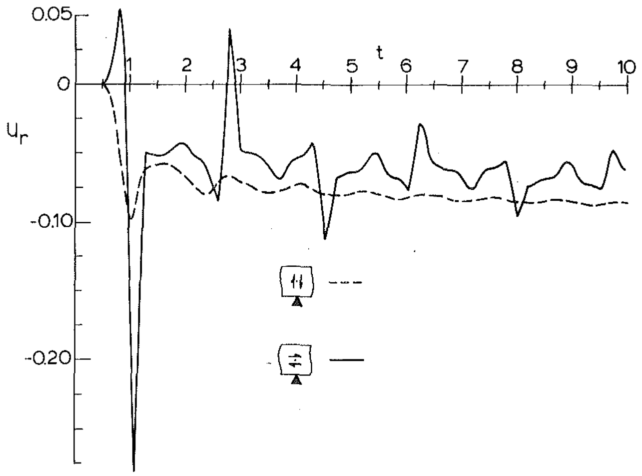

Fig. 7(*a*) Solid line **a** = (1, 0, 0), **b** = (0, 0, −1), dashed line **a** = (0, 0, 1), **b** = (1, 0, 0)

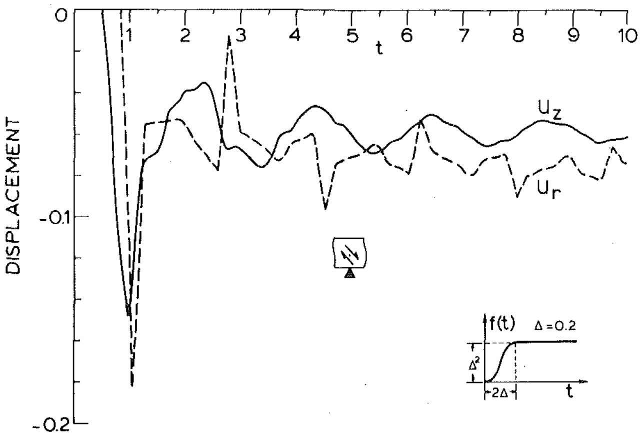

Fig. 7(*b*) Couple with oblique forces $\sqrt{2}\,\mathbf{a} = (1, 0, 1)$, $\sqrt{2}\,\mathbf{b} = (1, 0, -1)$

Fig. 7 Response of the surface $z = 1$ due to three different orientations of a single couple at $z_0 = 1/2$; the ordinate is the normalized nondimensional displacement $\pi\mu h^3 u_\alpha/M_0 (\alpha = r, z)$

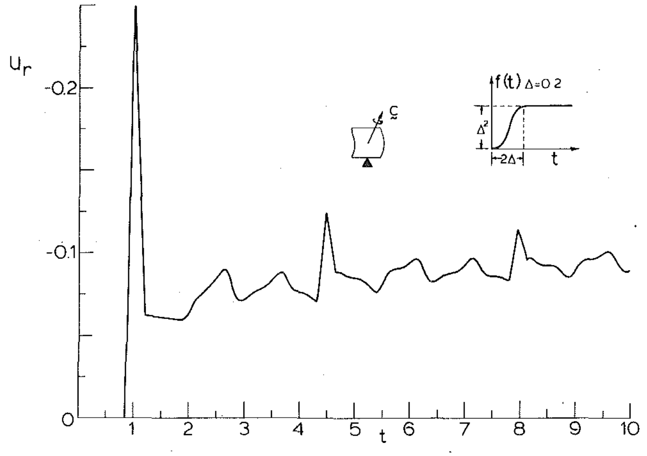

Fig. 8 Response of the surface $z = 1$ due to a center of rotation at $z_0 = 1/2$; *the ordinate is the normalized nondimensional displacement,* $\pi\mu h^3 u_r/(M_0 c_\theta)$

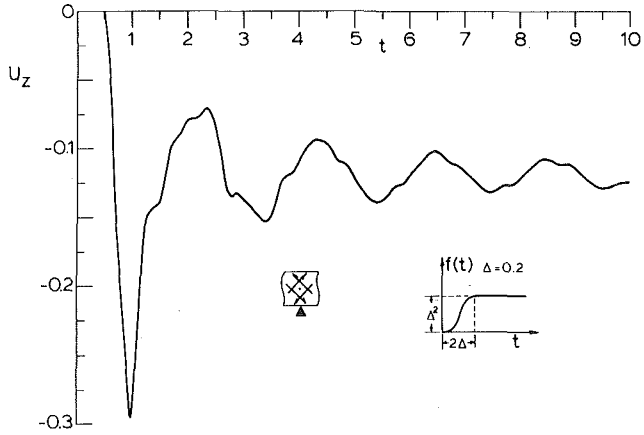

Fig. 9 (*a*) **a** = (1, 0, 0), **b** = (0, 0, −1)

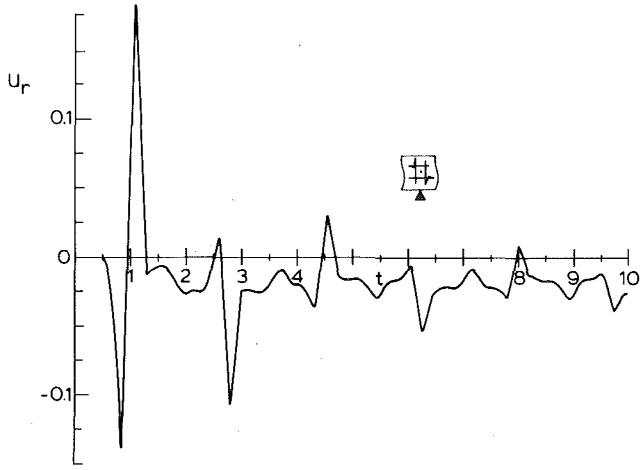

Fig. 9 (*b*) $\sqrt{2}\,\mathbf{a} = (1, 0, 1)$, $\sqrt{2}\,\mathbf{b} = (1, 0, -1)$

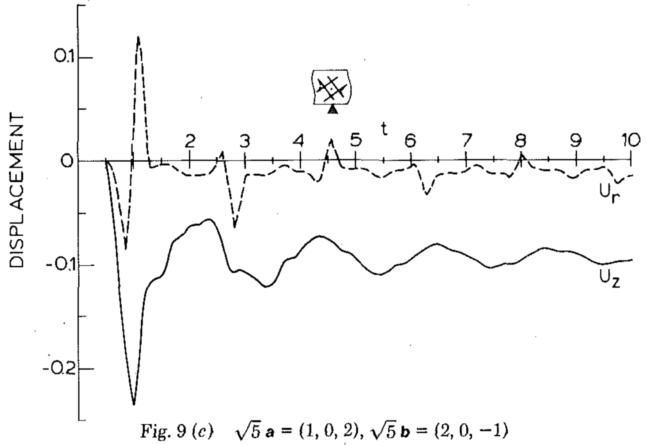

Fig. 9 (*c*) $\sqrt{5}\,\mathbf{a} = (1, 0, 2)$, $\sqrt{5}\,\mathbf{b} = (2, 0, -1)$

Fig. 9 Response of the surface $z = 1$ due to three different orientations of a buried double-couple without moment at $z_0 = 1/2$; the ordinate is the normalized nondimensional displacement $\pi\mu h^3 u_\alpha/D_0(\alpha = r, z)$

are generated upon reflections (see, equation (38)). Fig. 8 shows the response due to a buried center of rotation at $z_0 = 0.5$ with a parabolic ramp function of rise time 0.4 as its time-dependency. The ordinate in this figure is the normalized displacement $\pi\mu h^3 u_r/(M_\theta c_\theta)$ where $c_\theta = a_r b_z - a_z b_r$. The long-time behavior of the radial displacement has a period of $2h/C$.

4 **Double-Couple Without Moment.** Double-couple without moment is the most widely used self-equilibrating force system in modeling the earthquake mechanisms. Known also as the Type II force system of Honda, [36], it represents the strike slip motion of the fault where the unit vector **a** is along the direction of the slip motion [3, Chapter 3].

Fig. 9 shows the epicentral response of the plate due to three different orientations of the double-couple without moment, equation (35). In all these figures the time-dependency of the source is a parabolic ramp function with a rise time of 0.4. As seen from these figures, a period of $T^* = 2h/c$ and $T^* = 2h/C$ can be associated with the vertical and radial displacements, respectively. Note that the vertical displacement due to a double-couple without moment is very much similar to those due to a double-force and a center of explosion, hence these two sources can be distinguished only from the responses at off-center points.

References

31 Ko, H., and Scott, R. F., "Deconvolution Techniques for Linear Systems," *Bull. of Seismo. Soc. Am.*, Vol. 57, No. 6, 1967, pp. 1393–1408.

32 Sachse, W., and Hsu, N. N., "Ultrasonic Transducers for Materials Testing and Their Characterization," *Physical Acoustics*, Vol. 14, Chapter 4, ed., Mason, W. P., and Thurston, R., New York, 1979.

33 Goodier, J. N., Jashsman, W. E., and Ripperger, E. A., "An Experimental Surface-Wave Method for Recording Force-Time Curves in Elastic Impacts," ASME JOURNAL OF APPLIED MECHANICS, Vol. 26, 1959, pp. 3–7.

34 Breckendridge, F. R., Tschiegg, C. E., and Greenspan, M., "Acoustic Emission: Some Application of Lamb's Problem," *Journal of the Acoustical Society of America*, Vol. 57, 1975, pp. 626–631.

35 Sachse, W., and Ceranoglu, A., "Experiments With a Well-Characterized Acoustic Emission System," *Ultrasonics International 1979, Conference Proceedings*, IPC Science and Technology Press Ltd. Guildford, England, in press.

36 Stauder, W., "The Focal Mechanism of Earthquakes," *Advances in Geophysics*, Vol. 9, 1962, pp. 1–76.

APPENDIX *D*

Both the Green's dyadics and the third rank Green's tensor simplify considerably at the epicentral locations, i.e., r = 0. Going through the limiting procedure as explained in Section 4 of this paper we get for the Green's dyadic:

P-SV components. (j, k = 1 and 2 for P and SV-modes, respectively)

$$(\overline{G}^{jk}_{zz})_n = s \int S_j \Pi^n_{jk} D_{zk} e^{-sg_n} \xi d\xi$$

$$(\overline{G}^{jk}_{rr})_n = -\frac{s}{2} \int S'_j \, \Pi^n_{jk} D_{rk} e^{-sg_n} \xi d\xi$$

$$(\overline{G}^{jk}_{\theta\theta})_n = -\frac{s}{2} \int S'_j \, \Pi^n_{jk} D_{\theta k} e^{-sg_n} \xi d\xi$$

$$(\overline{G}^{jk}_{zr})_n = (\overline{G}^{jk}_{rz})_n = (\overline{G}^{jk}_{z\theta})_n = (\overline{G}^{jk}_{r\theta})_n = (\overline{G}^{jk}_{\theta r})_n = 0$$

SH-Components.

$$(\overline{G}^{H}_{rr})_n = \frac{s}{2} \int S_H \Pi^n_H D_{rH} e^{-sg_n} \xi d\xi$$

$$(\overline{G}^{H}_{\theta\theta})_n = \frac{s}{2} \int S_H \Pi^n_H D_{\theta H} e^{-sg_n} \xi d\xi$$

All other components are zero.

In the case of the third rank Green's tensor the only nonzero components are:

P-SV Components.

$$(\overline{\mathcal{G}}^{jk}_{zzz})_n = s^2 \int \mathcal{S}_j \Pi^n_{jk} D_{zk} e^{-sg_n} \xi d\xi$$

$$(\overline{\mathcal{G}}^{jk}_{zrr})_n = \frac{1}{2} s^2 \int \mathcal{S}'_j \, \Pi^n_{jk} D_{zk} e^{-sg_n} \xi^2 d\xi$$

$$(\overline{\mathcal{G}}^{jk}_{z\theta\theta})_n = (\overline{\mathcal{G}}^{jk}_{zrr})_n$$

$$(\overline{\mathcal{G}}^{jk}_{rzr})_n = -\frac{1}{2} s^2 \int \mathcal{S}''_j \, \Pi^n_{jk} D_{rk} e^{-sg_n} \xi d\xi$$

$$(\overline{\mathcal{G}}^{jk}_{rrz})_n = \frac{1}{2} s^2 \int \mathcal{S}'''_j \, \Pi^n_{jk} D_{rk} e^{-sg} \xi d\xi$$

$$(\overline{\mathcal{G}}^{jk}_{\theta\theta z})_n = \frac{1}{2} s^2 \int \mathcal{S}'''_j \, \Pi^n_{jk} D_{\theta k} e^{-sg_n} \xi d\xi$$

$$(\overline{\mathcal{G}}^{jk}_{\theta z\theta})_n = \frac{1}{2} s^2 \int \mathcal{S}''_j \, \Pi^n_{jk} D_{\theta k} e^{-sg_n} \xi d\xi$$

SH-Components.

$$(\overline{\mathcal{G}}^{H}_{rzr})_n = \frac{1}{2} s^2 \int \mathcal{S}'_H \, \Pi^n_H D_{rH} e^{-sg_n} \xi d\xi$$

$$(\overline{\mathcal{G}}^{H}_{\theta z\theta})_n = \frac{1}{2} s^2 \int \mathcal{S}'_H \Pi^n_H D_{rH} e^{-sg_n} \xi d\xi$$

For a center of rotation:

P-SV Components.

$$(\overline{\mathcal{G}}'^{k}_{r\theta})_n = s^2 \int S_2 \Pi^n_{2k} D_{rk} e^{-sg_n} \xi d\xi$$

$$(\overline{\mathcal{G}}'^{k}_{\theta z})_n = \frac{1}{2} s^2 \int S_2 \Pi^n_{2k} D_{\theta k} e^{-sg_n} \xi d\xi$$

SH-Components.

$$(\overline{\mathcal{G}}'^{H}_{r\theta})_n = -\frac{1}{2} s^2 \int S_H \Pi^n_H D_{rH} e^{-sg_n} \xi d\xi$$

$$(\overline{\mathcal{G}}'^{H}_{\theta r})_n = \frac{1}{2} s^2 \int S_H \Pi^n_H D_{\theta H} e^{-sg_n} \xi d\xi$$

A. N. Ceranoglu
Assistant Professor,
Bogazici University,
Istanbul, Turkey

Yih-Hsing Pao
Professor,
Department of Theoretical
and Applied Mechanics,
Cornell University,
Ithaca, N. Y. 14853
Mem. ASME

Propagation of Elastic Pulses and Acoustic Emission in a Plate

Part 3: General Responses

In the first part of this paper, the Laplace transformed solutions in terms of the generalized ray integrals for point sources in a plate are presented. The inverse transform and the exact solutions for the epicentral responses together with numerical results were given in Part 2. In this part a modified version of Cagniard's method is applied to obtain the transient response of the plate at any location due to point sources applied at the surface or the interior of the plate. Numerical results are shown for a concentrated force, a single-couple, a double-force, a double-couple without moment and a center of rotation, at locations up to six plate thicknesses from the source.

6 Source and Receiver on the Same Surface

The general expressions for the Laplace transformed displacement fields due to different point force systems are given by equations (22)–(29) in Part 1, [30]. It was also explained in Section 2.4 how to modify the ray integrals to take into account the cases when either the source or the receiver was on the bounding surface of a half space, or when they were on the opposite sides of a plate.

The problem where both the source and the receiver are on the *same* surface of a plate requires special attention. The solution for this problem is derived from the general plate solution by taking the limit as both z_0 and z approach zero. The order of this limiting process with respect to z and z_0 is immaterial.

Consider first two rays, P and S, and four reflected rays, Pp, Ps, Ss, and Sp as shown in Fig. 10. The three rays P, P_p, and Ps form a P-group in a half space or a plate and the remaining form a S-group. If we combine the three ray integrals of the P-group, as given by equations (9) and (20), and then take the limits when both z and z_0 approach zero, we obtain a single integral devoid of the exponential phase function because both exp $[-s\eta(z+z_0)]$ and exp $[-s\zeta(z+z_0)]$ reduce to unity. This ray integral represents a P-wave which propagates directly from the source to the receiver along the surface. The coefficient of the Bessel functions in the integrands can be expressed as $S_1\Pi^1_{11}D_{\alpha 1}$ and $S'_1\Pi^1_{11}D_{\alpha 1}$ where S_1 and S'_1 equals the *surface* P-source, S^*_p and S'^*_p, respectively, as given by equation (23a), and $D_{\alpha 1}$ equals the *interior* P-receiver function $D_{\alpha p}$ as listed in Table 2. The Π^1_{11} equals unity (no reflection) in this case.

Fig. 10 Three rays coalesce into a single P-ray, or a single S-ray as $z_0 \rightarrow 0$ and $z \rightarrow 0$

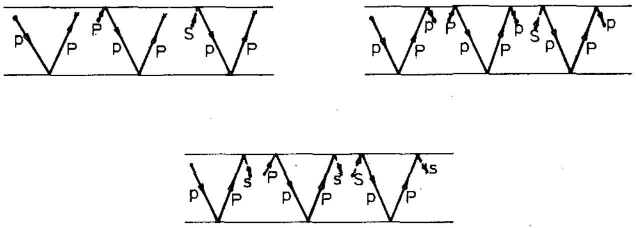

Fig. 11 A group of nine rays which coalesce into a pP ray as both receiver and source approach to the top surface of a plate

Combination of the three rays of the SV-group gives rise to a single SV-ray integral with similar results. The case of the SH components of a surface source can be treated in the same manner except that the resulting SH ray integral is formed by combining only two rays, H and Hh.

We note in passing that when the surface force is a vertical force ($a_r = 0$, $a_\theta = 0$, $a_z = 1$), the result so obtained is the solution for the surface response of a half space originally investigated by Lamb [37]. When the surface force is a horizontal force, the results so obtained agree with that obtained by Chao [38].

Next, consider the nine rays shown in Fig. 11. All these rays, in the limit as z and z_0 approach zero, coalesce into a single pP ray that starts at the source location as a P-wave and reaches the receiver as a P-wave after one reflection. Going through the same limiting process, we find

---

Contributed by the Applied Mechanics Division of THE AMERICAN SOCIETY OF MECHANICAL ENGINEERS, for presentation at the 1981 Joint ASME/ASCE Applied Mechanics, Fluids Engineering, and Bioengineering Conference, University of Colorado, Boulder, Colo., June 22–27, 1981.

Discussion on this paper should be addressed to the Editorial Department, ASME, United Engineering Center, 345 East 47th Street, New York, N. Y. 10017, and will be accepted until June 1, 1981. Readers who need more time to prepare a Discussion should request an extension from the Editorial Department. Manuscript received by ASME Applied Mechanics Division, August, 1979. Paper No. 81-APM-6.

that the resulting ray integrals will contain the products $S_1\Pi_{11}^2 D_{\alpha 1}$ and $S_1'\Pi_{11}^2 D_{\alpha 1}$. The S_1 and S_1' equal the *surface* P-source functions S_p^* and $S_p'^*$ but $D_{\alpha 1}$ equals the *surface* receiver function $D_{\alpha 1}^*$ of equation (24*a*), (see Tables 1 and 2 of Part 1), and $\Pi_{11}^2 = R_{pp}$.

Similarly, we can group nine rays to form a single pS ray, a sS ray, or a sP ray. The corresponding products Π_{jk}^2 are R_{pv}, R_{vv}, and R_{vp}, respectively.

In summary, when both source and receiver are on the same surface of the plate, the *surface* source and *surface* receiver functions are to be used in all ray integrals except the three rays, P, S, and H that travel from the source directly to the receiver along the surface. In the latter case, the *surface* source function and *interior* receiver function should be used.

7 Inverse Laplace Transform of the Generalized Rays

The integrals appearing in the general expressions for the components of the second rank Green's tensor $\bar{\mathbf{G}}(r,z,s)$ and the third rank Green's tensor $\bar{\mathcal{G}}(r,z,s)$ (Appendixes A and B in Part 1) are, in general, of two types: those that involve the Bessel function $J_0(s\xi r)$ and those that involve $J_1(s\xi r)$. For the jth ray propagating inside the medium, these integrals can be written in contracted notation as

$$\bar{I}(s) = \int_0^\infty E(\xi)e^{-sg(\xi,z)}\xi J_0(s\xi r)d\xi$$

$$\bar{I}'(s) = \int_0^\infty \xi E'(\xi)e^{-sg(\xi,z)}\xi J_1(s\xi r)d\xi \tag{51}$$

where E and E' are even functions of ξ, and involve the source function, receiver function, and the product of the reflection coefficients; $g(\xi,z)$ is the phase function of the jth ray, and s is the Laplace transform parameter. Once the inverse Laplace transforms of these integrals are obtained, the final solution due to the jth ray can be calculated through a convolution integral as explained in Section 4. Since the application of the Cagniard's method to the integrals, given by equation (51) were explained in detail in [7, 26], we simply state the results

$$I(t) = \frac{2}{\pi}\mathrm{H}(t - t_A)\ \mathrm{Im}\int_0^{\xi_1(r,z,t)} E(\xi)\frac{1}{K(r,z,t;\xi)}\xi d\xi$$

$$I'(t) = \frac{2}{\pi r}\mathrm{H}(t - t_A)\ \mathrm{Im}\int_0^{\xi_1(r,z,t)} E'(\xi)\frac{t - z_p\eta - z_s\zeta}{K(r,z,t;\xi)}\xi d\xi \tag{52}$$

where

$$K(r,z,t;\xi) = [\xi^2 r^2 + (t - \eta z_p - \zeta z_s)^2]^{1/2} \tag{53}$$

$$t_A = z_p + \kappa z_s \tag{54}$$

$$t = -i\xi_1 r + z_p(\xi_1^2 + 1)^{1/2} + z_s(\xi_1^2 + \kappa^2)^{1/2} \tag{55}$$

The symbol Im means that the imaginary part of these integrals are to be taken.

The integrations in equations (52) are along the Cagniard contour in the complex ξ-plane from the origin to ξ_1 as shown in Fig. 12. Along the imaginary axis, E at 1 and F at κ are two branch points, R is the Rayleigh pole, and M is a stationary point. At the point M, the value for t in equation (55) is stationary, that is when $\xi_1 = \xi_M$

$$\left(\frac{dt}{d\xi_1}\right)_{\xi_1=\xi_M} = 0 = -ir + z_p\xi_M(\xi_M^2 + 1)^{-1/2} + z_s\xi_M(\xi_M^2 + \kappa^2)^{-1/2}. \tag{56}$$

It can be shown that the foregoing equation has only one root and it is pure imaginary.

The upper limit of the integrals, $\xi_1(r,z,t)$, is obtained from equation (55) for a given value of t at a given point (r,z). When the point M lies below the point E (Fig. 12*a*), these integrals are all real-valued until ξ_1 reaches the point M where $\xi = \xi_M$ and $t = t_M$. Hence, $I(t)$ and $I'(t)$ are both zero until the time t_M is reached, and t_M is the arrival time of waves traveling along the direct-ray paths.

For rays with all segments in SV mode, it is possible to have the stationary point M situated above the point $E(|\xi_M| > 1$ in Fig. 12b).

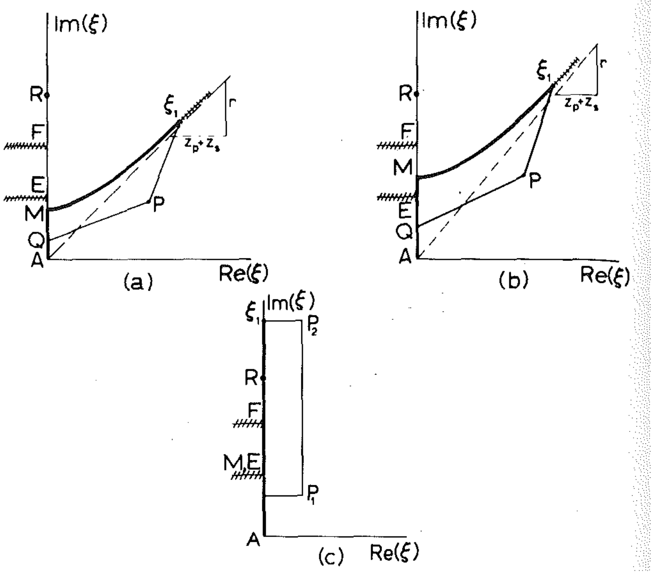

Fig. 12 Cagniard's contour (heavy line) and alternative paths for numerical integrations; (a) Direct and reflected rays; (b) Refracted rays; (c) First *P* and *S*-rays for the case where both the receiver and the source are on the same surface

In this case a part of the wave is refracted along the surface of the plate and it reaches the receiver faster than the waves along the direct-ray. The arrival time of this SV ray with refraction is obtained by setting $z_p = 0$ and $\xi_1 = +i$ (point E) in equation (55),

$$t_E = r + z_s(\kappa^2 - 1)^{1/2}. \tag{57}$$

Waves along this refracted ray are also known as "head waves."

When the integrands of all ray integrals are assembled as explained in Part 1, one is ready to carry out the numerical integrations of the integrals as represented by equation (52) along the path $AM\xi_1$ as shown in Fig. 12.

The upper limit of the integration, $\xi_1(r,z,t)$, in equation (52) moves along the imaginary ξ-axis from the origin. The integrand is real-valued when ξ_1 is below the point M, or the branch point E, the latter is for refracted or head waves. Since only the imaginary part of these integrals are used for the answer, the response is zero until the point M or E is reached. At the point M, Cagniard's path leaves the imaginary axis and stays in the first quadrant of the complex ξ-plane. Since the path itself is given by a complicated equation, equation (55), integration along it is difficult. Several methods have been proposed by Pekeris and Longman [39], Sherwood [40], and Abromovici and Alterman [41] to evaluate these integrals. A comparison of these methods is given by Gajewski [42], who also developed a method of direct numerical integration of the ray integrals. His method first reported in 1971 [43] will be applied in this paper.

The original path of integration $AM\xi_1$ is replaced by the path $QM\xi_1$ where Q is located below the point M or E since the value of the integral along AQ is zero. Note that the function $K(r,z,t;\xi)$ has a branch point at the point $\xi_1(r,z,t)$ and the required branch cut is taken to extend along Cagniard's path from ξ_1 to infinity such that K has positive real part on the left side of the branch cut. Cauchy's theorem is then applied to find an alternative path of integration $QP\xi_1$ as shown in Fig. 12. Since within the closed path $QM\xi_1PQ$ there are no singularities, the integral along $QM\xi_1$ is equal to that along $QP\xi_1$. Integration along the straight lines QP and $P\xi_1$ is much easier than the integration along the original path. The criteria that were used in the selection of the points Q and P were as follows:

1 $Q = 0.8|\xi_M|$ if ξ_M is below the first branch point (direct and reflected rays) and $Q = 0.8$ otherwise (for head waves).

2 P is fixed for a certain time interval, and hence a certain range of complex values of ξ_1. It is then shifted to another convenient location. As a starting value, P is taken as $(0.2 + i)|\xi_M|$.

3 The lengths of the path QP and $P\xi_1$ are kept approximately equal and as short as possible. In the case where both the source and the receiver are on the same surface of the plate, the alternative path $QP_1P_2\xi_1$ shown in Fig. 12(c) was used.

The new path of integration stays away from the singularities on the imaginary axis, namely, the branch points E and F, and the Rayleigh pole R (point where the denominator of the reflection coefficients vanish). However, the integrand is still singular of one half order at the upper limit of integration, which are the zeros of the function K in equations (52). This half-order singularity can be removed by introducing a new variable

$$\alpha = (\xi^2 - \xi_1^2)^{1/2} \tag{58}$$

Then the integrals in equation (52) along the path $P\xi_1$ transform into

$$I(t) = \mathrm{H}(t - t_A)\frac{2}{\pi}\,\mathrm{Im}\int_{\alpha_p}^{0} E[\xi(\alpha)]\,\frac{\alpha d\alpha}{K(r,z,t;\xi(\alpha)]}$$

$$I'(t) = \mathrm{H}(t - t_A)\frac{2}{\pi r}\,\mathrm{Im}\int_{\alpha_p}^{0} E'[\xi(\alpha)][t - z_p\eta(\alpha) - z_s\zeta(\alpha)]\,\frac{\alpha d\alpha}{K[r,z,t;\xi(\alpha)]} \tag{59}$$

where α_p is the value of α at the point P. Note that as $\xi \rightarrow \xi_1$ both α and K approach zero. To remove this indeterminancy, the function K is expanded into a Taylor series around the point $\alpha = 0$ where a common factor of α is factored out to cancel the α in the numerator. This power series expansion is only used when the point in the integration algorithm is near the point $\alpha = 0$.

Each of the integrals along the straight lines QP and $P\xi_1$, in the complex ξ-plane can be transformed into an integration with respect to a real variable v and w in the interval $[-1,1]$ [43]. The relations between ξ and v along QP is

$$\xi = \frac{1}{2}(\xi_P + \xi_Q) + \frac{1}{2}(\xi_P - \xi_Q)v; \quad \frac{d\xi}{dv} = \frac{1}{2}(\xi_P - \xi_Q) \tag{60}$$

and that between α and w along $P\xi_1$

$$\alpha = \frac{1}{2}(1 - w)\alpha_P; \quad \frac{d\alpha}{dw} = -\frac{1}{2}\alpha_P \tag{61}$$

Hence, the integrals in equation (59) become

$$I(t) = \mathrm{H}(t - t_A)\frac{2}{\pi}\left\{\int_{-1}^{1}\mathrm{Im}\left[E\frac{\xi}{K}\frac{d\xi}{dv}\right]dv + \int_{-1}^{1}\mathrm{Im}\left[E\frac{\alpha}{K}\frac{d\alpha}{dw}\right]dw\right\}$$

$$I'(t) = \mathrm{H}(t - t_A)\frac{2}{\pi r}\left\{\int_{-1}^{1}\mathrm{Im}\left[E'\frac{t - z_p\eta - z_s\zeta}{K}\,\xi\frac{d\xi}{dv}\right]dv + \int_{-1}^{1}\mathrm{Im}\left[E'\frac{t - z_p\eta - z_s\zeta}{K}\,\alpha\frac{d\alpha}{dw}\right]dw\right\} \tag{62}$$

These integrations can now be carried out by using standard numerical techniques for integration of real variables.

8 Numerical Results for Responses at the Surface of a Plate

In the following numerical examples the plate material was assumed to have $\lambda = \mu$, corresponding to $\kappa^2 = 3$. In evaluating integrals, given by equation (62), we have used Gaussian quadratures with 10 or 20 points.

1 **Concentrated Force (Figs. 13–19).** The case of a vertical force was discussed in some detail [9–13] but no off-central results were reported for a horizontal force. The surface motion of the plate at the locations $r = 2$, 4, and 6 due to step-time function are shown in Fig. 13 for a buried vertical force and in Fig. 14 for a horizontal force applied in the direction of $\theta = 0°$. The receiver for the latter is also at $\theta = 0°$. In both cases the force was located at the midplane. The ordinate in these figures is the normalized displacement $\pi\mu h^2 u_\alpha/F_0$, ($\alpha = r,z$) and the abcissa is the nondimensional time $t = ct^*/h$. Note that the initial stage of the response becomes weaker as the receiver is moved from $r = 2$ to 4, to 6. At equal r, the vertical motions of both surfaces due to a vertical force are in phase, while the radial displacements are antisymmetric with respect to the midplane. This shows that such a loading excites the antisymmetric modes of the plate [13]. In the case of a buried horizontal force, the vertical motions are antisymmetric while the radial motions are symmetric. Hence, the symmetric modes of the plate are excited.

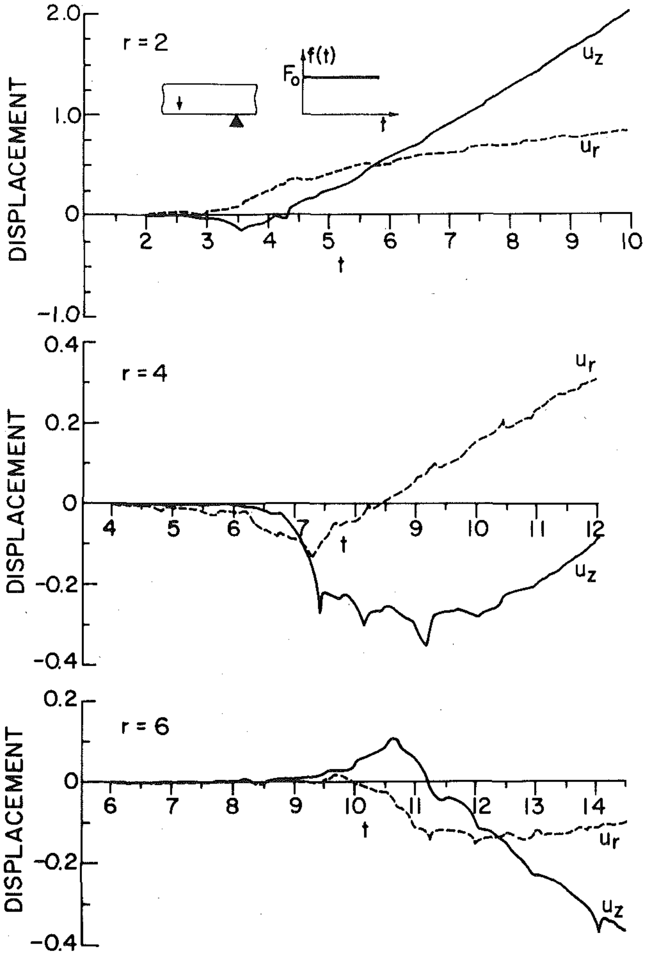

Fig. 13 Response of the surface $z = 1$ due to a buried vertical force at $z_0 = 1/2$; the ordinate is the nondimensional displacement $\pi\mu h^2 u_\alpha/F_0$ ($\alpha = r,z$), and the abscissa the dimensionless time

Figs. 15 and 16 show the response of the plate due to a vertical surface force; these results were first given in reference [13]. As seen, for same r, while the vertical motion of the both surfaces are in phase, except at the arrival of the Rayleigh wave, the radial motion is out of phase.

The responses of both surfaces due to a shear impact are shown in Figs. 17 and 18. The force is in the direction of **a**, its components in Cartesian coordinates being $a_x = 1$, $a_y = 0$, $a_z = 0$. In cylindrical coordinates, the components are calculated by the formulas

$$a_r = a_x \cos\theta + a_y \sin\theta$$

$$a_\theta = a_x \sin\theta + a_y \cos\theta$$

$$a_z = a_z \tag{63}$$

Comparison of Fig. 13 with Fig. 14; Fig. 15 with Fig. 17; and Fig. 16 with Fig. 18 shows an interesting relation between G_{zr} an G_{rz}. The G_{zr} is proportional to the vertical displacement due to a horizontal force, shown as u_z in Figs. 14, 17, and 18. The G_{rz} is proportional to the radial displacement due to a vertical force shown as u_r in Figs. 13, 15, and 16. Even though these two components are equal to each other for an unbounded medium, they may be different for a

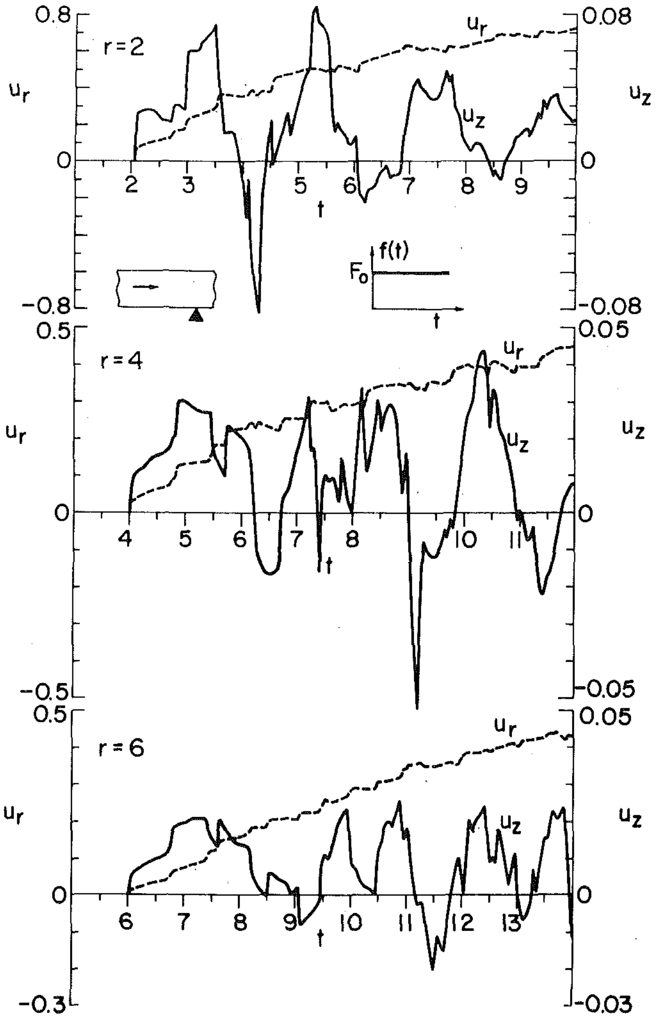

Fig. 14 Response of the surface $z = 1$ due to a buried horizontal force at $z_0 = 1/2$; the ordinate is the nondimensional displacement $\pi\mu h^2 u_\alpha/(F_0 \cos\theta)$ $(\alpha = r,z)$

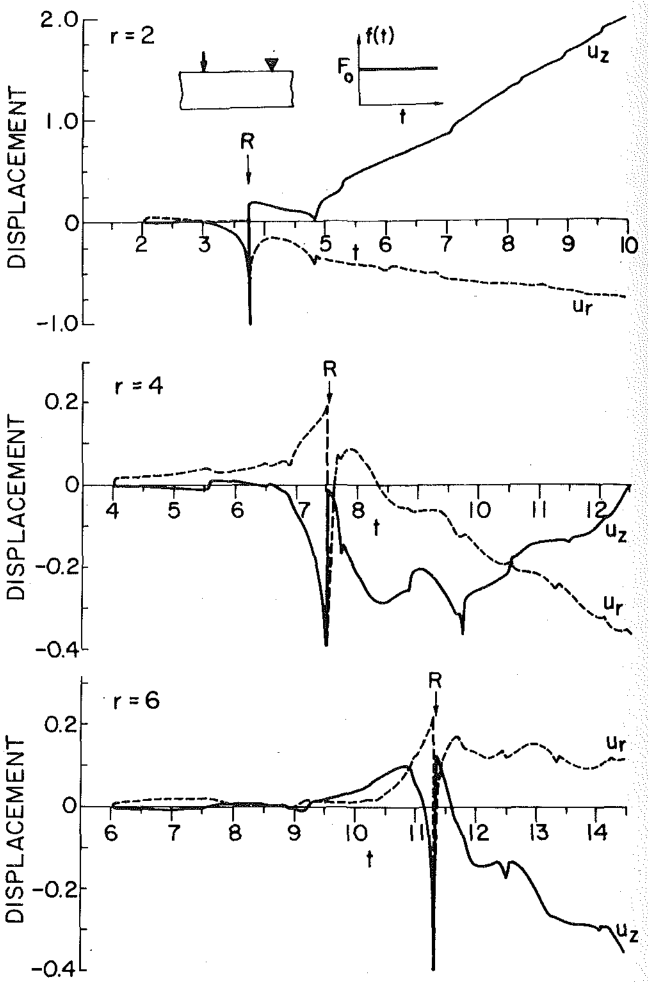

Fig. 15 Response of the surface $z = 0$ due to a vertical force on the same surface; the ordinate is the nondimensional displacement $\pi\mu h^2 u_\alpha/F_0$ $(\alpha = r,z)$

bounded medium. These components of the Green's dyadics are symmetric when the source and receiver are both buried in the plate or when they are on opposite sides (Figs. 16 and 18), but they are antisymmetric when both source and the receiver are located on the same surface of the plate (Figs. 15 and 17). However, they are completely unrelated if either the force or the receiver is buried while the other is on the surface (Figs. 13 and 14).

We have shown in Fig. 19 the angular variation of the displacement field on the surface $z = 0$ due to an oblique force ($\mathbf{a} = 1,0,1$) acting on the same surface.

2 **A Single Couple (Figs. 20–21).** The expressions for the displacement components due to a single couple were given by equation (29) in Part 1. There are 16 different integrals in these expressions; 11 of them appear in the radial displacement $\bar{u}_{rj}$ and 5 in $\bar{u}_{zj}$. Eventhough the inversion of these integrals are similar to those given by equation (51), the calculations of these many integrals become very laborious and expensive in computer time. Hence, only the numerical results pertaining to the displacement $u_z(r,t)$ are presented. Similar to the epicentral results presented in Part 2, a time-dependency of parabolic ramp function with a rise time of 0.6 will be considered for the source.

Fig. 20 show the response at the points $(r,\theta,1)$ $r = 2,4$, and 6 due to two different buried couples with vectors $\mathbf{a} = (1,0,0)$, $\mathbf{b} = (0,0,-1)$ and $\mathbf{a} = (0,0,1)$, $\mathbf{b} = (1,0,0)$, all in Cartesian components. The ordinate is the nondimensional displacement $\pi\mu h^3 u_z/(M_0 \cos\theta)$. Eventhough these two couples are statically equivalent, the transient response due to each one is quite different. The response of the plate is antisymmetric with respect to y-axis in Cartesian coordinates or $\theta = \pi/2$ and $3\pi/2$ in polar coordinates. Hence, these are nodal lines. Similar to the previous examples, the initial part of the signals becomes weaker as the receiver is moved further away from the source.

Fig. 21 shows the response due to a single-couple with moment axis along the z-axis. The two vectors are $\mathbf{a} = (1,0,0)$ and $\mathbf{b} = (0,-1,0)$. The ordinate in these sets of figures is $\pi\mu h^3 u_z/(M_0 \sin 2\theta)$. Hence, the $\theta = 0$, $\pi/2$, $3\pi/2$, and π are nodal lines.

3 **Double-Force (Figs. 22–23).** Pao, et al. [13], have studied the axisymmetric response of a plate due to a vertical double-force; their results along with the new results for a horizontal double-force are presented in Fig. 22. Again a parabolic ramp function with a rise time of 0.6 was considered as the time function of the source. The first large peak in all these curves is due to the arrivals of the first three ray groups, i.e., the rays with 0, 1, and 2 reflections. Note that except for a phase difference these two transient signals near the source are similar in their gross behavior.

Fig. 23 shows the angular dependency of the vertical displacement at $r = 4$ due to an oblique double-force whose generating forces act along $\mathbf{a} = (2,0,1)$ in Cartesian components. As noted in Section 5.2 of Part 2, the response due to an oblique and double-force cannot be obtained by superposing the responses due to the vertical and horizontal components of the oblique double-force.

4 **Double-Couple Without Moment (Fig. 24–26).** The transient motion of the surface $z = 1$ for two double-couples without moment at different orientations are shown in Figs. 24 and 25. In Fig. 24 the couple axis is along the y-axis with $\mathbf{a} = (1,0,0)$ and $\mathbf{b} = (0,0,-1)$.

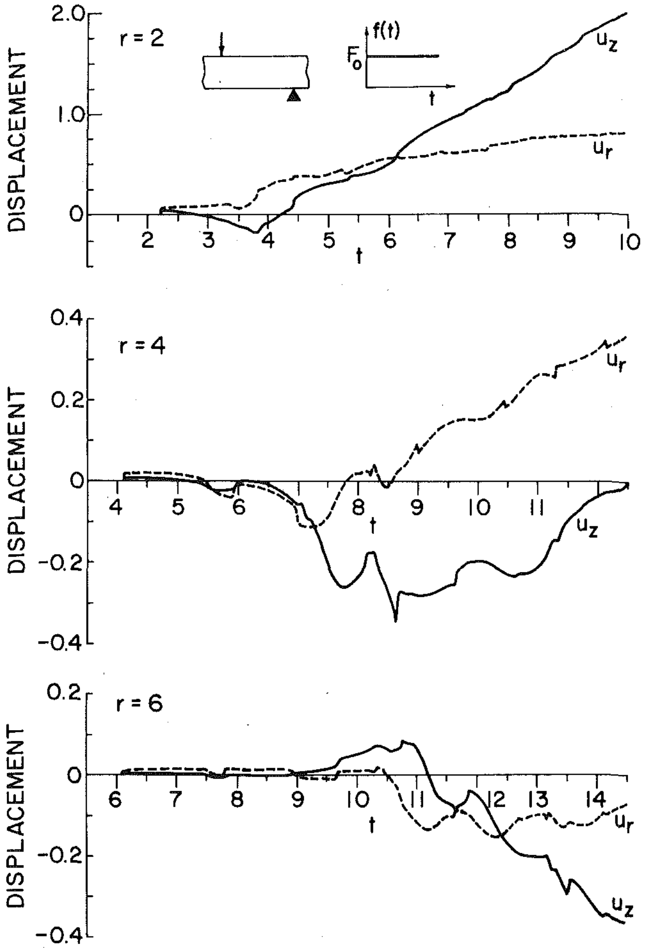

Fig. 16 Response of the surface $z = 1$ due to a vertical force on the surface $z = 0$; the ordinate is the nondimensional displacement $\pi\mu h^2 u_\alpha / F_0$ ($\alpha = r,z$)

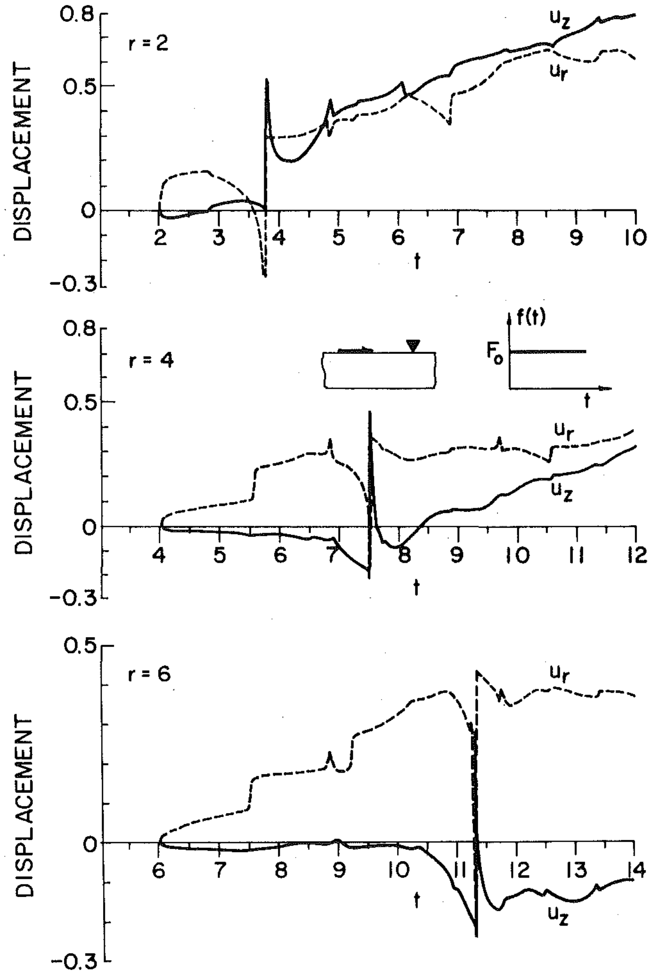

Fig. 17 Response of the surface $z = 0$ due to a horizontal force on the same surface; the ordinate is the nondimensional displacement $\pi\mu h^2 u_\alpha / (F_0 \cos\theta)$ ($\alpha = r,z$)

In Fig. 25, the axis of the couples is along the z-axis with $\mathbf{a} = (1,0,0)$ and $\mathbf{b} = (0,-1,0)$. The center of the couples is at $z_0 = 1/2$. The angular dependency of the vertical displacement for the first source is $\cos\theta$ and for the second source $\sin 2\theta$. These angular dependencies are the same as those for single-couples with same orientations, Figs. 20 and 21. It is also seen from Figs. 21 and 25, that while the two responses have exactly the same behavior, the one due to a double-couple without moment is twice that of due to a single-couple for this particular orientation of the sources. The effect can also be shown directly from the equations (29a) and equation (35a). Comparison of Fig. 25 with Fig. 22 shows that the responses due to a horizontal double-couple without moment and a horizontal double-force are very similar in nature. Such a similarity was noted by Stauder [36].

In Fig. 26 we show the angular variation of the u_z at $r = 4$ due to a double-couple without moment whose generating forces are along the vectors $\sqrt{3}\mathbf{a} = (1,1,1)$, $\sqrt{6}\mathbf{b} = (-1,2,-1)$. In all the aforementioned cases the time function was assumed to be a parabolic ramp function and the rise time was taken to be 0.6.

5 Center of Rotation (Fig. 27). Finally, in Fig. 27, we show both the radial and the vertical motion of the surface $z = 1$ due to a buried center of rotation at $z_0 = 1/2$. The axis of the couple (the unit vector $\mathbf{c}$) is along the arbitrary vector (c_r, c_θ, c_z). Eventhough only S-waves are generated at the source location, the initial response outside the critical range r_c is due to head waves which arrive prior to the direct S-waves to a receiver located on the surface. The critical distance r_c is related to the source depth z_0 and the wave speeds in the material through the relations

$$r_c = z_0 \tan\theta^*, \quad \sin\theta^* = C/c = 1/\kappa \qquad (64)$$

The ordinate in the Fig. 27 is the normalized displacement $\pi\mu h^3 u_\alpha / (c_\theta M_0)$, $\alpha = r,z$, where c_θ is the θ-components of the unit vector $\mathbf{c}$. Note that if $\mathbf{c}$ is parallel to the z-axis, both displacements u_r and u_z will vanish.

9 Conclusions

In this paper, we have shown the construction of the Laplace transformed Green's dyadics and triadics (the gradient of the dyadics) for nonaxisymmetric waves generated by a variety of point sources in a plate, based on the theory of generalized rays. The transient response of the plate is then determined from the inverse Laplace transform which is accomplished by applying the Cagniard method. Extensive numerical results are shown for the plate surface responses at radial distances equal to 0, 2, 4, and 6 plate thickness for an oblique concentrated force, a double-force, a couple, a center of rotation, and a double-couple without moment. The time function for the source is either a step function or a parabolic ramp function. The last mentioned source has been used widely in seismology to model the slip motion of a fault.

Since the integrand of the Green's dyadics have been decomposed into four parts, the source function, the reflection coefficients, the receiver function, and the phase function, the analytical results, and the computer codes for evaluating these integrals can easily be modified for other types of point sources, and boundary conditions of the plate. For instance, if one side of the plate is rigid, or if the plate is joined to a semiinfinite elastic solid, it is only necessary to change some of the reflection coefficients in the product for Π_{ij}^n. The Laplace transformed Green's dyadics could also be modified for a distribution

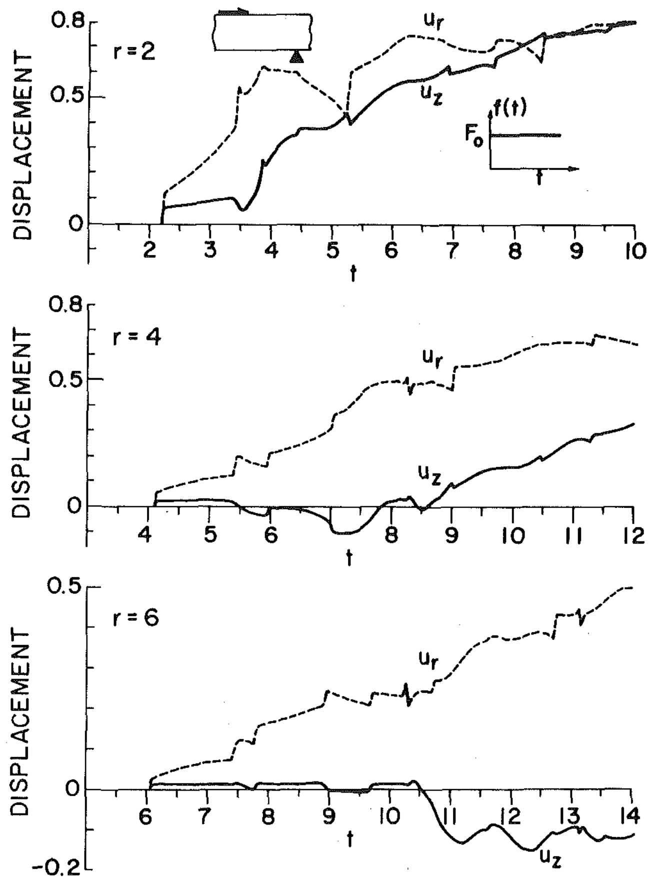

Fig. 18 Response of the surface $z = 1$ due to a horizontal force on the surface $z = 0$; the ordinate is the nondimensional displacement $\pi\mu h^2 u_\alpha/(F_0 \cos\theta)$ $(\alpha = r,z)$

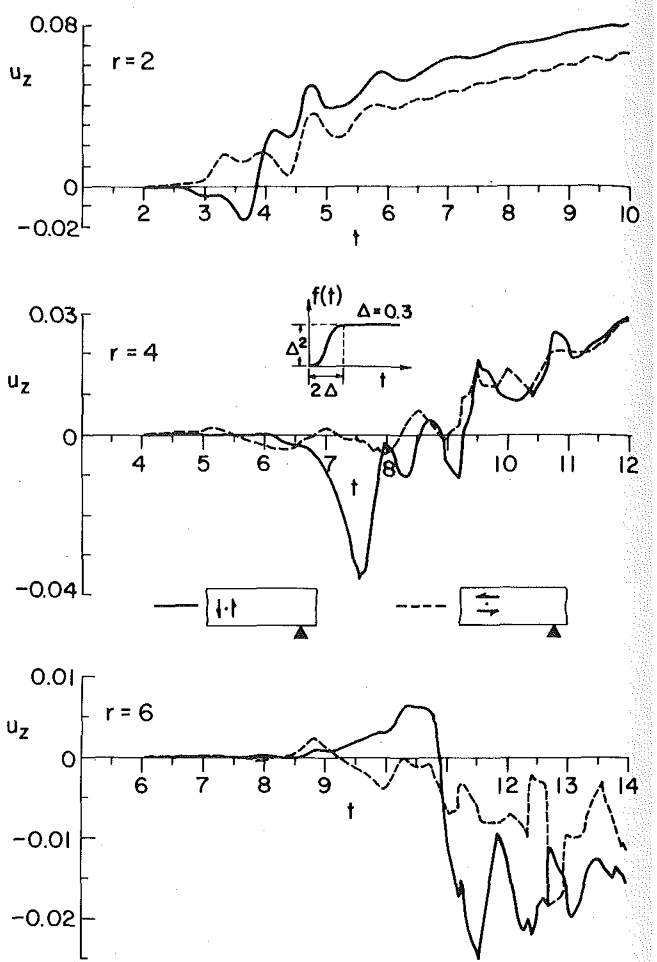

Fig. 20 Response of the surface $z = 1$ due to two different buried ($z_0 = 0.5$) single-couples with the same moment vector $c = (0,1,0)$; the ordinate is the nondimensional displacement $\pi\mu h^3 u_z/(M_0 \cos\theta)$

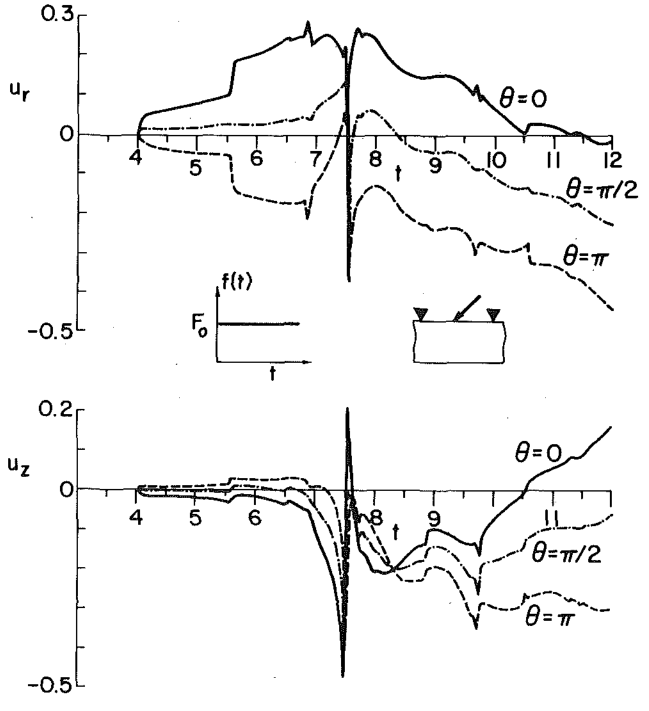

Fig. 19 Response of the points $(4,\theta,0)$ due to an oblique force, $a = (1,0,1)$, on the surface $z = 0$; the ordinates are the nondimensional displacement $\pi\mu h^2 u_\alpha/F_0$ $(\alpha = r,z)$

of point sources on an area, or in a volume, through a surface or volume integration [3, 44].

The results shown in all figures are exact for the time duration considered. At $r = 6$, a total of 1586 ray integrals are evaluated numerically for each type of sources. Many more ray integrals must be evaluated if a longer duration is desired. For such a case, the method of normal modes perhaps should be applied to determine the long time behavior.

From the analysis, we observe two interesting points about the Green's dyadics:

1 Although the Green's dyadics G_{ij} are symmetric in an infinite space, they are not symmetric when either the source or the receiver is on the surface, and the other is in the interior of the plate.

2 Eventhough the response due to a concentrated oblique force can be obtained by superposing the responses due to its two components, a vertical and a horizontal, such a superposition is not possible for double forces and double couples.

To apply these theoretical results to the study of acoustic emission, we note that one of the main objectives is to determine the location of the source of emission. This is done by the well-known method of triangulation [44], which requires *a priori* the knowledge of the speed of the predominant signal that is first recorded by a receiver. Although the fastest signal always travels along the direct path between the source and the receiver in P-wave mode, its strength may be too weak, when compared with slower signals, to be detected by a transducer. In this regard, the following conclusions as drawn from this analysis may be of interest.

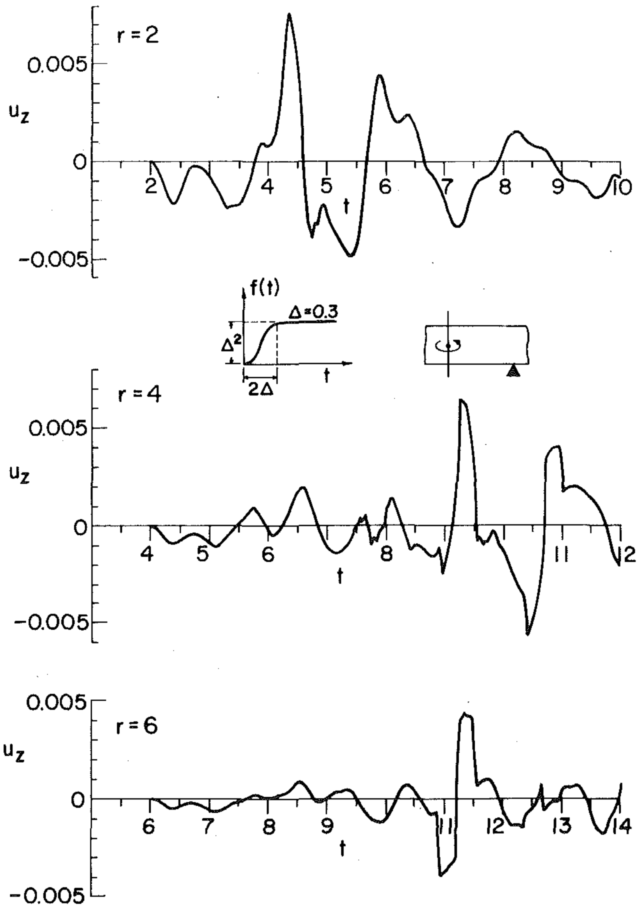

Fig. 21 Response of the surface $z = 1$ due to a buried ($z_0 = 0.5$) single-couple c = (0,0,−1); the ordinate is the nondimensional displacement $\pi\mu h^3 u_z/(M_0 \sin 2\theta)$

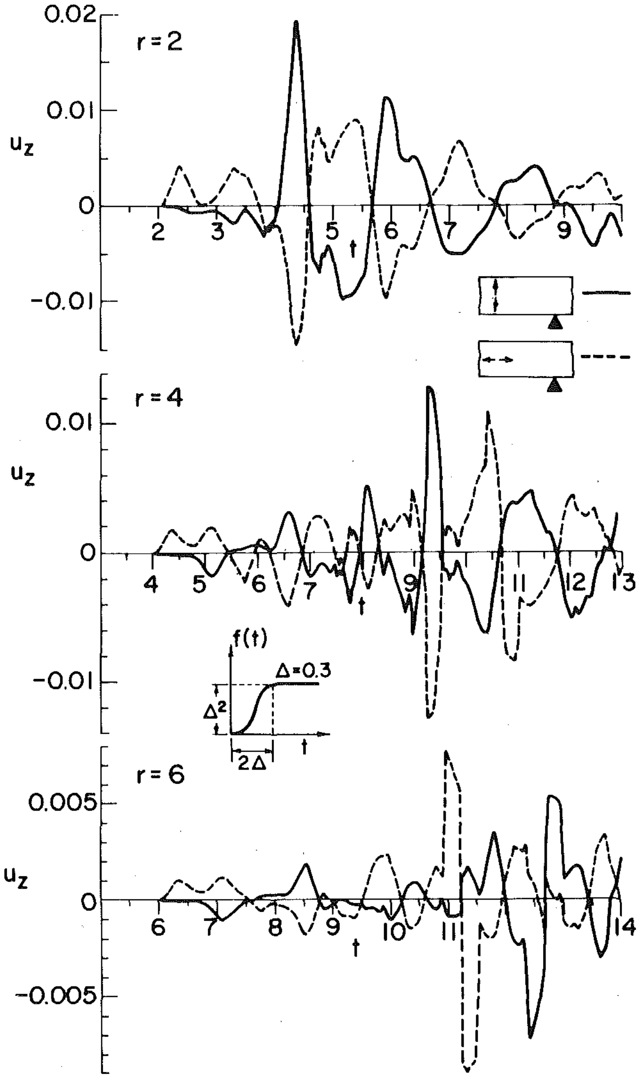

Fig. 22 Response of the surface $z = 1$ due to two different orientations of a buried double-force at $z_0 = 0.5$; the ordinate is the nondimensional displacement $\pi\mu h^3 u_z/D_0$, ($\theta = 0°$)

3 Epicentral responses of the plate due to all kinds of force systems considered are strong at both the initial and later period.

4 As the receiver is moved away from the epicenter, the strength of the initial part of the response is weakened for unbalanced force systems (a concentrated force, a single-couple, and a center of rotation). However, in the case of self-equilibrating force systems (a double-force, double-couple without moment, and center of explosion), the signal is relatively strong throughout, especially for the case where the generating forces lie in a plane parallel to the surface of the plate.

5 There is a clearly identifiable peak in the signals due to self-equilibrating force systems. This peak becomes conspicuous after the arrival of the first three groups of rays, namely, the source rays and those which have experienced one and two reflections from the surfaces. Arrival times of these rays depend on the thickness of the plate.

The aforementioned results could be also useful to characterize the nature of the source, which is another main objective of acoustic emission. In this regard, we offer the following observations:

6 As the rise time of the source increases, the signals become smoother. The surface response is very sensitive to the distance between the receiver and the source and to the depth of the source.

7 For sources without axisymmetry, the magnitude of the response is strongly dependent on the angular location of the receiver relative to the orientation of the source. This is evidenced by the results shown in the Figs. 17, 19, 23, 25, and 26.

8 Displacement fields due to a single-couple and a double-couple without moment with generating forces lying in a plane parallel to the surfaces of the plate have the same angular dependency, sin 2θ. However, the amplitude of the latter is twice that of the former.

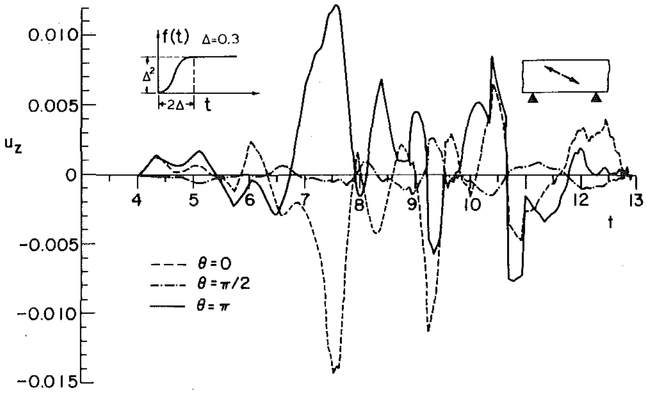

Fig. 23 Response of the points (4,θ,1) due to a buried ($z_0 = 0.5$) double-force, a = (2,0,1); the ordinate is the nondimensional displacement $\pi\mu h^3 u_z/D_0$

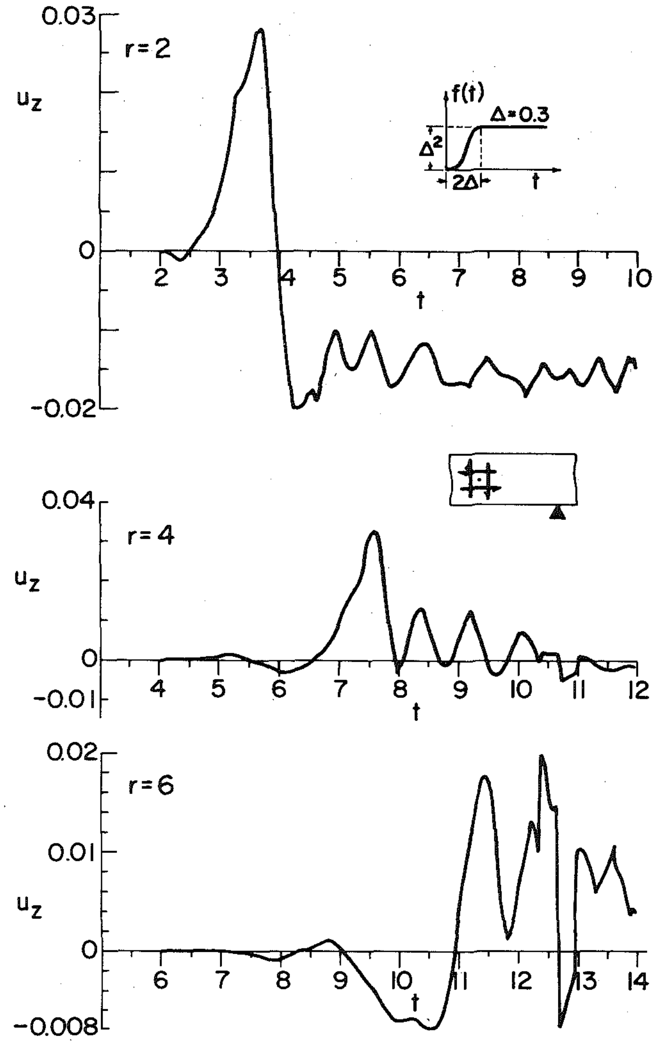

Fig. 24 Response of the surface $z = 1$ due to a buried ($z_0 = 0.5$) double-couple without moment c = (0,1,0); the ordinate is the nondimensional displacement $\pi \mu h^3 u_z / (M_0 \cos \theta)$

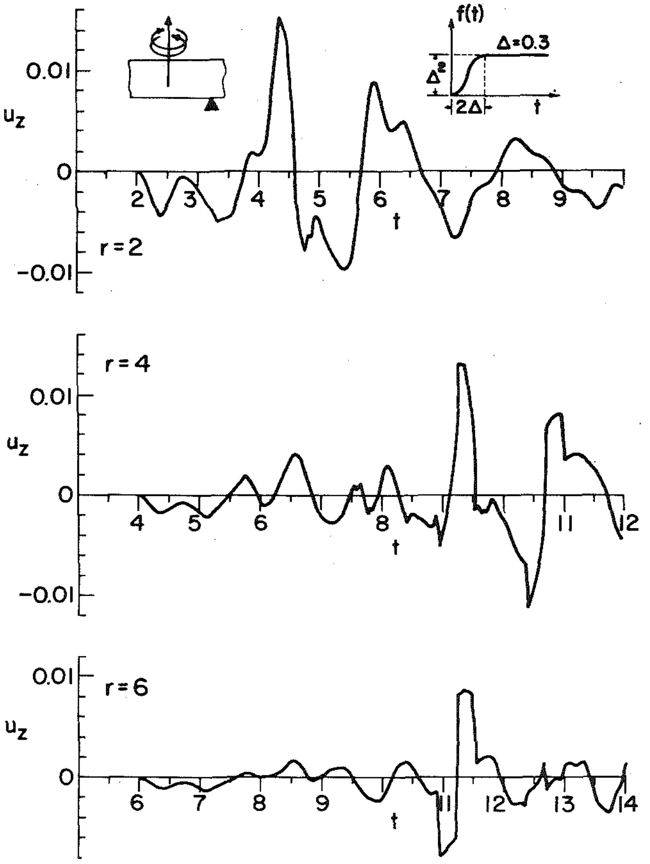

Fig. 25 Response of the surface $z = 1$ due to a buried ($z_0 = 0.5$) double-couple without moment, c = (0,0,−1); the ordinate is the nondimensional displacement $\pi \mu h^3 u_z / (M_0 \sin 2\theta)$

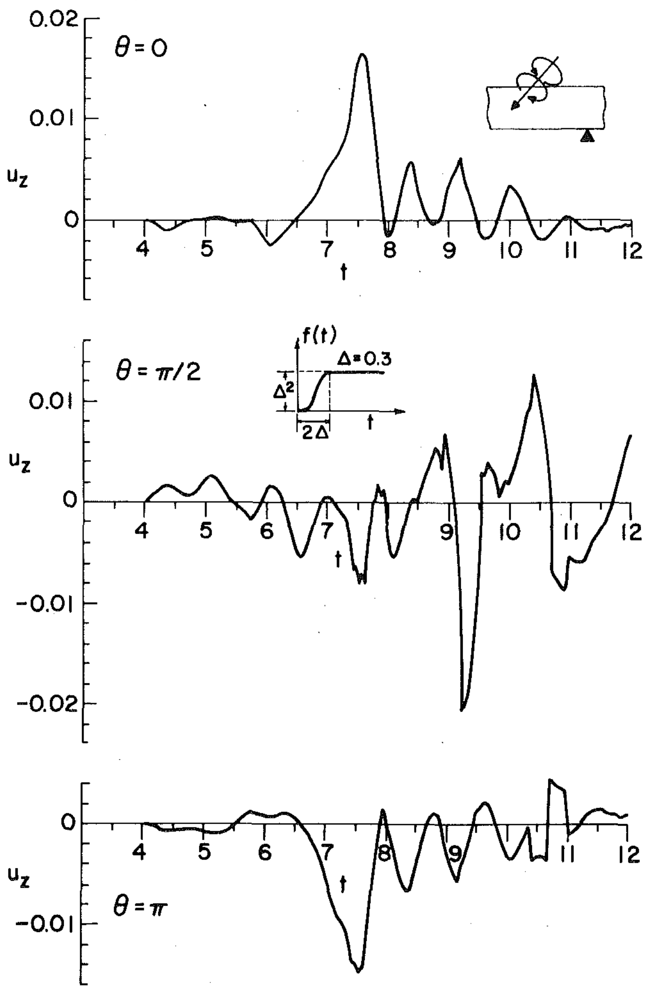

Fig. 26 Response of the points $(4,\theta,1)$ due to a buried double-couple without moment, $a = (1,1,1)/\sqrt{3}$, $b = (-1,2,-1)/\sqrt{6}$; the ordinate in the normalized displacement $\pi\mu h^3 u_z/M_0$

9 For a given type of source, the exact solution as given in this paper for a step time or parabolic ramp time function forms the kernal of a convolution integral, equation (49). The time function of the source can then be determined by an inverse process of deconvolution. Applications of such a procedure to characterizing a source or to calibrating transducers were mentioned in Section 4 of Part 2.

Finally, we note that although only solutions for point sources are discussed in this paper, those for stationary sources distributed over an area or a volume can be obtained directly from integrating numerically the response of point source [3, 44]. Recently, Israel and Kovach [45] have shown that, even for moving sources, such as a propagating strike-slip fault represented by the spreading of double-couple without movement over an area, the transient responses can be calculated effectively by an additional numerical integration over the time variable.

Acknowledgment

The authors acknowledge the support of this investigation provided by the Materials Science Center of Cornell University and a Grant from the Engineering Mechanics Division of the National Science Foundation.

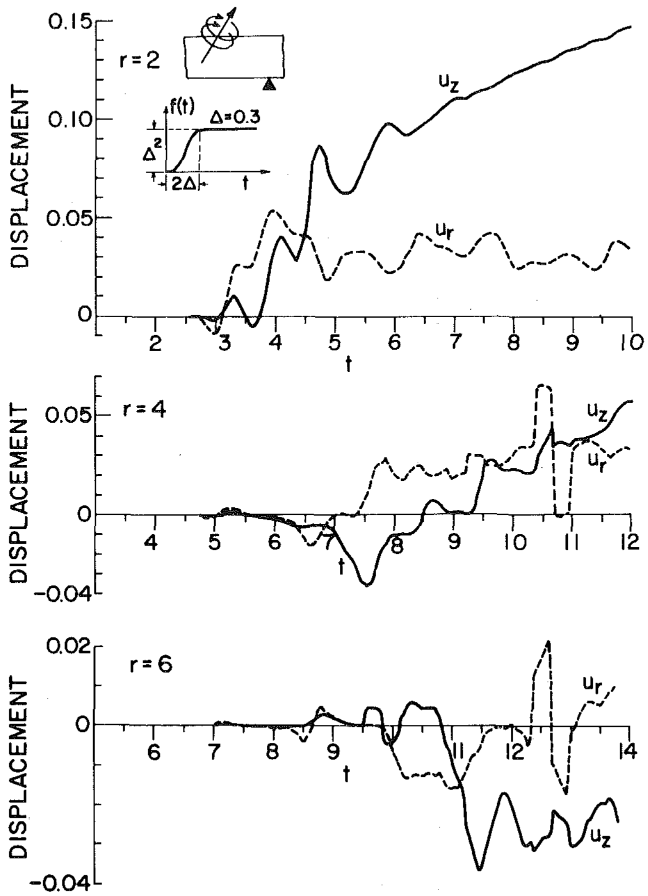

Fig. 27 Response of the surface $z = 1$ due to a buried $(z_0 = 0.5)$ center of rotation, with axis $c(c_r,c_\theta,c_z)$; the ordinate is the nondimensional displacement $\pi\mu h^3 u_\alpha/(M_0 c_\theta)$ $(\alpha = r,z)$

References

37 Lamb, H., "On the Propagation of Tremors Over the Surface of an Elastic Solid," *Philosophical Transactions of the Royal Society,* Series A, Vol. 203, 1904, pp. 1–42.

38 Chao, C. C., "Dynamical Response of an Elastic Half Space to Tangential Surface Loadings," ASME JOURNAL OF APPLIED MECHANICS, Vol. 27, 1960, pp. 559–567.

39 Pekeris, C. L., and Longman, I. M., "Ray Theory Solution of the Problem of Propagation of Explosive Sound in a Layered Liquid," *Journal of the Acoustical Society of America,* Vol. 30, 1958, pp. 323–328.

40 Sherwood, J. W. C., "Transient Sound Propagation in a Layered Liquid Medium," *Journal of the Acoustical Society of America,* Vol. 32, 1960, p. 1673.

41 Abromovici, F., and Alterman, Z., "Computations Pertaining to the Problem of Propagation of a Seismic Pulse in a Layered Solid," *Methods in Computational Physics,* eds., Alder B., Fernbach, S., and Rothenberg, M., Academic Press, New York, Vol. 4, 1965, p. 349.

42 Gajewski, R., Transient Response of Layered Elastic Solids to Uniform Pressure on a Spherical Cavity, PhD thesis, Cornell University, 1978.

43 Pao, Y. H., Gajewski, R. R., and Thau, S. A., "Analysis of Ground Wave Propagation in Layered Media," Final Report No. DASA 2694, Defense Nuclear Agency, Washington, D. C., 20305.

44 Pao, Y. H., "Theory of Acoustic Emission," in *Elastic Waves and Nondestructive Testing of Materials,* AMD Vol. 29, ASME, New York, ed., Pao, Y. H., 1978, pp. 107–128.

45 Israel, M., and Kovach, R. L., "Near-Field Motions From a Propagating Strike-Slip Fault in an Elastic Half Space," *Bulletin of Seismological Society of America,* Vol. 67, 1977, pp. 977–994.

Thomas P. Desmond

Research Engineer,
SRI International,
Engineering Mechanics Department,
Menlo Park, Calif. 94025

Theoretical and Experimental Investigation of Stress Waves at a Junction of Three Bars

When a longitudinal stress wave impinges on a junction of three elastic bars (where two bars are collinear and a third is noncollinear to the others), six separate stress waves are produced. A longitudinal stress wave and a flexural wave are reflected back along the first bar, and a stress wave of each type is transmitted into the second and third bars. For the theoretical treatment of these waves, the simple one-dimensional theory is used to describe the propagation of longitudinal (or axial) waves, and the Timoshenko beam theory is used to describe the propagation of transverse (or bending) waves. The method of characteristics is used to transform the partial differential equations into total differential equations. The total differential equations are then solved by a forward differencing finite-difference scheme. For solution at the junction, the junction is modeled as a rigid-body element. Impact experiments were performed to verify the analysis, and agreement between theory and experiment is very satisfactory.

Introduction

Previous studies [1, 2] have been made of reflections and transmissions of stress waves at a boundary discontinuity. Reflections and transmissions of longitudinal waves in a bar in which the discontinuity is formed by a change in cross-sectional area is treated by Ripperger and Abramson [3] and Yang and Hassett [4]. Reflections and transmissions of waves in which the discontinuity is formed by two noncollinear bars is treated by Lee and Kolsky [5], Atkins and Hunter [6], and Mandel, Mathur, and Chang [7].

In the present study, three bars meeting at a common junction form the discontinuity. Two bars are collinear to each other and a third is noncollinear to the first two, as shown in Fig. 1(*a*). In general, when a longitudinal wave in one of the three bars impinges on the intersection, six waves are produced. A longitudinal wave and a flexural wave are reflected back along the first bar, and one wave of each type is transmitted into the second and third bars. In the present paper, these waves are predicted in each of the connecting bars and are compared to experimentally measured waves. For the analysis, the junction is modeled as a rigid intersection element.

This work has applications in determining the internal equipment response of structures subjected to shock loading.

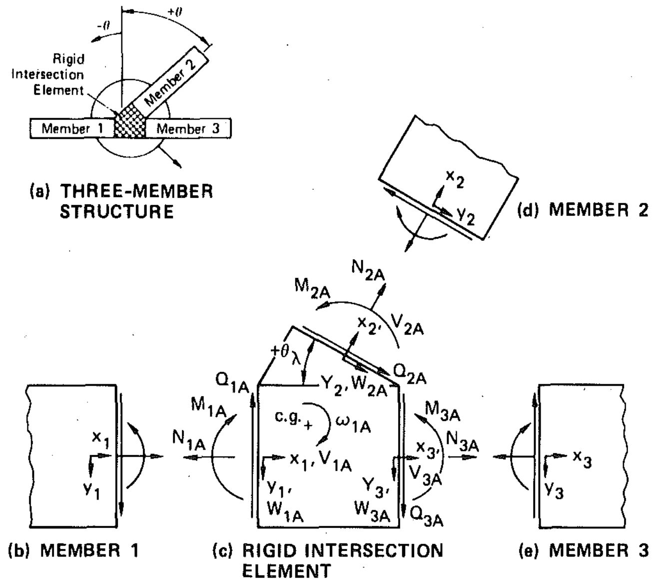

(a) THREE-MEMBER STRUCTURE

(d) MEMBER 2

(b) MEMBER 1

(c) RIGID INTERSECTION ELEMENT

(e) MEMBER 3

Fig. 1 Three-member intersection

Theory

Wave Propagation Through Connecting Bars. Two general types of waves propagate through elastic bar elements: a longitudinal (or axial) wave and a transverse (or bending) wave. Because the transverse deflections are small (relative to the bar's cross section),

---

Contributed by the Applied Mechanics Division of THE AMERICAN SOCIETY OF MECHANICAL ENGINEERS, for presentation at the 1981 Joint ASME/ASCE Applied Mechanics, Fluids Engineering, and Bioengineering Conference, University of Colorado, Boulder, Colo., June 22–27, 1981.

Discussion on this paper should be addressed to the Editorial Department, ASME, United Engineering Center, 345 East 47th Street, New York, N.Y. 10017, and will be accepted until June 1, 1981. Readers who need more time to prepare a Discussion should request an extension from the Editorial Department. Manuscript received by ASME Applied Mechanics Division, April, 1980; final revision, September, 1980. Paper No. 81-APM-16.

the two types of waves are not coupled in the bar segments. For propagation of longitudinal waves, a simple one-dimensional theory satisfactorily describes the longitudinal response. However, for the propagation of transverse waves, use of the Timoshenko beam theory rather than the Bernoulli-Euler beam theory is necessary because significant rotary inertia and transverse shear are produced. The Timoshenko beam theory accounts for rotary inertia of the cross section and for transverse shear, whereas the Bernoulli-Euler theory does not.

For the longitudinal waves, the deformations of the bar are specified by the longitudinal displacement u. It is related to the axial force N by the constitutive relationship.

$$N + EA\frac{\partial u}{\partial x} = 0, \tag{1}$$

where E is Young's modulus, A is the cross-sectional area of the bar, and x is the axial coordinate. The equation of motion is obtained by applying the dynamical equation to a differential bar element. The equation of motion for longitudinal waves is

$$\frac{\partial N}{\partial x} + \rho A\frac{\partial^2 u}{\partial t^2} = 0 \tag{2}$$

where ρ is the mass density and t is time.

For solution by the method of characteristics, equations (1) and (2) are transformed as follows. The longitudinal velocity is first defined by

$$V = \partial u/\partial t.$$

Then equation (1) is differentiated with respect to time such that the system of equations can be written in matrix form as

$$\begin{bmatrix} 0 & EA \\ \dfrac{1}{\rho A} & 0 \end{bmatrix}\begin{bmatrix} N \\ V \end{bmatrix}_x + \begin{bmatrix} N \\ V \end{bmatrix}_t = 0$$

or in symbolic form as

$$[\Gamma]\{U\}_x + \{U\}_t = 0 \tag{3}$$

These equations form a set of first-order partial differential equations in space x and time t. To transform these partial differential equations into total differential equations by the method of characteristics [8], each term in equation (3) is multiplied by the eigenvector l^i of $[\Gamma]$. The result is

$$\left(\lambda_i\frac{\partial}{\partial x} + \frac{\partial}{\partial t}\right)l^i\{U\} = l^i\{\Omega\}, \tag{4}$$

where λ_i is the eigenvalue corresponding to l^i and $\{\Omega\}$ is a column vector. Along the line $\lambda = dx/dt$, the partial derivatives combine to form a total derivative; thus the governing equations in differential form become

$$d(l^i\{U\}) = l^i\{\Omega\}dt. \tag{5}$$

The condition required for the foregoing transformation is that λ_i be an eigenvalue of matrix Γ; that is,

$$|[\Gamma] - \lambda_i[I]| = 0,$$

where $[I]$ is the identity matrix.

This requirement reduces to

$$\lambda = dx/dt = \begin{cases} +c_b = \sqrt{E/\rho} \text{ along } I^+ & (6a) \\ -c_b = \sqrt{E/\rho} \text{ along } I^-. & (6b) \end{cases}$$

Equations (6a) and (6b) define two straight characteristic lines, I^+ and I^-, in the $x - t$ plane. With a convenient set of eigenvectors, the governing equations (5) can be written as

$$I^+: \quad dN + c_b\rho A dV = 0 \tag{7a}$$

$$I^-: \quad dN - c_b\rho A dV = 0. \tag{7b}$$

For the transverse waves, the deformation of the bar element is specified by the transverse deflection v and the slope of the deflection curve Ψ. These quantities are related to the bending moment M and transverse shear force Q by the constitutive relationships

$$M + EI\frac{\partial \Psi}{\partial x} = 0 \tag{8a}$$

$$Q - k'AG\left(\frac{\partial v}{\partial x} - \Psi\right) = 0, \tag{8b}$$

where I is the moment of inertia, k' is the shear correction coefficient, and G is the shear modulus. The two equations of transverse motion are obtained by applying the dynamical equation to a differential beam element. The equation for rotary motion is

$$\frac{\partial M}{\partial x} - Q + \rho I\frac{\partial^2 \Psi}{\partial t^2} = 0, \tag{9a}$$

and the equation for translatory motion is

$$\frac{\partial Q}{\partial x} - \rho A\frac{\partial^2 y}{\partial t^2} = 0. \tag{9b}$$

The procedure for obtaining the characteristic equations is similar to that described for the longitudinal waves. The translational and rotational velocities are first defined by

$$\omega = \dot{\Psi}, \quad W = \dot{y}. \tag{10}$$

The force-displacement equations (8a) and (8b) are then differentiated with respect to time, and the system equations are written in matrix form.

$$\begin{bmatrix} 0 & 0 & EI & 0 \\ 0 & 0 & 0 & -k'AG \\ 1/\rho I & 0 & 0 & 0 \\ 0 & -1/\rho A & 0 & 0 \end{bmatrix}\begin{bmatrix} M \\ Q \\ \omega \\ W \end{bmatrix}_x + \begin{bmatrix} M \\ Q \\ \omega \\ W \end{bmatrix}_t = \begin{bmatrix} 0 \\ -k'AG\omega \\ Q/\rho I \\ 0 \end{bmatrix} \tag{11}$$

The procedure described for the longitudinal wave response gives the following characteristic lines for transverse wave response:

$$\lambda = \frac{dx}{dt} = \begin{cases} +c_b \text{ along II}^+ & (12a) \\ -c_b \text{ along II}^- & (12b) \\ +c_s \text{ along III}^+ & (12c) \\ -c_s \text{ along III}^-, & (12d) \end{cases}$$

where $c_s = \sqrt{k'G/\rho}$, and the corresponding characteristic equations are found to be

$$\text{II}^+: \quad dM + \rho I c_b d\omega = c_b Q dt \tag{13a}$$

$$\text{II}^-: \quad dM - \rho I c_b d\omega = -c_b Q dt \tag{13b}$$

$$\text{III}^+: \quad dQ - \rho A c_s dW = -k'AG\omega dt \tag{13c}$$

$$\text{III}^-: \quad dQ + \rho A c_s dW = -k'AG\omega dt. \tag{13d}$$

Wave Propagation Through the Junction. At the junction the intersection is modeled as a rigid intersection joining the three bars. Two bars are collinear, and the third intersects at an arbitrary angle θ as shown in Fig. 1.[1]

The response at the junction is governed by

1 The equation of motion for the rigid intersection element.

2 Equations of compatibility at the interfaces of the rigid element and the deformable bars.

3 Equations of motion for the three bars.

4 Constitutive relationships for the bars.

The equations of motion for the rigid intersection element are derived by considering the forces and moments acting on a rigid intersection of unit width shown in Fig. 1. The longitudinal and transverse

---

[1] For the analytical and experimental results discussed here, the three bars that form the junction are of the same cross-sectional dimensions and of the same material properties.

equations of motion are given with respect to coordinates x_1 and y_1, and the rotational equation of motion is given with respect to the intersection's mass center of gravity. The equations for axial, transverse, and rotational motion are then as follows:

$$-N_{1A} + N_{3A} + N_{2A} \sin\theta + Q_{2A} \cos\theta = \rho A_0 \frac{dV_1}{dt} \qquad (14a)$$

$$-Q_{1A} + Q_{3A} + Q_{2A} \sin\theta - N_{2A} \cos\theta = \rho A_0 \frac{dW_1}{dt} \qquad (14b)$$

$$M_{1A} - M_{2A} - M_{3A} + \xi_1 Q_{1A} - \xi_3 Q_{3A} - \xi_2 Q_{2A} - (N_{1A} - N_{3A})\eta_1 + N_{2A}\eta_2 = I_{cg} \frac{d\omega_{1A}}{dt} \qquad (14c)$$

where subscripts $1A$, $2A$, and $3A$ refer to the forces on the left, upper, and right faces of the rigid intersection; A_0 is the area of the rigid element; and I_{cg} is its moment of inertia of mass taken about the centroidal axis perpendicular to the planar area A_0. They are given as

$$A_0 = \frac{h_2}{\cos\theta}\left[h_1 + \frac{h_2}{2}\sin\theta\right]$$

$$I_{cg} = \frac{\rho h_1 h_2}{12\cos\theta}\left[h_1^2 + \frac{h_2^2}{\cos^2\theta} + 12 d_1^2\right] + \frac{\rho h_2^2 \tan\theta}{36}\left[h_2^2(1 + \tan^2\theta) + 18 d_2^2\right],$$

in which h_1 and h_2 are the depths of bars 1 and 2, and d_1 and d_2 are distances between the centers of gravity of the rigid intersection element and its component rectangle and triangle, respectively (Fig. 1). The vectorial distances ξ_i and η_i are in the x and y-direction, respectively, from the $x_i - y_i$ coordinate axes to the rigid intersection element's mass center of gravity.

After the derivatives are expressed in finite-difference form, the nondimensional forms of equations (14a), (14b), and (14c) become

$$-\epsilon_{12}\epsilon_{13}\overline{N}_{1A} + \epsilon_{12}\overline{N}_{3A} + \epsilon_{13}\overline{N}_{2A}\sin\theta + \beta^2\epsilon_{13}\overline{Q}_{2A}\cos\theta - \frac{\sqrt{3}}{2\gamma}\overline{A}_0\overline{V}_{1A} = -\frac{\sqrt{3}}{2\gamma}\overline{A}_0\overline{V}_{1G} \qquad (15a)$$

$$-\epsilon_{12}\epsilon_{13}\overline{Q}_{1A} + \epsilon_{12}\overline{Q}_{3A} + \epsilon_{13}\overline{Q}_{2A}\sin\theta - \frac{\epsilon_{13}}{\beta^2}\overline{N}_{2A}\cos\theta - \frac{\sqrt{3}\,\overline{A}_0}{\beta^2\gamma\cdot 2}\overline{W}_{1A} = -\frac{\sqrt{3}\,\overline{A}_0}{\beta^2\gamma\cdot 2}\overline{W}_{1G} \qquad (15b)$$

$$\epsilon_{12}^2\epsilon_{13}^2\overline{M}_{1A} - \epsilon_{13}^2\overline{M}_{2A} - \epsilon_{12}^2\overline{M}_{3A} + \epsilon_{12}^2\epsilon_{13}^2\beta^2\overline{\xi}_1\overline{Q}_{1A} - \epsilon_{12}^2\beta^2\overline{\xi}_3\overline{Q}_{3A} - \epsilon_{13}^2\beta^2\overline{\xi}_2\overline{Q}_{2A} - \epsilon_{12}^2\epsilon_{13}^2\overline{\eta}_1\overline{N}_{1A} + \epsilon_{13}^2\overline{\eta}_2\overline{N}_{2A} + \epsilon_{12}^2\overline{\eta}_1\overline{N}_{3A} - 6\sqrt{3}\,\overline{I}_{cg}\overline{\omega}_{1A} = -6\sqrt{3}\,\overline{I}_{cg}\overline{\omega}_{1G} \qquad (15c)$$

where $\epsilon_{ij} = h_i/h_j$, $\beta = c_s/c_b$, $\gamma = \Delta\tau/2$, and $r_i = h_i/\sqrt{12}$. The nondimensional components are expressed as

$$\overline{N} = N/(\rho h_i c_b^2)$$
$$\overline{Q} = Q/(\rho h_i c_s^2)$$
$$\overline{V} = V/c_b$$
$$\overline{W} = W/c_b$$
$$\overline{M} = M/(\rho h_i r_i c_b^2)$$
$$\overline{\omega} = \omega r_i/c_b$$
$$\overline{A}_0 = A_0/(h_2 h_3)$$
$$\overline{I}_{cg} = I_{cg}/(\rho h_2^2 h_3^2)$$
$$\overline{\eta}_i = \eta_i/r_i$$
$$\overline{\xi}_i = \xi_i/r_i$$

The equations of compatibility of motion are obtained by requiring that the rigid intersection element and its interfaces with the beam-columns have the same axial, transverse, and rotational velocity. These equations in nondimensional form are

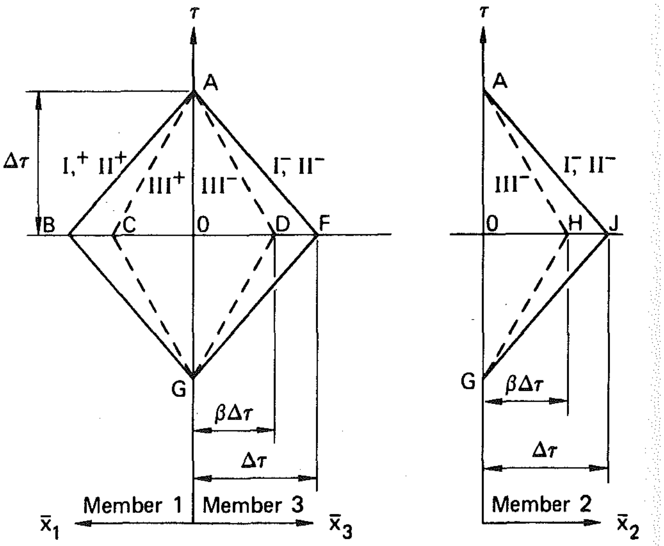

Fig. 2 Characteristic lines for three-member intersection

$$\overline{V}_{1A} = \overline{V}_{3A} \qquad (16a)$$

$$\overline{W}_{1A} + \overline{\omega}_{1A}\frac{|\xi_1|}{r_1} = \overline{W}_{3A} - \overline{\omega}_{3A}\frac{|\xi_3|}{r_3} \qquad (16b)$$

$$\overline{\omega}_{1A} = \epsilon_{13}\,\overline{\omega}_{3A} \qquad (16c)$$

$$\overline{V}_{1A} + \overline{\omega}_{1A}\frac{|\eta_1|}{r_1} = \left(\overline{V}_{2A} - \frac{\eta_2}{r_2}\overline{\omega}_{2A}\right)\sin\theta + \left(\overline{W}_{2A} - \overline{\omega}_{2A}\frac{|\xi_2|}{r_2}\right)\cos\theta \qquad (16d)$$

$$\overline{W}_{1A} + \overline{\omega}_{1A}\frac{|\xi_1|}{r_1} = \left(\overline{W}_{2A} - \overline{\omega}_{2A}\frac{|\xi_2|}{r_2}\right)\sin\theta + \left(\overline{\omega}_{2A}\frac{\eta_2}{r_2} - \overline{V}_{2A}\right)\cos\theta \qquad (16e)$$

$$\overline{\omega}_{1A} = \epsilon_{12}\overline{\omega}_{2A} \qquad (16f)$$

The equations of motion and constitutive relationships for each bar are expressed in characteristic form by equations (7) and (13). Disturbances propagated to the intersection element are governed by nine characteristic equations, three for each bar. These equations were derived above in dimensional form. The characteristic lines in the dimensionless, $\overline{x} - \tau$ spaces along which these equations apply, are graphically represented in Fig. 2. The dimensionless spacial coordinate $\overline{x} = x/r$, and the dimensionless temporal coordinate $\tau = c_b t/r$. The characteristic equations governing bending and shear apply along the characteristic lines of slopes ±1 and $\pm\beta$. The characteristics equations governing thrust apply only along the characteristic lines of slope ±1. From equations (7) and (13), the required dimensionless forms of the characteristic equations in finite difference form are

$$\overline{N}_{1A} - \overline{V}_{1A} = \overline{N}_{1B} - \overline{V}_{1B} \qquad (17a)$$

$$\overline{M}_{1A} + \overline{\omega}_{1A} - \beta^2\gamma\overline{Q}_{1A} = \overline{M}_{1B} + \overline{\omega}_{1B} + \beta^2\gamma\overline{Q}_{1B} \qquad (17b)$$

$$\beta\overline{Q}_{1A} - \overline{W}_{1A} + \beta\gamma\overline{\omega}_{1A} = \beta\overline{Q}_{1C} - \overline{W}_{1C} - \beta\gamma\overline{\omega}_{1C} \qquad (17c)$$

$$\overline{N}_{3A} + \overline{V}_{3A} = \overline{N}_{3F} + \overline{V}_{3F} \qquad (17d)$$

$$\overline{M}_{3A} - \overline{\omega}_{3A} + \beta^2\epsilon_{13}\gamma\overline{Q}_{3A} = \overline{M}_{3F} - \overline{\omega}_{3F} - \beta^2\epsilon_{13}\gamma\overline{Q}_{3F} \qquad (17e)$$

$$\beta\overline{Q}_{3A} + \overline{W}_{3A} + \beta\epsilon_{13}\gamma\overline{\omega}_{3A} = \beta\overline{Q}_{3D} - \beta\epsilon_{13}\gamma\overline{\omega}_{3D} + \overline{W}_{3D} \qquad (17f)$$

$$\overline{N}_{2A} + \overline{V}_{2A} = \overline{N}_{2J} + \overline{V}_{2J} \qquad (17g)$$

$$\overline{M}_{2A} - \overline{\omega}_{2A} + \beta^2\epsilon_{12}\gamma\overline{Q}_{2A} = \overline{M}_{2J} - \overline{\omega}_{2J} - \beta^2\epsilon_{12}\gamma\overline{Q}_{2J} \qquad (17h)$$

$$\beta\overline{Q}_{2A} + \overline{W}_{2A} + \beta\epsilon_{12}\gamma\overline{\omega}_{2A} = \beta\overline{Q}_{2H} + \overline{W}_{2H} - \beta\epsilon_{12}\gamma\overline{\omega}_{2H} \qquad (17i)$$

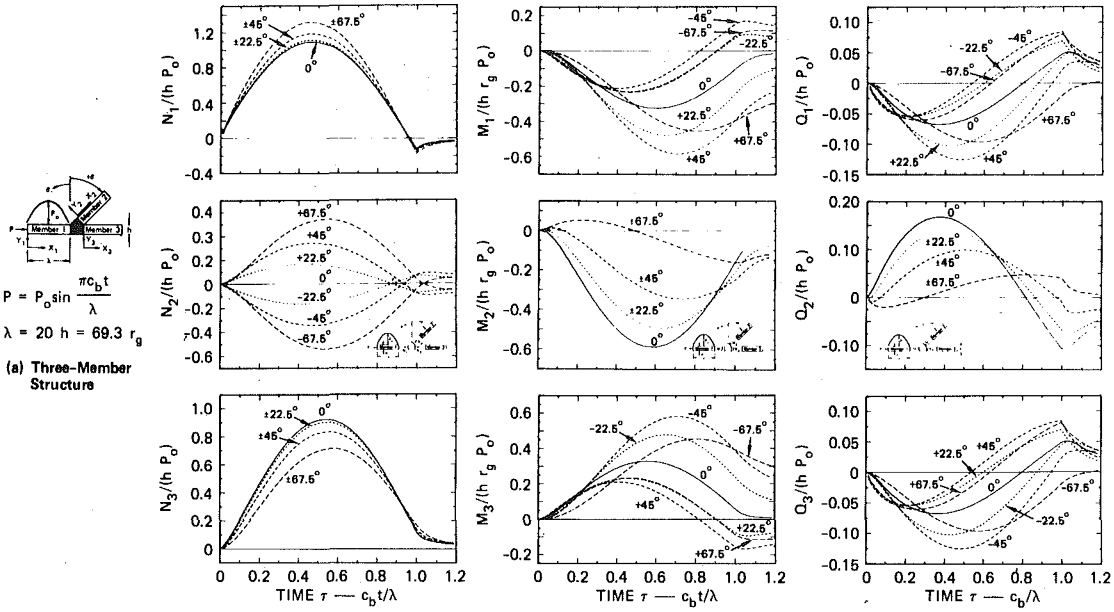

(b) Longitudinal Force History

(c) Bending Moment History

(d) Transverse Shear Force History

Fig. 3 Theoretical wave response at three-member junction

Equations (17*c*), (17*f*), and (17*i*) are expressed in terms of velocities and forces at points *A*, *C*, *D*, and *H* in Fig. 2. To simplify the finite-difference solution, quantities at points *C*, *D*, and *H* are expressed in terms of those at *A*, *B*, *F*, *J*, and *G*, thereby eliminating the characteristic lines of slope $\pm\beta$ from the computations. For example, the quantities at *C* in equation (17*c*) are expressed in terms of those at *B* and *O* by linearly interpolating along line *BOF*. Then the dependence on quantities at *O* is removed by interpolating along line *AOG*. Equation (17*c*) is then expressed in terms of quantities at *A*, *B*, and *G* as

$$\beta(\beta + 1)\overline{Q}_{1A} - (\beta + 1)\overline{W}_{1A} + \beta\gamma(3 - \beta)\,\overline{\omega}_{1A} = 2\beta[\beta\overline{Q}_{1B} - \overline{W}_{1B} - \beta\gamma\overline{\omega}_{1B}] + (1 - \beta)\,[\beta\overline{Q}_{1G} - \overline{W}_{1G} - \beta\gamma\overline{\omega}_{1G}]$$

The 18 unknown forces and velocities at point *A* are obtained by solution of 18 simultaneous equations: three equations of motion, equations (15*a*)–(15*c*); six compatibility equations, equations (16*a*)–(16*f*); and nine characteristic equations, equations (17*a*)–(17*i*). These equations can be expressed in matrix form as

$$[A]\{U\} = \{B\},$$

where $\{U\}$ is a column vector of the 18 unknown quantities at point *A* in Fig. 2; $\{B\}$ is a column vector whose 18 elements are combinations of known quantities at points *B*, *F*, *J*, and *G*; and $[A]$ is an 18×18 square matrix of constant coefficients.

In matrix notation, the solution for $\{U\}$ is

$$\{U\} = [A]^{-1}B,$$

where $[A]^{-1}$ is the inverse of $[A]$. Since $[A]$ is independent of time, it is inverted only once during the analysis; thus it is expedient to determine $[A]^{-1}$ numerically with an available computer subroutine. The intersection solution obtained in this way can then be combined with the solutions for the bars which are given in dimensionless finite-difference forms of the characteristic equations in [9] to give the solution for the three-member structure.

Theoretically Predicted Wave Response. To characterize the wave propagation through a junction, the structure shown in Fig. 3(*a*) was analyzed. Member 1 of this structure was loaded by a half-sine wave longitudinal pulse.

$$P = P_0 \sin \frac{\pi c_b t}{\lambda},$$

where c_b is the bar wave velocity, λ is the half-sine wavelength, and t is time.

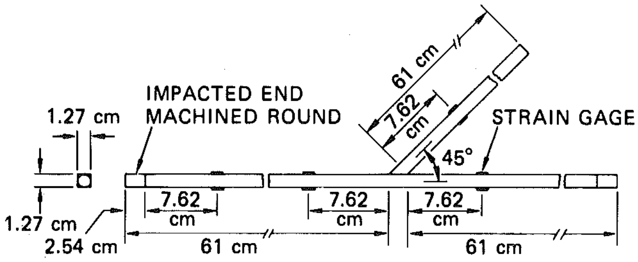

Fig. 4 Geometry of experimental structure and strain gage locations

Time histories of longitudinal force, bending moment, and shear force at the interface of the intersection and its three connecting members are shown in Figs. 3(*b*), (*c*), and (*d*) for several values of θ.

For member 1, Fig. 3(*b*) shows that the longitudinal or axial response increases with increasing absolute values of θ. Because the response at the interface of member 1 and the intersection element represents a superposition of the incident wave and the reflected wave, the peak axial response always exceeds the amplitude of the incident wave. Figs. 3(*c*) and 3(*d*) show that the bending moment and shear response in member 1 are a maximum at about θ equals $\pi/4$ rad (45 deg).

For member 2, Fig. 3(*b*) shows that the axial response increases for increases monotonically with θ. Figs. 3(*c*) and 3(*d*) show that the largest (absolute) values of bending moment and shear response occur at θ equals zero.

For member 3, Fig. 3(*b*) shows that the largest axial response occurs at θ equals zero and is less than the amplitude of the incident wave. Figs. 3(*c*) and 3(*d*) show that the largest (absolute) values of bending moment and shear occur at about θ equals $-\pi/4$ rad (-45 deg).

Experiments

Impact experiments were performed to measure the stress wave response at the junction. Fig. 4 shows a schematic of the structure used

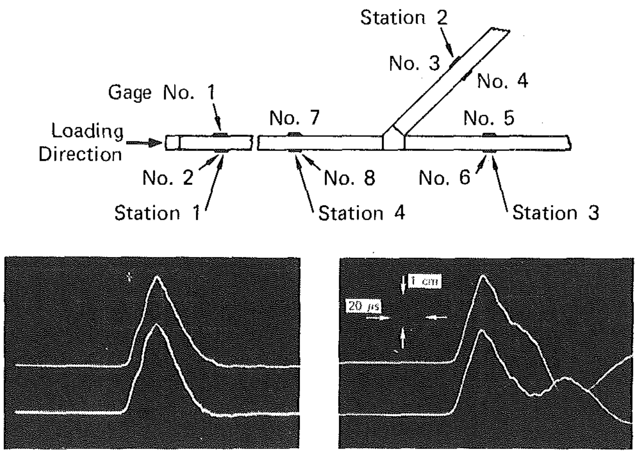

GAGES 1 (TOP) AND 2
STATION 1 (Delay Time after Impact = -57 μs)

GAGES 7 (TOP) AND 8
STATION 4 (Delay Time after Impact = +23 μs)

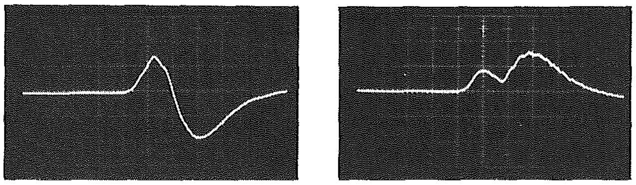

GAGE NO. 3 GAGE NO. 4
STATION 2 (Delay Time after Impact = +53 μs)

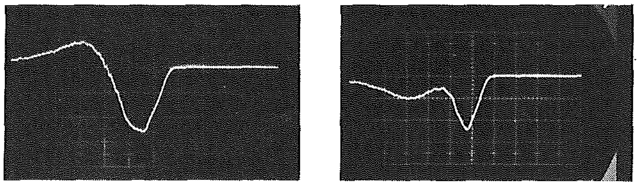

GAGE NO. 5 GAGE NO. 6
STATION 3 (Delay Time after Impact = +53 μs)

Fig. 5 Strain gage records for three-member structure where $\theta = +\pi/4$ rad

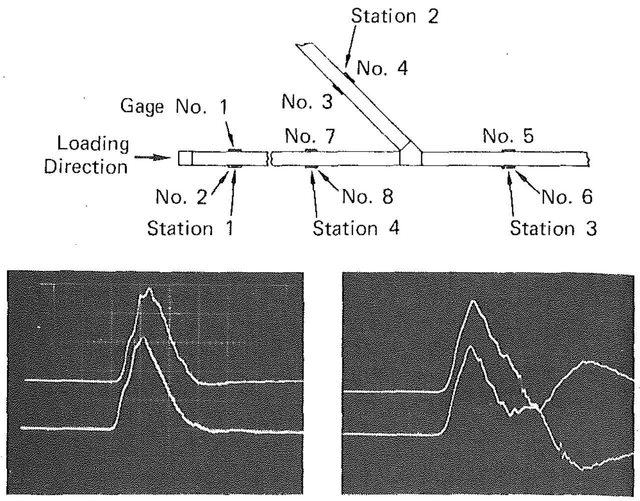

GAGES 1 (TOP) AND 2
STATION 1 (Delay Time after Impact = -45 μs)

GAGES 7 (TOP) AND 8
STATION 4 (Delay Time after Impact = +35 μs)

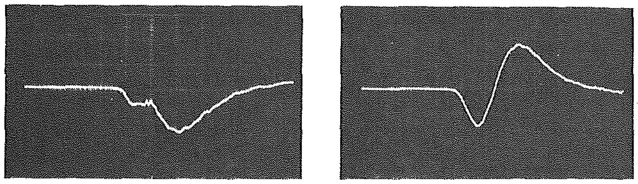

GAGE NO. 3 GAGE NO. 4
STATION 2 (Delay Time after Impact = +65 μs)

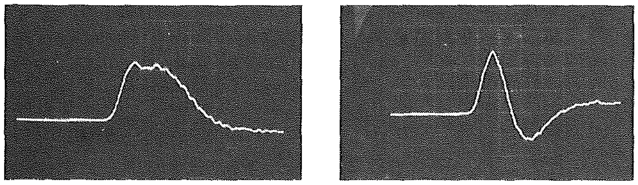

GAGE NO. 5 GAGE NO. 6
STATION 3 (Delay Time after Impact = +65 μs)

Fig. 6 Strain gage records for three-member structure where $\theta = -\pi/4$ rad

in the experiments. The structure was fabricated from 6061-T6 Aluminum rods of 1.27 cm (1/2 in.) sq cross section. The junction was formed by welding a noncollinear bar to a second bar at an angle of $\pi/4$ rad (45 deg) to form a junction of three bars as shown in the figure. The structure was heat-treated to the T6 condition to remove any residual stresses induced by welding.

A short-duration load was induced by impacting the structure at one end with a cylindrical brass projectile fired from a 1.204 cm dia gas gun. Each end of the target was machined round so that it could be inserted into the muzzle of the gas gun, thereby aligning the target with the projectile. A 0.318 cm thick Teflon disk was attached to the impacted end of the target to give the loading pulse a finite rise time. The impact velocity was about 15.2 m/sec.

Strains induced in the target by the impact loading were measured with foil-type strain gages. Gages were oriented to measure longitudinal strains in the bar segments of the structure; their locations are indicated in Fig. 4.

Measured strain-time histories are shown in Figs. 5 and 6. Fig. 5 shows the response for a structure in which the intersection angle is $+\pi/4$ rad, and Fig. 6 shows the response for a structure in which the intersection angle is $-\pi/4$ rad. The gages located at the impacted end measured the longitudinal or axial wave induced by the impact of the projectile. Those gages located immediately before and after the junction measured the superposition of axial and bending strains due to waves reflected from and transmitted through the intersection element.

Comparison Between Theory and Experiment

To verify the analysis for wave propagation through the junction, the predicted wave response was compared with that obtained from experiments. Figs. 7 and 8 compare the theoretically predicted strain-time histories with the experimentally measured strain-time histories. (Fig. 7 shows histories for a three-member structure with an intersection where $\theta = +\pi/4$ rad, and Fig. 8 shows histories for a three-member structure where $\theta = -\pi/4$ rad.) The loading for the theoretical analysis was taken as the axial strain history measured at station 1 in the experiment. Agreement between theory and experiment is good; however, the theory deviates slightly from the experiment in the latter portion of each strain-time history. This is due to the arrival of the measured bending pulse at a time of about 10 μs later than the arrival of the predicted bending pulse.

This effect is better shown in Fig. 9, where the axial and bending components are shown separately. The figure shows strain-time histories obtained by the finite-difference integration scheme using

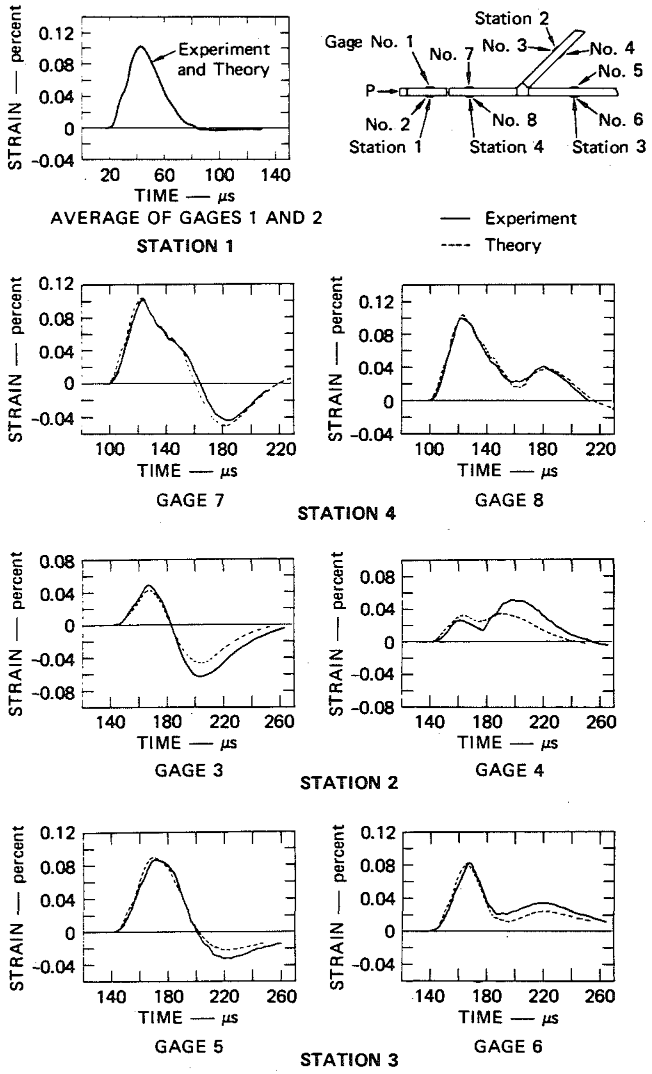

Fig. 7 Comparison of experimental and theoretical strain-time histories for three-member structure where $\theta = +\pi/4$ rad

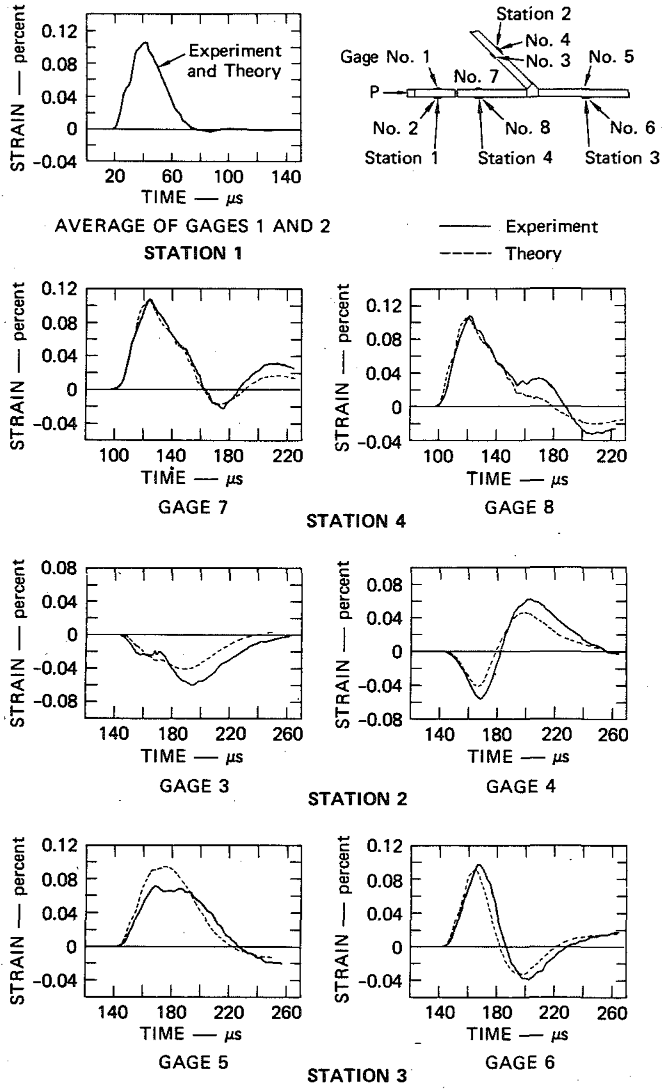

Fig. 8 Comparison of experimental and theoretical strain-time histories for three-member structure where $\theta = -\pi/4$ rad

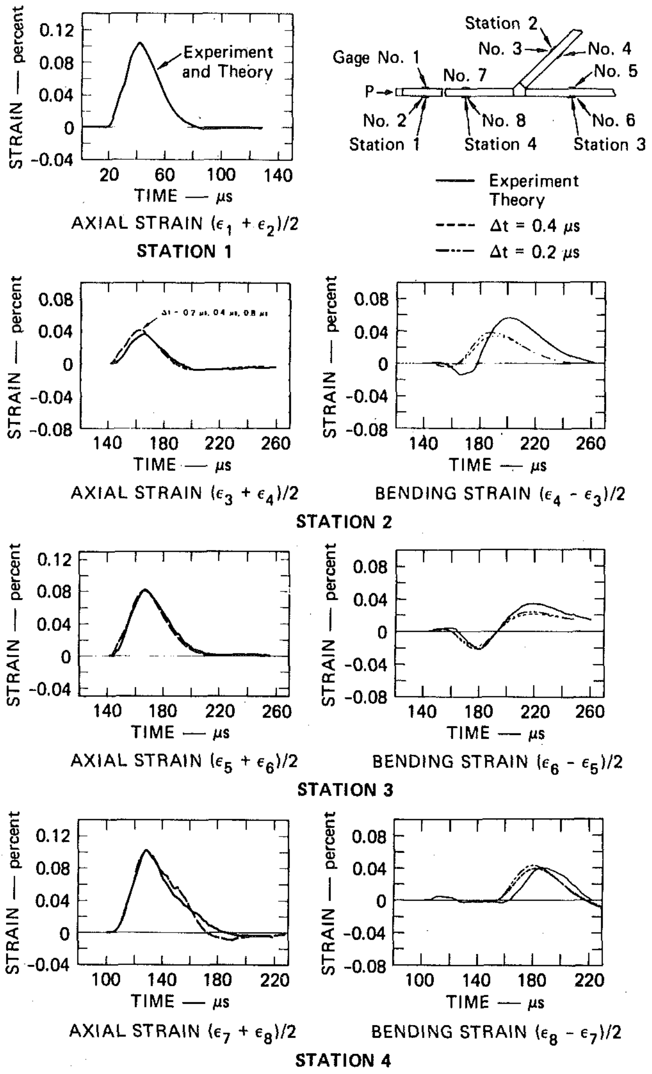

Fig. 9 Comparison of axial and bending strain-time histories for three-member structure where $\theta = +\pi/4$ rad

two different values of the time increment (grid size) Δt.[2] The axial response is virtually unchanged by a refined finite-difference grid, whereas the shape of the bending strain-time history is somewhat sensitive to grid size. The arrival time of the theoretically predicted bending pulse, however, is not sensitive to grid size; therefore, a more refined grid would not improve agreement in arrival times between theory and experiment.

There are two plausible reasons for the discrepancy between theoretical and experimental bending strains. First, the discrepancy may be due to the difference in the response of an intersection that is rigid, as modeled in the analysis, and an intersection that is elastic, as used in the experiment. An incident pulse of wavelength several times larger than the dimension of the intersection propagates through an elastic intersection and through a rigid intersection in roughly the same manner. However, an incident pulse of wavelength comparable to the intersection dimension is distorted when propagated through a rigid intersection. Although the experimentally measured incident pulse (which was also used as the loading pulse in the analysis) is dominated by long-wavelength components, it also contains some short-wavelength components. The distortion of these short-wavelength components when propagated through the rigid intersection is believed to cause the discrepancy between theory and experiment. Second, the discrepancy may be due to the bending (Timoshenko) equations being more susceptible to integration errors inherent in a linear-interpolation scheme compared to those of the axial motion equations. A more sophisticated integration scheme such as that given in [10] may have improved the correlation between theory and experiment.

In spite of the slight discrepancy in the bending response, the overall response is satisfactorily predicted by the theory.

Acknowledgment

This work was done under a contract with the Defense Nuclear Agency [11]. Their support is gratefully acknowledged. The author also wishes to thank J. D. Colton and H. E. Lindberg of SRI International for providing many key ideas and technical advice.

References

1 Kolsky, H., *Stress Waves in Solids*, Clarendon Press, Oxford, 1953, Dover Reprint, 1964.

2 Achenback, J. D., *Wave Propagation in Elastic Solids*, American Elsevier Publishing Co., New York, 1973.

3 Ripperger, E. A., and Abramson, H. N., "Reflection and Transmission of Elastic Pulses in a Bar at a Discontinuity in Cross Section," 3rd Midwestern Conference on Solid Mechanics, 1957.

4 Yang, J. C. S., and Hassett, R. J., "Stress Wave Propagation in Multilayered Axisymmetric Bodies of Varying Area," Naval Ordnance Laboratory Report (NOLTR 70-253), White Oak, Silver Spring, Md., Dec. 1970.

5 Lee, J. P., and Kolsky, H., "The Generation of Stress Pulses at the Junction of Two Noncollinear Rods," ASME JOURNAL OF APPLIED MECHANICS, Vol. 39, Sept. 1972, pp. 809–813.

6 Atkins, K. J., and Hunter, S. C., "The Propagation of Longitudinal Elastic Waves Around Right-Angled Corners in Rods of Square Cross Section," *Quarterly Journal of Mechanics and Applied Mathematics*, Vol. 28, May 1975, pp. 245–260.

7 Mandel, J. A., Mathur, R. K., and Chang, Y. C., "Stress Waves at Rigid Right Angle Joint," *Journal of the Engineering Mechanics Division*, ASCE, Vol. 97, No. EM4, Aug. 1971, pp. 1173, 1186.

8 Garabedian, P. R., *Partial Differential Equations*, Wiley, New York, pp. 95–99.

9 Colton, J. D., and Lindberg, H. E., "Stress Wave Approach to the Analysis of Internal Component Shock Response," Stanford Research Institute Annual Report for Contract DNA001-74-C-0140, May 1975.

10 Ranganath, S., and Clifton, R. J., "A Second-Order Accurate Difference Method for Systems of Hyperbolic Partial Differential Equations," *Computer Methods in Applied Mechanics and Engineering*, 1972, pp. 173–188.

11 Desmond, T. P., and Colton, J. D., "Generalization of the Wave Approach to the Analysis of Internal Equipment Response," SRI International Report for Contract DNA001-77-C-0198, Oct. 1978.

---

[2] A time increment of $\Delta t = 0.2$ μs was used in most calculations presented in this paper.

R. K. Miller
Associate Professor,
Department of Civil Engineering,
University of Southern California,
Los Angeles, Calif. 90007
Assoc. Mem. ASME

H. T. Tran
Graduate Student,
Department of Mechanical Engineering,
University of California,
Berkeley, Calif. 94720

Reflection, Refraction, and Absorption of Elastic Waves at a Frictional Interface: *P* and *SV* Motion

An approximate method of analysis is presented for determining the reflection, refraction, and absorption of obliquely incident planar time-harmonic P or SV waves at a frictional interface between dissimilar elastic solids. The solids are pressed together with sufficient pressure to prevent separation, and the angle of incidence is subcritical. General expressions for the amplitudes and phases of all reflected and refracted waves are developed in closed form for a broad class of models for bonding friction. Specific results are presented for the case of identical elastic solids bonded by Coulomb friction, as an example of application of the general approach.

Introduction

In a previous paper [1] the authors began an investigation of the effects of friction and slippage at an interface on the propagation of elastic body waves. The previous investigation was limited to the case of antiplane strain (*SH*) motion. Presented herein are the results of an extension of this investigation to the case of plane strain (*P* and *SV*) motion. In particular, attention is focused on the reflection, refraction and absorption of planar time-harmonic *P* and *SV* waves at a frictionally bonded interface between dissimilar elastic solids. The solids are pressed together with sufficient external pressure to prevent separation at the interface, and the angle of incidence is assumed to be subcritical.

The effect of bonding imperfections on the propagation of elastic waves is a subject of potential technological application in several areas, including soil-structure interaction of burried structures during earthquakes, and nondestructive testing of materials for bonding defects [2–4]. Several recent investigations have dealt with theoretical aspects of the subject. For time-harmonic body waves of *P* and *SV* type, Comninou and Dundurs have considered the effects of localized separation at a lubricated interface [5] and at an interface bonded by Coulomb friction [6], while Murty [7] considered the effects of slippage without separation along an interface with linear viscous bonding. Comninou and Dundurs have also considered the case of separation caused by transient (anharmonic) *P* and *SV* waves at a lubricated interface [8, 9]. Similar investigations of Stonely-type interface waves along an interface with imperfect bonding have been reported [10–12]. Each of these investigations employs an exact solution technique which depends on the bonding conditions which result for lubricated, viscous, or Coulomb friction laws at the interface. Any bonding laws which are more complex or realistic in their treatment of the boundary conditions at the interface are not tractable by the mathematical techniques used in the studies previously described. While simple models for bonding friction may be adequate for some applications, there exist applications for which the validity of such models may be questioned. For example, with regard to smooth metallic surfaces it is well known that the coefficient of friction in the Coulomb law may not remain constant, but instead may depend significantly on such variables as contact pressure, slip velocity, time of contact, temperature, and others [13, 14]. Furthermore, some experimental results [15] on the nature of friction between sliding steel plates reveal a behavior somewhat more complex than Coulomb friction would predict. With regard to interfaces between soil layers or soil and structural foundations, little is known about the frictional behavior. Experimental research on such interfaces is currently in progress to investigate appropriate constitutive laws between cyclic shear stress and relative slip [16]. In order to investigate the features introduced by these more complex and even empirical frictional models, it is necessary to use approximate techniques of analysis. The present investigation employs an approximate solution technique which relieves many of the mathematical difficulties and allows any of a broad class of models for bonding friction to be considered.

An approximate analytical technique is employed in this paper to

---

Contributed by the Applied Mechanics Division of THE AMERICAN SOCIETY OF MECHANICAL ENGINEERS, for presentation at the 1981 Joint ASME/ASCE Applied Mechanics, Fluids Engineering, and Bioengineering Conference, University of Colorado, Boulder, Colo., June 22–27, 1981.

Discussion on this paper should be addressed to the Editorial Department, ASME, United Engineering Center, 345 East 47th Street, New York, N. Y. 10017, and will be accepted until June 1, 1981. Readers who need more time to prepare a Discussion should request an extension from the Editorial Department. Manuscript received by ASME Applied Mechanics Division, March, 1980; final revision, September, 1980. Paper No. 81-APM-18.

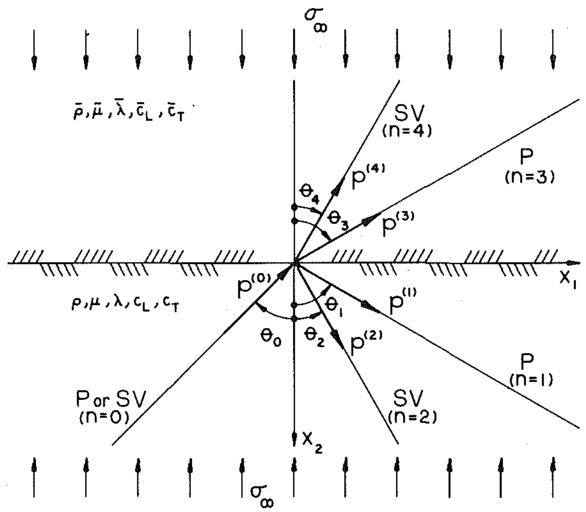

Fig. 1 **Orientation of coordinate directions, angles, and unit vectors relative to the interface between dissimilar elastic solids**

provide closed-form general expressions for the amplitude and phase of all reflected and refracted waves, and for the partitioning of energy in the system. The expressions are valid for a broad class of models for bonding friction at the interface. As an example of application of the general approach, specific results are presented for the case of bonding of identical elastic solids by Coulomb friction. The results in this case are shown to depend on the angle of incidence and Poisson's ratio in addition to the stress ratio τ^* identified earlier [1]. It is also shown that less energy is absorbed at the interface for incident waves of P or SV type than for an SH wave of equal shear stress amplitude.

Formulation

Consider two semi-infinite elastic solids with a common planar boundary at $x_2 = 0$, as shown in Fig. 1. Following standard notation, let λ and μ denote the Lamé constants, c_L and c_T the longitudinal and transverse wave velocities, respectively, ρ the mass density, u_i ($i = 1, 2$) the displacement field, and σ_{ij} ($i, j = 1, 2$) the stress field for this plane strain problem. An overbar is used to distinguish quantities associated with the upper solid from those of the lower solid.

The solids are pressed together by a static pressure σ_∞, and subjected to a planar time-harmonic incident wave of P or SV type in the lower solid. The incident wave propagates in the direction of the unit vector $\mathbf{p}^{(0)}$ at subcritical angle of incidence θ_0, as shown in Fig. 1. The incident wave is assumed to have displacement amplitude A_0 and frequency ω. The resulting reflected and refracted P and SV waves propagate along the directions $\mathbf{p}^{(n)}$ ($n = 1, 2, 3, 4$), with periodic but generally anharmonic time-dependence.

Contact between media occurs on the planar boundary $x_2 = 0$. It is assumed that the external pressure σ_∞ is sufficiently large to prevent separation, but that additional bonding between solids is provided by friction only. Thus, when A_0 is sufficiently large, local relative slip is allowed between solids. Let this local relative slip be defined as

$$s(x_1, t) \equiv u_1(x_1, 0, t) - \bar{u}_1(x_1, 0, t). \tag{1}$$

The boundary conditions at the frictionally bonded interface then require that

$$\bar{u}_2(x_1, 0, t) = u_2(x_1, 0, t) \tag{2}$$

$$\bar{\sigma}_{22}(x_1, 0, t) = \sigma_{22}(x_1, 0, t) \tag{3}$$

$$\bar{\sigma}_{12}(x_1, 0, t) = \tau_F[\sigma_\infty, s(x_1, t)] \tag{4}$$

$$\sigma_{12}(x_1, 0, t) = \tau_F[\sigma_\infty, s(x_1, t)] \tag{5}$$

where τ_F is the frictional stress developed at the interface. As previously explained [1], the functional $\tau_F[\cdot]$ represents a general constitutive law for the frictional shear stress τ_F in terms of the external pressure σ_∞ and the time history of relative slip.

Approximate Solution for a General Frictional Model, τ_F

For many realistic nonlinear models for the frictional stress τ_F, the problem just formulated is very difficult to solve. In fact, as far as the authors are aware, exact solutions for this problem have been presented [5–7] only for the special case in which τ_F is zero, determined by Coulomb friction, or is a linear function of s, such as the expression

$$\kappa s(x_1, t) + \zeta \frac{\partial s(x_1, t)}{\partial t} \tag{6}$$

where κ and ζ are constants.

No attempt is made here to find an exact solution for the case of general nonlinear frictional stress, τ_F. Instead, the approach presented earlier [1] is used to develop an approximate solution. The approach involves replacing the nonlinear frictional stress τ_F with a linearized expression of the form (6), with appropriately chosen constants κ and ζ. The solution to the resulting linearized problem is then regarded as an approximate solution to the original nonlinear problem. Clearly the accuracy of the approximate solution depends on the choice of the parameters κ and ζ. As previously shown, an optimal choice of the parameters depends on the amplitude of motion in the linearized solution and the nonlinear constitutive law $\tau_F[\cdot]$ through the integrals

$$\kappa = \kappa(\sigma_\infty, S) = \frac{1}{\pi S} \int_0^{2\pi} \tau_F(\sigma_\infty, S \cos \eta) \cos \eta \, d\eta \tag{7}$$

$$\zeta = \zeta(\sigma_\infty, S) = \frac{-1}{\pi \omega S} \int_0^{2\pi} \tau_F(\sigma_\infty, S \cos \eta) \sin \eta \, d\eta \tag{8}$$

where S is a constant representing the amplitude of the harmonic wave form of the linearized solution for s of equation (1). These integrals may be readily evaluated for any of a broad class of nonlinear frictional models.

Having obtained the linearized parameters κ and ζ, it remains to solve the resulting linearized problem. This may be done by well-known displacement potential techniques [7], the details of which will not be presented here. However, it is noteworthy that closed-form solutions for a broad class of frictional models may be obtained in terms of $\kappa(\sigma_\infty, S)$ and $\zeta(\sigma_\infty, S)$, and these solutions are presented in the following. In particular, it may be shown [17] that the linearized amplitude S of slip displacement is governed by the transcendental equation

$$\begin{aligned} S^2 \left[\left(\frac{\kappa(\sigma_\infty, S)}{\mu k_s} \right)^2 + \left(\frac{\omega \zeta(\sigma_\infty, S)}{\mu k_s} + \frac{2\upsilon_1 - (\upsilon_2^2 - 1) a_{21}}{1 - \upsilon_2 a_{21} - a_{31} - \upsilon_4 a_{41}} \right)^2 \right] \\ = \frac{A_0^2}{(1 + \upsilon_0^2)} \left\{ b_3 + (\upsilon_2^2 - 1) a_{22} \right. \\ \left. - \frac{(b_4 + \upsilon_2 a_{22} + a_{32} + \upsilon_4 a_{42}) \, [2\upsilon_1 - (\upsilon_2^2 - 1) a_{21}]}{1 - \upsilon_2 a_{21} - a_{31} - \upsilon_4 a_{41}} \right\}^2 \end{aligned} \tag{9}$$

where, if c_n ($n = 0, 1, 2, 3, 4$) represents the phase velocity of the nth wave shown in Fig. 1, the coefficients are given by

$$k_s = \omega / c_s; \quad c_s = c_0 / p_1^{(0)} \tag{10}$$

$$\upsilon_n = (c_s^2 / c_n^2 - 1)^{1/2} = \cot(\theta_n); \quad n = 0, 1, 2, 3, 4 \tag{11}$$

and for an incident SV wave,

$$b_1 = -1; \quad b_2 = -2\upsilon_2; \quad b_3 = (\upsilon_2^2 - 1); \quad b_4 = -\upsilon_2 \tag{12}$$

while for an incident P wave,

$$b_1 = \upsilon_1; \quad b_2 = (\upsilon_2^2 - 1); \quad b_3 = 2\upsilon_1; \quad b_4 = -1. \tag{13}$$

The remaining coefficients are given by

$$a_{21} = \frac{\begin{array}{r} 2\upsilon_1(1 - \upsilon_4{}^2 + 2\upsilon_3\upsilon_4) + 2\upsilon_3\,(1 - \upsilon_2{}^2 - 2\gamma\upsilon_1\upsilon_4) \\ - (\upsilon_4{}^2 - 1)[\gamma\upsilon_1(\upsilon_4{}^2 - 1) + \upsilon_3(\upsilon_2{}^2 - 1)] \end{array}}{\begin{array}{r} (\upsilon_2{}^2 - 1)\,(1 - \upsilon_4{}^2 + 2\upsilon_3\upsilon_4) + 4\upsilon_3(\upsilon_2 + \gamma\upsilon_4) \\ + (\upsilon_4{}^2 - 1)[\gamma(\upsilon_4{}^2 - 1) + 2\upsilon_2\upsilon_3] \end{array}} \tag{14}$$

$$a_{22} = \frac{\begin{array}{r} 2\upsilon_3(2\gamma\upsilon_4 b_1 - b_2) - b_3(1 - \upsilon_4{}^2 + 2\upsilon_3\upsilon_4) \\ + (\upsilon_4{}^2 - 1)[\gamma b_1(\upsilon_4{}^2 - 1) - \upsilon_3 b_2] \end{array}}{\begin{array}{r} (\upsilon_2{}^2 - 1)\,(1 - \upsilon_4{}^2 + 2\upsilon_3\upsilon_4) + 4\upsilon_3(\upsilon_2 + \gamma\upsilon_4) + \\ (\upsilon_4{}^2 - 1)[\gamma(\upsilon_4{}^2 - 1) + 2\upsilon_2\upsilon_3] \end{array}} \tag{15}$$

$$a_{31} = \frac{(1 - \upsilon_2{}^2 - 2\gamma\upsilon_1\upsilon_4) - 2(\upsilon_2 + \gamma\upsilon_4)a_{21}}{\gamma(1 - \upsilon_2{}^2 + 2\upsilon_3\upsilon_4)} \tag{16}$$

$$a_{32} = \frac{(2\gamma\upsilon_4 b_1 - b_2) - 2(\upsilon_2 + \gamma\upsilon_4)a_{22}}{\gamma(1 - \upsilon_2{}^2 + 2\upsilon_3\upsilon_4)} \tag{17}$$

$$a_{41} = \frac{-\gamma\upsilon_1(\upsilon_4{}^2 - 1) + \upsilon_3(\upsilon_2{}^2 - 1) + [\gamma(\upsilon_4{}^2 - 1) + 2\upsilon_2\upsilon_3]a_{21}}{\gamma(1 - \upsilon_4{}^2 + 2\upsilon_3\upsilon_4)} \tag{18}$$

$$a_{42} = \frac{-\upsilon_3 b_2 + \gamma(\upsilon_4{}^2 - 1)b_1 + [2\upsilon_2\upsilon_3 + \gamma(\upsilon_4{}^2 - 1)]a_{22}}{\gamma(1 - \upsilon_4{}^2 + 2\upsilon_3\upsilon_4)} \tag{19}$$

where

$$\gamma = \bar{\mu}/\mu. \tag{20}$$

Due to the trancendental nature of equation (9), numerical solutions for S will generally be required.

After S has been determined, the corresponding phase shift α_s (relative to the incident wave) of the wave form for the relative slip s may be obtained from the expression

$$\alpha_s = \tan^{-1}\left\{\left[\omega\zeta(\sigma_\infty, S) + \mu k_s \times \frac{2\upsilon_1 - (\upsilon_2{}^2 - 1)a_{21}}{1 - \upsilon_2 a_{21} - a_{31} - \upsilon_4 a_{41}}\right] \Big/ \kappa(\sigma_\infty, S)\right\}. \tag{21}$$

The displacement amplitudes A_n and corresponding phase shifts α_n (relative to the incident wave) of all reflected and refracted waves may be determined from S, α_s, and B_0, where

$$B_0 = A_0/(\upsilon_0{}^2 + 1)^{1/2}. \tag{22}$$

In particular,

$$(A_n/A_0) = (B_n/B_0)(\upsilon_n{}^2 + 1)^{1/2}/(\upsilon_0{}^2 + 1)^{1/2}; \quad n = 1, 2, 3, 4 \tag{23}$$

where

$$(B_1/B_0) = \frac{\begin{array}{r} \{(S/B_0)^2 \cos^2\alpha_s + [(S/B_0)\sin\alpha_s + b_4 \\ + \upsilon_2 a_{22} + a_{32} + \upsilon_4 a_{42}]^2\}^{1/2} \end{array}}{(1 - \upsilon_2 a_{21} - a_{31} - \upsilon_4 a_{41})} \tag{24}$$

$$\alpha_1 = \tan^{-1}\{[(S/B_0)\cos\alpha_s]/[(S/B_0)\sin\alpha_s + b_4 + \upsilon_2 a_{22} + a_{32} + \upsilon_4 a_{42}]\} \tag{25}$$

$$(B_n/B_0) = \{[a_{n1}(B_1/B_0)\cos\alpha_1 + a_{n2}]^2 + [a_{n1}(B_1/B_0)\sin\alpha_1]^2\}^{1/2} \quad n = 2, 3, 4 \tag{26}$$

$$\alpha_n = \tan^{-1}\{[a_{n1}(B_1/B_0)\sin\alpha_1]/[a_{n1}(B_1/B_0)\cos\alpha_1 + a_{n2}]\}; \quad n = 2, 3, 4. \tag{27}$$

Furthermore, the partitioning of incident wave energy into reflection, refraction, and absorption may be determined from the displacement amplitude ratios just presented. In particular, if E_n is the energy flux per unit area per cycle of oscillation associated with the wave of amplitude A_n (n = 0, 1, 2, 3, 4), then a measure of the portion of incident wave energy carried by this wave is given by the energy ratio e_n where

$$e_n \equiv (E_n/E_0)^{1/2} = \beta_n{}^{1/2}(A_n/A_0); \quad n = 1, 2, 3, 4 \tag{28}$$

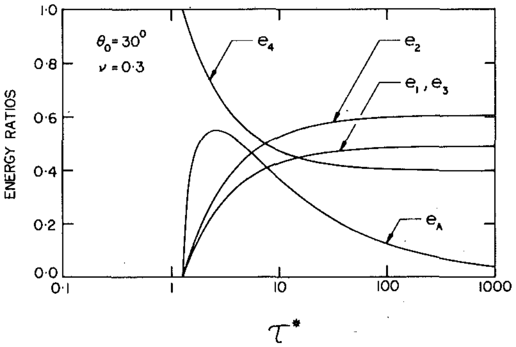

Fig. 2 Dependence of energy ratios on the stress ratio τ^* for the case of an incident SV wave

and where, for an incident SV wave,

$$\beta_1 = \frac{\upsilon_1(\upsilon_2{}^2 + 1)}{\upsilon_2(\upsilon_1{}^2 + 1)}; \quad \beta_2 = 1; \quad \beta_3 = \gamma\frac{\upsilon_3(\upsilon_4{}^2 + 1)}{\upsilon_2(\upsilon_3{}^2 + 1)}; \quad \beta_4 = \gamma\frac{\upsilon_4}{\upsilon_2} \tag{29}$$

or, for an incident P wave,

$$\beta_1 = 1; \quad \beta_2 = \frac{\upsilon_2(\upsilon_1{}^2 + 1)}{\upsilon_1(\upsilon_2{}^2 + 1)}; \quad \beta_3 = \gamma\frac{\upsilon_3(\upsilon_4{}^2 + 1)\,(\upsilon_1{}^2 + 1)}{\upsilon_1(\upsilon_2{}^2 + 1)\,(\upsilon_3{}^2 + 1)};$$

$$\beta_4 = \gamma\frac{\upsilon_4(\upsilon_1{}^2 + 1)}{\upsilon_1(\upsilon_2{}^2 + 1)}. \tag{30}$$

The amount of energy absorbed at the boundary may be obtained by subtracting the energy associated with each of the reflected and refracted waves from the energy associated with the incident wave. A convenient measure of the absorbed energy is provided by the absorption energy ratio e_A defined as

$$e_A \equiv (E_A/E_0)^{1/2} = (1 - e_1{}^2 - e_2{}^2 - e_3{}^2 - e_4{}^2)^{1/2} \tag{31}$$

where E_A is the energy flux per unit area per cycle of oscillation which is absorbed at the interface.

Results for Identical Solids Bonded by Coulomb Friction

As an illustration of the general approach presented in the previous section, consider the simple case in which bonding between solids is provided by Coulomb friction. At a given location along the interface, this model requires that the solids adhere so long as the local shear stress does not exceed a "slip stress," whose magnitude is the product of the local compressive stress and a constant coefficient of friction between surfaces. When the magnitude of the local shear stress builds up to the slip stress, local relative slipping occurs between solids. As a result, a pattern of alternate "stick" and "slip" zones will form at the interface during the passage of the train of incident waves, as discussed in a previous paper [1].

Let f denote the coefficient of friction between surfaces, and let $\sigma_c(x_1,t)$ denote the net compressive stress at any location along the interface. The local slip stress then becomes $f\sigma_c(x_1,t)$. Evaluating the integrals in equations (7) and (8) for this model of friction, it may be shown that

$$\kappa(\sigma_\infty, S) = 0; \quad \zeta(\sigma_\infty, S) = (4f\sigma_\infty)/(\pi\omega S). \tag{32}$$

Because of the mathematical simplicity of equations (32), it is possible even in the general case of dissimilar elastic solids, to obtain closed-form approximate solutions for the displacement amplitudes, phase shifts, and energies associated with each of the reflected and refracted waves. This may be accomplished by substituting from equations (32) for κ and ζ in equation (9), and solving for (S/A_0) in closed form. Closed-form expressions for the other amplitudes may then be obtained from the remaining equations in the previous section. However, in order to avoid the lengthy coefficients which result in the general case, attention will be focused on the special case of identical elastic solids for the remainder of this example.

For upper and lower solids with identical material properties, it may be shown that

$$\gamma = 1; \quad a_{21} = a_{41} = -(\upsilon_2^2 - 1)/2\upsilon_2$$
$$a_{22} = 0; \quad a_{31} = -1; \quad a_{32} = b_5; \quad a_{42} = (1 - b_5) \tag{33}$$

where, for an incident SV wave,

$$b_5 = 0 \tag{34}$$

while, for an incident P wave,

$$b_5 = 1. \tag{35}$$

Using equations (32) and (33), it may be shown for identical solids bonded by Coulomb friction that

$$(S/A_0) = \begin{cases} \dfrac{2\upsilon_2 b_3(\upsilon_2^2 + 1)}{(\upsilon_0^2 + 1)^{1/2}[4\upsilon_1\upsilon_2 + (\upsilon_2^2 - 1)^2]}\left(1 - \dfrac{4}{\pi\tau^*}\right); & \dfrac{b_3}{f|b_2|} > \tau^* \geq \dfrac{4}{\pi} \\ 0; & \dfrac{4}{\pi} \geq \tau^* \geq 0 \end{cases} \tag{36}$$

$$\alpha_s = \pi/2 \tag{37}$$

$$(A_1/A_0) = (\upsilon_1^2 + 1)^{1/2}(S/A_0)/(\upsilon_2^2 + 1); \; \alpha_1 = 0 \tag{38}$$

$$(A_2/A_0) = \frac{(\upsilon_2^2 - 1)}{2\upsilon_2(\upsilon_2^2 + 1)^{1/2}}(S/A_0); \; \alpha_2 = \pi \tag{39}$$

$$(A_3/A_0) = b_5 + (1 - 2b_5)(\upsilon_1^2 + 1)^{1/2}(S/A_0)/(\upsilon_2^2 + 1);$$

$$\alpha_3 = \pi(1 - b_5) \tag{40}$$

$$(A_4/A_0) = (1 - b_5) + (2b_5 - 1)\frac{(\upsilon_2^2 - 1)}{2\upsilon_2(\upsilon_2^2 + 1)^{1/2}}(S/A_0);$$
$$\alpha_4 = \pi b_5 \tag{41}$$

where

$$\tau^* \equiv [\mu k_s A_0 b_3/(\upsilon_0^2 + 1)^{1/2}]/(f\sigma_\infty)$$
$$= \max|\sigma_{12}^{(0)}(x_1, 0, t)|/(f\sigma_\infty). \tag{42}$$

As indicated in equation (42), the governing parameter τ^* may be interpreted as a ratio of the magnitude of $\sigma_{12}^{(0)}(x_1,0,t)$, the shear stress along the interface associated with the incident wave, to an average slip stress $f\sigma_\infty$. This stress ratio plays a central role in determining the nature of the response of the system.

When $\tau^* < (4/\pi)$, the approximate solution predicts that $S = 0$, so that no slip occurs, and the solids behave as though perfectly welded along the interface. For this range of small amplitude incident waves, equations (38)–(41) reveal that the incident wave is simply transmitted across the interface without causing any reflected or refracted waves, as expected. When $\tau^* = (4/\pi)$, a "break loose" condition is encountered, and relative slip begins to occur in alternate stick and slip zones which travel along the interface. As the amplitude of incident waves is increased so that $(4/\pi) < \tau^* < b_3/(f|b_2|)$, the energy associated with the incident wave is no longer carried across the interface by a single refracted wave. Instead, a mode conversion occurs at the interface, and some of the incident energy is carried by reflected P and SV waves, some by refracted P and SV waves, and some is absorbed at the interface. The energy ratios in this case may be obtained from equation (28) and equations (36)–(42) where, for identical elastic solids in the case of an incident SV wave,

$$\beta_1 = \beta_3 = [\upsilon_1(\upsilon_2^2 + 1)]/[\upsilon_2(\upsilon_1^2 + 1)]; \quad \beta_2 = \beta_4 = 1 \tag{43}$$

while, for an incident P wave,

$$\beta_1 = \beta_3 = 1; \quad \beta_2 = \beta_4 = [\upsilon_2(\upsilon_1^2 + 1)]/[\upsilon_1(\upsilon_2^2 + 1)]. \tag{44}$$

As the amplitude of incident waves is further increased so that $\tau^* = b_3/(f|b_2|)$, the local compressive stress vanishes at some locations along the interface, and zones of separation between solids begin to form. Since the formulation presented herein does not allow separation, the results do not apply in such a case. However, it should be noted that no separation will accompany the slip which occurs at the interface, even for rather large amplitude incident waves, if the coefficient of friction f is sufficiently small.

In addition to the stress ratio τ^*, it is clear from equations (36)–(42) that the solution also depends on υ_1 and υ_2. Furthermore, it is easily shown that υ_1 and υ_2 are functions of the angle of incidence θ_0 and Poisson's ratio ν for the identical solids. Thus the solution depends on θ_0 and ν in addition to τ^*. In contrast, the solution for the case of incident SH waves was shown in a previous paper [1] to depend on τ^* alone. The dependence on θ_0 and ν for the case of incident P or SV waves is a result of the mode conversion (P to SV and SV to P) which occurs at the interface in this case.

For the case of normally incident SV waves ($\theta_0 = 0$), the situation is identical to the case of normally incident SH waves and hence the energy ratios are independent of ν, and their dependence on the stress ratio τ^* is as shown in Fig. 2 of reference [1]. When the angle of incidence is increased to $\theta_0 = 30°$ in a solid with $\nu = 0.3$, plots of the energy ratios as functions of τ^* are shown in Fig. 2. (For $\nu = 0.3$ the critical angle is $\theta_{cr} = 32° \, 18.7'$). The curves are similar in shape to those for the case of SH motion, with the principal differences being the additional curves for the reflected and refracted P waves which occur in this case. For very small values of τ^* it is found that no slipping occurs, all the incident energy is carried by the refracted SV wave, and the interface behaves as though perfectly welded. At the opposite extreme, as $\tau^* \to \infty$ each curve approaches an asymptote which coincides with the corresponding energy ratio for a perfectly lubricated interface. At an intermediate value of τ^* ($\tau^* = 8/\pi$) it is found that the energy absorbed at the interface is maximized. These features are found to be independent of θ_0 and ν, and identical with the case of an incident SH wave. It is also found that as the angle of incidence θ_0 is increased to the critical angle θ_{cr}, the energy carried by the reflected and refracted P waves vanishes, and the curves are again identical with those for SH motion.

For the case of incident P waves, the solution presented herein is valid for all angles of incidence in the range of $0 < \theta_0 < \pi/2$. Shown in Fig. 3 are plots of the energy ratios as functions of the stress ratio τ^* for the case of a P wave incident at an angle of $\theta_0 = 60°$ in a solid with $\nu = 0.3$. Again it is found that for small values of τ^* the boundary behaves as though perfectly welded, and as $\tau^* \to \infty$ the boundary behaves as though perfectly lubricated. The asymptotic values of the energy ratios for large τ^* coincide with the corresponding values for a perfectly lubricated interface. Maximum energy absorption occurs at $\tau^* = 8/\pi$. These features are again found to be independent of θ_0 and ν. As shown in the figure, frictional slippage at the interface does not absorb much of the energy in this case, and most of the energy is carried by the refracted P wave. Furthermore, it can be shown that as $\theta_0 \to 0$ or as $\theta_0 \to \pi/2$, all of the energy is carried by the refracted P wave, and no energy is absorbed at the interface.

Energy Dissipation at the Interface. Of particular interest in this problem is the energy which is absorbed or dissipated at the interface. For the particular case of identical elastic solids bonded by Coulomb friction, it may be shown that the absorption energy ratio may be expressed as

$$e_A = \begin{cases} C\,(4/\pi\tau^*)^{1/2}\,(1 - 4/\pi\tau^*)^{1/2}; & b_3/(f|b_2|) > \tau^* \geq 4/\pi \\ 0; & 4/\pi \geq \tau^* \geq 0 \end{cases} \tag{45}$$

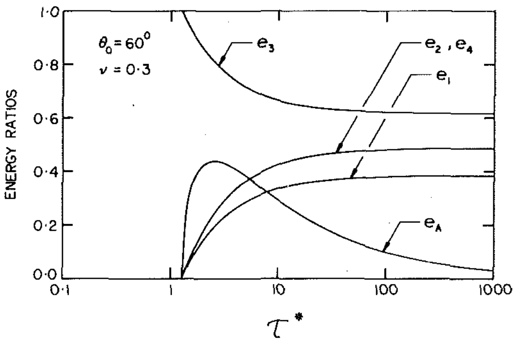

Fig. 3 Dependence of energy ratios on the stress ratio τ^* for the case of an incident *P* wave

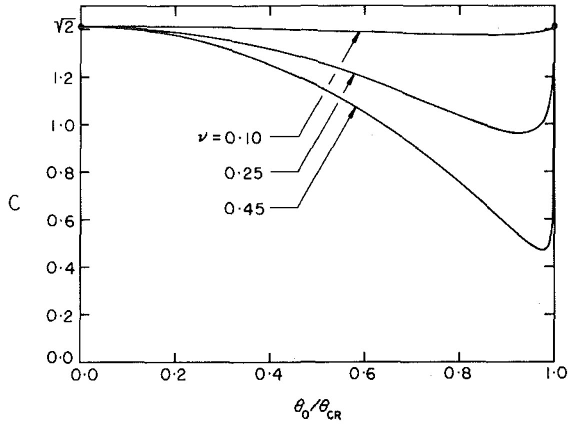

Fig. 4 Dependence of the energy dissipation coefficient *C* on the normalized angle of incidence θ_0 for the case of an incident *SV* wave

where C depends on the angle of incidence θ_0 and Poisson's ratio ν. For the case of an incident *SH* wave it can be shown [1] that $C = \sqrt{2}$, independent of θ_0 and ν.

Shown in Fig. 4 are plots of the dissipation coefficient C as a function of the angle of incidence θ_0 (normalized with respect to the critical angle) for various values of Poisson's ratio ν, for the case of an incident *SV* wave. Similar plots for the case of an incident *P* wave are shown in Fig. 5. As inferred from Fig. 4, except at normal and critical angles of incidence, less energy is absorbed at the interface for an incident *SV* wave than for an incident *SH* wave of equal amplitude. The maximum value of C is $\sqrt{2}$, and the minimum value depends on Poisson's ratio.

As inferred from Fig. 5, an incident *P* wave also results in less energy dissipation than an *SH* wave of equal amplitude. In this case, the minimum value of C is zero, while the maximum value depends on Poisson's ratio.

Conclusions

An approximate method of analysis is presented for determining the reflection, refraction, and absorption of obliquely incident planar harmonic *P* or *SV* waves at a frictional interface between dissimilar elastic solids. The solids are pressed together with pressure σ_∞, and the analysis applies only to the regime in which slip occurs at the interface without separation, and the angle of incidence is subcritical. The frictional stress at any location along the interface is assumed to depend in some prescribed manner on the local normal stress and the time history of the local slip across the interface, but remains otherwise arbitrary throughout the analyais. General results are presented for the linearized displacement amplitudes and phases of all reflected and refracted waves, and for partitioning of energy into reflection, refraction, and absorption.

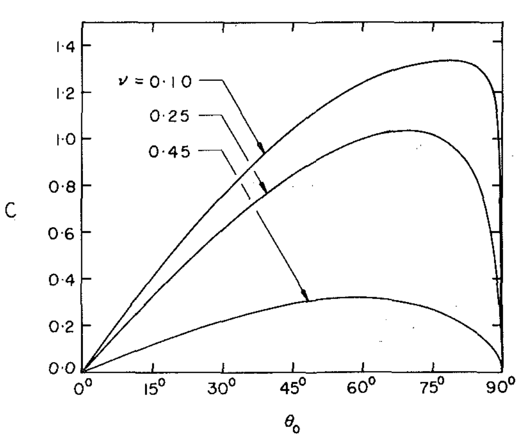

Fig. 5 Dependence of the energy dissipation coefficient *C* on the angle of incidence θ_0 for the case of an incident *P* wave

The special case of identical elastic solids bonded by Coulomb friction with coefficient of friction f is considered in detail as an example of the application of the general approach. With regard to the results for this special case, it is concluded that

1 The amount of slippage at the interface is dependent upon the stress ratio τ^*, which is the ratio of the magnitude of the peak shear stress along the interface associated with the incident wave, to an average slip stress, $f\sigma_\infty$. When $\tau^* < (4/\pi)$, the interface behaves as though perfectly welded, and no slippage occurs. When $\tau^* = (4/\pi)$, a "break loose" condition is encountered, and relative slip begins to occur in alternate stick and slip zones which travel along the interface. As $\tau^* \rightarrow \infty$, the interface behaves as though perfectly lubricated.

2 Zones of separation begin to form along the interface when the magnitude of peak normal stress along the interface associated with the incident wave equals or exceeds σ_∞. The results do not apply for such large amplitude incident waves.

3 In addition to τ^*, the energy partitioning in the system also depends on the angle of incidence, θ_0, and Poisson's ratio, ν. However, less energy is absorbed by slippage at the interface for either an incident *P* or *SV* wave than for an incident *SH* wave of equal stress amplitude.

Acknowledgments

Portions of this investigation were sponsored by the National Science Foundation under Grant No. PFR-7701096.

References

1 Miller, R. K., and Tran, H. T., "Reflection, Refraction, and Absorption of Elastic Waves at a Frictional Interface: *SH* Motion," ASME JOURNAL OF APPLIED MECHANICS, Vol. 46, 1979, pp. 625–630.

2 Aveyard, S., and Sharpe, R. S., "Applications of Ultrasonic Pulse Interference," *Proceedings, Fourth International Conference Nondestructive Testing*, Butterworth, London, 1964, pp. 150–154.

3 McClung, R. W., and Cook, K. Y., "Ultrasonic Detection of Nonbond in Clad Structures," *Proceedings, Fourth International Conference Nondestructive Testing*, Butterworth, London, 1964, pp. 267–271.

4 Ross, J. D., and Leep, R. W., "Ultrasonic Transmission Tester for Detection of Unbonded Areas," ASTM Special Technical Publication No. 223, 1958.

5 Comninou, M., and Dundurs, J., "Reflexion and Refraction of Elastic Waves in Presence of Separation," *Proceedings, Royal Society*, London, Series A, Vol. 356, 1977, pp. 509–528.

6 Comninou, M., and Dundurs, J., "Interaction of Elastic Waves With a Unilateral Interface," *Proceedings, Royal Society*, London, Series A, Vol. 368, 1979, pp. 141–154.

7 Murty, G. S., "Reflection, Transmission, and Attenuation of Elastic Waves at a Loosely Bonded Interface of Two Half Spaces," *Geophs. J. R. Astr. Soc.*, Vol. 44, 1976, pp. 389–404.

8 Dundurs, J., and Comninou, M., "Interface Separation Caused by a Plane Elastic Wave of Arbitrary Form," *Wave Motion*, Vol. 1, 1979, pp. 17–23.

9 Comninou, M., and Dundurs, J., "Interface Separation in the Transonic Range Caused by a Plane Stress Pulse," *Journal of Sound Vibration*, Vol. 62, 1979, pp. 317–325.

10 Comninou, M., and Dundurs, J., "Elastic Interface Waves Involving

Separation," ASME JOURNAL OF APPLIED MECHANICS, Vol. 44, 1977, pp. 222–226.

11 Comninou, M., and Dundurs, J., "Elastic Interface Waves and Sliding Between Two Solids," ASME JOURNAL OF APPLIED MECHANICS, Vol. 45, 1978, pp. 325–330.

12 Murty, G. S., "A Theoretical Model for the Attenuation and Dispersion of Stonely Waves at the Loosely Bonded Interface of Elastic Half Spaces," *Phys. Earth Plan. Int.*, Vol. 11, 1975, pp. 65–79.

13 Bowden, F. P., and Tabor, D., *The Friction and Lubrication of Solids—Part II*, London, Oxford University Press, 1964.

14 Rabinowicz, E., *Friction and Wear of Materials*, New York, Wiley, 1965.

15 Earles, S. W. E., and Philpot, M. G., "Energy Dissipation at Plane Surfaces in Contact," *Journal of the Mechanical Engineering Sciences*, Vol. 9, 1967, pp. 86–97.

16 Desai, C. S., personal communication.

17 Tran, H. T., "Reflection, Transmission, and Adsorption of Elastic Waves at a Frictional Boundary," MS Thesis, Department of Mechanical and Environmental Engineering, University of California, Santa Barbara, Calif., 1978.

S. Krenk
Risø National Laboratory,
4000 Roskilde,
Denmark

H. Schmidt
Structural Research Laboratory,
Technical University of Denmark,
2800 Lyngby,
Denmark

Vibration of an Elastic Circular Plate on an Elastic Half Space—A Direct Approach

The axisymmetric problem of a vibrating elastic plate on an elastic half space is solved by a direct method, in which the contact stresses and the normal displacements of the plate are taken as the unknown functions. First, the influence functions that give the displacements in terms of the stresses are determined for the half space and the plate. Displacement continuity then takes the form of an integral equation. Due to the half space the kernel is weakly singular, and a special solution technique that accounts for this is employed. The solution implies a direct matrix relation between the expansion coefficients of the contact stresses and plate deformations. The solution technique is valid for all frequencies and avoids asympototic expansion in terms of the frequency. The plate is represented by the theory of Reissner and Mindlin, which imposes physical limitations for high frequencies, but the method is easily extended to more general plate theories as well as nonsymmetric oscillations. The results include displacement and phase curves for rigid disks, power input for elastic plates, and typical stress and deformation distributions at selected phase angles. The results show considerable influence from the elastic properties of the plate.

1 Introduction

The problem of a vibrating circular plate on an elastic half space is of considerable technical interest, e.g., in connection with transducers or earthquake response of footings. It is therefore natural that a large number of papers have been devoted to the subject. Apart from the explicit solution by Reissner and Sagoci [1, 2] of the torsion problem, the problems have been formulated in terms of integral representations. Due to the mixed boundary conditions, dual integral equations are obtained for the Hankel transforms of the physical variables. A common approach has been to represent these Hankel transforms in terms of a Fourier transform, see, e.g., [3, 4]. This leads to a Fredholm integral equation of the second kind for the unknown function. This integral equation must be solved numerically.

As demonstrated by Sneddon [5], the combination of a Hankel transformation and a Fourier transformation leads to a relation in terms of Abel integrals. Thus the bulk of existing work uses an indirect method in the sense that the unknown function which is determined numerically is related to the physical variables of the problem by Abel integrals. These integrals are inconvenient for numerical calculations, and this may account for the absence of information about the distribution of the contact stresses. Another serious drawback of the indirect approach is the difficulty of incorporating more complicated boundary conditions such as those of the contact with a flexible plate.

Both these difficulties are overcome, if the contact stresses are used directly as the unknown function. However, in order to do this it is necessary to be able to represent the relation between surface stresses and surface displacements accurately numerically. This is possible by using a simple polynominal relation originally derived by Popov [6] and later extended by Krenk [7, 8]. The demonstration of this approach is the main purpose of this work, and its ability to treat rather complicated boundary conditions is illustrated through its application to the problem of an oscillating elastic circular plate on an elastic half space. Due to the difference in method reference is made to [9] for a review of previous work on rigid plates.

2 Basic Principles

In order not to obscure the basic principles of the method, the problem is limited to axisymmetric oscillations of an elastic circular plate of thickness H and radius a assumed to remain in frictionless contact with an elastic half space, Fig. 1. Vertical oscillations of any trigonometrical order including rocking and torsion can be considered in an entirely similar way by use of the formulas of [7, 8]. The problem of vibrations parallel to the half-space surface is slightly more complicated but is analogous to the problem of shear loading of a circular crack treated in [7]. Shear modulus, Poisson's ratio, and mass density are μ_p, ν_p, ρ_p for the plate and μ_h, ν_h, ρ_h for the half space. Cylindrical

---

Contributed by the Applied Mechanics Division for publication in the JOURNAL OF APPLIED MECHANICS.

Discussion on this paper should be addressed to the Editorial Department, ASME, United Engineering Center, 345 East 47th Street, New York, N. Y. 10017, and will be accepted until June 1, 1981. Readers who need more time to prepare a Discussion should request an extension from the Editorial Department. Manuscript received by ASME Applied Mechanics Division, January, 1980; final revision, July, 1980.

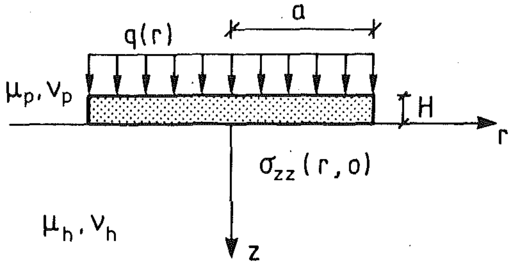

Fig. 1 A circular elastic plate on an elastic half space

coordinates $\{r, \theta, z\}$ are used with z directed into the half space. All the physical variables of the problem contain the factor exp $(i\omega t)$, where ω is the angular frequency and t is the time. When differentiation with respect to time $\partial/\partial t$ is replaced with the factor $i\omega$ and all variables are allowed to take complex values, the time factor can be omitted. This will be done here.

The vertical displacement of the contact surface of the plate is $w(r)$. The total load on the plate is composed of the external load $q(r)$ and the contact stresses $\sigma_{zz}(r)$. In the plate theory to be used in Section 4, the thickness of the plate remains unchanged, and the loads therefore only appear as the sum $p(r) = q(r) + \sigma_{zz}(r)$. When the plate is linear elastic, the surface displacement is related to the load through a relation of the form

$$w(r) = \int_0^a w_p(r, x)p(x)dx \tag{1}$$

$w_p(r, x)$ is the displacement at r due to a unit ring load at x. It is noted that within the plate theory to be used, $w_p(r, x)$ is bounded and continuous.

In order to be able to allow analysis of resonance phenomena, another load is provided for, namely, a surface displacement of the half space, $w^*(r)$, had the plate not been there. Thus the contact stresses $\sigma_{zz}(r)$ shall produce the surface displacement $w(r) - w^*(r)$ for $0 \le r < a$ in order to obtain continuity. As in the case of the plate, the field equations of the half space can be integrated to yield a relation of the form

$$w(r) - w^*(r) = \int_0^a w_h(r, x)\, \sigma_{zz}(x)\, dx \tag{2}$$

In contrast to $w_p(r, x)$, this influence function turns out to have a logarithmic singularity in $|r - x|$. This feature determines the expansions to be used.

In the case of a rigid plate $w(r)$ can be expressed directly in terms of the resulting force thus providing an integral equation that allows the determination of the contact stress $\sigma_{zz}(x)$ corresponding to a specified surface displacement. In the case of a flexible plate $w(r)$ is unknown and is eliminated between (1) and (2) yielding the following integral equation for the determination of $\sigma_{zz}(x)$.

$$\int_0^a [w_h(r, x) - w_p(r, x)]\, \sigma_{zz}(x)dx = -\, w^*(r) + \int_0^a w_p(r, x)q(x)dx \tag{3}$$

The integral equation (3) is of the first kind and therefore the logarithmic singularity contained in $w_h(r, x)$ leads to a square root singularity of the contact stress $\sigma_{zz}(r)$ at $r = a$. The object of the present method is to provide suitable representations for the integrals in (1) and (2) that accounts properly for the singularity of $\sigma_{zz}(x)$.

3 The Influence Function of the Half Space

The influence function $w_h(r, x)$ of the half space determines the nature of the solution and is therefore treated first. Introduce the dimenionless coordinates $\xi = x/a$, $\eta = r/a$, and $\zeta = z/a$. Following Bycroft [10], the displacement components $u(\eta, \zeta)$ and $w(\eta, \zeta)$ of the general solution are given as

$$u(\eta, \zeta) = a \int_0^\infty \left\{A(s)\frac{s}{\alpha(s)}e^{-\zeta\alpha(s)} + B(s)e^{-\zeta\beta(s)}\right\} sJ_1(s\eta)ds \tag{4}$$

and

$$w(\eta, \zeta) = a \int_0^\infty \left\{A(s)e^{-\zeta\alpha(s)} + B(s)\frac{s}{\beta(s)}e^{-\zeta\beta(s)}\right\} sJ_0(s\eta)ds \tag{5}$$

$J_n(\,)$ is the Bessel function of the first kind of order n [11]. $A(s)$ and $B(s)$ are arbitrary functions, while

$$\alpha(s) = \begin{cases} (s^2 - h^2)^{1/2} & s \ge h \\ i(h^2 - s^2)^{1/2} & |s| < h \\ -(s^2 - h^2)^{1/2} & s \le -h \end{cases} \tag{6}$$

and

$$\beta(s) = \begin{cases} (s^2 - k^2)^{1/2} & s \ge k \\ i(k^2 - s^2)^{1/2} & |s| < k \\ -(s^2 - k^2)^{1/2} & s \le -k \end{cases} \tag{7}$$

The dimensionless parameters h and k reflect the relative wavenumber of longitudinal and transverse waves, respectively.

$$h^2 = \frac{1}{2}\frac{1 - 2\nu_h}{1 - \nu_h}\frac{\omega^2 a^2 \rho_h}{\mu_h} \tag{8}$$

$$k^2 = \frac{\omega^2 a^2 \rho_h}{\mu_h} \tag{9}$$

The pertinent stress components are [10]

$$\sigma_{zz}{}^{22}(\eta, \zeta) = -\mu_h \int_0^\infty \left\{A(s)\frac{2s^2 - k^2}{\alpha(s)}e^{-\zeta\alpha(s)} + 2B(s)se^{-\zeta\beta(s)}\right\} sJ_0(s\eta)ds \tag{10}$$

and

$$\sigma_{rz}(\eta, \zeta) = -\mu_h \int_0^\infty \left\{2A(s)se^{-\zeta\alpha(s)} + B(s)\frac{2s^2 - k^2}{\beta(s)}e^{-\zeta\beta(s)}\right\} sJ_1(s\eta)ds \tag{11}$$

When the surface $\zeta = 0$ is assumed to be free of shear stress, the integral representation (11) provides a relation between $A(s)$ and $B(s)$. After elimination of $A(s)$ or $B(s)$ inversion of (10) and substitution into (5) yields the following relation:

$$w(\eta, 0) = \frac{ak^2}{4\mu_h}\int_0^\infty \frac{\alpha(s)sJ_0(s\eta)}{(s^2 - \tfrac{1}{2}k^2)^2 - s^2\alpha(s)\beta(s)} \times \int_0^1 \sigma_{zz}(\xi, 0)\xi J_0(s\xi)d\xi ds \tag{12}$$

The denominator in (12) has a zero between k and infinity corresponding to the occurrence of Rayleigh waves. As shown by Bycroft [10], the integral representation accounts properly for the Rayleigh waves, if the integration with respect to s is performed along a contour indented with positive imaginary part at the pole. The corresponding formula for $u(\eta, 0)$ in terms of $\sigma_{zz}(\xi, 0)$ is

$$u(\eta, 0) = -\frac{a}{2\mu_h}\int_0^\infty \frac{s^2 - \tfrac{1}{2}k^2 - \alpha(s)\beta(s)}{(s^2 - \tfrac{1}{2}k^2)^2 - s^2\alpha(s)\beta(s)} s^2 J_1(s\eta) \times \int_0^1 \sigma_{zz}(\xi, 0)\xi J_0(s\xi)d\xi ds \tag{13}$$

It is not immediately obvious that the order of integration in (12) can be reversed, and the asymptotic behavior for large s is therefore extracted. From the definitions (6)–(9)

$$\lim_{s/k\to\infty} \frac{k^2}{4(1 - \nu_h)}\frac{s\alpha(s)}{(s^2 - \tfrac{1}{2}k^2)^2 - s^2\alpha(s)\beta(s)} = -1 \tag{14}$$

It is noted that the limit process only involves the ratio s/k. In the case of a vibration problem $k \neq 0$, and the limit is used to extract the dominant part of the integral. Alternatively the limit process corresponds to $\omega \to 0$, i.e., the static problem, for any fixed value of s. Therefore the dominant part of the integral for the vibration problem is identical to that of the corresponding static problem. The dominant part of (12) is

$$w_s(\eta) = a \int_0^\infty J_0(s\eta) \left\{ -\frac{1-\nu_h}{\mu_h} \int_0^1 \sigma_{zz}(\xi, 0)\xi J_0(s\xi)d\xi \right\} ds \quad (15)$$

A change of the order of integration would lead to the kernel [12],

$$\int_0^\infty J_0(s\eta)J_0(s\xi)ds = \begin{cases} \dfrac{1}{\eta}\, {}_2F_1\left(\tfrac{1}{2}, \tfrac{1}{2}, 1, \left(\dfrac{\xi}{\eta}\right)^2\right) = \dfrac{2}{\pi\eta} K\left(\dfrac{\xi}{\eta}\right), & \xi < \eta \\ \dfrac{1}{\xi}\, {}_2F_1\left(\tfrac{1}{2}, \tfrac{1}{2}, 1, \left(\dfrac{\eta}{\xi}\right)^2\right) = \dfrac{2}{\pi\xi} K\left(\dfrac{\eta}{\xi}\right), & \eta < \xi \end{cases} \quad (16)$$

where $K(\ )$ is the complete elliptic integral of the first kind. Asymptotic analysis of (16) reveals a logarithmic singularity at $\xi = \eta$, and a bounded Hölder continuous function $w_s(\eta)$ in (15) therefore requires $\sigma_{zz}(\xi, 0)$ to have a square root singularity at $\xi = 1$.

What is needed is not a numerical calculation of the singular kernel (16), but an expansion of $\sigma_{zz}(\xi, 0)$ for which the corresponding expansion of $w(\eta, 0)$ can be easily evaluated. Such an expansion was found by Popov [6]. Let $\sigma_{zz}(\eta, 0)$ be given by

$$-\frac{1-\nu_h}{\mu_h}\sigma_{zz}(\eta, 0) = (1-\eta^2)^{-1/2} \sum_{j=0}^\infty S_j P_{2j}(\sqrt{1-\eta^2})/P_{2j}(0) \qquad 0 \le \eta \le 1 \quad (17)$$

where $P_m(\ )$ is the Legendre polynomial of degree m [12]. The polynomials are normalized at $\eta = 1$ by the constants

$$P_{2j}(0) = (-1)^j 2^{2j} \binom{2j}{j} \quad (18)$$

From Sonine's first integral and the recurrence relations for the Legendre polynomials and the Bessel functions, the following formula is derived, Krenk [8].

$$\frac{1}{P_{2j}(0)} \int_0^1 (1-\eta^2)^{-1/2} P_{2j}(\sqrt{1-\eta^2})\eta J_0(s\eta)d\eta = (-1)^j j_{2j}(s) \quad (19)$$

$j_m(\ )$ is the spherical Bessel function of the first kind [11],

$$j_m(s) = \sqrt{\frac{\pi}{2s}}\, J_{m+1/2}(s) \quad (20)$$

Substitution of (17) into (15) and use of (19) and the discontinuous Weber-Schafheitlin integral—Watson [13]—lead to

$$w_s(\eta) = a \sum_{j=0}^\infty (-1)^j S_j \int_0^\infty J_0(s\eta) j_{2j}(s)ds$$
$$= a \sum_{j=0}^\infty S_j P_{2j}(0) \begin{cases} \dfrac{\pi}{2} P_{2j}(\sqrt{1-\eta^2}), & 0 \le \eta < 1 \\ iQ_{2j}(i\sqrt{\eta^2-1}), & 1 < \eta \end{cases} \quad (21)$$

This formula is a special case of more general results derived by Gladwell [14] and Krenk [8]. In view of this result it is convenient to represent the normal displacement within the contact area in the form

$$w(\eta, 0) = a \sum_{m=0}^\infty W_m P_{2m}(\sqrt{1-\eta^2})P_{2m}(0), \quad 0 \le \eta < 1 \quad (22)$$

A similar expansion with coefficients W_m^* is used for the displacement $w^*(r)$.

The integral (12) is calculated by extracting the asymptotic value (14) and substituting the expansions (17) and (22)

$$\sum_{m=0}^\infty W_m P_{2m}(\sqrt{1-\eta^2})P_{2m}(0) = \sum_{j=0}^\infty S_j \left\{ \frac{\pi}{2} P_{2j}(\sqrt{1-\eta^2})P_{2j}(0) \right.$$
$$-(-1)^j \int_0^\infty \left(\frac{k^2}{4(1-\nu_h)} \frac{s\alpha(s)}{(s^2 - \tfrac{1}{2}k^2)^2 - s^2\alpha(s)\beta(s)} + 1 \right)$$
$$\left. \times J_0(s\eta) j_{2j}(s)ds \right\}, \qquad 0 \le \eta \le 1 \quad (23)$$

The coefficients W_m can be evaluated by use of the orthogonality relations for the Legendre polynomials, here in the form

$$\int_0^1 P_{2j}(\sqrt{1-\eta^2})P_{2m}(\sqrt{1-\eta^2}) \frac{\eta d\eta}{\sqrt{1-\eta^2}} = \begin{cases} 0, & j \neq m \\ \dfrac{1}{4m+1}, & j = m \end{cases} \quad (24)$$

As the asymptotic behavior has been extracted, the order of integration can be reversed, and use can again be made of (19).

$$W_m = \sum_{j=0}^\infty S_j \left\{ \frac{\pi}{2} - (-1)^{j+m}(4m+1) \right.$$
$$\left. \times \int_0^\infty \left(\frac{k^2}{4(1-\nu_h)} \frac{s\alpha(s)}{(s^2 - \tfrac{1}{2}k^2)^2 - s^2\alpha(s)\beta(s)} + 1 \right) j_{2m}(s) j_{2j}(s)ds \right\} \quad (25)$$

This formula can be written in the form

$$W_m = (4m+1) \sum_{j=0}^\infty (-1)^{j+m} S_j A_{jm}^h \quad (26)$$

which is the desired discretized form of the stress deformation relation (2) for the half space. Due to (14) the integral vanishes in the static case.

The expression for the matrix A_{jm}^h is reduced in two steps. First, it is observed that the term $\pi/2$ in (25) can be written in integral form by use of the orthogonality relation of the Bessel functions, thereby cancelling the constant 1. Thus explicit extraction of the singularity of the kernel proves unnecessary in the numerical calculations. Secondly, the integral can be reduced to integrals over finite intervals by calculus of residues. The necessary formulae are derived in the Appendix. The result is

$$A_{jm}^h = -\int_0^\infty \frac{k^2}{4(1-\nu_h)} \frac{s\alpha(s)}{(s^2 - \tfrac{1}{2}k^2)^2 - s^2\alpha(s)\beta(s)} j_{2j}(s) j_{2m}(s)ds$$
$$= -\frac{i\pi k}{4(1-\nu_h)} \frac{\xi_R^2(\xi_R^2 - \gamma^2)\sqrt{\xi_R^2 - 1}}{3(1-\gamma^2)\xi_R^4 - (3-2\gamma^2)\xi_R^2 + \tfrac{1}{2}} h_{2j}^{(2)}(k\xi_R) j_{2m}(k\xi_R)$$
$$- \frac{ik}{4(1-\nu_h)} \int_0^\gamma \frac{\xi\sqrt{\gamma^2 - \xi^2}}{(\xi^2 - \tfrac{1}{2})^2 + \xi^2\sqrt{1-\xi^2}\sqrt{\gamma^2-\xi^2}} h_{2j}^{(2)}(k\xi)\, j_{2m}(k\xi)d\xi$$
$$- \frac{ik}{4(1-\nu_h)} \int_\gamma^1 \frac{(\xi^2 - \gamma^2)\xi^3\sqrt{1-\xi^2}}{(\xi^2 - \tfrac{1}{2})^4 + \xi^4(1-\xi^2)(\xi^2-\gamma^2)} h_{2j}^{(2)}(k\xi)\, j_{2m}(k\xi)d\xi, \qquad j \le m \quad (27)$$

For $j > m$ it is used that $A_{mj}^h = A_{jm}^h$. The material constant γ is defined by

$$\gamma^2 = \frac{1}{2}\frac{1-2\nu_h}{1-\nu_h} \quad (28)$$

and ξ_R is the relative slowness of Rayleigh waves, i.e., the positive root of the denominator of the first intergral formula for A_{jm}^h. $h_m^{(2)}(s)$ is the spherical Bessel function of the third kind [11]. Bycroft, who assumed the pressure distribution of the static case and a rigid disk, was led to the particular case of $j = 0$ in (27), a fact that is not surprising in view of its derivation. The asymptotic method of Robertson [3, 4] leads to a similar expression but with the Bessel function products replaced with powers of s. The accuracy of the power series expansion thereby implied for the spherical Bessel functions clearly depends on the magnitude of the dimensionless frequency k.

4 The Influence Function of the Plate

The plate is described in terms of the plate equations of Mindlin [15]. They include the effect of transverse shear deformations, and account for the inertial terms through an assumption of straight normals. As shown by Reissner [16] this assumption is not true and is in fact unnecessary, but as shown by Mindlin [15] the rotatory inertia plays a minor role compared to the effect of transverse deformation.

The generalized displacements are the transverse deformation w of the middle surface and in the present case of axial symmetry the angle ψ between the normal and the z-axis. The nonvanishing moments and shear forces are

$$M_r = D\left[\frac{1}{r}\frac{\partial}{\partial r}(r\psi) - (1-\nu_p)\frac{\psi}{r}\right] \tag{29}$$

$$M_\theta = D\left[\nu_p\frac{1}{r}\frac{\partial}{\partial r}(r\psi) + (1-\nu_p)\frac{\psi}{r}\right] \tag{30}$$

$$Q_r = \kappa^2\mu_p H\left[\frac{\partial w}{\partial r} + \psi\right] \tag{31}$$

D is the flexural rigidity of the plate $D = H^3\mu_p/6(1-\nu_p)$, and κ^2 is a parameter that accounts for the averaging of the shear stress distribution. A parabolic distribution gives $\kappa^2 = 5/6$, while Mindlin [15] suggests $\kappa^2 = \pi^2/12$, because this value gives the correct thickness-shear frequency.

In terms of the generalized displacements the equations of motion are for rotation

$$D\frac{\partial}{\partial r}\left(\frac{1}{r}\frac{\partial}{\partial r}(r\psi)\right) - \kappa^2\mu_p H\left(\frac{\partial w}{\partial r} + \psi\right) + \frac{\rho_p H^3}{12}\omega^2\psi = 0 \tag{32}$$

and for translantion

$$\kappa^2\mu_p H\left(\frac{1}{r}\frac{\partial}{\partial r}\left(r\frac{\partial w}{\partial r}\right) + \frac{1}{r}\frac{\partial}{\partial r}(r\psi)\right) + \rho_p H\omega^2 w + p = 0 \tag{33}$$

where $p(r)$ is the total transverse load on the plate.

The following notation is introduced:

$$\tau = \frac{H}{a} \tag{34}$$

$$\omega_S^2 = \frac{12\kappa^2\mu_p}{H^2\rho_p} \tag{35}$$

$$\omega_E^2 = \frac{2\mu_p}{H^2(1-\nu_p)\rho_p} \tag{36}$$

where ω_S is the angular thickness-shear frequency.

It is convenient to replace ψ, which is a vector component, by

$$\varphi = \frac{1}{r}\frac{\partial}{\partial r}(r\psi) \tag{37}$$

which is the divergence of the vector $(\psi, 0)$. As $\psi(0) = 0$ (37) provides a unique relation between φ and ψ. When ψ is eliminated between (32) and (33), the resulting differential equation for w can be written as

$$\left[\left(\nabla^2 + \frac{12}{\tau^2}\left(\frac{\omega}{\omega_S}\right)^2\right)\left(\nabla^2 + \frac{1}{\tau^2}\left(\frac{\omega}{\omega_E}\right)^2\right) - \frac{12}{\tau^4}\left(\frac{\omega}{\omega_E}\right)^2\right]w = \left[1 - \tau^2\left(\frac{\omega_E}{\omega_S}\right)^2\nabla^2 - \left(\frac{\omega}{\omega_S}\right)^2\right]\frac{a^4 p}{D} \tag{38}$$

with the dimensionless radial coordinate $\eta = r/a$ and the differential operator

$$\nabla^2 = \frac{1}{\eta}\frac{\partial}{\partial\eta}\eta\frac{\partial}{\partial\eta}.$$

φ follows from (33),

$$a^2\varphi = -\left(\nabla^2 + \frac{12}{\tau^2}\left(\frac{\omega}{\omega_S}\right)^2\right)w - \tau^2\left(\frac{\omega_E}{\omega_S}\right)^2\frac{a^4 p}{D} \tag{39}$$

The equations are solved by factorizing (38) in the form

$$[\nabla^2 + \delta_1^2(\omega)][\nabla^2 + \delta_2^2(\omega)]\,w = \left[1 - \tau^2\left(\frac{\omega_E}{\omega_S}\right)^2\nabla^2 - \left(\frac{\omega}{\omega_S}\right)^2\right]\frac{a^4 p}{D} \tag{40}$$

with

$$2\tau^2\delta_{1,2}^2(\omega) = 12\left(\frac{\omega}{\omega_S}\right)^2 + \left(\frac{\omega}{\omega_E}\right)^2 \pm\sqrt{\left[12\left(\frac{\omega}{\omega_S}\right)^2 - \left(\frac{\omega}{\omega_E}\right)^2\right]^2 + 48\left(\frac{\omega}{\omega_E}\right)^2} \tag{41}$$

$\delta_1^2(\omega)$ is positive for all values of ω, whereas $\delta_2^2(\omega) < 0$ for $0 < \omega < \omega_S$ and $\delta_2^2(\omega) > 0$ for $\omega_S < \omega$. For $0 < \omega < \omega_S$ we introduce the notation $\delta_2^*(\omega)$, where $(\delta_2^*(\omega))^2 = -(\delta_2(\omega))^2$.

Now it is a rather simple matter to construct the solution corresponding to a concentrated ring load of magnitude 1 at x, when ω is not an eigenfrequency of the free plate. The solution of the homogeneous equation (38) with $p(r) = 0$ in the domains $0 \le r < x$ and $x < r \le a$ involves six arbitrary constants, which depend on x. The solution is given for $0 < \omega < \omega_S$, and the necessary changes for $\omega_S < \omega$ indicated afterwards. In terms of the dimensionless coordinates η and ξ

$$w_p(\eta,\xi)/a = C_1(\xi)J_0(\delta_1\eta) + C_2(\xi)I_0(\delta_2^*\eta), \quad 0 \le \eta \le \xi \tag{42}$$

$$w_p(\eta,\xi)/a = C_3(\xi)J_0(\delta_1\eta) + C_4(\xi)I_0(\delta_2^*\eta) \quad C_5(\xi)Y_0(\delta_1\eta) + C_6(\xi)K_0(\delta_2^*\eta), \quad \xi \le \eta \le 1 \tag{43}$$

$J_0(\ )$ and $Y_0(\ )$ are the Bessel functions of order zero. $I_0(\ )$ and $K_0(\ )$ are the corresponding modified Bessel functions [11]. φ follows from (39):

$$\varphi(\eta,\xi)a = C_1(\xi)\left[\delta_1^2 - \frac{12}{\tau^2}\left(\frac{\omega}{\omega_S}\right)^2\right]J_0(\delta_1\eta) + C_2(\xi)\left[\delta_2^2 - \frac{12}{\tau^2}\left(\frac{\omega}{\omega_S}\right)^2\right] \times I_0(\delta_2^*\eta), \quad 0 \le \eta \le \xi \tag{44}$$

$$\begin{aligned}\varphi(\eta,\xi)a = {} & C_3(\xi)\left[\delta_1^2 - \frac{12}{\tau^2}\left(\frac{\omega}{\omega_S}\right)^2\right]J_0(\delta_1\eta) \\ & + C_4(\xi)\left[\delta_2^2 - \frac{12}{\tau^2}\left(\frac{\omega}{\omega_S}\right)^2\right]I_0(\delta_2^*\eta) + C_5(\xi)\left[\delta_1^2 - \frac{12}{\tau^2}\left(\frac{\omega}{\omega_S}\right)^2\right]Y_0(\delta_1\eta) \\ & + C_6(\xi)\left[\delta_2^2 - \frac{12}{\tau^2}\left(\frac{\omega}{\omega_S}\right)^2\right]K_0(\delta_2^*\eta), \quad \xi \le \eta \le 1\end{aligned} \tag{45}$$

ψ follows by integration of (37)

$$\psi(\eta,\xi) = \frac{C_1(\xi)}{\delta_1}\left[\delta_1^2 - \frac{12}{\tau^2}\left(\frac{\omega}{\omega_S}\right)^2\right]J_1(\delta_1\eta) + \frac{C_2(\xi)}{\delta_2^*}\left[\delta_2^2 - \frac{12}{\tau^2}\left(\frac{\omega}{\omega_S}\right)^2\right]I_1(\delta_2^*\eta), \quad 0 \le \eta \le 1 \tag{46}$$

$$\begin{aligned}\psi(\eta,\xi) = {} & \frac{C_3(\xi)}{\delta_1}\left[\delta_1^2 - \frac{12}{\tau^2}\left(\frac{\omega}{\omega_S}\right)^2\right]J_1(\delta_1\eta) \\ & + \frac{C_4(\xi)}{\delta_2^*}\left[\delta_2^2 - \frac{12}{\tau^2}\left(\frac{\omega}{\omega_S}\right)^2\right]I_1(\delta_2^*\eta) + \frac{C_5(\xi)}{\delta_1}\left[\delta_1^2 - \frac{12}{\tau^2}\left(\frac{\omega}{\omega_S}\right)^2\right]Y_1(\delta_1\eta) \\ & - \frac{C_6(\xi)}{\delta_2^*}\left[\delta_2^2 - \frac{12}{\tau^2}\left(\frac{\omega}{\omega_S}\right)^2\right]K_1(\delta_2^*\eta), \quad \xi \le \eta \le 1\end{aligned} \tag{47}$$

The moment is given by (29)

$$M_r = D\left(\varphi - (1-\nu_p)\frac{\psi}{r}\right) \tag{48}$$

$\psi(\eta,\xi)$ is continuous for $0 \le \eta \le 1$, and it then follows from (48) that continuity of $M_r(\eta,\xi)$ is equivalent to continuity of $\varphi(\eta,\xi)$ as given by (44) and (45). The shear force is given by (31). After use of (35) and (36)

$$Q_r(\eta,\xi)\frac{1-\nu_p}{2\mu_p}\frac{\tau}{a}\left(\frac{\omega_E}{\omega}\right)^2 = -\frac{C_1(\xi)}{\delta_1}J_1(\delta_1\eta) - \frac{C_2(\xi)}{\delta_2^*}I_1(\delta_2^*\eta), \quad 0 \le \eta \le \xi \tag{49}$$

$$Q_r(\eta,\xi)\frac{1-\nu_p}{2\mu_p}\frac{\tau}{a}\left(\frac{\omega_E}{\omega}\right)^2=-\frac{C_3(\xi)}{\delta_1}J_1(\delta_1\eta)-\frac{C_4(\xi)}{\delta_2^*}I_1(\delta_2^*\eta)$$

$$-\frac{C_5(\xi)}{\delta_1}Y_1(\delta_1\eta)+\frac{C_6(\xi)}{\delta_2^*}K_1(\delta_2^*\eta),\quad \xi\le\eta\le 1 \qquad (50)$$

The parameters $C_1(\xi),\ldots,C_6(\xi)$ are determined from the boundary conditions $M_r=Q_r=0$ for $\eta=1$, continuity of w, ψ, and φ at $\eta=\xi$, and the discontinuity condition $Q_r(\xi-,\xi)-Q_r(\xi+,\xi)=1$. The resulting equations (51) follow from (42)–(50) by suitable linear combinations.

$$\begin{bmatrix} J_0(\delta_1\xi) & I_0(\delta_2^*\xi) & -J_0(\delta_1\xi) & -I_0(\delta_2^*\xi) & -Y_0(\delta_1\xi) & -K_0(\delta_2^*\xi) \\ \delta_1^2J_0(\delta_1\xi) & \delta_2^2I_0(\delta_2^*\xi) & -\delta_1^2J_0(\delta_1\xi) & -\delta_2^2I_0(\delta_2^*\xi) & -\delta_1^2Y_0(\delta_1\xi) & -\delta_2^2K_0(\delta_2^*\xi) \\ \delta_1J_1(\delta_1\xi) & -\delta_2^*I_1(\delta_2^*\xi) & -\delta_1J_1(\delta_1\xi) & -\delta_2^*I_1(\delta_2^*\xi) & -\delta_1Y_1(\delta_1\xi) & -\delta_2^*K_1(\delta_2^*\xi) \\ -\frac{1}{\delta_1}J_1(\delta_1\xi) & -\frac{1}{\delta_2^*}I_1(\delta_2^*\xi) & \frac{1}{\delta_1}J_1(\delta_1\xi) & \frac{1}{\delta_2^*}I_1(\delta_2^*\xi) & \frac{1}{\delta_1}Y_1(\delta_1\xi) & -\frac{1}{\delta_2^*}K_1(\delta_2^*\xi) \\ 0 & 0 & \frac{1}{\delta_1}J_1(\delta_1) & \frac{1}{\delta_2^*}I_1(\delta_2^*) & \frac{1}{\delta_1}Y_1(\delta_1) & -\frac{1}{\delta_2^*}K_1(\delta_2^*) \\ 0 & 0 & [\delta_1^2-\frac{12}{\tau^2}(\frac{\omega}{\omega_S})^2] & [\delta_2^2-\frac{12}{\tau^2}(\frac{\omega}{\omega_S})^2] & [\delta_1^2-\frac{12}{\tau^2}(\frac{\omega}{\omega_S})^2] & [\delta_2^2-\frac{12}{\tau^2}(\frac{\omega}{\omega_S})^2] \\ & & [J_0(\delta_1)-\frac{1-\nu_p}{\delta_1}J_1(\delta_1)] & [I_0(\delta_2^*)-\frac{1-\nu_p}{\delta_2^*}I_1(\delta_2^*)] & [Y_0(\delta_1)-\frac{1-\nu_p}{\delta_1}Y_1(\delta_1)] & [K_0(\delta_2^*)+\frac{1-\nu_p}{\delta_2^*}K_1(\delta_2^*)] \end{bmatrix} \begin{bmatrix} C_1(\xi) \\ C_2(\xi) \\ C_3(\xi) \\ C_4(\xi) \\ C_5(\xi) \\ C_6(\xi) \\ \\ \end{bmatrix} = \begin{bmatrix} 0 \\ 0 \\ -6\frac{1-\nu_p}{\mu_p}\frac{1}{\tau a}(\frac{\omega_E}{\omega_S})^2 \\ \frac{1-\nu_p}{2\mu_p}\frac{\tau}{a}(\frac{\omega_E}{\omega})^2 \\ 0 \\ 0 \\ \\ \end{bmatrix} \qquad (51)$$

For $\omega_S<\omega$ all coefficients to C_2, C_4, and C_6 are identical to those of C_1, C_3, and C_5, but with δ_2 instead of δ_1. The degenerate cases $\xi=0$, $\xi=1$, and $\omega=\omega_S$ can be evaluated by a similar procedure.

Discretization of $w_p(\eta,\xi)$ is divided into two steps because the contact stress $\sigma_{zz}(\eta,0)$ is singular at $\eta=1$, while the external load $q(\eta)$ will be assumed bounded. The following polynomial expansion for $w_p(\eta,\xi)$ is used.

$$\frac{\mu_p}{1-\nu_p}w_p(\eta,\xi)=\sum_{j=0}^{\infty}\sum_{m=0}^{\infty}(4j+1)A^p_{jm}\xi P_{2j}(\sqrt{1-\xi^2})$$
$$\times P_{2m}(\sqrt{1-\eta^2})P_{2j}(0)P_{2m}(0) \qquad (52)$$

The coefficient matrix A^p_{jm} is found by use of the orthogonality relation (24).

$$A^p_{jm}P_{2j}(0)P_{2m}(0)=\frac{\mu_p}{1-\nu_p}\int_0^1\int_0^1 w_p(\eta,\xi)\eta$$
$$\times\frac{P_{2m}(\sqrt{1-\eta^2})}{\sqrt{1-\eta^2}}\frac{P_{2j}(\sqrt{1-\xi^2})}{\sqrt{1-\xi^2}}d\eta d\xi \qquad (53)$$

Substitution of the contact stress in the form (17) and $w_p(\eta,\xi)$ from (52) gives the following expansion coefficients for the displacement of the plate due to contact stresses.

$$W_m=-\frac{1-\nu_p}{1-\nu_h}\frac{\mu_h}{\mu_p}(4m+1)\sum_{j=0}^{\infty}S_jA^p_{jm} \qquad (54)$$

The external load $q(\xi)$ is expanded as

$$\frac{1-\nu_h}{\mu_h}q(\xi)=\sum_{k=0}^{\infty}N_k\frac{P_{2k+1}(\sqrt{1-\xi^2})}{\sqrt{1-\xi^2}P'_{2k+1}(0)} \qquad (55)$$

where the normalizing factor is

$$P'_{2k+1}(0)=(-1)^k(2k+1)2^{-2k}\binom{2k}{k} \qquad (56)$$

When (55) and (52) are substituted into (1) the following formula is needed [17, p. 306].

$$\int_0^1 P_{2j}(s)P_{2k+1}(s)ds$$
$$=\frac{(-1)^{j+k}(2j)!(2k+1)!}{2^{2j+2k}(2k+1-2j)(2j+2k+2)(j!)^2(k!)^2} \qquad (57)$$

After a slight reduction the expansion coefficients for the displacement of the plate due to the external load (55) take the form

$$W_m=\frac{1-\nu_p}{1-\nu_h}\frac{\mu_h}{\mu_p}(4m+1)\sum_{j=0}^{\infty}\sum_{k=0}^{\infty}A^p_{jm}M_{jk}N_k \qquad (58)$$

where

$$M_{jk}=\frac{(4j+1)[P_{2j}(0)]^2}{(2k+1-2j)(2j+2k+2)} \qquad (59)$$

5 Numerical Solution and Results

By substitution of the appropriate series expansions into (3), the following infinite system of equations is obtained:

$$(4m+1)\sum_{j=0}^{\infty}\left[(-1)^{j+m}A^h_{jm}+\frac{1-\nu_p}{1-\nu_h}\frac{\mu_h}{\mu_p}A^p_{jm}\right]S_j$$
$$=-W^*_m+(4m+1)\sum_{j=0}^{\infty}\left[\frac{1-\nu_p}{1-\nu_h}\frac{\mu_h}{\mu_p}A^p_{jm}\sum_{k=0}^{\infty}M_{jk}N_k\right],$$
$$m=0,1,\ldots \qquad (60)$$

The solution is obtained by truncating all series to a maximum of N-terms. The total displacement follows from (2) by use of (26).

$$W_m=(4m+1)\sum_{j=0}^{\infty}[(-1)^{j+m}A^h_{jm}S_j]+W^*_m,\quad m=0,1,\ldots \qquad (61)$$

The bulk of the calculations is the evaluation of the matrices A^h_{jm} and A^p_{jm}. The matrix A^h_{jm} is calculated from (27) by Gauss-Jacobi quadrature accounting for the behavior of the integrands near the end points of the intervals of integration. The matrix A^p_{jm} is evaluated from (53) by Gauss-Legendre quadrature after a variable transformation. In both cases weights and abscissae were evaluated by the subroutine of Stroud and Secrest [18]. Due to the discontinuity of the derivatives of $w_p(\eta,\xi)$ at $\eta=\xi$ the number of integration points necessary for the evaluation of A^p_{jm} will be larger than N. The efficiency can be improved by extracting the discontinuities explicitly.

A Rigid Disk. In the limit $\mu_p\to\infty$, i.e., a rigid disk, the formulation must be modified. In this case $w(\eta)=aW_0$, and (1) is replaced by the equation of motion for the disk.

$$-\omega^2Mw=2\pi\int_0^a p(r)rdr \qquad (62)$$

where $M=\pi a^2H\rho_p$ is the mass of the disk. By substitution of the expansion (17) for $\sigma_{zz}(r)$ and (55) for $q(r)$ the relation (62) takes the form

$$W_0=\frac{2\rho_h}{k^2\rho_p\tau(1-\nu_h)}\left[S_0-\sum_{k=0}^{\infty}M_{0k}N_k\right] \qquad (63)$$

The modification of the equations (60) amounts to the following replacements:

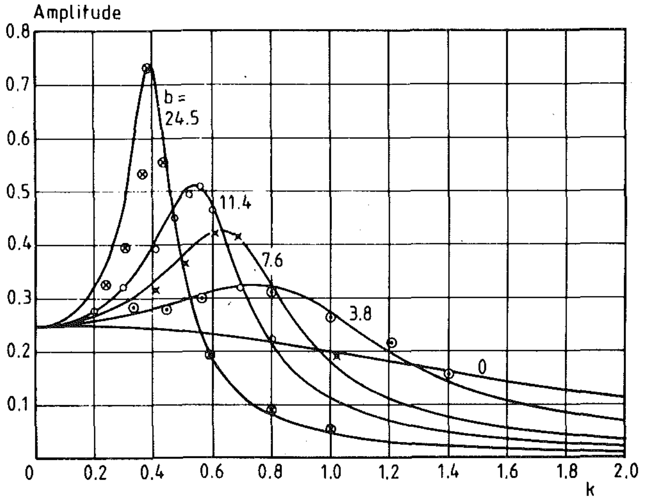

Fig. 2 Displacement amplitudes from present theory and experiments [19]

$$(4m+1)\frac{1-\nu_p}{1-\nu_h}\frac{\mu_h}{\mu_p}A^p_{jm} \rightarrow \begin{cases} \dfrac{-2\rho_h}{k^2\rho_p\tau(1-\nu_h)}, & m=j=0 \\ 0 & \text{else} \end{cases} \tag{64}$$

In any investigations restricted to rigid disks it will, of course, be more convenient to represent the external load $q(\xi)$ directly in terms of its resultant instead of using (55). In that particular case the effect of the mass can be accounted for explicitly because the resultant inertial force is in phase with the displacement [3, 10].

Experiments have been carried out by Arnold, et al. [19], using foam rubber for the half space. The experimental results are compared with theoretical curves obtained by the present method in Fig. 2. The dimensionless displacement amplitude $d = |\mu_h a w/F|$ is shown as function of the dimensionless frequency $k = \omega a\sqrt{\rho_h/\mu_h}$. F is the amplitude of the external force. The curves correspond to different values of the mass ratio $b = M/(\rho_h a^3) = \pi\tau\rho_p/\rho_h$. The calculated results show slight deviations from calculations given in [19] based on the static stress distribution [10]. There is a general tendency for the experimental points to fall below the theoretical curves for small frequencies. Apart from the case of $b = 24.5$ an excellent fit can be obtained for all frequencies by increasing the value of Poisson's ratio from $\nu_h = 0$ used in Fig. 2 and in [19] to $\nu_h \approx 0.05$.

The accuracy of the present method is supported by the excellent agreement with the results of Robertson [3] for $b = 0$ as well as regarding the resonant amplitudes and frequencies given in Table 3 of [3][1]. Also the static limit $d \rightarrow (1-\nu_h)/4$ is accurately reproduced.

In connection with ultrasonic and acoustic emission transducers a broader frequency range is needed and typical mass ratios will be much lower. Some results in the area of interest are shown in Fig. 3 for $\nu_h = 0.25$. Expansions with $N = 10$ terms for low frequencies increasing to $N = 20$ for the higher frequencies were used. Doubling of the number of terms only gave negligible changes.

Elastic Plates. In the case of elastic plates no single displacement parameter describes the response of the plate to an oscillating external load. The best single parameter seems to be the average power input $\langle P\rangle$. As no damping is assumed in the plate the power input can be expressed in terms of the contact stress and the surface velocity of the half space.

$$\langle P\rangle = 2\pi\int_0^a \langle \mathrm{Re}\,[\sigma_{zz}(r)e^{i\omega t}]\,\mathrm{Re}\,[i\omega w(r)e^{i\omega t}]\rangle r\,dr \tag{65}$$

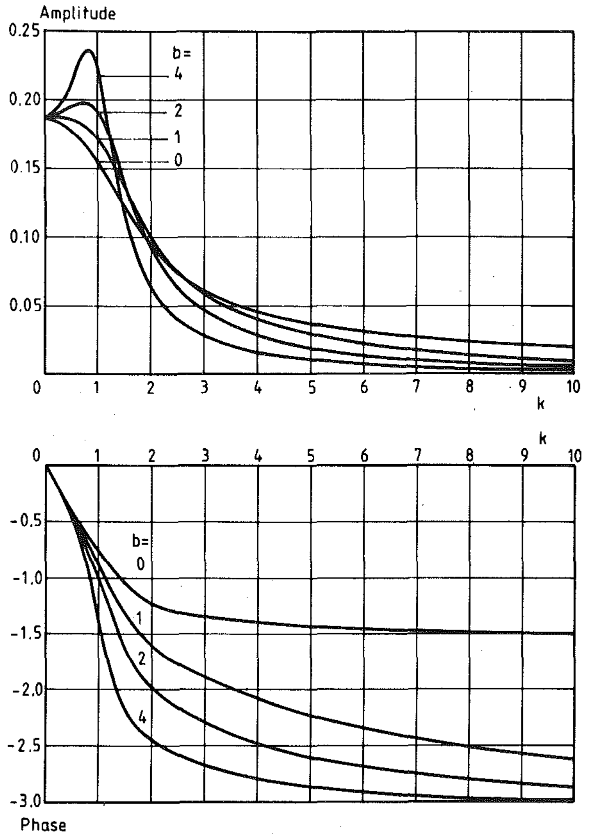

Fig. 3 Displacement amplitudes and phases for rigid disks with $\nu_h = 0.25$ and mass ratios $b = 0, 1, 2,$ and 4

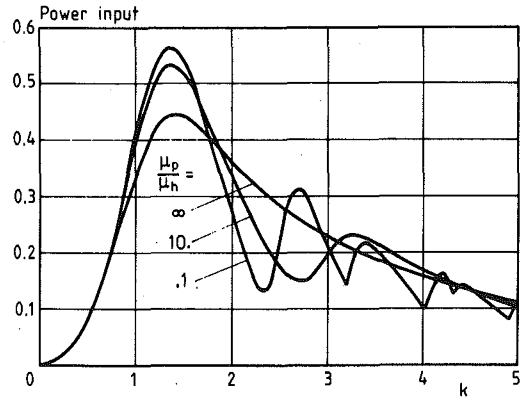

Fig. 4 Dimensionless power input for elastic plates

When use is made of the relation (Achenbach [20, p. 34]),

$$\langle \mathrm{Re}\,[F]\,\mathrm{Re}\,[f]\rangle = \tfrac{1}{2}\,\mathrm{Re}\,[F\bar{f}] \tag{66}$$

and the polynomial expansions (17) and (22), the following dimensionless expression is found for the power input:

$$\frac{1-\nu_h}{\mu_h}\sqrt{\frac{\rho_h}{\mu_h}}\frac{\langle P\rangle}{\pi a^2} = k\sum_{m=0}^{\infty}\frac{1}{4m+1}\,\mathrm{Re}\,[\overline{i(W_m)}S_m] \tag{67}$$

In the examples presented here the following parameters are used: $\tau = 0.2$, $\nu_h = 0.25$, $\nu_p = 0.33$, and $\rho_p/\rho_h = 3.0$. Three stiffness ratios are considered, $\mu_p/\mu_h = 0.1, 10.0, \infty$. The external load is uniformly distributed, i.e., $N_0 = 1$, $q(r) \equiv \mu_h/(1-\nu_h)$.

Fig. 4 shows the dimensionless power input (67) for $0 \le k \le 5$. The curves are based on calculations at 51 equally spaced abscissae, and the number of terms in the polynomial expansions increases from N

---

[1] η and γ should be γ^2 and η in the head of Table 3 in [3].

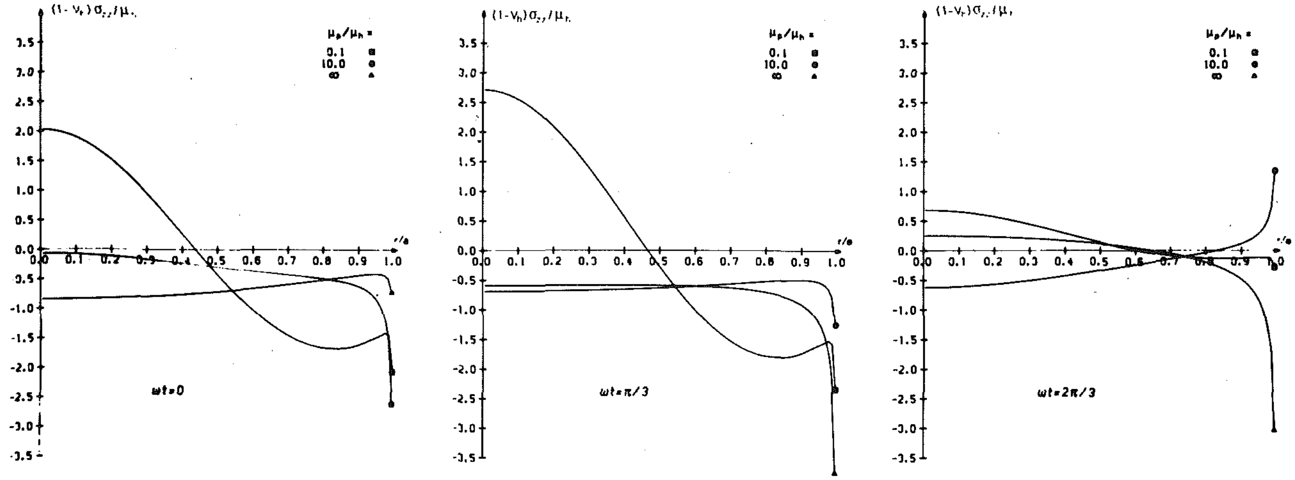

Fig. 5 Contact stress distributions for phase angles 0, π/3, 2π/3, and k = 2.5

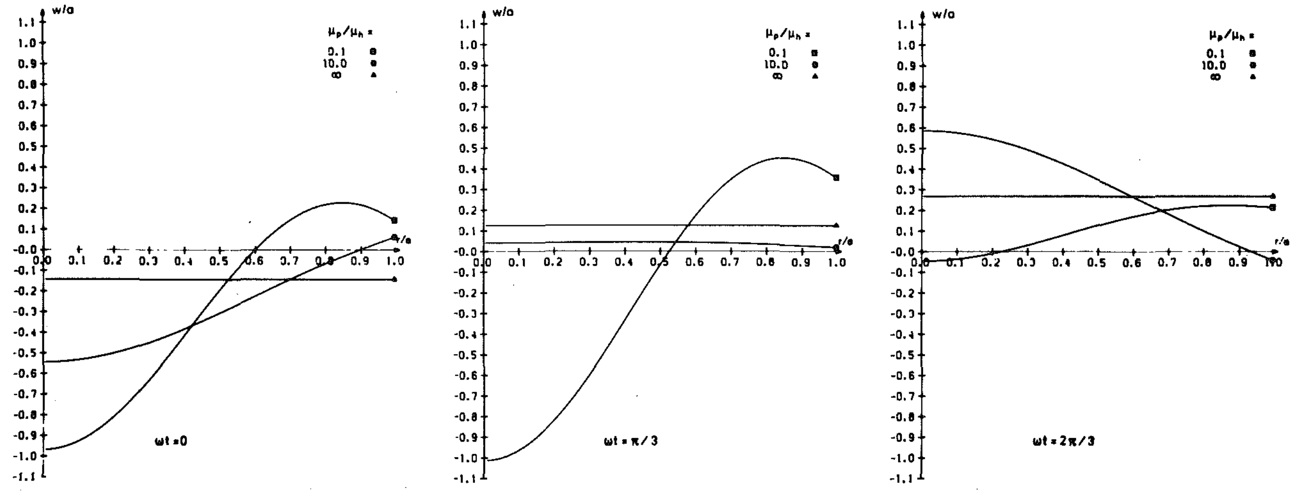

Fig. 6 Plate displacement distributions for phase angles 0, π/3, 2π/3, and k = 2.5

= 10 to $N = 23$ with increasing frequency. The matrix A_{jm}^p is evaluated by use of $3N$ integration points for the plate with $\mu_p/\mu_h = 0.1$ and $2N$ for $\mu_p/\mu_h = 10.0$. Increasing N to $1.5N$ only gave relative changes of less than 10^{-3} for the most flexible plate and less than 10^{-6} for the other two.

The figure shows a clear influence of the flexibility of the plate. While all three curves have a marked peak near the resonance frequency of the rigid plate, the flexible plates exhibit a number of secondary peaks at higher frequencies. This number increases with increasing flexibility of the plate.

The influence of the flexibility of the plate on the distribution of contact stresses and displacements is illustrated in Figs. 5 and 6. The distributions are plotted at phase intervals of $\pi/3$ and cover half of the oscillation at the dimensionless frequency $k = 2.5$. As expected increasing deviations from the rigid plate distributions are found for increasing flexibility. Additional calculations show the deviations to increase with frequency as well.

The ability of the present method to account for the flexibility of the plate is supported by the fact that the contact stresses and displacements for $\mu_p/\mu_h \rightarrow 0$ and $k \rightarrow 0$ approach those of the static problem of a constant load on a circular area [21].

Acknowledgment

The first author appreciates support from the Structural Research Laboratory of the Technical University of Denmark.

References

1 Reissner, E., and Sagoci, H. F., "Forced Torsional Oscillations of an Elastic Half Space. I," *Journal of Applied Physics*, Vol. 15, 1944, pp. 652–654.

2 Sagoci, H. F., "Forced Torsional Oscillations of an Elastic Half Space II," *Journal of Applied Physics*, Vol. 15, 1944, pp. 655–662.

3 Robertson, I. A., "Forced Vertical Vibration of a Rigid Circular Disc on a Semi-Infinite Elastic Solid," *Proceedings of the Cambridge Philosophical Society*, Vol. 62, 1966, pp. 547–553.

4 Gladwell, G. M. L., "Forced Tangential and Rotatory Vibration of a Rigid Circular Disc on a Semi-Infinite Solid," *International Journal of Engineering Science*, Vol. 6, 1968, pp. 591–607.

5 Sneddon, I. N., *The Use of Integral Transforms*, McGraw-Hill, New York, 1972.

6 Popov, G. Ia., "Some Properties of Classical Polynomials and Their Application to Contact Problems," *Journal of Applied Mathematics and Mechanics*, Vol. 27, 1963, pp. 1255–1271.

7 Krenk, S., "A Circular Crack Under Asymmetric Loads and Some Related Integral Equations," ASME JOURNAL OF APPLIED MECHANICS, Vol. 46, 1979, pp. 821–826.

8 Krenk, S., "Polynomial Solutions to Singular Integral Equations," Risö National Laboratory, Roskilde, Denmark, 1979.

9 Luco, J. R., and Westmann, R. A., "Dynamic Response of Circular Footings," *Journal of the Engineering Mechanics Division, Proceedings of the ASCE*, Vol. 97, 1971, pp. 1381–1395.

10 Bycroft, G. N., "Forced Vibrations of a Rigid Circular Plate on a Semi-Infinite Elastic Space and on an Elastic Stratum," *Philosophical Transactions of the Royal Society*, London, Series A, Vol. 248, 1956, pp. 327–368.

11 Abramowitz, M., and Stegun, I. A., *Handbook of Mathematical Functions*, Dover, New York, 1968.

12 Erdelyi, A., *"Higher Transcendental Functions,"* Vols. I, II, McGraw-Hill, New York, 1953.

13 Watson, G. N., *Theory of Bessel Functions*, Cambridge University Press, 1966.

14 Gladwell, G. M. L., "Polynomial Solutions for an Ellipse on an Anisotropic Half Space." *Quarterly Journal of Mechanics and Applied Mathematics*, Vol. 31, 1978, pp. 251–260.

15 Mindlin, R. D., "Influence of Rotatory Inertia and Shear on Flexural Motions of Isotropic, Elastic Plates," ASME JOURNAL OF APPLIED MECHANICS, Vol. 18, 1951, pp. 31–38.

16 Reissner, E., "On Transverse Bending of Plates, Including the Effect of Transverse Shear Deformation," *International Journal of Solids and Structures*, Vol. 11, 1975, pp. 569–573.

17 Whittaker, E. T., and Watson, G. N., *Modern Analysis*, Cambridge University Press, 1927.

18 Stroud, A. H., and Secrest, D., *Gaussian Quadrature Formulas*, Prentice-Hall, Englewood Cliffs, N. J., 1966.

19 Arnold, R. N., Bycroft, G. N., and Warburton, G. B., "Forced Vibrations of a Body on an Infinite Elastic Solid," ASME JOURNAL OF APPLIED MECHANICS, Vol. 22, 1955, pp. 391–400.

20 Achenbach, J. D., *Wave Propagation in Elastic Solids*, North-Holland, Amsterdam, 1973.

21 Timoshenko, S., and Goodier, J. N., *Theory of Elasticity*, McGraw-Hill, New York, 1951.

22 Scholte, J. G. J., "Rayleigh Waves in Isotropic and Anisotropic Elastic Media," *Mededelingen en Verhandelingen 72*, Koninklijk Nederlands Meteorologisch Instituut, 1958.

APPENDIX

An Integral Identity

Consider the integral

$$B_{jm} = -\frac{k^2}{4(1-\nu_h)}\frac{1}{2}\int_{-\infty}^{\infty}\frac{s\alpha(s)}{(s^2-{}^1\!/_2\,k^2)^2 - s^2\alpha(s)\beta(s)} \times h_{2j}^{(1)}(s)\,j_{2m}(s)ds \qquad m \geq j \tag{68}$$

The denominator is known to have only two roots, both of which are real [20], and the contour of integration is indented into the positive imaginary half plane at these points. The spherical Bessel functions of the third kind are defined as

$$\begin{aligned} h_m^{(1)}(s) &= j_m(s) + iy_m(s) \\ h_m^{(2)}(s) &= j_m(s) - iy_m(s) \end{aligned} \tag{69}$$

where $j_m(s)$ and $y_m(s)$, are the spherical Bessel funtions of the first and second kind, respectively, [11].

In the upper half of the complex plane the product of the two spherical Bessel functions in (68) is bounded and the contour can therefore be closed without changing the value of the integral. The integrand is analytic in the enclosed domain, which do not contain any poles, and thus $B_{jm} = 0$.

The integral is rewritten by introducing the dimensionless variable $\xi = s/k$ and rationalizing the integrand

$$B_{jm} = -\frac{k}{4(1-\nu_h)}\frac{1}{2}\int_{-\infty}^{\infty} \times \frac{(\xi^2-\frac{1}{2})^2\sqrt{\xi^2-\gamma^2} + (\xi^2-\gamma^2)\xi^2\sqrt{\xi^2-1}}{(\xi^2-\frac{1}{2})^4 - (\xi^2-\gamma^2)(\xi^2-1)\xi^4} \times \xi h_{2j}^{(1)}(k\xi)\,j_{2m}(k\xi)d\xi \tag{70}$$

The integration variable is now replaced by $\eta = -\xi$ on the negative part of the real axis, and B_{jm} is then given as the sum of two integrals along the positive real axis, with ξ passing over and η under the pole ξ_R. ξ_R is the positive root of the equation

$$(\xi^2 - {}^1\!/_2)^2 - \xi^2\sqrt{\xi^2-\gamma^2}\sqrt{\xi^2-1} = 0 \tag{71}$$

corresponding to the relative slowness of Rayleigh waves. Apart from $\pm\xi_R$ the denominator in (70) has four other roots corresponding to various interference phenomena, Scholte [22], but as they are also roots of the numerator, and it can be shown that they are outside the intervals $\gamma < |\xi| < 1$, Achenbach [20], they do not need explicit consideration.

The η contour is now changed to pass over the pole $\eta = \xi_R$, thus giving rise to an isolated contribution from the residue. The result is evaluated by use of the relations [11]

$$\begin{aligned} h_{2j}^{(1)}(-k\eta) &= h_{2j}^{(2)}(k\eta) \\ j_{2m}(-k\eta) &= j_{2m}(k\eta) \end{aligned} \tag{72}$$

After reduction of the residue the result is

$$\begin{aligned} B_{jm} = {} & \frac{i\pi k}{4(1-\nu_h)}\,\frac{\xi_R^2(\xi_R^2-\gamma^2)\sqrt{\xi_R^2-1}}{3(1-\gamma^2)\xi_R^4-(3-2\gamma^2)\xi_R^2+{}^1\!/_2} \times h_{2j}^{(2)}(k\xi_R)\,j_{2m}(k\xi_R) \\ & - \frac{k}{4(1-\nu_h)}\int_0^{\gamma}\frac{\xi(\xi^2-{}^1\!/_2)^2\sqrt{\xi^2-\gamma^2}}{(\xi^2-{}^1\!/_2)^4-(\xi^2-\gamma^2)(\xi^2-1)\xi^4} \times iy_{2j}(k\xi)\,j_{2m}(k\xi)d\xi \\ & - \frac{k}{4(1-\nu_h)}\int_{\gamma}^{\infty}\frac{\xi(\xi^2-{}^1\!/_2)^2\sqrt{\xi^2-\gamma^2}}{(\xi^2-{}^1\!/_2)^4-(\xi^2-\gamma^2)(\xi^2-1)\xi^4} \times j_{2j}(k\xi)\,j_{2m}(k\xi)d\xi \\ & - \frac{k}{4(1-\nu_h)}\int_0^{1}\frac{\xi^3(\xi^2-\gamma^2)\sqrt{\xi^2-1}}{(\xi^2-{}^1\!/_2)^4-(\xi^2-\gamma^2)(\xi^2-1)\xi^4} \times iy_{2j}(k\xi)\,j_{2m}(k\xi)d\xi \\ & - \frac{k}{4(1-\nu_h)}\int_1^{\infty}\frac{\xi^3(\xi^2-\gamma^2)\sqrt{\xi^2-1}}{(\xi^2-{}^1\!/_2)^4-(\xi^2-\gamma^2)(\xi^2-1)\xi^4} \times j_{2j}(k\xi)\,j_{2m}(k\xi)d\xi \end{aligned} \tag{73}$$

When use is made of the definitions (6) and (7) for the arguments of the square roots subtraction of $B_{jm} = 0$ from A_{jm}^h yields the result (27).

S. Narayanan[1]
Assistant Professor,
Department of Aeronautical Engineering.

J. P. Verma
Graduate Student.

A. K. Mallik
Assistant Professor,
Department of Mechanical Engineering.

Indian Institute of Technology, Kanpur,
Kanpur-208016, India

Free Vibration of Thin-Walled Open Section Beams With Unconstrained Damping Treatment

Free-vibration characteristics of a thin-walled, open cross-section beam, with unconstrained damping layers at the flanges, are investigated. Both uncoupled transverse vibration and the coupled bending-torsion oscillations, of a beam of a top-hat section, are considered. Numerical results are presented for natural frequencies and modal loss factors of simply supported and clamped-clamped beams.

1 Introduction

Thin-walled open section beams are used as stiffening members in various sheet metal constructions, such as aircraft skin-stringer panels, ship-hull structures, and vehicle bodies. In general, the asymmetry present in this type of sections results in a coupling of the bending and torsional modes of oscillation. Free-vibration characteristics of such beams in the coupled modes have been studied by Gere [1] and Gere and Lin [2].

The vibration of resonant structures can be controlled most effectively through applied damping treatments. Both unconstrained and constrained layers of viscoelastic materials are used for this purpose. Free and forced-vibration analyses of beams with additive damping layers have been investigated by several authors [3–9], who considered only beams and plates of uniform rectangular cross section. No analysis, however, has been reported of the vibration of a thin-walled open section beam with an additive damping treatment. This paper presents an analysis of free-vibration characteristics of such layered structures.

Another motivation for this study stems from the following considerations. In a recent paper, Sengupta [10] has proposed the concept of intrinsic structural tuning for reducing the low frequency vibrations of aircraft fuselage skins. For a typical skin-stringer combination, the frequency of peak response is very close to the natural frequency of the individual skin bay (say f_p), which is clamped along the stringers and simply supported along the frames. If the stringer and panel dimensions are such that the natural frequency of the stringer coincides with f_p, then the stringer can act as a tuned absorber for the skin vibrations. Additional damping, through the application of damping treatments to the stringers, will increase the effectiveness of the intrinsically tuned stringers, over a broad frequency range. The analysis presented in this paper will also be useful in the design of such intrinsically tuned damped stringers.

As an example, a top-hat section, with unconstrained damping layers at the flanges, is considered in this paper. Vibrations both in and out of the plane of symmetry are investigated. The vibration in the plane of symmetry is uncoupled and the analysis is exactly similar to those considered by previous workers [3–9]. This paper concentrates on the vibration in the coupled bending torsional modes. For this analysis, it is necessary to determine the location of the shear center and the torsional and warping rigidities of the composite cross section.

Numerical results are presented for natural frequencies and modal loss factors for simply supported as well as clamped end conditions. An efficient algorithm, based on a two-dimensional Newton-Raphson technique, is used for computations.

2 Theoretical Analysis

2.1 Vibration in the Plane of Symmetry. Fig. 1 shows a top-hat section with damping layers on the flanges. The composite neutral axis for bending in the plane of symmetry is shown as $\eta - \eta$, whereas $\eta_1 - \eta_1$ and $\eta_2 - \eta_2$ refer to the centroidal axes of the individual layers (1) and (2), respectively. In the present analysis, the base layer (1) is assumed to be nondissipative. Furthermore, the loss factor of the viscoelastic layer (2) is assumed to be frequency-independent, and the same in the shear and extensional modes of deformation.

Following the analysis presented by Ditaranto [5], the natural frequencies and the modal loss factors, for various cases, are obtained as follows:

For S-S Ends:

$$\omega_n^2 = \frac{n^4\pi^4}{l^4}\frac{B}{\mu}, \tag{1}$$

---

[1] Presently, Assistant Professor, Machine Dynamics Laboratory, Department of Applied Mechanics, Indian Institute of Technology, Madras, Madras, 600036, India.

Contributed by the Applied Mechanics Division for publication in the JOURNAL OF APPLIED MECHANICS.

Discussion on this paper should be addressed to the Editorial Department, ASME, United Engineering Center, 345 East 47th Street, New York, N. Y. 10017, and will be accepted until June 1, 1981. Readers who need more time to prepare a Discussion should request an extension from the Editorial Department. Manuscript received by ASME Applied Mechanics Division, November, 1979; final revision, May 1980.

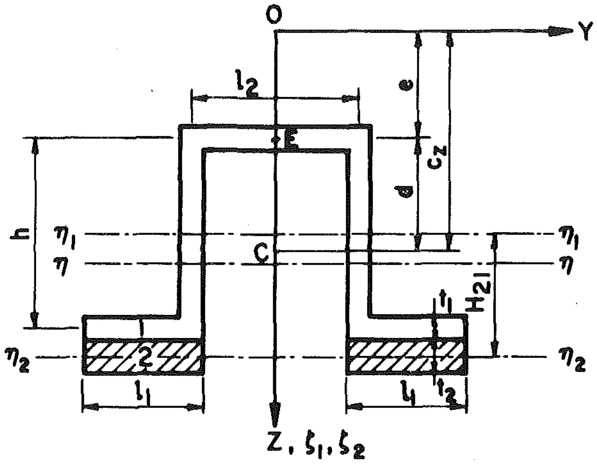

Fig. 1 Cross section of the composite beam

For C-C Ends:

$$\omega_n^2 \simeq \frac{(n+\frac{1}{2})^4\pi^4}{l^4}\frac{B}{\mu} \qquad n = 1, 2, 3, \ldots \tag{2}$$

where, under the usual assumption of $E_2 \ll E_1$, [11]

$$B \simeq E_1 I_{\eta 11} + E_2\,(I_{\eta 22} + A_2 H_{21}^2) \tag{3}$$

and the loss factor in all the modes, η, for both end conditions, is given by

$$\eta \simeq \beta\frac{E_2}{E_1}\,\frac{I_{\eta 22} + A_2 H_{21}^2}{I_{\eta 11} + \dfrac{E_2}{E_1}(I_{\eta 22} + A_2 H_{21}^2)} \tag{4}$$

2.2 Coupled Bending-Torsion Modes. Referring to Fig. 1, O and C are, respectively, the shear center and the mass center of the composite section. It is evident that

$$v_c = v_0 - c_z\psi \tag{5}$$

The equations of motion in the coupled modes are given by [2]

$$(E_1 I_{\zeta_1} + E_2^* I_{\zeta_2})\frac{\partial^4 v_0}{\partial x^4} + \mu\frac{\partial^2 v_c}{\partial t^2} = 0 \tag{6}$$

and

$$C_2\frac{\partial^4\psi}{\partial x^4} - C_1\frac{\partial^2\psi}{\partial x^2} - \mu c_z\frac{\partial^2 v_c}{\partial t^2} + (\rho_1 I_{c_1} + \rho_2 I_{c_2})\frac{\partial^2\psi}{\partial t^2} = 0 \tag{7}$$

where the constants C_1, C_2, and c_z are as derived in Appendix A. Assuming harmonic solutions of the form

$$v_0 = V_0(x)e^{i\omega^* t}$$

and

$$\psi = \Psi_0(x)e^{i\omega^* t}, \tag{8}$$

and using equations (5)–(7) for eliminating ψ and v_c, one gets the following equation in terms of nondimensional quantities:

$$\frac{d^8V_0}{d\xi^8} + \alpha_1\frac{d^6V_0}{d\xi^6} + \alpha_2\,\Omega_c^{*2}\frac{d^4V_0}{d\xi^4} + \alpha_3\Omega_c^{*2}\frac{d^2V_0}{d\xi^2} + \alpha_4\Omega_c^{*4}\,V_0 = 0 \tag{9}$$

The coefficients α_1, α_2, α_3, and α_4 are given in Appendix B. Substituting a trial solution of the form

$$V_0(\xi) = \sum_{s=1}^{8} Q_s\,e^{\lambda_s\xi} \tag{10}$$

in equation (9), the following characteristic polynomial equation for the λ's is obtained:

$$\lambda^8 + \alpha_1\lambda^6 + \alpha_2\Omega_c^{*2}\,\lambda^4 + \alpha_3\Omega_c^{*2}\lambda^2 + \alpha_4\Omega_c^{*4} = 0 \tag{11}$$

Applying the appropriate boundary conditions at the two ends of the beam, the frequency equation is obtained in the usual form

$$\det\,[A] = 0 \tag{12}$$

The boundary conditions, and the associated elements of the matrix $[A]$ for different end conditions, are also included in Appendix B.

3 Computational Procedure

It should be noted that two quantities, viz., Ω_c^2 and η_c, are to be determined from the zeros of det $[A]$. The solution of the determinantal equation (12) is somewhat cumbersome due to the complex arithmetic and the associated numerical problems [12]. This difficulty has been overcome by splitting the determinant into its real and imaginary parts and setting these separately equal to zero. The real and imaginary parts of the determinant are considered as functions of the two variables $\Omega_c^2$and $\eta_c\Omega_c^2$. The zeros of the functions are obtained by using a two-dimensional Newton-Raphson procedure. The iteration scheme proceeds according to the following sequence:

Let

$$A_R(m, n) = 0$$
$$A_I(m, n) = 0 \tag{13}$$

Nomenclature

A_1, A_2 = cross-sectional areas of the elastic layer (1) and the viscoelastic damping layer (2), respectively
A_{1f}, A_{2f} = flange areas of layers (1) and (2), respectively
l = length of the beam
t = time
x = lengthwise coordinate
z = coordinate along the axis of symmetry
y = coordinate perpendicular to x and z
E_1 = modulus of elasticity of layer (1)
E_2 = storage elastic modulus of layer (2)
v_0, v_c = deflections in Y-direction of the composite shear center and mass center, respectively
$I_{\eta 11}$, $I_{\eta 22}$ = second moments of area of layer (1) about $\eta_1 - \eta_1$ axis and of layer (2) about $\eta_2 - \eta_2$ axis, respectively
I_{ζ_1}, I_{ζ_2} = second moments of area about ζ_1 (or ζ_2) axis of layers (1) and (2), respectively
I_{c_1}, I_{c_2} = polar second moments of area of layers (1) and (2), respectively, about the longitudinal axis passing through the composite mass center
G_1 = shear modulus of layer (1)
G_2 = storage shear modulus of layer (2)
C_1 = Saint-Venant's torsional rigidity of the composite cross section
C_2 = warping rigidity of the composite cross section
M = bending moment
V = shear force
ρ_1, ρ_2 = mass densities of layers (1) and (2), respectively
μ = mass per unit length of the beam = $\rho_1 A_1 + \rho_2 A_2$
ψ = rotation of the cross section about X-axis
β = loss factor of the viscoelastic material in both shear and extension
$i = \sqrt{-1}$
$E_2^* = E_2(1 + i\beta)$
$G_2^* = G_2(1 + i\beta)$
ω_n, η = natural frequency and loss factor, respectively, *in the vertical uncoupled* mode
$\xi = x/l$
ω, η_c = natural frequency and loss factor, respectively, in the coupled bending-torsion mode
$\omega^* = \omega(1 + i\eta_c)^{1/2}$
Ω_c = nondimensional natural frequency in the coupled mode = $\omega l^2\,(\mu/E_1 I_{\zeta_1} + E_2 I_{\zeta_2})^{1/2}$
$\Omega_c^* = \Omega_c(1 + i\eta_c)^{1/2}$
γ = shear strain

Table 1 Natural frequencies and modal loss factors in coupled vibration

$$\frac{\rho_2}{\rho_1} = 0.2, \quad \frac{t_2}{t_1} = 1.50, \quad \frac{E_2}{E_1} = 0.001, \quad \beta = 1.00$$

Mode No.	Simply supported ends Ω_c	Simply supported ends η_c	Clamped-clamped ends Ω_c	Clamped-clamped ends η_c
1	3.8578	0.00350	7.5646	0.00172
2	13.3733	0.00175	20.2314	0.00129
3	16.8653	0.00124	39.2024	0.00108
4	29.1171	0.00126	65.6123	0.00103
5	51.1401	0.00106	103.6293	0.00098
6	66.5015	0.00101	133.6277	0.00090
7	79.4502	0.00097	177.6716	0.00088
8	114.0493	0.00092	202.9504	0.00096

where

$$A_R = \text{Real}(\det[A]), \quad A_I = \text{Imag}(\det[A]),$$

$$m = \Omega_c^2 \text{ and } n = \eta_c \Omega_c^2$$

Then, two successive iterations for the roots of equations (13) are related as

$$m_{j+1} = m_j + \left[\frac{A_I A_{Rn} - A_R A_{In}}{A_{Rm} A_{In} - A_{Rn} A_{Im}}\right]_j ; \qquad (14)$$

and

$$n_{j+1} = n_j + \left[\frac{A_R A_{Im} - A_I A_{Rm}}{A_{Rm} A_{In} - A_{Rn} A_{Im}}\right]_j \qquad (15)$$

In the foregoing equations, the subscripts m and n refer to the partial differentiation with respect to m and n, respectively, and the suffix j denotes the jth iteration.

The required partial derivatives are computed by using a central-difference scheme. Starting from the lower end of the frequency scale, the iterations are performed to obtain the natural frequencies and the modal loss factors in the various modes. For each natural frequency and its associated loss factor, the convergence is tested by a twofold criterion:

1 A specified limit on the percentage change in the relevant values in successive iterations.

2 A specified limit on the absolute value of the determinant.

The foregoing scheme converged, in most instances, within six or seven iterations. The initial starting point for the variables did not present any problem. The value of the determinant, however, was seen to vary, with frequency, over a wide range. To eliminate consequent problems in dealing with very large numbers, the determinant was suitably scaled at the start of the iteration scheme for the different modes.

4 Results and Discussions

Numerical computations are performed with the following dimensions and properties of the elastic layer (Fig. 1) $l_1 = 20$ mm, $l_2 = 26$ mm, $t_1 = 2$mm, and $h = 35$ mm. $E_1 = 6.87 \times 10^{10}$ N/m^2, $\rho_1 = 2700$ kg/m^3.

Table 1 shows some typical values of the natural frequencies and the loss factors in the coupled bending-torsion modes. It is seen that the modal loss factors for the coupled vibration, unlike those in the uncoupled vertical mode (see equation (4)), depend on the end conditions and as well as the modal number. This is attributed to the simultaneous extensional and shear deformation of the viscoelastic layer in the coupled modes. A similar situation is encountered in beams of solid cross section with constrained damping layers [5].

It can also be seen that for both end conditions, the loss factor in the first mode is appreciably larger than those in the higher modes. Moreover, the simply supported beam has higher loss factors as compared to a clamped-clamped beam. This is especially so in the case of lower-order modes.

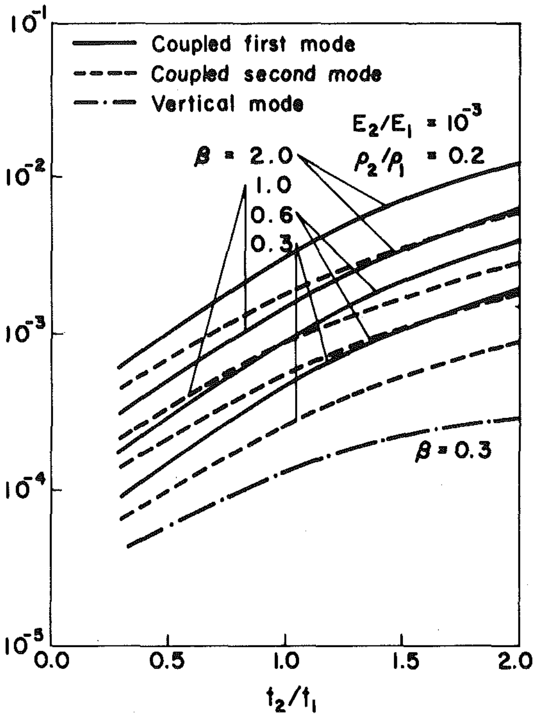

Fig. 2 Variation of composite loss factor with thickness ratio for a simple supported beam

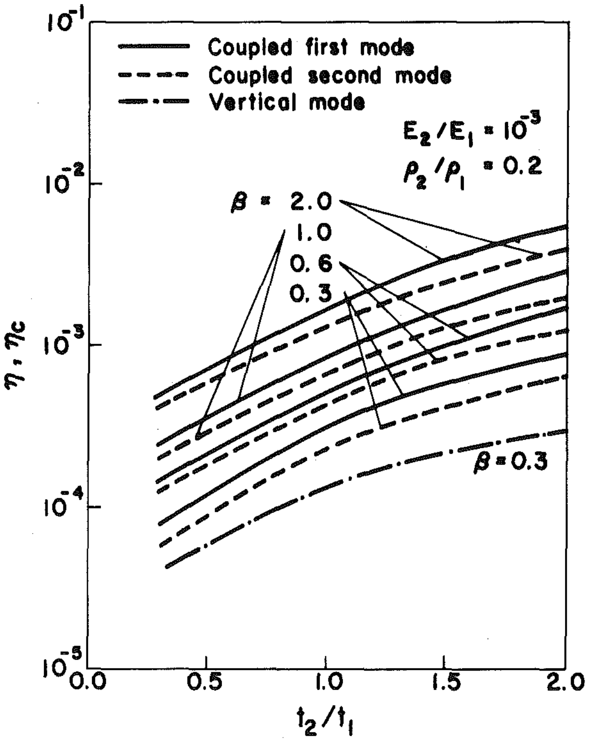

Fig. 3 Variation of composite loss factor with thickness ratio for a clamped-clamped beam

Figs. 2 and 3 show the variation of the loss factor with the thickness ratio, t_2/t_1, in the first two modes. The loss factor in the uncoupled vertical mode, given by equation (4), is also plotted in the same figures. It is clearly seen that an unconstrained damping layer is more effective

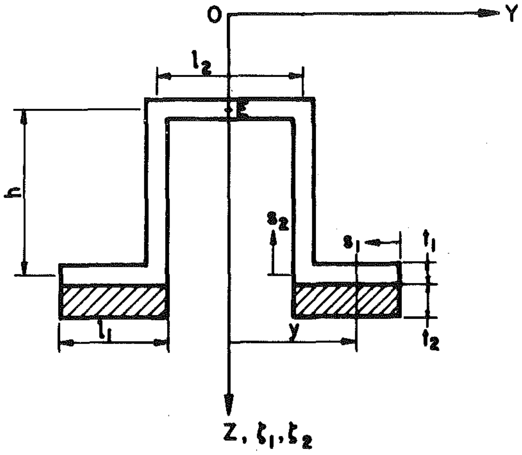

Fig. 4 Coordinates for shear flow calculations

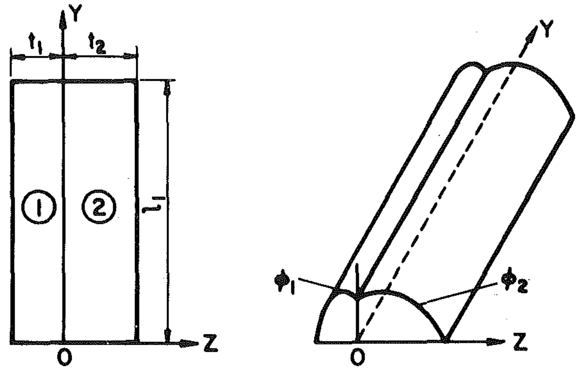

Fig. 5 Deflected surface of the membrane made of two materials

in the lower-order coupled modes, than in the uncoupled vertical mode. Extensive parametric investigation [11] also showed that η_c (just like η) varies linearly with β and E_2/E_1. However, the variation in Ω_c with β was found to be insignificant. Furthermore, in the range $0.2 < \rho_2/\rho_1 < 0.7$, the composite loss factor in the coupled mode, η_c, was seen to be independent of ρ_2/ρ_1.

An analysis of the free vibration of similar sections, with constrained damping layers, will be presented in a future paper.

5 Conclusions

An analysis of the free-vibration characteristics of a thin-walled open section beam, with unconstrained damping layers at the flanges, shows

1 For the coupled bending-torsion oscillation, the modal loss factors depend (even when the damping layer is unconstrained) on the end conditions and the mode number.

2 For the coupled as well as the uncoupled oscillations, the composite loss factor varies linearly with β and E_2/E_1.

3 The loss factor in the coupled mode, especially for the lower-order modes, is higher than that in the uncoupled vertical mode.

4 The unconstrained treatment is more effective in damping out the lower-order coupled modes.

References

1 Gere, J. M., "Torisonal Vibrations of Beams of Thin-Walled Open Section," ASME JOURNAL OF APPLIED MECHANICS, Vol. 21, 1954, pp. 381–387.

2 Gere, J. M., and Lin, Y. K., "Coupled Vibration of Thin-Walled Beams of Open Cross Section," ASME JOURNAL OF APPLIED MECHANICS, Vol. 25, 1958, pp. 373–378.

3 Kerwin, E. M., "Damping of Flexural Waves by a Constrained Viscoelastic Layer," *Journal of the Acoustical Society of America*, Vol. 31, 1959, pp. 952–962.

4 Ross, D., Ungar, E., and Kerwin, E. M., "Damping of Plate Flexural Vibrations by Means of Viscoelastic Laminae," *Structural Damping*, Section Three, ed., Ruzicka, J., Pergamon Press, Oxford, 1960.

5 Ditaranto, R. A., "Theory of Vibratory Bending for Elastic and Viscoelastic Layered Finite Length Beams," ASME JOURNAL OF APPLIED MECHANICS, Vol. 31, 1965, pp. 881—886.

6 Mead, D. J., and Markus, S., "The Forced Vibration of a Three Layer, Damped Sandwich Beam With Arbitrary Boundary Conditions," *Journal of Sound and Vibration*, Vol. 10, 1969, pp. 163–175.

7 Mead, D. J., and Markus, S., "Loss Factor and Resonant Frequencies of Encastre Damped Sandwich Beams," *Journal of Sound and Vibration*, Vol. 12, 1970. pp. 99–112.

8 Mead, D. J., "The Damping Properties of Elastically Supported Sandwich Plates," *Journal of Sound and Vibration*, Vol. 24, 1972, pp. 275–295.

9 Mead, D. J., "Loss Factors and Resonant Frequencies of Periodic Damped Sandwich Plates," ASME Paper No. 75-DET-19.

10 Sengupta, G., "Methods of Reducing Low Frequency Cabin Noise and Sonically Induced Stresses, Based on the Intrinsic Structural Tuning Concept," paper presented at the Eighteenth Structures, Dynamics Specialist Conference of AIAA, San Diego, 1977.

11 Verma, J. P., "Free Vibration of Thin-Walled Open Section Beams With Unconstrained Damping Layer," M. Tech. Thesis, Indian Institute of Technology, Kanpur, Sept. 1979.

12 Oravsky, V., Markus, S., and Simkova, O., "A New Approximate Method of Finding the Loss Factors of a Sandwich Cantilever," *Journal of Sound and Vibration*, Vol. 33, 1974, pp. 335–353.

13 Timoshenko, S. P., and Gere, J. M., *Theory of Elastic Stability*, McGraw-Hill, London, 1961.

14 Booker, J. R., and Kitipornchai, S., "Torsion of Multilayered Rectangular Section," *Journal of Engineering Mechanics Division, ASCE*, Vol. 97, No. EM5, Proceedings Paper 8415, Oct., 1971, pp. 1451–1468.

15 Thomson, A. F., and Woolf, A. "Dynamic Torsion of a Two-Layer Viscoelastic Beam," *Journal of Sound and Vibration*, Vol. 48, 1976, pp. 251–263.

APPENDIX *A*

Shear Center of Composite Section

Considering the bending, about the Z-axis, of the composite section shown in Fig. 4, the fractions of the bending moment resisted by Sections (1) and (2) are given by

$$M_1 = \frac{ME_1 I_{\zeta_1}}{E_1 I_{\zeta_1} + E_2^* I_{\zeta_2}}; \quad M_2 = \frac{ME_2^* I_{\zeta_2}}{E_1 I_{\zeta_1} + E_2^* I_{\zeta_2}} \tag{16}$$

The total shear flow in the flanges for Sections (1) and (2), at a distance y, is then obtained as

$$(q_{xy})_1 + (q_{xy})_2 = \frac{VE_1 \int_0^{s_1} yt_1 ds_1}{E_1 I_{\zeta_1} + E_2^* I_{\zeta_2}} + \frac{VE_2^* \int_0^{s_1} yt_2 ds_1}{E_1 I_{\zeta_1} + E_2^* I_{\zeta_2}} \tag{17}$$

Similarly, the shear flow in the webs is

$$(q_{xz})_1 = \frac{V}{E_1 I_{\zeta_1} + E_2^* I_{\zeta_2}} \left\{ \int_0^{l_1} (E_1 t_1 + E_2^* t_2) y \, ds_1 + \frac{l_2}{2} \int_0^{s_2} E_1 t_1 ds_2 \right\} \tag{18}$$

The shear center is located by considering the moment balance about the point E, and the distance e is obtained as

$$e = \frac{E_1 t_1 h}{E_1 I_{\zeta_1} + E_2^* I_{\zeta_2}} \left[\frac{l_2^2 h}{4} + \left(1 + \frac{E_2^* t_2}{E_1 t_1}\right)\left(\frac{l_1 l_2^2}{2} - \frac{2 l_1^3}{3}\right) \right] \tag{19}$$

Thus, from Fig. 1,

$$c_z = e + d$$

Torsional and Warping Rigidities of Composite Section

The Saint-Venant's torsional rigidity of a composite, thin, rectangular cross section was derived in references [14, 15] by using warping functions. A much simpler procedure, using the membrane analogy, is presented here. Consider a membrane made of two materials (Fig.

5) and subjected to an internal pressure. The membrane which is initially of the form $\phi = 0$ deflects to the shape $\phi = \phi(z, y)$.

If $l_1 \gg t_1 + t_2$, the deflected surface of the membrane can be considered independent of y, except near the ends. ϕ_1 and ϕ_2 are the deflected surfaces of the membranes of materials 1 and 2; these quantities also correspond to the Prandtl's stress functions. Let θ_0 be the uniform twist along the length. Then, by the membrane analogy, ϕ_1 and ϕ_2 are governed by

$$\frac{\partial^2\phi_1}{\partial z^2} = -2G_1\theta_0, \; -t_1 < z \leq 0;$$

and

$$\frac{\partial^2\phi_2}{\partial z^2} = -2G_2^*\theta_0, \; 0 \leq z < t_2 \qquad (20)$$

The functions ϕ_1 and ϕ_2 can be obtained by integration of equation (20) with the following boundary conditions:

$$\phi_1(-t_1) = \phi_2(t_2) = 0,$$

$$\phi_1(0) = \phi_2(0) \qquad (21)$$

at

$$z = 0, \quad (\gamma_{xy})_1 = (\gamma_{xy})_2.$$

The last condition implies the continuity of the shear strain at the interface, and can be rewritten as

$$\frac{1}{G_1}\frac{\partial\phi_1}{\partial z}\bigg|_{z=0} = \frac{1}{G_2^*}\frac{\partial\phi_2}{\partial z}\bigg|_{z=0} \qquad (22)$$

Finally, ϕ_1 and ϕ_2 are obtained as

$$\phi_1 = -G_1\theta(z^2 - t_1^2) + \Gamma G_1\theta(z + t_1)$$

and

$$\phi_2 = -G_2^*\theta(z^2 - t_2^2) + \Gamma G_2^*\theta(z - t_2)$$

where

$$\Gamma = \frac{G_2^*t_2^2 - G_1t_1^2}{G_2^*t_2 + G_1t_1} \qquad (23)$$

Under pure torsion, the torque resisted by the shear stresses in the flanges is

$$T_f = 2\iint \phi\, dzdy = 2\int_{A_{1f}} \phi_1 dA_{1f} + 2\int_{A_{2f}} \phi_2 dA_{2f} \qquad (24)$$

The torsional rigidity of the entire composite beam, including the torque resisted by the rest of the cross section, is

$$C_1 = 4l_1G_1(\tfrac{2}{3}t_1^3 + \tfrac{1}{2}\Gamma\, t_1^2) + 4l_1G_2^*(\tfrac{2}{3}t_2^3 - \tfrac{1}{2}\Gamma\, t_2^2) + G_1(\tfrac{2}{3}h + \tfrac{1}{3}l_2)\, t_1^3 \qquad (25)$$

Under nonuniform torsion, warping stresses are generated; these include shear stresses which, in turn, resist a part of the applied torque [13]. The warping torques of the two sections are given by

$$T_1 = -E_1C_{\omega1}\frac{\partial^3\psi}{\partial x^3} \quad \text{and} \quad T_2 = -E_2^*C_{\omega2}\frac{\partial^3\psi}{\partial x^3} \qquad (26)$$

where $C_{\omega1}$ and $C_{\omega2}$ are the warping constants of the Sections (1) and (2), respectively. Hence, the warping rigidity of the composite section, C_2, is obtained as

$$C_2 = E_1C_{\omega1} + E_2^*C_{\omega2} \qquad (27)$$

Expressions for $C_{\omega1}$ and $C_{\omega2}$, for a top-hat section, are given in reference [11].

APPENDIX *B*

Coefficients and Boundary Conditions of Equation (11)

The coefficients α, appearing in Equations (9) and (11), are as follows:

$$\alpha_1 = -\frac{C_1l^2}{C_2}$$

$$\alpha_2 = -(E_1I_{\zeta_1} + E_2I_{\zeta_2})\left(\frac{1}{(E_1I_{\zeta_1} + E_2^*I_{\zeta_2})} + \frac{c_z^2}{C_2} + \frac{\rho_1I_{c_1} + \rho_2I_{c_2}}{\mu C_2}\right]$$

$$\alpha_3 = -\alpha_1\frac{E_1I_{\zeta_1} + E_2I_{\zeta_2}}{E_1I_{\zeta_1} + E_2^*I_{\zeta_2}}$$

$$\alpha_4 = \frac{(E_1I_{\zeta_1} + E_2I_{\zeta_2})^2}{E_1I_{\zeta_1} + E_2^*I_{\zeta_2}}\frac{\rho_1I_{c_1} + \rho_2I_{c_2}}{\mu C_2} \qquad (28)$$

For simply supported ends, the boundary conditions are

$$\left.\begin{array}{l} V_0 = 0 \\ \dfrac{d^2V_0}{d\xi^2} = 0 \\ \Psi_0 = 0 \quad \text{or} \quad \dfrac{d^4V_0}{d\xi^4} = 0 \\ \text{and} \\ \dfrac{d^2\Psi_0}{d\xi^2} = 0 \quad \text{or} \quad \dfrac{d^6V_0}{d\xi^6} = 0 \end{array}\right\} \text{at} \quad \xi = 0 \quad \text{and} \quad \xi = 1 \qquad (29)$$

hence the elements of the matrix $[A]$ are obtained as

$$A_{1j} = 1,\ A_{2j} = e^{\lambda_j},\ A_{3j} = \lambda_j^2,\ A_{4j} = \lambda_j^2 e^{\lambda_j},\ A_{5j} = \lambda_j^4$$

$$A_{6j} = \lambda_j^4 e^{\lambda_j},\ A_{7j} = \lambda_j^6$$

$$A_{8j} = \lambda_j^6 e^{\lambda_j} \quad \text{for} \quad j = 1, 2, \ldots, 8 \qquad (30)$$

Similarly, for clamped-clamped ends, the boundary conditions and the matrix elements are given by

$$\left.\begin{array}{l} V_0 = 0 \\ \dfrac{dV_0}{d\xi} = 0 \\ \Psi_0 = 0 \quad \text{or} \quad \dfrac{d^4V_0}{d\xi^4} = 0 \\ \text{and} \\ \dfrac{d\Psi_0}{d\xi} = 0 \quad \text{or} \quad \dfrac{d^5V_0}{d\xi^5} = 0 \end{array}\right\} \text{at} \quad \xi = 0 \quad \text{and} \quad \xi = 1 \qquad (31)$$

$$A_{1j} = 1,\ A_{2j} = e^{\lambda_j},\ A_{3j} = \lambda_j,\ A_{4j} = \lambda_j e^{\lambda_j},\ A_{5j} = \lambda_j^4$$

$$A_{6j} = \lambda_j^4 e^{\lambda_j},\ A_{7j} = \lambda_j^5$$

$$A_{8j} = \lambda_j^5 e^{\lambda_j} \quad \text{for} \quad j = 1, 2, \ldots, 8 \qquad (32)$$

S. K. Shrivastava[1]

NRC-NASA Senior Research Associate,
Structures and Mechanics Division,
L. B. Johnson Space Center,
NASA,
Houston, Texas 77062

Stability Theorems for Multidimensional Linear Systems With Variable Parameters

Two equivalent theorems governing stability of multidimensional linear systems with variable parameters are derived which generalize some of the existing stability theorems. Illustrations include damped, gyroscopic, circulatory systems with varying parameters.

Introduction

Several stability theorems have been derived in the past two centuries which lead to a good understanding of a system even without the solution of its equations. Most of the theorems have been developed for systems with constant parameters. Some are applicable in presence of periodic coefficients. There are situations of importance where parameters may vary arbitrarily. Such systems will need attention.

Using a Liapunov-type approach, two equivalent theorems are derived here which govern stability of coupled linear systems with varying multiple parameters. Some of the existing theorems like the Sonin-Polya theorem [2] become special cases of the present theorems. These are applied, as illustrations, to mechanical systems with varying inertia, stiffness, gyroscopic, and damping terms, and velocity and position-dependent forces.

Analysis

Consider a set of n coupled nonautonomous linear equations,

$$a_2(x)z'' + a_1(x)z' + a_0(x)z = 0 \tag{1}$$

where x is independent variable, z is an n-dimensional vector, a_2, a_1, a_0 are $n \times n$ coefficient matrices varying with x. Matrices a_2 and a_0 should be nonsingular. Primes indicate derivatives with respect to x. Define

$$P(x) = \exp\,[\textstyle\int a_2{}^{-1}a_1 dx] \tag{2}$$

Note that P is a $n \times n$ positive-definite matrix. Using P, (1) can be written as

$$(Pz')' + Qz = 0 \tag{3}$$

where

$$Q(x) = Pa_2{}^{-1}a_0 \tag{4}$$

Let us assume $Q^{-1}P$ (hence $a_0{}^{-1}a_2$) to be "symmetrizable" [1], i.e., there exists a positive symmetric matrix $S(x)$, which makes $(SQ^{-1}P)$ or $(Sa_0{}^{-1}a_2)$ symmetric. Note that S can be found from $R^T = S^{-1}RS$, where $R = a_2{}^{-1}a_0$. Let a vector z be a nontrivial solution of (3). We can define a scalar F as

$$F = z^TSz + z'^TSQ^{-1}Pz' \tag{5}$$

If $(SQ^{-1}P)$ is positive-definite, F is positive-definite defining a region of possible solutions about the origin. Its derivative is given by

$$\begin{aligned} F' = {} & z'^TSz + z^TSz' + z^TS'z + (Pz')^{T'}(QS^{-1}P^T)^{-1}(Pz') \\ & + (Pz')^T(QS^{-1}P^T)^{-1}(Pz')' + (Pz')^T(QS^{-1}P^T)^{-1'}(Pz') \end{aligned} \tag{6}$$

Using (3) and symmetry of $(SQ^{-1}P)$, the first and second terms can be cancelled with the fifth and fourth terms, respectively. After some simplification we get

$$F' = z^TS'z - (Q^{-1T}S^Tz')^T(QS^{-1}P^T)'(Q^{-1T}S^Tz') \tag{7}$$

If $S' \leqslant 0$ and $(QS^{-1}P^T)' \geqslant 0$, F' will be negative semidefinite and F, defining the region of possible motion will be nonincreasing. If $F' < 0$, F will be asymptotically decreasing. Therefore F is a Liapunov functional. Hence, we can state the following:

Theorem 1. Let $P(x)$ be positive-definite and $Q(x)$ be nonsingular and continuously differentiable on an interval I. If there exists a positive-definite symmetric matrix S, such that $(SQ^{-1}P)$ is sym-

---

[1] Assistant Professor, Department of Aeronautical Engineering, Indian Institute of Science, Bangalore, India.

Contributed by the Applied Mechanics Division for publication in the JOURNAL OF APPLIED MECHANICS.

Discussion on this paper should be addressed to the Editorial Department, ASME, United Engineering Center, 345 East 47th Street, New York, N. Y. 10017, and will be accepted until June 1, 1981. Readers who need more time to prepare a Discussion should request an extension from the Editorial Department. Manuscript received by ASME Applied Mechanics Division, February, 1980.

metric and positive-definite, $S' \leqslant 0$, $(QS^{-1}P^T)' \geqslant 0$, then the region of possible solutions of the nonautonomous coupled system

$$[P(x)z']' + Q(x)z = 0$$

will be nonincreasing as x increases on I. It will be asymptotically decreasing if $(QS^{-1}P^T)' > 0$.

Application of the theorem in the present form may pose difficulties for large n, mainly in the computation of P. It is desirable to find conditions on the matrices a_2, a_1, and a_0 directly. Note that

$$SQ^{-1}P = Sa_0{}^{-1}a_2$$

and

$$P' = Pa_2{}^{-1}a_1 = a_2{}^{-1}a_1P \tag{8}$$

Using these, the definition of P and Q, and symmetry of $(Sa_0{}^{-1}a_2)$ we can write

$$(QS^{-1}P^T)' = P(Sa_0{}^{-1}a_2)^{-1}[Sa_0{}^{-1}a_1 + (Sa_0{}^{-1}a_1)^T - (Sa_0{}^{-1}a_2)'](Sa_0{}^{-1}a_2)^{-1T}P^T \tag{9}$$

This is positive-semidefinite if the matrix-pencil in the bracket is positive semidefinite.

It may be noted that this condition can be obtained directly from (1) by writing it as

$$Sa_0{}^{-1}a_2z'' + Sa_0{}^{-1}a_1z' + Sz = 0$$

and

$$F = z^TSz + z'^TSa_0{}^{-1}a_2z' \tag{10}$$

So the theorem can be restated as follows:

Theorem 2. Let $a_0(x)$, $a_2(x)$ be nonsingular and continuously differentiable on an interval I. If there exists a positive-definite symmetric matrix $S(x)$ such that $(Sa_0{}^{-1}a_2)$ is positive-definite symmetric (i.e., $a_0{}^{-1}a_2$ is symmetrizable), $S' \leqslant 0$ and $A = [Sa_0{}^{-1}a_1 + (Sa_0{}^{-1}a_1)^T - (Sa_0{}^{-1}a_2)'] \geqslant 0$, then the region of possible solutions of the coupled nonautonomous equations,

$$a_2(x)z'' + a_1(x)z' + a_0(x)z = 0$$

is nonincreasing as x increases. If $A > 0$, the region will decrease asymptotically.

These theorems generalize some of the existing theorems as observed in the following:

1 For a one-degree-of-freedom system [$n = 1, S = 1, P(x) = p(x), Q(x) = q(x)$], Theorem 1 reduces to the Sonin-Polya theorem [2], which states: Let $p(x) > 0$ and $q(x) \neq 0$ be continuously differentiable on an interval I, and suppose $p(x)q(x)$ is nonincreasing (nondecreasing) on I. Then the absolute values of the relative maxima and minima of every nontrivial solution of the equation

$$[p(x)y']' + q(x)y = 0$$

are nondecreasing (nonincreasing) as x increases.

2 If the parameters are all constant, S will also be a constant and most of the stability theorems of linear systems with constant parameters [1] can be shown to be special cases of the present theorems. For example, for a circulatory system with $a_1 = 0$, Theorem 2 reduces to Theorem 6.1 of reference [1], which in the present notations states: A circulatory system is stable if and only if there exists a symmetric and positive-definite matrix S_1 such that $(S_1a_2{}^{-1}a_0)$ is symmetric and positive-definite.

3 For the special situation of $(a_0a_2{}^T)$ (and hence $a_0{}^{-1}a_2$) being symmetric at all x over the interval, S = identity matrix and the theorems can be reduced to the following simple criteria of stability:

$$B = [a_0a_1{}^T + a_1a_0{}^T + a_0'a_2{}^T - a_2'a_0{}^T] \geqslant 0$$

and

$$a_0a_2{}^T > 0 \tag{11}$$

This is indeed a simple form of the condition, as there is no matrix inversion involved.

4 It may be noted that if the asymmetry of $(a_0a_2{}^T)$ is not significant, conditions (11) can still be used with a good approximation.

Stability of Dynamical Systems

For dynamical systems the independent variable is time t. The region of possible solutions is the motion envelope in a $2n$-dimensional hyper-phase-space. For stability, it should be nonincreasing. For asymptotic stability, it should decrease. The two theorems can thus be directly applied to such systems, as illustrated next.

(*a*) Torque-Free Rotating Systems With Variable Inertia. The equation of a torque-free system is given by

$$\dot{h} + w \times h = 0 \tag{12}$$

where h is angular momentum vector and w is rotation vector. The dot represents a derivative with respect to time. The equation can be linearized as

$$\dot{h} + gh = 0 \tag{13}$$

where g is a skew-symmetric gyroscopic matrix. Differentiating again,

$$\ddot{h} + \dot{g}h + g\dot{h} = 0 \tag{14}$$

Applying (13), it can be written as

$$\ddot{h} - \dot{g}g^{-1}h - ggh = 0 \tag{15}$$

Here $a_0a_2{}^T = -gg$ is symmetric and condition (11) is applicable, which leads to

$$B = [g^T\dot{g}^T - g\dot{g}] > 0$$

and

$$-gg > 0 \tag{16}$$

This is satisfied only if the body is symmetric, rotates about the axis of symmetry, and the variations in inertia are such that the body remains symmetric. Otherwise instability can occur in h-plane. This observation is made in reference [3] by decoupling the equations and applying the Sonin-Polya theorem to each equation separately.

(*b*) Damped Gyroscopic Systems With Velocity and Position-Dependent Forces and Variable Parameters. The general equation of a damped gyroscopic system with velocity and position-dependent forces can be written as [1]:

$$m(t)\ddot{z} + c(t)\dot{z} + k(t)z = 0 \tag{17}$$

where

m = a $n \times n$ real symmetric nonsingular inertia matrix.
c = a $n \times n$ real matrix containing gyroscopic, damping, and velocity-dependent forcing terms.
k = a $n \times n$ real nonsingular matrix containing symmetric stiffness (conservative) terms and skew-symmetric circulatory force (position-dependent) terms.

If km^T is symmetric or slightly asymmetric the stability conditions are

$$B = [ck^T + kc^T + \dot{k}m^T - \dot{m}k^T] \geqslant 0$$

and

$$km^T > 0 \tag{18}$$

In presence of strong circulatory forces km^T will be quite asymmetric. Then there must be a matrix S satisfying the conditions of Theorem 2 to insure stability. If no such S can be found, the system will generally be unstable.

Conclusion

Two equivalent theorems are derived which govern the stability of multidimensional linear systems with variable parameters. They generalize some of the existing theorems, applicable to systems with constant parameters and the Sonin-Polya theorem applicable to a single-degree-of-freedom system with variable coefficients. Although applied here to mechanical systems for illustration, they should be applicable to a wide range of systems.

Acknowledgment

The author wishes to thank Dr. R. C. Ried, Head, Aerothermodynamics Section, Structures and Mechanics Division, L. B. Johnson Space Center, NASA, for his encouragement and valuable discussions during this investigation.

References

1 Huseyin, K., *Vibrations and Stability of Multiple Parameter Systems*, Noordhoff Int. Pub., Alphen ann den Rijn, The Netherlands, 1978.

2 Kreider, D. L., et al., *An Introduction to Linear Analysis*, Addison-Wesley, Reading, Mass., 1966, pp. 237–239.

3 Sellappan, R., and Bainum, P. M., "Stability of Spacecraft During Asymmetrical Deployment of Appendages," *Journal of Guidance and Control*, Vol. 1, Nov.-Dec. 1978, pp. 446–447.

H. Hemami
F. C. Weimer

Department of Electrical Engineering,
The Ohio State University,
Columbus, Ohio

Modeling of Nonholonomic Dynamic Systems With Applications[1]

A feedback model of nonholonomically constrained dynamic system is presented with applications in analysis, control, and understanding of such systems under impulsive and friction forces.

1 Introduction

A feedback model of a nonholonomically constrained dynamic system is developed. This model contributes to better understanding of constrained dynamic systems and affords analysis and control of the evolution of such systems in time, allowing the constraints to be deliberately violated, maintained or, additionally imposed by external control. A general method of reduction of dimensionality for such systems is also provided. The model also renders some insight for analysis of dynamic systems with friction forces and those with impulsive inputs. Nonholonomic dynamic systems have been discussed by Kane [1, 2], Whittaker [3], and Rosenberg [4]. Friction has been discussed by Whittaker [5], Den Hartog [6], and Bowden and Tabor [7]. Impulsive forces are discussed in [2–4] and by Pars [8].

The feedback models of this paper are based on [9, 10] where it was shown that, in constrained motion of holonomically constrained dynamic systes, the Lagrange undetermined multipliers are explicit functions of the state (positions and velocities) and external inputs. This method is developed in Section 2. In Section 3, the reduction of dimensionality resulting from the imposition of the constraints is developed and compared with that of Kane [1]. In Section 4, the control problem and modeling of the friction forces are discussed. Finally, impulsive forces are treated in Section 5. Several examples are included in the text.

2 The Lagrangian Formulation

Let a dynamic system be characterized by l generalized coordinates Z, m external inputs U, and r nonholonomic constraints:

$$C(Z)\dot{Z} + G(Z) = 0 \tag{1}$$

where $C(Z)$ is a $r \times n$ matrix and $G(Z)$ is a r vector and $C(Z)$ and $G(Z)$ have first-order derivatives with respect to Z in the region of interest in the space of Z, and on its boundaries (where the constraints begin to be violated). Assume $C(Z)$ has rank r in this region. Let the kinetic energy, the potential energy, the incremented work of the external inputs, and the vector Γ of the forces of constraint be, respectively,

$$\begin{gathered} \tfrac{1}{2}\dot{Z}^T I(Z)\dot{Z} \\ V(Z) \\ dZ^T W(Z) U \\ \Gamma \end{gathered} \tag{2}$$

where I is an $l \times l$ symmetric positive-definite matrix, and $W(Z)$ is $n \times m$. The Lagrangian equations of motion for this system [1,3] are

$$\frac{d}{dt}\left(\frac{\partial L}{\partial \dot{Z}}\right) - \frac{\partial L}{\partial Z} = C^T\,\Gamma + W\,U \tag{3}$$

The left-hand side of equation (3) may be rewritten as

$$I(Z)\,\ddot{Z} + g(Z, \dot{Z}) = C^T\,\Gamma + W\,U \tag{4}$$

If equation (1) is differentiated with respect to time, one obtains

$$\frac{d}{dt}[C(Z)]\,\dot{Z} + C(Z)\,\ddot{Z} + \frac{\partial G^T}{\partial Z}\,\dot{Z} = 0 \tag{5}$$

From equations (4) and (5) one obtains uniquely the forces of constraint Γ as functions of state $X = [Z, \dot{Z}]^T$ and the inputs U

$$\Gamma = \Gamma(X, U) \tag{6}$$

The constraints can be in general classified into two classes: soft constraints and hard constraints. A soft constraint may be violated on either side of the constraint manifold (equation 1). A hard constraint can be violated only on one side of the surface of constraint. For soft constraints to be maintained, the force of constraint should satisfy certain inequalities as shown later in example 4. These inequalities can be written in the general form

$$L_1\Gamma + L_2U > 0 \tag{7}$$

where L_1 and L_2 are appropriate size matrices.

Hard constraints, on the other hand, retain the same polarity while the constraints are satisfied [9, 10].

$$\Gamma > 0 \tag{8}$$

---

[1] This work was in part supported by the National Science Foundation under Grants ENG74-21664 and ENG78-24440 and in part by the Department of Electrical Engineering, The Ohio State University, Columbus, Ohio.

Contributed by the Applied Mechanics Division of THE AMERICAN SOCIETY OF MECHANICAL ENGINEERS, for presentation at the 1981 Joint ASME/ASCE Applied Mechanics, Fluids Engineering, and Bioengineering Conference, University of Colorado, Boulder, Colo., June 22–27, 1981.

Discussion on this paper should be addressed to the Editorial Department, ASME, United Engineering Center, 345 East 47th Street, New York, N.Y. 10017, and will be accepted until June 1, 1981. Readers who need more time to prepare a Discussion should request an extension from the Editorial Department. Manuscript received by ASME Applied Mechanics Division, August, 1978; final revision, August, 1980. Paper No. 81-APM-12.

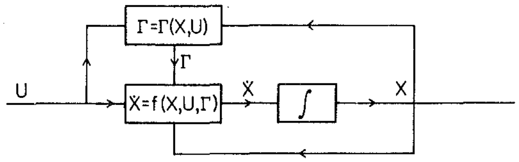

Fig. 1 Feedback model of a constrained system

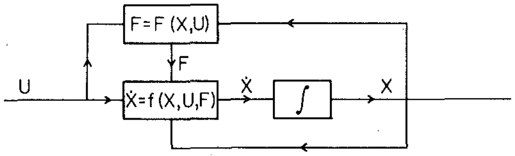

Fig. 2 Representation of a system with friction

When the hard constraints are violated, the forces of constraint become inactive

$$\Gamma = 0 \tag{9}$$

This development results in the feedback model of Fig. 1 encompassing both the constrained and unconstrained system.

In many nonholonomic systems, friction plays an important role. Consequently, friction forces must also be adequately modeled before control problems can be discussed.

Accurate modeling of friction is very difficult and involved [7, 11, 12]. Here it is assumed that friction forces F as functions of the state and the input are also available and well defined

$$F = F(X, U) \tag{10}$$

Therefore, a dynamic system with friction forces can be represented by the feedback model of Fig. 2. This model can also adequately represent other dissipative systems [3] but this subject is not to be considered here. If a dynamic system with friction is further constrained, the combination of Figs. 1 and 2 results in the model of Fig. 3, and can be described by the following equation:

$$\dot{X} = (X, U, F, \Gamma) \tag{11}$$

Example 1. Kane's two rigidly coupled disks rolling down an incline [1].

Let the parameters of the system be the same as Kane's with $Z = [\psi_1, \psi_2, x_1, x_2, \phi]^T$, the expressions for the kinetic, potential, and constraints are

$$T = m(\dot{x}_1^2 + \dot{x}_2^2) + m\left(r^2 + \frac{k^2}{2}\right)\dot{\phi}^2 + \tfrac{1}{2}J(\dot{\psi}_1^2 + \dot{\psi}_2^2)$$

where $J = mk^2$ is the moment of inertia.

$$V = -2x_1\, mg \sin\theta$$

$$C = \begin{bmatrix} r & -r & 0 & 0 & 2r \\ r\sin\phi & r\sin\phi & -2 & 0 & 0 \\ r\cos\phi & r\cos\phi & & 2 & 0 \end{bmatrix}$$

$$G = 0$$

Carrying out the calculations results in the following forces of constraint as functions of the state $[Z, \dot{Z}]^T$:

$$\Gamma = \begin{bmatrix} \gamma_1 \\ \gamma_2 \\ \gamma_3 \end{bmatrix} = m \begin{bmatrix} \dfrac{r^2\cos^2\phi + k^2}{r^2 + k^2} g \sin\theta - \dfrac{r}{2}\dot{\phi}\cos\theta\,(\dot{\psi}_1 + \dot{\psi}_2) \\ \dfrac{-r^2\sin\phi\cos\phi}{r^2 + k^2} g\sin\theta + \dfrac{r}{2}\dot{\phi}\sin\theta\,(\dot{\psi}_1 + \dot{\psi}_2) \end{bmatrix} \tag{12}$$

The equations of motion are

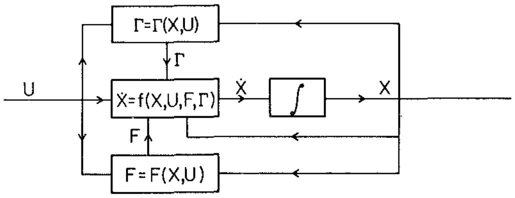

Fig. 3 Representation of a constrained system with friction

$$\begin{cases} \dot{Z} = \dot{Z} \\ \ddot{Z} = I^{-1}C^T\Gamma + I^{-1}[0, 0, 2mg\sin\theta, 0, 0]^T \end{cases} \tag{13}$$

where I is the diagonal 5×5 matrix

$$I_{11} = I_{22} = mk^2$$

$$I_{33} = I_{44} = 2m$$

$$I_{55} = m\left(r^2 + \frac{k^2}{2}\right)$$

If vector Γ is substituted in (13), the equations of motion, under constraint are

$$\begin{aligned} \ddot{\psi}_1 &= \frac{r\,g\sin\theta\sin\phi}{r^2 + k^2} \\ \ddot{\psi}_2 &= \frac{r\,g\sin\theta\sin\phi}{r^2 + k^2} \\ \ddot{x}_1 &= g\sin\theta\frac{r^2\sin^2\phi}{r^2 + k^2} + \frac{r}{2}\cos\phi\,(\dot{\psi}_1 + \dot{\psi}_2)\dot{\phi} \\ \ddot{x}_2 &= g\sin\theta\frac{-r^2\sin\phi\cos\phi}{r^2 + k^2} + \frac{r}{2}\sin\phi\,\dot{\phi}(\dot{\psi}_1 + \dot{\psi}_2) \\ \ddot{\phi} &= 0 \end{aligned} \tag{14}$$

These equations, naturally satisfy the equations of constraint, and are equivalent to those of Kane [1]. More will be said about the equivalence below.

3 Reduction of Dimensionality

When the r constraints are satisfied, the system's dimension reduces to $l - r$. Kane's method for derivation of the reduced equations is based on generalized active and inertial forces [1]. An alternative method of deriving Kane's results is provided later.

Consider the r dimensional subspace spanned by the rows of C. Let OC be the orthogonal complement of C, and let H be a $(l - r) \times n$ matrix whose rows span the subspace OC. By definition

$$HC^T = 0 \tag{15}$$

If both sides of equation (4) are premultiplied by H, the forces of constraint are eliminated and the following $l - r$ equations result

$$HI(Z)\ddot{Z} + Hg(Z, \dot{Z}) = MWU \tag{16}$$

Equations (1) and (16) are the reduced equations of the system.

Since H is not unique, the reduced equations of the system are not unique in form. Consequently, for the reduced system, a variety of representations are possible.

Example 2. In example 1, let the orthogonal complement of C be specified by

$$H = \begin{bmatrix} 1 & -1 & 0 & 0 & -1 \\ -1 & -1 & -r\sin\phi & r\cos\phi & 0 \end{bmatrix} \tag{17}$$

Then the reduced equations are

$$\begin{gathered} (3mk^2 + 2mr^2)\,\ddot{\phi} = 0 \\ \ddot{\psi}_1 + \ddot{\phi} = \frac{1}{k^2 + r^2} gr\sin\theta\sin\phi \end{gathered} \tag{18}$$

On the other hand, if H has the form

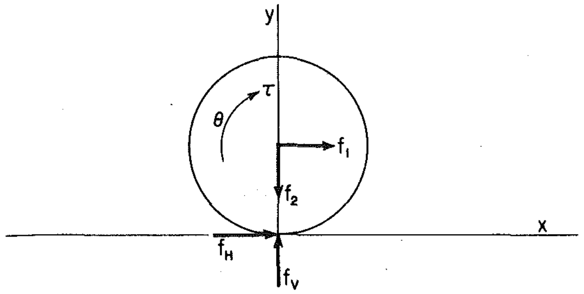

Fig. 4 Wheel on a plane

$$H = \begin{bmatrix} 2 & 2 & r\sin\phi & r\cos\phi & -1 \\ -1 & -1 & -r\sin\phi & r\cos\phi & 0 \end{bmatrix} \tag{19}$$

Then Kane's equations of motion (see reference [1]) result.

The computation of H may be eased by a variety of transformations. Suppose in equation (4) both sides are multiplied by I^{-1}

$$\ddot{Z} + I^{-1} g(Z,\dot{Z}) = I^{-1}C^T \Gamma + I^{-1} WU \tag{20}$$

Now H may be selected to correspond to the orthogonal complement of $(CI^{-1})^T$.

Alternatively, let $T(Z)$ be an $r \times r$ nonsingular transformation. Let the equations of constraint be premultiplied by T

$$T\,C\,\dot{Z} + T\,G = C_1\,\dot{Z} + G_1 = 0 \tag{21}$$

Computation of H as well as computation of the forces of constraint may be eased by the choice of T.

Example 3. In example 1, the transformation

$$T = \begin{bmatrix} 1 & 0 & 0 \\ -\sin\phi & 2 & 0 \\ -\cos\phi & 0 & 2 \end{bmatrix}$$

was applied to Kane's equations of constraint (see reference [1, equations (23, 25)]) which resulted in considerable simplification of the Lagrangian derivation.

Finally, if it is *a priori* known that certain constraints can never be violated, one may use part of H to eliminate only the corresponding forces of constraint and retain others.

While the derivation of Kane [1] is physically based and relies on D'Alembert's law, the derivation here is mathematically based and relies on the Lagrangian method. The latter allows manipulation of the computations by choice of matrices H and T.

4 The Control Problem

With the foregoing discussion, a dynamic system is represented by equations (1) and (11). The control of dynamic systems with hard holonomic constraints is discussed in [9, 10]. Here the control of systems with soft nonholonomic constraints are considered. For these systems, one must specify input reference signals V and feedback laws

$$U = U(X,V) \tag{22}$$

such that two major control problems can be solved.

1 The trajectory of the constrained motion is modified, while the constraint is maintained.

2 A transition is made from constrained motion to unconstrained motion and vice versa.

If the system had no constraints whatsoever, classical state variables or optimal control would be utilized. For maintaining the constraint, essentially two approaches are available:

1 One designs the control system such that the motion remains in the constrained subspace [9].

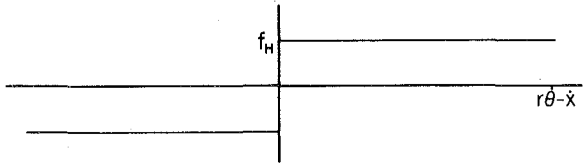

Fig. 5 Friction force versus relative velocity

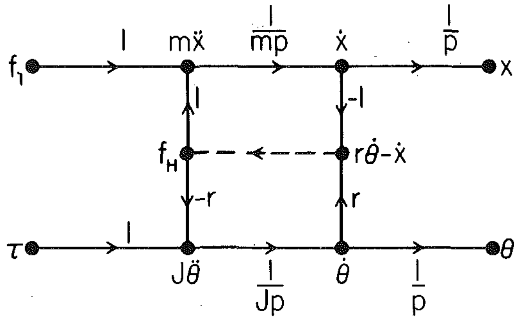

Fig. 6 Signal-flow graph

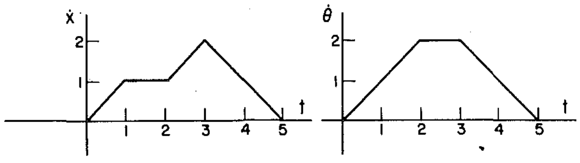

Fig. 7 Specified velocities for example

2 One indirectly controls the forces of constraint Γ, maintaining the constraint [10].

To be more specific, the second approach is applied to the control of a wheel in the following example.

Example 4. Consider a wheel [12, 13] of radius r, mass m, and moment of inertia J, on a place with both static and sliding friction as shown in Fig. 4. The inputs are the forces f_1 and f_2 and the torque τ. The forces at the point of contact are the vertical reaction force f_V and the friction force f_H, which is assumed to be a function of the relative velocity $(r\dot{\theta} - \dot{x})$. An example is shown in Fig. 5, and in this case equation (10) reduces to

$$f_H = \mu f_2 \operatorname{sgn}(r\dot{\theta} - \dot{x}) \tag{23}$$

where μ is the coefficient of friction.

If the wheel is in contact with the plane,

$$y = r \tag{24}$$

and

$$f_V = f_2. \tag{25}$$

The equations of motion (4) then become

$$m\ddot{x} = f_1 + f_H \tag{26}$$

$$J\ddot{\theta} = \tau - rf_H \tag{27}$$

and can be represented by the signal-flow graph of Fig. 6. A dotted line is used to represent the functional relationship of equation (23). When the wheel rolls without slipping, f_H can assume any value between $-\mu f_2$ and $+\mu f_2$ in order to make $\dot{x} = r\dot{\theta}$.

If $\dot{x}$ and $\dot{\theta}$ are specified as functions of time, it is possible to find f_1 and τ as follows. The required accelerations $\ddot{x}$ and $\ddot{\theta}$ can be found by differentiating the specified velocities. Then from equations (26) and (27)

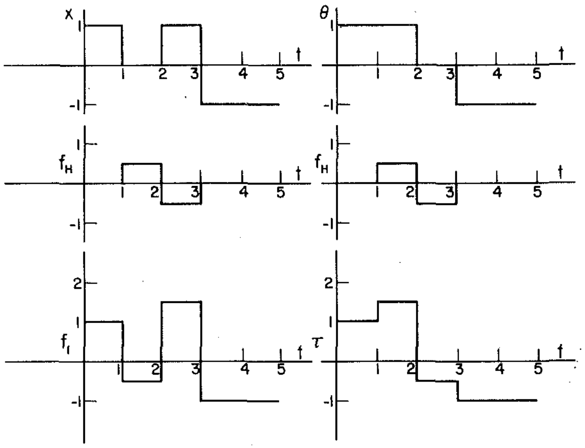

Fig. 8 Calculation of f_1 and τ

$$f_1 = m\ddot{x} - f_H \tag{28}$$

$$\tau = J\ddot{\theta} + rf_H \tag{29}$$

Three cases must be considered in order to find the value of f_H to be used in equations (28) and (29).

Case I. If $\dot{x} = r\dot{\theta}$, the wheel rolls without slipping, and f_H may have any value between $-\mu f_2$ and $+\mu f_2$.

Case II. If $\dot{x} < r\dot{\theta}$, the wheel must slip, and $f_H = +\mu f_2$.

Case III. If $\dot{x} > r\dot{\theta}$, the wheel must slip, and $f_H = -\mu f_2$.

This procedure can be illustrated by letting $m = J = r = 1$ for simplicity and calculating f_1 and τ for the velocities $\dot{x}$ and $\dot{\theta}$ in Fig. 7. This calculation is shown in Fig. 8. The maximum absolute value of f_H was assumed to be 0.5, and f_H was assumed to be zero when there was no slipping.

Feedback can be used to produce the required values of f_1 and τ from the commanded values $\dot{x}_c$ and $\dot{\theta}_c$. A simple feedback scheme is shown in Fig. 9, where K_x and K_θ are large values of gain.

If the system in Fig. 9 is linearized by assuming viscous friction between the wheel and the plane, the dotted line may be replaced by a branch of gain k. The four transfer functions then are

$$\frac{\dot{x}}{\dot{x}_c} = \frac{K_x(Jp + kr^2 + K_\theta)}{mJp^2 + (kJ + kmr^2 + K_xJ + K_\theta m)p + kK_\theta + kr^2K_x + K_xK_\theta}$$

$$\frac{\dot{\theta}}{\dot{\theta}_c} = \frac{K_\theta(mp + k + K_x)}{mJp^2 + (kJ + kmr^2 + K_xJ + K_\theta m)p + kK_\theta + kr^2K_x + K_xK_\theta}$$

$$\frac{\dot{x}}{\dot{\theta}_c} = \frac{K_\theta kr}{mJp^2 + (kJ + kmr^2 + K_xJ + K_\theta m)p + kK_\theta + kr^2K_x + K_xK_\theta}$$

$$\frac{\dot{\theta}_c}{\dot{x}_c} = \frac{K_xkr}{mJp^2 + (kJ + kmr^2 + K_xJ + K_\theta m)p + kK_\theta + kr^2K_x + K_xK_\theta}$$

If k, K_x, and K_θ are positive, all the poles of these transfer functions will be in the left half plane, and stability is assured.

Since the signal-flow graph of Fig. 9 contains a single nonlinearity, stability can be shown without the assumption of linear friction. If the inputs $\dot{x}_c$ and $\dot{\theta}_c$ are set equal to zero, the linear portion of Fig. 9 may be reduced to a single branch $G(p)$ as shown in Fig. 10.

where

$$G(p) = \frac{1}{1 + K_xmp} + \frac{r^2}{1 + K_\theta Jp} = \frac{1 + r^2 + (K_xmr^2 + K_\theta J)p}{(1 + K_xmp)(1 + K_\theta Jp)} \tag{30}$$

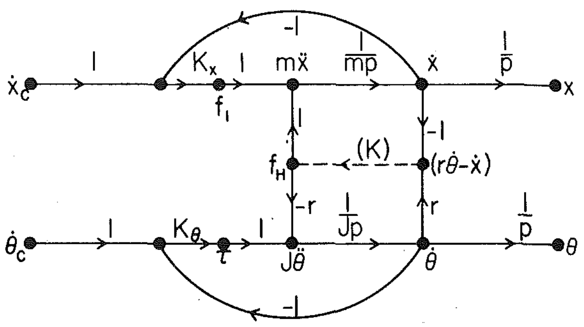

Fig. 9 Feedback control example

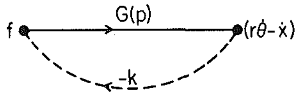

Fig. 10 Reduced flow graph

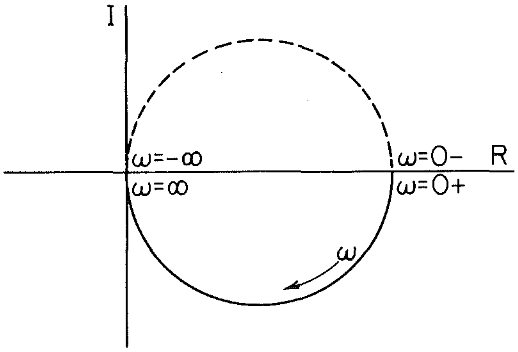

Fig. 11 Polar sketch of $G(j\omega)$

$G(p)$ has two poles and one zero, all of which are real and negative. Furthermore, the zero is between the two poles, and the phase angle of the frequency response $G(j\omega)$ lies between 0 and $-90°$ for all positive values of w. A sketch of $G(j\omega)$ is shown in Fig. 11. Since $G(j\omega)$ lies entirely in the right half plane and k, the equivalent gain of the nonlinearity, varies from 0 to $+\infty$, the system is seen to be stable by Popov's criterion.

5 Impulsive Inputs

Consider the system of equations (4) and (6) in state space form

$$\begin{aligned} \dot{Z} &= \dot{Z} \\ \ddot{Z} &= I^{-1}[-g(Z, \dot{Z}) + C^T\,\Gamma\,(Z, \dot{Z}, U) + WU] \end{aligned} \tag{31}$$

Suppose the system is under constrained motion. If U or components of U are impulsive or have impulsive components at time t, certain components of Γ are also impulsive from equation (6). Both of these impulses in U and Γ enter in equation (31) explicitly. If equation (31) is intergrated, the instantaneous changes in velocities can be computed

$$\Delta\dot{Z} = \dot{Z}\,(t_1^+) - \dot{Z}\,(t_1^-) \tag{32}$$

Example 5. Suppose the wheel in Example 4 is suddenly subjected to an impulsive input force $f_1 = \delta(t - t_1)$. This immediately violates the constraint that $\dot{x} = r\dot{\theta}$. Consequently, the system immediately (even through the application of impulse) loses the constraint and would be governed by equations (26). If the input torque τ is impulsive, the same argument holds, and the constraint is violated. If both f_1 and τ are impulsive at the same instant, and their ratio is such that f_H in equation (28) does not have any impulsive component, the constraint is not violated, and the wheel rolls without slipping.

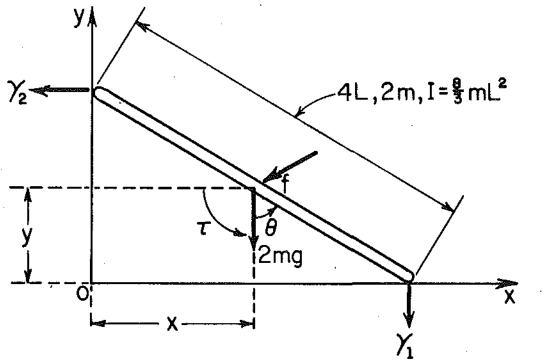

Fig. 12 A rod sliding down a vertical wall

Examples 6. Sliding movement of a rod down a wall from Kane [2, pp. 219–222].

Consider movement of a rod (Fig. 12) under the force of gravity and input force f and input torque τ. There is no friction and the rod slides down. At the instant that the rod leaves the wall, external impulsive force f and torque τ are applied to reverse the direction of motion, so that the rod starts sliding up the wall with prescribed velocity.

Let the weight, length, and the movement of inertia of the rod be, respectively, $2m$, $4L$ and $(8m/3)\,L^2$. Let the generalized coordinates of the system be $Z = [x, y, \theta]$.^{T} This is a holonomic system and the two constraints are

$$\begin{aligned} y - 2L, \cos\theta = 0 \\ x - 2L, \sin\theta = 0 \end{aligned} \tag{33}$$

Let the corresponding forces of constraint be $\Gamma = [\gamma_1, \gamma_2]^T$. Following the approach just presented, and in [9] with $X = [Z, Z]^T$. The equations of motion are

$$\begin{aligned} \dot Z &= \dot Z \\ &\frac{1}{2m}(-\gamma_2 - fx) \\ \ddot Z &= \frac{1}{2m}(-\gamma_1 - 2mg - fy) \\ &\frac{3}{8mL^2}(\tau + 2L\cos\theta\gamma_2 - 2\text{L}\sin\theta\gamma_1) \end{aligned} \tag{34}$$

or in summary

$$\dot X = F(X, \Gamma, U) \tag{35}$$

The constraint forces become the following functions of the state and the input:

$$\begin{aligned} \gamma_1 &= 4mL\dot\theta^2\cos\theta - \left(\frac{mg}{2} + \frac{fy}{4}\right)(1 + 3\cos^2\theta) \\ &\quad - \tfrac{3}{4}\sin\theta\cos\theta\, fx + \frac{3}{8L}\tau\sin\theta \\ \gamma_2 &= 4mL\dot\theta^2\sin\theta - \left(\frac{mg}{2} + \frac{fy}{4}\right)3\sin\theta\cos\theta \\ &\quad - \tfrac{1}{4}(1 + 3\sin^2\theta)\, fx - \frac{3}{8L}\tau\cos\theta \end{aligned} \tag{36}$$

For the constraints to be satisfied, both γ_1 and γ_2 must be negative.

Case 1. Sliding Down. Suppose only the force of gravity is active, matrix H of equation (11) is

$$H = [2L\cos\theta - 2L\sin\theta\ 1] \tag{37}$$

Following step of equation (12) and differentiating equations (33) twice one obtains

$$\ddot\theta = \frac{3g}{8L}\sin\theta \tag{38}$$

The rod leaves the wall when $\gamma_2 = 0$ or

$$\dot\theta^2 = \frac{3g}{8L}\cos\theta \tag{39}$$

Case 2. Sliding Up. It is desired to apply inpulsive force f and torque τ at the instant that the rod leaves the wall in order to reverse the movement's direction, but with, say, one half of the downward velocity.

From equation (36) it is obvious that one cannot do this with an impulsive torque τ alone. The impulsive torque τ must be negative, but then γ_2 becomes positive—a violation of constraint. Therefore at least a positive impulsive force fx is additionally necessary. Letting fx and τ be the amplitudes (positive or negative) of the impulses, from equation (36)

$$\begin{aligned} &-\tfrac{1}{4}(1 + 3\sin^2\theta)\, fx - \frac{3}{8L}\tau\cos\theta < 0 \\ &fx > \frac{-3}{2L}\frac{\cos\theta}{1 + 3\sin^2\theta}\tau \end{aligned} \tag{40}$$

Let equation (40) be satisfied. Equation (36) can be used to derive the impulsive components of Γ. The result is substituted in equation (34) and integrated to derive

$$\dot Z(t^+) - \dot Z(t^-) = I^{-1}\begin{bmatrix} -\tfrac{3}{4}\cos^2\theta & \dfrac{3}{8L}\cos\theta & \\ \dfrac{3\sin\theta\cos\theta}{4} & \dfrac{-3}{8L}\sin\theta & \\ \dfrac{-2L\cos\theta}{4} & \dfrac{2L\sin\theta}{4} & \tau \end{bmatrix} fx \tag{41}$$

From the requirement that the velocity of the upward motion be ½ of that of the downward motion one derives

$$\dot Z(t^+) - \dot Z(t^-) = \begin{bmatrix} -3L\dot\theta\cos\theta \\ 3L\dot\theta\sin\theta \\ -1.5\dot\theta \end{bmatrix} \tag{42}$$

From (41) and (42) fx and τ are related by

$$-\tfrac{3}{4}\cos\theta\, fx + \frac{3}{8L}\tau = 6L\dot\theta m \tag{43}$$

Let the following equality be substituted for equation (40)

$$fx = -\frac{2}{L}\frac{\cos\theta}{1 + 3\sin^2\theta}\tau \tag{44}$$

Then (43) and (44) can be solved for τ and fx. It also becomes apparent that the solution is not unique.

Impulse forces may also arise [4, 8] when the system is subjected to additional surfaces of constraint, not accounted for in equation (1). The approach here can also be extended to such systems. Further discussion of this point is found in Kane [2, p. 228]. Also an example when the foot of a walking biped kicks a rigid stationary obstacle is given in [14].

6 Conclusions

A model of a class of nonholonomically constrained dynamic systems is developed where the forces of constraint are explicit functions of the state and inputs. This model is useful in cases where the constraints may be violated and imposed at will.

A reduction of dimensionality method was discussed that is an alternative method to the method of generalized active forces and moments provided by Kane. As a matter of fact, it is a Lagrangian interpretation of Kane's results. It also shows that the representations of reduced systems are not unique in form. Some other uses can be cited:

1 The approach here may be used as a checking mechanism to prevent human error in the deriving equations of motion.

2 With *a priori* knowledge that certain constraints can never be violated, one may use this method to eliminate only the corresponding forces of constraint.

3 For large dimensional systems where computers may be used to derive equations of motion [15], it may facilitate and formalize Kane's method.

An example with Coulomb friction force was discussed in order to reduce the control of nonholonomic systems to that of holonomic systems and control and stability were considered.

Finally, one application of the model in analysis of systems with impulsive inputs was demonstrated for a holonomically constrained system.

Acknowledgment

The authors would like to thank Prof. H. C. Ko, Chairman of the Department of Electrical Engineering at The Ohio State University for his sustained encouragement and support of this work.

References

1 Kane, T. R., "Dynamics of Nonholonomic Systems," ASME JOURNAL OF APPLIED MECHANICS, Vol. 28, Dec. 1961, pp. 574–578.

2 Kane, T. R., *Dynamics*, Holt, Rinehart, and Winston, New York, 1968.

3 Whittaker, *A Treatise on the Analytical Dynamics of Particles and Rigid Bodies*, Dover Publications, Inc., New York, p. 214.

4 Rosenberg, R. M., *Analytical Dynamics of Discrete Systems*, Plenum Press, New York, 1977.

5 Whittaker, Ibid., p. 226.

6 Den Hartog, J. P., *Mechanics*, Dover Publications, Inc., New York, 1948.

7 Bowden, F. P., and Tabor, D., *Friction, An Introduction to Tribology*, Anchor Press, New York, 1968.

8 Pars, L. A., *A Treatise on Analytical Dynamics*, Wiley, New York, 1968.

9 Hemami, H., and Wyman, B., "Modeling and Control of Constrained Dynamic Systems With Application to Biped Locomotion in the Frontal Plane," *IEEE Transactions on Automatic Control*, Vol. AC-24, Aug. 1979, pp. 26–535.

10 Hemami, H., and Wyman, B. F., "Indirect Control of the Forces of Constraint in Dynamic Systems," ASME *Journal of Dynamic Systems, Measurement and Control*, Vol. 101, Dec. 79, pp. 355–360.

11 Moore, D. F., *The Friction of Pneumatic Tyres*, Elsevier Scientific Publishing Co., Amsterdam, 1975, Section 2.7.

12 Hays, D. F., and Browne, A. L., *The Physics of Tire Traction*, Plenum Press, May 1974.

13 Boyd, P. L., Neill, A. H., Jr., and Hinch, J. "The Use of the Mobile Tire Traction Dynamometer in Research," Paper No. 780196, presented at SAE Congress in Detroit, Mich., Feb. 1978.

14 Hemami, H., and Farnsworth, R. L., "Postural and Gait Stability of a Planar Five Link Biped by Simulation," *IEEE Trans. on Automatic Control*, Vol. AC-22, No. 3, June 1977, pp. 452–458.

15 Dillon, S. R., and Hemami, H., "Automated Equation Generation and Its Application to Problems in Control," *Proc. of Fifteenth Joint Automatic Control Conference*, Austin, Texas, June 1974.

K. Huseyin

Professor and Chairman,
Department of Systems Design,
University of Waterloo,
Waterloo, Ontario, N2L 3G1,
Canada

On the Stability of Equilibrium Paths Associated With Autonomous Systems

The postcritical behavior and stability distribution on the equilibrium paths emanating from a divergence point associated with an autonomous system are studied within a state-space formulation. The analysis concerning the stability of equilibrium paths is based on the eigenvalues of the Jacobian evaluated at arbitrary equilibrium points in the vicinity of a critical point. Explicit conditions of stability and instability concerning the initial and postcritical paths are obtained through a perturbation approach. It is shown that at an asymmetric point of bifurcation an exchange of stabilities between two paths occurs in complete analogy with conservative systems. Similarly, a symmetric point of bifurcation involves a postcritical path which is totally stable (unstable) if the initial path is unstable (stable).

1 Introduction

The stability of an equilibrium state associated with gradient systems can be studied on the basis of the extremum properties of a potential function. In the analysis of elastic conservative systems, for example, the "energy criterion" provides a powerful means for this purpose[1]. In the case of nongradient systems, however, the convenience of basing the formulation and analysis on a well-behaved potential function is lost, and other methods have to be adopted.

The postcritical behavior of nongradient systems has been studied by a number of authors. Plaut [2, 3], for example, analyzed the divergence behavior of a discrete nonconservative mechanical system statically by setting the frequency to zero in Lagrange's equations and assuming that the system exhibits a trivial fundamental equilibrium path. Mass distribution and dissipation are not incorporated in this analysis, and the author remarks in his conclusions [3] that stability cannot be studied in general terms. In other investigations [4, 5], a more general approach, involving a set of first-order autonomous differential equations, is adopted. In this approach both gradient and nongradient systems are covered under the same formulation which is capable of yielding information on dynamic behavior as well as divergence. Since the Lagrangian equations can be transformed into first-order state equations with a simple transformation of variables without losing information (e.g., mass distribution and dissipation), the method seems to be quite comprehensive.

The attention in references [4, 5], however, is focussed on the critical conditions and the equilibrium solutions rather than their stability. In fact, an analysis concerning the stability of equilibrium states would have been rather cumbersome if not impossible under the formulation of [4, 5]. In this paper, a further transformation is introduced which facilitates the stability analysis, and enables one to explore the stability distribution on the initial and postcritical paths *explicitly* on a comparative basis.

2 Bifurcating Stationary Solutions

Consider an autonomous dynamical system represented by the first-order differential equations

$$dy/dt = Y(y, \lambda) \qquad (1)$$

where y is the state vector of n-components in the Euclidean space E_n and λ is an independent real scalar parameter. The nonlinear vector function Y is assumed to be real analytic in the state variables $y^i (i = 1, 2, \dots n)$ and λ in a region (R) of interest. The equilibrium states of the system are described by the stationary solutions of (1),

$$Y(y, \lambda) = 0 \qquad (2)$$

Normally, the set of nonlinear equations (2) defines certain equilibrium paths which are one-dimensional manifolds of the $n + 1$ dimensional *state-space* E_{n+1} spanned by $y^i (i = 1, 2, \dots, n)$ and λ. Without loss of generality, suppose an *initially stable path* emerges from the origin of E_{n+1}; it is assumed that all the eigenvalues of the Jacobian matrix evaluated on this path have negative real parts in this neighborhood. As λ is increased, a *critical point* on the path may be

---

Contributed by the Applied Mechanics Division of THE AMERICAN SOCIETY OF MECHANICAL ENGINEERS, for presentation at the 1981 Joint ASME/ASCE Applied Mechanics, Fluids Engineering, and Bioengineering Conference, University of Colorado, Boulder, Colo., June 22–27, 1981.

Discussion on this paper should be addressed to the Editorial Department, ASME, United Engineering Center, 345 East 47th Street, New York, N. Y. 10017, and will be accepted until June 1, 1981. Readers who need more time to prepare a Discussion should request an extension from the Editorial Department. Manuscript received by ASME Applied Mechanics Division, March, 1980; final revision, July 1980. Paper No. 81-APM-9.

reached where the real part of at least a pair of complex eigenvalues vanishes and, with a further increase in λ, becomes positive, resulting in an oscillatory instability (flutter). At the onset of flutter instability, the system may bifurcate into limit cycles which will not be analyzed in this paper (Hopf bifurcation). Another type of instability occurs when at least one real eigenvalue of the Jacobian vanishes at a critical point and becomes positive with a further increase in λ (divergence instability). This phenomenon has been explored in [4, 5] with regard to *coincident* as well as *simple* critical points, and various equilibrium path configurations in the vicinity of a critical divergence point are obtained systematically through a convenient perturbation procedure which yields asymptotic results. In order to examine the stability of the equilibrium paths emanating from a critical point, however, a more appropriate formulation has to be introduced to facilitate the analysis.

Let the initial path have a critical divergence point on it in the region of interest (R), and be expressed in the form $y = f(\lambda)$ where the vector function f is assumed to be single-valued in the neighborhood of the critical point. A coordinate system $\bar{y}$ can then be attached to the initial path by the relation

$$y = f(\lambda) + \bar{y}. \tag{3}$$

Substituting (3) into (1), one obtains

$$d\bar{y}/dt = \bar{Y}(\bar{y}, \lambda) \tag{4}$$

with the properties

$$\bar{Y}(0, \lambda) = \bar{Y}'(0, \lambda) = \bar{Y}''(0, \lambda) = \ldots = 0 \tag{5}$$

which arise [1] from the derivation of (4). Here and in the sequel the primes on the functions are used to denote partial differentiation with respect to the parameter. It is understood that the assumption underlying the transformation (3) excludes the limit points from the analysis; see [4]. A further transformation

$$\bar{y} = Px, \tag{6}$$

will be introduced into (4) to obtain

$$dx/dt = X(x, \lambda) \tag{7}$$

such that its Jacobian matrix

$$J = \left[\frac{\partial X}{\partial x}\right]_c,$$

evaluated at the critical point $c(\lambda = \lambda_c)$ is in the canonical form

$$J = \operatorname{diag}[D, K_3, K_5, \ldots] \tag{8}$$

with real elements. Here

$$D = \begin{bmatrix} 0 & 0 \\ 0, & \alpha_2 \end{bmatrix}, \quad K_r = \begin{bmatrix} \alpha_r & -\beta_r \\ \beta_r & \alpha_r \end{bmatrix}, \quad r = (3, 5, \ldots) \tag{9}$$

in which $\alpha_2 < 0$, $\alpha_r < 0$, and the K_r correspond to complex conjugate eigenvalues $(\alpha_r \pm i\beta_r)$. The block D is chosen here as a 2×2 matrix solely for its simplicity and to avoid another subscript for real eigenvalues without loss of generality. In fact there can be m (2, 3, 4, 5, .) nonvanishing real eigenvalues, $\alpha_m < 0$, which would have no essential effect on the following analysis. It can readily be seen that the properties (5) are carried over to the vector function X, and one has

$$X(0, \lambda) = X'(0, \lambda) = X''(0, \lambda) = \ldots = 0. \tag{10}$$

Consider now a transformation of the form (6) but with a matrix $P = P(\lambda)$ such that, when λ varies in the neighborhood of $\lambda = \lambda_c$, the canonical form (8) of the Jacobian along the initial path $f(\lambda)$ is preserved. In other words, for each value of λ in the vicinity of $\lambda = \lambda_c$, an appropriate transformation matrix $P(\lambda)$ is formed in such a way that the Jacobian matrix $[\partial X/\partial x]$ evaluated on the *initial path* has the block-diagonal form of (8) with D always diagonal:

$$\left[\frac{\partial X}{\partial x}\right]_{x=0} = \left[\begin{array}{cc|cc|c} \alpha_1(\lambda) & 0 & & 0 & \\ 0 & \alpha_2(\lambda) & & & \\ \hline & & \alpha_3(\lambda) & -\beta_3(\lambda) & \\ & 0 & & & 0 \\ & & \beta_3(\lambda) & \alpha_3(\lambda) & \\ \hline & & & 0 & \end{array}\right] \tag{11}$$

where $\alpha_1(\lambda_c) = 0$, and the $\alpha_t (t = 2, 3, \ldots)$ remain negative in this neighborhood.

It follows that all the off-block-diagonal elements and their derivatives with respect to λ vanish along the initial path. This property will facilitate the stability analysis and will be used in the following sections. Thus, if the Jacobian is denoted by $X_{ij}(x^k, \lambda)$ one has for example,

$$X_{ij}(0, \lambda) = X'_{ij}(0, \lambda) = X''_{ij}(0, \lambda) = \ldots 0 \quad \text{for} \quad i \neq j \quad \text{where} \quad i = 1, 2. \tag{12}$$

Similar properties can be expressed for the remaining blocks on the diagonal.

Stationary solutions of (7) satisfy $X(x, \lambda) = 0$ which can also be expressed as

$$X_i(x^j, \lambda) = 0. \tag{13}$$

The formulation assumes that $x^i = 0$ is the initial equilibrium path, and the other possible paths in the vicinity of $\lambda = \lambda_c$ are sought in the parametric form

$$x = x(\sigma), \quad \lambda = \lambda(\sigma). \tag{14}$$

The scalar parameter σ is chosen such that the functions in (14) are single-valued in σ and can be expanded into power series around the point c. Introducing (14) into (13) one obtains the identities

$$X[x(\sigma), \lambda(\sigma)] \equiv 0 \tag{15}$$

which can be used to generate asymptotic solutions intrinsically by successive differentiations. Thus the first, second, and third-order perturbations yield

$$\partial_j X_i \dot{x}^j + \partial_0 X_i \dot{\lambda} = 0, \tag{16}$$

$$\partial_{jk} X_i \dot{x}^j \dot{x}^k + 2\partial_{j0} X_i \dot{x}^j \dot{\lambda} + \partial_j X_i \ddot{x}^j + \partial_{00} X_i (\dot{\lambda})^2 + \partial_0 X_i \ddot{\lambda} = 0 \tag{17}$$

and

$$\begin{aligned} \partial_{jkl} X_i \dot{x}^j \dot{x}^k \dot{x}^l + 3\partial_{jk0} \dot{X}_i \dot{x}^j \dot{x}^k \dot{\lambda} + 3\partial_{jk} X_i \ddot{x}^j \dot{x}^k \\ + 3\partial_{j00} X_i \dot{x}^j (\dot{\lambda})^2 + 3\partial_{j0} X_i \ddot{x}^j \dot{\lambda} + 3\partial_{j0} X_i \dot{x}^j \ddot{\lambda} \\ + \partial_j X_i \ddot{x}^j + 3\partial_{00} X_i \dot{\lambda}\, \ddot{\lambda} + \partial_{000} X_i (\dot{\lambda})^3 + \partial_0 X_i \ddot{\lambda} = 0 \end{aligned} \tag{18}$$

where the dots denote differentiation with respect to the parameter σ, the operators ∂_0, ∂_j, ∂_{j0}, etc., indicate differentiation with respect to λ, x^j, x^j, and λ, etc., respectively, and summation convention is adopted.

If the arc length of the equilibrium path (14), measured from the critical point c is used as the parameter σ, the analysis is simplified considerably. The unit tangent vector of the path (14) at c is then given by $(n + 1)$ components $\dot{x}$ and $\dot{\lambda}$, satisfying the relation

$$(\dot{x}^1)^2 + (\dot{x}^2)^2 + \ldots + (\dot{x}^n)^2 + (\dot{\lambda})^2 = 1 \tag{19}$$

Equations (16)–(19) will now be used to explore the properties of the postcritical path(s) in the vicinity of c. Evaluating (16) at c with the aid of (10) and (11) yields

$$\dot{x}^2 = 0, \quad \dot{x}^s = 0 \quad (s = 3, 4, \ldots n). \tag{20}$$

Similarly, evaluation (17) with the aid of (10), (11), and (20) results in

$$\left\{\begin{array}{r} \dot{x}^1 = 0 \\ \ddot{x}^2 = 0 \\ \\ \ddot{x}^r = \ddot{x}^{r+1} = 0 \end{array}\right\} \text{ or } \left\{\begin{array}{l} \dot{\lambda} = (-X_{111}/2X'_{11})\dot{x}^1 \\ \ddot{x}^2 = (-X_{211}/\alpha_2)(\dot{x}^1)^2 \\ \\ \begin{bmatrix} \alpha_r & -\beta_r \\ \beta_r & \alpha_r \end{bmatrix}\begin{bmatrix} \ddot{x}^r \\ \ddot{x}^{r+1} \end{bmatrix} = -\begin{bmatrix} X_{311} \\ X_{411} \end{bmatrix}(\dot{x}^1)^2, \end{array}\right\} \begin{array}{r} (21) \\ (22) \\ \\ (23) \end{array}$$

$$(r = 3, 5, \ldots)$$

where the derivatives of X_i evaluated at the critical point c are indicated by the obvious notation $[\partial_{jk}X_i]_c = X_{ijk}$, $[\partial_{j0}X_i]_c = X'_{ij}$, etc., and it is assumed that $X'_{11} \neq 0$ (see [1] for a discussion of the case $X'_{11} = 0$ associated with conservative systems).

The solution of these equations give the initial and postcritical paths asymptotically. The former path is thus defined by

$$x^1 = x^2 = x^3 = \ldots = 0 \tag{24}$$

as expected, and the latter is obtained upon setting $\sigma \equiv x^1$ and using $\lambda = \lambda_c + \varphi$, as

$$\begin{aligned} \varphi &= -\frac{1}{2}\frac{X_{111}}{X'_{11}}x^1 \\ x^2 &= -\frac{1}{2}\frac{X_{211}}{\alpha_2}(x^1)^2 \triangleq -\frac{1}{2}a_2(x^1)^2 \\ x^r &= -\frac{1}{2}\frac{\alpha_r X_{r11} + \beta_r X_{(r+1)11}}{(\alpha_r)^2 + (\beta_r)^2}(x^1)^2 \triangleq -\frac{1}{2}a_r(x^1)^2 \qquad (25) \\ x^{r+1} &= -\frac{1}{2}\frac{\alpha_r X_{(r+1)11} - \beta_r X_{r11}}{(\alpha_r)^2 + (\beta_r)^2}(x^1)^2 \triangleq -\frac{1}{2}a_{r+1}(x^1)^2 \end{aligned}$$

where $r = 3, 5 \ldots$. It is clear that allowing for more real eigenvalues α_m ($m = 2, 3, \ldots$) would simply result in more equations of the type shown on the second line in equation (25), in effect replacing subscripts and superscripts 2 by m.

Equation (25) defines the postdivergence path which intersects the initial path at the critical point c. It is seen that the critical point is an "asymmetric point of bifurcation" in complete analogy with gradient systems [1, 5].

It may turn out that certain key coefficient(s) vanish at c and, in fact, (25) indicates that if $X_{111} = 0$, one will have to resort to further perturbations in order to obtain the first-order equations of the postcritical path. To this end, evaluate the third-order perturbation equation (18) at the critical point c, with the aid of $X_{111} = 0$, to obtain the second derivative

$$\lambda_{11}(\equiv \ddot{\lambda}) = -\frac{1}{3X'_{11}}\left[X_{1111} - 3\frac{X_{121}X_{211}}{\alpha_2} - 3X_{1s1}a_s\right] \triangleq -a_0$$

where $s = 3, 4, \ldots n$. This second derivative can be expressed in the more compact form

$$\lambda_{11} = -a_0 = -\frac{1}{3X'_{11}}[X_{1111} - 3X_{1t1}a_t], \quad t = 2, 3, 4, \ldots n. \tag{26}$$

Using this derivative, the first-order equations of the postcritical path are expressed as

$$\begin{aligned} \varphi &= -\frac{1}{2}a_0(x^1)^2 \\ x^t &= -\frac{1}{2}a_t(x^1)^2 \quad (t = 2, 3, \ldots n) \end{aligned} \tag{27}$$

which represent a space curve in the state-space ($\varphi - x^i$) intersecting the fundamental path at $\lambda = \lambda_c$ and having a slope $\dot{\lambda} = 0$. It is recognized again, in complete analogy with gradient systems, that the critical point c is now a symmetric point of bifurcation. It also follows that postcritical equilibrium states exist either for $\lambda > \lambda_c$ or $\lambda < \lambda_c$ only.

3 Stability Distribution on the Equilibrium Paths

In order to examine the stability of the equilibrium states on the initial and postcritical paths, consider the expansion of $X_i(x^j, \lambda)$ into Taylor series around the critical point $\lambda = \lambda_c$,

$$\begin{aligned} X_i = {} & \left.\frac{\partial X_i}{\partial x^j}\right|_c x^j + \left.\frac{\partial X_i}{\partial \lambda}\right|_c (\lambda - \lambda_c) \\ & + \frac{1}{2}\left.\frac{\partial^2 X_i}{\partial x^j \partial x^k}\right|_c x^j x^k + \left.\frac{\partial^2 X_i}{\partial x^j \partial \lambda}\right|_c x^j(\lambda - \lambda_c) + \ldots \end{aligned} \tag{28}$$

The Jacobian of a given equilibrium state in the vicinity of the critical point can then be expressed in the general form

$$\partial_j X_i = X_{ij} + X_{ijk}x^k + X'_{ij}\varphi + \ldots, \tag{29}$$

and the evaluation of (29) on the initial and postcritical paths intersecting at the critical point c yields information about the stability of these paths. Thus, evaluating (29) on the initial path, which is identified by $x^i = 0$, by using the canonical form of X_{ij} and keeping to first-order approximations, one observes that the eigenvalues of the Jacobian are uncoupled for each block and that those associated with the complex conjugate blocks of X_{ij} continue to have negative real parts (this was in fact assumed in the beginning) for sufficiently small φ. On the other hand, the eigenvalues associated with the diagonal block can be obtained from

$$[\partial_j X_i]_{x_i=0} = \begin{bmatrix} 0 & 0 \\ 0 & \alpha_2 \end{bmatrix} + \begin{bmatrix} X'_{11} & 0 \\ 0 & X'_{22} \end{bmatrix}\varphi \tag{30}$$

as $(X'_{11}\varphi)$ and $(\alpha_2 + X'_{22}\varphi)$. The latter obviously remains negative for sufficiently small φ, and one has the following stability criterion for the initial path in the vicinity of $\lambda = \lambda_c$;

$$X'_{11}\varphi \begin{smallmatrix} < \\ = \\ > \end{smallmatrix} 0 \quad \text{for} \quad \left.\begin{array}{l} \text{stable} \\ \text{critical} \\ \text{unstable} \end{array}\right\} \text{equilibrium.} \tag{31}$$

In practical situations, as emphasized earlier $\alpha_1 < 0$ for $\lambda < \lambda_c$ and $\alpha_1 > 0$ for $\lambda > \lambda_c$ while $\alpha_1 = 0$ for $\lambda = \lambda_c$ (which means $X'_{11} > 0$) and the criterion (31) simply expresses the fact that the initial path is stable (unstable) for $\varphi < 0$ ($\varphi > 0$). Note, however, that the criterion (31) remains valid if the reverse situtation occurs, an unstable path gaining stability upon passing through the critical point.

Next, suppose the critical point is an asymmetric point of bifurcation, and evaluate the Jacobian (29) on the postcritical path (25). Thus substituting for x^t and x^1 yields

$$[\partial_j X_i]_{\text{p.c.p}} = X_{ij} + X_{ij1}(-2X'_{11}/X_{111}\varphi) + X'_{ij}\varphi + O(\varphi^2) + \ldots$$

in which (2×2) blocks are no longer in the uncoupled form as in the case of initial path. At the critical point $\varphi = 0$, the eigenvalues of the Jacobian are of course the same as before and it is assumed that the vanishing eigenvalue $\alpha_1 = \alpha_1(\varphi)$ ($\alpha_1 = 0$, for $\varphi = 0$) can be expanded into power series in the vicinity of the critical point while α_2 and $\alpha_r \pm i\beta_r$ stay away from zero and preserve their qualitative properties. Expressing $\alpha_1(\varphi)$ as

$$\alpha_1 = 0 + \alpha'_1\varphi + \ldots \quad \text{where } \alpha'_1 = \left.\frac{d\alpha_1}{d\varphi}\right|_{\varphi=0}$$

which describes the variation of α_1 along the postcritical path, one can obtain α'_1 by differentiating the determinant of the Jacobian with respect to φ. To this end, consider the characteristic equation

$$|\partial_j X_i - \alpha I| = 0 \tag{32}$$

If α_1 is a root, it should stasify (32), and differentiating by columns and evaluating at $\varphi = 0$ one observes that all determinants except the leading one vanish identically, resulting in

$$\begin{vmatrix} X'_{11} + X_{111}(-2X'_{11}\mathrm{X}_{111}) - \alpha'_1 & 0 & 0 & 0 & \dots \\ 0 + X_{211}(-2X'_{11}/\mathrm{X}_{111}) & \alpha_2 - 0 & 0 & 0 & \dots \\ 0 + \dots\dots\dots & 0 & \alpha_3 - 0 & -\beta_3 & \dots \\ \dots\dots\dots\dots & 0 & \beta_3 & \alpha_3 - 0 & \dots \\ \dots\dots\dots\dots\dots\dots\dots\dots\dots\dots\dots\dots\dots\dots \end{vmatrix} = 0 \quad (33)$$

which yields

$$\alpha'_1 = -X'_{11} \quad (34)$$

It follows that the eigenvalue $\alpha_1(\varphi)$ can be expressed as

$$\alpha_1 = X'_{11}\varphi + O(\varphi^2) + \dots, \quad (35)$$

and in the vicinity of $\varphi = 0$ (or $\lambda = \lambda_c$) one has the following stability criterion associated with the postcritical path:

$$X'_{11}\varphi \gtreqless 0 \quad \text{for} \quad \left.\begin{matrix} \text{stable} \\ \text{critical} \\ \text{unstable} \end{matrix}\right\} \text{equilibirum.} \quad (36)$$

If $X'_{11} > 0$, the postcritical path is unstable for $\varphi < 0$ and gains stability upon passing through the critical point $\lambda = \lambda_c$ in contrast with the initial path. More generally, the criteria (31) and (36) reveal that *an exchange of stabilities occurs at an asymmetric point of bifurcation* in complete analogy with gradient systems.

Finally, consider the symmetric point of bifurcation and the postcritical path (27). In this case, the Jacobian (29) can be expressed as

$$(\partial_j X_i)_{p.c.p} = X_{ij} + X_{ij1}x^1 + \tfrac{1}{2}X_{ij11}(x^1)^2 + X_{ijt}(-\tfrac{1}{2}a_t(x^1)^2) + X'_{ij}(-\tfrac{1}{2}a_0(x^1)^2) + \dots \quad (37)$$

and the eigenvalue $\alpha_1(x^1)$, along the postcritical path, as

$$\alpha_1 = 0 + \alpha_{1,1}x^1 + \tfrac{1}{2}\alpha_{1,11}(\mathrm{x}^1)^2 + \dots$$

where

$$\alpha_{1,1} = \left.\frac{d\alpha_1}{dx^1}\right|_{x^1=0}, \quad \text{etc.}$$

If $\alpha_1(x^1)$ is an eigenvalue of the Jacobian (37) it satisfies

$$|\partial_j X_i - \alpha_1 I| = 0, \quad (38)$$

and the first differentiation with respect to x^1 yields, upon evaluation at $\varphi = x^1 = 0$,

$$\begin{vmatrix} 0 -, \alpha_{1,1} & 0 & 0 & 0 & . & . \\ X_{211} & \alpha_2 - 0 & 0 & 0 & . & . \\ X_{311} & 0 & \alpha_3 & -\beta_3 & . & . \\ X_{411} & 0 & \beta_3 & \alpha_3 & . & . \\ \dots\dots\dots\dots\dots\dots\dots\dots\dots\dots \\ \dots\dots\dots\dots\dots\dots\dots\dots\dots\dots \end{vmatrix} = 0 \quad (39)$$

resulting in

$$\alpha_{1,1} = 0. \quad (40)$$

The second differentiation of (38) involves several determinants which upon evaluation at critical point and using (40) yields, after some algebra (see the Appendix),

$$\alpha_{1,11} = X_{1111} - 3X_{11t}a_t - X'_{11}a_0 \quad (41)$$

where a_t and a_0 are as defined in (25) and $t = 2, 3, 4, \dots n$.

In view of (26), however, $\alpha_{1,11}$ can be expressed as

$$\alpha_{1,11} = 2X'_{11}a_0$$

where

$$a_0 = \frac{1}{3X'_{11}}(X_{1111} - 3X_{1t1}a_t) \quad (42)$$

and it follows that

$$\alpha_1 = X'_{11}a_0(x^1)^2 + \dots \quad (43)$$

The stability criterion for the symmetric postcritical path is then given by

$$X'_{11}a_0 \lesseqgtr 0 \quad \text{for} \quad \left.\begin{matrix} \text{stable} \\ \text{critical} \\ \text{unstable} \end{matrix}\right\} \text{equilibrium} \quad (44)$$

In other words if we assume $X'_{11} > 0$ as before and the postcritical path (27) exists for $\varphi > 0$, then $a_0 < 0$, and the postcritical path is stable. On the other hand, if the postcritical path exists for $\varphi < 0$, then $a_0 > 0$ and the path is unstable. More generally, comparing (31) and (44) in conjunction with (27), one observes that *the postcritical path is totally stable (unstable) for all $\varphi > 0$ or $\varphi < 0$ if the initial path is unstable (stable) for the same range of φ.*

It is understood that the stability criterion in (44) is intended for a direct comparision with (31), and it can also be written as

$$(X_{1111} - 3X_{1t1}a_t) \lesseqgtr 0 \quad \text{for} \quad \left.\begin{matrix} \text{stable} \\ \text{critical} \\ \text{unstable} \end{matrix}\right\} \text{equilibrium}$$

which is independent of the parameter φ.

4 Discussion

It was assumed that all the eigenvalues of the Jacobian matrix on the initial path have negative real parts initially, and the stability is lost at a critical point where a real eigenvalue vanishes. This eigenvalue becomes positive upon passing through zero while the remaining eigenvalues maintain their character, and continue to have negative real parts.

If the equilibrium equations (25) and the stability criteria are examined, however, it is noted that the analysis and the results would still be valid if the real parts of some of the complex conjugate eigenvalues were zero and remained so in the vicinity of the critical point along the initial path as a real eigenvalue goes through zero. Here it is of course assumed that the imaginary parts are not repeated or the multiplicity of a repeated root is equal to its index [6] and nonlinear terms do not change stability characteristics. In some problems, all the eigenvalues can be imaginery, $\pm\beta_k$, as in the case of conservative systems, and the stability is lost when at least a pair goes through zero. The postcritical behavior in this case as well as in the case of multiple zeros has been studied in reference [5].

It was noted earlier that the formulation in this paper excludes limit points from the analyses automatically. It can be shown [7], however, that *if the equilibrium states are stable on one side of a limit point they have to be unstable on the other side.*

Acknowledgment

The financial support of NSERC of Canada is acknowledged.

References

1 Huseyin, K., *Nonlinear Theory of Elastic Stability,* Noordhoff International Publishing, The Netherlands, 1975.

2 Plaut, R., "Postbuckling Behaviour of Nonconservative Elastic Systems, *Journal of Structural Mechanics,* Vol. 4, 1976, pp. 395–416.

3 Plaut, R., Branching Analysis at Coincident Buckling Loads of Nonconservative Elastic Systems, ASME JOURNAL OF APPLIED MECHANICS, Vol. 44, 1977, pp. 317–321.

4 Mandadi, V., and Huseyin, K., "Nonlinear Instability Behaviour of Nongradient Systems," *Hadronic Journal,* Vol. 2, 1979, pp. 657–681.

5 Mandadi, V., and Huseyin, K., "Nonlinear Bifurcation Analysis of Nongradient Systems," *International Journal of Nonlinear Mechanics,* Vol. 15, 1980, pp. 159–172.

6 Huseyin, K., *Vibrations and Stability of Multiple-Parameter Systems,* Sijthoff and Noordhoff, The Netherlands, 1978.

7 Huseyin, K., and Mandadi, V., "On the Instability of Multiple-Parameter Systems," Sectional Lecture, *Proceedings of the 15th International Congress of Theoretical and Applied Mechanics*, Toronto, 1980, North Holland Publishing Co., to appear.

APPENDIX

In order to derive the second derivative (41) of the vanishing eigenvalue $\alpha_1(x^1)$, the determinant (38) is differentiated by columns with respect to x^1 for a second time and evaluated at the critical point $x^1 = 0$. Upon using (40), this operation yields

$$\begin{vmatrix} X_{1111} - X_{11t}a_t - X'_{11}a_0 - \alpha_{1,11} & 0 & 0 & 0 & \cdot \\ X_{2111} - X_{21t}a_t & \alpha_2 & 0 & 0 & \cdot \\ X_{3111} - X_{31t}a_t & 0 & \alpha_3 & -\beta_3 & \cdot \\ X_{4111} - X_{41t}a_t & 0 & \beta_3 & \alpha_3 & \cdot \\ \cdots & \cdots & \cdots & \cdots & \cdots \end{vmatrix}$$

$$+ \begin{vmatrix} 0 & X_{121} & 0 & 0 & \cdot \\ X_{211} & X_{221} & 0 & 0 & \cdot \\ X_{311} & X_{321} & \alpha_3 & -\beta_3 & \cdot \\ X_{411} & X_{421} & \beta_3 & \alpha_3 & \cdot \\ \cdots & \cdots & \cdots & \cdots & \cdots \end{vmatrix}$$

$$+ \begin{vmatrix} 0 & 0 & X_{131} & 0 & \cdot \\ X_{211} & \alpha_2 & X_{231} & 0 & \cdot \\ X_{311} & 0 & X_{331} & -\beta_3 & \cdot \\ X_{411} & 0 & X_{431} & \alpha_3 & \cdot \\ \cdots & \cdots & \cdots & \cdots & \cdots \end{vmatrix}$$

$$+ \begin{vmatrix} 0 & 0 & 0 & X_{141} & \cdot \\ X_{211} & \alpha_2 & 0 & X_{241} & \cdot \\ X_{311} & 0 & \alpha_3 & X_{341} & \cdot \\ X_{411} & 0 & \beta_3 & X_{441} & \cdot \\ \cdots & \cdots & \cdots & \cdots & \cdots \end{vmatrix}$$

$$+ \begin{vmatrix} 0 & X_{121} & 0 & 0 & \cdot \\ X_{211} & X_{221} & 0 & 0 & \cdot \\ X_{311} & X_{321} & \alpha_3 & -\beta_3 & \cdot \\ X_{411} & X_{421} & \beta_3 & \alpha_3 & \cdot \\ \cdots & \cdots & \cdots & \cdots & \cdots \end{vmatrix}$$

$$+ \begin{vmatrix} 0 & 0 & X_{131} & 0 & \cdot \\ X_{211} & \alpha_2 & X_{231} & 0 & \cdot \\ X_{311} & 0 & X_{331} & -\beta_3 & \cdot \\ X_{411} & 0 & X_{431} & \alpha_3 & \cdot \\ \cdots & \cdots & \cdots & \cdots & \cdots \end{vmatrix}$$

$$+ \begin{vmatrix} 0 & 0 & 0 & X_{141} & \cdot \\ X_{211} & \alpha_2 & 0 & X_{241} & \cdot \\ X_{311} & 0 & \alpha_3 & X_{341} & \cdot \\ X_{411} & 0 & \beta_3 & X_{441} & \cdot \\ \cdots & \cdots & \cdots & \cdots & \cdots \end{vmatrix}$$

$$+ \ldots = 0$$

which results in

$$\begin{aligned} \alpha_{1.111} = X_{1111} - X_{11t}a_t - X'_{11}a_0 - 2\,\frac{X_{121}X_{211}}{\alpha_2} \\ -2X_{131}\left(\frac{\alpha_3 X_{311} + \beta_3 X_{411}}{\alpha_3^2 + \beta_3^2}\right) \\ -2X_{141}\left(\frac{\alpha_3 X_{411} - \beta_3 X_{311}}{\alpha_3^2 + \beta_3^2}\right) - \ldots . \end{aligned}$$

Recognizing the definitions in (25), the fact that $X_{1t1} = X_{11t}$ for any $t = 2, 3, \ldots$, and generalizing the summations lead to the derivative (41).

Journal of Applied Mechanics

Brief Notes

A Brief Note is a short paper which presents a specific solution of technical interest in mechanics but which does not necessarily contain new general methods or results. A Brief Note should not exceed 1500 words *or equivalent* (a typical one-column figure or table is equivalent to 250 words; a one line equation to 30 words). Brief Notes will be subject to the usual review procedures prior to publication. After approval such Notes will be published as soon as possible. The Notes should be submitted to the Technical Editor of the JOURNAL OF APPLIED MECHANICS. Discussions on the Brief Notes should be addressed to the Editorial Department, ASME, United Engineering Center, 345 East 47th Street, New York, N. Y. 10017, or to the Technical Editor of the JOURNAL OF APPLIED MECHANICS. Discussions on Brief Notes appearing in this issue will be accepted until two months after publication. Readers who need more time to prepare a Discussion should request an extension of the deadline from the Editorial Department.

A Procedure to Generate Liapunov Functional for Distributed Parameter Systems

M. Seetharam Bhat[1] and S. K. Shrivastava[2]

Introduction

Liapunov's theory of stability [1] has become an important tool in the analysis of dynamical systems described by ordinary linear and nonlinear differential equations. Extensions to systems represented by a class of partial linear and nonlinear differential equations are also made [2–4, et al.]. For a general case of distributed parameter system, difficulties may be encountered in obtaining a Liapunov functional. Parks and Prichard [5], and Mockaitis [6] present some approaches to deal with the problem.

This paper gives a guideline for finding Liapunov functional for distributed parameter systems, represented by partial differential equations, based on the work of Schultz and Gibson [7] on lumped parameter systems. Two examples are also included to demonstrate applicability of the method.

Preliminaries

Let Ω be a bounded open domain in m-dimensional x-space and $\partial\Omega$ be its boundary. Let the system under consideration be described on the space-time domain $\Omega \times T$ by the following general vector partial differential equation:

$$\mathbf{M}\,\mathbf{u}_t = \alpha\mathbf{u}(\mathbf{x}, t) \qquad (1)$$

where $\mathbf{u}(\mathbf{x}, t)$ is a n-dimensional vector, $\mathbf{u} \in H^n$, representing the physical variables of the system. Subscript t denotes partial derivative with respect to time. $\mathbf{M}$ is a $n \times n$ symmetric, invertible, time-invariant matrix operator. α is a $n \times n$ linear or nonlinear spatial differential operator defined on Ω. H^n is a Cartesian product of n real Hilbert spaces over the spatial domain $H^n = H_1 x H_2 x \ldots .H_n$, in which the inner product is defined by

$$\langle u, v\rangle_{H^n} = \sum_{i=1}^{n} \langle u_i, v_i\rangle_{H_i}\,; \quad \mathbf{u}, \mathbf{v} \in H^n \qquad (2)$$

and the norm is induced by (2). The inner product between $a(\mathbf{x}, t) \in H_i$ and $b(x, t) \in H_i$ is given by

$$\langle a, b\rangle = \int_{\mathbf{x}\in\Omega} a \cdot b d\mathbf{x} \qquad (3)$$

Assume that the solution to equation (1) with a set of initial and boundary data exists. The equilibrium state of the system with homogeneous boundary conditions is trivial for a linear system and it is nontrivial for nonlinear systems. With nonhomogeneous boundary conditions, a number of equilibrium states can exist for a nonlinear system. Here we wish to study the stability in the neighborhood of equilibrium or null solution (s) via Liapunov's direct method.

Liapunov's theorem for asymptotic stability may be stated as follows [4]:

Suppose there exists a functional $J[\mathbf{u}(\mathbf{x}, t)] = V(t)$, differentiable (Frechet) in t along $\mathbf{u}(\mathbf{x}, t)$ such that $J[0] = 0$, and

(*i*) $J[\mathbf{u}(\mathbf{x}, t)] = V(t)$ is positive-definite, that there exists a continuous nondecreasing function β_1 such that $\beta_1(0) = 0$ for all t and all $\mathbf{u}(\mathbf{x}, t) \neq 0, 0 < \beta_1(\rho(t)) \leq V(t); (\rho(t) \subset H^n);$

(*ii*) The derivative $\dot{V}(t)$ is negative-semidefinite, i.e., there exists a $\gamma(t)$ such that $\gamma(0) = 0$ and for all $t > 0$ and $\mathbf{u}(\mathbf{x}, t) \neq 0$, $\dot{V}(t) \leq -\gamma(\rho(t)) \leq 0$;

(*iii*) There exists a continuous nondecreasing scalar functional β_2 such that $\beta_2(0) = 0$ for all t and $V(t) \leq \beta_2(\rho(t))$;

(*iv*) $\beta_1(\rho) \rightarrow \infty$ as $\rho \rightarrow \infty$, then the equilibrium solution of equation (1) is asymptotically stable. The functional $V(t)$ is called "Liapunov functional."

Formulation of Liapunov Functional

We develop a procedure to obtain a Liapunov functional V as well as its derivative $\dot{V}$, which may be used directly to establish stability. The procedure essentially extends the "variable gradient method," developed for autonomous ordinary differential equations by Schultz and Gibson [7], to a distributed parameter system. We can rewrite equation (1) as

$$\frac{\partial\mathbf{u}(\mathbf{x}, t)}{\partial t} = \mathbf{A}\mathbf{u}(\mathbf{x}, t); \quad \mathbf{u} \in H^n; \quad t \in T; \quad \mathbf{x} \in \Omega \qquad (4)$$

where $\mathbf{A} = \mathbf{M}^{-1}\alpha$.

We assume that the null solution $\mathbf{u} = \theta$ exists and $\nabla\mathbf{V}(\theta)$ is equal to zero. Then the gradient in the vicinity of the null solution is given by

$$\nabla\mathbf{V} = \nabla\mathbf{V}(\theta) + (\nabla\mathbf{V}'(\mathbf{u}))^T\mathbf{u} = \mathbf{G}(\mathbf{u})^T\mathbf{u} \qquad (5)$$

---

[1] Research Scholar, Department of Aeronautical Engineering, Indian Institute of Science, Bangalore 560012, India.

[2] Assistant Professor, Department of Aeronautical Engineering, Indian Institute of Technology, Bangalore 560012, India.

Manuscript received by ASME Applied Mechanics Division, October, 1979; final revision, June, 1980.

The operator $\mathbf{G(u)}$ is similar to the Hessian of the functional V. The Liapunov functional can be obtained from the path integral of the assumed gradient function (5) as

$$V(u) = \langle \nabla \mathbf{V(u)} \cdot \mathbf{u} \rangle_{H^n} = \oint \nabla \mathbf{V(u)}^T \mathbf{u} ds \tag{6}$$

The time derivative of the Liapunov functional along the equation of motion is given by

$$\dot{V}(\mathbf{u}) = \langle \nabla \mathbf{V(u)} \cdot \dot{\mathbf{u}} \rangle_{H^n} = \langle \nabla \mathbf{V(u)} \cdot \mathbf{Au} \rangle_{H^n}$$
$$= \oint \mathbf{u}^T \mathbf{N}^T \mathbf{u} ds \tag{7}$$

where $N = \mathbf{G(u)A(u)}$.

The path integral of $\nabla \mathbf{V}$ to obtain $\mathbf{V}$ and $\dot{V}$ will be path-independent, if $\mathbf{G(u)}$ is symmetric [8]. This is equivalent to the curl condition in finite dimensional systems. The unknown operator $\mathbf{G(u)}$ is determined by (a) using symmetry or "curl" condition and (b) making functional $\dot{V}(\mathbf{u})$ at least negative semidefinite. To check the semidefiniteness of the functional $\dot{V}(\mathbf{u})$, the integral inequalities [9] can be used. Then the stability of the distributed parameter system is insured by checking the positive-definiteness of the Liapunov functional.

To summarize, the procedure is as follows:

1 Assume the gradient $\nabla \mathbf{V}$ in the form of (5).

2 Use symmetry conditions on $\mathbf{G(u)}$.

3 Obtain the functional $\dot{V}$ and make $\dot{V}$ at least negative-definite. Obtain $\mathbf{N} = \mathbf{G}\ \mathbf{(u)A(u)}$ and make the off-diagonal elements of $\mathbf{N}$ antisymmetric and thus determine all the unknowns in $\mathbf{G(u)}$.

4 Obtain the Liapunov functional V and check for sign definiteness.

Illustrations

To demonstrate the applicability of the approach to a general class of problems, we shall now consider two examples.

1 **Turbluence.** Let us consider Berger's linear model of turbulence given by [10]:

$$\frac{D^2u}{R} + u - u_t = 0; \quad 0 \le x \le 1, \quad u \in R^1, \quad t \in [0, \infty),$$
$$D^i = \partial^i / \partial x^i \tag{8}$$

and associated boundary conditions are

$$u(0, t) = u(1, t) = 0 \tag{9}$$

while R is a positive parameter which may be varied at will. The equation can be rewritten as

$$u_t = \frac{D^2u}{R} + u; \quad u \in R^1, \quad x \in [0, 1], \quad t \in [0, \infty) \tag{10}$$

$u = 0$ is the equilibrium state of the system. Assume $\nabla \mathbf{V}(u) = u$; from (6)–(8)

$$V = \int_0^1 \nabla V \cdot u dx = \int_0^1 u^2 dx \tag{11}$$

$$\dot{V} = \int_0^1 u \cdot \left(\frac{D^2u}{R} + u \right) dx \tag{12}$$

Using (8), (9), and (12)

$$\dot{V} = \int_0^1 u^2 (R - \pi^2)/R dx. \tag{13}$$

From (11) one can see that the Liapunov functional is positive-definite. If $R < \pi^2$, $\dot{V}$ is negative-definite and hence the system will be asymptotically stable. For $R > \pi^2$, it will be unstable.

2 **Whirling Motion of a Viscoelastic Continuous Shaft.** The equations of motion in a coordinate system rotating at a constant rate Ω with the shaft are [11]

$$m(x)u_{1tt} + 2Cu_{1t} + 2\Omega u_{2t} - \Omega^2 u_1 + D^2(p(x)D^2u_1) + D^2(q(x)D^2u_{1t}) = 0$$
$$m(x)u_{2tt} + 2Cu_{2t} - 2\Omega u_{1t} - \Omega^2 u_2 + D^2(p(x)D^2u_1) + D^2(q(x)D^2u_{2t}) = 0$$
$$m(x) > 0, \quad p(x) > 0, \quad q(x) > 0, \quad C \ge 0, \quad \Omega > 0,$$
$$x \in [0, 1], \quad t \in [0, \infty) \tag{14}$$

and the associated boundary conditions are

$$u_1(0, t) = u_2(0, t) = Du_1(0, t) = Du_2(0, t) = 0$$
$$D^2u_1(1, t) = D^2u_2(1, t) = 0$$
$$D(p(x)D^2u_1(1, t)) = D(p(x)D^2u_2(1, t)) = 0$$

For simplicity we shall assume m, p, q to be constant throughout the shaft. The equations can be written as

$$\mathbf{u}_t = \frac{1}{m} \begin{bmatrix} 0 & 0 & m & 0 \\ 0 & 0 & 0 & m \\ \Omega^2 - pD^4 & 0 & -2C - qD^4 & -2\Omega \\ 0 & \Omega^2 - pD^4 & 2\Omega & -2C - qD^4 \end{bmatrix} \begin{bmatrix} u_1 \\ u_2 \\ u_3 \\ u_4 \end{bmatrix} \tag{15}$$

where $u_3 = u_{1t}$, $u_4 = u_{2t}$. Following the suggested procedure (section, " Formulation of Liapunov Functional,"), with a judical choice of $\mathbf{G}$ and some effort, the gradient vector is found to be

$$\nabla \mathbf{V} = \frac{1}{2m} \begin{bmatrix} -\Omega^2 u_1 + (2C + p)D^4 u_1 + qD^4 u_1 D^4 + mD^4 u_3 \\ -\Omega^2 u_2 + (2C + p)D^4 u_2 + qD^4 u_2 D^4 + mD^4 U_4 \\ mD^4 u_1 + mu_3 \\ mD^4 u_2 + mu_4 \end{bmatrix} \tag{16}$$

From equations (7), (15), and (16) after simplification,

$$\dot{V} = -\frac{1}{m} \int_0^1 [2C(u_3{}^2 + u_4{}^2) + (q - 2m)((D^2u_3)^2 + (D^2u_4)^2) + (D^2u_4 + \Omega D^2u_1)^2 + (D^2u_3 - \Omega D^2u_2)^2 + p((D^4u_1)^2 + (D^4u_2)^2)] dx \tag{17}$$

It is negative-definite if $q > 2m$. From equation (6) and (16), Liapunov functional is

$$V = \frac{1}{2m} \int_0^1 [-\Omega^2(u_1{}^2 + u_2{}^2) + (2C + p)((D^2u_1)^2 + (D^2u_2)^2) + q((D^4u_1)^2 + (D^4u_2)^2) + m(u_3{}^2 + u_4{}^2) + m((D^2u_1)^2 + (D^2u_2)^2)_t] dx \tag{18}$$

Using integral inequalities [9],

$$V \ge \frac{1}{2m} \int_0^1 [(u_1{}^2 + u_2{}^2)(-\Omega^2 + \pi^4(2C + p) + \pi^8 q) + m(u_3{}^2 + u_4{}^2) + 2\pi^4 m(u_1{}^2 + u_2{}^2 + u_2{}^2)_t] dx \tag{19}$$

V is positive-definite if

$$\Omega^2 < (2C + p)\pi^4 + q\pi^8 \tag{20}$$

Thus the system is stable if $q > 2m$ and the condition (20) is satisfied.

These illustrations establish the applicability and simplicity of the suggested approach to obtain Liapunov functional for continuous systems.

References

1 Liapunov, A. M., *Stability of Motion*, Academic Press, 1967.

2 Hahn, W., *Theory and Applications of Liapunov's Direct Method*, Prentice-Hall, Englewood Cliffs, N.J., 1963.

3 Watson, F. E., and Kastenberg, W. E., "On the Stability of a Class of Nonlinear Continuous System," *International Journal of Control*, Vol. 20, 1974, pp. 997–1014.

4 Caughey, T. K., and Ellison, J., "Existence, Uniqueness and Stability of Solutions of a Class of Nonlinear Partial Differential Equations," *Journal of Mathematical Analysis and Applications*, Vol. 51, 1975, pp. 1–32.

5 Parks, P. C., and Pritchard, A. J., "Stability Analysis of Structural Dynamics Using Liapunov Functionals," *Journal of Sound and Vibration*, Vol. 25, 1972, pp. 609–621.

6 Mockaitis, A., "Explicit Synthesis of Liapunov Functionals for Continuous Systems," PhD Thesis, Mechanical Engineering, University of Pennsylvania, 1972.

7 Schultz, D. G., and Gibson, J. E., "The Variable Gradient Method for Generating Liapunov Functions," *Trans. of the AIEE, Part II: Applications and Industry*, Vol. 81, Sept. 1962, pp. 203–209.

8 Williamson, R. E., and Trotter, H. F., *Multivariable Mathematics*, Prentice-Hall, Englewood Cliffs, N.J., 1974, Chapter 18.

9 Laxmikantham, V., and Leela, S., *Differential and Integral Inequalities. Vol. 2: Functionsl, Partial, Abstract and Complex Differential Equations*, Academic Press, 1969.

10 Eckhaus, W., *Studies in Nonlinear Stability Theory*, Springer-Verlag, 1965, pp. 4–5.

11 Genin, J., and Maybee, J. S., "Whirling Motion of a Viscoelastic Continuous Shaft," *International Journal of Engineering Science*, Vol. 8, 1970, pp. 671–686.

Basic Transport Equations in Ascending Equiangular Spiral Polar Coordinates

S. Ali[1]

Basic transport equations have been expressed in a coordinate system suitable for the analytical study of momentum, heat, and mass transport processes in ascending equiangular spiral tube coils. The chosen coordinate system for the representation of these equations is orthogonal curvilinear possessing proper transformation to the rectangular Cartesian coordinate system. Various tensorial quantities appearing in the tensorial form of the general basic transport equations have been obtained in expanded form in the chosen curvilinear coordinate system. Substitution of these quantities, readily expands all the basic transport equations in their various forms. Illustration has been made for the equation of continuity, the general equation of motion, the Navier-Stokes equation, the equation of energy, and the equation of mass transport. The resulting equations are in forms suitable for analytical and numerical solution.

Introduction

Various biomedical appliances, continuous flow chemical reactors, and heat and mass transfer equipment are preferred to be in the geometrical configuration of spirally and helically curved closed channels. As compared to straight channels, apart from the advantage of compactness of geometry, transport through these curved channels also has enhanced heat and mass transfer coefficients and closer approximation to plug flow. Also, as noticed by Ali and Zaidi [1], the only disadvantage of higher head loss in these channels disappears within a range of flow limited by the two critical Reynolds numbers of the curved channel flow.

So far, as appears in literature, torus is the only continuously curved closed channel geometry for which basic transport equations have been obtained and solved. A toroidal geometry can be thought to be an approximation to a small pitch helical coil. With the help of these analytical studies and other experimental works, the transport features of flow and heat transfer through helically coiled tubes are now fairly well analyzed and understood.

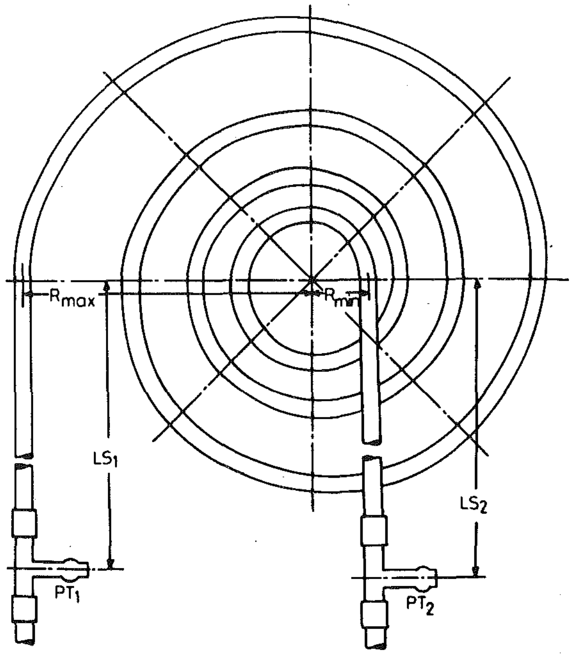

Fig. 1 Configuration of an ascending equiangular spiral coil; *LS*, straight lengths; *PT*, pressure taps; R_{max}, maximum radius of the coil; R_{min}, minimum radius of the coil

Although spirally bent coils form equally useful and interesting continuously curved closed channel geometries, no analytical study for transport problems concerning any type of them has been made. As a first step toward these studies, basic transport equations of momentum, heat, and mass transfer have been obtained in the following work for a well-defined spiral coil geometry known as ascending equiangular spiral coil. As compared to the other type of spiral coils, the ascending equiangular spiral coil geometry possesses analytically attackable transport equations and, as observed by Ali and Zaidi [1], minimum resistance for flow.

Choosing a Suitable Coordinate System

Ascending equiangular spiral coils are formed by bending tubes of circular cross section such that their axis takes the shape of a plannular curve called ascending equiangular spiral. The family of the curve is described by the polar equation

$$R = K\,e^{m\Theta}, \tag{1}$$

where K is the radius of the inner asymptotic circle, m is a positive constant characterizing rate of ascent, and Θ ranges from 0 to ∞. The shape of the curve is shown in Fig. 1.

A suitable choice of coordinate system for the mathematical description of transport processes in the spiral coil has to be only curvilinear, preferably if possible orthogonal. To arrive at such a choice, we proceed as follows.

We shall assign a rectangular Cartesian coordinate system (X, Y, Z) whose XY-plane coincides with the plane of the axis of the coil, X-axis is same as the initial line of the polar coordinate (R, Θ) and origin O is same as the origin of the polar coordinate. The rectangular Cartesian coordinate of a point inside the coil will then be represented by (X, Y, Z).

Now, as shown in Fig. 2, a curvilinear coordinate system can be chosen in which any point P on the axis of the spiral coil is located by an angle Ω such that for a given Ω there is a perpendicular PQ to its ray OQ which is tangent to the spiral axis at the point P to be located. The angle Ω is measured in anticlockwise direction from the initial line OX. Now, we consider a cross section of the coil through the point

---

[1] Presently, at the DRPD Division of Research and Development Centre, Steel Authority of India Ltd., Ranchi 834002, India; formerly, Department of Chemical Engineering, University of Roorkee, Roorkee, India.

Manuscript received by ASME Applied Mechanics Division, November, 1979.

3 Watson, F. E., and Kastenberg, W. E., "On the Stability of a Class of Nonlinear Continuous System," *International Journal of Control*, Vol. 20, 1974, pp. 997–1014.

4 Caughey, T. K., and Ellison, J., "Existence, Uniqueness and Stability of Solutions of a Class of Nonlinear Partial Differential Equations," *Journal of Mathematical Analysis and Applications*, Vol. 51, 1975, pp. 1–32.

5 Parks, P. C., and Pritchard, A. J., "Stability Analysis of Structural Dynamics Using Liapunov Functionals," *Journal of Sound and Vibration*, Vol. 25, 1972, pp. 609–621.

6 Mockaitis, A., "Explicit Synthesis of Liapunov Functionals for Continuous Systems," PhD Thesis, Mechanical Engineering, University of Pennsylvania, 1972.

7 Schultz, D. G., and Gibson, J. E., "The Variable Gradient Method for Generating Liapunov Functions," *Trans. of the AIEE, Part II: Applications and Industry*, Vol. 81, Sept. 1962, pp. 203–209.

8 Williamson, R. E., and Trotter, H. F., *Multivariable Mathematics*, Prentice-Hall, Englewood Cliffs, N.J., 1974, Chapter 18.

9 Laxmikantham, V., and Leela, S., *Differential and Integral Inequalities. Vol. 2: Functionsl, Partial, Abstract and Complex Differential Equations*, Academic Press, 1969.

10 Eckhaus, W., *Studies in Nonlinear Stability Theory*, Springer-Verlag, 1965, pp. 4–5.

11 Genin, J., and Maybee, J. S., "Whirling Motion of a Viscoelastic Continuous Shaft," *International Journal of Engineering Science*, Vol. 8, 1970, pp. 671–686.

Basic Transport Equations in Ascending Equiangular Spiral Polar Coordinates

S. Ali[1]

Basic transport equations have been expressed in a coordinate system suitable for the analytical study of momentum, heat, and mass transport processes in ascending equiangular spiral tube coils. The chosen coordinate system for the representation of these equations is orthogonal curvilinear possessing proper transformation to the rectangular Cartesian coordinate system. Various tensorial quantities appearing in the tensorial form of the general basic transport equations have been obtained in expanded form in the chosen curvilinear coordinate system. Substitution of these quantities, readily expands all the basic transport equations in their various forms. Illustration has been made for the equation of continuity, the general equation of motion, the Navier-Stokes equation, the equation of energy, and the equation of mass transport. The resulting equations are in forms suitable for analytical and numerical solution.

Introduction

Various biomedical appliances, continuous flow chemical reactors, and heat and mass transfer equipment are preferred to be in the geometrical configuration of spirally and helically curved closed channels. As compared to straight channels, apart from the advantage of compactness of geometry, transport through these curved channels also has enhanced heat and mass transfer coefficients and closer approximation to plug flow. Also, as noticed by Ali and Zaidi [1], the only disadvantage of higher head loss in these channels disappears within a range of flow limited by the two critical Reynolds numbers of the curved channel flow.

So far, as appears in literature, torus is the only continuously curved closed channel geometry for which basic transport equations have been obtained and solved. A toroidal geometry can be thought to be an approximation to a small pitch helical coil. With the help of these analytical studies and other experimental works, the transport features of flow and heat transfer through helically coiled tubes are now fairly well analyzed and understood.

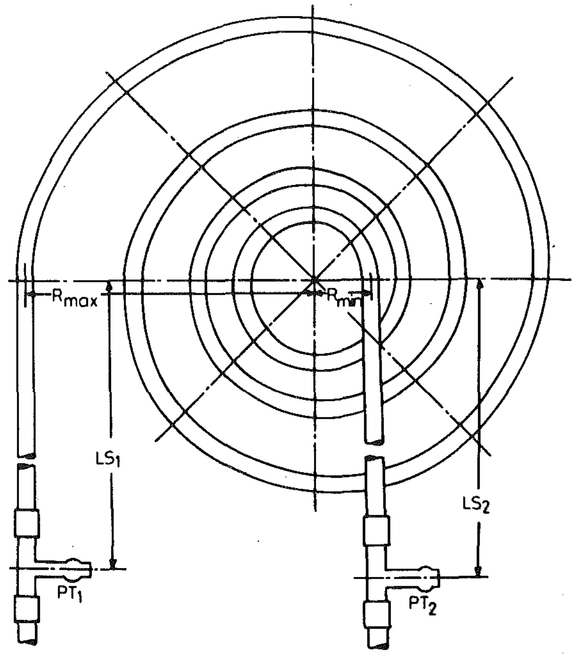

Fig. 1 Configuration of an ascending equiangular spiral coil; *LS*, straight lengths; *PT*, pressure taps; R_{max}, maximum radius of the coil; R_{min}, minimum radius of the coil

Although spirally bent coils form equally useful and interesting continuously curved closed channel geometries, no analytical study for transport problems concerning any type of them has been made. As a first step toward these studies, basic transport equations of momentum, heat, and mass transfer have been obtained in the following work for a well-defined spiral coil geometry known as ascending equiangular spiral coil. As compared to the other type of spiral coils, the ascending equiangular spiral coil geometry possesses analytically attackable transport equations and, as observed by Ali and Zaidi [1], minimum resistance for flow.

Choosing a Suitable Coordinate System

Ascending equiangular spiral coils are formed by bending tubes of circular cross section such that their axis takes the shape of a plannular curve called ascending equiangular spiral. The family of the curve is described by the polar equation

$$R = K\, e^{m\Theta}, \tag{1}$$

where K is the radius of the inner asymptotic circle, m is a positive constant characterizing rate of ascent, and Θ ranges from 0 to ∞. The shape of the curve is shown in Fig. 1.

A suitable choice of coordinate system for the mathematical description of transport processes in the spiral coil has to be only curvilinear, preferably if possible orthogonal. To arrive at such a choice, we proceed as follows.

We shall assign a rectangular Cartesian coordinate system (X, Y, Z) whose XY-plane coincides with the plane of the axis of the coil, X-axis is same as the initial line of the polar coordinate (R, Θ) and origin O is same as the origin of the polar coordinate. The rectangular Cartesian coordinate of a point inside the coil will then be represented by (X, Y, Z).

Now, as shown in Fig. 2, a curvilinear coordinate system can be chosen in which any point P on the axis of the spiral coil is located by an angle Ω such that for a given Ω there is a perpendicular PQ to its ray OQ which is tangent to the spiral axis at the point P to be located. The angle Ω is measured in anticlockwise direction from the initial line OX. Now, we consider a cross section of the coil through the point

---

[1] Presently, at the DRPD Division of Research and Development Centre, Steel Authority of India Ltd., Ranchi 834002, India; formerly, Department of Chemical Engineering, University of Roorkee, Roorkee, India.

Manuscript received by ASME Applied Mechanics Division, November, 1979.

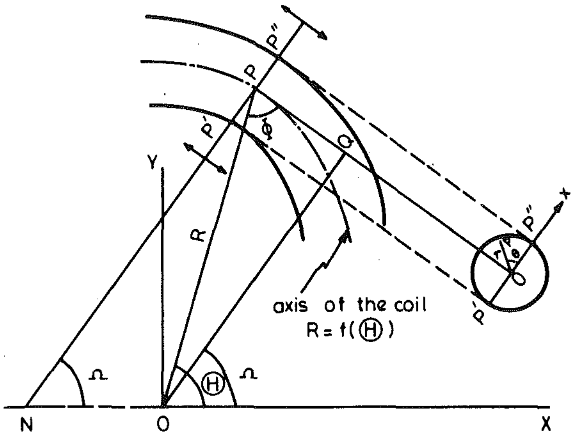

Fig. 2 Coordinate system

P, whose plane is normal to the foregoing tangent. Any point p on this circular cross section is located by the usual polar coordinates r and θ such that its initial line ox coincides with the line $P'P''$, its origin o coincides with the point P, and θ is measured in anticlockwise direction. This choice of the coordinate system (Ω, r, θ) is such that Ω = constant is a plane, r = constant is a curved circular cylinder, and θ = constant is a spirally bent curved surface. At any point p inside the coil, all these surfaces meet at right angle to each other, hence the chosen coordinate system is orthogonal. The coordinates Ω and θ are dimensionless and r has the dimension of length.

The sequence Ω, r, and θ forms a left-hand screw system.

Transformation of Coordinates

Transformation from the defined curvilinear coordinate system (Ω, r, θ) to the defined Cartesian coordinate system (X, Y, Z) is given by

$$X = R\cos\Theta + r\cos\theta\cos\Omega,$$

$$Y = R\sin\Theta + r\cos\theta\sin\Omega,$$

$$Z = r\sin\Theta, \tag{2}$$

where Θ is related to Ω by the equation

$$\Omega = \Theta - \pi/2 + \cot^{-1}m \tag{3}$$

It is shown by Ali [2] that transformation (2) is proper, i.e., one-to-one correspondence between the two coordinate systems exists in the region inside the coils bounded by the finite values of Ω.

Required Tensorial Quantities

Since basic transport equations consist of terms which are various tensorial quantities, these quantities are obtained in the chosen coordinate system and given later. For the dimensional consistency, these are given in their physical component form. Definition of these quantities can be found in any book on general tensor analysis. Eringen [3] has also described them.

Matrix of the Fundamental Metric Tensor, g_{ij}

$$\bar{\bar{g}} = \begin{bmatrix} g_{11} & 0 & 0 \\ 0 & 1 & 0 \\ 0 & 0 & r^2 \end{bmatrix} \tag{4}$$

where

$$\sqrt{g_{11}} = \sqrt{(1+m^2)}\,K\,e^{m\Theta} + r\cos\theta, \tag{5}$$

Gradient of a Scalar Field ϕ

$$\nabla\phi = \frac{1}{\sqrt{g_{11}}}\frac{\delta\phi}{\delta\Omega}\mathbf{e}_1 + \frac{\delta\phi}{\delta r}\mathbf{e}_2 + \frac{1}{r}\frac{\delta\phi}{\delta\theta}\mathbf{e}_3, \tag{6}$$

where $\mathbf{e}_1$, $\mathbf{e}_2$, and $\mathbf{e}_3$ are unit base vectors in the ascending equiangular spiral polar coordinate.

Divergence of a Vector Field $\mathbf{A}$

$$\nabla\cdot\mathbf{A} = \frac{1}{\sqrt{g_{11}}}\frac{\delta A_\Omega}{\delta\Omega} + \frac{\delta A_r}{\delta r} + \frac{1}{r}\frac{\delta A_\theta}{\delta\theta} + \left(\frac{1}{r} + \frac{\cos\theta}{\sqrt{g_{11}}}\right)A_r - \frac{\sin\theta}{\sqrt{g_{11}}}A_\theta, \tag{7}$$

where A_Ω, A_r, and A_θ are physical components of the vector $\mathbf{A}$.

Laplacian of a Scalar Field ϕ

$$\begin{aligned}\nabla^2\phi = {}& \frac{1}{g_{11}}\frac{\delta^2\phi}{\delta\Omega^2} + \frac{\delta^2\phi}{\delta r^2} + \frac{1}{r^2}\frac{\delta^2\phi}{\delta\theta^2} - \frac{m}{g_{11}}\left(\frac{\sqrt{g_{11}} - r\cos\theta}{\sqrt{g_{11}}}\right)\frac{\delta\phi}{\delta\Omega} \\ & + \left(\frac{1}{r} + \frac{\cos\theta}{\sqrt{g_{11}}}\right)\frac{\delta\phi}{\delta r} - \frac{\sin\theta}{r\sqrt{g_{11}}}\frac{\delta\phi}{\delta\theta}.\end{aligned} \tag{8}$$

Divergence of a Second-Order Symmetric Tensor $\bar{\tau}$

$$\begin{aligned}\nabla\cdot\boldsymbol{\tau} = {}& \left[\frac{1}{\sqrt{g_{11}}}\frac{\delta\tau_{\Omega\Omega}}{\delta\Omega} + \frac{\delta\tau_{\Omega r}}{\delta r} + \frac{1}{r}\frac{\delta\tau_{\Omega\theta}}{\delta\theta}\right. \\ & \left. + \left(\frac{1}{r} + \frac{2\cos\theta}{\sqrt{g_{11}}}\right)\tau_{\Omega r} - \frac{2\sin\theta}{\sqrt{g_{11}}}\tau_{\Omega\theta}\right]\mathbf{e}_\Omega \\ & + \left[\frac{1}{\sqrt{g_{11}}}\frac{\delta\tau_{\Omega r}}{\delta\Omega} + \frac{\delta\tau_{rr}}{\delta r} + \frac{1}{r}\frac{\delta\tau_{r\theta}}{\delta\theta} - \frac{\cos\theta}{\sqrt{g_{11}}}\tau_{\Omega\Omega}\right. \\ & \left. + \left(\frac{1}{r} + \frac{\cos\theta}{\sqrt{g_{11}}}\right)\tau_{rr} - \frac{\sin\theta}{\sqrt{g_{11}}}\tau_{r\theta} - \frac{1}{r}\tau_{\theta\theta}\right]\mathbf{e}_r \\ & + \left[\frac{1}{\sqrt{g_{11}}}\frac{\delta\tau_{\Omega\theta}}{\delta\Omega} + \frac{\delta\tau_{r\theta}}{\delta r} + \frac{1}{r}\frac{\delta\tau_{\theta\theta}}{\delta\theta} + \frac{\sin\theta}{\sqrt{g_{11}}}\tau_{\Omega\Omega}\right. \\ & \left. + \left(\frac{2}{r^2} + \frac{\cos\theta}{\sqrt{g_{11}}}\right)\tau_{r\theta} - \frac{\sin\theta}{\sqrt{g_{11}}}\tau_{\theta\theta}\right]\mathbf{e}_\theta.\end{aligned} \tag{9}$$

Laplacian of a Vector Field $\mathbf{v}$

$$\begin{aligned}\nabla^2\mathbf{v} = {}& \left[\frac{1}{g_{11}}\frac{\delta^2 v_\Omega}{\delta\Omega^2} + \frac{\delta^2 v_\Omega}{\delta r^2} + \frac{1}{r^2}\frac{\delta^2 v_\Omega}{\delta\theta^2}\right. \\ & - \frac{m}{g_{11}}\left(\frac{\sqrt{g_{11}} - r\cos\theta}{\sqrt{g_{11}}}\right)\frac{\delta v_\Omega}{\delta\Omega} + \left(\frac{1}{r} + \frac{\cos\theta}{\sqrt{g_{11}}}\right) + \frac{\delta v_\Omega}{\delta r} \\ & - \frac{\sin\theta}{r\sqrt{g_{11}}}\frac{\delta v_\Omega}{\delta\theta} + \frac{2\cos\theta}{g_{11}}\frac{\delta v_r}{\delta\Omega} - \frac{2\sin\theta}{g_{11}}\frac{\delta v_\theta}{\delta\Omega} \\ & - \frac{v_\Omega}{g_{11}} - \frac{m\cos\theta}{g_{11}}\left(\frac{\sqrt{g_{11}} - r\cos\theta}{\sqrt{g_{11}}}\right)v_r \\ & \left. + \frac{m\sin\theta}{g_{11}}\left(\frac{\sqrt{g_{11}} - r\cos\theta}{\sqrt{g_{11}}}\right)v_\theta\right]\mathbf{e}_\Omega \\ & + \left[\frac{1}{g_{11}}\frac{\delta^2 v_r}{\delta\Omega^2} + \frac{\delta^2 v_r}{\delta r^2} + \frac{1}{r^2}\frac{\delta^2 v_r}{\delta\theta^2} - \frac{2\cos\theta}{g_{11}}\frac{\delta v_\Omega}{\delta\Omega}\right. \\ & - \frac{m}{g_{11}}\left(\frac{\sqrt{g_{11}} - r\cos\theta}{\sqrt{g_{11}}}\right)\frac{\delta v_r}{\delta\Omega} + \left(\frac{1}{r} + \frac{\cos\theta}{\sqrt{g_{11}}}\right)\frac{\delta v_r}{\delta r} \\ & - \frac{\sin\theta}{r\sqrt{g_{11}}}\frac{\delta v_r}{d\theta} - \frac{2}{r^2}\frac{\delta v_\theta}{\delta\theta} + \frac{m\cos\theta}{g_{11}}\left(\frac{\sqrt{g_{11}} - r\cos\theta}{\sqrt{g_{11}}}\right)v_\Omega \\ & \left. - \left(\frac{1}{r^2} + \frac{\cos^2\theta}{g_{11}}\right)v_r + \left(\frac{\sin\theta}{r\sqrt{g_{11}}} + \frac{\sin\theta\cos\theta}{g_{11}}\right)v_\theta\right]\mathbf{e}_r \\ & + \left[\frac{1}{g_{11}}\frac{\delta^2 v_\theta}{\delta\Omega^2} + \frac{\delta^2 v_\Omega}{\delta r^2} + \frac{1}{r^2}\frac{\delta^2 v_\theta}{\delta\theta^2} + \frac{2\sin\theta}{g_{11}}\frac{\delta v_\Omega}{\delta\Omega}\right. \\ & + \frac{2}{r^2}\frac{\delta v_r}{\delta\theta} - \frac{m}{g_{11}}\left(\frac{\sqrt{g_{11}} - r\cos\theta}{\sqrt{g_{11}}}\right)\frac{\delta v_\theta}{\delta\Omega} + \left(\frac{1}{r} + \frac{\cos\theta}{\sqrt{g_{11}}}\right)\frac{\delta v_\theta}{\delta r} \\ & - \frac{\sin\theta}{r\sqrt{g_{11}}}\frac{\delta v_\theta}{\delta\theta} - \frac{m\sin\theta}{g_{11}}\left(\frac{\sqrt{g_{11}} - r\cos\theta}{\sqrt{g_{11}}}\right)v_\Omega \\ & \left. - \frac{\sin\theta}{r\sqrt{g_{11}}}\left(\frac{\sqrt{g_{11}} - r\cos\theta}{\sqrt{g_{11}}}\right)v_r - \left(\frac{1}{r^2} + \frac{\sin^2\theta}{g_{11}}\right)v_\theta\right]\mathbf{e}_\theta.\end{aligned} \tag{10}$$

Material Derivative of a Scalar Field ϕ

$$\frac{D\phi}{Dt} = \frac{\delta\phi}{\delta t} + \frac{v_\Omega}{\sqrt{g_{11}}}\frac{\delta\phi}{\delta\Omega} + v_r\frac{\delta\phi}{\delta r} + \frac{v_\theta}{r}\frac{\delta\phi}{\delta\theta}. \tag{11}$$

Material Derivative of a Vector Field **v**

$$\frac{D\mathbf{v}}{Dt}=\left[\frac{\delta v_\Omega}{\delta t}+\frac{v_\Omega}{\sqrt{g_{11}}}\frac{\delta v_\Omega}{\delta\Omega}+\frac{\cos\theta}{\sqrt{g_{11}}}v_\Omega v_r-\frac{\sin\theta}{\sqrt{g_{11}}}v_\Omega v_\theta+v_r\frac{\delta v_\Omega}{\delta r}+\frac{v_\theta}{r}\frac{\delta v_\Omega}{\delta\theta}\right]\mathbf{e}_\Omega$$
$$+\left[\frac{\delta v_r}{\delta t}+\frac{v_\Omega}{\sqrt{g_{11}}}\frac{\delta v_r}{\delta\Omega}-\frac{\cos\theta}{\sqrt{g_{11}}}v_\Omega^2+v_r\frac{\delta v_r}{\delta r}+\frac{v_\theta}{r}\frac{\delta v_r}{\delta\theta}-\frac{v_\theta^2}{r}\right]\mathbf{e}_r$$
$$+\left[\frac{\delta v_\theta}{\delta t}+\frac{v_\Omega}{\sqrt{g_{11}}}\frac{\delta v_\theta}{\delta\Omega}+\frac{\sin\theta}{\sqrt{g_{11}}}v_\Omega^2+v_r\frac{\delta v_\theta}{\delta r}+\frac{v_\theta}{r}\frac{\delta v_\theta}{\delta\theta}+\frac{v_r v_\theta}{r}\right]\mathbf{e}_\theta. \tag{12}$$

Basic Transport Equations

Having obtained the expansion for the required tensor quantities, almost all basic transport equations in their various forms can be readily written down by simple substitution for terms. This is illustrated for few important basic transport equations of common occurrence in the following.

Equation of Continuity

$$\frac{\delta\rho}{\delta t}+\nabla\cdot(\rho\mathbf{v})=0 \tag{13}$$

in the chosen coordinate system takes the form

$$\frac{\delta\rho}{\delta t}+\frac{1}{\sqrt{g_{11}}}\frac{\delta}{\delta\Omega}(\rho v_\Omega)+\frac{\delta}{\delta r}(\rho v_r)+\frac{1}{r}\frac{\delta}{\delta\theta}(\rho v_\theta)+\left(\frac{1}{r}+\frac{\cos\theta}{\sqrt{g_{11}}}\right)\rho v_\Omega-\frac{\sin\theta}{\sqrt{g_{11}}}\rho\, v_\theta=0. \tag{14}$$

General Equation of Motion

$$\rho\mathbf{a}=\rho\mathbf{f}+(\nabla\cdot\tau), \tag{15}$$

where **a** is the acceleration vector, **f** is the body force, and τ is stress tensor, takes the form

$$\rho\frac{D\mathbf{v}}{Dt}=\rho f_\Omega\,\mathbf{e}_\Omega+\rho f_r\,\mathbf{e}_r+\rho f_\theta\,\mathbf{e}_\theta+(\nabla\cdot\tau), \tag{16}$$

where first and last terms can be substituted from equations (12) and (9), respectively.

For fluids of known constitutive equations, expressions for stress components in terms of velocity gradients and fluid properties may be substituted to get more useful form of equation of motion. Navier-Stokes equation of motion, which uses constitutive equation corresponding to Newtonian fluid with the assumption of constant density and viscosity, is given by

$$\rho\mathbf{a}=-\nabla p+\mu\nabla^2\mathbf{v}+\rho\mathbf{g}, \tag{17}$$

where p is pressure and **g** is the gravitational force assumed to be the only body force present. In the ascending equiangular spiral polar coordinate system, the Navier-Stokes equation is easily obtained by substituting for $\rho\mathbf{a}$ and $\rho\mathbf{g}$ from equation (16), for ∇p from equation (6) and for $\nabla^2\mathbf{v}$ from equation (10).

Equation of Thermal Energy

For the cases where viscous heat dissipation is not important and coefficient of thermal conductivity is constant, the equation of energy is given by

$$\rho\hat{C}_v\frac{DT}{Dt}=k\nabla^2T-T\left(\frac{\delta p}{\delta T}\right)_\rho(\nabla\cdot\mathbf{v})+\rho S, \tag{18}$$

and in the required coordinate system becomes

$$\rho\hat{C}_v\left[\frac{\delta T}{\delta t}+\frac{v_\Omega}{\sqrt{g_{11}}}\frac{\delta T}{\delta\Omega}+v_r\frac{\delta T}{\delta r}+\frac{v_\theta}{r}\frac{\delta T}{\delta\theta}\right]=k\left[\frac{1}{g_{11}}\frac{\delta^2T}{\delta\Omega^2}+\frac{\delta^2T}{\delta r^2}+\frac{1}{r^2}\frac{\delta^2T}{\delta\theta^2}-\frac{m}{g_{11}}\right. \tag{19}$$

$$\left.\times\left(\frac{\sqrt{g_{11}}-r\cos\theta}{\sqrt{g_{11}}}\right)\frac{\delta T}{\delta\Omega}+\left(\frac{1}{r}+\frac{\cos\theta}{\sqrt{g_{11}}}\right)\frac{\delta T}{\delta r}-\frac{\sin\theta}{r\sqrt{g_{11}}}\frac{\delta T}{\delta\theta}\right]-T\left(\frac{\delta p}{\delta T}\right)_\rho\left[\frac{1}{\sqrt{g_{11}}}\frac{\delta v_\Omega}{\delta\Omega}+\frac{\delta v_r}{\delta_r}+\frac{1}{r}\frac{v_\theta}{\delta\theta}+\left(\frac{1}{r}+\frac{\cos\theta}{\sqrt{g_{11}}}\right)v_r-\frac{\sin\theta}{\sqrt{g_{11}}}v_\theta\right]+\rho S. \tag{19 (Cont.)}$$

Equation of Diffusion

For binary mixtures obeying Fick's law and having constant mass density and diffusion coefficient, the equation of mass diffusion is

$$\frac{DC_A}{Dt}=D_{AB}\nabla^2C_A+R_A \tag{20}$$

which expands as

$$\frac{\delta C_A}{\delta t}+\frac{v_\Omega}{\sqrt{g_{11}}}\frac{\delta C_A}{\delta\Omega}+v_r\frac{\delta C_A}{\delta r}+\frac{v_\theta}{r}\frac{\delta C_A}{\delta\theta}=D_{AB}\left[\frac{1}{g_{11}}\frac{\delta^2C_A}{\delta\Omega^2}+\frac{\delta^2C_A}{\delta r^2}+\frac{1}{r^2}\frac{\delta^2C_A}{\delta\theta^2}-\frac{m}{g_{11}}\left(\frac{\sqrt{g_{11}}-r\cos\theta}{\sqrt{g_{11}}}\right)\frac{\delta C_A}{\delta\Omega}+\left(\frac{1}{r}+\frac{\cos\theta}{\sqrt{g_{11}}}\right)\frac{\delta C_A}{\delta r}-\frac{\sin\theta}{r\sqrt{g_{11}}}\frac{\delta C_A}{\delta\theta}\right]+R_A. \tag{21}$$

Concluding Remarks

Apart from the basic transport equations, expansions, which have previously illustrated almost all other forms of transport equations, can readily be written down in the developed ascending equiangular spiral polar coordinate system by simple substitution for their tensorial terms expansion which has been obtained in the foregoing.

References

1 Ali, S., and Zaidi, A. H., "Head Loss and Critical Reynolds Number for Flow in Ascending Equiangular Spiral Tube Coils," *Ind. Eng. Chem. Process Des. Dev.*, Vol. 18, No. 2, Apr. 1979, pp. 349–352.

2 Ali, S., "Steps Toward the Theoretical Study of Secondary Flow in Spirally Coiled Channels (Basic Transport Equations and a Solution by the Method of Weighted Residual)," PhD Thesis, IIT Kanpur, India, 1974.

3 Eringen, A. C., *Nonlinear Theory of Continuous Media,* McGraw-Hill, New York, 1962.

Linear Spatial Stability of Developing Flow in a Parallel Plate Channel

S. C. Gupta[1] **and V. K. Garg**[2]

It is found that even a 5 percent change in the velocity profile produces a 100 percent change in the critical Reynolds number for the stability of developing flow very close to the entrance of a two-dimensional channel.

Introduction

The temporal stability characteristics of the developing flow in a

---

[1] Assistant Professor, Department of Mechanical Engineering, University of Jodhpur, Jodhpur, India.

[2] Professor, Department of Mechanical Engineering, Indian Institute of Technology, Kanpur 208016, India.

Manuscript received by ASME Applied Mechanics Division, October, 1979; final revision, February, 1980.

Material Derivative of a Vector Field v

$$\frac{D\mathbf{v}}{Dt} = \left[\frac{\delta v_\Omega}{\delta t} + \frac{v_\Omega}{\sqrt{g_{11}}}\frac{\delta v_\Omega}{\delta \Omega} + \frac{\cos\theta}{\sqrt{g_{11}}} v_\Omega v_r - \frac{\sin\theta}{\sqrt{g_{11}}} v_\Omega v_\theta + v_r \frac{\delta v_\Omega}{\delta r} + \frac{v_\theta}{r}\frac{\delta v_\Omega}{\delta\theta}\right]\mathbf{e}_\Omega + \left[\frac{\delta v_r}{\delta t} + \frac{v_\Omega}{\sqrt{g_{11}}}\frac{\delta v_r}{\delta\Omega} - \frac{\cos\theta}{\sqrt{g_{11}}} v_\Omega^2 + v_r\frac{\delta v_r}{\delta r} + \frac{v_\theta}{r}\frac{\delta v_r}{\delta\theta} - \frac{v_\theta^2}{r}\right]\mathbf{e}_r + \left[\frac{\delta v_\theta}{\delta t} + \frac{v_\Omega}{\sqrt{g_{11}}}\frac{\delta v_\theta}{\delta\Omega} + \frac{\sin\theta}{\sqrt{g_{11}}} v_\Omega^2 + v_r\frac{\delta v_\theta}{\delta r} + \frac{v_\theta}{r}\frac{\delta v_\theta}{\delta\theta} + \frac{v_r v_\theta}{r}\right]\mathbf{e}_\theta. \quad (12)$$

Basic Transport Equations

Having obtained the expansion for the required tensor quantities, almost all basic transport equations in their various forms can be readily written down by simple substitution for terms. This is illustrated for few important basic transport equations of common occurrence in the following.

Equation of Continuity

$$\frac{\delta\rho}{\delta t} + \nabla\cdot(\rho\mathbf{v}) = 0 \quad (13)$$

in the chosen coordinate system takes the form

$$\frac{\delta\rho}{\delta t} + \frac{1}{\sqrt{g_{11}}}\frac{\delta}{\delta\Omega}(\rho v_\Omega) + \frac{\delta}{\delta r}(\rho v_r) + \frac{1}{r}\frac{\delta}{\delta\theta}(\rho v_\theta) + \left(\frac{1}{r} + \frac{\cos\theta}{\sqrt{g_{11}}}\right)\rho v_\Omega - \frac{\sin\theta}{\sqrt{g_{11}}}\rho\, v_\theta = 0. \quad (14)$$

General Equation of Motion

$$\rho\mathbf{a} = \rho\mathbf{f} + (\nabla\cdot\tau), \quad (15)$$

where **a** is the acceleration vector, **f** is the body force, and τ is stress tensor, takes the form

$$\rho\frac{D\mathbf{v}}{Dt} = \rho f_\Omega\,\mathbf{e}_\Omega + \rho f_r\,\mathbf{e}_r + \rho f_\theta\,\mathbf{e}_\theta + (\nabla\cdot\tau), \quad (16)$$

where first and last terms can be substituted from equations (12) and (9), respectively.

For fluids of known constitutive equations, expressions for stress components in terms of velocity gradients and fluid properties may be substituted to get more useful form of equation of motion. Navier-Stokes equation of motion, which uses constitutive equation corresponding to Newtonian fluid with the assumption of constant density and viscosity, is given by

$$\rho\mathbf{a} = -\nabla p + \mu\nabla^2\mathbf{v} + \rho\mathbf{g}, \quad (17)$$

where p is pressure and **g** is the gravitational force assumed to be the only body force present. In the ascending equiangular spiral polar coordinate system, the Navier-Stokes equation is easily obtained by substituting for $\rho\mathbf{a}$ and $\rho\mathbf{g}$ from equation (16), for ∇p from equation (6) and for $\nabla^2\mathbf{v}$ from equation (10).

Equation of Thermal Energy

For the cases where viscous heat dissipation is not important and coefficient of thermal conductivity is constant, the equation of energy is given by

$$\rho\hat{C}_v\frac{DT}{Dt} = k\nabla^2 T - T\left(\frac{\delta p}{\delta T}\right)_\rho(\nabla\cdot\mathbf{v}) + \rho S, \quad (18)$$

and in the required coordinate system becomes

$$\rho\hat{C}_v\left[\frac{\delta T}{\delta t} + \frac{v_\Omega}{\sqrt{g_{11}}}\frac{\delta T}{\delta\Omega} + v_r\frac{\delta T}{\delta r} + \frac{v_\theta}{r}\frac{\delta T}{\delta\theta}\right] = k\left[\frac{1}{g_{11}}\frac{\delta^2 T}{\delta\Omega^2} + \frac{\delta^2 T}{\delta r^2} + \frac{1}{r^2}\frac{\delta^2 T}{\delta\theta^2} - \frac{m}{g_{11}} \quad (19)$$

$$\times\left(\frac{\sqrt{g_{11}} - r\cos\theta}{\sqrt{g_{11}}}\right)\frac{\delta T}{\delta\Omega} + \left(\frac{1}{r} + \frac{\cos\theta}{\sqrt{g_{11}}}\right)\frac{\delta T}{\delta r} - \frac{\sin\theta}{r\sqrt{g_{11}}}\frac{\delta T}{\delta\theta}\right] - T\left(\frac{\delta p}{\delta T}\right)_\rho\left[\frac{1}{\sqrt{g_{11}}}\frac{\delta v_\Omega}{\delta\Omega} + \frac{\delta v_r}{\delta_r} + \frac{1}{r}\frac{v_\theta}{\delta\theta} + \left(\frac{1}{r} + \frac{\cos\theta}{\sqrt{g_{11}}}\right)v_r - \frac{\sin\theta}{\sqrt{g_{11}}}v_\theta\right] + \rho S. \quad (19)\ (Cont.)$$

Equation of Diffusion

For binary mixtures obeying Fick's law and having constant mass density and diffusion coefficient, the equation of mass diffusion is

$$\frac{DC_A}{Dt} = D_{AB}\,\nabla^2 C_A + R_A \quad (20)$$

which expands as

$$\frac{\delta C_A}{\delta t} + \frac{v_\Omega}{\sqrt{g_{11}}}\frac{\delta C_A}{\delta\Omega} + v_r\frac{\delta C_A}{\delta r} + \frac{v_\theta}{r}\frac{\delta C_A}{\delta\theta} = D_{AB}\left[\frac{1}{g_{11}}\frac{\delta^2 C_A}{\delta\Omega^2} + \frac{\delta^2 C_A}{\delta r^2} + \frac{1}{r^2}\frac{\delta^2 C_A}{\delta\theta^2} - \frac{m}{g_{11}}\left(\frac{\sqrt{g_{11}} - r\cos\theta}{\sqrt{g_{11}}}\right)\frac{\delta C_A}{\delta\Omega} + \left(\frac{1}{r} + \frac{\cos\theta}{\sqrt{g_{11}}}\right)\frac{\delta C_A}{\delta r} - \frac{\sin\theta}{r\sqrt{g_{11}}}\frac{\delta C_A}{\delta\theta}\right] + R_A. \quad (21)$$

Concluding Remarks

Apart from the basic transport equations, expansions, which have previously illustrated almost all other forms of transport equations, can readily be written down in the developed ascending equiangular spiral polar coordinate system by simple substitution for their tensorial terms expansion which has been obtained in the foregoing.

References

1 Ali, S., and Zaidi, A. H., "Head Loss and Critical Reynolds Number for Flow in Ascending Equiangular Spiral Tube Coils," *Ind. Eng. Chem. Process Des. Dev.*, Vol. 18, No. 2, Apr. 1979, pp. 349–352.

2 Ali, S., "Steps Toward the Theoretical Study of Secondary Flow in Spirally Coiled Channels (Basic Transport Equations and a Solution by the Method of Weighted Residual)," PhD Thesis, IIT Kanpur, India, 1974.

3 Eringen, A. C., *Nonlinear Theory of Continuous Media,* McGraw-Hill, New York, 1962.

Linear Spatial Stability of Developing Flow in a Parallel Plate Channel

S. C. Gupta[1] **and V. K. Garg**[2]

It is found that even a 5 percent change in the velocity profile produces a 100 percent change in the critical Reynolds number for the stability of developing flow very close to the entrance of a two-dimensional channel.

Introduction

The temporal stability characteristics of the developing flow in a

---

[1] Assistant Professor, Department of Mechanical Engineering, University of Jodhpur, Jodhpur, India.

[2] Professor, Department of Mechanical Engineering, Indian Institute of Technology, Kanpur 208016, India.

Manuscript received by ASME Applied Mechanics Division, October, 1979; final revision, February, 1980.

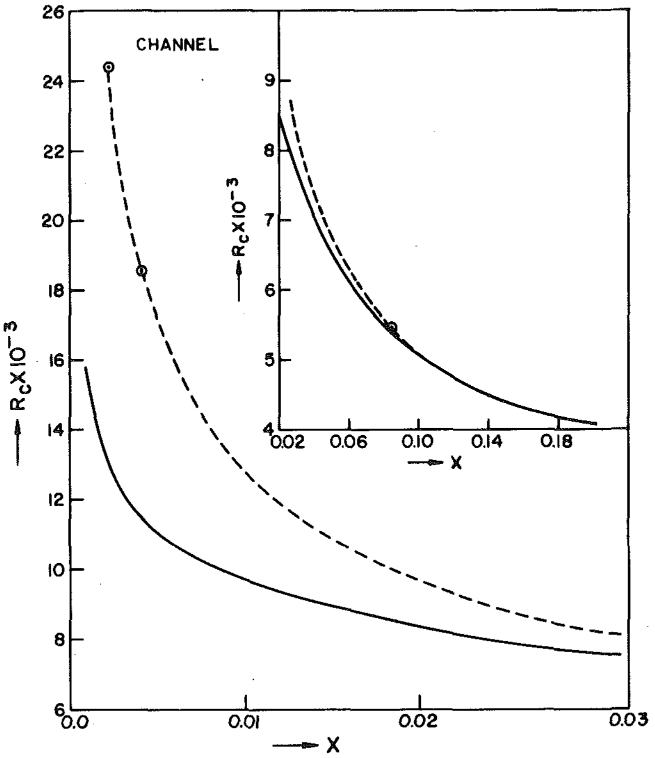

Fig. 1 Variation of critical Reynolds number with *X*; —, present work; - - -, Chen's results with finite-difference technique [1]; ⊙ present results for Sparrow's profile [2]

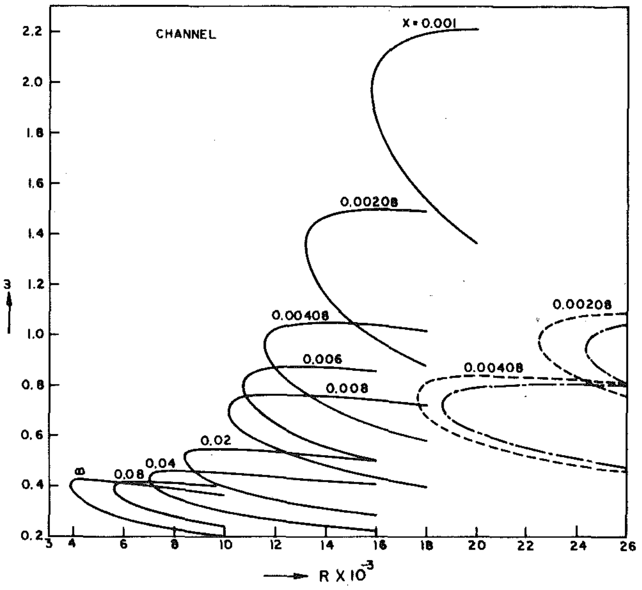

Fig. 2 Neutral curves at various axial locations; —, present work; — - —, present results with Sparrow's profile [2]; - - -, Chen's results [1]

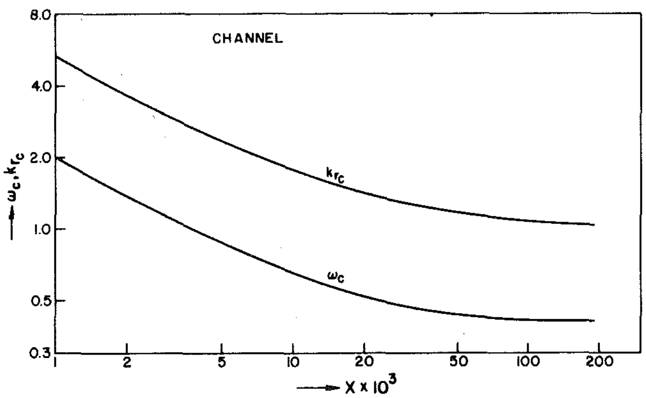

Fig. 3 Variation of critical frequency and critical wave number with *X*

two-dimensional channel were determined by Chen [1] using the Sparrow profile, the velocity profile determined by the linearization method of Sparrow, et al. [2]. However, it is now widely accepted that the velocity profile, hereafter referred to as the *B-O* profile, obtained by Bodoia and Osterle's method [3] gives a better velocity field description. The present study, therefore, aims to study the linear spatial stability characteristics of the *B-O* profile and to compare them with those of the Sparrow profile. Symmetric disturbances of the type $\chi(x, y, t) = \phi(y) \exp\{i(kx - \omega t)\}$ are considered, where χ is the stream function of the disturbance, x and y are the dimensionless streamwise and transverse coordinates measured from the inlet section and the center line of the channel, respectively, ω and t are the dimensionless frequency and time, respectively, k is the complex number whose real part k_r is the wave number and imaginary part k_i is the spatial growth rate. Nondimensionalization is carried out with respect to half width of the channel and average velocity of the flow. This leads to the Orr-Sommerfeld problem.

Solution

The eigenvalue problem is solved by means of the fourth-order Runge-Kutta method while using selectively the Gram-Schmidt orthonormalization procedure [4]. Convergence to the eigenvalue is achieved by Muller's method [5]. By numerical experimentation it was found that a step size of 0.0025 gives an error of $0(10^{-6})$ in the eigenvalues when computation is done in double precision mode on DEC 1090. Iteration to the neutral point was terminated for $|k_i| \leq 10^{-6}$.

Results

Fig. 1 shows the variation of critical Reynolds number, R_c, with X for the present analysis and for the Sparrow profile as obtained by Chen [1] using the finite-difference scheme of Thomas [6]. Here $X = x/R$, where R is the Reynolds number. It is observed that the critical Reynolds number for the *B-O* profile is much lower than that for the Sparrow profile in the near-entry region. At $X = 0.002$, R_c for the Sparrow profile is about twice that for the *B-O* profile. This difference between the R_c-values decreases as X increases to about $X = 0.09$ where the two curves appear to coincide with each other and remain so thereafter. This behavior is to be expected since the two velocity profiles are found to merge into one at $X \approx 0.084$. One, therefore, draws the conclusion that the large difference in R_c-values in the near-entry region is due to the difference in the two velocity profiles. The three critical points, obtained for the Sparrow profile by the present technique and shown in the figure by points marked ⊙, show the agreement of our results with those of Chen obtained by the finite-difference method.

Fig. 2 shows the neutral curves at $X = 0.001, 0.00208, 0.00408, 0.006$, and 0.008 to ∞ for the *B-O* profile. Also shown on this figure are the neutral curves at $X = 0.00208$ and 0.00408 for the Sparrow profile obtained by the present method as well as by Chen using regular viscous solutions for the full channel profile. Comparison of the neutral curves at $X = 0.00208$ and 0.00408 reveals that the *B-O* profile is unstable for a wider range of frequencies at any given X and R. We also note that neutral curves reported by Chen for the Sparrow profile are not accurate. It may be observed that the area of unstable region for the *B-O* profile decreases with increasing X.

Fig. 3 shows the variation of the critical wave number, k_{rc}, and critical frequency, ω_c, with X. We note that both k_{rc} and ω_c decrease with increasing axial distance in the entrance region and approach asymptotically the corresponding values for the fully developed flow; the curves being nearly parallel.

Conclusions

Though the Sparrow and *B-O* velocity profiles differ by 5 percent at most in the near-entry region, the critical Reynolds number for the former is twice of that for the latter at $X = 0.001$. It is difficult to say which velocity profile predicts the stability of the actual developing flow more accurately due to lack of experimental stability characteristics. However, since the superiority of the *B-O* profile over the Sparrow profile has been widely accepted, one has the intuitive feeling that the stability results reported herein for the *B-O* profile should be closer to the actual one.

Acknowledgment

This forms part of the PhD thesis submitted by S. C. Gupta to the Indian Institute of Technology, Kanpur.

References

1 Chen, T. S., "Hydrodynamic Stability of Developing Flow in a Parallel Plate Channel," PhD Thesis, Department of Mechanical Engineering, University of Minnesota, 1966.

2 Sparrow, E. M., Lin, S. H., and Lundgren, T. S., "Flow Development in the Hydrodynamic Entrance Region of Tubes and Ducts," *Physics of Fluids*, Vol. 7, 1964, pp. 338–347.

3 Bodoia, J. R., and Osterle, J. F., "Finite-Difference Analysis of Plane Poiseuille Flow and Couette Flow Development," *Applied Scientific Research*, Section A, Vol. 10, 1961, pp. 265–276.

4 Garg, V. K., "Improved Shooting Techniques for Linear Boundary-Value Problems," *Computer Methods in Applied Mechanics and Engineering*, Vol. 22, 1980, pp. 87–99.

5 Muller, D. E., "A Method for Solving Algebraic Equations Using an Automatic Computer," *Mathematical Tables and Other Aides to Computers*, Vol. 10, 1956, pp. 208–215.

6 Thomas, L. H., "Stability of Plane Poiseuille Flow," *Physical Review*, Vol. 91, 1953, pp. 780–783.

Note on the Energy-Release Rate for a Crack Starting From the Apex of a Wedge

C. Yatomi[1]

We show that for a Mode III crack starting from the apex of a wedge, the initial value of the energy-release rate is zero, although the stresses at the crack tip are unbounded.

Introduction

Griffith [1] was apparently the first to employ the energy-release rate $\mathcal{G}$ as a critical condition of crack extension. In this Note we will show, however, that if a crack starts from the apex of a wedge (cf. Fig. 1 with $n \neq 1$), the initial value of $\mathcal{G}$ is zero, although the stresses at the crack tip are unbounded. This example suggests that you cannot use the initial energy-release rate as a critical condition of crack extension unless the opening-angle of the crack faces in the reference is *precisely zero*. Since the order of the singularity of the strain-energy density is less than one, this result may be predicted mathematically but it is not trivial physically.

We confine our problem to a simple Mode III crack; the given solutions are then simple and of closed form, so that we can examine the precise dependence of $\mathcal{G}$ on the crack length a. To the author's knowledge, no such closed-form solution for an arbitrary crack length a has been presented (see, for example, Khrapkov [2] for Modes I and II).

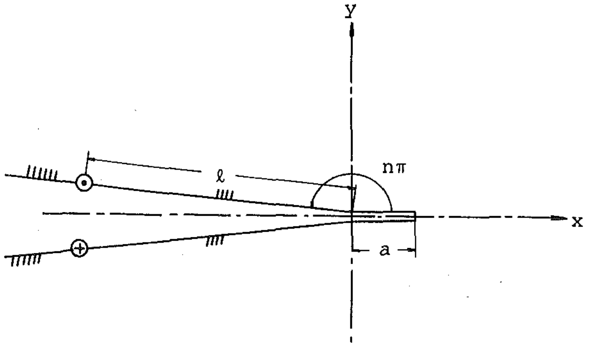

Fig. 1 A crack starting from the apex of a wedge

Brief Methods of Solutions

Following the theory developed by Sih [3], we will analyze Mode III crack of length a which starts from the apex of an infinite wedge subjected to concentrated forces P acting in opposite directions at $z = \ell e^{\pm i n \pi}$ (Fig. 1).

We employ a function

$$z = w(\zeta) = e^{-n\pi i}(\zeta^2 - a^{1/n})^n, \quad 0 < n \leq 1, \tag{1}$$

which maps the upper side of the crack to $-a^{1/2n} \leq \text{Real}\ (\zeta) \leq 0$, the lower side to $O \leq \text{Real}\ (\zeta) \leq a^{1/2n}$, and the points at which the forces P are acting to $\beta = \pm\ (\ell^{1/n} + a^{1/n})^{1/2}$, respectively.

With the aid of equation (16) of Sih [3], the relevant stress function is

$$F(\zeta) = \frac{P}{\pi G} \log \frac{\zeta + \beta}{\zeta - \beta}, \tag{2}$$

where G is the shear modulus. The stresses are then given in the form

$$\begin{aligned} \sigma_{xz} - i\sigma_{yz} &= G\frac{F'(\zeta)}{w'(\zeta)} \\ &= \frac{P}{\pi}\frac{2\beta}{\beta^2 - \zeta^2}\frac{1}{2ne^{-n\pi i}\zeta(\zeta^2 - a^{1/n})^{n-1}} \end{aligned}$$

in the ζ-plane, or

$$= \frac{P}{\pi}\frac{(\ell^{1/n} + a^{1/n})^{1/2}}{\ell^{1/n} + z^{1/n}}\frac{-1}{n(a^{1/n} - z^{1/n})^{1/2} z^{1-1/n}}, \tag{3}$$

$$= \frac{p}{\pi}\frac{\ell^{1/2n}}{\ell^{1/n} + z^{1/n}}\frac{i}{nz^{1-1/2n}} \quad \text{for} \quad a = 0 \tag{4}$$

in the z-plane.

Equations (3) and (4) show, as is expected, that the stress singularity of order ½ has changed discontinuously order to 1 − ½n at $a = 0^+$. (This is another example of simple closed-form solution exhibiting the singularity transition phenomenon which was studied by Nuismer and Sendeckyj [4].)

Inserting equations (1) and (2) into equation (7) of [3] yields the solution for the stress-intensity factor:

$$K(a) = \frac{P}{\pi}\frac{\sqrt{2}}{(\ell^{1/n} + a^{1/n})^{1/2}}\frac{a^{1/2n-1/2}}{n^{1/2}}.$$

Since $\mathcal{G} = \pi K^2/2G$, the energy-release rate is given by

$$\mathcal{G}(a) = \frac{p^2}{\pi G}\frac{a^{1/n-1}}{(\ell^{1/n} + a^{1/n})n}. \tag{5}$$

Equation (5) shows that

$$\mathcal{G}(a) \sim a^{1/n-1} \quad \text{as} \quad a \to 0,$$

---

[1] Department of Aeronautical Engineering, Kyoto University, Kyoto, Japan; formerly, Department of Mathematics, Carnegie-Mellon University, Pittsburgh, Pa. 15213.

Manuscript received by ASME Applied Mechanics Division, June, 1980.

asymptotically the corresponding values for the fully developed flow; the curves being nearly parallel.

Conclusions

Though the Sparrow and *B-O* velocity profiles differ by 5 percent at most in the near-entry region, the critical Reynolds number for the former is twice of that for the latter at $X = 0.001$. It is difficult to say which velocity profile predicts the stability of the actual developing flow more accurately due to lack of experimental stability characteristics. However, since the superiority of the *B-O* profile over the Sparrow profile has been widely accepted, one has the intuitive feeling that the stability results reported herein for the *B-O* profile should be closer to the actual one.

Acknowledgment

This forms part of the PhD thesis submitted by S. C. Gupta to the Indian Institute of Technology, Kanpur.

References

1 Chen, T. S., "Hydrodynamic Stability of Developing Flow in a Parallel Plate Channel," PhD Thesis, Department of Mechanical Engineering, University of Minnesota, 1966.

2 Sparrow, E. M., Lin, S. H., and Lundgren, T. S., "Flow Development in the Hydrodynamic Entrance Region of Tubes and Ducts," *Physics of Fluids*, Vol. 7, 1964, pp. 338–347.

3 Bodoia, J. R., and Osterle, J. F., "Finite-Difference Analysis of Plane Poiseuille Flow and Couette Flow Development," *Applied Scientific Research*, Section A, Vol. 10, 1961, pp. 265–276.

4 Garg, V. K., "Improved Shooting Techniques for Linear Boundary-Value Problems," *Computer Methods in Applied Mechanics and Engineering*, Vol. 22, 1980, pp. 87–99.

5 Muller, D. E., "A Method for Solving Algebraic Equations Using an Automatic Computer," *Mathematical Tables and Other Aides to Computers*, Vol. 10, 1956, pp. 208–215.

6 Thomas, L. H., "Stability of Plane Poiseuille Flow," *Physical Review*, Vol. 91, 1953, pp. 780–783.

Note on the Energy-Release Rate for a Crack Starting From the Apex of a Wedge

C. Yatomi[1]

We show that for a Mode III crack starting from the apex of a wedge, the initial value of the energy-release rate is zero, although the stresses at the crack tip are unbounded.

Introduction

Griffith [1] was apparently the first to employ the energy-release rate $\mathcal{G}$ as a critical condition of crack extension. In this Note we will show, however, that if a crack starts from the apex of a wedge (cf. Fig. 1 with $n \neq 1$), the initial value of $\mathcal{G}$ is zero, although the stresses at the crack tip are unbounded. This example suggests that you cannot use the initial energy-release rate as a critical condition of crack extension unless the opening-angle of the crack faces in the reference is *precisely zero.* Since the order of the singularity of the strain-energy density is less than one, this result may be predicted mathematically but it is not trivial physically.

We confine our problem to a simple Mode III crack; the given solutions are then simple and of closed form, so that we can examine the precise dependence of $\mathcal{G}$ on the crack length a. To the author's knowledge, no such closed-form solution for an arbitrary crack length a has been presented (see, for example, Khrapkov [2] for Modes I and II).

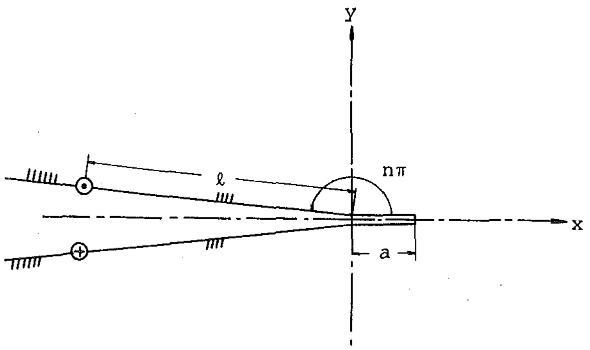

Fig. 1 A crack starting from the apex of a wedge

Brief Methods of Solutions

Following the theory developed by Sih [3], we will analyze Mode III crack of length a which starts from the apex of an infinite wedge subjected to concentrated forces P acting in opposite directions at $z = \ell e^{\pm in\pi}$ (Fig. 1).

We employ a function

$$z = w(\zeta) = e^{-n\pi i}(\zeta^2 - a^{1/n})^n, \quad 0 < n \leq 1, \tag{1}$$

which maps the upper side of the crack to $-a^{1/2n} \leq \text{Real}\,(\zeta) \leq 0$, the lower side to $O \leq \text{Real}\,(\zeta) \leq a^{1/2n}$, and the points at which the forces P are acting to $\beta = \pm\,(\ell^{1/n} + a^{1/n})^{1/2}$, respectively.

With the aid of equation (16) of Sih [3], the relevant stress function is

$$F(\zeta) = \frac{P}{\pi G} \log \frac{\zeta + \beta}{\zeta - \beta}, \tag{2}$$

where G is the shear modulus. The stresses are then given in the form

$$\sigma_{xz} - i\sigma_{yz} = G\frac{F'(\zeta)}{w'(\zeta)}$$

$$= \frac{P}{\pi}\frac{2\beta}{\beta^2 - \zeta^2}\frac{1}{2ne^{-n\pi i}\zeta(\zeta^2 - a^{1/n})^{n-1}}$$

in the ζ-plane, or

$$= \frac{P}{\pi}\frac{(\ell^{1/n} + a^{1/n})^{1/2}}{\ell^{1/n} + z^{1/n}}\frac{-1}{n(a^{1/n} - z^{1/n})^{1/2}z^{1-1/n}}, \tag{3}$$

$$= \frac{p}{\pi}\frac{\ell^{1/2n}}{\ell^{1/n} + z^{1/n}}\frac{i}{nz^{1-1/2n}} \quad \text{for} \quad a = 0 \tag{4}$$

in the z-plane.

Equations (3) and (4) show, as is expected, that the stress singularity of order ½ has changed discontinuously order to $1 - \frac{1}{2}n$ at $a = 0^+$. (This is another example of simple closed-form solution exhibiting the singularity transition phenomenon which was studied by Nuismer and Sendeckyj [4].)

Inserting equations (1) and (2) into equation (7) of [3] yields the solution for the stress-intensity factor:

$$K(a) = \frac{P}{\pi}\frac{\sqrt{2}}{(\ell^{1/n} + a^{1/n})^{1/2}}\frac{a^{1/2n-1/2}}{n^{1/2}}.$$

Since $\mathcal{G} = \pi K^2/2G$, the energy-release rate is given by

$$\mathcal{G}(a) = \frac{p^2}{\pi G}\frac{a^{1/n-1}}{(\ell^{1/n} + a^{1/n})n}. \tag{5}$$

Equation (5) shows that

$$\mathcal{G}(a) \sim a^{1/n-1} \quad \text{as} \quad a \to 0,$$

---

[1] Department of Aeronautical Engineering, Kyoto University, Kyoto, Japan; formerly, Department of Mathematics, Carnegie-Mellon University, Pittsburgh, Pa. 15213.

Manuscript received by ASME Applied Mechanics Division, June, 1980.

and the initial value of $G(a)$ at $a = 0^+$ is zero unless $n = 1$ as noted in the Introduction.

Acknowledgment

The authors would like to thank Profs. M. E. Gurtin and J. W. Hutchinson for valuable comments and discussions. This work was supported by the Air Force Office of Scientific Research.

References

1 Griffith, A. A., "The Phenomena of Rupture and Flow in Solids," *Philosophical Transactions of the Royal Society*, London, Series A, Vol. 221, 1921, pp. 163–198.

2 Khrapkov, A. A., "The First Basic Problem for a Notch at the Apex of an Infinite Wedge," *International Journal of Fracture Mechanics*, Vol. 7, 1971, pp. 373–382.

3 Sih, G. C., "Stress Distribution Near Internal Crack Tips for Longitudinal Shear Problems," ASME JOURNAL OF APPLIED MECHANICS, Vol. 32, 1965, pp. 51–58.

4 Nuismer, R. J., and Sendeckyj, G. P., "On the Changing Order of Singularity at a Crack Tip," ASME JOURNAL OF APPLIED MECHANICS, Vol. 44, 1977, pp. 625–630.

On the Polygon-Circle Paradox

K. Rajaiah[1] and A. K. Rao[2]

Introduction

The problem of the polygon-circle paradox in thin plate theory [1] has attracted sustained attention during the last decade [2–7] primarily due to its implications in thin plate and finite-element analyses. There have been some earlier investigations [8–10] too on the subject some of which were considered by Hanuska [11]. Inspite of such continued interest, a satisfactory resolution of the paradox does not seem to have appeared in the literature. The resolution of the paradox, based on an earlier study [12], is presented in this Note.

Statement of the Paradox

Consider a two-dimensional physical phenomenon in a regular polygonal domain with an inscribed circle of radius a and also in a circular domain with the same radius a, both fields being subject to identical physical boundary conditions (Fig. 1). One would expect that, as the number of sides n of the polygon is increased indefinitely ($n \to \infty$), the solution for the polygon should approach that for the circle. Numerical results from different sources referred to in [1] for the flexure of regular polygonal plates under uniform transverse pressure, show diverging trends in relation to this anticipation when the edges are simply supported, although they are all in agreement with the anticipation when the edges are clamped.

Resolution

The paradox shows that, even though the limiting polygon ($n \to \infty$) and the corresponding circular plate under identical loading conditions are governed by the same differential equation, their flexural behavior is identical for conditions of edge fixity, but is entirely different for edge conditions of simple support. Obviously one should shift attention from the complete solution of the problem to the boundary conditions. For simplicity the discussion can be in relation to axisymmetric load distributions.

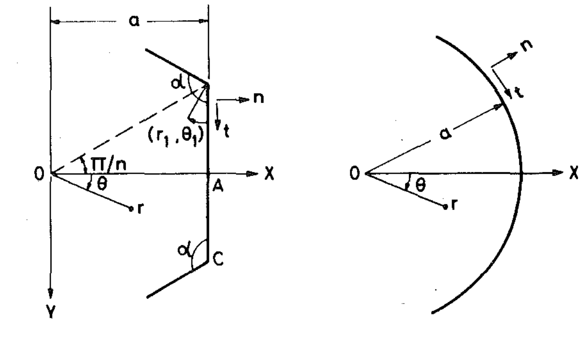

REGULAR POLYGONAL PLATE CIRCULAR PLATE

Fig. 1 Coordinate axes

(*i*) **Clamped Edges.** Consider the conditions along a clamped circular edge. On such an edge, the clamped condition implies $w = 0$, $w_n = 0$, and $w = 0$ itself yields $w_t = 0$ and due to axisymmetry $M_{nt} = 0$. Thus four quantities w, w_n, w_t, and M_{nt} become zero on the edge of a clamped circular plate.

On any edge of a clamped regular polygonal plate, once again the conditions are $w = 0$, $w_n = 0$. Further more $w = 0$ leads to $w_t = 0$ while $w_n = 0$ yields $M_{nt} = 0$. Also from an eigenfunction analysis due to Williams [13], it is clear that there are no singularities at the corners of the polygonal plate. All these conditions hold good however large the number of sides, even in the limit $n \to \infty$.

Comparing the conditions on the clamped circular edge with those of the limiting clamped polygon, it is observed that the same four quantities (w, w_n, w_t, and M_{nt}) vanish on the edge in either case. There are apparently no other physical quantities that may produce any discrepancy. Hence the limiting clamped polygon, as $n \to \infty$, should be and is identical with the corresponding clamped circular plate.

(*ii*) **Simply Supported Edges.** First, consider the circular edge. By definition, $w = 0$ and $M_n = 0$. Due to axisymmetry, $M_{nt} = 0$. But from the exact solution for the circular plate [14] it is clear that $M_t \neq 0$, and therefore $\nabla^2 w \neq 0$.

Next, consider the edges of the polygon. The simple edge support needs $w = 0$ and $M_n = 0$. As a consequence, $w_{tt} = 0$ and $M_t = 0$ and also $\nabla^2 w = 0$. It is also realized that $M_{nt} \neq 0$ anywhere except at the midpoints. These conditions apply for all n. On the other hand, in the corresponding circular plate w_{tt}, M_t, $\nabla^2 w \neq 0$ while $M_{nt} = 0$. Clearly, in this case the limiting polygonal plate solution must be different from the circular plate solution.

Now let us proceed to consider the effect of the corners in the limiting simply supported polygon. From an eigenfunction study [13], one finds that when $n \geq 4$, the corners C are points of moment (M_r, M_θ, $M_{r\theta}$) singularities. The singular part of the deflection function is given by $A_1 r_1^{\pi/\alpha} \sin(\pi/\alpha)\,\theta_1$ where $\pi/\alpha = n/(n-2)$ and A_1 is the strength of the singularity. The corresponding second derivative in r (contributing to the moments M_r, M_θ, and $M_{r\theta}$) is found to be

$$A_1 \frac{\pi}{\alpha}\left(\frac{\pi}{\alpha} - 1\right) r_1^{\pi/\alpha - 2} \sin(\pi/\alpha)\,\theta_1.$$

It is also observed that, at each corner, the slopes in two different directions are zero and as such each corner behaves like a clamped point. In view of this, the simply supported condition along the straight edges is effectively augmented by periodic corner clamping. Thus the limiting polygon is supported by an alternating system of "infinitesimally short" simple straight supports and stiff point supports. As such the stiffness of the limiting polygon should be between the stiffnesses of the simply supported and clamped circular plates. This is confirmed by the central deflections and edge rotations for the three cases which are shown in Table 1.

In fact it can be readily shown that a circular plate with an elastic

---

[1] Professor, Department of Aeronautical Engineering, Indian Institute of Technology, Powai, Bombay, 400 076 India.

[2] Professor, Department of Aeronautical Engineering, Indian Institute of Science, Bangalore, India.

Manuscript received by ASME Applied Mechanics Division, April, 1980; final revision, June, 1980.

and the initial value of $G(a)$ at $a = 0^+$ is zero unless $n = 1$ as noted in the Introduction.

Acknowledgment

The authors would like to thank Profs. M. E. Gurtin and J. W. Hutchinson for valuable comments and discussions. This work was supported by the Air Force Office of Scientific Research.

References

1 Griffith, A. A., "The Phenomena of Rupture and Flow in Solids," *Philosophical Transactions of the Royal Society*, London, Series A, Vol. 221, 1921, pp. 163–198.

2 Khrapkov, A. A., "The First Basic Problem for a Notch at the Apex of an Infinite Wedge," *International Journal of Fracture Mechanics*, Vol. 7, 1971, pp. 373–382.

3 Sih, G. C., "Stress Distribution Near Internal Crack Tips for Longitudinal Shear Problems," ASME JOURNAL OF APPLIED MECHANICS, Vol. 32, 1965, pp. 51–58.

4 Nuismer, R. J., and Sendeckyj, G. P., "On the Changing Order of Singularity at a Crack Tip," ASME JOURNAL OF APPLIED MECHANICS, Vol. 44, 1977, pp. 625–630.

On the Polygon-Circle Paradox

K. Rajaiah[1] **and A. K. Rao**[2]

Introduction

The problem of the polygon-circle paradox in thin plate theory [1] has attracted sustained attention during the last decade [2–7] primarily due to its implications in thin plate and finite-element analyses. There have been some earlier investigations [8–10] too on the subject some of which were considered by Hanuska [11]. Inspite of such continued interest, a satisfactory resolution of the paradox does not seem to have appeared in the literature. The resolution of the paradox, based on an earlier study [12], is presented in this Note.

Statement of the Paradox

Consider a two-dimensional physical phenomenon in a regular polygonal domain with an inscribed circle of radius a and also in a circular domain with the same radius a, both fields being subject to identical physical boundary conditions (Fig. 1). One would expect that, as the number of sides n of the polygon is increased indefinitely ($n \to \infty$), the solution for the polygon should approach that for the circle. Numerical results from different sources referred to in [1] for the flexure of regular polygonal plates under uniform transverse pressure, show diverging trends in relation to this anticipation when the edges are simply supported, although they are all in agreement with the anticipation when the edges are clamped.

Resolution

The paradox shows that, even though the limiting polygon ($n \to \infty$) and the corresponding circular plate under identical loading conditions are governed by the same differential equation, their flexural behavior is identical for conditions of edge fixity, but is entirely different for edge conditions of simple support. Obviously one should shift attention from the complete solution of the problem to the boundary conditions. For simplicity the discussion can be in relation to axisymmetric load distributions.

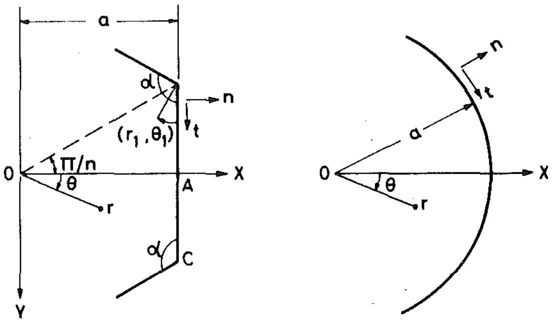

REGULAR POLYGONAL PLATE CIRCULAR PLATE

Fig. 1 Coordinate axes

(*i*) **Clamped Edges.** Consider the conditions along a clamped circular edge. On such an edge, the clamped condition implies $w = 0$, $w_n = 0$, and $w = 0$ itself yields $w_t = 0$ and due to axisymmetry $M_{nt} = 0$. Thus four quantities w, w_n, w_t, and M_{nt} become zero on the edge of a clamped circular plate.

On any edge of a clamped regular polygonal plate, once again the conditions are $w = 0$, $w_n = 0$. Further more $w = 0$ leads to $w_t = 0$ while $w_n = 0$ yields $M_{nt} = 0$. Also from an eigenfunction analysis due to Williams [13], it is clear that there are no singularities at the corners of the polygonal plate. All these conditions hold good however large the number of sides, even in the limit $n \to \infty$.

Comparing the conditions on the clamped circular edge with those of the limiting clamped polygon, it is observed that the same four quantities (w, w_n, w_t, and M_{nt}) vanish on the edge in either case. There are apparently no other physical quantities that may produce any discrepancy. Hence the limiting clamped polygon, as $n \to \infty$, should be and is identical with the corresponding clamped circular plate.

(*ii*) **Simply Supported Edges.** First, consider the circular edge. By definition, $w = 0$ and $M_n = 0$. Due to axisymmetry, $M_{nt} = 0$. But from the exact solution for the circular plate [14] it is clear that $M_t \neq 0$, and therefore $\nabla^2 w \neq 0$.

Next, consider the edges of the polygon. The simple edge support needs $w = 0$ and $M_n = 0$. As a consequence, $w_{tt} = 0$ and $M_t = 0$ and also $\nabla^2 w = 0$. It is also realized that $M_{nt} \neq 0$ anywhere except at the midpoints. These conditions apply for all n. On the other hand, in the corresponding circular plate w_{tt}, M_t, $\nabla^2 w \neq 0$ while $M_{nt} = 0$. Clearly, in this case the limiting polygonal plate solution must be different from the circular plate solution.

Now let us proceed to consider the effect of the corners in the limiting simply supported polygon. From an eigenfunction study [13], one finds that when $n \geq 4$, the corners C are points of moment (M_r, M_θ, $M_{r\theta}$) singularities. The singular part of the deflection function is given by $A_1 r_1^{\pi/\alpha} \sin{(\pi/\alpha)}\, \theta_1$ where $\pi/\alpha = n/(n-2)$ and A_1 is the strength of the singularity. The corresponding second derivative in r (contributing to the moments M_r, M_θ, and $M_{r\theta}$) is found to be

$$A_1 \frac{\pi}{\alpha}\left(\frac{\pi}{\alpha} - 1\right) r_1^{\pi/\alpha - 2} \sin{(\pi/\alpha)}\, \theta_1.$$

It is also observed that, at each corner, the slopes in two different directions are zero and as such each corner behaves like a clamped point. In view of this, the simply supported condition along the straight edges is effectively augmented by periodic corner clamping. Thus the limiting polygon is supported by an alternating system of "infinitesimally short" simple straight supports and stiff point supports. As such the stiffness of the limiting polygon should be between the stiffnesses of the simply supported and clamped circular plates. This is confirmed by the central deflections and edge rotations for the three cases which are shown in Table 1.

In fact it can be readily shown that a circular plate with an elastic

---

[1] Professor, Department of Aeronautical Engineering, Indian Institute of Technology, Powai, Bombay, 400 076 India.

[2] Professor, Department of Aeronautical Engineering, Indian Institute of Science, Bangalore, India.

Manuscript received by ASME Applied Mechanics Division, April, 1980; final revision, June, 1980.

Table 1 Relative stiffness of simply supported circle, simply supported limiting polygon and clamped circle

Load	Type of plate	Central deflection $W_{\max}/(Pa^2/\pi D)$	Edge rotation $-(\partial w/\partial r)_{r=a}$ $(Pa/\pi D)$
Uniform pressure q (Total load $P = q\pi a^2$)	Simply supported circle	$\frac{1}{64}\left(\frac{5+\nu}{1+\nu}\right)$	$\frac{1}{16}\left(\frac{2}{1+\nu}\right)$
	Simply supported limiting polygon	$\frac{1}{64}(3)$	$\frac{1}{16}$
	Clamped circle	$\frac{1}{64}$	0
Central concentrated load P	simply supported circle	$\frac{1}{16}\left(\frac{3+\nu}{1+\nu}\right)$	$\frac{1}{8}\left(\frac{2}{1+\nu}\right)$
	Simply supported limiting polygon	$\frac{1}{16}(2)$	$\frac{1}{8}$
	Clamped circle	$\frac{1}{16}$	0

edge rotational restraint of finite stiffness $K = (1 - \nu)D/a$ would reproduce the behavior of the limiting polygon. For such a circular plate, the edge conditions are found to be $w = \nabla^2 w = 0$.

References

1 Rao, A. K., and Rajaiah, K., "Polygon-Circle Paradox of Simply Supported Thin Plates Under Uniform Pressure," *AIAA Journal*, Vol. 6, No. 1, 1968, pp. 155–156.

2 Rajaiah, K., and Rao, A. K., "Effect of Boundary Condition Description on Convergence of Solution in a Boundary-Value Problem," *Journal of Computational Physics*, Vol. 3, No. 2, 1968, pp. 190–201.

3 Rajaiah, K., and Rao, A. K., "On Limiting Cases in the Flexure of Simply Supported Regular Polygonal Plates," *Proceedings of the Cambridge Philosophical Society*, Vol. 65, 1969, pp. 831–834.

4 Murray, N. W., "The Polygon-Circle Paradox and Convergence in Thin Plate Theory," *Proceedings of the Cambridge Philosophical Society*, Vol. 73, 1973, pp. 279–283.

5 Rossow, M. P., "Efficient C° Finite-Element Solution of Simply Supported Plates of Polygonal Shape," ASME JOURNAL OF APPLIED MECHANICS, Vol. 44, June 1977, pp. 347–349.

6 Rossow, M. P., "Observations on Numerical Modeling of an Obtuse Corner of a Simply Supported Plate," ASME JOURNAL OF APPLIED MECHANICS, Vol. 45, 1978, pp. 689–690.

7 Krauthammer, T., "Accuracy of the Finite-Element Method Near a Curved Boundary," *International Journal of Computers and Structures*, Vol. 10, Dec. 1979, pp. 921–929.

8 Sapondschan, O. M., "Biegung einer frei gelagerten Polygonalplatte," (Russian), *Izv. Akad. Nauk. Arm. SSR.*, T.V. No. 2, 1952, pp. 29–46.

9 Babuska, I., "Die Stabilitat mit Rucksicht auf das Definitions-gebiet und Frage der Formulierung des Plattenproblems," *Aplikace Matematiky*, Vol. 7, No. 6, 1962, pp. 463–470.

10 Babuska, I., "The Theory of Small Changes in the Domain of Existence in the Theory of Partial Differential Equations and Its Applications," chapter in *Differential Equations and Their Applications*, Czechoslovak Academy of Sciences, Academic Press, New York, 1962.

11 Hanuska, A., "Zu den Theorien der Plattenbiegung," *Beton-und Stahlbetongau*, Vol. 9, 1969, pp. 214–217.

12 Rajaiah, K., "Some Studies in Thin Plate Flexure," Doctoral Thesis, Faculty of Engineering, Indian Institute of Science, Bangalore, India, 1972.

13 Williams, M. L., "Surface Stress Singularities Resulting From Various Boundary Conditions in Angular Corners of Plates Under Bending," *Proceedings of the First U.S. National Congress of Applied Mechanics*, 1952, pp. 325–329.

14 Timoshenko, S., and Woinowsky-Krieger, S., *Theory of Plates and Shells*, 2nd ed., McGraw-Hill, New York, 1959.

Vibrations of Free Circular Plates Having Elastic Constraints and Added Mass Distributed Along Edge Segments

A. Leissa[1] and Y. Narita[2]

Introduction

Although numerous references exist which treat the free vibrations of circular plates [1], the vast majority analyze cases having classical boundary conditions (i.e., clamped, simply supported, or free). Several papers can be found (cf., [2, 3]) which deal with elastic constraints uniformly distributed around the edge, and at least one [4] treats the boundary having uniformly distributed, additional mass.

Recently, free-vibration problems for circular plates having rotational and/or translational springs distributed around segments of the edge have been solved [5, 6]. The analytical method utilized there is now applied to a more general problem wherein additional mass also appears along a segment of the edge (see Fig. 1). Numerical results are presented for some interesting problems for which the intensities of the partial springs and masses are varied.

Analysis

The free transverse vibration of a thin, homogeneous plate is governed by the differential equation

$$D\nabla^4 W - \rho\omega^2 W = 0 \tag{1}$$

where, in polar coordinates, $W = W(r, \theta)$. An exact solution to equation (1) for a solid circular plate is given by

$$W(r, \theta) = \sum_{n=0}^{\infty} W_n(kr)\cos n\theta + \sum_{n=1}^{\infty} W_n{}^*(kr)\sin n\theta \tag{2}$$

where

$$W_n(kr) = A_n J_n(kr) + C_n I_n(kr) \tag{3a}$$

$$W_n{}^*(kr) = A_n{}^* J_n(kr) + C_n{}^* I_n(kr) \tag{3b}$$

Consider a free circular plate elastically constrained along parts of the edge as shown in Fig. 1. Translational and rotational springs having stiffnesses K_w and K_ψ, respectively, are attached to typical portions of the edge. An additional strip of mass m and rotary inertia I_G (per unit of length) also acts upon a segment of the boundary. The following boundary conditions are required along typical portions of the edge:

$$V_r(a, \theta) = -(K_w - m\omega^2)W(a, \theta) \tag{4a}$$

$$M_r(a, \theta) = (K_\psi - I_G\omega^2)\frac{\partial W}{\partial r}(a, \theta) \tag{4b}$$

where the edge reaction and bending moment are related to the deflection by

$$V_r(r, \theta) = -D\left[\frac{\partial}{\partial r}(\nabla^2 W) + \frac{1-\nu}{r}\frac{\partial}{\partial r}\left(\frac{1}{r}\frac{\partial^2 W}{\partial \theta^2}\right)\right] \tag{5a}$$

$$M_r(r, \theta) = -D\left[\frac{\partial^2 W}{\partial r^2} + \nu\left(\frac{1}{r}\frac{\partial W}{\partial r} + \frac{1}{r^2}\frac{\partial^2 W}{\partial \theta^2}\right)\right] \tag{5b}$$

and where the coefficients K_w, K_ψ, m, and I_G are, in general, not constants, but functions of θ, either continuous or piecewise contin-

---

[1] Professor of Engineering Mechanics, Ohio State University Columbus, Ohio 43210. Mem. ASME

[2] Lecturer, Computer Center, Hokkaido Institute of Technology Teine, Sapporo 061-24, Japan.

Manuscript received by ASME Applied Mechanics Division, July, 1980.

Table 1 Relative stiffness of simply supported circle, simply supported limiting polygon and clamped circle

Load	Type of plate	Central deflection $W_{\max}/(Pa^2/\pi D)$	Edge rotation $\dfrac{-(\partial/w/\partial r)_{r=a}}{(Pa/\pi D)}$
Uniform pressure q (Total load $P = q\pi a^2$)	Simply supported circle	$\frac{1}{64}\left(\frac{5+\nu}{1+\nu}\right)$	$\frac{1}{16}\left(\frac{2}{1+\nu}\right)$
	Simply supported limiting polygon	$\frac{1}{64}(3)$	$\frac{1}{16}$
	Clamped circle	$\frac{1}{64}$	0
Central concentrated load P	simply supported circle	$\frac{1}{16}\left(\frac{3+\nu}{1+\nu}\right)$	$\frac{1}{8}\left(\frac{2}{1+\nu}\right)$
	Simply supported limiting polygon	$\frac{1}{16}(2)$	$\frac{1}{8}$
	Clamped circle	$\frac{1}{16}$	0

edge rotational restraint of finite stiffness $K = (1 - \nu)D/a$ would reproduce the behavior of the limiting polygon. For such a circular plate, the edge conditions are found to be $w = \nabla^2 w = 0$.

References

1 Rao, A. K., and Rajaiah, K., "Polygon-Circle Paradox of Simply Supported Thin Plates Under Uniform Pressure," *AIAA Journal*, Vol. 6, No. 1, 1968, pp. 155–156.

2 Rajaiah, K., and Rao, A. K., "Effect of Boundary Condition Description on Convergence of Solution in a Boundary-Value Problem," *Journal of Computational Physics*, Vol. 3, No. 2, 1968, pp. 190–201.

3 Rajaiah, K., and Rao, A. K., "On Limiting Cases in the Flexure of Simply Supported Regular Polygonal Plates," *Proceedings of the Cambridge Philosophical Society*, Vol. 65, 1969, pp. 831–834.

4 Murray, N. W., "The Polygon-Circle Paradox and Convergence in Thin Plate Theory," *Proceedings of the Cambridge Philosophical Society*, Vol. 73, 1973, pp. 279–283.

5 Rossow, M. P., "Efficient C° Finite-Element Solution of Simply Supported Plates of Polygonal Shape," ASME JOURNAL OF APPLIED MECHANICS, Vol. 44, June 1977, pp. 347–349.

6 Rossow, M. P., "Observations on Numerical Modeling of an Obtuse Corner of a Simply Supported Plate," ASME JOURNAL OF APPLIED MECHANICS, Vol. 45, 1978, pp. 689–690.

7 Krauthammer, T., "Accuracy of the Finite-Element Method Near a Curved Boundary," *International Journal of Computers and Structures*, Vol. 10, Dec. 1979, pp. 921–929.

8 Sapondschan, O. M., "Biegung einer frei gelagerten Polygonalplatte," (Russian), *Izv. Akad. Nauk. Arm. SSR.*, T.V. No. 2, 1952, pp. 29–46.

9 Babuska, I., "Die Stabilitat mit Rucksicht auf das Definitions-gebiet und Frage der Formulierung des Plattenproblems," *Aplikace Matematiky*, Vol. 7, No. 6, 1962, pp. 463–470.

10 Babuska, I., "The Theory of Small Changes in the Domain of Existence in the Theory of Partial Differential Equations and Its Applications," chapter in *Differential Equations and Their Applications*, Czechoslovak Academy of Sciences, Academic Press, New York, 1962.

11 Hanuska, A., "Zu den Theorien der Plattenbiegung," *Beton-und Stahlbetongau*, Vol. 9, 1969, pp. 214–217.

12 Rajaiah, K., "Some Studies in Thin Plate Flexure," Doctoral Thesis, Faculty of Engineering, Indian Institute of Science, Bangalore, India, 1972.

13 Williams, M. L., "Surface Stress Singularities Resulting From Various Boundary Conditions in Angular Corners of Plates Under Bending," *Proceedings of the First U.S. National Congress of Applied Mechanics*, 1952, pp. 325–329.

14 Timoshenko, S., and Woinowsky-Krieger, S., *Theory of Plates and Shells*, 2nd ed., McGraw-Hill, New York, 1959.

Vibrations of Free Circular Plates Having Elastic Constraints and Added Mass Distributed Along Edge Segments

A. Leissa[1] and Y. Narita[2]

Introduction

Although numerous references exist which treat the free vibrations of circular plates [1], the vast majority analyze cases having classical boundary conditions (i.e., clamped, simply supported, or free). Several papers can be found (cf., [2, 3]) which deal with elastic constraints uniformly distributed around the edge, and at least one [4] treats the boundary having uniformly distributed, additional mass.

Recently, free-vibration problems for circular plates having rotational and/or translational springs distributed around segments of the edge have been solved [5, 6]. The analytical method utilized there is now applied to a more general problem wherein additional mass also appears along a segment of the edge (see Fig. 1). Numerical results are presented for some interesting problems for which the intensities of the partial springs and masses are varied.

Analysis

The free transverse vibration of a thin, homogeneous plate is governed by the differential equation

$$D\nabla^4 W - \rho\omega^2 W = 0 \tag{1}$$

where, in polar coordinates, $W = W(r, \theta)$. An exact solution to equation (1) for a solid circular plate is given by

$$W(r, \theta) = \sum_{n=0}^{\infty} W_n(kr)\cos n\theta + \sum_{n=1}^{\infty} W_n{}^*(kr)\sin n\theta \tag{2}$$

where

$$W_n(kr) = A_n J_n(kr) + C_n I_n(kr) \tag{3a}$$

$$W_n{}^*(kr) = A_n{}^* J_n(kr) + C_n{}^* I_n(kr) \tag{3b}$$

Consider a free circular plate elastically constrained along parts of the edge as shown in Fig. 1. Translational and rotational springs having stiffnesses K_w and K_ψ, respectively, are attached to typical portions of the edge. An additional strip of mass m and rotary inertia I_G (per unit of length) also acts upon a segment of the boundary. The following boundary conditions are required along typical portions of the edge:

$$V_r(a, \theta) = -(K_w - m\omega^2)W(a, \theta) \tag{4a}$$

$$M_r(a, \theta) = (K_\psi - I_G\omega^2)\frac{\partial W}{\partial r}(a, \theta) \tag{4b}$$

where the edge reaction and bending moment are related to the deflection by

$$V_r(r, \theta) = -D\left[\frac{\partial}{\partial r}(\nabla^2 W) + \frac{1-\nu}{r}\frac{\partial}{\partial r}\left(\frac{1}{r}\frac{\partial^2 W}{\partial \theta^2}\right)\right] \tag{5a}$$

$$M_r(r, \theta) = -D\left[\frac{\partial^2 W}{\partial r^2} + \nu\left(\frac{1}{r}\frac{\partial W}{\partial r} + \frac{1}{r^2}\frac{\partial^2 W}{\partial \theta^2}\right)\right] \tag{5b}$$

and where the coefficients K_w, K_ψ, m, and I_G are, in general, not constants, but functions of θ, either continuous or piecewise contin-

---

[1] Professor of Engineering Mechanics, Ohio State University Columbus, Ohio 43210. Mem. ASME

[2] Lecturer, Computer Center, Hokkaido Institute of Technology Teine, Sapporo 061-24, Japan.

Manuscript received by ASME Applied Mechanics Division, July, 1980.

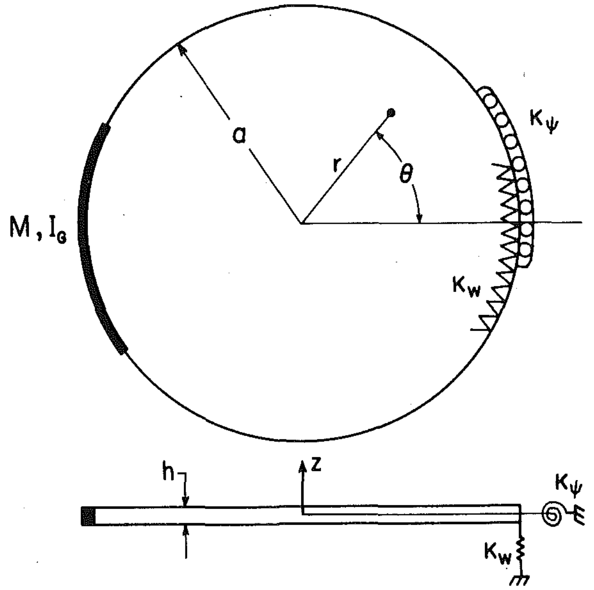

Fig. 1 Circular plate having elastic constraints and added mass along boundary segments

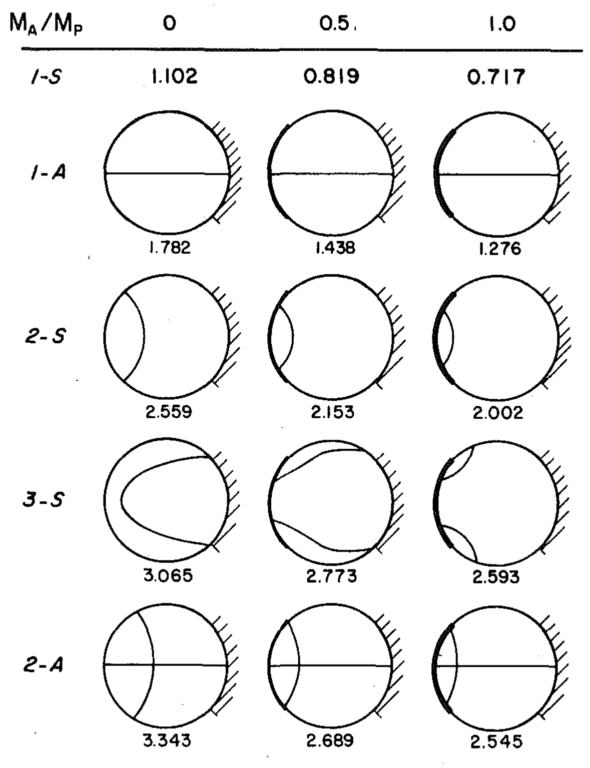

Fig. 2 Frequency parameters $\lambda = (\omega a^2\sqrt{\rho/D})^{1/2}$ and nodal patterns for clamped-free circular plates having added partial strip mass.

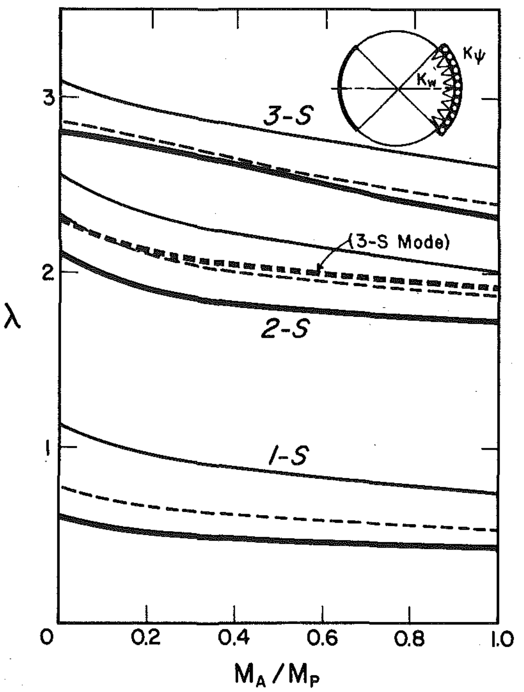

(a) Symmetric Modes

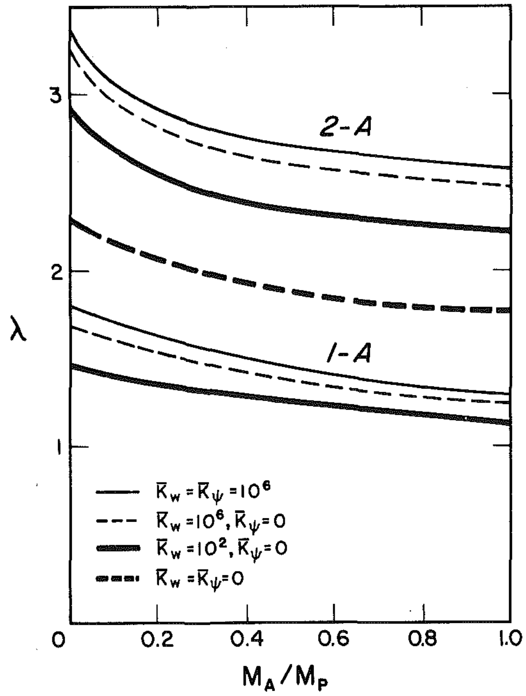

(b) Anti-symmetric Modes

Fig. 3 Frequency parameter $\lambda = (\omega a^2\sqrt{\rho/D})^{1/2}$ versus ratio of added mass for four cases of elastic edge constraint

uous, as shown. The coefficients can be expanded into Fourier series; that is,

$$K_w(\theta) = \sum_{i=0}^{\infty} K_m \cos i\theta + \sum_{i=1}^{\infty} K_m{}^* \sin i\theta \tag{6a}$$

$$K_\psi(\theta) = \sum_{i=0}^{\infty} L_m \cos i\theta + \sum_{i=1}^{\infty} L_m{}^* \sin i\theta \tag{6b}$$

$$m(\theta) = \sum_{i=0}^{\infty} m_i \cos i\theta + \sum_{i=1}^{\infty} m_i{}^* \sin i\theta \tag{6c}$$

$$I_G(\theta) = \sum_{i=0}^{\infty} I_{G_i} \cos i\theta + \sum_{i=1}^{\infty} I_{G_i}{}^* \sin i\theta \tag{6d}$$

where the Fourier coefficients are determined in the usual manner.

Substituting equations (2), (3), (5), and (6) into (4), and utilizing trigonometric identities of the type

$$\sin i\theta \cos n\theta = \frac{1}{2}[\sin(i+n)\theta + \sin(i-n)\theta] \tag{7}$$

allows the products of two infinite sums on the right-hand sides of equations (4) to be replaced by single infinite sums, yielding an infinite characteristic determinant for the eigenvalues (or nondimensional frequency parameters) of free vibration (cf., [5, 6]).

Numerical Results

Fig. 2 shows the lowest five frequency parameters $\lambda = (\omega a^2\sqrt{\rho/D})^{1/2}$ and the corresponding nodal patterns of circular plates elastically constrained along $-\pi/4 < \theta < \pi/4$ and having uniformly distributed mass along $3\pi/4 < \theta < 5\pi/4$. The nodal patterns are either symmetric (S) or antisymmetric (A) with respect to the symmetry diameter. The fundamental (i.e., lowest frequency) mode has no interior node lines. The constrained part of the plate can be regarded as effectively clamped due to the large stiffness $\overline{K}_w = \overline{K}_\psi = 10^6$ ($\overline{K}_w = a^3K_w/D$, $\overline{K}_\psi = aK_\psi/D$) [5, 6]. The attached mass is increased with the ratio of $M_A/M_P = 0, 0.5, 1$ (M_A, total mass of the added mass; M_p, mass of the plate by itself). In the present calculations, Poisson's ratio is taken as $\nu = 0.33$ and the rotary inertia of the added mass is zero. A 60th-order determinant is used to yield the frequencies which can be considered as accurate within three significant figures, as found in previous convergence studies [6].

Fig. 3 shows the variation of the frequency parameter in the same problem for four different degrees of elastic constraint along the boundary segment $-\pi/4 < \theta < \pi/4$, ranging from fully free to fully clamped. Symmetric and antisymmetric modes are presented in Figs. 3(a) and (b), respectively. As the mass ratio M_A/M_P is increased, the frequencies decrease monotonically, as expected. But the rate of change depends upon the mode of vibration and, in one case, the curves (3-S and 2-A) cross each other. For $\overline{K}_w = \overline{K}_\psi = 0$, the 1-$S$, 1-$A$, and 2-$S$ modes correspond to rigid body motions of translation and rotation; i.e., $\lambda = 0$.

References

1 Leissa, A. W., *Vibration of Plates*, NASA SP-160, U.S.Government Printing Office, 1969.

2 Kantham, C. L., "Bending and Vibration of Elastically Restrained Circular Plates," *Journal of The Franklin Institute*, Vol. 265, No. 6, 1958, pp. 483–491.

3 Laura, P. A. A., Paloto, J. C., and Santos, R. D , "A Note on the Vibration and Stability of a Circular Plate Elastically Restrained Against Rotation," *Journal of Sound and Vibration*, Vol. 41, No. 2, 1975, pp. 177–180.

4 Takahashi, S., "The Vibration of a Circular Plate With Weights or a Bar on Its Outer Boundary," *Bulletin JSME*, Vol. 10, No. 40, 1967, pp. 463–471.

5 Narita, Y., and Leissa, A. W., "Transverse Vibration of Simply Supported Circular Plates Having Partial Elastic Constraints," *Journal of Sound and Vibration*, Vol. 70, No. 1, 1980, pp. 103–116.

6 Narita, Y., and Leissa, A. W., "Flexural Vibrations of Free Circular Plates Elastically Constrained Along Parts of the Edges," *International Journal of Solids and Structures*, Vol. 17, No. 1, 1981, pp. 83–92.

Stabilization of an Unstable Linear System by Parametric White Noise

J. E. Prussing[1]

In this Note a simple illustrative example demonstrates that an unstable deterministic system can be stabilized by parametric white noise excitation. Nevelson and Khas'minskii [1] and Nakamizo and Sawaragi [2] show that it is impossible for a linear system excited by parametric white noise to be stable if the deterministic system is unstable. However, these results are based on mathematical white noise rather than physical white noise which is the limiting case of a stationary stochastic process for which the correlation time tends to zero. For physical white noise the correlation between the noise and the system response at the same instant of time must be accounted for.

In the analysis which follows it is shown using the Wong and Zakai correction [3] which is a special case of the stochastic averaging procedure of Stratonovich [4] and Khas'minskii [5] that parametric physical white noise can stabilize an unstable deterministic system. This fact was first reported by Mitchell and Kozin [6] in Example 4 of that reference and verified by simulation. The motivation for finding a simple illustrative example stems from recent analyses of helicopter rotor blade aeroelastic stability in turbulent flow [7–9] for which parametric white noise in certain cases stabilizes the system [7].

Consider a linear autonomous second-order system with parametric random excitation:

$$\ddot{X}(t) + [c + c_\xi\xi(t)]\dot{X}(t) + [k + k_\xi\xi(t)]X(t) = 0 \tag{1}$$

The variable $\xi(t)$ is a scalar physical white noise process having zero mean value. It is convenient to write (1) in terms of the state vector $\mathbf{X}^T = (X\dot{X})$ as

$$\dot{\mathbf{X}}(t) = (A + \xi(t)P)\mathbf{X}(t) \tag{2}$$

where A and P are constant matrices containing the deterministic coefficients c, k, and the parametric noise coefficients c_ξ, k_ξ, respectively. In the stochastic averaging procedure the state $\mathbf{X}(t)$ is approximated by a Markov process $\mathbf{x}(t)$ which is continuous with probability one and satisfies an associated Itô equation. This approximation is valid because the relaxation time of the system (2) is large compared to the correlation time of the noise, which is zero for white noise.

To investigate first moment (mean) stability the equation for the vector of first moments $\overline{\mathbf{M}}(t) = E[\mathbf{x}(t)]$ is calculated to be

$$\dot{\overline{\mathbf{M}}}(t) = (A + \pi\Phi_\xi P^2)\overline{\mathbf{M}}(t) \triangleq \overline{B}\overline{\mathbf{M}}(t) \tag{3}$$

using the Wong and Zakai correction summarized in Appendix A of [8]. The variable Φ_ξ is the (constant) spectral density of the white noise process: $E[\xi(t)\xi(t+\tau)] = 2\pi\Phi_\xi\delta(\tau)$. The matrix $\overline{B}$ for the system (1) is given by

$$\overline{B} = \begin{bmatrix} 0 & 1 \\ \pi\Phi_\xi c_\xi k_\xi - k & \pi\Phi_\xi {c_\xi}^2 - c \end{bmatrix} \tag{4}$$

and the Routh-Hurwitz conditions for first moment asymptotic stability are

$$c - \pi\Phi_\xi {c_\xi}^2 > 0 \tag{5}$$

$$k - \pi\Phi_\xi c_\xi k_\xi > 0 \tag{6}$$

The deterministic system is asymptotically unstable if $c < 0$ or $k < 0$. From the stability criteria (5) and (6) it is evident that since $\Phi_\xi \geq 0$ the only unstable deterministic system which can be stabilized by white noise has $c > 0$ and $k < 0$. In addition (6) implies that $c_\xi k_\xi < 0$ for the noise to be stabilizing and (5) implies that a sufficiently high noise intensity will destabilize the system. Under these conditions the system is first moment stable for the range of noise intensity:

$$\frac{k}{c_\xi k_\xi} < \pi\Phi_\xi < \frac{c}{{c_\xi}^2} \tag{7}$$

To investigate second moment (mean square) stability the equation for the vector of second moments $\overline{\overline{\mathbf{M}}}(t)$ having components $E[{x_1}^2]$, $E[x_1x_2]$, and $E[{x_2}^2]$ is calculated to be

$$\dot{\overline{\overline{\mathbf{M}}}}(t) = \overline{\overline{B}}\,\overline{\overline{\mathbf{M}}}(t) \tag{8}$$

where

$$\overline{\overline{B}} = \begin{bmatrix} 0 & 2 & 0 \\ \pi\Phi_\xi c_\xi k_\xi - k & \pi\Phi_\xi {c_\xi}^2 - c & 1 \\ 2\pi\Phi_\xi {k_\xi}^2 & 2(3\pi\Phi_\xi c_\xi k_\xi - k) & 2(2\pi\Phi_\xi {c_\xi}^2 - c) \end{bmatrix} \tag{9}$$

---

[1] Associate Professor, Department of Aeronautical and Astronautical Engineering, University of Illinois, Urbana, Ill. 61801.

Manuscript received by ASME Applied Mechanics Division, November, 1979; final revision, August, 1980.

allows the products of two infinite sums on the right-hand sides of equations (4) to be replaced by single infinite sums, yielding an infinite characteristic determinant for the eigenvalues (or nondimensional frequency parameters) of free vibration (cf., [5, 6]).

Numerical Results

Fig. 2 shows the lowest five frequency parameters $\lambda = (\omega a^2\sqrt{\rho/D})^{1/2}$ and the corresponding nodal patterns of circular plates elastically constrained along $-\pi/4 < \theta < \pi/4$ and having uniformly distributed mass along $3\pi/4 < \theta < 5\pi/4$. The nodal patterns are either symmetric (S) or antisymmetric (A) with respect to the symmetry diameter. The fundamental (i.e., lowest frequency) mode has no interior node lines. The constrained part of the plate can be regarded as effectively clamped due to the large stiffness $\overline{K}_w = \overline{K}_\psi = 10^6$ ($\overline{K}_w = a^3K_w/D, \overline{K}_\psi = aK_\psi/D$) [5, 6]. The attached mass is increased with the ratio of $M_A/M_P = 0, 0.5, 1$ (M_A, total mass of the added mass; M_p, mass of the plate by itself). In the present calculations, Poisson's ratio is taken as $\nu = 0.33$ and the rotary inertia of the added mass is zero. A 60th-order determinant is used to yield the frequencies which can be considered as accurate within three significant figures, as found in previous convergence studies [6].

Fig. 3 shows the variation of the frequency parameter in the same problem for four different degrees of elastic constraint along the boundary segment $-\pi/4 < \theta < \pi/4$, ranging from fully free to fully clamped. Symmetric and antisymmetric modes are presented in Figs. 3(a) and (b), respectively. As the mass ratio M_A/M_P is increased, the frequencies decrease monotonically, as expected. But the rate of change depends upon the mode of vibration and, in one case, the curves (3-S and 2-A) cross each other. For $\overline{K}_w = \overline{K}_\psi = 0$, the 1-$S$, 1-$A$, and 2-$S$ modes correspond to rigid body motions of translation and rotation; i.e., $\lambda = 0$.

References

1 Leissa, A. W., *Vibration of Plates,* NASA SP-160, U.S.Government Printing Office, 1969.

2 Kantham, C. L., "Bending and Vibration of Elastically Restrained Circular Plates," *Journal of The Franklin Institute,* Vol. 265, No. 6, 1958, pp. 483–491.

3 Laura, P. A. A., Paloto, J. C., and Santos, R. D , "A Note on the Vibration and Stability of a Circular Plate Elastically Restrained Against Rotation," *Journal of Sound and Vibration,* Vol. 41, No. 2, 1975, pp. 177–180.

4 Takahashi, S., "The Vibration of a Circular Plate With Weights or a Bar on Its Outer Boundary," *Bulletin JSME,* Vol. 10, No. 40, 1967, pp. 463–471.

5 Narita, Y., and Leissa, A. W., "Transverse Vibration of Simply Supported Circular Plates Having Partial Elastic Constraints," *Journal of Sound and Vibration,* Vol. 70, No. 1, 1980, pp. 103–116.

6 Narita, Y., and Leissa, A. W., "Flexural Vibrations of Free Circular Plates Elastically Constrained Along Parts of the Edges," *International Journal of Solids and Structures,* Vol. 17, No. 1, 1981, pp. 83–92.

Stabilization of an Unstable Linear System by Parametric White Noise

J. E. Prussing[1]

In this Note a simple illustrative example demonstrates that an unstable deterministic system can be stabilized by parametric white noise excitation. Nevelson and Khas'minskii [1] and Nakamizo and Sawaragi [2] show that it is impossible for a linear system excited by parametric white noise to be stable if the deterministic system is unstable. However, these results are based on mathematical white noise rather than physical white noise which is the limiting case of a stationary stochastic process for which the correlation time tends to zero. For physical white noise the correlation between the noise and the system response at the same instant of time must be accounted for.

In the analysis which follows it is shown using the Wong and Zakai correction [3] which is a special case of the stochastic averaging procedure of Stratonovich [4] and Khas'minskii [5] that parametric physical white noise can stabilize an unstable deterministic system. This fact was first reported by Mitchell and Kozin [6] in Example 4 of that reference and verified by simulation. The motivation for finding a simple illustrative example stems from recent analyses of helicopter rotor blade aeroelastic stability in turbulent flow [7–9] for which parametric white noise in certain cases stabilizes the system [7].

Consider a linear autonomous second-order system with parametric random excitation:

$$\ddot{X}(t) + [c + c_\xi\xi(t)]\dot{X}(t) + [k + k_\xi\xi(t)]X(t) = 0 \tag{1}$$

The variable $\xi(t)$ is a scalar physical white noise process having zero mean value. It is convenient to write (1) in terms of the state vector $\mathbf{X}^T = (X\dot{X})$ as

$$\dot{\mathbf{X}}(t) = (A + \xi(t)P)\mathbf{X}(t) \tag{2}$$

where A and P are constant matrices containing the deterministic coefficients c, k, and the parametric noise coefficients c_ξ, k_ξ, respectively. In the stochastic averaging procedure the state $\mathbf{X}(t)$ is approximated by a Markov process $\mathbf{x}(t)$ which is continuous with probability one and satisfies an associated Itô equation. This approximation is valid because the relaxation time of the system (2) is large compared to the correlation time of the noise, which is zero for white noise.

To investigate first moment (mean) stability the equation for the vector of first moments $\overline{\mathbf{M}}(t) = E[\mathbf{x}(t)]$ is calculated to be

$$\dot{\overline{\mathbf{M}}}(t) = (A + \pi\Phi_\xi P^2)\overline{\mathbf{M}}(t) \triangleq \overline{B}\overline{\mathbf{M}}(t) \tag{3}$$

using the Wong and Zakai correction summarized in Appendix A of [8]. The variable Φ_ξ is the (constant) spectral density of the white noise process: $E[\xi(t)\xi(t + \tau)] = 2\pi\Phi_\xi\delta(\tau)$. The matrix $\overline{B}$ for the system (1) is given by

$$\overline{B} = \begin{bmatrix} 0 & 1 \\ \pi\Phi_\xi c_\xi k_\xi - k & \pi\Phi_\xi c_\xi^2 - c \end{bmatrix} \tag{4}$$

and the Routh-Hurwitz conditions for first moment asymptotic stability are

$$c - \pi\Phi_\xi c_\xi^2 > 0 \tag{5}$$

$$k - \pi\Phi_\xi c_\xi k_\xi > 0 \tag{6}$$

The deterministic system is asymptotically unstable if $c < 0$ or $k < 0$. From the stability criteria (5) and (6) it is evident that since $\Phi_\xi \geq 0$ the only unstable deterministic system which can be stabilized by white noise has $c > 0$ and $k < 0$. In addition (6) implies that $c_\xi k_\xi < 0$ for the noise to be stabilizing and (5) implies that a sufficiently high noise intensity will destabilize the system. Under these conditions the system is first moment stable for the range of noise intensity:

$$\frac{k}{c_\xi k_\xi} < \pi\Phi_\xi < \frac{c}{c_\xi^2} \tag{7}$$

To investigate second moment (mean square) stability the equation for the vector of second moments $\overline{\overline{\mathbf{M}}}(t)$ having components $E[x_1^2]$, $E[x_1x_2]$, and $E[x_2^2]$ is calculated to be

$$\dot{\overline{\overline{\mathbf{M}}}}(t) = \overline{\overline{B}}\overline{\overline{\mathbf{M}}}(t) \tag{8}$$

where

$$\overline{\overline{B}} = \begin{bmatrix} 0 & 2 & 0 \\ \pi\Phi_\xi c_\xi k_\xi - k & \pi\Phi_\xi c_\xi^2 - c & 1 \\ 2\pi\Phi_\xi k_\xi^2 & 2(3\pi\Phi_\xi c_\xi k_\xi - k) & 2(2\pi\Phi_\xi c_\xi^2 - c) \end{bmatrix} \tag{9}$$

---

[1] Associate Professor, Department of Aeronautical and Astronautical Engineering, University of Illinois, Urbana, Ill. 61801.

Manuscript received by ASME Applied Mechanics Division, November, 1979; final revision, August, 1980.

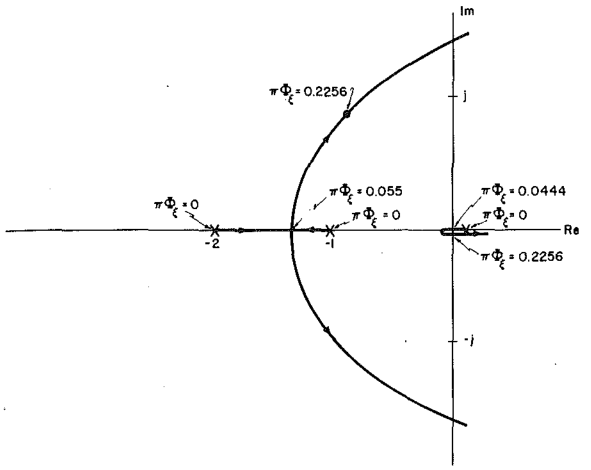

Fig. 1 Locus of eigenvalues of the second moment stability matrix $\bar{B}$

The Routh-Hurwitz conditions for second moment asymptotic stability are

$$3c - 5\pi\Phi_\xi c_\xi^2 > 0 \tag{10}$$

$$2(\pi\Phi_\xi)^2 c_\xi^3 k_\xi - \pi\Phi_\xi(k^2_\xi + 2kc^2_\xi + cc_\xi k_\xi) + kc > 0 \tag{11}$$

$$-10(\pi\Phi_\xi)^3 c_\xi^6 + (\pi\Phi_\xi)^2 c_\xi^3(21cc_\xi + 16k_\xi) - 2\pi\Phi_\xi[c_\xi^2(7c^2 + 3k) + k_\xi(5cc_\xi - k_\xi)] + c(3c^2 + 4k) > 0 \tag{12}$$

As an illustrative numerical example of an unstable deterministic system which is stabilized by parametric white noise, consider the case $c = c_\xi = 1$, $k = -0.01$, and $k_\xi = -0.5$. The first moment stability condition (7) is satisfied for

$$0.02 < \pi\Phi_\xi < 1.0 \tag{13}$$

and the second moment stability conditions (10)–(12) are satisfied for the smaller range:

$$0.0444 < \pi\Phi_\xi < 0.2256 \tag{14}$$

where condition (11) determines both the upper and lower bounds in (14). The locus of the eigenvalues of the second moment coefficient matrix $\bar{B}$ is shown in Fig. 1 with the value of $\pi\Phi_\xi$ as a parameter.

A physical example of a system (1) which has a stochastic spring constant with a negative deterministic value ($k < 0$) is an inverted pendulum with random vertical acceleration of the support. This has been analyzed by several authors including Mitchell [10] for deterministic damping. For the case of stochastic damping it is difficult to cite a realistic mechanical damping model which provides the necessary relationship between random damping and support motion to provide stability ($c_\xi k_\xi < 0$). A realistic physical application is in aeroelastic problems for which stochastic damping is due to aerodynamic turbulence [7–9].

Acknowledgment

This Note is based on work supported by the U.S. Army Research Office under Grant DAAG 29-78-G-0039 directed by Prof. Y. K. Lin.

References

1 Nevelson, M. B., and Khas'minskii, R. Z., "Stability of Stochastic Systems," *Problems of Information Transmission,* Vol. 2, No. 3, 1966., pp. 61–74.

2 Nakamizo, T., and Sawaragi, Y., "Analytical Study on *n*th-Order Linear System With Stochastic Coefficients," *Lecture Notes in Mathematics 294, Stability of Stochastic Dynamical Systems,* Springer-Verlag, Berlin, 1972, pp. 173–185.

3 Wong, E., and Zakai, M. "On the Relation Between Ordinary and Stochastic Equations," *International Journal of Engineering Science,* Vol. 3, No. 2, 1965, pp. 213–229.

4 Stratonovich, R. L., *Topics in the Theory of Random Noise,* Vol. II, Gordon and Breach, N.Y., 1967.

5 Khas'minskii, R. Z., "A Limit Theorem for the Solutions of Differential Equations With Random Right-Hand Sides," *Theory of Probability and Its Applications,* Vol. 11, 1966, pp. 390–401.

6 Mitchell, R., and Kozin, F., "Sample Stability of Second-Order Linear Differential Equations With Wide Band Noise Coefficients," *SIAM Journal of Applied Mathematics,* Vol. 27, No. 4, 1974, pp. 571–605.

7 Prussing, J. E., and Lin, Y. K., "Rotor Blade Flap-Lag Stability in Turbulent Flows," to be published.

8 Lin, Y. K., Fujimori, Y., and Ariaratnam, S. T., "Rotor Blade Stability in Turbulent Flows—Part I," *AIAA Journal,* Vol. 17, No. 6, 1979, pp. 545–552.

9 Fujimori, Y., Lin, Y. K., and Ariaratnam, S. T., "Rotor Blade Stability in Turbulent Flows—Part II," *AIAA Journal,* Vol. 17, No. 7, 1979, pp. 673–678.

10 Mitchell, R., "Stability of the Inverted Pendulum Subjected to Almost Periodic and Stochastic Base Motion—An Application of the Method of Averaging," *International Journal of Nonlinear Mechanics,* Vol. 7, 1972, pp. 101–123.

Folding of Elastica-Similarity Solutions

C.-Y. Wang[1]

Introduction

The folding of thin elastic sheets (paper, sheet metal, cloth, etc.) is extremely important in manufacturing processes. If the thickness of the sheet is small compared to its minimum radius of curvature, the elastica equations may be used [1]

$$EI\frac{d\theta}{ds'} = M + Fx' + Gy' \tag{1}$$

$$\frac{dx'}{ds'} = \cos\theta, \frac{dy'}{ds'} = \sin\theta \tag{2}$$

Here EI is the flexural rigidity, θ is the local angle of inclination, s' is the arc length, x',y' are Cartesian coordinates, M,F,G are moment, vertical force, horizontal force at $s' = 0$, respectively. Fig. 1 shows three different folding processes. In Case 1 the elastica is compressed by two parallel approaching plates. In Case 2 the elastica is folded by two symmetric rollers moving to the right. In Case 3 it is folded between a moving roller and a flat plane. The boundary conditions are

Case 1

$$s' = 0, \theta = \pi/2, x' = y' = 0 \tag{3}$$

$$s' = L, \theta = \pi, \frac{d\theta}{ds'} = 0 \tag{4}$$

$$G = 0 \tag{5}$$

Case 2

$$s' = 0, \theta = \pi/2, x' = y' = 0 \tag{6}$$

$$s' = L, \theta = \pi, y' = 0 \tag{7}$$

$$G = 0 \tag{8}$$

Case 3

$$s' = 0, \theta = \frac{d\theta}{ds'} = x' = y' = 0 \tag{9}$$

---

[1] Professor, Department of Mathematics, Michigan State University, East Lansing, Mich. 48824.

Manuscript received by ASME Applied Mechanics Division, August, 1980; final revision, October, 1980.

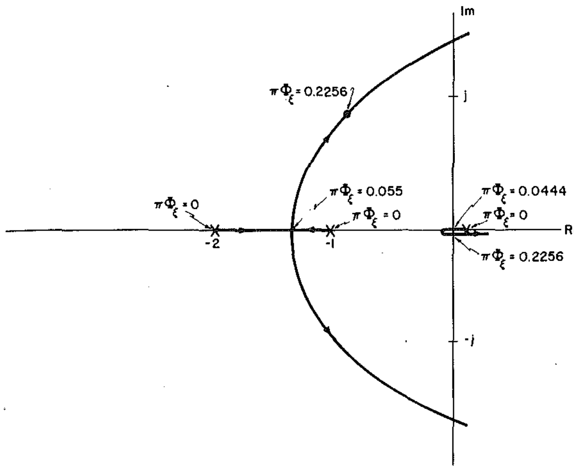

Fig. 1 Locus of eigenvalues of the second moment stability matrix $\overline{B}$

The Routh-Hurwitz conditions for second moment asymptotic stability are

$$3c - 5\pi\Phi_\xi c_\xi{}^2 > 0 \tag{10}$$

$$2(\pi\Phi_\xi)^2 c_\xi{}^3 k_\xi - \pi\Phi_\xi(k^2{}_\xi + 2kc^2{}_\xi + cc_\xi k_\xi) + kc > 0 \tag{11}$$

$$\begin{aligned} -10(\pi\Phi_\xi)^3 c_\xi{}^6 + (\pi\Phi_\xi)^2 c_\xi{}^3(21cc_\xi + 16k_\xi) \\ - 2\pi\Phi_\xi[c_\xi{}^2(7c^2 + 3k) + k_\xi(5cc_\xi - k_\xi)] \\ + c(3c^2 + 4k) > 0 \end{aligned} \tag{12}$$

As an illustrative numerical example of an unstable deterministic system which is stabilized by parametric white noise, consider the case $c = c_\xi = 1$, $k = -0.01$, and $k_\xi = -0.5$. The first moment stability condition (7) is satisfied for

$$0.02 < \pi\Phi_\xi < 1.0 \tag{13}$$

and the second moment stability conditions (10)–(12) are satisfied for the smaller range:

$$0.0444 < \pi\Phi_\xi < 0.2256 \tag{14}$$

where condition (11) determines both the upper and lower bounds in (14). The locus of the eigenvalues of the second moment coefficient matrix $\overline{B}$ is shown in Fig. 1 with the value of $\pi\Phi_\xi$ as a parameter.

A physical example of a system (1) which has a stochastic spring constant with a negative deterministic value ($k < 0$) is an inverted pendulum with random vertical acceleration of the support. This has been analyzed by several authors including Mitchell [10] for deterministic damping. For the case of stochastic damping it is difficult to cite a realistic mechanical damping model which provides the necessary relationship between random damping and support motion to provide stability ($c_\xi k_\xi < 0$). A realistic physical application is in aeroelastic problems for which stochastic damping is due to aerodynamic turbulence [7–9].

Acknowledgment

This Note is based on work supported by the U.S. Army Research Office under Grant DAAG 29-78-G-0039 directed by Prof. Y. K. Lin.

References

1 Nevelson, M. B., and Khas'minskii, R. Z., "Stability of Stochastic Systems," *Problems of Information Transmission,* Vol. 2, No. 3, 1966., pp. 61–74.

2 Nakamizo, T., and Sawaragi, Y., "Analytical Study on *n*th-Order Linear System With Stochastic Coefficients," *Lecture Notes in Mathematics 294, Stability of Stochastic Dynamical Systems,* Springer-Verlag, Berlin, 1972, pp. 173–185.

3 Wong, E., and Zakai, M. "On the Relation Between Ordinary and Stochastic Equations," *International Journal of Engineering Science,* Vol. 3, No. 2, 1965, pp. 213–229.

4 Stratonovich, R. L., *Topics in the Theory of Random Noise,* Vol. II, Gordon and Breach, N.Y., 1967.

5 Khas'minskii, R. Z., "A Limit Theorem for the Solutions of Differential Equations With Random Right-Hand Sides," *Theory of Probability and Its Applications,* Vol. 11, 1966, pp. 390–401.

6 Mitchell, R., and Kozin, F., "Sample Stability of Second-Order Linear Differential Equations With Wide Band Noise Coefficients," *SIAM Journal of Applied Mathematics,* Vol. 27, No. 4, 1974, pp. 571–605.

7 Prussing, J. E., and Lin, Y. K., "Rotor Blade Flap-Lag Stability in Turbulent Flows," to be published.

8 Lin, Y. K., Fujimori, Y., and Ariaratnam, S. T., "Rotor Blade Stability in Turbulent Flows—Part I," *AIAA Journal,* Vol. 17, No. 6, 1979, pp. 545–552.

9 Fujimori, Y., Lin, Y. K., and Ariaratnam, S. T., "Rotor Blade Stability in Turbulent Flows—Part II," *AIAA Journal,* Vol. 17, No. 7, 1979, pp. 673–678.

10 Mitchell, R., "Stability of the Inverted Pendulum Subjected to Almost Periodic and Stochastic Base Motion—An Application of the Method of Averaging," *International Journal of Nonlinear Mechanics,* Vol. 7, 1972, pp. 101–123.

Folding of Elastica-Similarity Solutions

C.-Y. Wang[1]

Introduction

The folding of thin elastic sheets (paper, sheet metal, cloth, etc.) is extremely important in manufacturing processes. If the thickness of the sheet is small compared to its minimum radius of curvature, the elastica equations may be used [1]

$$EI\frac{d\theta}{ds'} = M + Fx' + Gy' \tag{1}$$

$$\frac{dx'}{ds'} = \cos\theta,\ \frac{dy'}{ds'} = \sin\theta \tag{2}$$

Here EI is the flexural rigidity, θ is the local angle of inclination, s' is the arc length, x', y' are Cartesian coordinates, M, F, G are moment, vertical force, horizontal force at $s' = 0$, respectively. Fig. 1 shows three different folding processes. In Case 1 the elastica is compressed by two parallel approaching plates. In Case 2 the elastica is folded by two symmetric rollers moving to the right. In Case 3 it is folded between a moving roller and a flat plane. The boundary conditions are

Case 1

$$s' = 0,\ \theta = \pi/2,\ x' = y' = 0 \tag{3}$$

$$s' = L,\ \theta = \pi,\ \frac{d\theta}{ds'} = 0 \tag{4}$$

$$G = 0 \tag{5}$$

Case 2

$$s' = 0,\ \theta = \pi/2,\ x' = y' = 0 \tag{6}$$

$$s' = L,\ \theta = \pi,\ y' = 0 \tag{7}$$

$$G = 0 \tag{8}$$

Case 3

$$s' = 0,\ \theta = \frac{d\theta}{ds'} = x' = y' = 0 \tag{9}$$

---

[1] Professor, Department of Mathematics, Michigan State University, East Lansing, Mich. 48824.

Manuscript received by ASME Applied Mechanics Division, August, 1980; final revision, October, 1980.

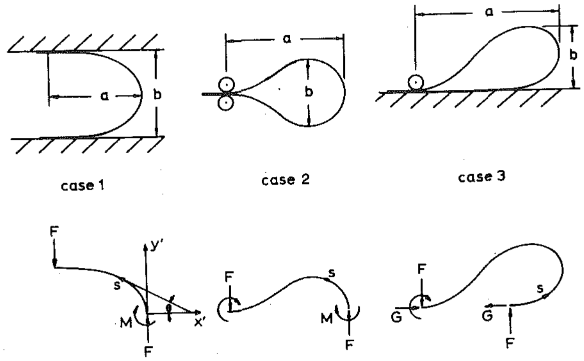

Fig. 1 The three cases of folding

$$s' = L, \theta = \pi, y' = 0 \tag{10}$$

Here L is the unknown free length of the elastica.

Similarity Solutions

Since there are no natural length scales we expect similarity solutions, i.e., the shapes of the elastica are invariant. Let us normalize all lengths by $(EI/F)^{1/2}$.

$$s = (F/EI)^{1/2}\, s', \quad x = (F/EI)^{1/2}\, x', \quad y = (F/EI)^{1/2}\, y' \tag{11}$$

Equation (1), after differentiating once, and equation (2) become

$$\frac{d^2\theta}{ds^2} = \cos\theta + \left(\frac{G}{F}\right)\sin\theta \tag{12}$$

$$\frac{dx}{ds} = \cos\theta, \frac{dy}{ds} = \sin\theta \tag{13}$$

Equation (12) can be integrated to give

$$\frac{1}{2}\left(\frac{d\theta}{ds}\right)^2 = \sin\theta - \left(\frac{G}{F}\right)\cos\theta + C \tag{14}$$

where C is a constant of integration. For Case 1, equations (4), (5), and (14) give $C = 0$ and

$$\frac{1}{2}\left(\frac{d\theta}{ds}\right)^2 = \sin\theta \tag{15}$$

Hence

$$\frac{d\theta}{ds}(0) = \sqrt{2} \tag{16}$$

Since $G = 0$ we can integrate equations (12), (13), (3), and (16) as an initial value problem by the Runge-Kutta algorithm. A mini computer (HP 9820A) using a step size $\Delta s = 0.025$ was found to be sufficient. The integration terminates at $\theta = \pi$, where we note the value of s, say, equal to s^*. Thus we find L indirectly by

$$s^* = (F/EI)^{1/2} L \tag{17}$$

For Case 2, a one-parameter shooting method is used. We guess $d\theta/ds$ at $s = 0$ and integrate until $\theta = \pi$. The initial guess is adjusted until $y = 0$ at $\theta = \pi$. Similarly, for Case 3, we guess the value of (G/F) and integrate equations (9), (12), and (13) until $y = 0$ at $\theta = \pi$. After (G/F) is found one can compute the maximum moment from equations (14) and (9).

Results and Discussion

Although the solutions to the elastica equations can be expressed in terms of elliptic functions, it is much more convenient and accurate to use numerical integration as outlined in this paper. Case 1 was first studied by Sonntag [2] using elliptic functions. Cases 2 and 3 was formulated in a general way by Born [3], but he had neither numerical values nor recognized their application to the folding process. Although the solution to elastica problems may be expressed in terms of elliptic functions, in some cases the process is extremely inconvenient [4], even with up-to-date elliptic tables [5].

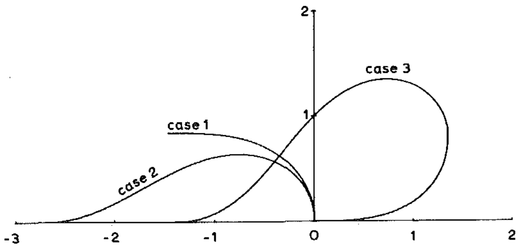

Fig. 2 The similarity shapes

Table 1

	Case 1	Case 2	Case 3
G/F	0	0	0.45532
Curvature at $s' = 0$: $\frac{d\theta}{ds}(0)$	$\sqrt{2}$	1.71018	0
Curvature at $s' = L$: $\frac{d\theta}{ds}(s^*)$	0	−0.96163	−1.34954
Arc length integrated: s^*	1.85407	3.14844	5.26292
Maximum width: $a(F/EI)^{1/2}$	$\sqrt{2}$	2.67181	2.70745
Maximum height: $b(F/EI)^{1/2}$	1.69443	1.28591	1.34972
Maximum moment: $\frac{d\theta}{ds}\vert\max$	$\sqrt{2}$	1.71018	1.76301

Table 1 shows our results. For the same force F and rigidity EI we see Case 1 has the smallest width, and Case 2 has the smallest height. Case 3, having the largest width and largest maximum moment, does not compare as favorably. Sontag [2] obtained four figure accuracy for Case 1.

Fig. 2 shows the three similarity shapes in terms of the normalized coordinates. The actual dimensions are proportional to $(F/EI)^{-1/2}$. As the elastica is being folded, the force F approaches infinity as the inverse square of the dimensions. The present theory, of course, ceases to be valid at the final stages of collapse, where the dimensions of the loop would be comparable to the thickness of the elastica.

References

1 Frisch-Fay, R., *Flexible Bars,* Butterworth, Washington D.C., 1962.

2 Sonntag, R., "Zur Theorie des geschlossenen Kreisringes mit grosser Formänderung," *Ingenieur-Archiv,* Vol. 13, 1943, pp. 380–397.

3 Born, M., "Untersuchungen über die Stabilität der elastischen Linie in Ebene und Raum unter verschiedenen Grenzbedingungen," Dissertation, Göttingen, 1906.

4 Wang, C. Y., and Watson, L. T., "On the Large Deformation of C-Shaped Springs," *International Journal of Mechanical Sciences,* Vol. 22, 1980, pp. 395–400.

5 Fettis, H. E., and Caslin, J. C., *Ten Place Tables of the Jacobian Elliptic Functions,* Aerospace Research Laboratories, 1965.

Pendulum With a Rotational Vibration

B. A. Schmidt[1]

This work involves a pendulum made up of a mass, a pivoted

---

[1] Assistant Professor, Department of Mathematics, Central Michigan University, Mt. Pleasant, Mich. 48859

Manuscript received by ASME Applied Mechanics Division, May, 1980; final revision, September, 1980.

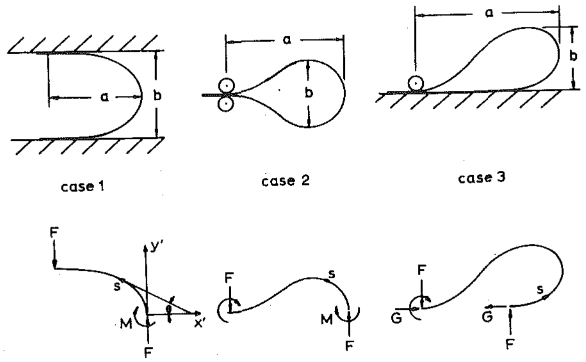

Fig. 1 The three cases of folding

$$s' = L, \theta = \pi, y' = 0 \tag{10}$$

Here L is the unknown free length of the elastica.

Similarity Solutions

Since there are no natural length scales we expect similarity solutions, i.e., the shapes of the elastica are invariant. Let us normalize all lengths by $(EI/F)^{1/2}$.

$$s = (F/EI)^{1/2} s', \quad x = (F/EI)^{1/2} x', \quad y = (F/EI)^{1/2} y' \tag{11}$$

Equation (1), after differentiating once, and equation (2) become

$$\frac{d^2\theta}{ds^2} = \cos\theta + \left(\frac{G}{F}\right)\sin\theta \tag{12}$$

$$\frac{dx}{ds} = \cos\theta, \frac{dy}{ds} = \sin\theta \tag{13}$$

Equation (12) can be integrated to give

$$\frac{1}{2}\left(\frac{d\theta}{ds}\right)^2 = \sin\theta - \left(\frac{G}{F}\right)\cos\theta + C \tag{14}$$

where C is a constant of integration. For Case 1, equations (4), (5), and (14) give $C = 0$ and

$$\frac{1}{2}\left(\frac{d\theta}{ds}\right)^2 = \sin\theta \tag{15}$$

Hence

$$\frac{d\theta}{ds}(0) = \sqrt{2} \tag{16}$$

Since $G = 0$ we can integrate equations (12), (13), (3), and (16) as an initial value problem by the Runge-Kutta algorithm. A mini computer (HP 9820A) using a step size $\Delta s = 0.025$ was found to be sufficient. The integration terminates at $\theta = \pi$, where we note the value of s, say, equal to s^*. Thus we find L indirectly by

$$s^* = (F/EI)^{1/2} L \tag{17}$$

For Case 2, a one-parameter shooting method is used. We guess $d\theta/ds$ at $s = 0$ and integrate until $\theta = \pi$. The initial guess is adjusted until $y = 0$ at $\theta = \pi$. Similarly, for Case 3, we guess the value of (G/F) and integrate equations (9), (12), and (13) until $y = 0$ at $\theta = \pi$. After (G/F) is found one can compute the maximum moment from equations (14) and (9).

Results and Discussion

Although the solutions to the elastica equations can be expressed in terms of elliptic functions, it is much more convenient and accurate to use numerical integration as outlined in this paper. Case 1 was first studied by Sonntag [2] using elliptic functions. Cases 2 and 3 was formulated in a general way by Born [3], but he had neither numerical values nor recognized their application to the folding process. Although the solution to elastica problems may be expressed in terms of elliptic functions, in some cases the process is extremely inconvenient [4], even with up-to-date elliptic tables [5].

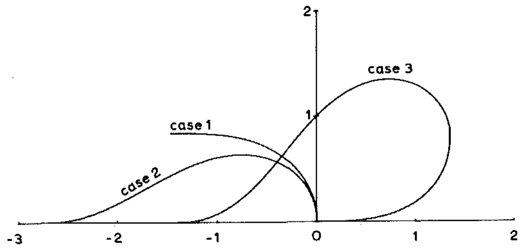

Fig. 2 The similarity shapes

Table 1

	Case 1	Case 2	Case 3
G/F	0	0	0.45532
Curvature at $s' = 0$: $\frac{d\theta}{ds}(0)$	$\sqrt{2}$	1.71018	0
Curvature at $s' = L$: $\frac{d\theta}{ds}(s^*)$	0	−0.96163	−1.34954
Arc length integrated: s^*	1.85407	3.14844	5.26292
Maximum width: $a(F/EI)^{1/2}$	$\sqrt{2}$	2.67181	2.70745
Maximum height: $b(F/EI)^{1/2}$	1.69443	1.28591	1.34972
Maximum moment: $\frac{d\theta}{ds}\vert\max$	$\sqrt{2}$	1.71018	1.76301

Table 1 shows our results. For the same force F and rigidity EI we see Case 1 has the smallest width, and Case 2 has the smallest height. Case 3, having the largest width and largest maximum moment, does not compare as favorably. Sontag [2] obtained four figure accuracy for Case 1.

Fig. 2 shows the three similarity shapes in terms of the normalized coordinates. The actual dimensions are proportional to $(F/EI)^{-1/2}$. As the elastica is being folded, the force F approaches infinity as the inverse square of the dimensions. The present theory, of course, ceases to be valid at the final stages of collapse, where the dimensions of the loop would be comparable to the thickness of the elastica.

References

1 Frisch-Fay, R., *Flexible Bars,* Butterworth, Washington D.C., 1962.

2 Sonntag, R., "Zur Theorie des geschlossenen Kreisringes mit grosser Formänderung," *Ingenieur-Archiv,* Vol. 13, 1943, pp. 380–397.

3 Born, M., "Untersuchungen über die Stabilität der elastischen Linie in Ebene und Raum unter verschiedenen Grenzbedingungen," Dissertation, Göttingen, 1906.

4 Wang, C. Y., and Watson, L. T., "On the Large Deformation of *C*-Shaped Springs," *International Journal of Mechanical Sciences,* Vol. 22, 1980, pp. 395–400.

5 Fettis, H. E., and Caslin, J. C., *Ten Place Tables of the Jacobian Elliptic Functions,* Aerospace Research Laboratories, 1965.

Pendulum With a Rotational Vibration

B. A. Schmidt[1]

This work involves a pendulum made up of a mass, a pivoted

---

[1] Assistant Professor, Department of Mathematics, Central Michigan University, Mt. Pleasant, Mich. 48859

Manuscript received by ASME Applied Mechanics Division, May, 1980; final revision, September, 1980.

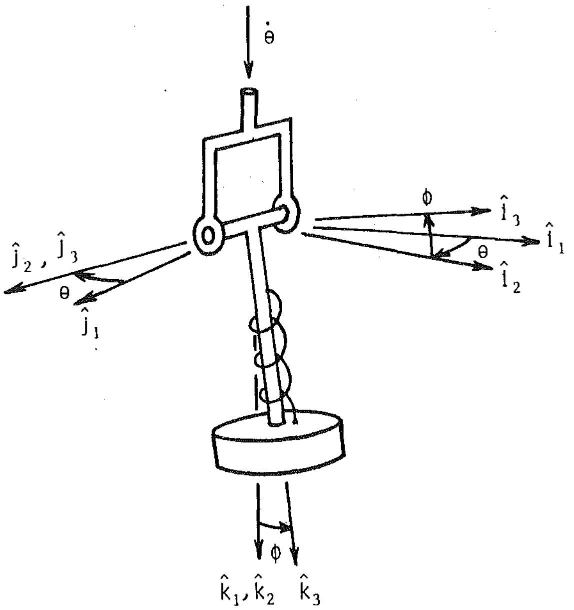

Fig. 1 The pendulum

weightless rod, and a spring. The mass is constrained to maintain its axial position on the rod, but is allowed to move rotationally on the rod under the influence of the spring. The pivot is vibrated rotationally at a high frequency about a vertical axis. It is found that, in some conditions, the vibration causes new stable equilibrium positions.

Introduction

The vibrated pendulum has been studied by many investigators. Stephenson [1] considered the plane pendulum subjected to a vertical vibration applied at the pivot. Lowenstern [2] considered several devices including the vibrated spherical pendulum. Phelps and Hunter [3] provided a thorough exposition of the plane pendulum with a vertical harmonic vibration at an unrestricted frequency. Miles [4] considered the stability of the downward vertical position of a spherical pendulum subjected to a horizontal vibration. Sethna and Hemp [5] studied the gyroscopic pendulum to which a high frequency vertical vibration was applied. Several authors including Howe [6] and Bogdanoff and Citron [7] have investigated the effects of random vertical vibrations applied to plane pendulums. Ryland and Meirovitch [8] considered the plane flexible pendulum with a vertical harmonic vibration at an unrestricted frequency.

In this work, the effect of a rotational vibration is investigated. The pendulum is allowed to have torsional flexibility so that gyroscopic forces can occur. The pendulum is shown in Fig. 1. The mass is a wheel whose axis coincides with the axis of the rod. There is a constraint which prohibits the mass from moving along the rod but the mass is allowed to rotate on the rod under the influence of the spring. A small rotational harmonic vibration is applied to the pivot about a vertical axis. The frequency of the vibration is large with respect to the natural frequency of the motion of the pendulum under the influence of gravity, while the frequency of the vibration is not large with respect to the natural frequency of the rotational motion of the mass on the rod under the influence of the spring.

The method of averaging [9] is used to replace the equations of motion by differential equations which approximately describe the motion. These equations are examined to find stable equilibrium positions. It is found that there are new stable equilibrium positions that occur because of inertia forces caused by the vibration.

The Analysis

The position of the pendulum is described by the variables θ, ϕ, and ψ. ϕ is a rotation of the pendulum about $\hat{j}_3$ and ψ is a rotation of the mass about $\hat{k}_3$. The vibration is given by $\theta = \epsilon \sin \nu t$. The equations of motion are

$$(I_2 + m\,r^2)\ddot{\phi} + (I_3 - I_1 - mr^2) \sin\phi \cos\phi\, \epsilon^2 \nu^2 \cos^2 \nu t$$
$$+ I_3 \dot{\psi} \sin\phi\, \epsilon\nu \cos \nu t + mrg \sin\phi + c_1 \dot{\phi} = 0$$

and

$$I_3(\ddot{\psi} - \epsilon\nu^2 \sin \nu t \cos\phi - \dot{\phi} \sin\phi\, \epsilon\nu \cos \nu\tau) + c_2\dot{\psi} + K\psi = 0,$$

where I_1, I_2, and I_3 are moments of inertia about axes through the center of the mass parallel to $\hat{i}_3$, $\hat{j}_3$, and $\hat{k}_3$, respectively, m is the mass, r is the distance from the pivot to the center of the mass, K is the spring constant, c_1 and c_2 are damping coefficients, t is time, and the dot indicates the derivative with respect to time.

The problem is restricted so that the amplitude of the vibration, ϵ, is positive and near zero and the frequency ν is of the order ϵ^{-1} and the spring constant K is of order ν^2. These restrictions allow the equations of motion to be presented in terms of the small parameter ϵ. Let $\tau = \nu t$, $I = I_3\,(I_2 + mr^2)^{-1}$, $k^2 = KI_3{}^{-1}\,\nu^{-2}$, $\epsilon^2\delta = mrg\,(I_2 + mr^2)^{-1}\nu^{-2}$, $\epsilon a_1 = c_1\nu^{-1}(I_2 + mr^2)^{-1}$, $\epsilon a_2 = c_2\,\nu^{-1}\,I_3{}^{-1}$, and let the prime indicate differentiation with respect to τ. The equations of motion become

$$\phi'' + \epsilon^2(I - 1) \sin\phi \cos\phi \cos^2\tau$$
$$+ \epsilon I\psi' \sin\phi \cos\tau + \epsilon^2\,\delta \sin\phi + \epsilon a_1\phi' = 0$$

and

$$\psi'' - \epsilon \cos\phi \sin\tau - \epsilon\phi' \sin\phi \cos\tau$$
$$+ k^2\psi + \epsilon a_2\psi' = 0. \quad (1a,b)$$

In this representation of the equations of motion, the variables, and parameters are dimensionless. The parameter ϵ is restricted to be positive and near zero, the parameters I, δ, k^2, a_1, and a_2 are positive and independent of ϵ. In this analysis, two other restrictions are imposed. They are

1 k^2 is not near 1, i.e., $k^2 - 1$ is independent of ϵ.
2 The initial conditions $\psi(0)$ and $\psi'(0)$ are of order ϵ.

To change the equations of motion, (1), into four equations in the standard form for the method of averaging the following transformation is made. Let

$$\phi' = \epsilon\omega$$
$$\psi = \epsilon u \cos k\tau + \epsilon v \sin k\tau + \epsilon(k^2 - 1)^{-1} \cos\phi \sin\tau$$
$$\psi' = -\epsilon uk \sin k\tau + \epsilon vk \cos k\tau$$
$$- \epsilon(k^2 - 1)^{-1}\,\phi' \sin\phi \sin\tau + \epsilon(k^2 - 1)^{-1} \cos\phi \cos\tau. \quad (2\,a,b,c)$$

Equations (2) transform equations (1) into four first-order differential equations in the variables ϕ, ω, u, and v. Equations (2*b*) and (2*c*) are used with the variation of parameters technique. The third term in (2*b*) and the third and fourth terms in (2*c*) are included to remove large terms in the first-order differential equations. Differentiation of (2*a*) and substitution of (1*a*), (2*a*), and (2*c*) give an equation involving ω', ϕ, ω, u, and v. Differentiation of (2*c*) and substitution of (1*b*), (2*a*), and (2*c*) give an equation involving u' and v'. This, along with the variation of parameters technique gives an equation for u' and an equation for v'. Then, if (2*a*) is included, there are four first-order equations in the standard form for the method of averaging. They are

$$\phi' = \epsilon\omega$$

$$\omega' = -\epsilon(I - 1) \sin\phi \cos\phi \cos^2\tau + \epsilon Iku \sin\phi \sin k\tau \cos\tau$$
$$- \epsilon\, Ikv \sin\phi \cos k\tau \cos\tau - \epsilon I(k^2 - 1)^{-1} \sin\phi \cos\phi \cos^2\tau$$
$$- \epsilon\,\delta \sin\phi - \epsilon a_1\,\omega$$

$$u' = -\,\epsilon k^{-1}[\omega \sin\phi \cos\tau + a_2ku \sin k\tau - a_2kv \cos k\tau$$
$$- a_2(k^2 - 1)^{-1} \cos\phi \cos\tau + 2(k^2 - 1)^{-1}\,\omega \sin\phi \cos\tau] \sin k\tau.$$
$$(3a\text{–}c)$$

$$\begin{aligned} v' = \epsilon k^{-1} [&\omega \sin\phi \cos\tau + a_2 k u \sin k\tau - a_2 k v \cos k\tau \\ &- a_2(k^2-1)^{-1} \cos\phi \cos\tau \\ &+ 2(k^2-1)^{-1} \omega \sin\phi \cos\tau] \cos k\tau. \end{aligned} \tag{3d}$$

These equations are in the standard form for the method of averaging. Averaging equations (3) gives

$$\begin{aligned} \Phi' &= \epsilon\Omega \\ \Omega' &= -\epsilon \tfrac{1}{2}(I-1)\sin\Phi\cos\Phi - \epsilon\tfrac{1}{2}I(k^2-1)^{-1}\sin\Phi\cos\Phi \\ &\quad - \epsilon\delta\sin\Phi - \epsilon a_1\Omega \\ U' &= -\epsilon\tfrac{1}{2}a_2 U \\ V' &= -\epsilon\tfrac{1}{2}a_2 V, \end{aligned} \tag{4a–d}$$

where Φ, Ω, U, and V are the averaged variables corresponding to ϕ, ω, u, and v.

Equations (4) can be analyzed in a variety of ways. In this investigation, equilibrium solutions are found and stability of these solutions is determined. By means of a theorem of Sethna [10] it can be stated that there exists an almost periodic solution of equations (3) which approaches an equilibrium solution of equations (4) as $\epsilon \to 0$ (for all τ) and that the stability properties of this solution of equations (3) are the same as the stability properties of the zero solution of the variation equations. In the remainder of this work, the equilibrium solutions of equations (4) are found and stability is judged by the variation equations.

Equations (4) indicate there is equilibrium if

$$\begin{aligned} 0 &= \Omega e \\ 0 &= (\beta\cos\Phi_e + \delta)\sin\Phi_e \\ 0 &= U_e \\ 0 &= V_e, \end{aligned} \tag{5a–d}$$

where Φ_e, Ω_e, U_e, and V_e are equilibrium values of Φ, Ω, U, and V, and $\beta = \frac{1}{2}(I - 1 + I(k^2-1)^{-1})$. From equations (5) it can be seen that equilibrium requires that $\sin\Phi_e$ is zero or

$$\beta\cos\Phi_e + \delta = 0. \tag{6}$$

Equilibrium is considered when Ω_e, U_e, and V_e are all zero and

1: $\Phi_e = 0$,

or

2: $\Phi_e = \pi$,

or

3: Φ_e is an angle described by equation (6) with $\Phi_e \neq 0, \pi$.

Equilibrium when $\sin\Phi_e = 0$ and $\beta\cos\Phi_e + \delta = 0$ is not considered. For this case, Sethna's theorem does not apply and the variation equation is not useful. Stability could be judged, however, by analysis of the right-hand side of equation (5*b*).

Stability of these equilibrium positions and of the corresponding almost periodic solutions of equations (3) can be determined by examining the variation equations. The variation equations are

$$\begin{aligned} \Phi_1' &= \epsilon\Omega_1 \\ \Omega_1' &= -\epsilon(\beta\cos 2\Phi_e + \delta\cos\Phi_e)\Phi_1 - \epsilon a_1\Omega_1 \\ U_1' &= -\epsilon\tfrac{1}{2}a_2 U_1 \\ V_1' &= -\epsilon\tfrac{1}{2}a_2 V_1, \end{aligned} \tag{7a–d}$$

where Φ_1, Ω_1, U_1, and V_1 are the variations of Φ, Ω, U, and V from their equilibrium values Φ_e, Ω_e, U_e, and V_e. Since the zero solutions for (7*c*) and (7*d*) are stable they need not be considered further. Stability depends only on equations (7*a*) and (7*b*) and since the coefficient of Ω_1 in (7*b*) is negative, stability depends only on the coefficient of Φ_1 in equation (7*b*). If it is negative, there is stability.

For the equilibrium position in Case 1, i.e., $\Phi_e = 0$, the coefficient of Φ_1 is $-\epsilon(\beta+\delta)$ and then the requirement for stability is

$$\beta > -\delta$$

For the equilibrium position in Case 2, i.e., $\Phi_e = \pi$, the coefficient of Φ_1 is $-\epsilon(\beta-\delta)$ and then the requirement for stability is

$$\beta > \delta.$$

Consider the equilibrium positions mentioned in Case 3. Equation (6) indicates that if $\beta < -\delta$, there is equilibrium in either the first or fourth quadrants and if $\beta > \delta$, there is equilibrium in either the second or third quadrants. Using equation (6) to remove Φ_e from the coefficient of Φ_1, in equation (7), this coefficient becomes

$$-\frac{\epsilon(\delta-\beta)(\delta+\beta)}{\beta}$$

For Φ_e in the first or fourth quadrants, i.e., $\beta < -\delta$, this coefficient is negative which indicates stability. For Φ_e in the second or third quadrants, i.e., $\beta > \delta$, the coefficient of Φ_1 is positive which indicates instability.

It can be noted that $U_e = 0$ and $V_e = 0$ implies an equilibrium value for ψ: $\psi_e = 0$. Then in summary, it can be said that the stable equilibrium positions are

1: $\psi_e = 0$, $\Phi_e = 0$, when $\beta > -\delta$
2: $\psi_e = 0$, $\Phi_e = \pi$, when $\beta > \delta$

and

3: $\psi_e = 0$, Φ_e is a first or fourth quadrant angle given by equation (6) when $\beta < -\delta$.

The unstable equilibrium positions are

1: $\psi_e = 0$, $\Phi_e = 0$, when $\beta < -\delta$
2: $\psi_e = 0$, $\Phi_e = \pi$, when $\beta < \delta$

and

3: $\psi_e = 0$, Φ_e is a second or third quadrant angle given by equation (6), when $\beta > \delta$.

From Sethna's theorem, it is known that there are almost periodic solutions of (3) (or (1)) which approach these equilibrium solutions as $\epsilon \to 0$.

Conclusion and Remarks

The analysis shows that, depending on the frequency of the vibration, the spring constant, the moments of inertia, the radius, gravity, and the initial conditions, there can be stable motion near several fixed positions. They are (*a*) the downward vertical position; (*b*) the upward vertical position; and (*c*) two downward nonvertical positions (first and fourth quadrants of ϕ). The positions mentioned in (*b*) and (*c*) are caused by two inertia forces created by the vibration. One of these is centrifugal in nature. The other could be described in gyroscopic.

The first of these inertia forces, the centrifugal force, is shown by the first term on the right of equation (4*b*) and it comes from the term $(I_3 - I_1 - mr^2)\sin\phi\cos\phi\,\epsilon^2\nu^2\cos^2\nu\tau$ in the first of the original equations of motion. This force has a stabilizing effect on the positions at $\phi = 0, \pi$ if $mr^2 < I_3 - I_2$, i.e., if the pendulum is short and wide, and it has a destabilizing effect on these positions if the pendulum is long ($mr^2 > I_3 - I_2$). Also, this force has a stabilizing effect on the positions in the first and fourth quadrants of ϕ if the pendulum is long ($mr^2 > I_3 - I_2$) and it has a destabilizing effect on these positions if the pendulum is short ($mr^2 < I_3 - I_2$).

The gyroscopic force is shown by the second term on the right of equation (4*b*). This comes from the term $\epsilon\nu I_3\dot{\psi}\sin\phi\cos\nu\tau$ in the first of the original equations of motion. This force can be a much stronger influence than the centrifugal force because of $k^2 - 1$ in the denominator. The quantity $k^2 - 1$ can be close to zero but it is restricted to be independent of ϵ. If $k^2 - 1$ were of order ϵ a different analysis would be needed. The gyroscopic force has a stabilizing influence on the positions at $\phi = 0, \pi$ if $k^2 > 1$ and a destabilizing influence on these positions if $k^2 < 1$. The gyroscopic force has a stabilizing influence on the positions in the first and fourth quadrants of ϕ if $k^2 < 1$ and a destabilizing influence on these positions if $k^2 > 1$.

References

1 Stephenson, A., "On a New Type of Dynamical Stability," *Memoirs and Proceedings of the Manchester Literary and Philosophical Society,* Vol. 52, 1907, pp. 1–10.

2 Lowenstern, E. R., "The Stabilizing Effect of Imposed Oscillations of High Frequency on a Dynamical System," *Philosophical Magazine,* Vol. 13, 1932, pp. 458–486.

3 Phelps, F. M., III, and Hunter, J. H., Jr., "An Analytical Solution of the Inverted Pendulum," *American Journal of Physics,* Vol. 33, 1965, pp. 285–295.

4 Miles, J. W., "Stability of Forced Oscillations of a Spherical Pendulum," *Quarterly of Applied Mathematics,* Vol. 20, No. 1, Apr. 1962, pp. 21–32.

5 Sethna, P. R., and Hemp, G. W., "Nonlinear Oscillations of a Gyroscopic Pendulum With an Oscillating Point of Suspension," *Proc. Colloq. International du Center National de la Recherche Scientifique,* N-148, Les Vibrations Forcees dans les Systems Non-Lineares, 1964, pp. 375–392.

6 Howe, M. S., "The Mean Square Stability of an Inverted Pendulum Subject to Random Parametric Excitation," *Journal of Sound and Vibration,* Vol. 32(3), 1974, pp. 407–421.

7 Bogdanoff, J. L., and Citron, S. J., "Experiments With an Inverted Pendulum Subject to Random Parametric Excitation," *Journal of the Acoustical Society of America,* Vol. 38, 1965, pp. 447–452.

8 Ryland, G., II, and Meirovitch, L., "Stability Boundaries of a Swinging Spring With Oscillatory Support," *Journal of Sound and Vibration,* Vol. 51(4), 1977, pp. 547–560.

9 Bogoliuboff, N. M., and Mitropolskii, Yu. A., *Asymptotic Methods in the Theory of Nonlinear Oscillations,* Chapters 5 and 6, Gordon and Breach, New York, 1962.

10 Sethna, P. R., "An Extension of the Method of Averaging," *Quarterly of Applied Mathematics,* Vol. 25, 1967, pp. 205–211.

Stress Distribution Around a Circular Hole in Square Plates, Loaded Uniformly in the Plane, on Two Opposite Sides of the Square

M. Erickson[1] **and A. J. Durelli**[2]

The complete stress distribution around a circular hole, located in the center of a square plate, has been determined photoelastically for the case of the plate loaded uniformly on two opposite sides. The study was conducted parametrically for a range of the ratio D/W of the diameter of the hole to the side of the square from 0.20 to 0.83. The results obtained permit the determination of the stresses for any biaxial condition and verify a previous solution obtained for the case of the pressurized hole. The experimental procedure is briefly described.

Introduction

The classical problem of the stress distribution around a circular hole in an infinite plate subjected to a uniaxial uniform loading in the plane of the plate was solved by Kirsch [1] in closed form. The appreciably more complicated case of the finite plate with the circular hole was solved by Howland [2] using an infinite series solution, but results were evaluated only for $D/W < 0.5$, D being the diameter of the hole and W the width of the plate. The distribution of stress for the cases when $D/W > 0.5$ was obtained experimentally by Wahl and Beeuwkes [3]. The stress-concentration factors referred to both the gross area and the net area, for the total range of D/W values are given in [4]. The case of the very large hole in the plate, when D/W approaches one presented some problems of interpretation, which have been dealt with in [5].

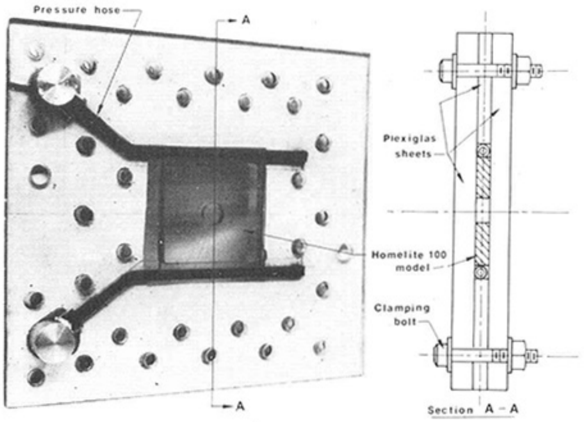

Fig. 1 Loading device used to apply uniform pressure to two opposite sides of a square plate

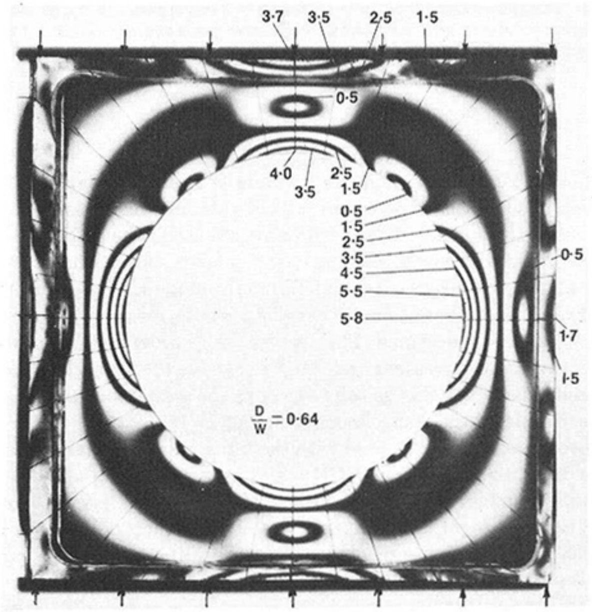

Fig. 2 Typical isochromatic pattern around a circular hole in a square plate subjected to uniform pressure on two opposite sides

The stress distribution for the case of a square plate with a circular hole was solved experimentally [6] when a uniform pressure is applied inside the hole, or what is equivalent [7], when the four sides of the square are subjected to uniform pressure. The problem of the square plate with a circular hole, subjected to in-plane uniform pressure applied to two opposite sides of the plate, has not been solved. The problem is important and if the solution were available, the solution of the previously mentioned problem for any ratio of biaxiality could be obtained as a special case by superposition. That is the problem dealt with in this Note. The solution is obtained photoelastically for a range of D/W values from 0.20 to 0.83.

Test Procedure

The analysis was conducted in a 3-in-sq, $\frac{1}{4}$-in-thick (Homalite 100)

---

[1] Adjunct Professor, School of Engineering, Oakland University, Rochester, Mich. 48063.

[2] Professor, Department of Mechanical Engineering, University of Maryland, College Park, Md. 20742. Fellow ASME.

Manuscript received by ASME Applied Mechanics Division, April, 1980; final revision, October, 1980.

positions at $\phi = 0, \pi$ if $k^2 > 1$ and a destabilizing influence on these positions if $k^2 < 1$. The gyroscopic force has a stabilizing influence on the positions in the first and fourth quadrants of ϕ if $k^2 < 1$ and a destabilizing influence on these positions if $k^2 > 1$.

References

1 Stephenson, A., "On a New Type of Dynamical Stability," *Memoirs and Proceedings of the Manchester Literary and Philosophical Society,* Vol. 52, 1907, pp. 1–10.

2 Lowenstern, E. R., "The Stabilizing Effect of Imposed Oscillations of High Frequency on a Dynamical System," *Philosophical Magazine,* Vol. 13, 1932, pp. 458–486.

3 Phelps, F. M., III, and Hunter, J. H., Jr., "An Analytical Solution of the Inverted Pendulum," *American Journal of Physics,* Vol. 33, 1965, pp. 285–295.

4 Miles, J. W., "Stability of Forced Oscillations of a Spherical Pendulum," *Quarterly of Applied Mathematics,* Vol. 20, No. 1, Apr. 1962, pp. 21–32.

5 Sethna, P. R., and Hemp, G. W., "Nonlinear Oscillations of a Gyroscopic Pendulum With an Oscillating Point of Suspension," *Proc. Colloq. International du Center National de la Recherche Scientifique,* N-148, Les Vibrations Forcees dans les Systems Non-Lineares, 1964, pp. 375–392.

6 Howe, M. S., "The Mean Square Stability of an Inverted Pendulum Subject to Random Parametric Excitation," *Journal of Sound and Vibration,* Vol. 32(3), 1974, pp. 407–421.

7 Bogdanoff, J. L., and Citron, S. J., "Experiments With an Inverted Pendulum Subject to Random Parametric Excitation," *Journal of the Acoustical Society of America,* Vol. 38, 1965, pp. 447–452.

8 Ryland, G., II, and Meirovitch, L., "Stability Boundaries of a Swinging Spring With Oscillatory Support," *Journal of Sound and Vibration,* Vol. 51(4), 1977, pp. 547–560.

9 Bogoliuboff, N. M., and Mitropolskii, Yu. A., *Asymptotic Methods in the Theory of Nonlinear Oscillations,* Chapters 5 and 6, Gordon and Breach, New York, 1962.

10 Sethna, P. R., "An Extension of the Method of Averaging," *Quarterly of Applied Mathematics,* Vol. 25, 1967, pp. 205–211.

Stress Distribution Around a Circular Hole in Square Plates, Loaded Uniformly in the Plane, on Two Opposite Sides of the Square

M. Erickson[1] **and A. J. Durelli**[2]

The complete stress distribution around a circular hole, located in the center of a square plate, has been determined photoelastically for the case of the plate loaded uniformly on two opposite sides. The study was conducted parametrically for a range of the ratio D/W of the diameter of the hole to the side of the square from 0.20 to 0.83. The results obtained permit the determination of the stresses for any biaxial condition and verify a previous solution obtained for the case of the pressurized hole. The experimental procedure is briefly described.

Introduction

The classical problem of the stress distribution around a circular hole in an infinite plate subjected to a uniaxial uniform loading in the plane of the plate was solved by Kirsch [1] in closed form. The appreciably more complicated case of the finite plate with the circular hole was solved by Howland [2] using an infinite series solution, but results were evaluated only for $D/W < 0.5$, D being the diameter of the hole and W the width of the plate. The distribution of stress for the cases when $D/W > 0.5$ was obtained experimentally by Wahl and Beeuwkes [3]. The stress-concentration factors referred to both the gross area and the net area, for the total range of D/W values are given in [4]. The case of the very large hole in the plate, when D/W approaches one presented some problems of interpretation, which have been dealt with in [5].

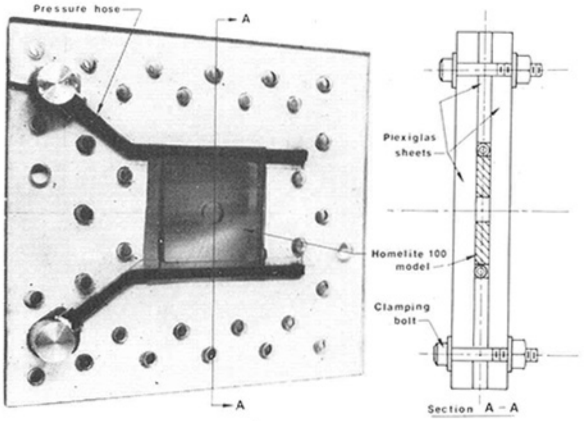

Fig. 1 Loading device used to apply uniform pressure to two opposite sides of a square plate

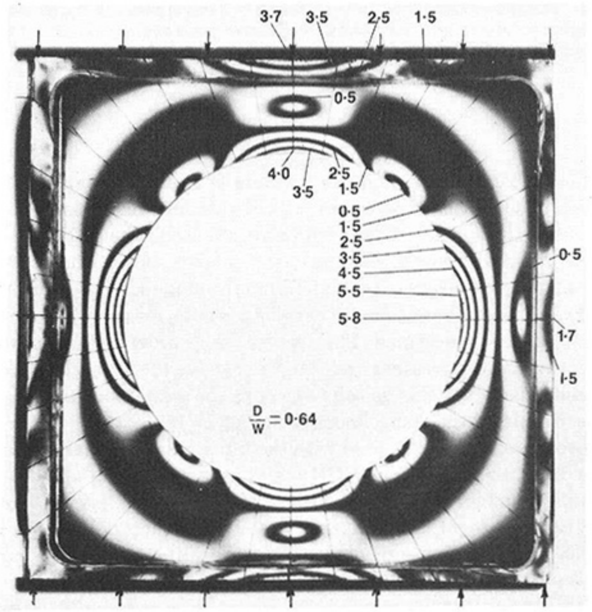

Fig. 2 Typical isochromatic pattern around a circular hole in a square plate subjected to uniform pressure on two opposite sides

The stress distribution for the case of a square plate with a circular hole was solved experimentally [6] when a uniform pressure is applied inside the hole, or what is equivalent [7], when the four sides of the square are subjected to uniform pressure. The problem of the square plate with a circular hole, subjected to in-plane uniform pressure applied to two opposite sides of the plate, has not been solved. The problem is important and if the solution were available, the solution of the previously mentioned problem for any ratio of biaxiality could be obtained as a special case by superposition. That is the problem dealt with in this Note. The solution is obtained photoelastically for a range of D/W values from 0.20 to 0.83.

Test Procedure

The analysis was conducted in a 3-in-sq, $\frac{1}{4}$-in-thick (Homalite 100)

---

[1] Adjunct Professor, School of Engineering, Oakland University, Rochester, Mich. 48063.

[2] Professor, Department of Mechanical Engineering, University of Maryland, College Park, Md. 20742. Fellow ASME.

Manuscript received by ASME Applied Mechanics Division, April, 1980; final revision, October, 1980.

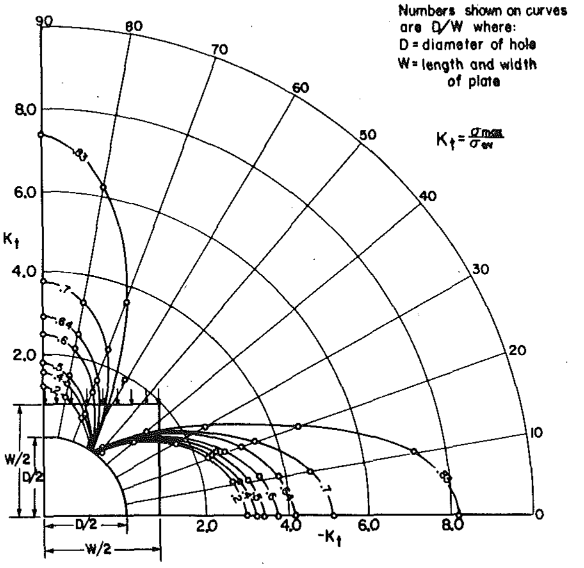

Fig. 3 **Stress distributions on inner boundary of a round hole in a square plate subjected to uniform pressure on two opposite sides (average stress on the net section used for comparison)**

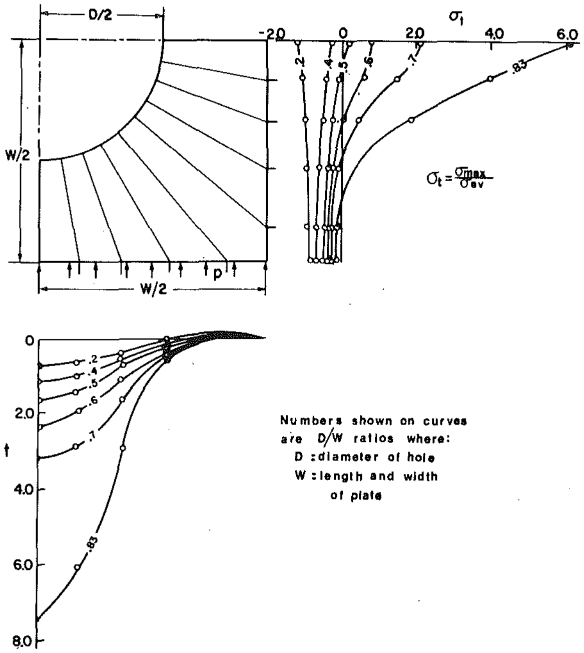

Fig. 4 **Stress distributions on outer boundary of a square plate with a round hole subjected to uniform pressure applied to two opposite sides of the plate (average stress on the net section used for comparison)**

specimen (Fig. 1). The uniform pressure is applied by means of a specially built device as described in [8]. Two rubber hoses, one placed on each of the opposite sides of the plate are used. The deformation of the pressurized hose is restrained by Plexiglass sheets. The loading frame had to be calibrated to determine the amount of pressure actually applied to the specimen. For this purpose, a strain gaged load cell was specially designed. The average fringe order was computed using the applied pressure and the fringe value of the material and a check obtained by algebraically averaging the areas above and below the zero axis for those specimens with high D/W.

Seven specimens were used with the inner hole diameter varying from 0.6 in. to 2.5 in. giving D/W values from 0.2 to 0.83, where D is the hole diameter and W the width of the specimen. Dark field and light field photographs were taken in a diffused light polariscope of the seven specimens, subjected to pressure sufficient to produce a maximum of about 5 fringes (Fig. 2). Fractional fringe orders were recorded using Tardy's method of compensation at every 10° at the edge of the hole from 0° (horizontal) to 90° (vertical). Readings were also taken on the outer edge of the plate at the 0° and 90° points. A calibration test on a 2.5-in-dia round disk of the material gave a material constant of 156 lb/in./fringe.

The results obtained are given as stress distributions along the inside and the outside boundaries (Figs. 3 and 4), and as stress concentrations at the intersection of the longitudinal and transverse axes with the boundary of the hole. All values are given parametrically as functions of D/W. These results permit, by superposition, the determination of stresses for any ratio of biaxial loading of the plate. The case of equal biaxiality was computed and is shown in Fig. 5. The values obtained verify those previously published for the case of the hydrostatically loaded hole [6], using the transformation explained in [7].

It may be noted that, in the present problem, K_t increases as D/W increases while for the case of circular holes in long rectangular plates, K_t decreases as D/W increases.

Acknowledgments

The research program from which this Note was developed was supported, in part, by the Office of Naval Research (Contract No. N00014-76-C-0487). The authors are grateful to N. Perrone and N. Basdekas of ONR for their support. The photoelastic specimens have been prepared by S. Nygren and the manuscript reproduction by P. Baxter.

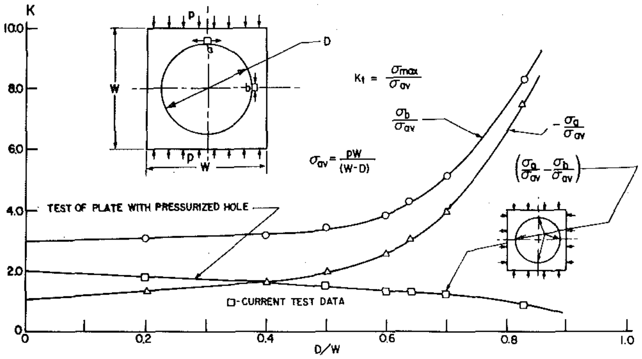

Fig. 5 **Stress-concentration factors for a round hole in a square plate subjected to a uniaxial uniform pressure and computations for the biaxial case**

References

1 Kirsch G., "Die Theorie der Elastizitaet and die Beduerfnisse der Festigkeitlehre," *Z. Ver. deut. Ing. W.*, Vol. 32, 1898, pp. 797–807.

2 Howland C. J., "On the Stresses in the Neighborhood of a Circular Hole in a Strip Under Tension," *Transactions of the Royal Society*, London, Series A, Vol. 229, 1929–1930, pp. 49–86.

3 Wahl, M., and Beeuwkes, R., "Stress Concentration Produced by Holes and Notches," ASME TRANS., Vol. 56, Aug. 1934, pp. 617–623.

4 Durelli A. J., Phillips, E. A., and Tsao, C. J., *Introduction to the Theoretical and Experimental Analysis of Stress and Strain*, McGraw-Hill, New York, 1958.

5 Durelli A. J., Parks, V. J., and Buhler-Vidal, J. O., "Linear and Nonlinear Elastic and Plastic Strains in a Plate With a Large Hole Loaded Axially in Its Plane," *International Journal of Nonlinear Mechanics*, Vol. 11, pp. 207–211.

6 Riley, W. F., Durelli, A. J., and Theocaris, P. S., "Further Stress Studies on a Square Plate With a Pressurized Central Circular Hole," *Proceedings of the 4th Midwestern Conference on Solid Mechanics*, Austin, Texas, Sept. 1959.

7 Parks, V. J., and Durelli, A. J., "Transfer of Hydrostatic Loading From One Boundary to Another," *Experimental Mechanics*, Vol. 15, No. 4, pp. 148–149, Apr. 1975.

8 Durelli A. J., *Applied Stress Analysis*, Prentice-Hall, Englewood Cliffs, N.J., 1967, pp. 78–79.

Planar Motion of a Rigid Body With a Friction Rotor

E. V. Wilms[1] and H. Cohen[2]

We consider a rigid body in planar motion which is free of all external forces. A rigid rotor of radius r is inserted in a cylindrical cavity inside the body and is acted upon by a normal force, and a friction force at the circumference. The combined system is illustrated in Fig. 1, and the forces acting on the rotor are indicated in Fig. 2. The system has similarities to those considered in [1, 2], except that in the present study the analysis is exact, and not dependent on a small angle approximation. The present problem has possible application in the damping of spacecraft rotations.

The center of mass of the outer body is at point 0, and the centers of mass of the entire system and of the rotor are at points G and A, respectively. The xy-axes are attached to the outer body. The angular velocity of the outer body is $\dot{\phi}$ and that of the rotor is $\dot{\phi} + \dot{\theta}$. Since there are no external forces applied, the point G remains fixed, and the angular momentum h with respect to G is a constant. We then have

$$h = \dot{\phi} I + \dot{\theta} I_A. \tag{1}$$

Here $I = m_0\eta_0{}^2 + m_A\eta_A{}^2 + I_0 + I_A$, where η_0 and η_A are the distances indicated in Fig. 1, m_0 and m_A are the masses of the outer body and of the rotor, respectively, I_0 and I_A are the moments of inertia of the outer body and the rotor with respect to 0 and A, respectively.

The equations of motion of the rotor are then

$$N(\cos\psi + \mu s \sin\psi) = m_A\eta_A\,\dot{\phi}^2, \tag{2a}$$

$$N(\sin\psi - \mu s \cos\psi) = -m_A\eta_A\,\ddot{\phi}, \tag{2b}$$

$$I_A(\ddot{\phi} + \ddot{\theta}) = \mu N r\, s. \tag{2c}$$

Here μ is the coefficient of friction, and $s = \operatorname{sgn}\dot{\theta}$.

Combining equations (2a) and (2b)

$$N = \frac{m_A\eta_A}{(1+\mu^2)^{1/2}}(\ddot{\phi}^2 + \dot{\phi}^4)^{1/2}. \tag{3}$$

Combining equations (1), (2c), and (3)

$$\ddot{\phi} = \frac{\mu r\, m_A\eta_A}{I'(1+\mu^2)^{1/2}}\, s(\ddot{\phi}^2 + \dot{\phi}^4)^{1/2}. \tag{4}$$

Equation (4) may be written

$$\ddot{\phi} = s\,\beta\dot{\phi}^2, \tag{5}$$

where

$$\alpha = \frac{\mu r\, m_A\eta_A}{I'(1+\mu^2)^{1/2}}, \quad I' = I - I_A, \quad \beta = \alpha/(1-\alpha^2)^{1/2}.$$

Equation (5) indicates that we will obtain real solutions for $\dot{\phi}$ only as long as β is real. This will be true only as long as $\alpha < 1$. Physically it is always possible to construct a system so that this inequality is violated. The difficulty encountered is an illustration of Painleve's paradox, some of the earliest examples of which are found in [3, 4]. The need for further study of problems of this kind was suggested by Klein in [4]. The difficulty arises because the Coulomb friction law is not always compatible with the equations of rigid-body dynamics, and some elasticity must be taken into account.

Equation (5) may be solved to yield

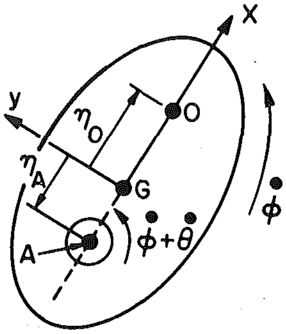

Fig. 1 The system

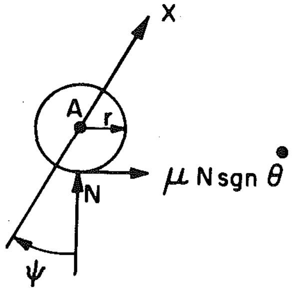

Fig. 2 The forces acting on the rotor

$$\dot{\phi} = \frac{\dot{\phi}_0}{1 - s\beta\dot{\phi}_0 t}. \tag{6}$$

Here $\dot{\phi}_0$ is the initial value of $\dot{\phi}$ at $t = 0$.

Equations (2a), (2b), and (5) yield

$$\tan\psi = s\,\frac{\beta + \mu}{1 - \beta\mu}. \tag{7}$$

Equations (1) and (6) yield

$$I_A(\dot{\theta} - \dot{\theta}_0) = -s\,\frac{I\beta\dot{\phi}_0{}^2\, t}{1 - s\beta\dot{\phi}_0 t}. \tag{8}$$

Here $\dot{\theta}_0$ is the initial value of $\dot{\theta}$. Equation (8) is valid only if s is constant over $(0,t)$.

We rewrite equations (6) and (8) as

$$\dot{\phi} = \frac{\dot{\phi}_0}{1 - st'}, \tag{9}$$

$$\dot{\theta}' = \dot{\theta}_0{}' - \frac{st'}{1 - st'}, \tag{10}$$

where

$$t' = \beta\dot{\phi}_0 t \text{ and } \dot{\theta}' = \frac{I_A}{I\dot{\phi}_0}\dot{\theta}.$$

There are 3 cases which must be considered. We will take $\dot{\phi}_0 > 0$ throughout with no loss in generality.

Case 1: $\dot{\theta}'_0 \geq 0$. Then equations (9) and (10) become

$$\dot{\phi} = \frac{\dot{\phi}_0}{1 - t'}; \quad \dot{\theta}' = \dot{\theta}'_0 - \frac{t'}{1 - t'}. \tag{11}$$

Equations (11) indicate that $\dot{\theta}' = 0$, when $t' = \dot{\theta}'_0/1 + \theta'_0$. At this time $\dot{\phi} = \dot{\phi}_0(1 + \dot{\theta}'_0)$. After this time the system rotates with a constant angular velocity and no relative motion between the rotor and the outer body.

Case 2: $\dot{\theta}'_0 \leq -1$. Then equations (9) and (10) become

$$\dot{\phi} = \frac{\dot{\phi}_0}{1 + t'}; \quad \dot{\theta}' = \dot{\theta}'_0 + \frac{t'}{1 + t'}. \tag{12}$$

Equations (12) yield $\dot{\theta}' \to 1 + \dot{\theta}'_0$ and $\dot{\phi} \to 0$ as $t \to \infty$.

Case 3: $-1 < \dot{\theta}'_0 \leq 0$. Equations (12) indicate that $\dot{\theta}' = 0$ and $\dot{\phi}$

---

[1] Associate Professor, Department of Civil Engineering, University of Manitoba, Winnipeg, Canada, R3T 2N2.

[2] Professor, Department of Civil Engineering, University of Manitoba, Winnipeg, Canada, R3T 2N2.

Manuscript received by ASME Applied Mechanics Division, August, 1980; final revision, November, 1980.

$= \dot{\phi}_0(1 + \dot{\theta}'_0)$ when $t' = -\dot{\theta}'_0/1 + \dot{\theta}'_0$. After this time the two bodies rotate with no relative motion. We see that the behavior is quite different in Cases 2 and 3.

Acknowledgment

The authors would like to thank Prof. L. E. Goodman for pointing out that the inequality $\alpha < 1$ is similar to the ones studied in [3, 4].

References

1 Wilms, E.V., and Cohen, H., "A Two-Degree-of-Freedom System With Coulomb Bearing Friction," ASME JOURNAL OF APPLIED MECHANICS, Vol. 46, 1979, pp. 217–218.

2 Wilms, E.V., and Cohen, H., "Displacement, Velocity, and Acceleration Dependent Damping in a Two-Degree-of-Freedom System," *Journal of Applied Mathematics and Physics (ZAMP)*, Vol. 30, 1979, pp. 533–540.

3 Lecornu, L., "Sur le frottement de glissement," *Comptes Rendus*, Vol. 140, 1905, pp. 635–637.

4 Klein, F., "Zu Painleve's Kritik der Coulombschen Reibungsgesetze," *Zeitschrift für Mathematik und Physik*, Vol. 58, 1909, pp. 186–191.

Viscoelastic Responses of Finite Bodies by Quadrature Form of Correspondence Principle[1]

G. Dasgupta[2]

Alternative forms of the elastic-viscoelastic analogy for numerically obtained frequency response functions have been reported for solids of similarly and dissimilarly viscoelastic in bulk and shear in [1, 2], respectively. It is herein demonstrated that the same integrals can be numerically evaluated to obtain viscoelastic responses of finite bodies even though the harmonic response functions have singularities at the resonance frequencies. Crucial aspects of the algorithm regarding the truncation of numerical quadrature in the neighborhood of the poles are addressed in this Note.

Introduction

The frequency response functions for field variables, such as stresses, displacements, etc., of mechanical systems of practical engineering interest, are generally computed with time harmonic inputs using computer codes based on spatial discretization methods. These functions grow indefinitely at the resonance frequencies for bounded elastic systems, as depicted in Fig. 1. In fact, it is customary to undertake a separate eigenvalue search to evaluate numerically the resonance frequencies to a satisfactory degree of accuracy. For the purpose of design-analysis it is essential to obtain the frequency response functions with various damping characteristics of the system. The classical form for the elastic-viscoelastic analogy cannot be employed directly since a closed-form solution for the response function is seldom available for bodies of arbitrary shapes. It is, therefore, computationally economical to implement the numerical form of the elastic-viscoelastic correspondence principle rather than perform fresh computations of the entire system with different damping properties.

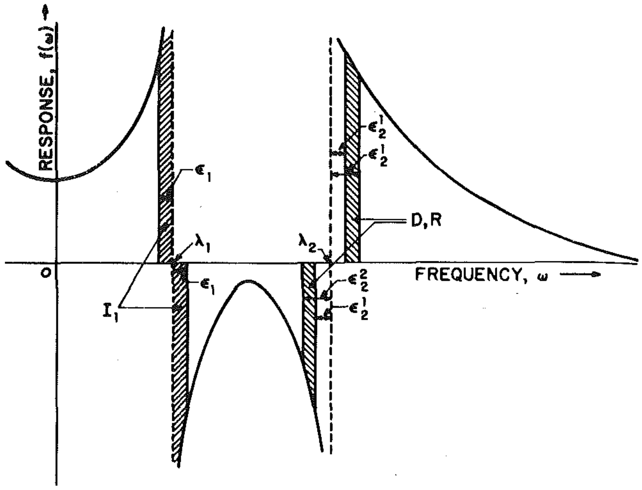

Fig. 1 Elastic frequency response function with resonance poles

The form of the quadrature expressions in [1, 2] suggests that the poles, which are introduced by the kernel to transform the elastic solutions to the viscoelastic domain, will be inside the bottom half of the complex plane. For infinite and semi-infinite bodies the response functions decay rapidly as the frequency increases indefinitely. These functions are also smooth and bounded. There is no computational difficulty encountered in implementing the numerical integration along the real line, say by employing a Simpson-type rule. However, for finite bodies the response functions will have singularities in the form of poles at the resonant frequencies, refer to Fig. 1. A straightforward numerical integration in the neighborhood of the poles on the real axis can incur undesirable computational errors. A pertinent step in this context is to determine the contribution of the kernel in the computation of the residue arising out of the resonance poles. The objective of this Note is to demonstrate that reliable viscoelastic responses can still be obtained via the quadrature forms of the correspondence principle if adequate care is taken to select the limits of the numerical integration in the neighborhood of the resonance poles. The local antisymmetry of frequency response functions yields zero net contribution when the quadrature is interpreted as the Cauchy principal value. The analysis is presented in the following section.

Effects of Poles

The kernels for the alternative representations of the elastic-viscoelastic correspondence principle for complex shear modulus [1], and for the complex Poisson's ratio [2], associated with solids similarly and dissimilarly viscoelastic in bulk and shear, respectively, have very similar structures. In this Note only the first case, i.e., with a frequency-dependent complex shear modulus, μ^*, is illustrated for brevity. A general nondimensional elastic frequency response function is indicated by $f(\omega)$, in which ω is the nondimensional frequency of excitation associated with the elastic shear modulus μ. An n-degree-of-freedom system has $2n$ real resonance frequencies at $\pm \lambda_j$, $j = 1$ to n. It will be assumed, without any loss in generality, that the frequency response function can be represented in the following form:

$$f(\omega) = F(\omega)/\prod_{j=1}^{n} \{\omega^2 - \lambda_j{}^2\} \qquad (1)$$

in which $F(\omega)$ is an infinitely smooth real function. It is recognized in the aforementioned form that the only singularities for the frequency response function are due to the resonance frequencies and they occur symmetrically about the origin.

Now the nondimensional viscoelastic response function $f^*(\omega)$ can be obtained in the form

$$\begin{aligned} f^*(\omega) &= f(\omega^*) \quad \text{[classical analogy]} \\ &= \int_{-\infty}^{\infty} f(\omega) \cdot K(\omega, \alpha, \beta) d\omega \quad \text{[alternative analogy]} \qquad (2) \end{aligned}$$

---

[1] Research is sponsored by a grant of the National Science Foundation ENV77-22524.

[2] Assistant Professor of Civil Engineering and Engineering Mechanics, Columbia University, New York, N.Y. Mem. ASME.

Manuscript received by ASME Applied Mechanics Division, June, 1980; final revision, September, 1980.

$= \dot{\phi}_0(1 + \dot{\theta}'_0)$ when $t' = -\dot{\theta}'_0/1 + \dot{\theta}'_0$. After this time the two bodies rotate with no relative motion. We see that the behavior is quite different in Cases 2 and 3.

Acknowledgment

The authors would like to thank Prof. L. E. Goodman for pointing out that the inequality $\alpha < 1$ is similar to the ones studied in [3, 4].

References

1 Wilms, E.V., and Cohen, H., "A Two-Degree-of-Freedom System With Coulomb Bearing Friction," ASME JOURNAL OF APPLIED MECHANICS, Vol. 46, 1979, pp. 217–218.

2 Wilms, E.V., and Cohen, H., "Displacement, Velocity, and Acceleration Dependent Damping in a Two-Degree-of-Freedom System," *Journal of Applied Mathematics and Physics* (*ZAMP*), Vol. 30, 1979, pp. 533–540.

3 Lecornu, L., "Sur le frottement de glissement," *Comptes Rendus*, Vol. 140, 1905, pp. 635–637.

4 Klein, F., "Zu Painleve's Kritik der Coulombschen Reibungsgesetze," *Zeitschrift für Mathematik und Physik*, Vol. 58, 1909, pp. 186–191.

Viscoelastic Responses of Finite Bodies by Quadrature Form of Correspondence Principle[1]

G. Dasgupta[2]

Alternative forms of the elastic-viscoelastic analogy for numerically obtained frequency response functions have been reported for solids of similarly and dissimilarly viscoelastic in bulk and shear in [1, 2], respectively. It is herein demonstrated that the same integrals can be numerically evaluated to obtain viscoelastic responses of finite bodies even though the harmonic response functions have singularities at the resonance frequencies. Crucial aspects of the algorithm regarding the truncation of numerical quadrature in the neighborhood of the poles are addressed in this Note.

Introduction

The frequency response functions for field variables, such as stresses, displacements, etc., of mechanical systems of practical engineering interest, are generally computed with time harmonic inputs using computer codes based on spatial discretization methods. These functions grow indefinitely at the resonance frequencies for bounded elastic systems, as depicted in Fig. 1. In fact, it is customary to undertake a separate eigenvalue search to evaluate numerically the resonance frequencies to a satisfactory degree of accuracy. For the purpose of design-analysis it is essential to obtain the frequency response functions with various damping characteristics of the system. The classical form for the elastic-viscoelastic analogy cannot be employed directly since a closed-form solution for the response function is seldom available for bodies of arbitrary shapes. It is, therefore, computationally economical to implement the numerical form of the elastic-viscoelastic correspondence principle rather than perform fresh computations of the entire system with different damping properties.

The form of the quadrature expressions in [1, 2] suggests that the poles, which are introduced by the kernel to transform the elastic solutions to the viscoelastic domain, will be inside the bottom half of the complex plane. For infinite and semi-infinite bodies the response functions decay rapidly as the frequency increases indefinitely. These functions are also smooth and bounded. There is no computational difficulty encountered in implementing the numerical integration along the real line, say by employing a Simpson-type rule. However, for finite bodies the response functions will have singularities in the form of poles at the resonant frequencies, refer to Fig. 1. A straightforward numerical integration in the neighborhood of the poles on the real axis can incur undesirable computational errors. A pertinent step in this context is to determine the contribution of the kernel in the computation of the residue arising out of the resonance poles. The objective of this Note is to demonstrate that reliable viscoelastic responses can still be obtained via the quadrature forms of the correspondence principle if adequate care is taken to select the limits of the numerical integration in the neighborhood of the resonance poles. The local antisymmetry of frequency response functions yields zero net contribution when the quadrature is interpreted as the Cauchy principal value. The analysis is presented in the following section.

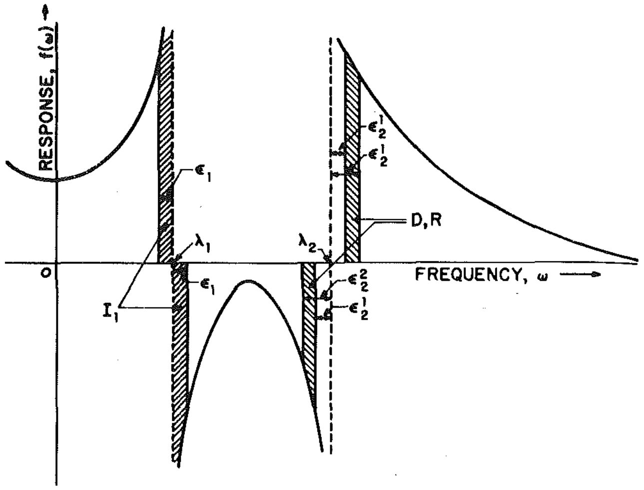

Fig. 1 Elastic frequency response function with resonance poles

Effects of Poles

The kernels for the alternative representations of the elastic-viscoelastic correspondence principle for complex shear modulus [1], and for the complex Poisson's ratio [2], associated with solids similarly and dissimilarly viscoelastic in bulk and shear, respectively, have very similar structures. In this Note only the first case, i.e., with a frequency-dependent complex shear modulus, μ^*, is illustrated for brevity. A general nondimensional elastic frequency response function is indicated by $f(\omega)$, in which ω is the nondimensional frequency of excitation associated with the elastic shear modulus μ. An n-degree-of-freedom system has $2n$ real resonance frequencies at $\pm\lambda_j$, $j = 1$ to n. It will be assumed, without any loss in generality, that the frequency response function can be represented in the following form:

$$f(\omega) = F(\omega)/\prod_{j=1}^{n}\{\omega^2 - \lambda_j{}^2\} \qquad (1)$$

in which $F(\omega)$ is an infinitely smooth real function. It is recognized in the aforementioned form that the only singularities for the frequency response function are due to the resonance frequencies and they occur symmetrically about the origin.

Now the nondimensional viscoelastic response function $f^*(\omega)$ can be obtained in the form

$$f^*(\omega) = f(\omega^*) \quad \text{[classical analogy]}$$

$$= \int_{-\infty}^{\infty} f(\omega)\cdot K(\omega, \alpha, \beta)d\omega \quad \text{[alternative analogy]} \qquad (2)$$

---

[1] Research is sponsored by a grant of the National Science Foundation ENV77-22524.

[2] Assistant Professor of Civil Engineering and Engineering Mechanics, Columbia University, New York, N.Y. Mem. ASME.

Manuscript received by ASME Applied Mechanics Division, June, 1980; final revision, September, 1980.

$$\equiv \int_{-\infty}^{\infty} G(\omega)d\omega, \text{ say} \qquad (2)\ (Cont.)$$

in which $\omega^* = \sqrt{[\mu^*/\mu]}\cdot\omega = \alpha - i\beta;\ \alpha, \beta > 0, i = \sqrt{-1}$.

The kernel, $K(\omega, \alpha, \beta)$, is given by

$$K(\omega, \alpha, \beta) = \frac{-\beta}{\pi\{\beta^2 + [\alpha - \omega]^2\}}$$

and is defined on the bottom half of the complex plane. The integral in (2) when interpreted as the Cauchy principal value can accommodate the singularities produced by the form of the frequency response function in (1). The error due to truncation in the neighborhood of a resonant singularity, λ_j is

$$I_j = \int_{\lambda_j-\epsilon_j}^{\lambda_j+\epsilon_j} f(\omega) \cdot K(\omega, \alpha, \beta)d\omega$$

This is evaluated as a line integral along a semicircular arc of radius ϵ_j centered at λ_j on the lower half of the complex plane leading to

$$I_j = \text{Real }[(i/2\ \lambda_j) \cdot Q_j]$$

in which

$$Q_j = \frac{F(\lambda_j) \cdot K(\lambda_j, \alpha, \beta}{\prod_{k \neq j}^{n} (\lambda_j{}^2 - \lambda_k{}^2)}$$

Thus, from the foregoing two equations, I_j is an imaginary number; hence, zero contribution of the kernel is due to a resonant frequency. The fact that a numerical scheme is possible employing the quadrature representation (2) to compute the viscoelastic response is thus established.

Error Estimation

In a numerical evaluation of the integral in expression (2) the computation is to be terminated at a distance ϵ from the pole. It is, therefore, desirable to obtain an error bound for such a truncation. The integral in (2) is examined between two closely spaced truncation points, as illustrated in Fig. 1, $\epsilon_j{}^1$ and $\epsilon_j{}^2$, $\epsilon_j{}^2 > \epsilon_j{}^1$, in the neighborhood of a pole λ_j, and will be indicated by D_j. As dictated by the Cauchy principal value definition the sum is computed from either side of the pole. This leads to

$$D_j = \frac{Q_j}{2\lambda_j} \log \frac{(2\lambda_j + \epsilon_j{}^1)\,(2\lambda_j - \epsilon_j{}^2)}{(2\lambda_j + \epsilon_j{}^2)\,(2\lambda_j - \epsilon_j{}^1)}$$

The limiting value of the aforementioned expression as $\epsilon_j{}^1$ tends to 0 and $\epsilon_j{}^2$ tends to ϵ_j is

$$R_j = \frac{Q_j}{2\lambda_j} \log \frac{(2\lambda_j - \epsilon_j)}{(2\lambda_j + \epsilon_j)}$$

and the error term

$$e(\lambda) = \Sigma R_j(\lambda_j) \qquad \text{[for all poles]}$$

This suggests that in order to improve upon the accuracy the contribution of the kernel in the neighborhood of the singularity, $e(\lambda)$, could be added to the numerical sum with truncated limits.

Conclusions

The alternative quadrature form of the elastic-viscoelastic analogy is formally extended to account for the singularities of the frequency response function pertaining to bounded elastic continua. It has been demonstrated that leaving equal intervals of the real axis on either side of the poles (due to the resonance phenomenon) errors due to numerical quadrature can be avoided. It is further illustrated that an estimated compensation due to the truncation can be incorporated in the viscoelastic responses so obtained by employing a numerical integration. Thus the alternative form of (2) can be reduced to

$$f^*(\omega) = \Sigma\,\{R_j(\lambda_j) + R_j(-\lambda_j) + T_j\}$$

in which

$$T_j = \int_{-\lambda_{j+1}+\epsilon}^{-\lambda_j-\epsilon} G(\omega)d\omega + \int_{\lambda_j-\epsilon}^{\lambda_{j+1}-\epsilon} G(\omega)d\omega$$

with the anticipation that λ_{n+1} is infinity (i.e., numerically set to a large number).

The aforementioned quadrature formula avoids the singularities on the real axis and contains an estimated correction factor. The form suggests that the expression holds for a more relaxed condition on the elastic frequency response function, $f(\omega)$. Piecewise continuous functions with finite jumps may be allowed between the resonant poles in the description of $f(\omega)$; even then [1, 2] remain valid.

Acknowledgment

The author wishes to thank Dr. Richard M. Christensen of the Lawrence Livermore Laboratory, Livermore, Calif., for pointing out the necessity of the present investigation. The suggestions and advice of Prof. Morton B. Friedman of Columbia University, New York, are greatly appreciated.

References

1 Dasgupta, G., and Sackman, J. L., "An Alternative Representation of the Elastic-Viscoelastic Correspondence Principle for Harmonic Oscillations," ASME JOURNAL OF APPLIED MECHANICS, Vol. 44, Mar. 1977, pp. 57–60.

2 Dasgupta, G., and Sackman, J. L., "A Quadrature Representation of the Viscoelastic Analogy in the Frequency Domain," ASME JOURNAL OF APPLIED MECHANICS, Vol. 45, Dec. 1978, pp. 955–956.

How to Optimally Support a Plate

W. H. Yang[1]

In practical applications, plates are often not supported along their boundaries. Properly located interior supports can greatly increase the load-carrying capacity of a plate. The optimal locations of N point symmetrical support for a uniformly loaded circular plate are calculated to substantiate the claim. The solutions are obtained for $1 \leq N \leq \infty$ under the theory of limit analysis of plates. The collapse load in each case is maximized by a search for the optimal support location.

The Problem

Optimal structural design [1] including optimal load and support distributions are nonlinear problems. Plasticity [2] of materials plays an important role in the optimal solutions. The limit analysis for plates is used in this Note as the basis such that the collapse load as a measure of load-carrying capacity of a plate is maximized by a search of optimal support location.

The problem considered is a uniformly loaded circular plate with a constant yield moment M_0, resting on a set of symmetrically located point supports. We seek the optimal support location in terms of the distance, d, from a support to the center of the plate such that the limit load q_0 is maximized.

The number, N, of supports starts with one at $d = 0$, and increases to ∞ as the points approach a line support along a circle of optimal radius d. For each N, the optimal support location and the maximum limiting load q_L^* are obtained.

---

[1] Department of Mechanical Engineering and Applied Mechanics, The University of Michigan, Ann Arbor, Mich. 48109. Mem. ASME.

Manuscript received by ASME Applied Mechanics Division, December, 1979; final revision, October, 1980.

$$\equiv \int_{-\infty}^{\infty} G(\omega)d\omega, \text{ say} \qquad (2)\ (Cont.)$$

in which $\omega^* = \sqrt{[\mu^*/\mu]}\cdot\omega = \alpha - i\beta;\ \alpha, \beta > 0,\ i = \sqrt{-1}$.

The kernel, $K(\omega, \alpha, \beta)$, is given by

$$K(\omega, \alpha, \beta) = \frac{-\beta}{\pi\{\beta^2 + [\alpha - \omega]^2\}}$$

and is defined on the bottom half of the complex plane. The integral in (2) when interpreted as the Cauchy principal value can accommodate the singularities produced by the form of the frequency response function in (1). The error due to truncation in the neighborhood of a resonant singularity, λ_j is

$$I_j = \int_{\lambda_j-\epsilon_j}^{\lambda_j+\epsilon_j} f(\omega)\cdot K(\omega, \alpha, \beta)d\omega$$

This is evaluated as a line integral along a semicircular arc of radius ϵ_j centered at λ_j on the lower half of the complex plane leading to

$$I_j = \text{Real}\,[(i/2\,\lambda_j)\cdot Q_j]$$

in which

$$Q_j = \frac{F(\lambda_j)\cdot K(\lambda_j, \alpha, \beta}{\prod_{k\neq j}^{n} (\lambda_j{}^2 - \lambda_k{}^2)}$$

Thus, from the foregoing two equations, I_j is an imaginary number; hence, zero contribution of the kernel is due to a resonant frequency. The fact that a numerical scheme is possible employing the quadrature representation (2) to compute the viscoelastic response is thus established.

Error Estimation

In a numerical evaluation of the integral in expression (2) the computation is to be terminated at a distance ϵ from the pole. It is, therefore, desirable to obtain an error bound for such a truncation. The integral in (2) is examined between two closely spaced truncation points, as illustrated in Fig. 1, $\epsilon_j{}^1$ and $\epsilon_j{}^2$, $\epsilon_j{}^2 > \epsilon_j{}^1$, in the neighborhood of a pole λ_j, and will be indicated by D_j. As dictated by the Cauchy principal value definition the sum is computed from either side of the pole. This leads to

$$D_j = \frac{Q_j}{2\lambda_j} \log \frac{(2\lambda_j + \epsilon_j{}^1)\,(2\lambda_j - \epsilon_j{}^2)}{(2\lambda_j + \epsilon_j{}^2)\,(2\lambda_j - \epsilon_j{}^1)}$$

The limiting value of the aforementioned expression as $\epsilon_j{}^1$ tends to 0 and $\epsilon_j{}^2$ tends to ϵ_j is

$$R_j = \frac{Q_j}{2\lambda_j} \log \frac{(2\lambda_j - \epsilon_j)}{(2\lambda_j + \epsilon_j)}$$

and the error term

$$e(\lambda) = \Sigma R_j(\lambda_j) \qquad [\text{for all poles}]$$

This suggests that in order to improve upon the accuracy the contribution of the kernel in the neighborhood of the singularity, $e(\lambda)$, could be added to the numerical sum with truncated limits.

Conclusions

The alternative quadrature form of the elastic-viscoelastic analogy is formally extended to account for the singularities of the frequency response function pertaining to bounded elastic continua. It has been demonstrated that leaving equal intervals of the real axis on either side of the poles (due to the resonance phenomenon) errors due to numerical quadrature can be avoided. It is further illustrated that an estimated compensation due to the truncation can be incorporated in the viscoelastic responses so obtained by employing a numerical integration. Thus the alternative form of (2) can be reduced to

$$f^*(\omega) = \Sigma\,\{R_j(\lambda_j) + R_j(-\lambda_j) + T_j\}$$

in which

$$T_j = \int_{-\lambda_{j+1}+\epsilon}^{-\lambda_j-\epsilon} G(\omega)d\omega + \int_{\lambda_j-\epsilon}^{\lambda_{j+1}-\epsilon} G(\omega)d\omega$$

with the anticipation that λ_{n+1} is infinity (i.e., numerically set to a large number).

The aforementioned quadrature formula avoids the singularities on the real axis and contains an estimated correction factor. The form suggests that the expression holds for a more relaxed condition on the elastic frequency response function, $f(\omega)$. Piecewise continuous functions with finite jumps may be allowed between the resonant poles in the description of $f(\omega)$; even then [1, 2] remain valid.

Acknowledgment

The author wishes to thank Dr. Richard M. Christensen of the Lawrence Livermore Laboratory, Livermore, Calif., for pointing out the necessity of the present investigation. The suggestions and advice of Prof. Morton B. Friedman of Columbia University, New York, are greatly appreciated.

References

1 Dasgupta, G., and Sackman, J. L., "An Alternative Representation of the Elastic-Viscoelastic Correspondence Principle for Harmonic Oscillations," ASME JOURNAL OF APPLIED MECHANICS, Vol. 44, Mar. 1977, pp. 57–60.

2 Dasgupta, G., and Sackman, J. L., "A Quadrature Representation of the Viscoelastic Analogy in the Frequency Domain," ASME JOURNAL OF APPLIED MECHANICS, Vol. 45, Dec. 1978, pp. 955–956.

How to Optimally Support a Plate

W. H. Yang[1]

In practical applications, plates are often not supported along their boundaries. Properly located interior supports can greatly increase the load-carrying capacity of a plate. The optimal locations of N point symmetrical support for a uniformly loaded circular plate are calculated to substantiate the claim. The solutions are obtained for $1 \leq N \leq \infty$ under the theory of limit analysis of plates. The collapse load in each case is maximized by a search for the optimal support location.

The Problem

Optimal structural design [1] including optimal load and support distributions are nonlinear problems. Plasticity [2] of materials plays an important role in the optimal solutions. The limit analysis for plates is used in this Note as the basis such that the collapse load as a measure of load-carrying capacity of a plate is maximized by a search of optimal support location.

The problem considered is a uniformly loaded circular plate with a constant yield moment M_0, resting on a set of symmetrically located point supports. We seek the optimal support location in terms of the distance, d, from a support to the center of the plate such that the limit load q_0 is maximized.

The number, N, of supports starts with one at $d = 0$, and increases to ∞ as the points approach a line support along a circle of optimal radius d. For each N, the optimal support location and the maximum limiting load q_L^* are obtained.

---

[1] Department of Mechanical Engineering and Applied Mechanics, The University of Michigan, Ann Arbor, Mich. 48109. Mem. ASME.

Manuscript received by ASME Applied Mechanics Division, December, 1979; final revision, October, 1980.

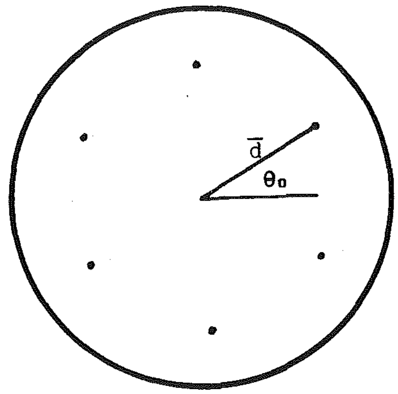

Fig. 1 **Circular plate and support configuration**

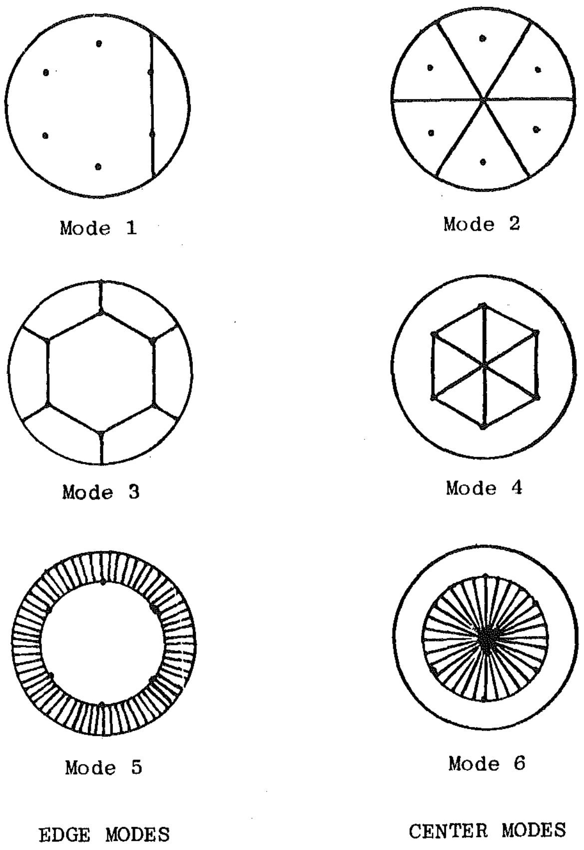

Fig. 2 **Collapse modes**

The method of analysis involves the standard upper bound formulation and a minimization procedure over a set of test functions or collapse modes. The upper bound formulation begins with the virtual work statement,

$$\iint_D w\nabla \cdot (\nabla \cdot M)dA = q_0 \iint_D wdA \qquad (1)$$

where $M(x, y)$ is a 2×2 moment matrix function in D, $\nabla = (\partial/\partial x, \partial/\partial y)$ is a vector operator and $w(x, y)$ is any kinematically admissible function [4]. If we integrate the left-hand side of (1) by parts using the divergence theorem and denote the scalar product operator of two matrices by: [3], equation (1) can be rewritten as a quotient,

$$q_0(M) = \iint_D M{:}\nabla\nabla wdA \Big/ \iint_D wdA \qquad (2)$$

provided that $\iint_D wdA \neq 0$ and M and w satisfy certain boundary conditions [3]. $w(x, y)$ in (3) is now restricted to a class of functions which satisfy the kinematical boundary conditions and its second derivatives contained in the Hessian matrix $\nabla\nabla w$ are defined in the sense of distributions (such as line delta functions). The functions in this class are continuous and its first derivatives may possess finite jumps.

An upper bound to $q_0(M)$ can be obtained by replacing M in (2) with a constitutively admissible one which is associated with a kinematically admissible w such that they together produce the largest integral in the numerator of (2). For a specific yield function, $\|M\|_2 - M_0 \leq 0$, this upper bound has the form,

$$q_0(M) \leq \iint_D \left\{\left|\frac{\partial^2 w}{\partial \xi^2}\right| + \left|\frac{\partial^2 w}{\partial \eta^2}\right|\right\}|J|d\xi d\eta \Big/ \left|\iint_D w|J|d\xi d\eta\right| = q^*(w) \qquad (3)$$

where $\|M\|_2$ is the Euclidean norm of M, (ξ, η) is the principal coordinate of M along which M is diagonal and J is the Jacobian of the transformation from (x, y) to (ξ, η). $M_0 = 1$ is assumed.

Since $q^*(w)$ is a function of w only, the least upper bound q_L^* can be obtained by minimization in the space of kinematically admissible functions. The mathematical operations described thus far can be written in the form of a minimax problem

$$q_L^* = \min_{\|w\|_1=1} \max_{\|M\|_2=1} \left|\iint_D M{:}\nabla\nabla wdA\right| \qquad (4)$$

where $\|w\|_1 = |\iint_D wdA|$, which is not a norm, only serves to normalize the kinematically admissible functions.

The choice of w in (4) is still very wide. For regularly shaped plates in applications, the possible collapse modes as kinematically admissible functions can often be enumerated. If the complete set of possible collapse modes $\{w_i \mid i = 1, 2, .., I\}$ is identified, the search for minimum of (4) over w is in a finite (I) dimensional space. The problem becomes computationally feasible.

The algorithm used in the next section begins with a set of assumed collapse modes $\{\tilde{w}_i(r, \theta, d)|i = 1, 2, .., I\}$ where (r, θ) is the polar coordinate and d the radial position of a support is regarded as a parameter. Each mode produces necessarily an upper bound to q_L^* such that

$$q_L^* \leq q_i^+ (d) = \max_{\|M\|_2=1} \left|\iint_D M{:}\nabla\nabla\tilde{w}_i(d)dA\right|, \quad \iint_D \tilde{w}_i dA = 1 \qquad (5)$$

The minimum envelope of the set $\{q_i^+|i = 1, 2, .., I\}$ is a function of d. The maximum of the envelope function gives the collapse load at the optimal d. Formally we can summarize the entire procedure described in this section as a max-min-max problem

$$q_L^* = \max_d \min_i \max_{\|M\|_2=1} \left|\iint_D M{:}\nabla\nabla\tilde{w}_i dA\right|, \quad \iint_D \tilde{w}_i dA = 1 \qquad (6)$$

assuming that $\{w_i|i = 1, 2, .., I\}$ is the complete set of all possible collapse modes.

Optimal Solutions

Let the dimensions be normalized with respect to the radius of the plate, a. The dimensionless support distance $\bar{d} = d/a$ and the angle $\theta_0 = \pi/N$ are shown in Fig. 1. Six possible collapse modes are shown in Fig. 2. In each mode, the $\nabla\nabla\tilde{w}$ assumes either a jump discontinuity such that

$$\|\nabla\nabla\tilde{w}\|_2 = |[\partial\tilde{w}/\partial n]| \qquad (7)$$

along some yield lines with normal n or a constant curvature on a conical surface such that

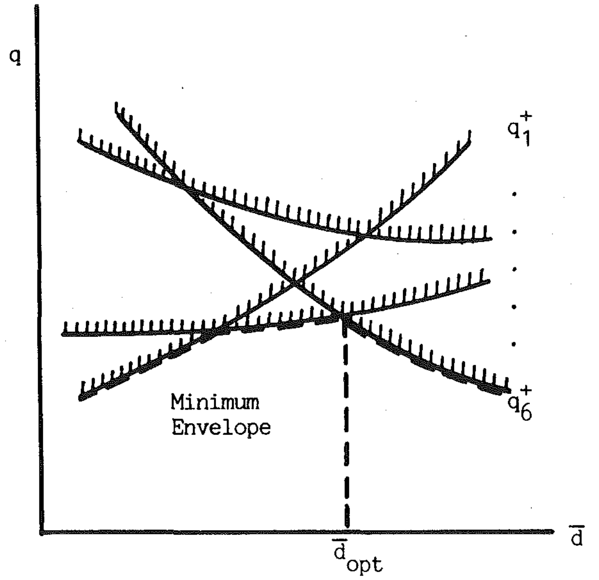

Fig. 3 Minimum envelope

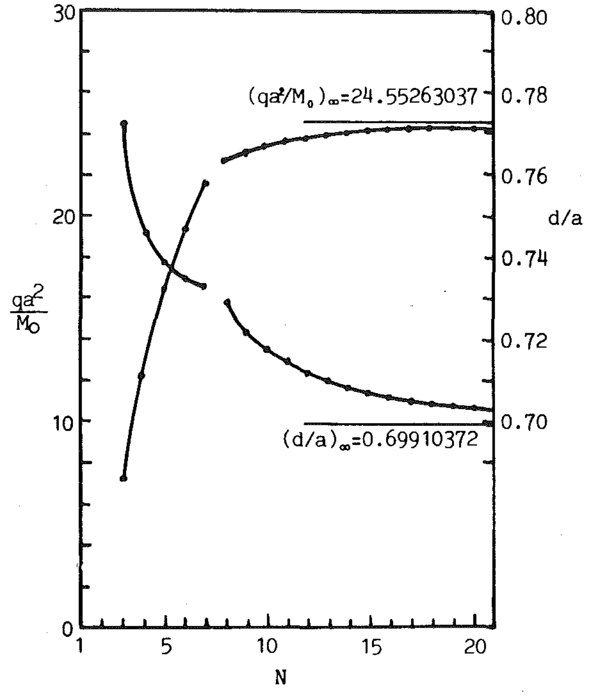

Fig. 4 Optimal solutions

$$\|\nabla\nabla\tilde{w}\|_2 = \left|\frac{\Delta}{r}\right| \tag{8}$$

where [ ] denotes the jump and Δ is the height of the cone. For the remaining area $\nabla\nabla w \equiv 0$.

The solution for each mode can be obtained by integrating (3). They are functions of $\bar{d}$ and N.

$$\begin{aligned}
\bar{q}_1^+ &= \mu \bigg/ \left[\frac{1}{3}\mu^3 - \frac{\lambda}{2}\left(\frac{\pi}{2} - \sin^{-1}\lambda - \lambda\mu\right)\right] \\
\bar{q}_2^+ &= \sin\theta_0 \bigg/ \left(\frac{1}{2}\bar{d}\theta_0 - \frac{1}{3}\sin\theta_0\right) \\
\bar{q}_3^+ &= 6[\bar{d} + (1-\bar{d})\cos\theta_0] \bigg/ \left(\bar{d}^3\cos^2\theta_0 - 3\bar{d}\,\frac{\theta_0\cos\theta_0}{\sin\theta_0} + 2\right) \\
\bar{q}_4^+ &= 12/(\bar{d}^2\cos^2\theta_0) \\
\bar{q}_5^+ &= 6/(\bar{d}^3 - 3\bar{d} + 2) \\
\bar{q}_6^+ &= 12/\bar{d}^2
\end{aligned} \tag{9}$$

where $\lambda = \bar{d}\cos\theta_0$, $\mu = \sqrt{1-\lambda^2}$, and $\bar{q}_i^+ = q_i^+ a^2/M_0$.

The least upper bound solution $\bar{q}(\bar{d})$ over the set $\{q_i^+\}$

$$\bar{q}(\bar{d}) = \min_i \{\bar{q}_i^+(\bar{d})\} \tag{10}$$

is the minimum envelope shown in Fig. 3 schematically. The optimal solution can be obtained by a one-dimensional search on $\bar{q}(\bar{d})$.

For each N, $\bar{q}_{opt}$ and $\bar{d}_{opt}$ are computed. $\bar{q}_{opt}$ is always the intersection of two or more modal solutions $\bar{q}_i^+$. Some modal solutions approach ∞ at $\bar{d} = 0$ or $\bar{d} = 1$. These points which are of little interest, should be avoided in the computation.

The $\bar{q}_{opt}$ and the associated $\bar{d}_{opt}$ are shown in Fig. 4 as functions of N. These are discrete functions. The curves between the function values only serve to connect the solutions with common mode combination. For $N = 1$, modes 1, 2, 3, 5 intersect. The $N = 2$ case involves modes 1 and 3. For $N = 3$ through $N = 7$, modes 2 and 3 prevail. For $N \geq 8$, the active modes are 3 and 6 with additional modes 4 and 5 as $N \rightarrow \infty$. The intersection of $\bar{q}_5^+$ and $\bar{q}_6^+$ gives the asymptotic solutions

$$\begin{aligned}
(\bar{q}_{opt})_\infty &= 24.55263037 \\
(\bar{d}_{opt})_\infty &= 0.69910372
\end{aligned} \tag{11}$$

The gaps between the connecting curves indicate mode changes.

Final Remark

Internal supports greatly increase the load capacity of a plate. A mere three point support optimally located provides 24.3 percent more load capacity than a simply supported plate along its entire boundary. A plate with a ring support of radius $r = (\bar{d}_{opt})_\infty$ can ultimately carry more than twice the load of the same plate clamped along its boundary and more than four times of a simply support one.

Intuitively, the benefit of internal support is obvious as many structures are built with them. But the exact locations of the supports to achieve maximum benefit are not known. Experimentally, these locations are not easy to find. First of all, the tests are destructive. Many specimens are needed to find the location for just one case. Second, the minimum envelope forms a cusp at $\bar{d}_{opt}$. The maximum load capacity falls sharply away from that point.

References

1 Niordson, F. L., and Peterson, P., "A Review of Optimal Structure Design," Report No. 31, Danish Center for Applied Mathematics and Mechanics, Tech University, Denmark, 1972.

2 Yang, W. H., "On a Class of Optimization Problem for Framed Structures," *Comp. Meth. Applied Mechanics Eng.*, Vol. 15, 1978, pp. 85–97.

3 Yang, W. H., "Minimization Approach to Limit Solutions of Plates," *Comp. Meth. Applied Mechanics Eng.*, Vol. 28, 1981.

4 Hodge, P. G., Jr., *Limit Analysis of Rotationally Symmetric Plates and Shells,* Prentice-Hall, Englewood Cliffs, N. J., 1963.

Journal of Applied Mechanics Discussion

An Application of Mixture Theory to Particulate Sedimentation[1]

E. M. Tory[2] and D. K. Pickard.[3] Constitutive equations for dispersions suffer from an inability to describe individual behavior. Even uniform spheres show a tremendous diversity of velocities, especially in dilute dispersions where cluster settling is important. (Much of the massive evidence of this diversity is summarized in [1].) Only the mean is important in many applications [2, 3], but variability and autocorrelation of velocity are necessary to explain diffuse interfaces, depletion of upper levels, and the difference between the mean velocity and that of the interface [4].

The variability of particle velocity occurs at all concentrations [1–3]. It does not emerge from the instability of some ordered arrangement, but is born with the random initial dispersion. Slurries may be uniform in the large, but their densities vary considerably from region to region. In very dilute dispersions, it is the paired particles which settle most quickly. The nonuniformity of spacing, reflected in variability of velocity, leads to a decrease in velocity (with increasing concentration) which is proportional to ϕ rather than $\phi^{1/3}$ as it would be for any ordered arrangement [5]. At $\phi \simeq 0.001$, the mean sedimentation velocity increases with time [6] as the suspension evolves from its original randomness to a "demixed" state [6]. The mechanism proposed for this "demixing" is a gradual buildup of cluster size as pairs overtake singles, triplets overtake pairs and singles, etc. [7]. In these instances and at higher concentrations, it is precisely the dense regions which have the highest velocity. Particle flux occurs predominantly in the denser regions and return flow in the regions of lower density. This effect is so great that mean velocities for $0.001 < \phi < 0.03$ exceed the Stokes velocity [8, 9]. At higher concentrations, there is more interaction among particles [1]; associations are more transient [1] and times to traverse a fixed distance reflect this averaging effect by becoming much less variable [9]. The variability and autocorrelation of velocity (which arise from the formation, persistence, and breakup of clusters) are incorporated in a Markov model for sedimentation [1–4].

The alleged instability of sedimentation under small perturbations in concentration arises from the assumption that $u = f(\phi)$ where f is monotone decreasing. Neither the assumption nor the view of perturbations holds in general. Though fluctuations in small regions can be substantial, global concentrations in a cylindrical section of a large tank change only slightly [3]. With small cylinder/particle diameter-ratios, global fluctuations are much larger [3] and there is little opportunity for cluster settling because wall effects for large clusters are huge [8]. Thus small columns provide the best opportunity to observe instabilities. The column which verified Jackson's predictions [10] had a diameter ratio of only 20.

Despite the caveats just noted, there is ample scope for the application of a deterministic version of a stochastic model for sedimentation. We commend the authors for smoothly merging the gravitational and diffusive aspects of sedimentation into a useful form.

References

1 Tory, E. M., and Pickard, D. K., "A Three-Parameter Markov Model for Sedimentation," *Canadian Journal of Chemical Engineering,* Vol. 55, 1977, pp. 655–665.

2 Pickard, D. K., and Tory, E. M., "A Markov Model for Sedimentation," *Journal of Mathematical Analysis and Applications,* Vol. 60, 1977, pp. 349–369.

3 Pickard, D. K., and Tory, E. M., "Experimental Implications of a Markov Model for Sedimentation," *Journal of Mathematical Analysis and Applications,* Vol. 72, 1979, pp. 150–176.

4 Tory, E. M., and Pickard, D. K., "Extensions and Refinements of a Markov Model for the Slow Sedimentation of Small Particles in a Viscous Fluid," Canadian Symposium on Fluid Dynamics, June 8–12, 1980, University of Calgary, Calgary, Alberta.

5 Batchelor, G. K., "Sedimentation in a Dilute Dispersion of Spheres," *Journal of Fluid Mechanics,* Vol. 52, 1972, pp. 245–268.

6 Koglin, B., "Dynamic Equilibrium of Settling Velocity Distribution in Dilute Suspensions of Spherical and Irregularly Shaped Particles," *Proceedings of the Conference on Particle Technology,* Chicago, 1973, pp. 265–271.

7 Kamel, M. T., Tory, E. M., and Jodrey, W. S., "The Distribution of *k*th Nearest Neighbors and Its Application to Cluster Settling in Dispersions of Equal Spheres," *Powder Technology,* Vol. 24, 1979, pp. 19–34.

8 Koglin, B., "Untersuchungen zur Sedimentationsgeschwindigkeit in niedrig konzentrierten Suspensionen," PhD Dissertation, Universität Karlsruhe, 1971.

9 Kaye, B. H., and Boardman, R. P., "Cluster Formation in Dilute Suspensions," *Proceedings of the Symposium on Interaction Between Fluids and Particles,* Institution of Chemical Engineers, 1962, pp. 17–21.

10 Jackson, R., "The Mechanics of Fluidized Beds: Part I: The Stability of the State of Uniform Fluidisation," *Transactions of the Institution of Chemical Engineers,* Vol. 41, 1963, pp. 13–28.

Authors' Closure

The authors wish to thank Professors Tory and Pickard for their interesting comments and for bringing to our attention their work on a statistical theory of sedimentation. We anticipate that the continuum and statistical approaches to the analysis of sedimentation will both continue to be useful. The field of gas dynamics provides an excellent analogy. The molecules of a gas also exhibit a "tremendous diversity of velocities," and large local variations in concentration as well, yet this has not prevented the continuum theories of gases from providing useful predictions when characteristic dimensions are large compared to the mean free path. The statistical theory of gases also continues to provide new results and insight, particularly at low densities. Neither approach shows the slightest tendency to supplant the other.

In our paper we applied a very simple continuum theory for a liquid-particle mixture to the problem of particle sedimentation. We included concentration gradients in the theory, which several authors

---

[1] By C. D. Hill, A. Bedford, and D. S. Drumheller, and published in the June, 1980, issue of ASME JOURNAL OF APPLIED MECHANICS, Vol. 47, pp. 261–265.

[2] Professor of Mathematics and Computer Science, Mount Allison University, Sackville, N. B., E0A 3C0, Canada.

[3] Associate Professor of Statistics, Harvard University, Cambridge, Mass. 02138.

have conjectured—and we concur—can model the effects of particle-particle impacts, or diffusivity. Given the simplicity of the theory, we consider the agreement with experiment which we presented in Fig. 2 of our paper to be very encouraging. We regard the relative smoothness of the experimental data that was obtained by Whelan, et al. (reference [29] and Fig. 2 of our paper) to be one indication of the appropriateness of a continuum approach.

Professors Tory and Pickard observe that the simple theory which we have used cannot model such phenomena as the formation and breakup of clusters of particles, which occur particularly at low particle concentrations. Thus the continuum theory which we used would not be expected to be applicable to low concentrations, i.e., in the neighborhood of the cell interface. It is therefore interesting that the prediction of the experimentally observed cell interface position is so accurate (Fig. 3 of our paper).

We note parenthetically that, in addition to the clumping which occurs due to hydrodynamic effects in the sedimentation of inert particles, red blood cells also collect into stacks (*rouleaux*) as a result of as yet undetermined physical or chemical processes. The theory we have used is certainly deficient in not modeling the effects of such clumping. However, in light of the current intense development of continuum theories having internal state variables and microstructural content, we do not believe that such effects are beyond the scope of a continuum theory.

With regard to their comments on our result concerning stability, what we have shown is that the *equations* of the continuum theory are stable under perturbations of the state of uniform sedimentation when the coefficient of the diffusivity term is sufficiently large and are unstable otherwise. (We do not understand their comment about the velocity being assumed to be a monotone decreasing function of the concentration. Our stability result does not depend on such an assumption either explicitly or implicitly.) The perturbations, in order to have meaning in the context of the continuum theory, must have wavelengths which are large compared to the distances between particles. They cannot correspond to the local fluctuations mentioned by Professors Tory and Pickard.

In closing, we reiterate our belief that the statistical and continuum approaches will be mutually complementary in the study of sedimentation.

Constitutive Equations of Elastoplastic Materials With Elastic-Plastic Transition[1]

Y. F. Dafalias.[2] The author presented a constitutive model which falls within the general framework of the "Bounding Surface" plasticity theories [1–6]. It will be instructive if the model can be viewed within this framework and this will be attempted here together with an effort to inform the interested reader about other publications of similar content.

The salient feature of the paper under discussion is that if G represents the inverse plastic modulus associated with the so-called fully plastic state and determined by the consistency condition for the yield surface, the inverse plastic modulus $\tilde{G}$ for points on loading surfaces within the yield surface (subyield states) is given by $\tilde{G} = UG$ for metals, equation (19*a*), and $\tilde{G} = \hat{G}\ (G, U, u)$ for soils, abbreviated symbolic form of equation (19*b*), with $\hat{G}\ (G, 0, u) = 0$ and $\hat{G}\ (G, 1, 0) = G$. The variables U and u change within the range $0 \leq U \leq 1$ and $u \leq 0$ as $0 \leq R \leq 1$, where R represents the ratio of the size of the loading to that of the yield surface.

The foregoing is a particular case of the general formulation in [2–5], where if $\tilde{K} = 1/\tilde{G}$ and $K = 1/G$ a relation of the form $\tilde{K} = \hat{K}\ (K, \delta, \delta_{in})$ was postulated (the notation here is changed slightly to conform with that of the author's). The δ represents the distance in stress space between the stress point within the bounding surface (which is called a yield surface by the author) and a corresponding image point on the bounding surface, and δ_{in} is the value of δ at loading initiation. The $\hat{K}$ satisfies the conditions $\hat{K}\ (K, \delta_{in}, \delta_{in}) = \infty$ and $\hat{K}\ (K, 0, \delta_{in}) = K$, with K always obtained from the consistency condition for the hardening bounding surface. If yield initiates always from the center of the bounding surface and the actual and "image" stress points lie on the same radius emanating from the center [3, 5], δ_{in} represents this radius and one immediately has the correspondence $R \leftrightarrow 1 - (\delta/\delta_{in})$. This particular form of the bounding surface formulation assumes that any stress point within the surface is at a quasi-elastic state, i.e., plastic deformation occurs always for stress rates directed "outward" with respect to the center and elastic unloading for "inward" direction [3, 5, 7]. A finite purely elastic range for any direction can be easily introduced [5] as pointed out also by the author. On that basis and with the aforementioned definition of K, $\tilde{K}$ and correspondence between R and δ/δ_{in}, the author's formulation is entirely equivalent to the bounding surface formulation. In fact, equation (33) of [2] can be recast here as

$$\tilde{K} = K + h\frac{\delta}{\delta_{in} - \delta} \tag{1}$$

with h a material function. For metals $K > 0$ and by writing $h = K\bar{h}$ [2], one has a complete correspondence between equation (19*a*) of the paper and equation (1) with

$$1 + \bar{h}\frac{\delta}{\delta_{in} - \delta} \leftrightarrow U^{-1}(R) \tag{2}$$

The form (1) for metals has been recently interpreted by means of statistical dislocation mechanics [7], and the importance of an associated kinematic hardening rule has been demonstrated by linking it to the "back" residual dislocation stresses, contrary to the author's comment in his discussion about the relative unimportance of such hardening.

Coming now to soils, the form (1) with zero kinematic hardening was used in a series of papers for a critical state bounding surface soil plasticity [3–5] with both qualitative and quantitative predictions of experimental results. The inclusion of $\tilde{G} = 1/\tilde{K}$ in the loading criterion by the author, equation (24) of the paper, in order to account for softening behavior when $\tilde{G} < 0$, has been already presented in [3–5]. In relation to this point observe from equation (1) that with $K < 0$ for a contracting bounding surface and stress ratios above the critical state line (shear loading at heavily overconsolidated state), it is possible to have a $\tilde{K}$ varying from positive to zero to negative and zero again values as δ diminishes and $K \rightarrow 0$ from negative values, indicating unstable softening behavior (rising and falling stress-strain curve) until critical failure [3–5]. Thus, despite the difference in functional form, but not in essence, between equation (19*b*) of the paper and equation (1) the author's model formulation and response for soils is essentially that of a bounding surface formulation.

It is encouraging that Mr. Hashiguchi has independently reached a formulation within the general concept of the bounding surface which seems to offer a unifying approach for the characterization of materials with bounding states. In this sense it is hoped that the present discussion can be proved useful to the interested reader.

References

1 Dafalias, Y. F., and Popov, E. P., "A Model of Nonlinearly Hardening Materials for Complex Loadings," *Acta Mechanica*, Vol. 21, 1975, pp. 173–192.

2 Dafalias, Y. F., and Popov, E. P., "Plastic Internal Variables Formalism of Cyclic Plasticity," ASME JOURNAL OF APPLIED MECHANICS, Vol. 98, 1976, pp. 645–650.

3 Dafalias, Y. F., "A Bounding Surface Plasticity Model," *Proc. 7th Canadian Congress of Applied Mechanics*, Sherbrooke, May 1979, pp. 89–90.

4 Dafalias, Y. F., "A Model for Soil Behavior Under Monotonic and Cyclic Loading Conditions," *Trans. 5th International Conference on Structural Mechanics in Reactor Technology*, Berlin, Aug. 1979, paper K 1/8.

---

[1] By K. Hashiguchi, and published in the June, 1980, issue of the ASME JOURNAL OF APPLIED MECHANICS, Vol. 47, pp. 266–272.

[2] Associate Professor, Department of Civil Engineering, University of California, Davis, Calif. 95616.

have conjectured—and we concur—can model the effects of particle-particle impacts, or diffusivity. Given the simplicity of the theory, we consider the agreement with experiment which we presented in Fig. 2 of our paper to be very encouraging. We regard the relative smoothness of the experimental data that was obtained by Whelan, et al. (reference [29] and Fig. 2 of our paper) to be one indication of the appropriateness of a continuum approach.

Professors Tory and Pickard observe that the simple theory which we have used cannot model such phenomena as the formation and breakup of clusters of particles, which occur particularly at low particle concentrations. Thus the continuum theory which we used would not be expected to be applicable to low concentrations, i.e., in the neighborhood of the cell interface. It is therefore interesting that the prediction of the experimentally observed cell interface position is so accurate (Fig. 3 of our paper).

We note parenthetically that, in addition to the clumping which occurs due to hydrodynamic effects in the sedimentation of inert particles, red blood cells also collect into stacks (*rouleaux*) as a result of as yet undetermined physical or chemical processes. The theory we have used is certainly deficient in not modeling the effects of such clumping. However, in light of the current intense development of continuum theories having internal state variables and microstructural content, we do not believe that such effects are beyond the scope of a continuum theory.

With regard to their comments on our result concerning stability, what we have shown is that the *equations* of the continuum theory are stable under perturbations of the state of uniform sedimentation when the coefficient of the diffusivity term is sufficiently large and are unstable otherwise. (We do not understand their comment about the velocity being assumed to be a monotone decreasing function of the concentration. Our stability result does not depend on such an assumption either explicitly or implicitly.) The perturbations, in order to have meaning in the context of the continuum theory, must have wavelengths which are large compared to the distances between particles. They cannot correspond to the local fluctuations mentioned by Professors Tory and Pickard.

In closing, we reiterate our belief that the statistical and continuum approaches will be mutually complementary in the study of sedimentation.

Constitutive Equations of Elastoplastic Materials With Elastic-Plastic Transition[1]

Y. F. Dafalias.[2] The author presented a constitutive model which falls within the general framework of the "Bounding Surface" plasticity theories [1–6]. It will be instructive if the model can be viewed within this framework and this will be attempted here together with an effort to inform the interested reader about other publications of similar content.

The salient feature of the paper under discussion is that if G represents the inverse plastic modulus associated with the so-called fully plastic state and determined by the consistency condition for the yield surface, the inverse plastic modulus $\tilde{G}$ for points on loading surfaces within the yield surface (subyield states) is given by $\tilde{G} = UG$ for metals, equation (19*a*), and $\tilde{G} = \hat{G}\ (G, U, u)$ for soils, abbreviated symbolic form of equation (19*b*), with $\hat{G}\ (G, 0, u) = 0$ and $\hat{G}\ (G, 1, 0) = G$. The variables U and u change within the range $0 \leq U \leq 1$ and $u \leq 0$ as $0 \leq R \leq 1$, where R represents the ratio of the size of the loading to that of the yield surface.

The foregoing is a particular case of the general formulation in [2–5], where if $\tilde{K} = 1/\tilde{G}$ and $K = 1/G$ a relation of the form $\tilde{K} = \hat{K}\ (K, \delta, \delta_{in})$ was postulated (the notation here is changed slightly to conform with that of the author's). The δ represents the distance in stress space between the stress point within the bounding surface (which is called a yield surface by the author) and a corresponding image point on the bounding surface, and δ_{in} is the value of δ at loading initiation. The $\hat{K}$ satisfies the conditions $\hat{K}\ (K, \delta_{in}, \delta_{in}) = \infty$ and $\hat{K}\ (K, 0, \delta_{in}) = K$, with K always obtained from the consistency condition for the hardening bounding surface. If yield initiates always from the center of the bounding surface and the actual and "image" stress points lie on the same radius emanating from the center [3, 5], δ_{in} represents this radius and one immediately has the correspondence $R \leftrightarrow 1 - (\delta/\delta_{in})$. This particular form of the bounding surface formulation assumes that any stress point within the surface is at a quasi-elastic state, i.e., plastic deformation occurs always for stress rates directed "outward" with respect to the center and elastic unloading for "inward" direction [3, 5, 7]. A finite purely elastic range for any direction can be easily introduced [5] as pointed out also by the author. On that basis and with the aforementioned definition of K, $\tilde{K}$ and correspondence between R and δ/δ_{in}, the author's formulation is entirely equivalent to the bounding surface formulation. In fact, equation (33) of [2] can be recast here as

$$\tilde{K} = K + h\frac{\delta}{\delta_{in} - \delta} \tag{1}$$

with h a material function. For metals $K > 0$ and by writing $h = K\bar{h}$ [2], one has a complete correspondence between equation (19*a*) of the paper and equation (1) with

$$1 + \bar{h}\frac{\delta}{\delta_{in} - \delta} \leftrightarrow U^{-1}(R) \tag{2}$$

The form (1) for metals has been recently interpreted by means of statistical dislocation mechanics [7], and the importance of an associated kinematic hardening rule has been demonstrated by linking it to the "back" residual dislocation stresses, contrary to the author's comment in his discussion about the relative unimportance of such hardening.

Coming now to soils, the form (1) with zero kinematic hardening was used in a series of papers for a critical state bounding surface soil plasticity [3–5] with both qualitative and quantitative predictions of experimental results. The inclusion of $\tilde{G} = 1/\tilde{K}$ in the loading criterion by the author, equation (24) of the paper, in order to account for softening behavior when $\tilde{G} < 0$, has been already presented in [3–5]. In relation to this point observe from equation (1) that with $K < 0$ for a contracting bounding surface and stress ratios above the critical state line (shear loading at heavily overconsolidated state), it is possible to have a $\tilde{K}$ varying from positive to zero to negative and zero again values as δ diminishes and $K \rightarrow 0$ from negative values, indicating unstable softening behavior (rising and falling stress-strain curve) until critical failure [3–5]. Thus, despite the difference in functional form, but not in essence, between equation (19*b*) of the paper and equation (1) the author's model formulation and response for soils is essentially that of a bounding surface formulation.

It is encouraging that Mr. Hashiguchi has independently reached a formulation within the general concept of the bounding surface which seems to offer a unifying approach for the characterization of materials with bounding states. In this sense it is hoped that the present discussion can be proved useful to the interested reader.

References

1 Dafalias, Y. F., and Popov, E. P., "A Model of Nonlinearly Hardening Materials for Complex Loadings," *Acta Mechanica*, Vol. 21, 1975, pp. 173–192.

2 Dafalias, Y. F., and Popov, E. P., "Plastic Internal Variables Formalism of Cyclic Plasticity," ASME JOURNAL OF APPLIED MECHANICS, Vol. 98, 1976, pp. 645–650.

3 Dafalias, Y. F., "A Bounding Surface Plasticity Model," *Proc. 7th Canadian Congress of Applied Mechanics*, Sherbrooke, May 1979, pp. 89–90.

4 Dafalias, Y. F., "A Model for Soil Behavior Under Monotonic and Cyclic Loading Conditions," *Trans. 5th International Conference on Structural Mechanics in Reactor Technology*, Berlin, Aug. 1979, paper K 1/8.

---

[1] By K. Hashiguchi, and published in the June, 1980, issue of the ASME JOURNAL OF APPLIED MECHANICS, Vol. 47, pp. 266–272.

[2] Associate Professor, Department of Civil Engineering, University of California, Davis, Calif. 95616.

5 Dafalias, Y. F., and Herrmann, L. R., "A Bounding Surface Soil Plasticity Model," *Proc. International Symposium on Soils Under Cyclic and Transient Loading*, Swansea, G. N. Pande and O. C. Zienkiewicz, eds., A. A. Balkema, publishers, Jan. 1980, Vol. 1, pp. 335–345.

6 Krieg, R. D., "A Practical Two-Surface Plasticity Theory," ASME JOURNAL OF APPLIED MECHANICS, Vol. 42, 1975, pp. 641–646.

7 Popov, E. P., and Ortiz, M., "Macroscopic and Microscopic Cyclic Metal Plasticity," *Proc. 3rd ASCE/EMD Specialty Conference*, Austin, 1979, Keynote Address.

Journal of Applied Mechanics

Book Reviews

Analysis and Performance of Fiber Composites. By Bhagwan D. Agarwal and Lawrence J. Broutman. John Wiley & Sons, Inc., New York. 1980. Pages xi–355. Price, $24.50.

REVIEWED BY C. W. BERT[1]

As the composite materials field unfolds, there is a need for text and reference books with more diversified viewpoints. Many of the early books were overbalanced in favor of the materials aspects, later books were perhaps overbalanced in favor of the mechanics aspects. This book aims to reach the middle ground between these two viewpoints. Thus it is more mechanics-oriented and less "descriptive" than Broutman and Krock's early text (*Modern Composite Materials,* Addison-Wesley, Reading, Mass., 1967), yet it is definitely oriented more toward materials and less toward structural mechanics than Robert M. Jones' more recent text (*Mechanics of Composite Materials,* McGraw-Hill, New York, 1975).

This book was commissioned and reviewed by the Society of Plastics Engineers and is part of its monograph series. Thus it is understandable that it is perhaps most suitable as a textbook in an introductory course on composites for undergraduates majoring in materials science, aerospace, mechanical, or civil engineering, rather than as a reference book or textbook for graduate students in mechanics.

The first chapter is a very general introduction. Chapter 2 covers the strength, failure modes, and thermal expansion of unidirectional composites. Chapter 3 is devoted entirely to short-fiber composites, which is believed to be unique to this book. This topic is especially timely due to the current strong interest of the automotive industry in this kind of composite, due to its potential for large-volume, low-cost production. Chapter 4 treats the elastic stiffness of a single orthotropic layer and its behavior under in-plane biaxial loading. Chapter 5 is concerned with the small-deflection, linearly elastic behavior of a thin laminate, based on the Kirchhoff hypothesis.

Chapter 6 is a *pot pourri:* laminated behavior after first-ply failure, free-edge effects, fracture mechanics (including the recently proposed Whitney-Nuismer criteria), and an elementary treatment of the design of adhesive and mechanical joints. Chapter 7 is a very extensive treatment of the critically important topic of material damage due to fatigue, impact, and environmental interaction. In Chapter 8 is presented what is believed to be the first treatment in a textbook (as opposed to a reference book) of the usually neglected, yet truly important, topic of experimental characterization.

The book is both well written and well illustrated. It is especially gratifying to see some of the failure modes introduced by means of actual microphotographs, supplemented by the usual schematic diagrams and mathematical analyses. Example problems suitable for individual attack or classroom assignment are interspersed throughout the book. For persons with less background in applied mathematics and advanced mechanics, there are Appendices on matrices and tensors and on the theory of elasticity.

This book is highly recommended as an introductory textbook on the analysis and prediction of performance of composites. It is especially suitable for those persons with only an elementary background in solid mechanics. However, by the same token it may not contain much information of a reference nature for the experienced researcher in the field. Those interested in the structural analysis of composite-material plates must still turn to the aforementioned book by Jones or to a more recent book by Richard M. Christensen (*Mechanics of Composite Materials,* John Wiley & Sons, Inc., New York, 1979).

Similarity, Self-Similarity and Intermediate Asymptotics. By G. I. Barenblatt. Plenum Publishing Corp., New York. 1979. Pages xvii–218. Price $35.

REVIEWED BY J. D. COLE[2]

Have you ever wondered why some authors can write down similarity forms for solutions (to p.d.e's say), based on simple dimensional considerations, others have to struggle to find the right form, to use deep analysis to uncover the critical exponents. This question is the starting point of the study by Dr. Barenblatt in a book which is an excellent translation from the earlier Russian edition.

In a series of short chapters the author develops a general classification for self-similar solutions illustrating his points by means of concrete examples, the only practical way here. The logical thread is the following:

The basic concepts of dimensional analysis (Π-theorem) are carefully presented first and used throughout. The examples of fundamental solution of the one-dimensional heat equation, and the propagation of a strong blast wave due to a point explosion are given as examples where pure dimensional analysis works to give self-similar solutions. Self-similarity is defined by $u(r, t) = u_0(t)\, f\,(r/r_0(t))$. The idea that these solutions are intermediate asymptotics valid after some time for a finite source, but for not too long or far (due to boundaries or weak shocks) is explained next. It is pointed out that the limit from the general solution (nonself-similar) to intermediate asymptotic (self-similar) is, more often than not, not uniform. This means that pure dimensional analysis does not suffice to characterize the self-similar solution. Examples for this are one-dimensional heat flow with diffusivity κ if $\partial u/\partial t > 0$, κ_1 if $\partial u/\partial t < 0$, or the point explosion with energy release at the shock front. In the first case the self-similar solution can no longer be interpreted as that due to a point source Q but rather Ql^α = constant; l = characteristic length of initial distribution, α = exponent found from a nonlinear eigenvalue problem and

$$u = \frac{Ql^\alpha}{(\kappa t)^{1+\alpha/2}}\, f\left(\frac{x}{\sqrt{\kappa t}}; \frac{\kappa_1}{\kappa}\right)$$

Self-similar solutions are classified as follows: the first kind—passage

---

[1] Benjamin H. Perkinson Professor of Engineering, School of Aerospace, Mechanical and Nuclear Engineering, The University of Oklahoma, Norman, Okla. 73069. Mem. ASME.

[2] Professor, Department of Mechanics and Structures, University of California, Los Angeles, Los Angeles, Calif. 90024.

to the limit (as the crucial $\Pi \rightarrow 0$) yields complete self-similarity and dimensional analysis works; the second kind—the limit is irregular, the critical exponent must be found from a nonlinear eigenvalue problem and the scale of the solution is unknown from similarity reasoning alone. Progressive waves $V = V(x - \lambda t + c)$ are connected to self-similar solutions by, $V = \log u$, $x = \log \xi$, $t = \log \tau$, and solutions of the first and second kind also exist. Self-similarity is identical with invariance for solutions under the affine group. It is next shown how to widen the concept of stability to apply to self-similar solutions. The example of Sternberg and Koiter of the elastic stress in a plane wedge angle (2α) is used to illustrate transition from solutions of the first kind to second kind at a critical parameter value. ($\alpha = \alpha_*$). The final chapters deal with similarity and turbulence, and are quite different since there are really no basic equations.

A criticism is that some of the problems seem physically artificial; in pratical cases it is very often easy to tell if the similarity is complete or incomplete. For problems nonlinear in highest order it is clear that point singularities characterized by delta functions are suspect. The reviewer would have liked to see discussion of more general similarity solutions $u = u_0(t) f(\xi)$, $\xi = \xi(x, t)$, based on group theory, and the connection with the ideas presented here.

In summary the book is a unique and very useful contribution to the literature of similarity. It is to be recommened as partial text for a graduate course on dimensions and similarity. The book is self-contained, the writing is clear, and it is a good introduction to the extensive Russian literature. Applied scientists in various fields would also benefit from reading this book and making connections with their own work.

Dislocations in Solids: Moving Dislocations. Vol. 3. Edited by F. R. N. Nabarro. North-Holland Publishing Co., 1980. Pages 353. Price $61.

REVIEWED BY T. MURA[3]

This is the third of five volumes devoted to the behavior of dislocations and their influence on the properties of solids. It contains four review papers concerned with the effects of moving dislocations. The author, title of paper, and summary of contents of each of these papers are listed as follows:

J. Weertman and J. R. Weertman, "Moving Dislocations," pp. 1–59. Moving dislocations that are straight and remain straight during their motion are treated. The velocity of a dislocation may be subsonic, transonic, or supersonic. They show the basic equation of motion, its solution, the associated energy calculation, and the force on the dislocation in each case. The stress field of a screw dislocation is contracted in the direction of motion. This distortion is analogous to the contraction and expansion of the electric field surrounding a moving electron.

The interaction between two moving dislocations, the dislocation mass, smeared-out dislocation (continuous distribution of dislocations), and dislocations in a discrete crystal lattice are also discussed. Several models for the stress-displacement relation on slip planes are discussed for the moving smeared-out dislocation.

G. Schöck, "Thermodynamics and Thermal Activation of Dislocations," pp. 64–163. This chapter reviews the thermodynamic properties of dislocations in crystalline solids and the various problems of thermal activation involving dislocations.

The quantity of interest to describe solids with defects under isothermal conditions is the Gibbs free energy of a body. The free energy is minimum for the equilibrium state.

The free energy is calculated for a separation of two partial dislocations, for an evaluation of volume change due to a dislocation, an elastic entropy of a dislocation, a configuration entropy of a dislocation, etc.

The movement of dislocation through a crystal lattice is controlled by thermally activated process. Various theories of thermal activation are reviewed: the transition-state theory, dynamic theory, diffusion theory, and quantum-mechanical theories.

When dislocations move in their glide planes they will often find randomly positioned localized obstacles which can only be overcome with the aid of thermal activation. The author reviews quite extensively these localized dispersed obstacles since he sees considerable confusion in existing literature about the thermodynamic interpretation and the connection between the theoretical and the experimental parameters.

J. W. Christian and A. G. Crocker, "Dislocations and Lattice Transformations," pp. 165–249. The main topics discussed in this chapter are the dislocation description of coherent or semicoherent grain or interphase boundaries, and the ways in which lattice dislocations interact with these boundaries. Fully coherent boundaries arise in twinning and in a few martensitic transformations. Semicoherent boundaries include low-angle grain boundaries and many martensitic boundaries. The first part of the chapter describes the mathematical treatment of finding an affine transformation which will carry one set of lattice points into another. The concept of a fully coherent interface then requires that one plane be invariant during this deformation, and the conditions for this are examined. When a coherent interface is geometrically impossible, the misfit at a planar interface may be described formally in terms of dislocations.

The last main topic to be considered concerns the generation and multiplication of twinning and transformation dislocations. A single partial dislocation moving across a glide plane leaves a stacking fault in its wake. A group of partial dislocations moving across adjacent parallel glide planes may convert the crystal into its twin, or may cause a phase transition.

J. C. Savage, "Dislocations in Seismology," pp. 251–339. This chapter shows how the methods of dislocation theory may be applied on a large scale (Burgers vectors of the order of a meter) to the analysis of earthquakes and to problems of plate tectonics. According to the author, however, at the present time the usefulness of dislocation theory in seismology is restricted by the absence of detailed knowledge of either the tectonic stress or the fault plane resistance and by the absence of detailed observations of deformation preceding, accompanying, and following an earthquake.

The first part of the chapter introduces the terminology used to describe faulting and outlines current thinking on how faulting occurs. The faulting problem may be approached either by prescribing the distribution of dislocations and calculating the consequent stress distribution or by prescribing both the tectonic stress and the slip law on the fault and calculating the dislocation distribution as done by J. Weertman. Weertman has suggested a slip law which may be important in priming a fault for catastrophic failure. The author further introduces Burridge and Halliday's solution for the longitudinal faulting in a half space, three-dimensional models of faulting, and dynamic solutions.

Analysis of Mechanisms and Robot Manipulators. By Joseph Duffy. Halstead Press (John Wiley & Co.). 1980. Pages 419. Price $114.95.

REVIEWED BY B. ROTH[4]

This book presents a unified method for the analysis of planar, spherical, and spatial linkwork. The main problem treated in the book

---

[3] Professor, The Technological Institute, Department of Civil Engineering, Northwestern University, Evanston, Ill. 60201.

[4] Professor, Department of Mechanical Engineering, Stanford University, Stanford, Calif. 94305.

is that of obtaining input-output equations for closed loop systems.

Duffy starts with a chapter on planar mechanisms and then goes on to develop the equations for spherical and spatial triangles that are basic to his methods.

The rest of the book is essentially a compilation of the spatial analysis work which Duffy and his students have published over the past 10 years. This material comprises the last 6 chapters of this 10 chapter book and runs for about 250 pages. The book is a good presentation of Duffy's techniques and is a consolidated source of results that were heretofore scattered in the literature. A special feature of the book is the inclusion of mechanical manipulators. These systems are analyzed by the same methods as the closed loop linkages.

This book is the most complete compilation of spatial analysis equations presently available. As such, it should be of interest to researchers and practicing engineers dealing with the kinematics, dynamics, and control of closed loop mechanisms and open loop chains of links.

ERRATUM

Erratum for "On the Influence of a Rigid Circular Inclusion on the Twisting and Shearing of a Shallow Spherical Shell," by E. Reissner, and published in the September, 1980, issue of the ASME JOURNAL OF APPLIED MECHANICS, Vol. 47, No. 3, pp. 586–588.

The factor "2" in equation (16) as well as the factor "8" in equation (17) should be replaced by factors "4."